

Gaetan Kerschen · M. R. W. Brake
Ludovic Renson *Editors*

Nonlinear Structures and Systems, Volume 1

Proceedings of the 37th IMAC, A Conference and
Exposition on Structural Dynamics 2019



Conference Proceedings of the Society for Experimental Mechanics Series

Series Editor

Kristin B. Zimmerman, Ph.D.
Society for Experimental Mechanics, Inc.,
Bethel, CT, USA

More information about this series at <http://www.springer.com/series/8922>

Gaetan Kerschen • M. R. W. Brake • Ludovic Renson
Editors

Nonlinear Structures and Systems, Volume 1

Proceedings of the 37th IMAC, A Conference and Exposition
on Structural Dynamics 2019

Editors

Gaetan Kerschen
Space Structures & Systems Lab., Bldg B52/3
University of Liège, Space
Liège, Belgium

M. R. W. Brake
Rice University
Houston, TX, USA

Ludovic Renson
University of Bristol
Bristol, UK

ISSN 2191-5644 ISSN 2191-5652 (electronic)
Conference Proceedings of the Society for Experimental Mechanics Series
ISBN 978-3-030-12390-1 ISBN 978-3-030-12391-8 (eBook)
<https://doi.org/10.1007/978-3-030-12391-8>

© Society for Experimental Mechanics, Inc. 2020

This work is subject to copyright. All rights are reserved by the Publisher, whether the whole or part of the material is concerned, specifically the rights of translation, reprinting, reuse of illustrations, recitation, broadcasting, reproduction on microfilms or in any other physical way, and transmission or information storage and retrieval, electronic adaptation, computer software, or by similar or dissimilar methodology now known or hereafter developed.

The use of general descriptive names, registered names, trademarks, service marks, etc. in this publication does not imply, even in the absence of a specific statement, that such names are exempt from the relevant protective laws and regulations and therefore free for general use.

The publisher, the authors, and the editors are safe to assume that the advice and information in this book are believed to be true and accurate at the date of publication. Neither the publisher nor the authors or the editors give a warranty, express or implied, with respect to the material contained herein or for any errors or omissions that may have been made. The publisher remains neutral with regard to jurisdictional claims in published maps and institutional affiliations.

This Springer imprint is published by the registered company Springer Nature Switzerland AG.
The registered company address is: Gewerbestrasse 11, 6330 Cham, Switzerland

Preface

Nonlinear Structures and Systems represents one of eight volumes of technical papers presented at the 37th IMAC, A Conference and Exposition on Structural Dynamics, organized by the Society for Experimental Mechanics, and held in Orlando, Florida, on January 28–31, 2019. The full proceedings also include volumes on Dynamics of Civil Structures; Model Validation and Uncertainty Quantification; Dynamics of Coupled Structures; Special Topics in Structural Dynamics & Experimental Techniques; Rotating Machinery, Optical Methods & Scanning LDV Methods; Sensors and Instrumentation, Aircraft/Aerospace, Energy Harvesting & Dynamic Environments Testing; and Topics in Modal Analysis & Testing.

Each collection presents early findings from experimental and computational investigations on an important area within structural dynamics. Nonlinearity is one of these areas.

The vast majority of real engineering structures behave nonlinearly. Therefore, it is necessary to include nonlinear effects in all the steps of the engineering design: in the experimental analysis tools (so that the nonlinear parameters can be correctly identified) and in the mathematical and numerical models of the structure (in order to run accurate simulations). In so doing, it will be possible to create a model representative of the reality which, once validated, can be used for better predictions.

Several nonlinear papers address theoretical and numerical aspects of nonlinear dynamics (covering rigorous theoretical formulations and robust computational algorithms) as well as experimental techniques and analysis methods. There are also papers dedicated to nonlinearity in practice where real-life examples of nonlinear structures are discussed.

The organizers would like to thank the authors, presenters, session organizers, and session chairs for their participation in this track.

Liège, Belgium
Houston, TX
Bristol, UK

G. Kerschen
M. R. W. Brake
Ludovic Renson

Contents

1	Nonsmooth Modal Analysis of a Non-internally Resonant Finite Bar Subject to a Unilateral Contact Constraint	1
	Carlos Yoong and Mathias Legrand	
2	A New Iwan/Palmov Implementation for Fast Simulation and System Identification	11
	Drithi Shetty and Matthew S. Allen	
3	Analysis of Transient Vibrations for Estimating Bolted Joint Tightness	21
	M. Brøns, J. J. Thomsen, S. M. Sah, D. Tcherniak, and A. Fidlin	
4	Spider Configurations for Models with Discrete Iwan Elements	25
	Aabhas Singh, Mitchell Wall, Matthew S. Allen, and Robert J. Kuether	
5	Predicting S4 Beam Joint Nonlinearity Using Quasi-Static Modal Analysis	39
	Mitchell Wall, Matthew S. Allen, and Iman Zare	
6	The Best Linear Approximation of MIMO Systems: First Results on Simplified Nonlinearity Assessment ..	53
	Péter Zoltán Csurscia, Bart Peeters, and Johan Schoukens	
7	Forced Response of Nonlinear Systems Under Combined Harmonic and Random Excitation	65
	Alwin Förster, Lars Panning-von Scheidt, and Jörg Wallaschek	
8	Gerrymandering for Interfaces: Modeling the Mechanics of Jointed Structures	81
	T. Dreher, Nidish Narayanaa Balaji, J. Groß, Matthew R. W. Brake, and M. Krack	
9	An Analysis of the Gimballed Horizontal Pendulum System for Use as a Rotary Vibrational Energy Harvester	87
	D. Sequeira, J. Little, and B. P. Mann	
10	On the Dynamic Response of Flow-Induced Vibration of Nonlinear Structures	91
	Banafsheh Seyed-Aghazadeh, Hamed Samandari, and Reza Abrisham Baf	
11	Potential and Limitation of a Nonlinear Modal Testing Method for Friction-Damped Systems	95
	Maren Scheel, Tobias Schulz, and Malte Krack	
12	Dynamics of a Magnetically Excited Rotational System	99
	Xue-She Wang and Brian P. Mann	
13	Experimental Nonlinear Dynamics of a Post-buckled Composite Laminate Plate	103
	John I. Ferguson, Stephen M. Spottswood, David A. Ehrhardt, Ricardo A. Perez, Matthew P. Snyder, and Matthew B. Obenchain	
14	Simulation of a Self-Resonant Beam-Slider-System Considering Geometric Nonlinearities	115
	Florian Müller and Malte Krack	
15	Reinforcement Learning for Active Damping of Harmonically Excited Pendulum with Highly Nonlinear Actuator	119
	James D. Turner, Levi H. Manring, and Brian P. Mann	

16 Investigation of Nonlinear Dynamic Phenomena Applying Real-Time Hybrid Simulation	125
Markus J. Hochrainer and Anton M. Puhwein	
17 Experimental and Numerical Aeroelastic Analysis of Airfoil-Aileron System with Nonlinear Energy Sink	133
Claudia Fernandez-Escudero, Miguel Gagnon, Eric Laurendeau, Sebastien Prothin, Annie Ross, and Guilhem Michon	
18 On the Modal Surrogacy of Joint Parameter Estimates in Bolted Joints	137
Nidish Narayanaa Balaji and Matthew R. W. Brake	
19 Vehicle Escape Dynamics on an Arbitrarily Curved Surface	141
Levi H. Manring and Brian P. Mann	
20 Nonlinear Dynamical Analysis for Coupled Fluid-Structure Systems	151
Q. Akkaoui, E. Capiez-Lernout, C. Soize, and R. Ohayon	
21 Experimental Nonlinear Vibration Analysis of a Shrouded Bladed Disk Model on a Rotating Test Rig	155
Ferhat Kaptan, Lars Panning-von Scheidt, and Jörg Wallaschek	
22 The Measurement of Tangential Contact Stiffness for Nonlinear Dynamic Analysis	165
C. W. Schwingshackl and D. Nowell	
23 Investigating Nonlinearity in a Bolted Structure Using Force Appropriation Techniques	169
Benjamin R. Pacini, Daniel R. Roettgen, and Daniel P. Rohe	
24 Techniques for Nonlinear Identification and Maximizing Modal Response	173
D. Roettgen, B. R. Pacini, and R. Mayes	
25 Influences of Modal Coupling on Experimentally Extracted Nonlinear Modal Models	189
Benjamin J. Moldenhauer, Aabhas Singh, Phil Thoenen, Daniel R. Roettgen, Benjamin R. Pacini, Robert J. Kuether, and Matthew S. Allen	
26 Dynamic Response of a Curved Plate Subjected to a Moving Local Heat Gradient	205
David A. Ehrhardt, B. T. Gockel, and T. J. Bebermiss	
27 A Test-Case on Continuation Methods for Bladed-Disk Vibration with Contact and Friction	209
Z. Saeed, G. Jenovencio, S. Arul, J. Blahoš, A. Sudhakar, L. Pesaresi, J. Yuan, F. El Haddad, H. Hetzler, and L. Salles	
28 Dynamics of Geometrically-Nonlinear Beam Structures, Part 1: Numerical Modeling	213
D. Anastasio, J. Dietrich, J. P. Noël, G. Kerschen, S. Marchesiello, J. Häfele, C. G. Gebhardt, and R. Rolfes	
29 Dynamics of Geometrically-Nonlinear Beam Structures, Part 2: Experimental Analysis	217
D. Anastasio, J. Dietrich, J. P. Noël, G. Kerschen, S. Marchesiello, J. Häfele, C. G. Gebhardt, and R. Rolfes	
30 Constructing Backbone Curves from Free-Decay Vibrations Data in Multi-Degrees of Freedom Oscillatory Systems	221
Mattia Cenedese and George Haller	
31 Nonlinear 3D Modeling and Vibration Analysis of Horizontal Drum Type Washing Machines	225
Cem Baykal, Ender Cigeroglu, and Yigit Yazicioglu	
32 Comparison of Linear and Nonlinear Modal Reduction Approaches	229
Erhan Ferhatoglu, Tobias Dreher, Ender Cigeroglu, Malte Krack, and H. Nevzat Özgüven	
33 Reduced Order Modeling of Bolted Joints in Frequency Domain	235
Gokhan Karapistik and Ender Cigeroglu	
34 Comparison of ANM and Predictor-Corrector Method to Continue Solutions of Harmonic Balance Equations	239
Lukas Woiwode, Nidish Narayanaa Balaji, Jonas Kappauf, Fabia Tubita, Louis Guillot, Christophe Vergez, Bruno Cochelin, Aurélien Grolet, and Malte Krack	

35	A Priori Methods to Assess the Strength of Nonlinearities for Design Applications	243
	E. Rojas, S. Punla-Green, C. Broadman, Matthew R. W. Brake, B. R. Pacini, R. C. Flicek, D. D. Quinn, C. W. Schwingshackl, and E. Dodgen	
36	Predictive Modeling of Bolted Assemblies with Surface Irregularities	247
	Matthew Fronk, Gabriela Guerra, Matthew Southwick, Robert J. Kuether, Adam Brink, Paolo Tiso, and Dane Quinn	
37	A Novel Computational Method to Calculate Nonlinear Normal Modes of Complex Structures	259
	Hamed Samandari and Ender Cigeroglu	
38	Experimental-Numerical Comparison of Contact Nonlinear Dynamics Through Multi-level Linear Mode Shapes	263
	Elvio Bonisoli, Domenico Lisitano, and Christian Conigliaro	
39	Dynamic Behavior and Output Charge Analysis of a Bistable Clamped-Ends Energy Harvester	273
	Masoud Derakhshani and Thomas A. Berfield	



Chapter 1

Nonsmooth Modal Analysis of a Non-internally Resonant Finite Bar Subject to a Unilateral Contact Constraint

Carlos Yoong and Mathias Legrand

Abstract The present contribution describes a numerical technique devoted to the nonsmooth modal analysis (natural frequencies and mode shapes) of a non-internally resonant elastic bar of length L subject to a Robin condition at $x = 0$ and a frictionless unilateral contact condition at $x = L$. When contact is ignored, the system of interest exhibits non-commensurate linear natural frequencies, which is a critical feature in this study. The *nonsmooth modes of vibration* are defined as one-parameter continuous families of nonsmooth periodic orbits satisfying the local equation together with the boundary conditions. In order to find a few of the above families, the unknown displacement is first expressed using the well-known d'Alembert's solution incorporating the Robin boundary condition at $x = 0$. The unilateral contact constraint at $x = L$ is reduced to a conditional switch between Neumann (open gap) and Dirichlet (closed gap) boundary conditions. Finally, T -periodicity is enforced. It is also assumed that only one contact switch occurs every period. The above system of equations is numerically solved for through a simultaneous discretization of the space and time domains, which yields a set of equations and inequations in terms of discrete displacements and velocities. The proposed approach is non-dispersive, non-dissipative and accurately captures the propagation of waves with discontinuous fronts, which is essential for the computation of periodic motions in this study. Results indicate that in contrast to its linear counterpart (bar without contact constraints) where modal motions are sinusoidal functions "uncoupled" in space and time, the system of interest features nonsmooth periodic displacements that are intricate *piecewise* sinusoidal functions in space and time. Moreover, the corresponding frequency-energy "nonlinear" spectrum shows backbone curves of the hardening type. It is also shown that nonsmooth modal analysis is capable of efficiently predicting vibratory resonances when the system is periodically forced. The pre-stressed and initially grazing bar configurations are also briefly discussed.

Keywords Nonsmooth systems · Modal analysis · Internal resonance · Unilateral contact constraints · Wave equation

1.1 Introduction

The concept of linear modes (natural frequencies and mode shapes) is a widely studied subject in the field of structural dynamics [7]. A possible extension of this notion to nonlinear conservative systems sees a mode of vibration as a one-parameter continuous family of periodic orbits displaying similar qualitative features [5]. In the phase space, nonlinear modes emerge as invariant surfaces of periodic trajectories, referred to as *invariant manifolds* [10], where invariant implies that the motion initiated on the manifold stays on it as time unfolds. To some extent, nonlinear modal analysis can be employed for predicting vibratory resonances, computing the nonlinear spectra of vibration or performing model-order reduction. Techniques traditionally employed for nonlinear modal analysis require a certain degree of smoothness in the nonlinearities [11] and thus fail for systems with *nonsmooth nonlinearities* such as unilateral contact constraints. Certainly, an accurate characterization of the vibratory response of these systems is essential to achieving enhanced and safer engineering applications [12]. Modal analysis of nonsmooth mechanical systems, also called *nonsmooth modal analysis*, has been recently proposed for a finite elastic bar of length L subject to a Dirichlet boundary condition at $x = 0$ and a unilateral contact constraint at $x = L$ [13]. This system satisfies a *complete internal resonance* condition, i.e. all linear natural frequencies are commensurate with the first one, which has drastic consequences on the nonlinear modal response. Despite the simplicity of the system, the computed *nonsmooth modes* (NSMs) indicate highly intricate vibratory behaviour. Corresponding periodic displacements were observed to be unseparated piecewise linear functions of space and time, as opposed to their linear counterparts which are sinusoidal functions separated in space and time. Moreover, for certain NSMs such internal resonance

C. Yoong (✉) · M. Legrand
Department of Mechanical Engineering, McGill University, Montréal, QC, Canada
e-mail: carlos.yoong@mail.mcgill.ca

generates a discontinuity between the linear and nonlinear portions of the invariant manifold. To further explore the nonlinear dynamics of this one-dimensional contact problem, a non-internally resonant configuration is investigated in the present work. The complete internal resonance condition is annihilated by changing the boundary condition (BC) at $x = 0$ from Dirichlet type $u(0, t) = 0$ to a Robin type $\partial_x u(0, t) - \alpha u(0, t) = 0$ which reflects that the elastic bar is now connected to a rigid support through a simple linear spring.¹ Analytical derivations are first proposed to facilitate the construction of the sought NSMs. Then, a numerical scheme based on the simultaneous discretization of the space and time domains is employed and the nonsmooth modes of vibration are constructed.

1.2 Non-internally Resonant Elastic Bar

The system of interest is a homogeneous elastic bar of length $L > 0$ and constant cross-sectional area $S > 0$ subject to a conservative unilateral constraint at its right end. Its left end is connected to a rigid support through a spring of stiffness $\kappa > 0$, as depicted in Fig. 1.1. The displacement, velocity, strain and stress fields are denoted by $u(x, t)$, $v(x, t)$, $\epsilon(x, t)$ and $\sigma(x, t)$ respectively where x is the coordinate of a point of the bar in the initial configuration and t denotes time. Young's modulus is denoted by $E > 0$ and $\rho > 0$ stands for the mass per unit volume, which are both, by assumption, space and time independent. Hence, the propagation speed of any longitudinal wave is $\sqrt{E/\rho}$. In the framework of linear elasticity, the stresses read $\sigma = E\epsilon$, where $\epsilon = \partial_x u$ should be infinitesimal and satisfy $|\partial_x u| < 1$ [1, p. 5]. The unilateral contact force $r(t)$ is related to the stresses by $\sigma(L, t) = E\partial_x u(L, t) = r(t)/S$. Further, the signed distance between the right extremity of the bar and the rigid obstacle, termed *gap function*, is defined as $g(u(L, t)) = g_0 - u(L, t)$, where g_0 is the signed distance between the unrestricted resting configuration and the obstacle: it is strictly negative in the pre-stressed configuration, for instance. Unless stated otherwise, there is no external excitation on the system. The full formulation reads:

$$\text{Local equation} \quad \partial_t^2 u(x, t) - c^2 \partial_{xx}^2 u(x, t) = 0, \quad \forall x \in]0; L[, \quad \forall t > 0, \quad (1.1)$$

$$\text{Robin BC} \quad \partial_x u(0, t) - \alpha u(0, t) = 0, \quad \forall t > 0, \quad (1.2)$$

$$\text{Signorini BC} \quad g(u(L, t)) \geq 0, \quad r(t) \leq 0, \quad r(t)g(u(L, t)) = 0, \quad \forall t > 0, \quad (1.3)$$

$$\text{Initial conditions} \quad u(x, 0) = u_0(x), \quad v(x, 0) = v_0(x), \quad \forall x \in]0; L[. \quad (1.4)$$

where $\alpha = \kappa/(ES)$. This formulation possesses a unique solution which conserves the total energy [9]. It is worth noting that the local equation (1.1) is the well-known *wave equation* (a hyperbolic partial differential equation) defined on a one-dimensional finite domain. The natural frequencies ω_k and Ω_k of the underlying linear system are solutions to the transcendental equations:

$$\text{spring-free BCs} \quad \omega_k - \alpha c \cot(\omega_k L/c) = 0, \quad k \in \mathbb{N}_{>0}, \quad (1.5)$$

$$\text{spring-fixed BCs} \quad \Omega_k + \alpha c \tan(\Omega_k L/c) = 0, \quad k \in \mathbb{N}_{>0}. \quad (1.6)$$

The corresponding natural periods are $\mathcal{T}_k = 2\pi/\omega_k$ and $\mathcal{P}_k = 2\pi/\Omega_k$. In both configurations, the natural frequencies are incommensurate, in the sense that ω_k and Ω_k for $k = 2, 3, \dots, \infty$ are not multiples of ω_1 nor Ω_1 , respectively [8, p. 245]. Accordingly, the complete internal resonance condition emerging when the bar is clamped at $x = 0$ no longer holds [13].

Non-trivial solutions of the unilateral contact problem described by Eqs. (1.1)–(1.4) are successions of free phases (open gap) and contact phases (closed gap) [2]. Hence, these solutions can be perceived as the combination of motions satisfying the wave equation together with a switching boundary condition at $x = L$ between $\partial_x u(L, \cdot) = 0$ when the gap is open, referred

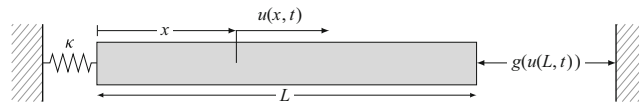


Fig. 1.1 One-dimensional finite elastic bar attached to a spring at its left extremity and subject to unilateral contact constraint on its right tip

¹In this document, operators $\partial_\xi (\bullet)$ and $\partial_{\xi\xi}^2 (\bullet)$ stand for the first and second derivatives of (\bullet) with respect to the argument ξ .

to as “spring–free BCs” (or equivalently Robin–Neumann BCs), and prescribed displacement $u(L, \cdot) = g_0$ which implies $v(L, \cdot) = 0$ when the gap is closed, named “spring–fixed BCs” (or equivalently Robin–Dirichlet BCs). The nonlinearity in the formulation arises in the dependence of the solution to the unknown switching time. To further elaborate on this statement, consider the general solution to the local equation (1.1) comprising the superposition of forward h and backward f travelling waves defined on the real line \mathbb{R} [1, p. 91]

$$u(x, t) = f(ct + x) + h(ct - x), \quad (1.7)$$

At $x = 0$, the effect of the attached spring on the reflection of an incident backward wave f is computed by inserting the general solution (1.7) in (1.2), yielding $(\partial_\xi f(\xi) - \partial_\xi h(\xi)) = \alpha(f(\xi) + h(\xi))$, $\forall \xi \in \mathbb{R}$, which in turns leads to the identity

$$h(\xi) = f(\xi) + e^{-\alpha\xi} \left(\beta - 2\alpha \int_0^\xi e^{\alpha s} f(s) ds \right), \quad \forall \xi \in \mathbb{R} \quad (1.8)$$

Without going into the details, it is straightforward to check that the BC at $x = L$ imply that $\beta = 0$. Incorporating (1.8) in (1.7) leads to an integral expression of the displacement in terms of f only

$$u(x, t) = f(ct + x) + f(ct - x) - 2\alpha e^{\alpha(ct-x)} \int_0^{ct-x} e^{\alpha s} f(s) ds, \quad (1.9)$$

which incorporates the reflection mechanism of the travelling waves at $x = 0$. At $x = L$, the boundary condition successively switches from Neumann to Dirichlet and vice-versa. The corresponding reflections require additional considerations elaborated later in the text.

Let us first denote by $f|_{[a;b]}$ the set of all ordered pairs $(\xi, f(\xi))$, $\forall \xi \in [a; b]$, which is also referred to as the graph of function f over the interval $[a; b]$. Provided that $f|_{[0;L]}$ is known, the boundary condition at $x = L$ is utilized to specify $f(\xi)$ over the remaining portions of the real axis \mathbb{R} , that is for $\xi \in]-\infty; 0[$ and $\xi \in]L; \infty[$. During free phases (open gap), a homogeneous Neumann BC is active at $x = L$, that is $\partial_x u(L, \cdot) = 0$. Inserting Eq. (1.7) into the latter yields $\partial_\xi f(\xi + 2L) = \partial_\xi h(\xi)$, which in turn results in $f(\xi + 2L) - h(\xi) = f(2L) - h(0)$. Incorporating the influence of the attached spring via Eq. (1.8), the latter is re-formulated in terms of the backward wave f only, that is

$$f(\xi + 2L) - f(\xi) + 2\alpha e^{-\alpha\xi} \int_0^\xi e^{\alpha s} f(s) ds = f(2L) - f(0). \quad (1.10)$$

During contact phases (closed gap), the right end of the bar satisfies a non-homogeneous Dirichlet BC, corresponding to a prescribed displacement at $x = L$, which reads $u(L, \cdot) = g_0$. Again, combining this boundary condition and the general solution (1.7), the interaction of forward and backward travelling waves shall satisfy $f(\xi + 2L) + h(\xi) = g_0$, which can also be expressed in terms of f only as follows:

$$f(\xi + 2L) + f(\xi) - 2\alpha e^{-\alpha\xi} \int_0^\xi e^{\alpha s} f(s) ds = g_0, \quad (1.11)$$

Accordingly, if f is known in any region of length $2L$, it can be expanded over the real axis, via (1.10) for a free phase (open gap) and (1.11) for a contact phase (closed gap). It is then employed in (1.9) to calculate the corresponding displacement.

During each of the above phases, $f|_{[0;2L]}$ is obtained from the associated initial and boundary conditions [4, p. 80]. For the free phase, knowing that the displacement and velocity waves reflect at a free BC without changing signs, $f|_{[0;2L]}$ satisfies

$$f|_{[0;2L]} = \begin{cases} \frac{u_0(\xi)}{2} + \frac{1}{2c} \int_0^\xi v_0(s) ds & \xi \in [0; L], \\ \frac{u_0(2L - \xi)}{2} + \frac{1}{2c} \int_0^L v_0(s) ds + \frac{1}{2c} \int_L^\xi v_0(2L - s) ds & \xi \in]L; 2L]. \end{cases} \quad (1.12)$$

However, for the contact phase, knowing that $u_0(L) = g_0$ and that the displacement and velocity waves reflect with opposite sign, $f|_{[0;2L]}$ shall satisfy

$$f|_{[0;2L]} = \begin{cases} \frac{u_0(\xi)}{2} + \frac{1}{2c} \int_0^\xi v_0(s) ds & \xi \in [0; L], \\ g_0 - \frac{u_0(2L - \xi)}{2} + \frac{1}{2c} \int_0^L v_0(s) ds - \frac{1}{2c} \int_L^\xi v_0(2L - s) ds & \xi \in]L; 2L], \end{cases} \quad (1.13)$$

Consequently, f can be completely defined over \mathbb{R} for every phase. To summarize, the displacement of the elastic bar with Robin BC on the left end is obtained through Eq. (1.9) provided that f is defined everywhere on the real axis. The successive switches in boundary conditions at $x = L$, reflecting the unilateral contact constraint, are incorporated through appropriate extensions: Eq. (1.10) for the free phase or Eq. (1.11) for contact phase. The following section is concerned with analytical derivations for the computation of periodic solutions by employing the expressions (1.9)–(1.11).

1.3 Periodic Solutions and Nonsmooth Modal Analysis

Nonsmooth modes of vibration of the spring–bar system depicted in Fig. 1.1 are defined as continuous families of periodic solutions satisfying the formulation (1.1)–(1.4) together with periodicity conditions in displacement and velocity: $\exists T > 0$ such that $u(x, t + T) = u(x, t)$ and $v(x, t + T) = v(x, t)$, $\forall x \in [0; L]$ and $\forall t > 0$. Finding such solutions translates into finding corresponding initial conditions u_0 and v_0 and period T which generate periodic motions. Without loss of generality, it is assumed that within one period, over the interval $t \in [0; T]$, the initial time segment is a free phase that initiates at $t = 0^+$ and the final time segment is a contact phase that ends at $t = T^-$ and switches back to the initial free phase state at $t = T^+$. In general, various successions of free and contact phases might arise within one period. Knowing that the motion of the bar can be uniquely defined by a single function f , the targeted trajectory is then an unknown periodic sequence of functions u in the form (1.9) where f switches between (1.10) and (1.11).

Let us consider the simplest combination of one free phase and one contact phase of duration t_f and $t_c = T - t_f$, respectively. When the gap is open, displacement and velocity satisfy the following equalities $\forall x \in [0; L]$ and $\forall t \in [0; t_f]$:

$$u_1(x, t) = f_0(ct + x) + f_0(ct - x) - 2\alpha e^{\alpha(x-ct)} \int_0^{ct-x} e^{\alpha s} f_0(s) ds, \quad (1.14a)$$

$$\frac{1}{c} v_1(x, t) = \partial_t f_0(ct + x) + \partial_t f_0(ct - x) - 2\alpha f_0(ct - x) + 2\alpha^2 e^{\alpha(x-ct)} \int_0^{ct-x} e^{\alpha s} f_0(s) ds, \quad (1.14b)$$

where $f_0|_{[0;2L]}$, calculated via Eq. (1.12) with the initial conditions u_0 and v_0 , is then expanded throughout the real axis \mathbb{R} via (1.10). During gap closure, the motion is described by the composite function $f_1(f_0(\cdot))$ corresponding to a boundary condition switch. This function arises by defining the graph $f_1|_{[0;2L]}$ with $u_1(\cdot, t_f)$ and $v_1(\cdot, t_f)$ as the “initial conditions” in Eq. (1.13) and then expanding it on \mathbb{R} via Eq. (1.11). During a contact phase, the displacement and velocity read $\forall x \in [0; L]$ and $\forall t \in]t_f; T]$

$$u_2(x, t) = f_1(c(t - t_f) + x) + f_1(c(t - t_f) - x) - 2\alpha e^{\alpha(x-c(t-t_f))} \int_0^{c(t-t_f)-x} e^{\alpha s} f_1(s) ds, \quad (1.15a)$$

$$\frac{1}{c} v_2(x, t) = \partial_t f_1(c(t - t_f) + x) + \partial_t f_1(c(t - t_f) - x) - 2\alpha f_1(c(t - t_f) - x) + 2\alpha^2 e^{\alpha(x-c(t-t_f))} \int_0^{c(t-t_f)-x} e^{\alpha s} f_1(s) ds. \quad (1.15b)$$

Accordingly, *admissible* T -periodic motions involving one lasting contact phase per period are described by functions $f_1 \circ f_0$ and f_0 that satisfy the following *periodicity condition*, arising from $u_0(x) = u_2(x, T)$ and $v_0(x) = v_2(x, T)$, $\forall x \in [0; L]$

$$u_0(x) = f_1(ct_c + x) + f_1(ct_c - x) - 2\alpha e^{\alpha(x-ct_c)} \int_0^{ct_c-x} e^{\alpha s} f_1(s) ds, \quad (1.16a)$$

$$\frac{1}{c} v_0(x) = \partial_t f_1(ct_c + x) + \partial_t f_1(ct_c - x) - 2\alpha f_1(ct_c - x) + 2\alpha^2 e^{\alpha(x-ct_c)} \int_0^{ct_c-x} e^{\alpha s} f_1(s) ds. \quad (1.16b)$$

together with the *admissibility conditions* reflecting Signorini’s conditions at $x = L$ in Eq. (1.3):

- the elastic bar shall not contact the obstacle during a free phase except at gap closure when $t = t_f$; grazing is permitted during free phase

$$g_0 - f_0(ct + L) - f_0(ct - L) + 2\alpha e^{\alpha(L-ct)} \int_0^{ct-L} e^{\alpha s} f_0(s) ds \geq 0, \quad \forall t \in [0; t_f], \quad (1.17a)$$

$$g_0 - f_0(ct_f + L) - f_0(ct_f - L) + 2\alpha e^{\alpha(L-ct_f)} \int_0^{ct_f-L} e^{\alpha s} f_0(s) ds = 0, \quad (1.17b)$$

- the contact force should be non-positive during gap closure until contact separation at $t = t_f + t_c = T$

$$\partial_x f_1(ct + L) - \partial_x f_1(ct - L) + 2\alpha f_1(ct - L) - 2\alpha^2 e^{\alpha(L-ct)} \int_0^{ct-L} e^{\alpha s} f_1(s) ds \leq 0, \quad \forall t \in [0; t_c], \quad (1.18a)$$

$$\partial_x f_1(ct_c + L) - \partial_x f_1(ct_c - L) + 2\alpha f_1(ct_c - L) - 2\alpha^2 e^{\alpha(L-ct_c)} \int_0^{ct_c-L} e^{\alpha s} f_1(s) ds = 0. \quad (1.18b)$$

From Eq. (1.16), the equality $c\partial_x u_0(x) + v_0(x) = c\partial_x u_2(x, T) + v_2(x, T)$ provides an additional relationship between f_0 and f_1 for potential periodic motions to exist: $f_1(ct_c + x) - f_1(ct_c) = f_0(x) - f_0(0), \forall x \in [0; L]$.

Finding solutions to Eqs. (1.16)–(1.18) is a noticeably challenging task. The complexity for solving such problems lies in the difficulty of defining a simple relationship between functions f_0 and f_1 incorporating the BC switching mechanism. Additionally, the effect of the spring, arising as a delay integral term in the displacement (1.9) further complicates the identification of admissible periodic motions.

1.4 Numerical Scheme

The main objective of the proposed numerical scheme is to simultaneously discretize the space and time domains of the above formulation in order to accurately mimic the propagation of discontinuous waves along the characteristics lines: $x \pm ct = \text{constant}$. The main limitation of the proposed technique is the fact that the *travelling-wave solution* shall be partially known (in the sense that identities such as Eqs. (1.16)–(1.18) can be derived) before discretization.

To compute families of periodic orbits, the space and time domains of the integral equations (1.16) are simultaneously discretized in order to approximate the initial conditions that generate a periodic motion. Space is divided into N intervals of identical length $\Delta x = x_{i+1} - x_i = L/N$ with $i = 0, 1, \dots, N$. Since travelling waves are required to propagate along the characteristic lines, the time-step shall satisfy $\Delta t = t_{n+1} - t_n = \Delta x/c$ for $n = 0, 1, \dots, n_T$, where n_T satisfies $n_T \Delta t = T$. To approximate f_1 in Eq. (1.16), the discretization of the real axis emerges from the discretized space-time coupling argument $x \pm ct$ of the travelling-wave solution, hence the discretized f_1 function is denoted as $f_{1j} \approx f_1(\xi_j)$ such that $\xi_j = x_i \pm ct_n$ where $j = i \pm n$ for $i = 0, 1, \dots, N$ and $n = 0, 1, \dots, n_T$. Similar notations also apply to f_0j . The discretization of the displacement and velocity during free phase produces $u_{1i}^{(n)} \approx u_1(x_i, t_n)$ and $v_{1i}^{(n)} \approx v_1(x_i, t_n)$ respectively, and in a similar fashion during contact phase for u_2 and v_2 . The discretized initial conditions read $u_{0i} \approx u_0(x_i)$ and $v_{0i} \approx v_0(x_i)$.

Since the duration of the free phase is $t_f = n_f \Delta t$ and the duration of the contact phase is $t_c = n_c \Delta t$, the approximations of $f_0|_{[0;2L]}$ and $f_1|_{[0;2L]}$ needed to approximately solve (1.16) are computed via a trapezoidal rule to compute the integrals:

- for a free phase via discretization of Eq. (1.12) with discrete initial conditions $u_{0i} \approx u_0(x_i)$ and $v_{0i} \approx v_0(x_i)$

$$f_{0j} = \begin{cases} \frac{u_{0j}}{2} + \frac{1}{4c} \sum_{i=0}^j \Delta x (v_{0i} + v_{0(i+1)}) & j = 0, 1, \dots, N, \\ a + \frac{u_{0(2N-j)}}{2} + \frac{1}{4c} \sum_{i=N+1}^j \Delta x (v_{0(2N-i)} + v_{0(2N-i+1)}) & j = N+2, N+3, \dots, 2N, \end{cases} \quad (1.19)$$

- for a contact phase via discretization of Eq. (1.13) with discrete “initial conditions” $u_{1i}^{(n_f)} \approx u_1(x_i, t_f)$ and $v_{1i}^{(n_f)} \approx v_1(x_i, t_f)$

$$f_{1j} = \begin{cases} \frac{u_{1j}^{(n_f)}}{2} + \frac{1}{4c} \sum_{i=0}^j \Delta x (v_{1i}^{(n_f)} + v_{1(i+1)}^{(n_f)}) & j = 0, 1, \dots, N, \\ b - \frac{u_{1(2N-j)}^{(n_f)}}{2} - \frac{1}{4c} \sum_{i=N+1}^j \Delta x (v_{1(2N-i)}^{(n_f)} + v_{1(2N-i+1)}^{(n_f)}) & j = N+2, N+3, \dots, 2N, \end{cases} \quad (1.20)$$

where $4ac = \sum_{i=0}^N \Delta x (v_{0i} + v_{0(i+1)})$ and $4bc = \sum_{i=0}^N \Delta x (v_{1i}^{(n_f)} + v_{1(i+1)}^{(n_f)}) + 4g_0c$. The above expressions (1.19) and (1.20) known for $j = 0, 1, \dots, 2N$ are then expanded on the real axis:

$$f_{0(j+2N)} - f_{0(j)} + \text{sgn}(j)\alpha e^{-\alpha j} \Delta x \sum_{k=0}^j (e^{\alpha \xi_k} f_{0(k)} + e^{\alpha \xi_{k+1}} f_{0(k+1)}) = f_{0(2N)} - f_{0(0)}, \quad (1.21)$$

$$f_{1(j+2N)} + f_{1(j)} + \text{sgn}(j)\alpha e^{-\alpha j} \Delta x \sum_{k=0}^j (e^{\alpha \xi_k} f_{1(k)} + e^{\alpha \xi_{k+1}} f_{1(k+1)}) = g_0, \quad (1.22)$$

where $\text{sgn}(\bullet)$ is the sign function. Since the period $T = t_f + t_c = n_T \Delta t$ is known, where $n_T = n_f + n_c$, the approximated displacement can be calculated for each phase as follows:

- free phase, via discretization of Eq. (1.14), for $i = 0, 1, \dots, N$ and $n = 0, 1, 2, \dots, n_f$

$$u_{1i}^{(n)} = f_{0(n+i)} + f_{0(n-i)} - \text{sgn}(n-i)\alpha e^{\alpha(x_i - ct_n)} \sum_{k=0}^{n-i} \Delta x (e^{\alpha \xi_k} f_{0(k)} + e^{\alpha \xi_{k+1}} f_{0(k+1)}), \quad (1.23)$$

- contact phase, via discretization of Eq. (1.15), for $i = 0, 1, \dots, N$ and $n = n_f + 1, n_f + 2, \dots, n_T$

$$u_{2i}^{(n)} = f_{1(n-n_f+i)} + f_{1(n-n_f-i)} - \text{sgn}(n-n_f-i)\alpha e^{\alpha(x_i - c(t_n - t_f))} \sum_{k=0}^{n-n_f-i} \Delta x (e^{\alpha \xi_k} f_{1(k)} + e^{\alpha \xi_{k+1}} f_{1(k+1)}). \quad (1.24)$$

The corresponding velocity is calculated through a numerical time-differentiation scheme, such as the forward Euler method $v_i^{(n)} = (u_i^{(n+1)} - u_i^{(n)})/\Delta t$. It is worth remarking that because f_{1j} in Eq. (1.24) is compounded with f_{0j} , and the latter is computed from discrete initial conditions, then all displacements points $u_{1i}^{(n)}$ and $u_{2i}^{(n)}$ can be expressed in terms of u_{0i} and v_{0i} .

The discretization of the periodicity condition (1.16) together with the unilateral contact condition yields a constrained system of linear equations written in terms of the discrete initial conditions u_{0i} and v_{0i} , free-phase time-steps n_f and contact-phase time-steps n_c :

$$\text{periodicity:} \quad u_{0i} - u_{2i}^{(n_f+n_c)} = 0 \text{ and } v_{0i} - v_{2i}^{(n_f+n_c)} = 0, \quad i = 0, 1, \dots, N \quad (1.25)$$

$$\text{impenetrability:} \quad g_0 - u_{1N}^{(n)} \geq 0, \quad n = 0, 2, \dots, n_f \quad (1.26)$$

$$\text{compressive contact:} \quad E \epsilon_{2N}^{(n)} \leq 0, \quad n = n_f + 1, n_f + 2, \dots, n_f + n_c \quad (1.27)$$

where $\epsilon_{2N}^{(n)}$ is the strain at $x = L$ at time t_n calculated from the numerical space-differentiation of discrete displacements $u_{2i}^{(n)}$; for instance, the implementation of the forward Euler scheme yields discrete strains in the form of $\epsilon_{2i}^{(n)} = (u_{2i}^{(n)} - u_{2(i-1)}^{(n)})/\Delta x$. The discretized formulation given by Eqs. (1.25)–(1.27) is solved through the following steps:

1. Set number of time-steps n_f and n_c .
2. Calculate *potential* initial conditions u_{0i} and v_{0i} that generate a periodic motion satisfying Eq. (1.25) only.
3. Verify that the generated periodic motion satisfies the conditions of impenetrability (1.26) and compressive contact (1.27): the corresponding initial conditions are *admissible*.

4. If the initial conditions are admissible, compute and store the period of vibration and total energy.
5. Change values of n_f and n_c .

For the identification of families of periodic orbits, every feasible pair $(n_f, n_c) \in \mathbb{N}_{>0}^2$ is examined. Nevertheless, verifying among all potential combinations is computationally very inefficient. For that reason, the iteration intervals are bounded for each family of admissible periodic motions by analyzing every possible combination of n_f and n_c on coarse meshes.

1.5 Spectrum of Nonsmooth Vibration

Three initial configurations of the bar are explored: unstressed ($g_0 > 0$), prestressed ($g_0 < 0$) and initially grazing ($g_0 = 0$). Without loss of generality, the mechanical parameters E , ρ , S and L are arbitrarily chosen to be unity and units are discarded. The autonomous dynamics of the bar is investigated for two spring-bar stiffness ratios α . The *linear* natural frequencies $\omega_k(\alpha)$ and $\Omega_k(\alpha)$ respectively calculated using Eqs. (1.5) and (1.6), now only depend on the parameter α . The proposed discretization technique with $\Delta t = \Delta x/c = 10^{-3}$ is implemented. Modal responses were obtained with $g_0 = \pm 10^{-3}$ in both unstressed and prestressed configurations. The response of the autonomous elastic bar is depicted in *frequency-energy plots* (FEPs) where a *backbone curve* (also known as *branch*) represents a NSM. Each point pertaining to a backbone curve represents a modal motion whose frequency is indicated on the horizontal axis and constant total energy along the vertical axis. The frequencies in the FEPs are not normalized while the energy is normalized with respect to the energy of the first linear mode grazing orbit.

NSMs computed for $\alpha = 1$ and $\alpha = 1/2$ are now investigated. In contrast to the results exposed in [13], the intricate dynamics caused by the spring complicates the identification of NSM branches and a highly fine discretization is required to discern how admissible periodic solutions organize to form a continuum. The backbone curves, emerging in the frequency range $[\omega_1; \Omega_1]$ are depicted in Fig. 1.2 as sets of scattered points supposedly belonging to NSMs. Contrary to main NSMs of the internally resonant bar studied in [13] where the energy continuously depends on the frequency, the depicted scattered points indicate more complicated backbone curves. Figure 1.2 suggests that a “nicely” connected continuum representing a possible “main NSM” does not exist. However, several independent branches emerge around subharmonics frequencies lying in the range for the unstressed configuration. This agrees with NSMs in discrete systems without linear internal resonance [6, 12]. An equivalent phenomenon occurs for the prestressed configuration where independent branches align in a seemingly softening branch. For the initially grazing configuration, the NSMs emerge as vertical lines embedding periodic solutions with identical frequency and increasing energy. It also appears that every given collection of scattered points represents a purely independent subharmonic vibration, as opposed to the internally resonant bar which features subharmonic as well as

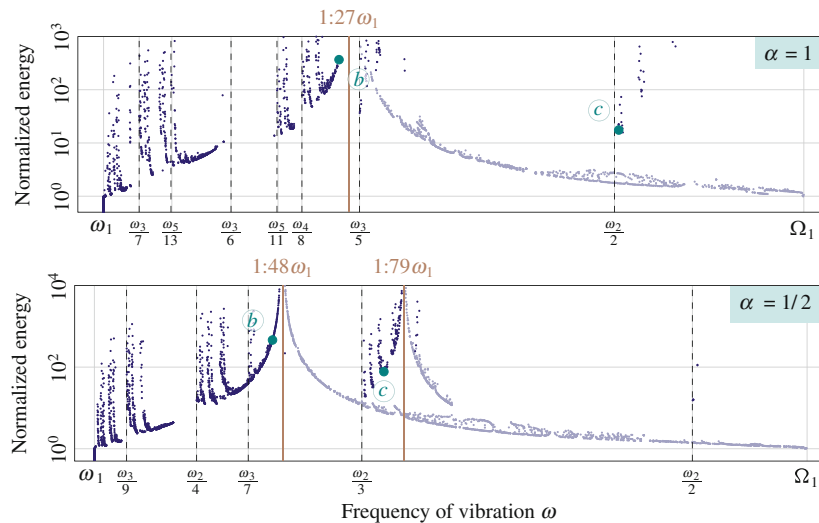


Fig. 1.2 Backbone curves in the frequency interval $[\omega_1; \Omega_1]$ for $\alpha = 1$ and $\alpha = 1/2$ with bar configurations: unstressed [blue solid line], prestressed [grey solid line] and initially grazing [brown solid line]. Subharmonics frequencies [dashed line]

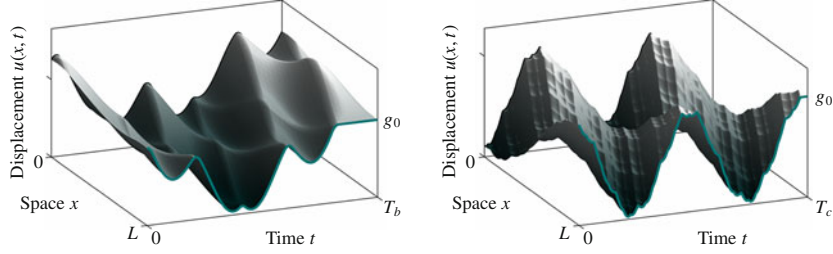


Fig. 1.3 Periodic displacement fields for $\alpha = 1$ corresponding to points (b) (left) and (c) (right) in Fig. 1.2

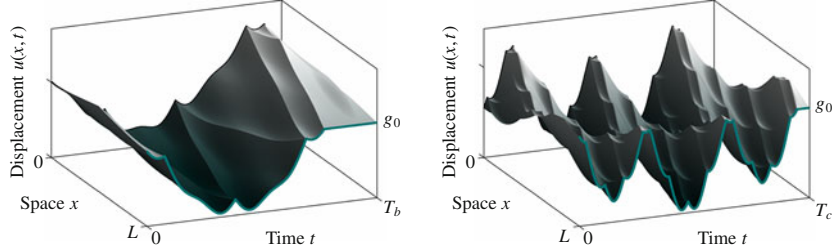


Fig. 1.4 Periodic displacement fields for $\alpha = 1/2$ corresponding to points (b) (left) and (c) (right) in Fig. 1.2

internally resonant NSMs [13]. This observation coincides with the fact that the system of interest does not satisfy the full internal resonance condition.

Figures 1.3 and 1.4 depict NSM periodic displacement fields, for $\alpha = 1$ and $\alpha = 1/2$ respectively, corresponding to points (b) and (c) in Fig. 1.2. Both points (b) represent periodic motions belonging to backbone curves that emerge in the vicinity of the respective ω_1 . On the other hand, points (c) live in apparent NSM branches that arise in the neighborhood of linear subharmonic frequencies. The complicated pattern of each solution is caused by an intricate interplay between various travelling waves embedding the Robin and Signorini boundary conditions. In contrast to linear modes that are purely harmonic functions, the nonsmooth modes of the non-internally resonant system are nonsmooth piecewise-sinusoidal functions. The velocity fields shall present several jump discontinuities per period, which would not be accurately described by traditional semi-discretization strategies [3]. From the reported motions, it also seems that the displacement field for $t \in [0; t_f]$ presents an axis of symmetry in time located at the middle of the free phase: $t = t_f/2$. This observation could facilitate the derivation of closed-form expressions; this is left to future investigations.

1.6 Response to Periodic External Forcing

This section numerically investigates the relationships between NSMs and the system response under periodic excitation. A slight amount of structural viscous damping is introduced in the governing equation (1.1) and a weak external damper is attached at $x = 0$ so that the system can possibly reach a periodic steady-state with bounded energy. The system is forced via a harmonically moving rigid wall that periodically compresses the bar, as seen in Fig. 1.5. The formulation for the forced spring–bar system, to be compared to Eqs. (1.1)–(1.4), reads

$$\partial_t^2 u(x, t) + \zeta_1 \partial_t u(x, t) - c^2 \partial_{xx}^2 u(x, t) = 0, \quad \forall x \in]0; L[, \quad \forall t > 0, \quad (1.28)$$

$$\partial_x u(0, t) - \alpha u(0, t) - \zeta_2 \partial_t u(0, t) = 0, \quad \forall t > 0, \quad (1.29)$$

$$g(u(L, t), w(t)) \geq 0, \quad r(t) \leq 0, \quad r(t)g(u(L, t), w(t)) = 0, \quad \forall t > 0, \quad (1.30)$$

$$u(x, 0) = u_0(x), \quad v(x, 0) = v_0(x), \quad \forall x \in]0; L[, \quad (1.31)$$

where ζ_1 and ζ_2 are respectively the structural and external damping coefficients. The moving wall excitation corresponds to $w(t) = w_0 \sin \omega t$. For an elastic bar initially at rest, the response of the periodically-forced system is constructed by

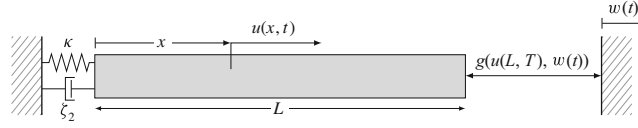


Fig. 1.5 Spring–bar system excited by a moving rigid wall

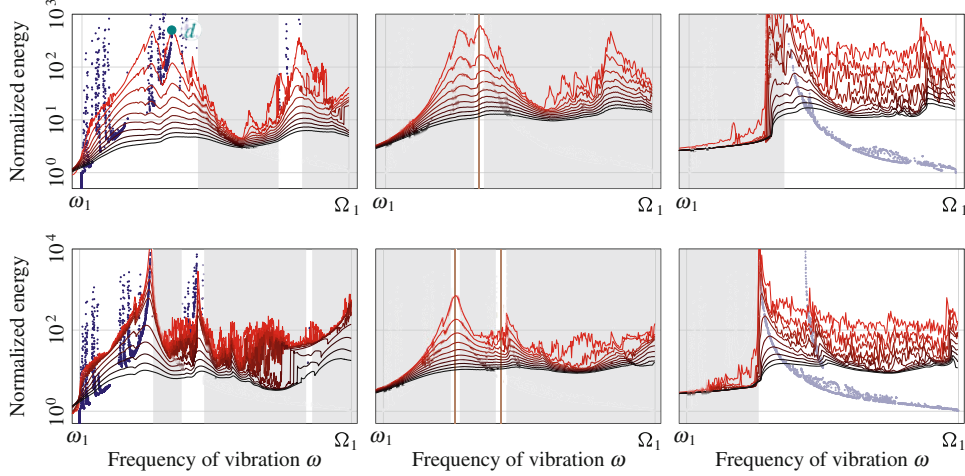
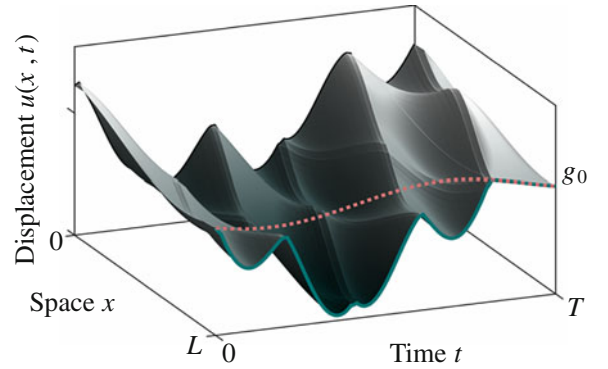


Fig. 1.6 Response to periodic forcing over $[\omega_1 ; \Omega_1]$ of the spring–bar system under various damping coefficients: $\alpha = 1$ (top) and $\alpha = 1/2$ (bottom). Bar configuration at rest: unstressed $g_0 > 0$ (left), grazing $g_0 = 0$ (center) and prestressed $g_0 < 0$ (right). Bar damping coefficient ξ_1 : low [red solid line] to high [solid line]. Grayed regions where NSMs were not found and forced-responses are not periodic

Fig. 1.7 Displacement over one steady-state period due to external excitation via moving wall [pink dashed line]. Result computed with $(\omega, \alpha) = (1.25, 1)$ and $g_0 > 0$. It corresponds to point (d) in Fig. 1.6 in the vicinity of NSM motion (b) in Fig. 1.2 top and Fig. 1.3 left



computing, when possible, the steady-state solution for each frequency of excitation. In this study, such solutions are obtained via the Wave Finite Element Method [13]. The total energy of the steady-state solution, averaged over one forcing period, for increasing frequencies of excitation and various damping coefficients is illustrated in Fig. 1.6 in the interval $[\omega_1 ; \Omega_1]$. In the frequency intervals where NSMs possibly do not exist,² highlighted with grayed areas in Fig. 1.6, the forced system does not seem to exhibit periodic steady-states. When non-periodic forced responses are detected, corresponding portions of the response curves in the frequency diagram consider, for each frequency of excitation, the total energy of the forced motion averaged over ten periods of the external forcing. It is observed that forced responses with high-energy periodic steady-state align well with the NSM backbone curves. Also, Fig. 1.7 illustrates a steady-state displacement of the slightly-damped bar under periodic forcing computed in the vicinity of an NSM. It clearly resembles the corresponding NSM motion, see Fig. 1.3. Although this forced solution seems to be identical to the autonomous oscillation, its free phase is actually not symmetric with respect to a time axis located in the middle of the free phase.

²The number of computable NSMs depends on the mesh size, and finer meshes should provide a more detailed spectrum.

1.7 Conclusions

This contribution targeted the nonsmooth modal analysis of a non-internally resonant bar through a numerical strategy based on simultaneous space-time discretization of the travelling-wave solution. The system of interest consisted of a finite elastic bar of length L subject to a Robin boundary condition at $x = 0$ and a unilateral contact constraint at $x = L$. Such configuration annihilates the full internal resonance condition featured by its internally resonant counterpart [13]. In addition, the Robin BC, physically corresponding to a simple spring attachment, causes a distortion in the waveform that complicates the numerical construction of nonsmooth modes. A semi-analytical approach is derived from the exact solution to the autonomous wave equation together with a switch in the boundary condition where unilateral contact arises. As nonsmooth periodic solutions in closed form are inaccessible, a discretization strategy is proposed to find families of periodic motions. The periodic nonsmooth motions are piecewise-*sinusoidal* functions, as opposed to the internally resonant counterparts where modal displacements are piecewise-linear functions. The forced response plots illustrated the capability of the Nonsmooth Modal Analysis to predict the vibratory resonances of the one-dimensional periodically-forced elastic bar. Even though the vibratory characterization is more challenging than for the internally resonant counterpart [13], the computed NSMs forecast most intervals involving nonlinear resonances.

References

1. Achenbach, J.: Wave Propagation in Elastic Solids. Elsevier, Amsterdam (1973). <https://doi.org/10.1016/C2009-0-08707-8>
2. Amerio, L.: Continuous solutions of the problem of a string vibrating against an obstacle. *Rendiconti del Seminario Matematico della Università di Padova* **59**, 67–96 (1978). EUDML: [107691](#)
3. Doyen, D., Ern, A., Piperno, S.: Time-integration schemes for the finite element dynamic Signorini problem. *SIAM J. Sci. Comput.* **33**(1), 223–249 (2011). OAI: [hal-00440128](#)
4. Graff, K.: Wave Motion in Elastic Solids. Dover, New York (1975)
5. Kerschen, G., Worden, K., Vakakis, A., Golinval, J.-C.: Past, present and future of nonlinear system identification in structural dynamics. *Mech. Syst. Signal Process.* **20**(3), 505–592 (2006). OAI: [hal-01863233](#)
6. Legrand, M., Junca, S., Heng, S.: Nonsmooth modal analysis of a n -degree-of-freedom system undergoing a purely elastic impact law. *Commun. Nonlinear Sci. Numer. Simul.* **45**, 190–219 (2017). OAI: [hal-01185980](#)
7. Meirovitch, L.: Analytical Methods in Vibrations. Macmillan, New York (1967)
8. Rao, S.: Vibration of Continuous Systems. Wiley, London (2007). DOI: [10.1002/9780470117866](#)
9. Schatzman, M., Bercovier, M.: Numerical approximation of a wave equation with unilateral constraints. *Math. Comput.* **53**(187), 55–79 (1989). OAI: [hal-01295436](#)
10. Shaw, S., Pierre, C.: Non-linear normal modes and invariant manifolds. *J. Sound Vib.* **150**(1), 170–173 (1991). OAI: [hal-01310674](#)
11. Thorin, A., Legrand, M.: Nonsmooth modal analysis: from the discrete to the continuous settings. In: Leine, R., Acary, V., Brüls, O. (eds.) *Advanced Topics in Nonsmooth Dynamics*. Transactions of the European Network for Nonsmooth Dynamics, chapter 5, pp. 191–234. Springer, Berlin (2018). OAI: [hal-01771849](#)
12. Thorin, A., Delezoide, P., Legrand, M.: Non-smooth modal analysis of piecewise-linear impact oscillators. *SIAM J. Appl. Dyn. Syst.* **16**(3), 1710–1747 (2017). OAI: [hal-01298983](#)
13. Yoong, C., Thorin, A., Legrand, M.: Nonsmooth modal analysis of an elastic bar subject to a unilateral contact constraint. *Nonlinear Dyn.* **91**(4), 2453–2476 (2018). OAI: [hal-01471341](#)



Chapter 2

A New Iwan/Palmov Implementation for Fast Simulation and System Identification

Drithi Shetty and Matthew S. Allen

Abstract While Iwan elements have been shown to be an effective model for the stiffness and energy dissipation in bolted joints, they are presently somewhat expensive to integrate. Currently, the Newmark-beta algorithm is used to integrate the equations of motion when a structure contains Iwan elements, and a small time step is needed to maintain accuracy. This paper presents a new way of simulating Iwan elements that speeds up the simulations dramatically by using closed form expressions for the micro-slip regime and using an averaging method for regions of time in which no external force is applied. With this method the response can be computed in about a hundredth of the time. The proposed algorithm is demonstrated on a single degree-of-freedom (SDOF) system to understand the range over which it retains accuracy. Although current implementation is applicable to SDOF systems, it can simulate the response of each mode in a structure that is modeled using the modal Iwan approach (i.e. assuming uncoupled, weakly-nonlinear modes).

Keywords Non-linear damping · Iwan model · method of averaging · Newmark-beta integration · Runge-Kutta

2.1 Introduction

Built-up structures are typically modeled using linear solvers with springs approximating the joints and using modal or proportional damping to account for energy dissipation. However, mechanical joints are a major contributor to the overall damping of structures [1]. Their behavior is predominantly non-linear and the development of a predictive model for the same is a challenge [2]. At lower amplitudes, only the edges of the joint surfaces slide relative to each other while a majority of the joint remains intact, known as micro-slip. In the micro-slip regime, the stiffness of the joint decreases only slightly, but there is significant energy loss [3]. Hence, the response is nearly linear although the damping is observed to change significantly with the amplitude of vibration [4]. As the amplitude increases, the slip region gradually expands until macro-slip occurs. In this case, relative motion occurs between the surfaces and the stiffness of the joint is significantly affected.

While the physics just described could be captured by modeling each joint in detail with a suitable friction law between parts, to compute the dynamic response with such an approach would take months or years on current computers. As a result, it is more common to use a reduced model with nonlinear elements between each component to account for micro- and macro-slip in the joints. The Iwan element, initially introduced for metal elasto-plasticity [5], has been shown to be effective in capturing joint behavior [4]. It is a lumped, hysteretic model consisting of a parallel system of spring-slider units known as Jenkins elements. The most common Iwan model is Segalman's four parameter model [6], with the four parameters accounting for the joint stiffness, the force at which the joint slips completely and the power law energy dissipation that many joints have been found to exhibit in microslip. While this is far less computationally expensive than modeling the contact in detail, the computational burden is significant when many joints are present or when performing parameter studies. As an alternative, Segalman proposed a modal approach [7], which exploits the fact that the modes of a structure tend to be mostly uncoupled when the joints remain in the micro-slip regime [8] and hence, each mode can be modeled as a single degree of freedom system but with an Iwan element to account for the nonlinearity.

In either case, the response of a structure that contains Iwan elements is typically found using the average acceleration Newmark-beta integration method [9], with a Newton-Raphson iteration loop for the nonlinear force in the Iwan model. This method is effective and quite reliable, but requires a small time step, making it computationally expensive. This paper presents an alternative that is much less expensive. One study that is relevant to the current work is that on the RIPP joint,

D. Shetty (✉) · M. S. Allen
University of Wisconsin, Madison, WI, USA
e-mail: ddshetty@wisc.edu; msallen@engr.wisc.edu

presented by Brake in [10], which uses somewhat similar concepts in an effort to accelerate integration of Iwan joints, while preserving the ability of the joint to capture macro-slip.

This work makes use of the analytical formulas for the behavior of an Iwan joint in microslip but limits the solution to the micro-slip regime and uses the averaging method to compute the time response much more quickly. The averaging method is applicable to systems in which the amplitude and phase vary slowly with time [11]. The following integration technique takes advantage of this behavior to improve the simulation time without significantly affecting the accuracy. It also has the advantage that the instantaneous natural frequency and damping are computed in the course of the time integration. The subsequent section explains the algorithm and the relevant theory behind it. Its applicability for a single degree of freedom system is then examined through a case study and future research is proposed.

2.2 Understanding the Algorithm

The algorithm presented in this work considers a single degree of freedom system (shown in Fig. 2.1) consisting of a linear spring, linear damper and a single non-linear Iwan joint. The simulation is divided into two parts:

- Integration in the presence of an external impulsive force and
- Simulating the free decay response after the external force goes to zero.

Matlab's adaptive fourth–fifth order Runge-Kutta (RK) algorithm (i.e. ode45), is used for both parts. This requires that the differential equation be defined in the form $\dot{\mathbf{x}} = f(\mathbf{x}, t)$ with the initial conditions provided as input. It is important to note that the traditional Iwan element cannot be integrated using Runge-Kutta, because it is hysteretic by definition and so it cannot be written in the form described above (without some kind of approximation). For that reason, the Newmark-beta algorithm has been used with a fixed time step in most cases in the literature. The procedure for obtaining the initial conditions is explained below.

2.2.1 When the External Force is Non-zero

The forced equation of motion can be approximated as follows when the Iwan joint remains in the micro-slip regime,

$$\ddot{x} + 2\zeta(A)\omega_n(A)\dot{x} + (\omega_n(A))^2x = F(t)/m \quad (2.1)$$

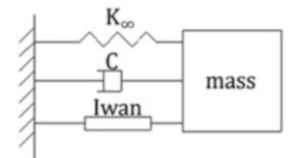
where A is the amplitude of vibration, which is elaborated below. The closed form expressions of dissipation per cycle (D) and secant stiffness (K_j) derived in [6] are used after converting the physical Iwan parameters $[F_s, K_t, \chi, \beta]$ to their mathematical equivalents $[R, S, \chi, \phi_{\max}]$

$$D = \frac{4RA^{\chi+3}}{(\chi+3)(\chi+2)} \quad (2.2)$$

$$r = \frac{A}{\phi_{\max}} \quad (2.3)$$

$$K_j = K_t \left(1 - \frac{r^{\chi+1}}{(\chi+2)(\beta+1)} \right) \quad (2.4)$$

Fig. 2.1 Schematic of the single degree of freedom system



Equations 2.2–2.4 are then substituted in the expressions below to obtain the effective natural frequency and damping ratio.

$$\omega_n(A) = \frac{\sqrt{K_j(A) + K_\infty}}{m} \quad (2.5)$$

$$\zeta(A) = \frac{D(A)}{2\pi m \omega_n^2 A^2} + \zeta_{linear} \quad (2.6)$$

By assuming that the change in amplitude is negligible over each cycle, a relationship between amplitude and response can be established as shown in Eqs. 2.7–2.9,

$$x \cong A \cos(\omega_d t) \quad (2.7)$$

$$\dot{x} \cong -A \omega_d \sin(\omega_d t) \quad (2.8)$$

$$A = \sqrt{x^2 + \left(\frac{\dot{x}}{\omega_d}\right)^2} \quad (2.9)$$

where

$$\omega_d = \omega_n \sqrt{1 - \zeta^2} \quad (2.10)$$

As seen in the equations above, the amplitude, natural frequency and damping ratio are interdependent variables in that the amplitude also changes with changing ω_n and ζ . This makes it necessary to solve this iteratively. To do so, a simple recursive scheme is implemented. The amplitude (and corresponding ω_n and ζ) is calculated within a loop, and the loop is repeated until the absolute difference between the amplitude calculated in successive iterations falls within a pre-defined tolerance. It was observed that a reduction in tolerance below 10^{-10} led to negligible change in the simulated response. Three to four loop iterations were typically needed. The instantaneous natural frequency and damping ratio thus obtained are then substituted in the equation of motion which is used to define the ODE that is solved.

The solution at the time at which the force ends (i.e. assuming the force is impulsive or otherwise short in duration) is used to define the initial amplitude and phase of the solution for the averaging algorithm, which solves for the rest of the transient response and is described in the next subsection.

2.2.2 When the External Force is Zero

The equation of motion in the absence of external force becomes the following.

$$\ddot{x} + 2\zeta(A)\omega_n(A)\dot{x} + (\omega_n(A))^2 x = 0 \quad (2.11)$$

While the previous method could be used for the transient part of the response as well, a quicker solution can be achieved by using the averaging method. On analyzing the response, it can be seen that while the response itself changes quickly with time, the amplitude and phase of the response change slowly with time (as seen in Fig. 2.2). Under these circumstances, the averaging method can be used to change the variables in the differential equation from displacement and velocity to amplitude and phase, allowing larger time steps to be taken and thus achieving a less computationally expensive solution. The differential equations used in this algorithm are derived in [12] by replacing displacement and velocity as states with amplitude and phase and then integrating over a cycle (i.e. assuming that amplitude and phase change slowly with time). The result is given in Eqs. 2.12 and 2.13.

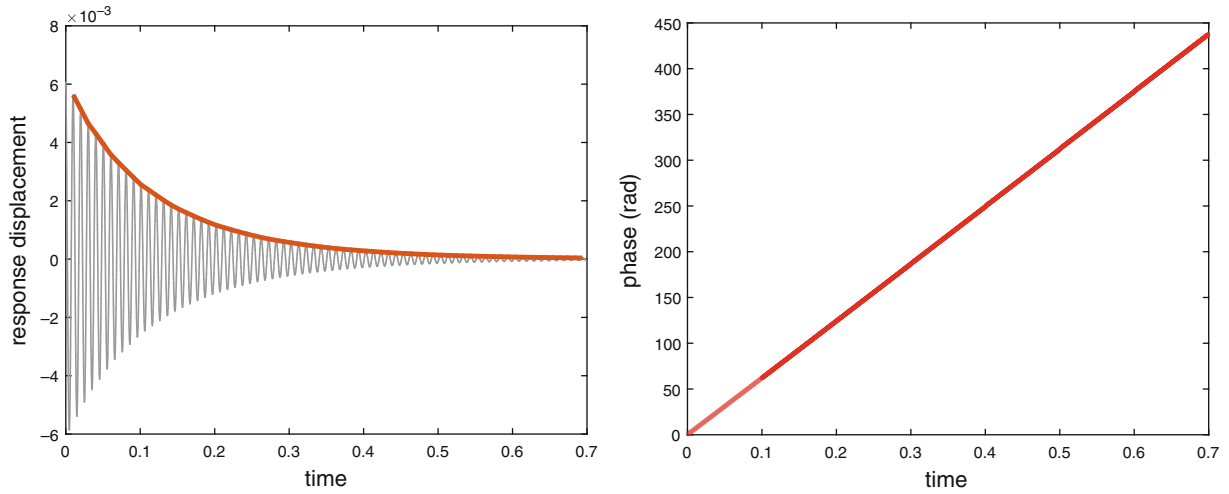


Fig. 2.2 Response amplitude and phase vs. time

$$\dot{A} = -A\omega_n\zeta \quad (2.12)$$

$$\dot{\phi} = \omega_n\sqrt{(1 - \zeta^2)} \quad (2.13)$$

As given in the derivation in [12], once these are found as a function of time, the displacement and velocity can then be recovered (if desired), using the following.

$$x = Ae^{i\phi} \quad (2.14)$$

$$\dot{x} = \dot{A}e^{i\phi} + A\dot{\phi}e^{i\phi}i \quad (2.15)$$

2.3 Application to Single Degree of Freedom System

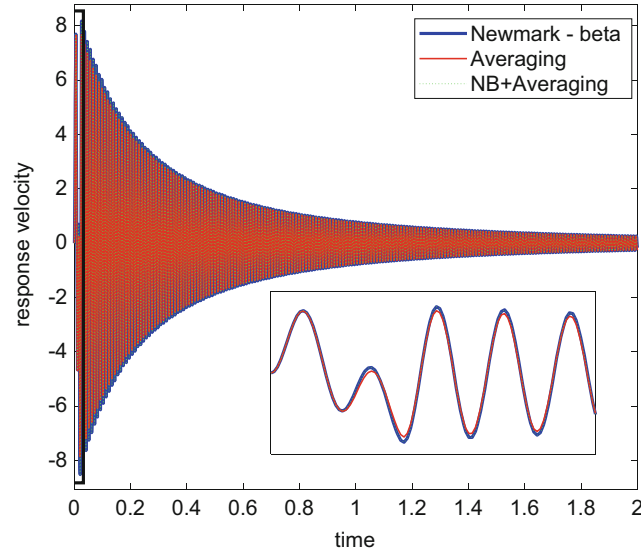
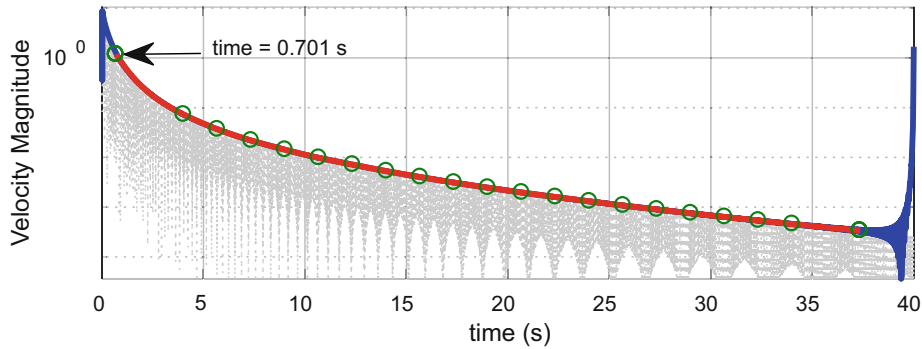
The algorithm described was tested against the Newmark-beta integration technique for speed and accuracy. The accuracy was measured by quantifying the error in the effective damping ratio and natural frequency as a function of amplitude and the speed was measured as the time taken for integration on an Intel[®] Core[™] i7-950 (3.07 GHz) processor. The response displacement (and velocity) were simulated using three methods:

- Newmark-beta integration.
- The algorithm described in Sects. 2.1 and 2.2, which is referred to here simply as the ‘‘Averaging’’ algorithm.
- A combination of the Newmark-beta algorithm (replacing the algorithm in Sect. 2.1) with the averaging algorithm of Sect. 2.2, which is here referred to as ‘‘NB + Averaging’’

Table 2.1 lists the parameters defining the test case being considered. A half sinusoidal impulse force of width 0.02 s was applied at various amplitudes, focusing on the micro-slip regime. This was verified by checking the displacement of the sliders in the Iwan joint. The time responses obtained by each method were then processed using the Hilbert transform, as described in [13], to obtain the instantaneous damping ratio and natural frequency. The errors in these estimations were calculated treating the Newmark-beta result as the truth solution, although some difficulty was encountered when doing this, as explained in the subsequent section.

Table 2.1 Parameters used in the test case

Parameter	Value
K_{∞}	$1.4 \times 10^5 \text{ N/m}$
ζ_{linear}	1×10^{-4}
Iwan Joint:	
• $[F_s, K_t, \chi, \beta]$	$[40000 \text{ N}, 2.5 \times 10^5 \text{ N/m}, -0.5, 1.0]$
Half sinusoidal pulse:	
• Amplitude	(varies)
• Pulse-width	0.02 s

**Fig. 2.3** Response velocity predicted by the three methods**Fig. 2.4** Trimming the velocity vector after computing the Hilbert transform to eliminate end effects

2.3.1 Results and Analysis

Accuracy

Figure 2.3 shows a sample of the responses obtained from the three simulation methods, corresponding to the case where the force amplitude was 10 kN, (or $E_r = 0.9$, as will be defined subsequently). The response was found for 40 s in each case. Then, the Hilbert transform was computed and trimmed to mitigate the end effects, as shown in Fig. 2.4. To maintain consistency, the same trim points were used for all simulation methods. The damping ratio and natural frequency obtained from the Hilbert transform were then plotted against the response velocity amplitude to observe the power-law behavior. It must be noted here that these graphs progress from right to left (i.e. from higher velocity amplitudes to lower velocity amplitudes) since the response velocity decreases with time. To generalize the results, the non-dimensional velocity was

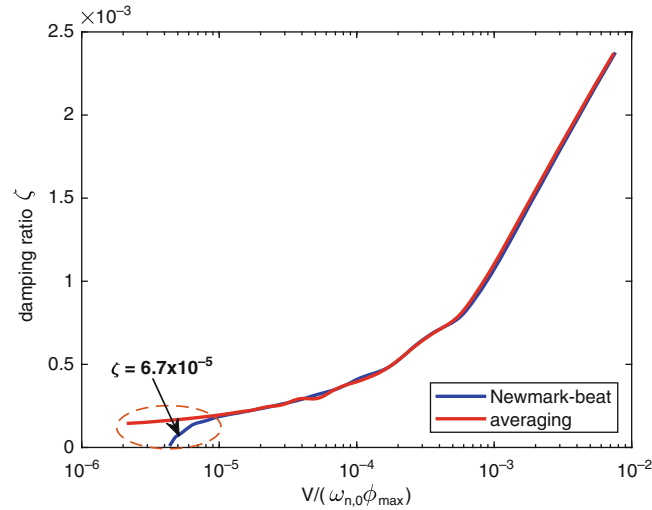


Fig. 2.5 Damping ratio vs. non-dimensional velocity when residual tolerance = 10^{-8}

defined as the ratio of the velocity to the product $(\omega_{n,0}\phi_{max})$, where $\omega_{n,0}$ is the natural frequency when the joint is stuck and ϕ_{max} , the displacement of the joint at macro-slip. The error in damping ratio and natural frequency was then calculated as a percentage of the Newmark-beta solution, which was considered to be the truth solution.

On performing the simulation for the test case described above, it was initially observed that the damping ratio (and natural frequency) estimated using the derived algorithm deviated from that obtained using the Newmark-beta (NB) integration at low velocities. As seen in Fig. 2.5, the damping ratio calculated by the NB method decreases to values below linear damping at lower velocities. On further investigation, it was noted that the response simulated by the NB method was sensitive to the residual tolerance criterion set in the Newton-Raphson Iteration loop. This was surprising, because the tolerance of 10^{-13} had been used in many previous studies without difficulty, and it was already approaching machine precision. The tolerance was reduced gradually until further reduction did not have a significant effect on the output. Finally, a tolerance of 10^{-15} was found suitable for the range of forces analyzed in this work. The arbitrary nature of this selection highlights a possible drawback of the existing integration method and further warrants development of a more accurate technique.

Figure 2.6 compares the damping ratio and natural frequency calculated by each of the methods after changing the tolerance described above. It can be observed that the results obtained are now in good agreement with the truth solution. The averaging method is found to give quite accurate results over a large range of vibration amplitude, with errors of less than 0.04% in the natural frequency over the whole range of amplitude and errors in damping of less than 8% (of the true value, which ranged from $\zeta = 0.0001$ to 0.003). The error is most pronounced at a non-dimensional velocity of 10^{-4} , which is possibly due to the noise introduced in the predictions by the Hilbert transform process. As expected, when the averaging method is augmented by using the NB algorithm to compute the initial portion of the response (during which the force is active), the error decreases relative to using the RK integration for initial portion. Note that the first instant shown in Fig. 2.6 (highest amplitude) corresponds to 0.70 s whereas the force pulse lasts 0.02 s.

The above plots used the Hilbert transform, which is susceptible to noise and end effects, to estimate the damping ratio and natural frequency from time histories. The Averaging method, however, also estimates the same during the course of the integration (i.e. Eqs. 2.5 and 2.6). To evaluate the potential errors in the damping and frequency due to the Hilbert transform Fig. 2.7 compares the damping estimated directly from the algorithm with those obtained from the Hilbert transform from the NB method and the Averaging method. All three solutions agree very well for non-dimensional velocities below $5 \cdot 10^{-5}$, but the values calculated directly using the Averaging method deviate from those estimated using the Hilbert transform at higher velocities. The damping found by the Hilbert Transform shows a slight waviness that is not expected from theory, whereas the damping found directly by the Averaging method shows exactly the expected power law behavior (i.e. the damping is linear on a log-log plot). Another advantage of the averaging method is that one does not need to truncate the first 0.70 seconds of data, as is required in the Hilbert transform to minimize end effects.

While the results above clearly show that the Averaging method produces a transient response that closely follows the desired frequency versus amplitude and damping versus amplitude curves, they do not prove that the same transient response will be obtained by each algorithm. Specifically, when the joint approaches macro-slip the initial response may deviate significantly, causing the averaging solution to estimate inaccurate amplitudes in the initial phase. An example of this is

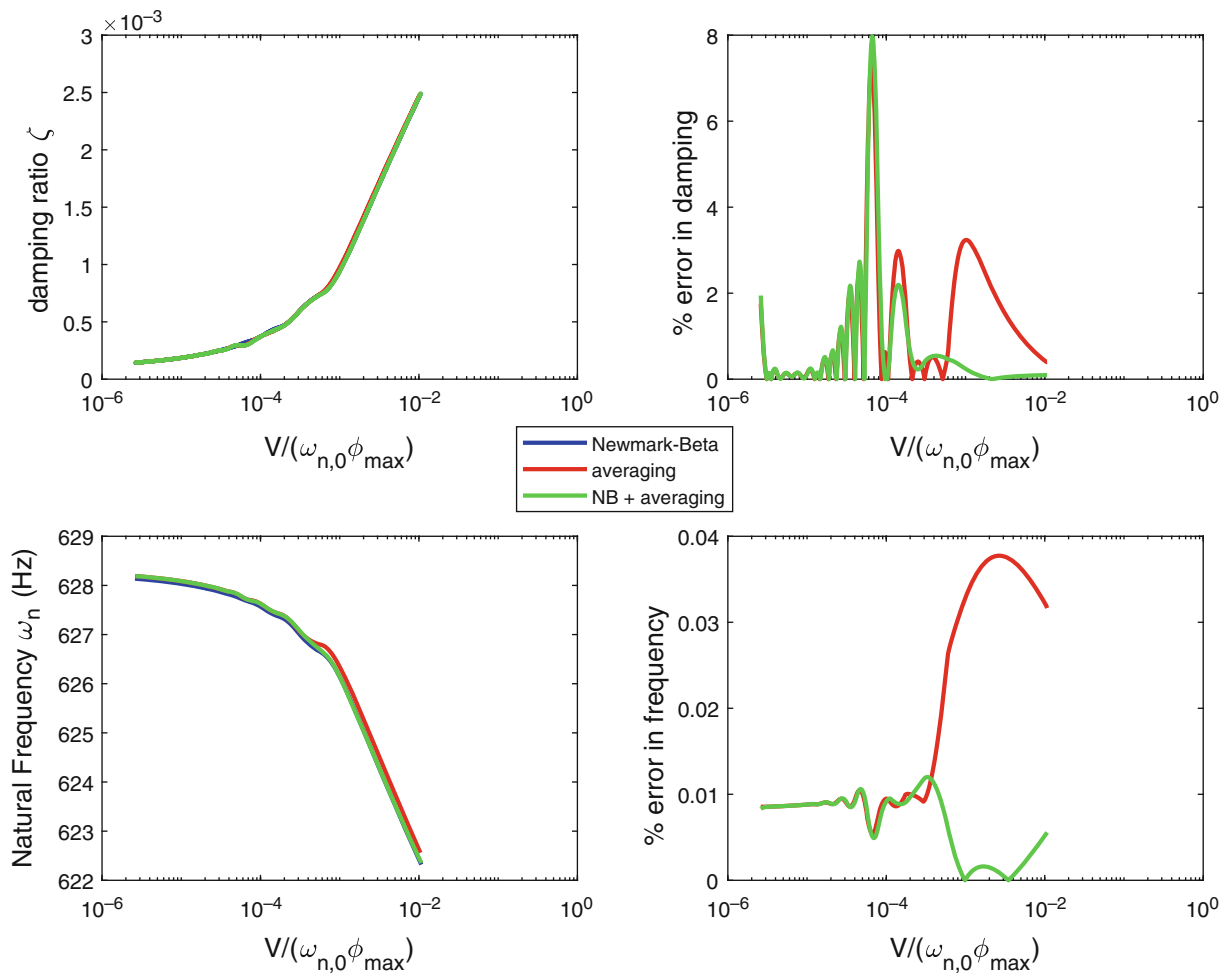


Fig. 2.6 Damping ratio and natural frequency vs. non-dimensional velocity

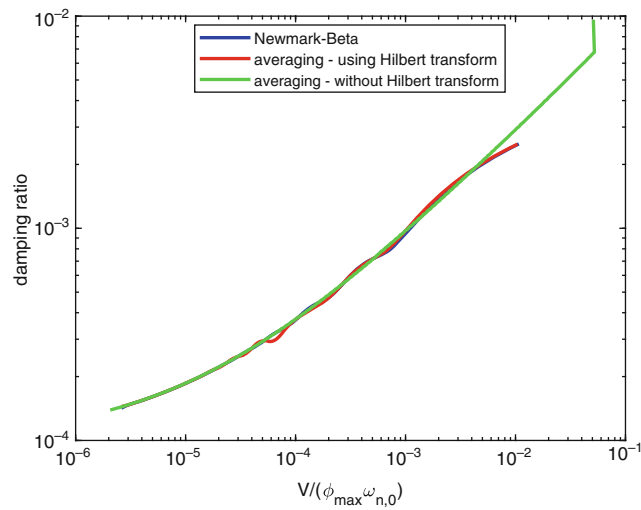


Fig. 2.7 Damping ratio calculated using closed form expressions

shown in Fig. 2.8, for the case where the force amplitude was $3 \cdot 10^5$ N (or $E_r = 685$). The averaging method behaves differently over the 0.02 s force pulse, resulting in a higher velocity during the transient part of the response.

To further quantify this, the amplitude of the response was estimated from each method for various force amplitudes and the results are summarized in Fig. 2.9. To generalize the results, the non-dimensional force amplitude was expressed as an energy ratio $E_r = E_{imp}/PE_{max}$ where the numerator is the energy imparted by the impulse (Eq. 2.16) and the denominator is the approximate potential energy for which the joint fully slips (Eq. 2.17). The results show that the averaging method predicts the transient response amplitude well up until an energy ratio of unity, and still produces acceptable results up until a ratio of 10. Beyond that point, it begins to significantly under-estimate the response amplitude, presumably because it doesn't have the ability to account for macro-slip.

$$E_{imp} = \frac{1}{2m} \left(\int f(t) dt \right)^2 \quad (2.16)$$

$$PE_{max} = \frac{1}{2} (K_{\infty} + K_T) \phi_{max}^2 \quad (2.17)$$

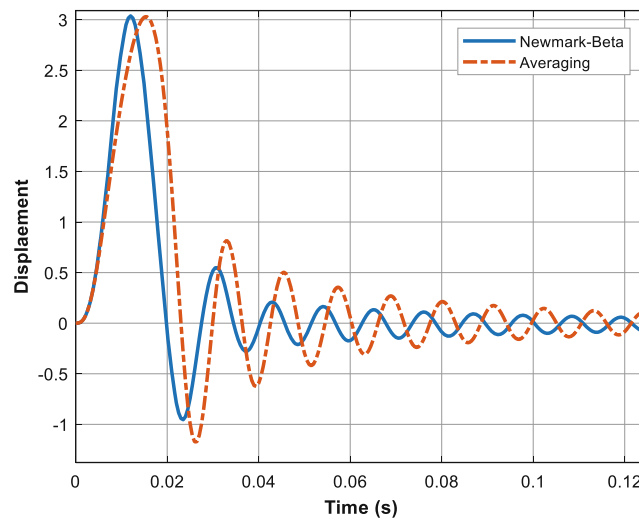


Fig. 2.8 Response velocity vs. time, macro-slip

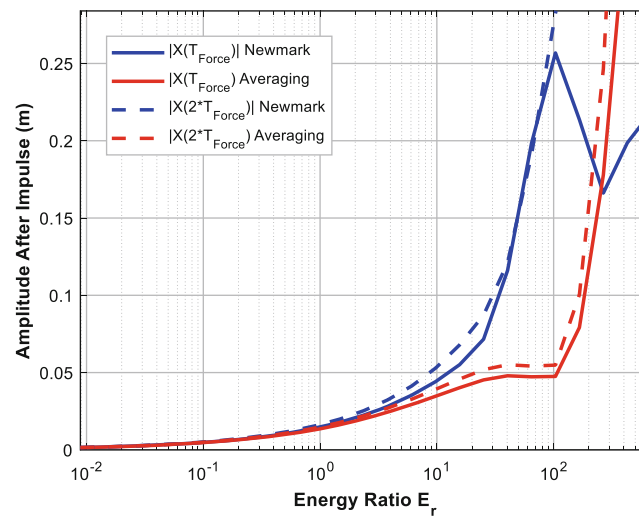


Fig. 2.9 Response amplitude after the impulse has ended for Newmark-beta method and Averaging method. The horizontal axis expresses the force in terms of the energy relative to that which initiates macro-slip, as described above

Table 2.2 Average simulation time for each of the three methods

Integration method	Simulation time (in seconds)
Newmark-beta	214.24
Averaging	1.961
Newmark beta and averaging combined (NB + Averaging)	14.303

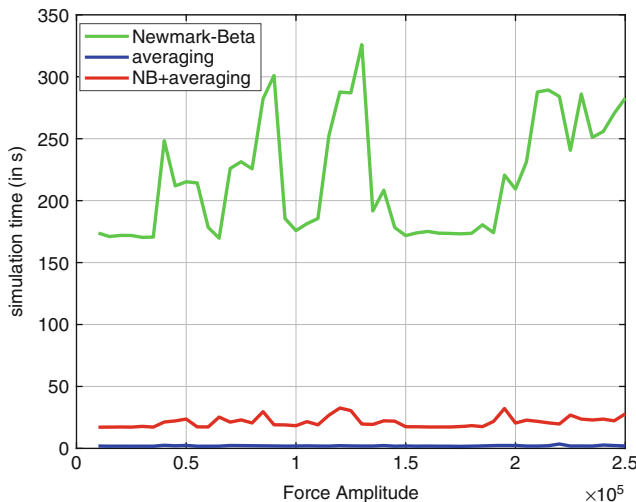


Fig. 2.10 Variation of simulation time with input force amplitude

Speed

As a measure of speed, the average simulation time was compared for the range of force amplitudes considered. Table 2.2 shows the time taken by each of the three methods being compared to simulate the response. It is evident that the method of averaging speeds up the integration process significantly. This was anticipated as applying the concept of averaging allows for a larger time step to be considered, thus lowering the number of integration steps. For example, for the cases shown in Fig. 2.10, 79,976 time steps were required for the NB method (200 samples per period) whereas for the same duration of interest, with the method of averaging, the RK integrator used an average of 2984 time steps. It can also be observed that varying the amplitude of the impulse force applied does not result in a considerable change in simulation time (2.10).

2.4 Conclusions

This work has shown that the method of averaging can be effectively used to speed up the integration of a single degree of freedom system with an Iwan joint with minimal loss in accuracy up to surprisingly large forces. In the micro-slip regime, the damping ratio, natural frequency and response amplitude estimated were found to be comparable to those from the Newmark-beta method. In fact, in some cases the averaging method was more reliable and accurate (i.e. didn't require adjusting the ad-hoc convergence tolerance in the Newton loop). It is also preferable if the final goal is to estimate damping and frequency versus time, because no further processing (i.e. with the Hilbert transform) is required to obtain these.

However, the averaging algorithm is fundamentally limited to micro-slip only. One can obtain the best of both worlds by using the Newmark-beta method until the external force dies down and the method of averaging can be used thereafter. With this approach the computation time is reduced significantly, but not as much so as when only the averaging method is used (i.e. the computation time is only reduced by a factor of ~ 10 rather than a factor of ~ 100).

Future work will seek to couple this with a suitable optimization tool, allowing one to determine the modal Iwan parameters for a weakly non-linear mode using frequency domain data. Such an approach could be critical in cases in which modal filtering or bandpass filtering is not applicable.

References

1. Gaul, L., Lenz, J.: Nonlinear dynamics of structures assembled by bolted joints. *Acta Mech.* **125**(1), 169–181 (1997)
2. Brake, M.R.W.: *The Mechanics of Jointed Structures*. Springer Science+Business Media, New York, NY (2017)
3. Segalman, D.J.: An Initial Overview of Iwan Modeling for Mechanical Joints. Sandia National Laboratories, Albuquerque, NM. SAND2001–0811 (2001). <https://doi.org/10.2172/780307>
4. Segalman, D.J.: Modelling joint friction in structural dynamics. *Struct. Control. Health Monit.* **13**(1), 430–453 (2006)
5. Iwan, W.D.: A distributed-element model for hysteresis and its steady-state dynamic response. *J. Appl. Mech.* **33**(4), 893–900 (1966)
6. Segalman, D.J.: A four-parameter Iwan model for lap-type joints. *J. Appl. Mech.* **72**, 752–760 (2005)
7. D. J. Segalman, “A modal approach to modeling spatially distributed vibration energy dissipation.,” SAND2010–4763, 993326, 2010 Sandia National Laboratories, Albuquerque, NM
8. Deaner, B.J., Allen, M.S., Starr, M.J., Segalman, D.J.: Investigation of modal Iwan models for structures with bolted joints. In: *Topics in Experimental Dynamic Substructuring*, vol. 2, pp. 9–25 (2014)
9. Cook, R.D., Malkus, D.S., Plesha, M.E., Witt, R.J.: *Concepts and Applications of Finite Element Analysis*, vol. 4. Wiley, New York (1974)
10. Brake, M.R.W.: A reduced Iwan model that includes pinning for bolted joint mechanics. *Nonlinear Dyn.* **87**(2), 1335–1349 (2017)
11. Nayfeh, A.H.: *Introduction to Perturbation Techniques*, 1st edn. Wiley, New York (1993)
12. Haslam, A.H., et al.: Non-linear system identification in the presence of modal coupling. In: *Nonlinear Dynamics, Conference Proceedings of the 36th IMAC*, p. 20 (2018)
13. Sumali, A.: Calculating Damping from Ring-Down Using Hilbert Transform and Curve Fitting, p. 20. Sandia National Laboratories, Albuquerque, NM (2011)



Chapter 3

Analysis of Transient Vibrations for Estimating Bolted Joint Tightness

M. Brøns, J. J. Thomsen, S. M. Sah, D. Tcherniak, and A. Fidlin

Abstract It is difficult to determine and control the tension level in a bolt; however, there is a great need for that to ensure safe operation of large structures. Bolts come in all sizes, but when properly tightened a bolt can roughly be considered an axially stressed clamped-clamped beam. A novel technique is proposed to quantify the level of bolt tightness by analysing natural frequencies and damping ratios of the bolt, based on simple hammer impacts. To study the application potential of the technique a set of real bolted joints, holding together machinery parts for a fluid mechanic setup, are impulse hammer impacted and the vibration response analysed. The tests aim to capture obstacles induced by working with bolts outside a controlled laboratory.

Keywords Bolted joints · Tension estimation · Transient vibrations · Signal processing · Practical application

3.1 Introduction

Bolted joints are present in many different engineering structures, from wind turbines to heavy machinery, some of which are critical joints where failure can have catastrophic consequences and is unacceptable. In those cases, it is of interest to be able to monitor the tension level in the bolt by a simple measure. A newly proposed technique is to impulse hammer impact the bolt and estimate the tension by analyzing the recorded dynamic response. An advantage of this method is that a tightening procedure with heavy equipment, such as hydraulic tensioners, will only be performed on the bolts that are in fact loose, potentially reducing maintenance cost.

Existing techniques count torque control [1], turn control [1] and ultrasonic methods [2, 3]. The new technique has been studied experimentally by measuring accelerations of freely decaying vibrations of different bolts. At low tension the squared natural frequency of the first bending mode increases strongly with tension. As the bolt is gradually tightened the squared natural frequency starts changing more weakly and approximately linearly with tension [4]. A one-dimensional linear beam model with clamped boundary conditions subjected to axial stress can theoretically explain the linear increase, while the nonlinear transition can be explained by the increased effective boundary stiffness accompanying tension [4].

In this work, the knowledge obtained in the laboratory is applied to a real structure with multiple bolts, with the purpose of exposing practical obstacles when using this novel technique in practice. One of the challenges when working with a real structure with multiple bolts is to properly identify the first bending natural frequency of the impacted bolt, as damping and signal noise is more pronounced, and the vibrations from other bolts and the structure itself are interfering.

M. Brøns (✉) · J. J. Thomsen · S. M. Sah
Department of Mechanical Engineering, Technical University of Denmark, Kgs. Lyngby, Denmark
e-mail: maribr@mek.dtu.dk

D. Tcherniak
Brüel and Kjær Sound and Vibration Measurements A/S, Nærum, Denmark

A. Fidlin
Institute of Engineering Mechanics, Karlsruhe Institute of Technology, Karlsruhe, Germany

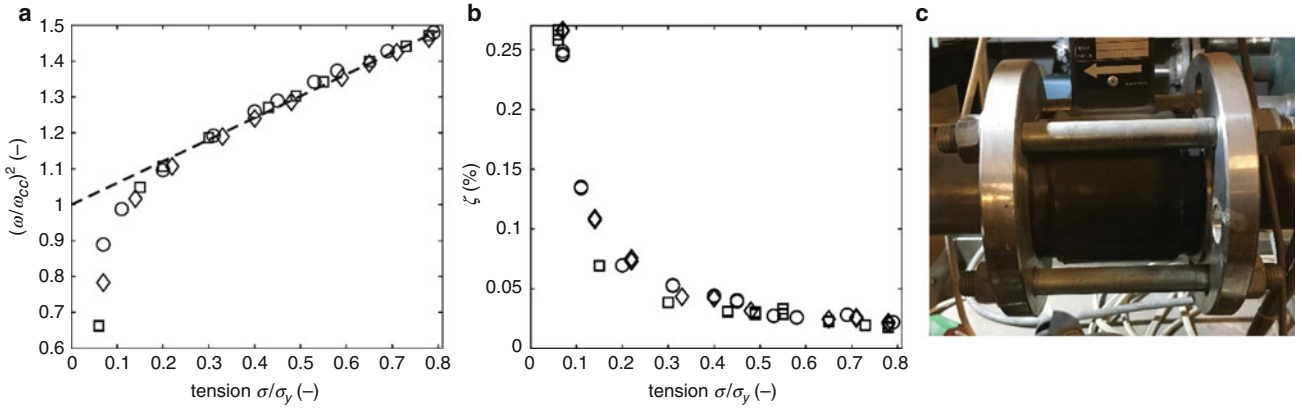


Fig. 3.1 (a) Measured first natural frequency squared as a function of tension for reference measurement. Three different test series indicated by \circ , \square , \diamond . Dashed line: Theoretical squared natural frequency for a clamped-clamped beam as a function of axial tension (cf. Eq. (3.1)); (b) Damping ratio ζ as a function of tension; (c) Real test structure

3.2 Background

A rough model of a tightened bolt is to assume it as a clamped-clamped beam exposed to axial tension. The j 'th natural frequency can in that case be calculated as [5]:

$$\omega_j = \frac{\lambda_j^2}{ls} \sqrt{\frac{E}{\rho} \left(1 + \frac{\sigma}{E} \left(\frac{K_j s}{\lambda_j^2} \right)^2 \right)}, \quad (3.1)$$

where l is the effective bolt length (from head to nut), λ_j is the eigenvalue for mode j , E Young's modulus, ρ density, σ applied axial stress, K_j a mode shape dependent constant, and s the slenderness ratio which is $2l/r$ for a circular cross section, when r is the radius of the bolt. It appears from Eq. (3.1) that the squared natural frequency increases linearly with tension, with a proportion that depends on the slenderness of the bolt: the more slender the bolt, the bigger is the change in natural frequency with respect to the axial stress σ .

Measurements with two different bolts have shown that this model assumption is reasonable, especially for slender bolts and for higher tension [4]. Adapted from [4] Fig. 3.1 shows reference results of an M12 \times 250 bolt tightened in a single structure. Figure 3.1a shows the squared first natural bending frequency normalized with the natural frequency ω_{cc} of an un-tensioned clamped-clamped beam as a function of tension, and Fig. 3.1b the corresponding damping ratio. The yield stress of the bolt is $\sigma_y = 640$ MPa, and σ is the actual stress. For tensions exceeding about 20% of the yield stress, the experimentally obtained natural frequency agrees with the model (dashed line). The damping ratio decreases with tension.

The idea is to go backwards and use the linear relation in Eq. (3.1) to estimate the tension of the bolts. The damping ratio can support an estimation, as a low damping ratio indicates a tight bolt. The technique is tested for a real structure used for fluid mechanic experiments. Figure 3.1c shows the setup, consisting of four bolts clamping two pipes and a flowmeter together, via two flanges. Each bolt is impulse hammer impacted, and the accelerations recorded by a 4397 B&K accelerometer mounted on the shaft of the bolt. The bolts in the setup was tightened by a torque wrench to three different torque levels: approximately [100, 150, 200] Nm. Depending on the chosen nut factor these levels correspond to [20–40, 30–60, 45–80] % of yield stress (which also illustrates the need for better tension estimation techniques) [1]. The nominal tension in a bolt is typically around 70% of yield stress [1]. The tightening order was counter-clockwise: Bolt 4-3-2-1. The bolts are mounted in the same structure and tightening one bolt will therefore affect the other bolts. To try to minimize the effect, the 100 Nm tightening was done in two steps: first tightening all the bolts to 50 Nm and then to 100 Nm. For 150 and 200 Nm, the torque wrench was applied twice on all bolts to try to prevent that the bolt tightened first did not loosen, as the others were tightened.

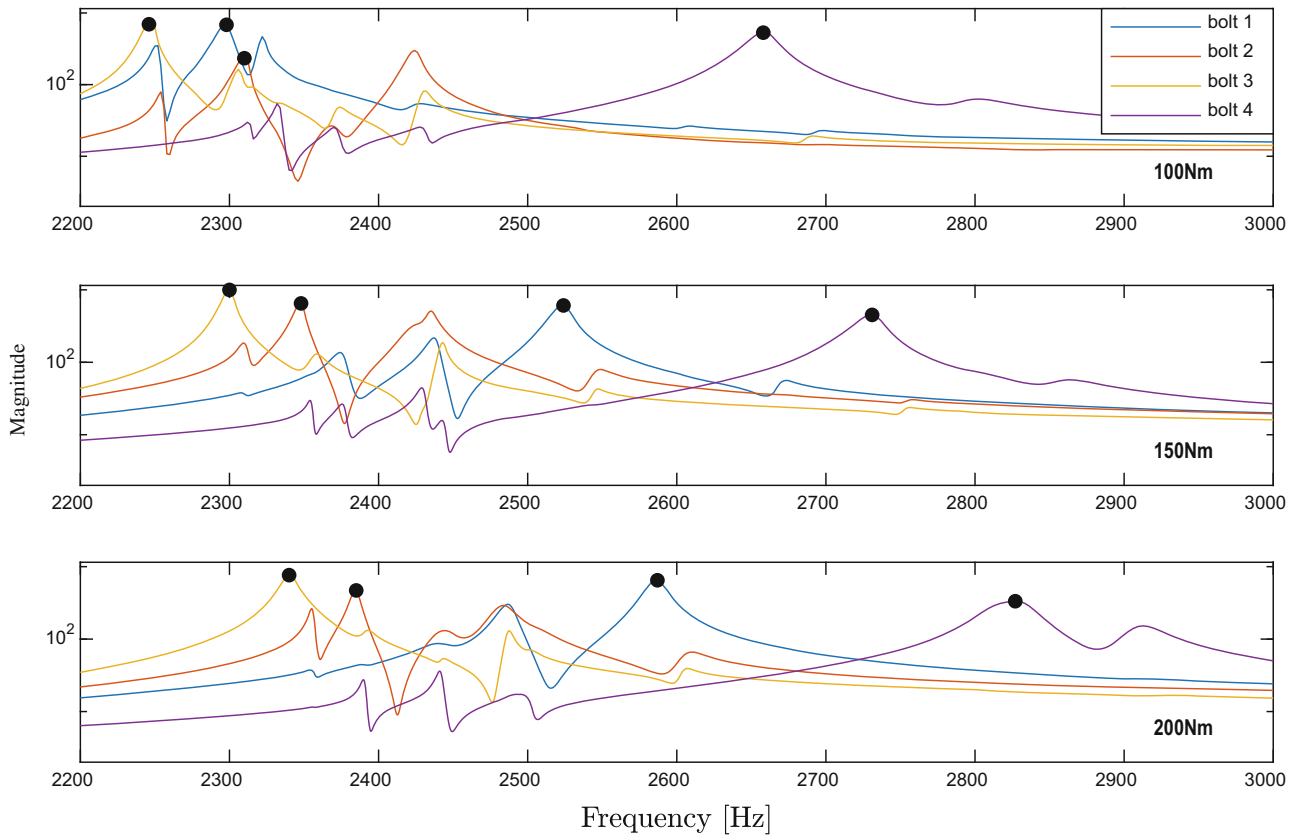


Fig. 3.2 FRF for the four bolts at three torque levels [100, 150, 200] Nm. The identified natural frequencies • (cf. Table 3.1)

Table 3.1 Natural frequencies and damping ratios for the four bolts at the three torque levels

		Bolt 1	Bolt 2	Bolt 3	Bolt 4
1st natural frequency [Hz]	100 Nm	2298	2310	2246	2658
	150 Nm	2524	2348	2300	2731
	200 Nm	2587	2385	2340	2827
Damping ratio [%]	100 Nm	0.18	0.19	0.16	0.42
	150 Nm	0.32	0.16	0.19	0.42
	200 Nm	0.31	0.15	0.29	0.44

3.3 Analysis

Figure 3.2 shows the frequency response function for each of the four bolts at the three levels of torque. Firstly, the figure illustrates how the identification of the natural frequency corresponding to that of the impacted and measured bolt is not trivial, as several peaks appear in one response. The multiple peaks arise from the response of the other bolts, and since the bolts are symmetric, there is a peak for each transverse direction. In this case it is assumed that the frequency with the largest magnitude is that of the impacted bolt (in the impact direction); however, that may not always be the case. Secondly, the frequencies for the four bolts are different within the same torque, despite the fact that the attempt was to tighten all bolts to the same level by the torque wrench. It indicates that the obtained tension is not the same, though the tightening torque nominally is. Table 3.1 shows the identified natural frequencies and damping ratios. The damping ratio is generally small and varies only little between torques, with the exception of Bolt 4, which is more damped than the other bolts and has significantly higher frequencies. A possible explanation is that the bolt was mounted a little off center in the setup, with the shaft of the bolt touching a flange clearance hole (cf. Fig. 3.1c) (which implies a shorter effective length and thus higher stiffness.).

The natural frequencies of all four bolts increase with the torque, but they cannot be modelled with the same parameters in Eq. (3.1) and still give meaningful tension estimations. One of the obstacles is the effective length: it is the only tunable

parameter in Eq. (3.1), why it covers any discrepancy between model and experiment. The frequencies of Bolt 1 and 3 can only fit to Eq. (3.1) if the effective length is unrealistically long. It suggests that the boundary stiffness does not entirely correspond to a clamped-clamped boundary, and the model is not sufficient in that case.

3.4 Conclusion

Experiments has been performed with a real bolted structure to illustrate the challenges when working with real structures and multiple bolts. It was possible to measure and identify the first natural bending frequency of each mounted bolt and determine a damping ratio. However, the simple clamped-clamped beam model cannot in this case sufficiently explain the behaviour of the bolts. The experiments also showed a need to develop the experimental technique and signal processing to better separate the frequency peaks.

Acknowledgments This work is financially supported by the Danish Council for Independent Research, grant DFF-6111-00385.

References

1. Bickford, J.H.: Introduction to the Design and Behavior of Bolted Joints – Non-gasketed Joints, 4th edn. CRC Press, Boca Raton, FL (2007)
2. Joshi, S.G., Pathare, R.G.: Ultrasonic instrument bolt stress. *Ultrasonics*. **22**(6), 270–274 (1984)
3. Nassar, S.A., Veeram, A.B.: Ultrasonic control of fastener tightening using varying wave speed. *J Press Vessel Technol.* **128**(3), 427 (2006)
4. Sah, S.M., Thomsen, J.J., Brøns, M., Fidlin, A., Tcherniak, D.: Estimating bolt tightness using transverse natural frequencies. *J Sound Vib.* **431**, 137–149 (2018). <https://doi.org/10.1016/j.jsv.2018.05.040>
5. Thomsen, J.J.: *Vibrations and Stability: Advanced Theory, Analysis, and Tools*. Springer, New York (2003)

Chapter 4

Spider Configurations for Models with Discrete Iwan Elements



Aabhas Singh, Mitchell Wall, Matthew S. Allen, and Robert J. Kuether

Abstract Lacayo et al. (Mechanical Systems and Signal Processing, 118: 133–157, 2019) recently proposed a fast model updating approach for finite element models that include Iwan models to represent mechanical joints. The joints are defined by using RBE3 averaging constraints or RBAR rigid constraints to tie the contact surface nodes to a single node on each side, and these nodes are then connected with discrete Iwan elements to capture tangential frictional forces that contribute to the nonlinear behavior of the mechanical interfaces between bolted joints. Linear spring elements are used in the remaining directions to capture the joint stiffness. The finite element model is reduced using a Hurty/Craig-Bampton approach such that the physical interface nodes are preserved, and the Quasi-Static Modal Analysis approach is used to quickly predict the effective natural frequency and damping ratio as a function of vibration amplitude for each mode of interest. Model updating is then used to iteratively update the model such that it reproduces the correct natural frequency and damping at each amplitude level of interest. In this paper, Lacayo’s updating approach is applied to the S4 Beam (Singh et al., IMAC XXXVI, 2018) giving special attention to the size and type of the multi-point constraints used to connect the structures, and their effect on the linear and nonlinear modal characteristics.

Keywords Iwan elements · Joints · Quasi-static modal analysis · Nonlinear updating · Model updating

4.1 Introduction

Mechanical structures with complicated geometry can be accurately modeled with finite element techniques if the structure is monolithic and manufactured from a single piece of material. However, even with additive manufacturing, most structures cannot be manufactured as such and therefore mechanical interfaces are introduced between sub-assemblies, which are then jointed with bolts, rivets or welds. These joints introduce uncertainty and significant modeling challenges due to the physics involved with frictional contact. While joints in general can introduce strong nonlinearity, resulting in complicated phenomena such as modal coupling, response at higher harmonics, and even chaos, in many structures of practical interest the nonlinearity is weak and is observed as a change in the effective natural frequency and damping of some of the structure’s vibration modes as vibration amplitude increases.

While commercial finite element analysis or multi-body dynamics software can presumably solve contact problems with friction [1], most practitioners do not appreciate the level to which the mesh must be refined near the interface in order to obtain a predictive model. This was illustrated recently by Jewel et al. [2] who found that tens of hours were required to obtain accurate solutions for the static response of a structure with only one or two joints when the joint was meshed with adequate refinement and the solver settings were tuned to accurately solve the contact problem. It would be extremely expensive to perform dynamic simulations with such a model, and even more so for realistic structures with hundreds of joints. As a result, the majority of dynamic models use relatively coarse meshes and then spider regions of the structure to connect different parts through linear springs, whose stiffnesses can be tuned when the model is updated to correlate with test data.

In some cases, nonlinear hysteretic models are used in place of linear springs when using this whole-joint approach. These models represent the nonlinearity through constitutive equations between the degrees of freedom of a single set of

A. Singh · M. Wall · M. S. Allen (✉)
University of Wisconsin, Madison, WI, USA
e-mail: singh36@wisc.edu; mwall4@wisc.edu; msallen@engr.wisc.edu

R. J. Kuether
Sandia National Laboratories, Albuquerque, NM, USA
e-mail: rjkueth@sandia.gov

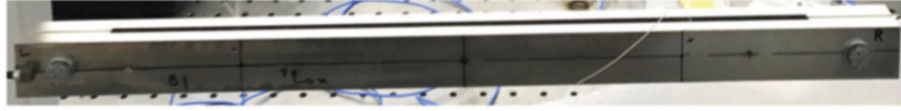


Fig. 4.1 The S4 Beam side view

nodes. When introduced into a reduced order model (ROM), such as a Hurty/Craig-Bampton (HCB) reduced model, they can capture nonlinear behavior while maintaining tractable computational cost. An example of the whole-joint model is the four parameter Iwan joint introduced by Segalman in 2006 [3], which was derived based on analytical solutions to contact problems and empirical data to best capture the energy dissipation observed in joints. These joint models can often be used to capture the amplitude dependent frequency or damping measured in experiments, so long as the joints remain in the micro-slip regime.

The parameters of a whole-joint model such as an Iwan element cannot currently be predicted from first principles, so measurements must be taken and model updating used to update the joint parameters until the model reproduces the measured response. The Hilbert Transform can be used to extract the frequency and damping as a function of amplitude from transient response measurements [4]. Then the recently developed Quasi-Static Modal Analysis (QSMA) approach [5, 6] can be used to quickly compute these quantities. Lacayo et al. [6] recently demonstrated this workflow to update a reduced model of the Brake-Reuss (BRB) beam. Similarly, this paper investigates the model updating procedure and applicability of the four parameter Iwan joint with a new benchmark structure studied at Sandia's Nonlinear Mechanics and Dynamics Institute in 2017 that is shown in Fig. 4.1.

The S4 Beam was studied experimentally by Singh et al. [7], and data from their study is used in this work. First, an HCB model is made for each beam and linear springs are inserted and updated to match the measured linear frequencies. Then, Iwan joints are inserted in place of some of the springs and QSMA is used to compute and iterate on the amplitude dependent damping and frequency in an effort to reproduce the experimentally measured frequency and damping. The experimental structure showed a high degree of nonlinearity in the first shearing mode (Mode 6), so the goal is to use the methodology to calibrate the model to capture this mode. In doing so, prior works have shown that a pareto front is often observed, a case in which the model cannot be updated to capture both the stiffness and damping. This work explores this issue by creating models with various types of spiders, or various ways to define the Multi-Point Constraints (MPCs) used to reduce the contact surfaces to a single node.

4.2 Modeling Approach

4.2.1 Hurty/Craig Bampton Reduction

To incorporate the high geometric detail of the structures of interest, finite element models can quickly become excessively large and computationally expensive. As a result, ROMs are used to approximate the full-order model at a set of reduction nodes between the mechanical interfaces. The approximation requires that these components remain linear and that the only source of nonlinearity within in the joined system is at the contact interface [8]. Although many methods of model reduction exist, this paper will focus on the HCB method as discussed in [9]. The FE discretized equations of motion for an undamped multi-degree of freedom (MDOF) system are given by Eq. 4.1, where \mathbf{M} is the mass matrix, \mathbf{K} is the stiffness matrix, \mathbf{F} is the external forcing, $\mathbf{F}_J(\mathbf{u})$ is the joint force (either linear or nonlinear) and \mathbf{u} is the physical displacement.

$$\mathbf{M}\ddot{\mathbf{u}} + \mathbf{K}\mathbf{u} + \mathbf{F}_J(\mathbf{u}) = \mathbf{F} \quad (4.1)$$

The system can be equivalently written with matrices partitioned between the boundary and interface DOFs as

$$\begin{bmatrix} \mathbf{M}_{ii} & \mathbf{M}_{ib} \\ \mathbf{M}_{bi} & \mathbf{M}_{bb} \end{bmatrix} \begin{Bmatrix} \ddot{\mathbf{u}}_i \\ \ddot{\mathbf{u}}_b \end{Bmatrix} + \begin{bmatrix} \mathbf{K}_{ii} & \mathbf{K}_{ib} \\ \mathbf{K}_{bi} & \mathbf{K}_{bb} \end{bmatrix} \begin{Bmatrix} \mathbf{u}_i \\ \mathbf{u}_b \end{Bmatrix} + \begin{Bmatrix} 0 \\ \mathbf{F}_{J,b}(\mathbf{u}_b) \end{Bmatrix} = \begin{Bmatrix} 0 \\ \mathbf{F}_b \end{Bmatrix} \quad (4.2)$$

where subscripts b and i represent the boundary and interface DOF respectively. Note that only the boundary DOF are assumed to be forced either externally or internally through the joint. Then, a small number of fixed interface modes,¹ Φ , are

¹Fixed interface modes are normal modes obtained by fixing the interface between two subcomponents.

computed and that basis is augmented with constraint modes,² Ψ , as detailed [10] to obtain the HCB transformation matrix in Eq. 4.3.

$$\begin{Bmatrix} \mathbf{u}_i \\ \mathbf{u}_b \end{Bmatrix} = \mathbf{T}^{HCB} \begin{Bmatrix} \mathbf{q}_k \\ \mathbf{u}_b \end{Bmatrix} = \begin{bmatrix} \Phi & \Psi \\ \mathbf{0} & \mathbf{I} \end{bmatrix} \begin{Bmatrix} \mathbf{q}_k \\ \mathbf{u}_b \end{Bmatrix} \quad (4.3)$$

This transformation then reduces the equations of motion to those shown in Eq. 4.4.

$$\left(\mathbf{T}^{HCB}\right)^T \begin{bmatrix} \mathbf{M}_{ii} & \mathbf{M}_{ib} \\ \mathbf{M}_{bi} & \mathbf{M}_{bb} \end{bmatrix} \mathbf{T}^{HCB} \begin{Bmatrix} \ddot{\mathbf{q}}_k \\ \ddot{\mathbf{u}}_b \end{Bmatrix} + \left(\mathbf{T}^{HCB}\right)^T \begin{bmatrix} \mathbf{K}_{ii} & \mathbf{K}_{ib} \\ \mathbf{K}_{bi} & \mathbf{K}_{bb} \end{bmatrix} \mathbf{T}^{HCB} \begin{Bmatrix} \mathbf{q}_k \\ \mathbf{u}_b \end{Bmatrix} + \begin{Bmatrix} \mathbf{0} \\ \mathbf{F}_{J,b}(\mathbf{u}_b) \end{Bmatrix} = \begin{Bmatrix} \mathbf{0} \\ \mathbf{F}_b \end{Bmatrix} \quad (4.4)$$

The ROM can be used to analyze the dynamic response of a structure more efficiently than a dynamic simulation of a full finite element model.

4.2.2 Spidering

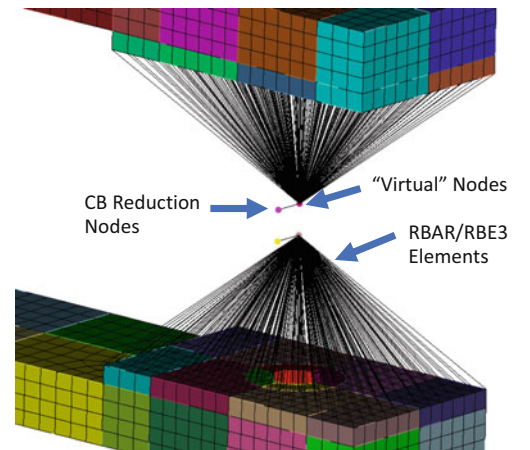
In order to connect the contact surfaces with one-dimensional linear or nonlinear elements, two types of spider elements were used in this work, which shall be referred to as RBAR and RBE3 elements (i.e. using NASTRAN's naming convention). An RBAR element is a rigid beam that rigidly constrains each node to a single node with 6 DOF, whereas an RBE3 is an averaging element that ties the average displacement and rotation of the surface to that of the slave node [11]. Both are types of MPCs (Fig. 4.2). Depicts an example of the MPC spiders on the S4B. Note that separate virtual and HCB reduction nodes had to be created because the implementation of the HCB method within Sandia National Laboratories Sierra Structural Dynamics (Sierra/SD) code doesn't allow a virtual node to be used as an interface node in a HCB model [11]. These are shown expanded for visualization, but in fact they are all coincident.

The spiders reduce an area of nodes to a single point that can be used to connect the surfaces. These spiders can be used to attach linear springs or Iwan elements to capture the linear/nonlinear dynamics of the system.

4.2.3 Whole-Joint Model

One of the most well-developed whole-joint models is Segalman's 4-parameter Iwan element. It was developed as part of a large research effort at Sandia National Laboratories that considered both analytical solutions for contact and empirical evidence that showed that joints exhibit power-law energy dissipation versus force (or vibration amplitude) [3]. An Iwan

Fig. 4.2 Finite element model of the S4B depicting the CS



²Constraint modes are obtained by deflecting a single mode by a unit displacement while fixing the other DOF.

Table 4.1 Definition of Iwan parameters (physical description)

F_s	The force necessary to cause macroslip
K_T	The tangential stiffness of the Jenkins elements (i.e. the joint stiffness when no slip occurs)
χ	The exponent that describes the slope of the energy dissipation curve
β	The ratio of the number of Jenkins elements that slip before micro-slip and then at macroslip

element is simply a collection of slider or Jenkins elements in parallel, in which the slip force³ for each slider is chosen to create an element that exhibits power-law energy dissipation. This approach simplifies joint modeling significantly; typical joint models consider every point in the interface to be independent and governed by several parameters, i.e. the friction coefficient, normal force, etc. . . . When one multiplies these unknowns by the number of contact elements there may be hundreds or thousands of free parameters. Segalman's model recognizes that the net effect of all of these parameters must be to produce power-law dissipation versus vibration amplitude, which is governed by only two of the four parameters in the Iwan model. The other two parameters control the transition to macro-slip when the joint slips completely. Macro-slip is typically not observed in engineered joints if they are tightened properly, except perhaps under extreme loading.

The four parameter Iwan model can be represented by four parameters: F_s , K_T , χ , and β , given in Table 4.1. For an in-depth discussion of the Iwan element, refer to [3].

For the nonlinear analysis, the Iwan joint replaces a linear spring between two spiders, and the corresponding spring constant becomes the K_T parameter of the Iwan element.

4.2.4 Linear Model Updating

Between the single point reduced interfaces, six DOF springs are attached to calibrate the linear natural frequencies of the model to the experimental data. Linear springs are attached with three translational and three rotational spring constants. These constants were varied from 1e4 to 1e10 (lb/in or in-lb/rad) in a Monte Carlo study to minimize the difference between the model and experimental frequencies as shown in Eq. 4.5.

$$\text{Objective Function} = \sum_{i=1}^n \left(\frac{\omega_{\text{model},i} - \omega_{\text{test},i}}{\omega_{\text{test},i}} \right)^2 \quad (4.5)$$

The results of the Monte Carlo updating are presented in Sects. 4.3 and 4.4.

4.2.5 Nonlinear Model Updating

Quasi-Static Modal Analysis (QSMA) was originally proposed by Festjens et al. [5] as a method that replaces a dynamic simulation of a joint with a quasi-static problem that can be solved to estimate the effective natural frequency and damping of a single mode due to the joints in the structure. A quasi-static distributed force is applied that replicates the inertial loading experienced during vibration in that mode and coupling between the vibration modes is ignored. Lacayo and Allen further extended QSMA, developing an even faster algorithm for the case where the joints are represented by Iwan elements [14]. The theory is presented in depth in that paper and for brevity it will not be repeated here other than key points. The HCB model still has the general form given in Eq. 4.1, and the nonlinear joints can be represented through a nonlinear force $\mathbf{F}_J(\mathbf{u})$ as shown in Eq. 4.6.

$$\mathbf{M}\ddot{\mathbf{u}} + \mathbf{K}\mathbf{u} + \mathbf{F}_J(\mathbf{u}) = \mathbf{F} \quad (4.6)$$

QSMA consists of solving the equation above for a static case, i.e. $\ddot{\mathbf{u}} = 0$, where the forcing is $\mathbf{F} = \alpha[\mathbf{M}]\varphi_i$. After solving Eq. 4.6, one obtains the static response, $\mathbf{u}(\alpha)$, from which the modal velocity amplitude, natural frequency, and damping ratio can be written as function of α as shown in Eqs. 12–17 in [14]. The damping ratio is obtained from a load-displacement

³If all sliders have the same friction coefficient then the slip force is defined by the normal force for each slider.

hysteresis curve that is derived using Masing's Rules. Given that all three variables are functions of amplitude, the damping and natural frequency can be plotted in terms of modal velocity amplitude and this is the convention that will be used in this work.

4.3 Application to S4 Beam: Linear Updating

The finite element model used for the S4 Beam is shown in Fig. 4.3. This high-fidelity model incorporates two C shaped beams that are held together by bolts. The bolts were modeled separately and glued to the top and bottom of the beam, but with the contact interfaces between the beams left free to slide relative to each other or to penetrate.

Prior to adding the linear springs or nonlinear Iwan elements, the FEM was reduced by creating a HCB model in which only the spider DOF were retained as interface nodes to create a compact and efficient model for the linear and nonlinear structure. The resulting model had 24 interface DOF (a six DOF virtual node at each of the four interfaces) and 30 fixed interface modes. This reduced the FEM to 54 DOF. The output transfer matrices were saved so that the response could be computed at 22 observation nodes, which were spaced every $2.5l$ along the top and bottom of the beam.

For this paper, the spiders were defined over two different areas: the full interface and a reduced interface, both of which are shown in Fig. 4.4. The full interface consists of all nodes on the flat portion where contact is possible whereas the reduced interface consists of nodes that were found to be in contact in a nonlinear contact simulation that was performed in Abaqus. The result of this contact simulation is also shown in Fig. 4.4. Note that this simulation approximates the surfaces as perfectly smooth and flat, and there is some evidence, as reported in [7], that the surfaces were not truly flat. Nevertheless, these models are in line with the typical approach, considering the information that might be available during the design of a structure. For each of the interface areas, two models were created, one using RBAR elements and one using RBE3s, resulting in a total of four candidate HCB models.

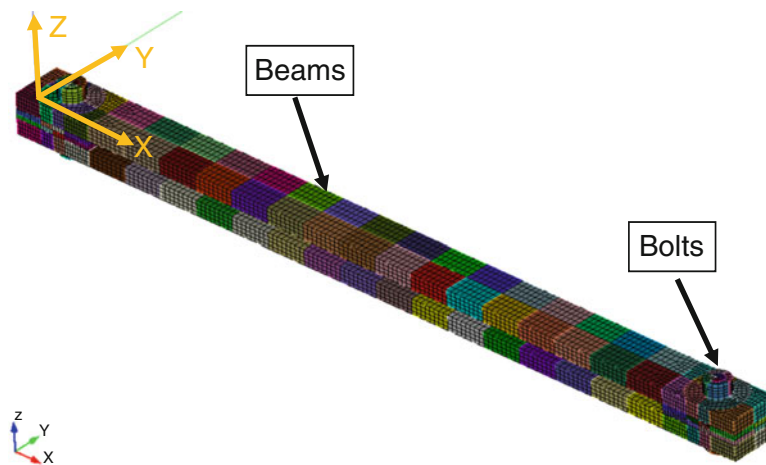


Fig. 4.3 Finite element model of the S4B depicting the coordinate system. The beam is segmented into blocks with nodes corresponding to measurement points

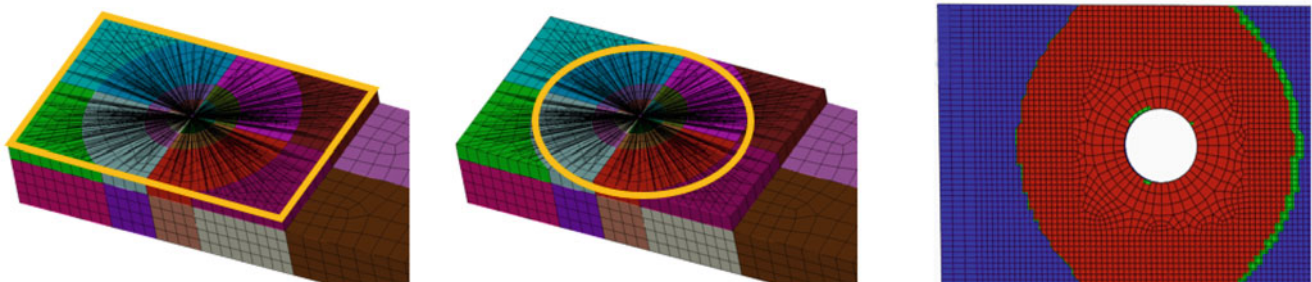


Fig. 4.4 (Left) Full contact area, (Middle) Reduced contact area, (Right) Abaqus Contact Simulation

Table 4.2 Modes of a single beam (half of the S4 assembly) vs. model frequencies

Mode	Description	Experimental frequency (Hz)	Single beam model frequency (Hz)	Percent error (%)
1	1st Bending	177.87	177.29	-0.33
2	2nd Bending	497.84	498.09	0.05
3	1st Stiff Bending	576.00	576.84	0.14
4	2nd Stiff Bending	979.84	988.44	0.88
5	Torsion	1474.67	1471.22	-0.23
6	-	1556.46	-	-
7	Torsion	1585.58	1595.47	0.62

Table 4.3 Single beam material property updating

	Nominal	Optimal
Elastic Modulus	29,000 (ksi)	27,245 (ksi) (-6.05%)
Poisson Ratio	0.29	0.29 (0.00%)

4.3.1 Single Beam Calibration

Prior to calibrating the whole-joint models with linear springs, a finite element model for a single beam was used to calibrate the material properties for steel. Table 4.2 lists the adjusted elastic modulus and Poisson ratio for the single beam and shows the resulting agreement between the experimental natural frequencies and those of the model. All model frequencies were within 1% of the experimental frequencies, with the highest error in a second stiff bending mode. The densities of the model were calibrated by measuring the mass of the experimental beams and dividing by the volume of the FEM to ensure that the FEM has correct mass. The first four elastic bending modes were used to tune the elastic modulus and the fifth and seventh modes (torsion) were used to tune the Poisson ratio. Although, Mode 6 for the single beam was identified by the experimental setup, it was not matched within the FEM and thus was not used in the calibration of the beam. These properties were then used in all subsequent modeling (Table 4.3).

4.3.2 Whole-Joint Spring Calibration


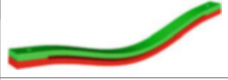
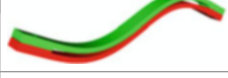



Linear model updating was performed for all four candidate models, and after using a Monte Carlo Simulation to minimize the objective function in Eq. 4.5, a set of values was found for each of the six spring constants. The springs on either end of the S4 beam were assumed to be identical. Tables 4.4 and 4.5 depict the percent error natural frequencies of the assembly after optimization and the spring stiffnesses for each of the cases respectively.

The S4 Beam has several different types of mode shapes, and each is influenced by different springs depending on how the joint is loaded. The mode shapes shown in Table 4.4 can be used to deduce these differences. For example, Modes 1 and 5 involve opening of the joint and hence are most sensitive to the Z-direction translational stiffness, whereas Mode 4 is completely insensitive to the joint stiffness.

While the overall agreement was similar for each candidate model, a few differences are noted between the results obtained using RBE3 and RBAR elements. Most notably, the models with RBE3s were not able to capture Mode 2 as accurately; this mode is sensitive to the axial stiffness of the joint, loading it in the fashion of the lap joints that have been studied in many prior works [6, 12]. The RBE3 models have very high values for T_x and yet they still under-predict the frequency of this mode. On the other hand, the RBE3 models do slightly better at predicting the frequencies of Mode 1, and this might have been expected since the RBE3 doesn't artificially rigidize the interface and Mode 1 would tend to be sensitive to this because it bends the interface region.

In comparing the results with the reduced and full interfaces, one can see that the reduced interface typically required higher spring stiffnesses than the full interface (e.g. consider R_Y in Table 4.5). This result makes sense, as reducing the interface area effectively decreases the stiffness of the joint region, and so the spring constants must be increased to compensate. To get a sense of how sensitive the natural frequencies are to the spring constants found in each case, the constants for the full interface RBAR case were used in the three other models and the natural frequencies were computed. As expected, the natural frequencies of modes 3 and 4 didn't change significantly. However, the models gave frequency errors ranging from 1 to 7% for the other modes. For conciseness, these results are presented in the Appendix.

Table 4.4 Natural frequency errors for each of the candidate models

Mode #	Test [Hz]	Full interface RBAR (%)	Full interface RBE3 (%)	Reduced interface RBAR (%)	Reduced interface RBE3 (%)	Reduced, bonded interface (%)	Mode shape
1	258.0	0.60	0.43	0.63	0.29	3.65	
2	331.7	0.37	-1.65	-0.47	-2.12	-0.48	
3	478.6	-0.78	-0.98	-0.87	-0.99	-0.88	
4	567.7	-2.20	-2.24	-2.22	-2.23	-2.25	
5	708.3	-0.78	-0.05	-0.25	-0.12	3.71	
6	851.5	-0.34	0.33	0.16	0.12	4.26	

The four candidate models contain different spider areas (full vs. reduced) and different constraint elements (RBAR vs. RBE3)

Table 4.5 Linear spring stiffnesses for each candidate model

Spring	Full interface <i>RBAR</i> spring	Full interface <i>RBE3</i> spring	Reduced interface <i>RBAR</i> spring	Reduced interface <i>RBE3</i> spring
T_X [lb/in]	1.00E+08	1.65E+10	6.71E+12	5.04E+11
T_Y [lb/in]	1.43E+12	1.68E+05	1.20E+05	1.43E+09
T_Z [lb/in]	4.61E+03	1.64E+02	1.48E+03	3.00E+04
R_X $\left[\frac{\text{in-lb}}{\text{rad}} \right]$	2.55E+07	8.59E+04	1.25E+06	2.85E+06
R_Y $\left[\frac{\text{in-lb}}{\text{rad}} \right]$	3.66E+05	1.89E+06	6.10E+05	1.04E+07
R_Z $\left[\frac{\text{in-lb}}{\text{rad}} \right]$	2.08E+06	7.72E+11	4.15E+07	1.82E+07

In the end, considering only the ability of the models to capture the linear natural frequencies, the best models contained RBAR elements, as those were able to best capture Mode 2. Overall, the area of influence had a weaker effect than the choice of spider elements (i.e. RBAR vs. RBE3). These effects are somewhat overshadowed by the errors in Modes 3 and 4, which were not sensitive to any spring constants. All modes, apart from Mode 4, were correlated to below one percent error. Mode 4 is the only mode that involves bending in the y-direction (stiff direction), and the six springs all have negligible effect on this mode since the joint is not loaded when the structure bends into this mode. It was thought that this mode may be sensitive to the mass of the bolts or accelerometers, but those were included in the model and their values verified and even then, the agreement shown is the best that could be obtained within the timeline of the project. Furthermore, since this mode is linear, this mode was not one of interest and no further steps were taken to improve correlation and as a result, these spring stiffnesses can be then applied as a basis for QSMA.

The uncertainty of these spring parameters must be evaluated prior to nonlinear updating, i.e. can different sets of parameters produce the same linear natural frequencies? If so, there is additional uncertainty and these parameters must be variable during nonlinear updating. Figure 4.5 shows the objective function for each iteration of the Monte Carlo study versus each of the spring stiffnesses.

This figure illustrates that the objective function, and hence the percent error in each natural frequency, is governed primarily by the Y rotation spring stiffness. The objective function can be small even when the other spring stiffnesses vary by several orders of magnitude, but it is only small if Y is between about $2e5$ and $8e5$ in-lb/rad. In other words, there are no other local minima that might produce similar results. Additionally, the X translation spring and the Z rotation spring must be above about 10^6 in order to obtain good correlation. To further illustrate which parameters are important in linear updating

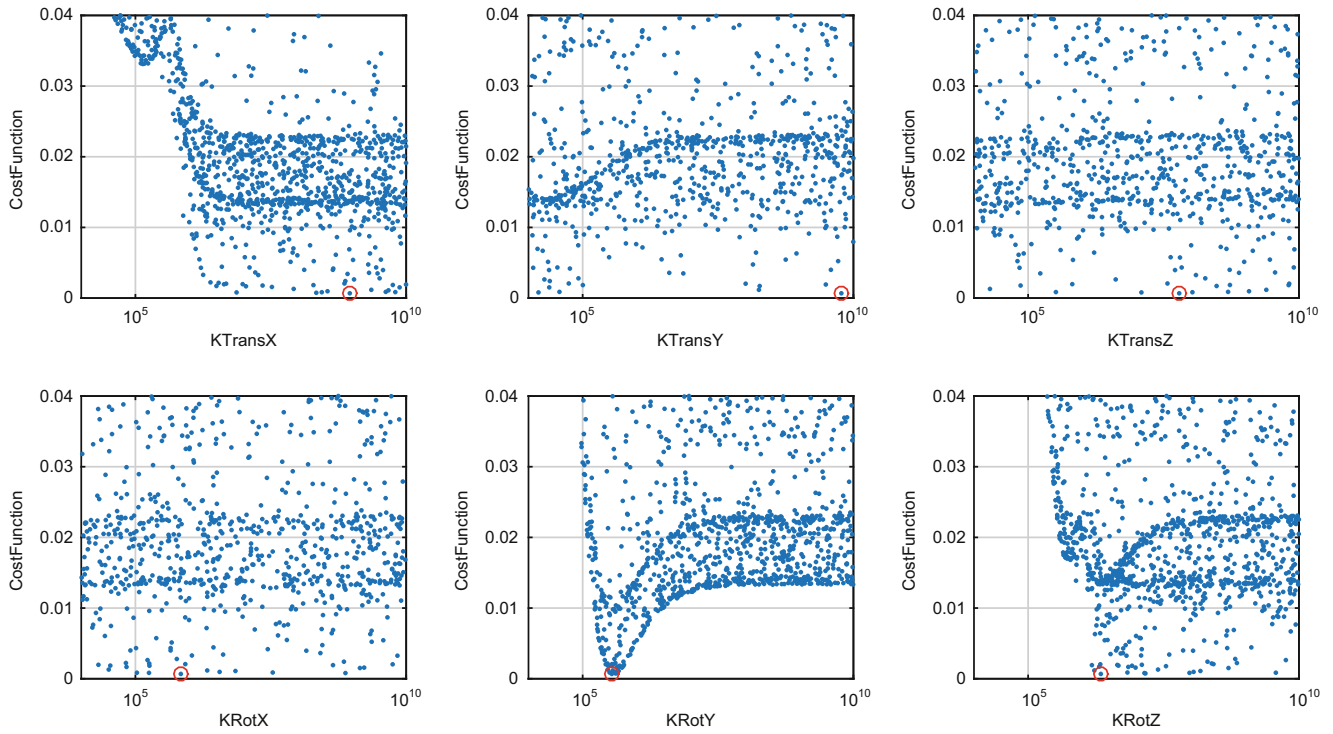


Fig. 4.5 Monte Carlo study depicting the objective function as a function of the spring stiffnesses for the Full Interface RBAR model

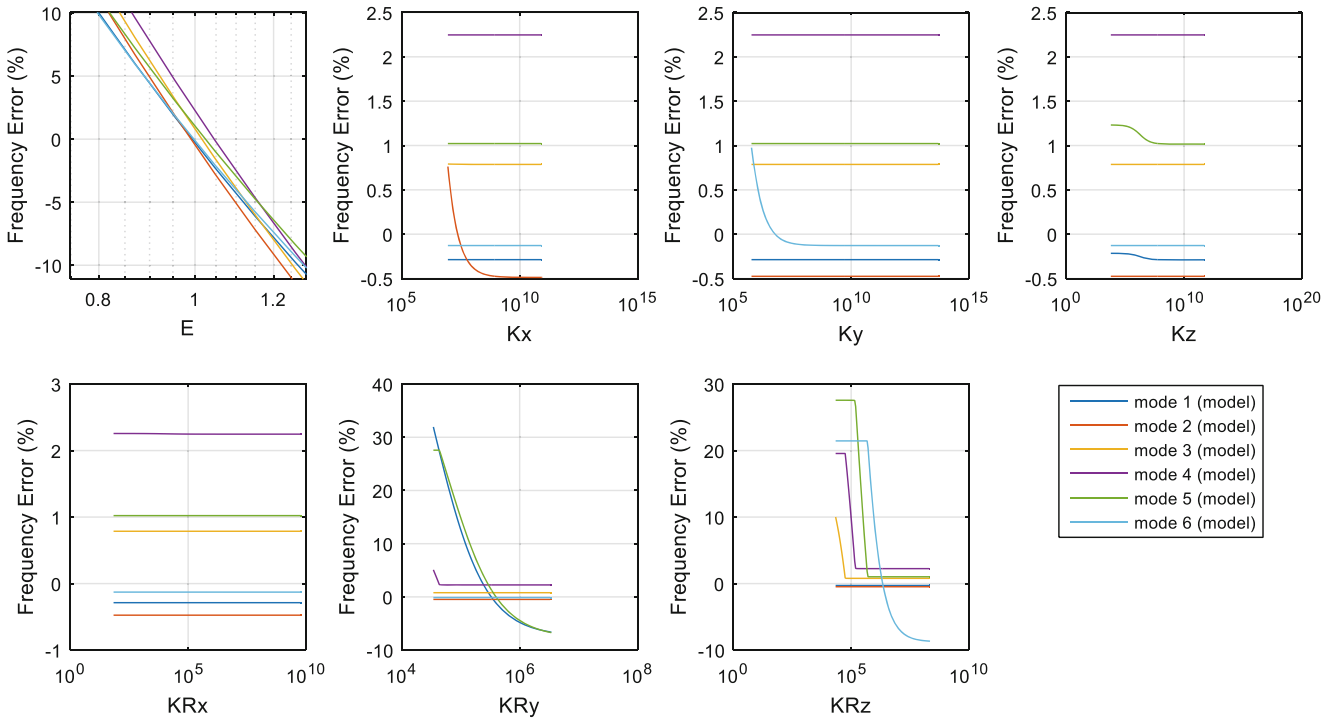


Fig. 4.6 Frequency Error as each spring stiffness is varied separately for the full interface RBAR model

and what ranges for these parameters might be reasonable, Fig. 4.6 depicts the percent error in each natural frequency (compared to the experimental) as each design variable changes relative to the values in Table 4.5.

Although the elastic modulus was established with the single beam study, it was varied in the parameter study to see if the second beam affected the modulus of the system. It changes the frequencies of every mode in approximately the same

way. Furthermore, no value of the X rotation spring stiffness can better correlate the model since the joints and modes do not exercise this rotation within the frequency range of interest. For the other parameters, there exists an optimal value that can improve the correlation of some modes, while not affecting the other modes. Mode 2 is only sensitive to X translation spring stiffness but has a large range of applicable values that result in little change in the other linear frequencies. This allows the freedom to vary the parameter in nonlinear updating in order to improve correlation. For Mode 6, a mode involving shearing of the joint, the Y translation and Z rotation springs can be selected to minimize the error, while marginally affecting the other modes. However, there is little freedom to vary the Z rotation spring stiffness before one begins to reduce the correlation of the fifth and sixth natural frequencies.

4.4 Nonlinear Model Updating

This paper uses the methodology discussed in Sect. 4.2 to identify the Iwan parameters of the whole-joints. In the results that follow, since only Mode 6 was considered, an Iwan element was only placed in the Z rotation direction since that affects the shearing of the joint and is assumed to cause the nonlinearity observed in this mode. The tangential stiffness (K_t) of the joint is chosen as the linear stiffness obtained from the linear model updating, while the other three parameters are free parameters to be calibrated. In order to ensure that a global optimum is obtained, Monte Carlo simulation (MCS) is used to explore the parameter space and find an optimal solution for unknown Iwan parameters. Before running MCS, it is informative to first perform a sweep of some of the parameters to understand what effect they have and to define limits over which to vary the parameters in the MCS. The power law exponent, χ , is measured from the slope of the experimental damping vs. amplitude curve [3, 13], and therefore is treated as a known parameter in this study; however since F_s and β cannot be measured, they are allowed to vary. To illustrate the effect of these parameters, using $\chi = -0.12$ and an arbitrary $\beta = 1$ for both of the joints (in the z-rotation direction), and allowing F_s to vary over a large range, we see the behavior shown in Fig. 4.7. The model predictions are compared with the measurement for Mode 6 at an impact level of 22.5 lbf and a torque levels of 25.1 N-m (18.5 ft-lb).

This preliminary test shows excellent correlation between model and experiment for both damping and frequency trends for $F_s = 0.599$, and gives an idea of how large of a change in F_s might be needed to probe the parameter space. This was repeated for various values of β , revealing that β had a much weaker effect. This provided an initial guess for F_s and established the range of these parameters to use in the Monte Carlo simulation.

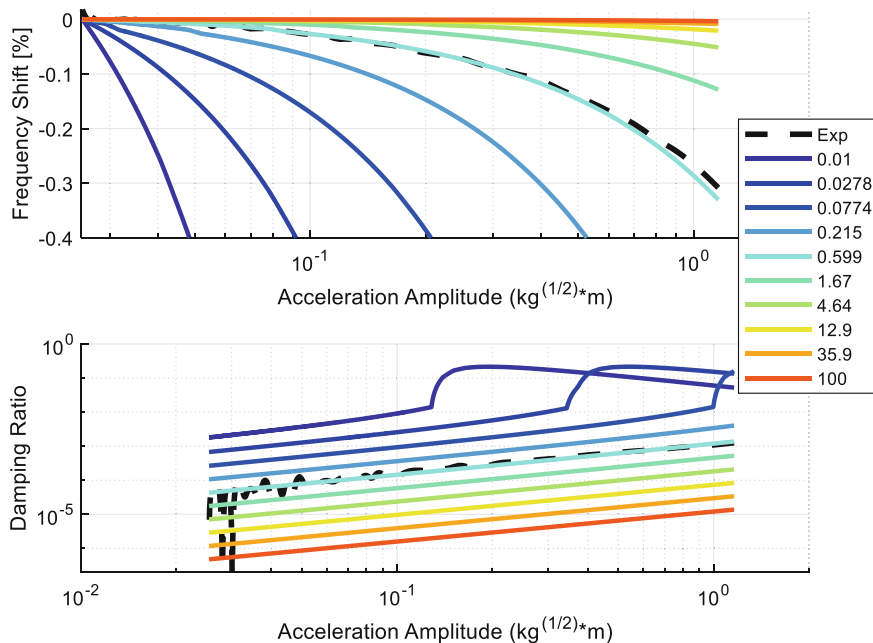


Fig. 4.7 Frequency shift and Damping ratio amplitude dependency for different F_s values for the full interface RBAR model

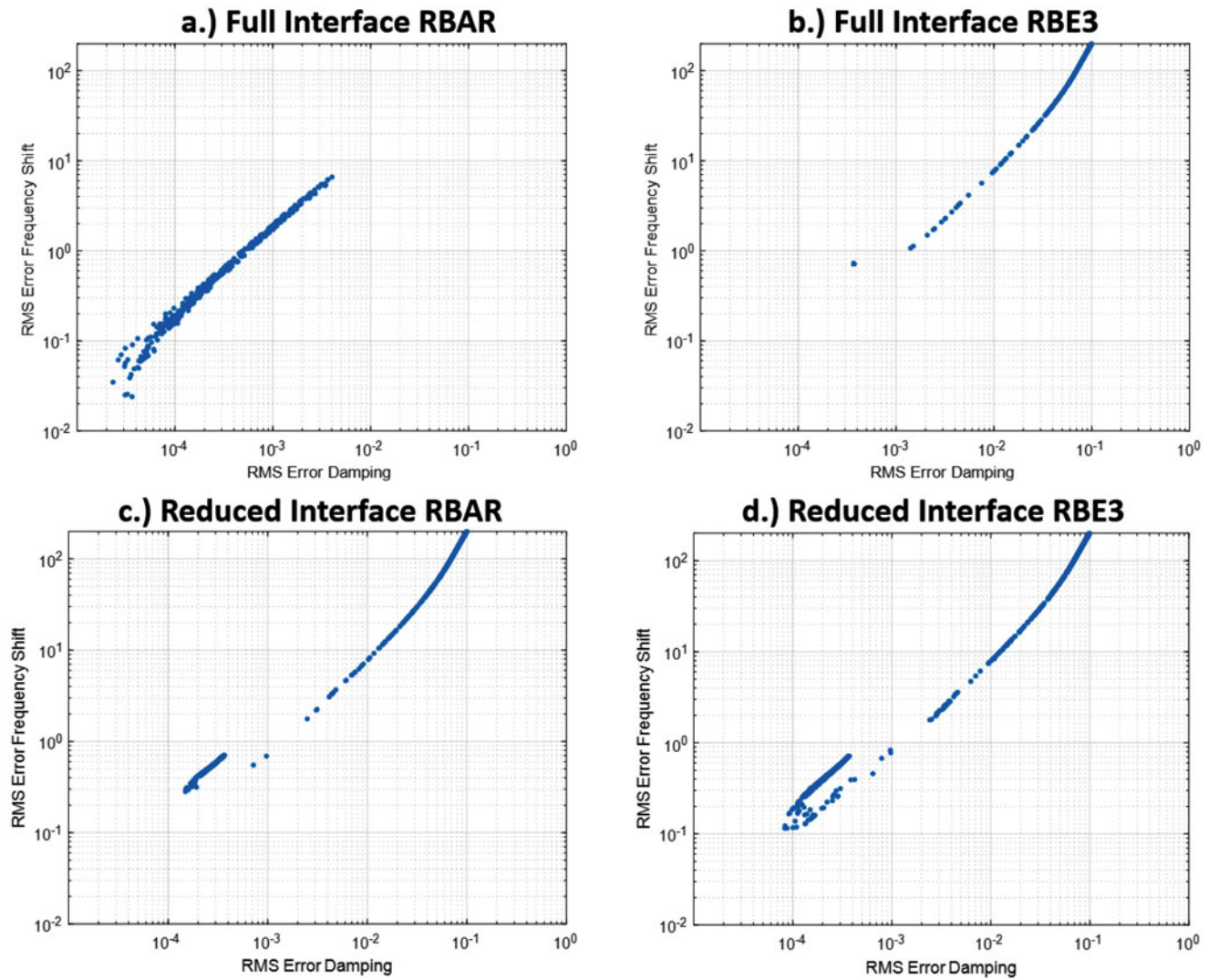


Fig. 4.8 RMS error for frequency shift and damping for the Monte Carlo simulations with (a) Full Interface RBAR, (b) Full Interface RBE3, (c) Reduced Interface RBAR, and (d) Reduced Interface RBE3 models

Table 4.6 Iwan parameters and errors from the Monte Carlo simulations

Interface	F_s	K_t	χ	β	RMS ω_n shift error (Hz)	RMS damping error
Full RBAR	0.4472	2.08e6	-0.1697	2.3521	0.023	2.62e-5
Reduced RBAR	0.0971	4.15e7	-0.1833	7.589e-5	0.274	1.567e-4
Full RBE3	0.0945	7.72e11	-0.112	0.00307	0.716	3.6975e-4
Reduced RBE3	0.1207	1.83e7	-0.1905	0.000951	0.113	1.155e-4

A large Monte Carlo simulation was then conducted for full/reduced interfaces and RBAR/RBE3 joint models where β was uniformly distributed in a logarithmic sense over 6 orders of magnitude, centered on $\beta = 0.1$, and F_s as well over 2 orders of magnitude centered on $F_s = 0.1$, while χ was varied linearly between 0 and -0.2 . Figure 4.8 depicts the root mean square (RMS) error in damping and frequency shift for each iteration of the MCS, and Table 4.6 gives the numerical value of the RMS errors and the Iwan parameters obtained for the optimal solution.

In the study in [14] a Pareto front was observed where one was forced to choose between low error in frequency or damping. In contrast, in this study the RMS error in frequency and damping are found to tend to zero together. However, the minimum errors obtained in each model vary quite significantly, with the Full Interface RBAR model obtaining an order of magnitude smaller error in frequency and damping than the others (see Table 4.6). Furthermore, the maximum errors varied greatly for each of the models, with the Full RBAR model having the least maximum RMS error in both frequency and

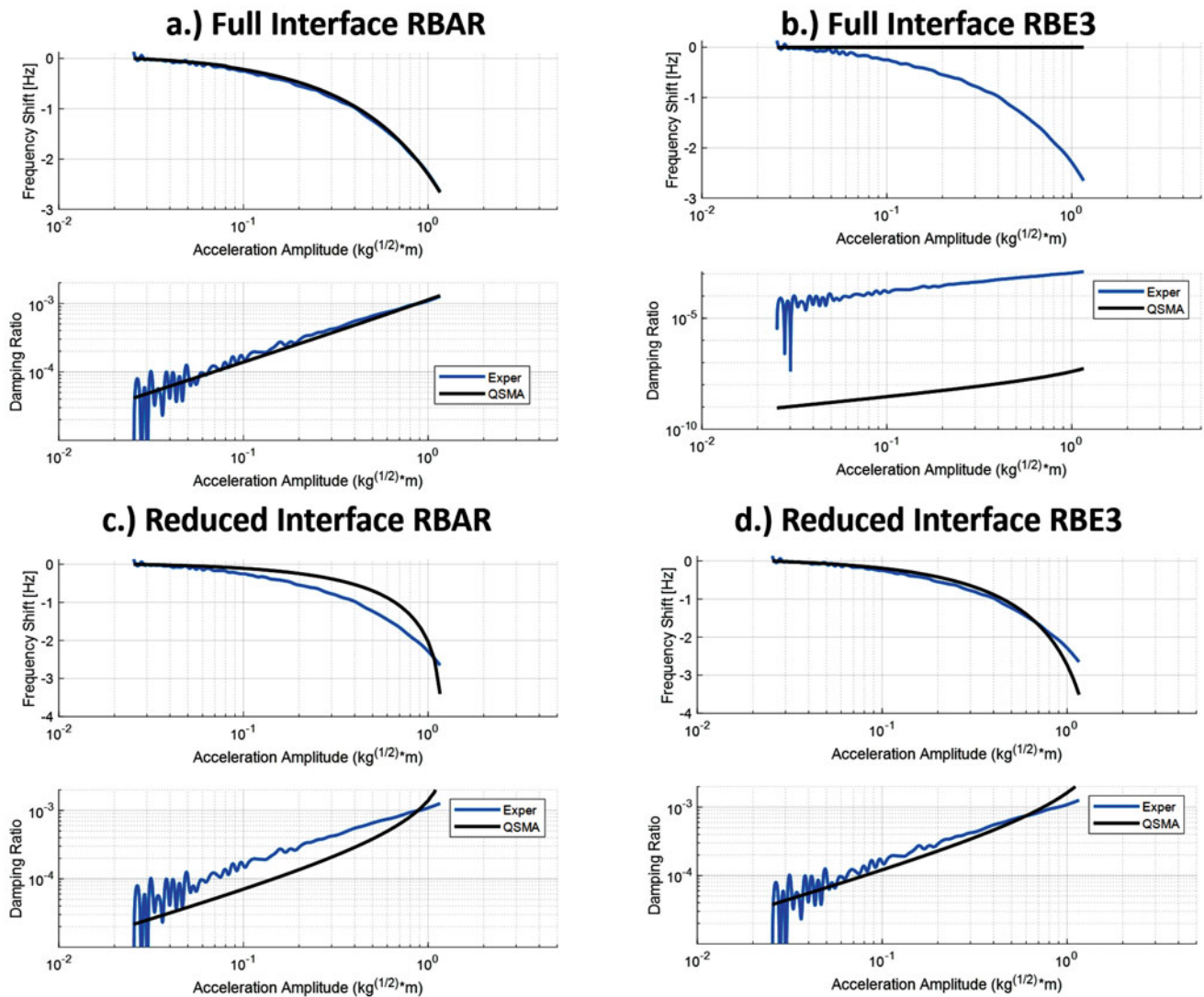


Fig. 4.9 Experimental damping and frequency shift versus QSMA predictions for the candidate models after optimization for (a) Full Interface RBAR, (b) Full Interface RBE3, (c) Reduced Interface RBAR, and (d) Reduced Interface RBE3 models

damping. So, in a sense, each of these models is limited in how well it can fit the measurements for any value of the Iwan parameters, as was the model in [6].

The amplitude dependent frequency and damping for each set of optimal Iwan parameters are shown in Fig. 4.9, where the best solution is obtained by the Full Interface RBAR model and the Full Interface RBE3 model gave very poor results. The optimization routine was able to find reasonably good correlation for the other two models, however, the curve in the damping vs. amplitude plots reveals that the parameters of the Iwan joints are tuned such that the models are nearing macro-slip. As a result, the models do not agree very well at higher amplitudes, and if the model was forced a little too high then it might exhibit macro-slip whereas the measurements show no sign that macro-slip is imminent. Interestingly, this same behavior was observed in the study by Lacayo et al. [6], and was the primary deficiency in their reduced model. The authors have had similar experiences with other models.

In an effort to understand why the Full Interface RBAR model was superior, a parameter study was conducted in the spring stiffness was varied for the Full Interface RBAR model and the resulting frequency and damping curves are shown in Fig. 4.10. In this case study, the optimal F_s , χ and β values were used, and the spring stiffness was varied from 1 to 10,000% of the value obtained from linear updating. This parameter study shows that a small decrease in K_t leads to an increase in damping. However, as K_t is decreased further, the damping begins to decrease. In other words, there is not a single, simple

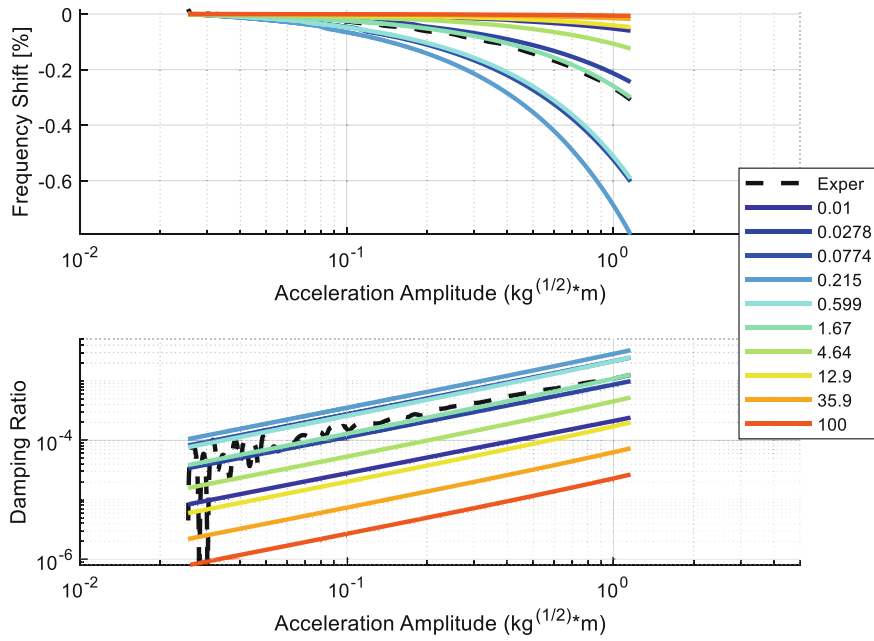


Fig. 4.10 Natural frequency and damping versus amplitude when the Iwan joint stiffness (K_t) is scaled and varied with the other parameters held at their optimal values for the Full Interface RBAR model

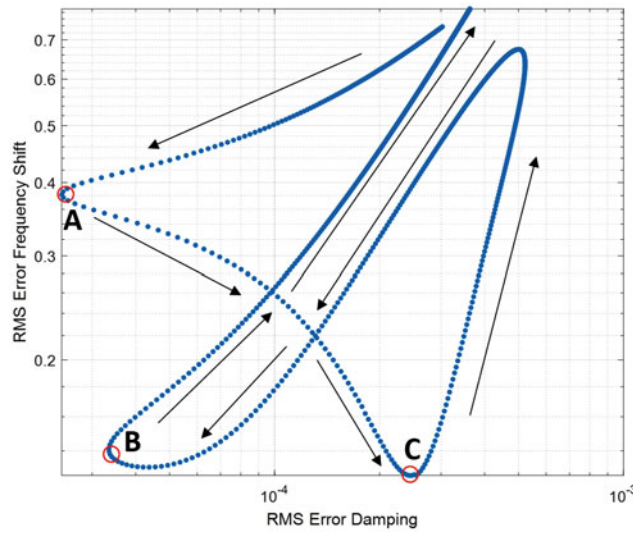


Fig. 4.11 Error plot for the case study where the Iwan joint stiffness (K_t) is varied and F_s is held at the optimal value for the Full Interface RBAR model

rule of thumb governing how K_t will affect the results. To explore this further, QSMA was performed for 1000 values of K_t between 1 and 10,000% and the RMS Error in frequency and damping is shown in Fig. 4.11.

The results in Fig. 4.11 further show that the frequency shift and damping do not depend monotonically on K_t , and that one might observe several Pareto fronts, depending on the range used for K_t . The arrows show the direction of increasing stiffness. A solution in Region A will yield only excellent damping correlation, whereas a solution in region B will yield only excellent frequency correlation. Region B will yield the optimal solution for both damping and frequency. Clearly the quasi-static solution depends strongly on K_t , and yet, for a single spidering method one has little leeway in adjusting the value of K_t , without impairing the model’s ability to capture the linear natural frequencies of the structure. Furthermore, this case study was conducted with an F_s value that correlates to an optimal solution using the nominal K_t , and different results might be obtained for other values of F_s .

It is very interesting that, although these models all produced relatively similar results for linear updating, they produce completely different results for the nonlinear damping. Furthermore, since the reduced interface of the S4B was established through a nonlinear contact simulation, it was expected that the reduced interface would yield the most optimal results; however, this was not the case as the full interface was most accurately able to capture the measured dynamic behavior.

4.5 Conclusion

This paper explored the applicability of linear and nonlinear model updating to a new nonlinear benchmark structure, the S4 Beam. High fidelity models were created using RBAR and RBE3 spidered joints to understand the effects of the area of influence for the joint (i.e. using full and reduced contact interface areas). The viability of the models was studied by evaluating their ability to reproduce the linear natural frequencies of the assembly (i.e. by updating linear springs at the interface) and their ability to capture the amplitude dependent frequency and damping caused by the joints (i.e. by updating the parameters of nonlinear Iwan elements at the interfaces).

The linear updating exercise showed that all models were quite similar, although the models with spiders constructed with rigid bar elements captured the second mode more accurately, and this was significant because the second mode was sensitive to shearing of the joint due to bending of the beam, a phenomenon that is often observed in lap joints. We also explored simply bonding all nodes in the interface that were found to be in contact by a high fidelity simulation of preload, but we did not obtain as good of agreement using that approach as was seen by Fronk et al. [14] although that aspect of this study deserves further investigation.

Quasi-static modal analysis was then used to update the parameters of the nonlinear Iwan elements, using the joint stiffnesses found in the linear updating step. Although the models captured the linear modes quite similarly, they produced a widely varying results for the nonlinear damping and for the change in frequency with vibration amplitude. The model with a full interface spidered with RBAR elements resulted in the excellent correlation between the experimental nonlinear frequency and damping curves, perhaps the best that has been observed in this type of study to date, whereas the model that used the Full Interface with RBE3 spiders gave very poor results. Both of the models using a reduced interface area gave reasonable correlation, but the Iwan joints were forced to the verge of macro-slip and so one would not have high confidence in simulations from these models. The preliminary conclusion of this work is that the method of spidering the interface does indeed matter very much for this type of modeling. Future work will be needed to understand this further and to develop best practices.

Acknowledgments This research was funded by Sandia National Laboratories. Sandia National Laboratories is a multi-mission laboratory managed and operated by National Technology and Engineering Solutions of Sandia, LLC., a wholly owned subsidiary of Honeywell International, Inc., for the U.S. Department of Energy's National Nuclear Security Administration under contract DE-NA-0003525. SAND2018-11919 C.

Appendix: Full Interface RBAR Springs for all Models

In this case study, the full interface RBAR case linear spring stiffnesses were used to attach the four interfaces for the other three models. The tables below depict their results with Table 4.7 showing the linear frequencies and Table 4.8 showing the percent errors.

Table 4.7 Linear frequencies for each model using the spring stiffnesses of the full interface RBAR case

Mode #	Experimental (Hz)	Full interface RBAR (Hz)	Full interface RBE3 (Hz)	Reduced interface RBAR (Hz)	Reduced interface RBE3 (Hz)
1	258.01	259.56	246.92	253.41	244.39
2	331.73	332.97	325.90	329.80	324.34
3	478.55	474.81	473.86	474.40	473.83
4	567.69	555.22	555.00	555.10	555.03
5	708.29	702.80	670.48	687.05	663.68
6	851.54	848.68	812.16	817.12	797.27

Table 4.8 Percent errors for the modes for each model using the spring stiffnesses of the full interface RBAR case

Mode #	Full interface RBAR (%)	Full interface RBE3 (%)	Reduced interface RBAR (%)	Reduced interface RBE3 (%)
1	0.60	-4.30	-1.78	-5.28
2	0.37	-1.76	-0.58	-2.23
3	-0.78	-0.98	-0.87	-0.99
4	-2.20	-2.24	-2.22	-2.23
5	-0.78	-5.34	-3.00	-6.30
6	-0.34	-4.62	-4.04	-6.37

In comparison to the optimal models, the frequencies for Modes 3 and 4 did not change. However, for all other modes, the frequency errors increased significantly though not dramatically

References

1. Abaqus analysis user's guide. Simulia, (2014)
2. Jewell, E., Allen, M.S., Lacayo, R.: Predicting damping of a cantilever beam with a bolted joint using quasi-static modal analysis. In: Presented at the Proceedings of the ASME 2017 International Design Engineering Technical Conference & 13th International Conference on Multibody Systems, Nonlinear Dynamics, and Control IDETC/MSNDC 2017, (2017)
3. Segalman, D.J.: A four-parameter Iwan model for lap-type joints. *J. Appl. Mech.* **72**(5), 752–760 (2005)
4. Feldman, M.: Non-linear system vibration analysis using Hilbert transform–I. Free vibration analysis method 'Freevib'. *Mech. Syst. Signal Process.* **8**(2), 119–127 (1994)
5. Festjens, H., Chevallier, G., Dion, J.-L.: A numerical quasi-static method for the identification of frictional dissipation in bolted joints. In: Presented at the ASME 2012 International Design Engineering Technical Conferences and Computers and Information in Engineering Conference, IDETC/CIE 2012, August 12, 2012–August 12, 2012, 2012, vol. 1, pp. 353–358
6. Lacayo, R.M., Allen, M.S.: Updating structural models containing nonlinear Iwan joints using quasi-static modal analysis. *Mech. Syst. Signal Process.* **2017**, (2017)
7. Singh, A. et al.: Experimental characterization of a new benchmark structure for prediction of damping nonlinearity. In: Presented at the 36th International Modal Analysis Conference (IMAC XXXVI), Orlando, Florida (2018)
8. Kuether, R.J., Coffin, P.B., Brink, A.R.: On Hurty/Craig-Bampton substructuring with interface reduction on contacting surfaces. In: International Design Engineering Technical Conferences, Cleveland, Ohio (2017)
9. Craig, R.R.J., Bampton, M.C.C.: Coupling of substructures for dynamic analysis. *AIAA J.* **6**(7), 1313–1319 (1968)
10. Krattiger, D., et al.: Interface reduction for Hurty/Craig-Bampton substructured models: review and improvement. *Mech. Syst. Signal Process.* **114**, 579–603 (2017)
11. Sierra/SD – Theory manual. Sandia National Laboratories, Albuquerque, NM (2018)
12. Segalman, D.J., et al.: Handbook on Dynamics of Jointed Structures, vol. 87185. Sandia National Laboratories, Albuquerque, NM (2009)
13. Deaner, B.: Modeling the Nonlinear Damping of Jointed Structures Using Modal Models. University of Wisconsin-Madison, Madison, WI (2013)
14. Fronk, M. et al.: Inverse methods for characterization of contact areas in mechanical systems. In: Presented at the 36th International Modal Analysis Conference (IMAC XXXVI) (2018)

Chapter 5

Predicting S4 Beam Joint Nonlinearity Using Quasi-Static Modal Analysis



Mitchell Wall, Matthew S. Allen, and Iman Zare

Abstract Recently, a new algorithm was presented (Festjens et al., *Int J Mech Sci* 75 (2013) 170–177) that allows one to predict the effective natural frequency and damping ratio as a function of amplitude for a structure with bolted joints. This paper applies a variant on that algorithm to a finite element model of the “S4 Beam” (two C-shaped beams bolted together on their ends) and compares the results with the measurements described in (Singh et al., *IMAC* 2019). The algorithm, which is here referred to as Quasi-Static Modal Analysis (QSMA), is applied to a detailed finite element model of the beam in the commercial software package, Abaqus[®]. Coulomb friction is assumed to govern the contact interface. Amplitude dependent damping and natural frequency curves are calculated for the structure and compared to experimental measurement. Several studies are included which explore the solver tolerances and preload values needed to reach agreement with experimental measurements. Additionally, the shape of the actual contact interfaces is measured using a profilometer and fed into the model to quantify the effect of slight curvature in the contact.

Keywords Quasi-static modal analysis · Nonlinearity · FEA · Damping · Natural frequency

5.1 Introduction

The dynamic response of large structures is determined by their inertia, stiffness and damping properties. While mass and stiffness properties can be readily deduced from design data, the prediction of damping properties is difficult, particularly in the case of nonlinear damping caused by friction in joints. Although mechanical joints are integral parts of most engineering structures, their effects on structural dynamics are not yet fully understood. Frequently, our ability to design dynamically loaded structures is hampered by the linear and nonlinear behavior of joints; because the joints aren't well understood, they are represented using simplified elements whose parameters must be identified or tuned through testing. As pointed out by Berger [1], joints are governed by physics at a length scale orders of magnitude smaller than the structures, so analysts are faced with a trade-off in the spatial resolution of the nonlinear degrees of freedom within a joint interface versus the computational effort required to evaluate such a model.

Although bolted joints are needed in almost all structures, they are a large source of uncertainty in the stiffness of the structure, and that stiffness is typically weakly nonlinear due to the joints. Furthermore, dissipation due to frictional slip in joints typically far exceeds the material damping, and the damping tends to nonlinear, increasing by a factor of 2–10 at high vibration amplitudes. Energy dissipation helps to reduce vibration amplitudes and decreases the loads on a structure. Hence, any predictions of the life of a structure may be erroneous if this effect is not taken into account in the design phase. If a more accurate estimate of a structure's capacity for energy dissipation can be computed for different levels of environment loading, then engineers can be better informed so as to create more lightweight designs for aircraft and spacecraft, and perhaps even design joints to exploit this effect to maximize dissipation.

The energy dissipation in joints comes about due to the slip in the contacts between components. In each cycle of vibration, the loads on the joints cause some regions within the contact to slip relative to each other while other regions remain stuck [2]. Depending on the transmitted load, the contact interface is divided into stick and slip zones. Bolted joints exhibit two types of motion during vibration, micro-slip, in which only the outer edges of the contact region experience slip, and macro slip, in which the entire joint experiences slip [3].

M. Wall · M. S. Allen · I. Zare (✉)
Department of Engineering Physics, University of Wisconsin, Madison, WI, USA
e-mail: zareestakhra@wisc.edu

In analyzing the dynamic response of structures, it is common to represent the friction that occurs at contact surfaces by means of Coulomb friction law. As simple Coulomb models with few parameters oversimplify the description of frictional joints, a continuous model with the ability to include micro-slip seems to be advantageous. Moreover, we should consider that the coefficient of friction is also not constant. It depends primarily on the contact surface properties which change during slip, and on the magnitude of the clamping pressure exerted by the bolts. In [4], it is shown that the coefficient of friction decreases with increasing clamping pressure. According to [5], for “practical surfaces” the coefficient of friction decreases approximately linearly with an increasing normal load.

In order to represent micro-slip friction accurately, the finite element model typically requires a mesh of elements having far greater density in the region of the joint compared to the rest of the structure. Computationally, high-fidelity models may be feasible for simple structures that contain one or a few joints, though some simplifications may be employed to speed up the computational time such as model-order reduction of the linear domain away from the joint. Using the best of these approaches, the time required to simulate the response to a dynamic loading is still on the order of hours, and this time would stretch to weeks or months for more realistic structures, such as the turbofan jet engine, which can contain hundreds of bolted joint interfaces.

It can be claimed that when a structure vibrates in the shape of one of its modes, the joints dissipate energy and lose stiffness in a manner that is unique to that mode. When the structure is excited to higher response amplitudes, the loss in stiffness and increase in energy dissipation can be observed experimentally as a decrease in the natural frequency and increase in the damping ratio, respectively, for that mode. Both the natural frequency and the damping can be retrieved for each mode using well-established experimental practices and signal processing techniques. The current techniques for extracting the frequency and damping from a model are based on signal processing of the simulated response. Both the signal processing techniques and dynamic simulations are prohibitively expensive to compute, which devalues their use in a practical model updating routine.

The problem of computational expense in dynamic simulations was overcome by treating the joint as a quasi-static subcomponent in an otherwise linear, dynamic global model. The groundwork for this solution was laid out in a paper by Festjens et al. [6]. They used the fact that the contact nonlinearity is governed by micro and meso-scale parameters (geometry, roughness, local pressure, etc.) and as a result cannot be included in a macro-size model of a whole structure because of the computational cost. They investigate the idea of using the normal modes of the linearized structure as boundary conditions on a detailed model reduced to the joints only. It has been observed that after a number of repetitive loading cycles, the response of a bolted joint structure may lead to a stabilized state called limit cycle and in the case of an assumed linear structure, this limit cycle is known [6]. Moreover, we can consider the fact that under linear assumption the use of modal coordinates is useful to reduce the size of vibrational problems [7, 8].

After a few modifications to the approach of Festjen et al. [6], Allen et al. [9] later presented a fast and efficient computational method for extracting the amplitude-dependent modal properties from a finite element model and applied it to structures where the joints were modeled as discrete Iwan elements. The new method termed “quasi-static modal analysis” (QSMA), estimates the effective modal natural frequency and damping from a single, static deflection in response to a monotonically-increasing load distributed over the entire structure in the shape of one of its modes. Masing’s rules are then applied to the force-deflection relationship to quantify the amount of energy dissipated and stiffness lost in the all joints when the structure vibrates in the mode of interest [9]. For Allen et al.’s work, Iwan elements were selected since they can capture microslip efficiently, which gives rise to energy dissipation and nonlinear behavior of the joint. However, Iwan elements require four parameter inputs that must be tuned based upon prototype results since they cannot be deduced from first principles but must be measured experimentally [10, 11].

The method of QSMA dramatically reduces the computational effort because the change in the natural frequency and damping of each mode with modal amplitude can be completely determined from a single set of quasi-static, monotonic loading cases. This is in stark contrast to a dynamic simulation, where the free-response history must be computed until its amplitude decays to the smallest level of interest [12]. This advancement prompted Jewell, Allen & Lacayo [13] to apply this technique to detailed finite element models that included nonlinear contact between the bolted interfaces using a commercial software package. While their results showed that such an analysis is feasible, they struggled to obtain accurate results and noted that, once the structure had been meshed with adequate fidelity to capture micro-slip, the computational cost was very significant even to perform a single static analysis.

Zare and Allen [14, 15] explored a more computationally efficient alternative that follows the work of Ahn and Barber [16, 17] in that they combined QSMA with a static reduction technique, retaining only those DOF on the interface. They implemented the QSMA for structures where the joint is modeled in detail, using a block Gauss-Seidel algorithm to solve the nonlinear contact problem in Matlab.

In this paper, a model of the S4 Beam is constructed in the commercial finite element analysis software package, Abaqus[®], with a Coulomb friction law assigned at the interfaces between the parts. The model is loaded using Quasi-Static

Modal analysis, and the nonlinear frequency and damping behavior is predicted and compared to experimentally measured properties for a single mode. Several parameters are studied in order to create an efficient and accurate model, such as, convergence tolerances, preload, and small perturbations in the flatness of the surface.

5.2 Background

The Quasi-Static Modal Analysis method implemented in this paper is similar to one developed by Festjens, Chevallier, and Dion, [6], where the effective natural frequency and modal damping ratios are extracted from a nonlinear static analysis. This is done by imposing a quasi-static load to the model that would excite only a single mode of the linearized structure. Allen and Lacayo, [12] recently elaborated on this method, and used the modal load-displacement curves to construct a hysteresis curve from which the effective natural frequency and damping were estimated. The method is reviewed below.

Suppose that a preload is applied to a structure such that the members come into contact in at least one location. The equation of motion for the coupled structure(s) can then be written as

$$\mathbf{M}\ddot{\mathbf{x}} + \mathbf{C}\dot{\mathbf{x}} + \mathbf{K}\mathbf{x} + \mathbf{f}_J(\mathbf{x}, \boldsymbol{\theta}) = \mathbf{f}_{ext}(t) \quad (5.1)$$

where \mathbf{M} , \mathbf{C} , and \mathbf{K} are, respectively, the mass, damping, and stiffness matrices of the system, and \mathbf{x} , $\dot{\mathbf{x}}$, and $\ddot{\mathbf{x}}$ are the displacement, velocity, and acceleration vectors, respectively. The vector \mathbf{f}_J represents the internal forces due to a joint model containing internal sliders, and $\boldsymbol{\theta}$ is a vector that captures the state (slip or stick) of each slider element.

At low vibration amplitudes, the joints can be replaced with springs equivalent to the preloaded stiffness of the joints (when vibratory loads are small),

$$\mathbf{K}_T = \left. \frac{\partial \mathbf{f}_J}{\partial \mathbf{x}} \right|_{\mathbf{x}=\mathbf{0}} \quad (5.2)$$

where $\mathbf{x} = \mathbf{0}$ corresponds to the preloaded state and an eigenvalue problem can be solved to estimate the mass-normalized mode shapes, φ_r , of the structure.

$$([\mathbf{K} + \mathbf{K}_T] - \lambda \mathbf{M}) \varphi_r = 0 \quad (5.3)$$

At this point, Festjens et al. [6] divided Eq. (5.1) into a nonlinear domain near the joint and a linear domain away from the joint. While their approach could reduce the computational burden, it does require a specialized implementation and introduces additional uncertainties as there is an additional convergence tolerance governing the connection between the linear and nonlinear domains. Allen and Lacayo instead let the nonlinear domain encompass the entire structure, in which case only one nonlinear static analysis is needed per mode. Using their approach [9], the following quasi-static problem is solved.

$$\mathbf{K}\mathbf{x} + \mathbf{f}_J(\mathbf{x}, \boldsymbol{\theta}) = \mathbf{M}\varphi_r \alpha \quad (5.4)$$

where α is a scalar which sets the load amplitude. A finite element package returns the response, $\mathbf{x}(\alpha)$, which can then be mapped onto the r th mode using:

$$q_r(\alpha) = \boldsymbol{\varphi}_r^T \mathbf{M}\mathbf{x}(\alpha) \quad (5.5)$$

Then using Masing's rules, the force (and similarly displacement) over a full loading cycle can be estimated yielding the following forward and reverse curves. To avoid the computing of a complete cycle for each energy E , it is assumed that the hysteretic behaviors of the joint follow the Masing rules [18]. This description simplifies the modeling of hysteretic behaviors if a full cycle in a force-amplitude hysteresis can be extrapolated from the initial loading (so-called backbone curve) [6].

$$\begin{aligned} \hat{f}_1(q_r) &= 2f_r \left(\frac{q_r + q_r(\alpha)}{2} \right) - \alpha \\ \hat{f}_2(q_r) &= \alpha - 2f_r \left(\frac{q_r(\alpha) - q_r}{2} \right) \end{aligned} \quad (5.6)$$

The secant of this hysteresis curve is then used to estimate the instantaneous natural frequency of the mode in question:

$$\omega_r(\alpha) = \sqrt{\frac{\alpha}{q_r(\alpha)}} \quad (5.7)$$

The energy dissipated for each vibration cycle is the area under the hysteresis curve,

$$\begin{aligned} D_r(\alpha) &= \int_{-q_r(\alpha)}^{q_r(\alpha)} (\hat{f}_1(q_r) - \hat{f}_2(q_r)) dq_r \\ &= 2 \int_{-q_r(\alpha)}^{q_r(\alpha)} \left(f_r\left(\frac{q_r+q_r(\alpha)}{2}\right) + f_r\left(\frac{q_r(\alpha)-q_r}{2}\right) - \alpha \right) dq_r \end{aligned} \quad (5.8)$$

The integral above is readily evaluated using the trapezoid rule and then the effective damping ratio $\zeta_r(\alpha)$ may be determined by analogy with a linear system [9, 12].

$$\zeta_r(\alpha) = \frac{D(\alpha)}{2\pi(q_r(\alpha)\omega_r(\alpha))^2} \quad (5.9)$$

5.3 Model Creation

The structure of interest was named the S4 Beam in [19] and is shown in Fig. 5.1. The structure consists of two C shaped beams, bolted together at each end. Impact testing was used to determine the amplitude dependent natural frequency and damping for the first several modes of the structure. These experimental measurements will be compared with the amplitude dependent natural frequency and damping predicted from various finite element models. A detailed explanation of experimental setup for the S4 Beam can be found in [19].

The finite element model used in this work borrowed from the 3D model created in [20], using the parameters, mesh density, etc. previously found to give reasonable results. For the S4 Beam, the mesh density very close to the hole (where slip does not occur until very large loads), as well as along the long beam section was coarsened to reduce computational cost. Tangential contact behavior was defined using the penalty method and $\mu = 0.6$. Normal behavior was also defined with the penalty method with “Hard” contact defined as the pressure-overclosure parameter and a contact stiffness scale factor of 10. The tangential penalty constraint was set to 10^{-6} , which is much tighter than the default, as was found to be necessary in [20]. The model consists of 386,666 user defined nodes and 348,818 user defined elements. All models with reported solve times were solved on a computer with 16 Gb of memory allocated to the solution (of 32 Gb) and a 3.6 GHz, Intel® i7-7700 processor using 2 cores (of the 8 available; Windows® treats the four physical cores as 8). The time to solve on two cores was only about 5–10% less than the time required to solve on a single core, so additional parallelization was not explored.

The simulation was split into two steps. First, the preload was applied in a nonlinear loading step in Abaqus and the modes shapes were found using a linear modal analysis. Inertial relief was applied so that preload analysis could be performed on this free-free model. The inertia relief process was apparently not perfect, so an additional rotational constraint was applied

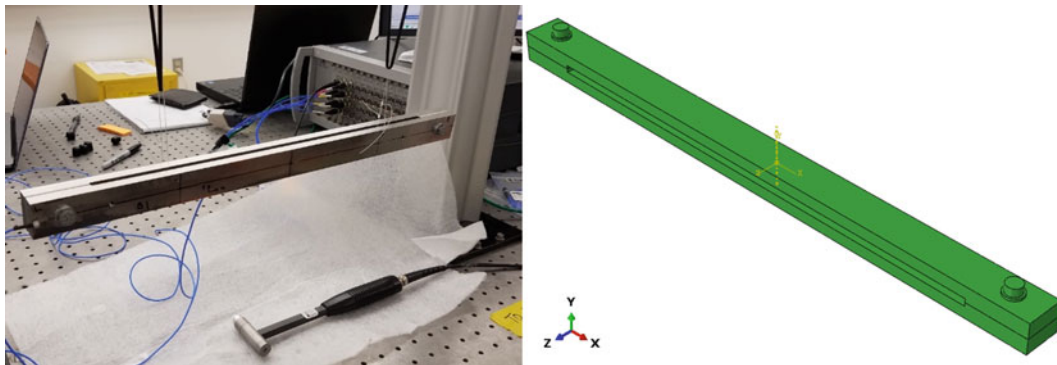


Fig. 5.1 (left) Photo of a test on the S4 Beam. (right) S4 Beam finite element model

to the center of the beams during the preload process. The nodes in contact were then welded together (according to Abaqus's default practice) for the modal analysis. Then the quasi static modal force was calculated in Matlab[®] as described in Eq. (5.4) and applied to the structure. The amplitude of the deflection will be referred to in units of thicknesses of the beam (i.e. in some models, the beam was deflected to 0.01 thicknesses of the beam). Inertial relief was also applied in the quasi static loading step, but in this step no additional constraints were needed.

5.3.1 Bolt Preload

Bolt preload was an important parameter to experiment with because it has a high level of uncertainty. In some cases, the preload of the bolt can vary $\pm 35\%$ for a given torque level [21]. For the $5/16 \times 24$ grade 8 bolts used in the actual experiment, one can calculate the nominal preload force using a torque-tension relationship. In this case the Motosh Eq. (5.10) was used [22].

$$T = F \left(\frac{P}{2\pi} + \frac{\mu_r r_t}{\cos(\beta)} + \mu_n r_n \right) \quad (5.10)$$

Here in Eq. (5.10), the torque applied to the bolt, T , is related to the preload force, F , and multiplied by three terms. The first accounts for the load transferred due to the pitch of the threads, P . The second term is the frictional loss incurred in the threads, where μ_r is the coefficient of friction between the threads on the bolt and the nut, r_t is the effective diameter of the threads, and β is the half angle of the threads. The last term is the friction loss incurred between the head of the bolt and the clamped member, where μ_n is the coefficient of friction between the head and the clamped member and r_n is the effective diameter of the bolt head contact region. For the purposes of these calculations, a coefficient of friction of 0.1 was used for both the threads and head of the bolt, though these numbers can vary widely. A load of 21.2 Kn. is calculated after using data from [23] to estimate the effective diameter of the threads and bolt head contact region. This load will be varied to quantify its effect on the amplitude dependent natural frequency and damping of the S4 Beam model.

5.3.2 Modeling Surface Curvature

The joint interfaces on the beams were machined to be nominally flat, but measurements revealed that there was some curvature, and so an effort was made to quantify the curvature of the contact patches and apply this to the FEM. In later sections of this paper, the measured surface contours of the beams were applied to the nodal positions on the joint interface to model a more realistic contact. In order to do this, surface contour plots were constructed which showed that the nominally flat surfaces had variation of up to $150 \mu\text{m}$ in height. Two measurements were used to extrapolate a surface contour. Referring to the coordinate system in Fig. 5.1, one measurement was parallel with the X axis and one with the Y, both measurements intersecting at the center of the bolt hole. Each measurement was fit with a sixth degree polynomial. All fits had R^2 values of greater than 0.97. The curvatures in x - and y - were then added together to approximate the surface of the real machined components. For brevity, the measurements and the fits to them were not included here, but plots of the surface profiles are shown in Fig. 5.2. The titles above each surface indicate which interface they belong to, referring to the coordinate system in Fig. 5.1. For example, the $+Y$, $+X$ surface is on the top beam on the right joint in Fig. 5.1, and $-Y$, $-X$ would be on the bottom beam on the left.

It should be clearly stated that the surface contours for this model are gross approximations meant only to roughly represent the variations in the surfaces. This method is likely a poor approximation of the edges of the interfaces, but as is shown later, the edges of the interface likely play no role in the contact of the joint.

5.4 Test Cases

In seeking to obtain agreement between the simulations and the experimental measurements, three main variables were studied. The solver tolerances were varied to find the settings that provide the minimum solve time without sacrificing significant accuracy. The preload of the bolt was varied over multiples of the nominal value to span any uncertainty in the

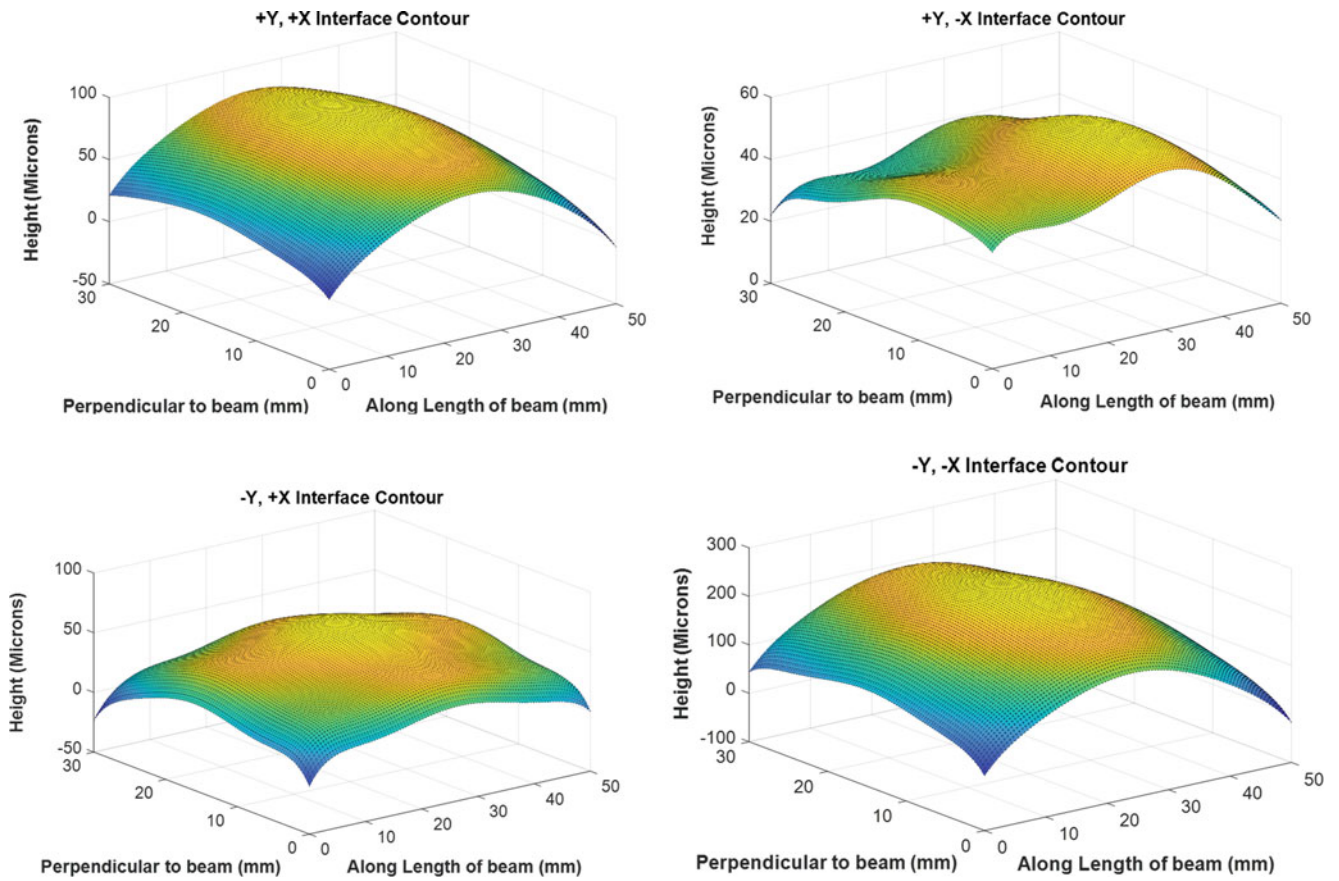


Fig. 5.2 Polynomial fit to surface shapes for the S4 Beam. Four surfaces were fit, two on each end of the beam. The bolt hole, which is not shown in these fits, would be at the center of each of the surfaces shown

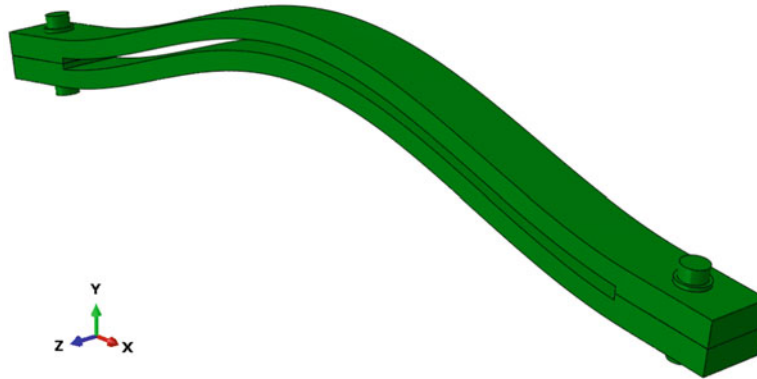


Fig. 5.3 Mode 2 of the S4 Beam

actual load. And finally, the measured surface contour was applied to the interfaces of the FEM to quantify the effect of small but realistic changes to the interface geometry on the results. In all models, mode 2 of the S4 Beam was used. Figure 5.3 shows that mode 2 is first order, in phase bending mode with motion in the Y-direction.

Table 5.1 Solve time (hours) and convergence tolerances for the 0.02 thickness deflection models

	C_n^α				
R_n^α	–	2×10^{-2}	2×10^{-1}	2×10^0	2×10^1
	5×10^{-3}	N/A	N/A	N/A	–
	5×10^{-2}	10.59	12.57	10.96	–
	5×10^{-1}	5.82	5.07	5.60	–
	5×10^0	–	–	–	5.77

N/A signifies models that did not solve after 2+ days

5.4.1 Solver Tolerances

When initially creating many of the models in this paper, convergence issues caused the models to take several days to solve and many did not converge at all. Computation time was also a topic of discussion in [20], which was a precursor to this work. Hence, the solver settings were explored further to seek to speed up the computations. The default solution control parameters defined in Abaqus/Standard are designed to provide reasonably optimal solution of complex problems involving combinations of nonlinearities as well as efficient solution of simpler nonlinear cases. However, the most important consideration in the choice of the control parameters is that any solution accepted as “converged” is a close approximation to the exact solution of the nonlinear equations. We can reset many solution control parameters related to the tolerances used for field equations. If we define less strict convergence criteria, results may be accepted as converged when they are still close to the exact solution of the system but with the less computational cost. In this research, we’ve changed two parameters to get the accurate results in the acceptable amount of time, C_n^α and R_n^α . Most nonlinear engineering calculations will be sufficiently accurate if the error in the residuals is less than ($\frac{1}{2}\%$). Therefore, Abaqus/Standard normally uses:

$$r_{max}^\alpha \leq R_n^\alpha \overline{q^\alpha} \quad (5.11)$$

where r_{max}^α is the largest residual in the balance equation for field α and $\overline{q^\alpha}$ is the instantaneous magnitude of the force for field α at time t , averaged over the entire model.

If this inequality is satisfied, convergence is accepted if the largest correction to the solution, C_{max}^α , is also small compared to the largest incremental change in the corresponding solution variable Δu_{max}^α ,

$$C_{max}^\alpha \leq C_n^\alpha \Delta u_{max}^\alpha \quad (5.12)$$

where C_{max}^α is the largest correction to any nodal variable of type of α provided by the current Newton iteration.

The defaults are 5×10^{-3} for R_n^α and 2×10^{-2} for C_n^α . Table 5.1 presents the results of a study in which, the convergence tolerances were varied and the corresponding solve times are listed. The solve time is given in what Abaqus defines as “wall clock time”, or the total time from the submission of the job to the completion.

The solve time was improved drastically by increasing R_n^α . Up until 100 times the default value the solve time decreased. Furthermore, while the results of these computations are not shown here for brevity, each of these solutions gave damping curves that differed by less than 0.001% after the results were processed with QSMA. Since R_n^α governs the largest residual in the model, it appears that, if the value is set too low, the solver spends a lot of time iterating between solutions when it is already very close to being converged. Relaxing this tolerance still gives good results while also decreasing the solve time drastically. To obtain the maximum speed while keeping the tolerance as small as possible, $R_n^\alpha = 5 \times 10^{-1}$, or 100× the default, was used for many of the subsequent models in this paper.

5.4.2 Bolt Preload

In the experimental measurements presented in [19], the only parameter measured to estimate the preload of the bolt was the torque applied. Given the possible variation in the coefficient of friction as well as the nonlinear dependence of coefficient of friction with pressure [4], a large uncertainty is assumed in the experimental bolt preload. The max tensile strength of a grade 8, 5/16" × 24 bolt is about 31.1 kN loads up to 84.4 kN were tested in order to span all possible loads and then exceeding the possible loads to show the level of preload needed to obtain correlation with experimental results. In total, factors of 0.5×,

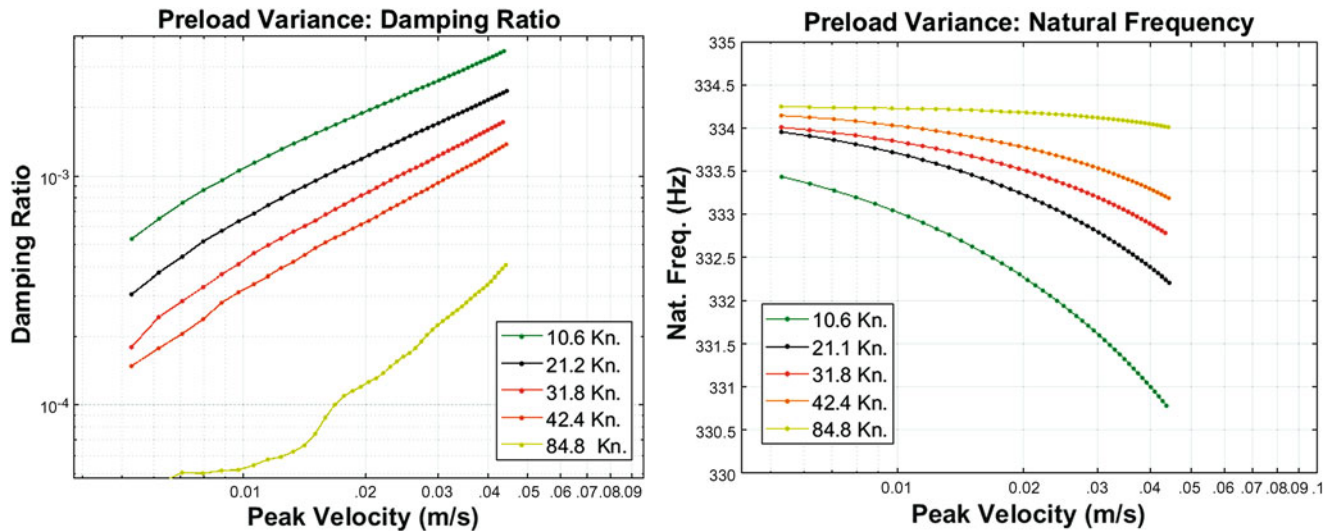


Fig. 5.4 Variation in effective damping ratio and natural frequency with preload

Table 5.2 Solve time vs. preload

Preload (kN.)	Solve times (hours, abaqus wall clock time)
42.4	21.8
31.8	7.46
21.2 (nominal)	9.97
10.6	18.92

1.5 \times , 2 \times and 4 \times were applied to the nominal bolt preload of 21.2 kN calculated in Sect. 5.3. The general trend is that as the preload increases the structures natural frequency is increased and the damping is decreased (Fig. 5.4).

It is also worth noting that the preload in the joint, and thus the amount of microslip occurring, had a substantial effect on solve time. For all the load cases within the physical limitation of the bolt, the solve time decreases with preload, likely because of reduced slip and hence the reduced computational cost of modeling slip. Though once very high loads were reached, computational costs increased rapidly. Solve times for the preceding models are shown in Table 5.2: Solve time vs. preload. The solve times are from models with $R_n^\alpha = 5 \times 10^{-2}$ and $C_n^\alpha = 2 \times 10^{-1}$.

These results are not presented for the purpose of showing which model is most efficient, but only to show that there are other factors that may slow down or speed up the simulation depending on the preload in the model. At the moment, the exact causes of the spike in computational cost at very high preloads are unclear, but it is likely that the high preload is causing some nodes to jump in and out of contact, and the solver tolerances may be too strict to address this in an efficient manner.

Figure 5.5 compares the damping from these simulations with the measured damping. When damping values are compared to experimental data, extremely high preloads are needed to bring the model near agreement with the experimental damping measurements. The cyan curve shows the raw experimental data, and the subsequent curves account for the lack of material, and any other form of linear damping in the FEM by subtracting a constant value from the experimental curve. Values of $\zeta = 0.0004$, $\zeta = 0.0006$ and $\zeta = 0.0008$ are shown to span reasonable values for damping in the linear regime, although the curve using, $\zeta = 0.0006$ produces damping from the joint that most closely obeys a power-law model [24] and is thought to be the most reliable curve.

When frequency shift is plotted in Fig. 5.6, it is clear that the 84.8 kN model agrees with the experimental data the best. But, the frequency shift is very small so all models show reasonably good agreement with experimental measurements, always being less than 1% away from the measured values.

The results in Fig. 5.6 (left) show that the linear natural frequency predicted by the model is 0.9% higher than the measured value. In [19], additional correlation was performed to reach agreement in the experimental modes of one half of the S4 Beam and a FEM. The elastic modulus needed to be shifted -6.05% in order to bring the FEM into agreement, which may explain why some discrepancy in the experimental measurements and the FEM presented here. The effect of the contact on the linear natural frequencies was studied in detail in [23] and so was not investigated further here.

In summary, this preload study shows that the model does show promise in predicting the nonlinear stiffness and damping of this structure, as the simulations and experiments agree in a qualitative sense and are not so far off quantitatively. However,

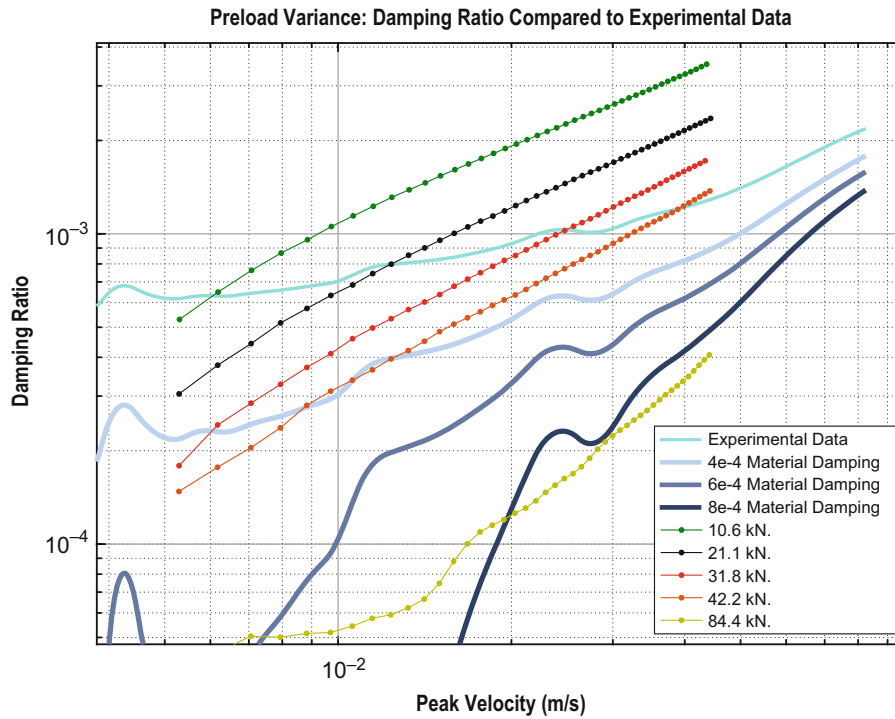


Fig. 5.5 Preload variance and experimental data with various values of material damping

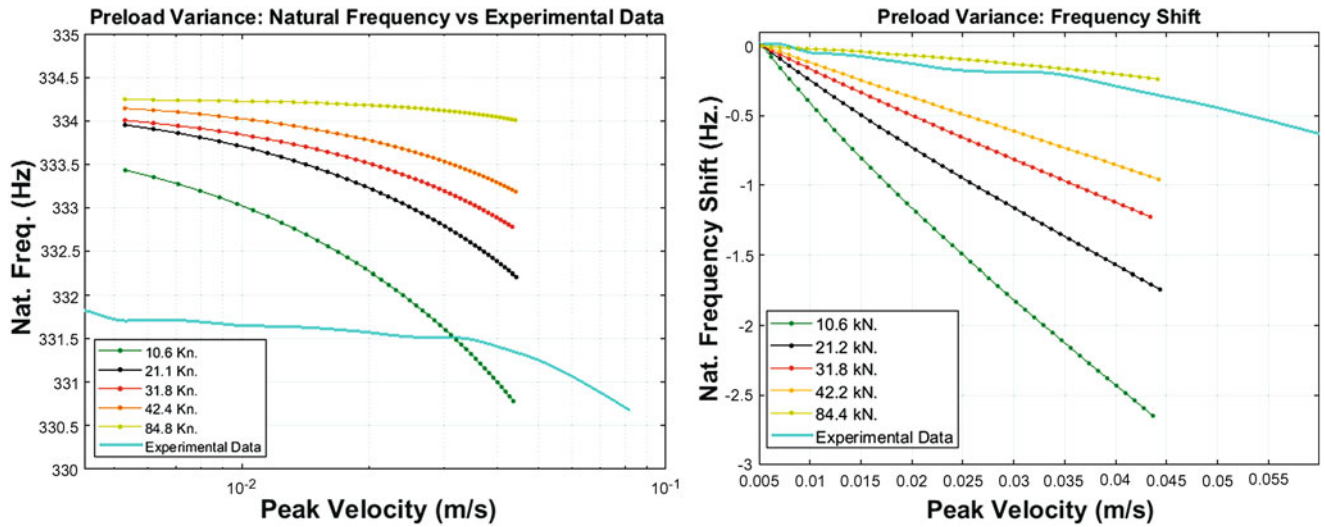


Fig. 5.6 (left) Preload variance and experimental natural frequency curves, (right) frequency shift for preload variance models and experimental data

it is not possible to bring both natural frequency and damping ratio into agreement without an impossibly high preload on the bolt, so clearly there are unmodeled physics that must be addressed.

5.4.3 Surface Contours

To explore the issues previously stated, efforts were made to model the geometry of the contact more precisely. Efforts were made in [19] to use profilometry to measure the actual roughness and topography of the surface. While the measurements

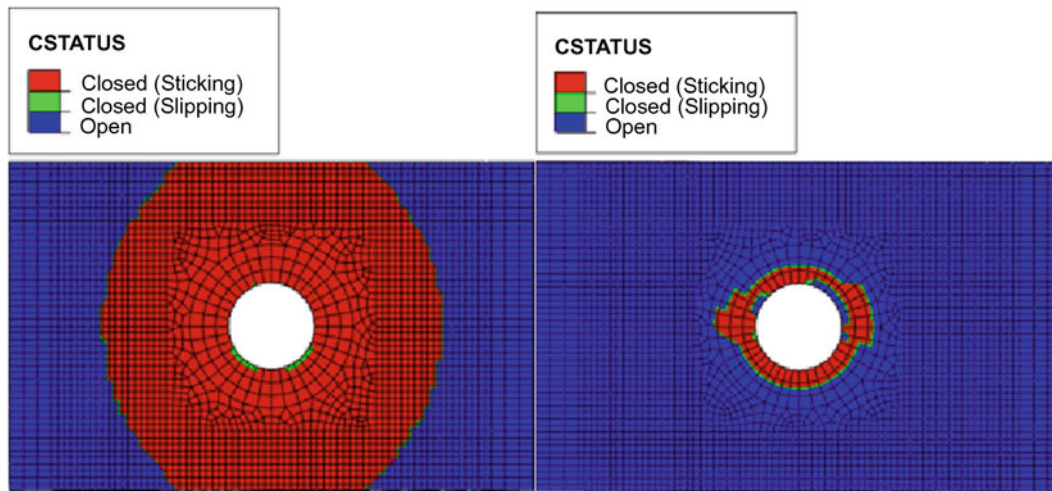


Fig. 5.7 Abaqus CSTATUS for flat surface vs. modified surface, 21.2 Kn. Preload

were not completely successful (the sample was too large for the machine used), sizeable variation in the surface shape was discovered. As described in Sect. 5.3, these measurements were used to estimate the profile of the surface and this was applied to the FEM by moving the nodes in the contact surface. The models were then solved as described previously under various preloads. First, the contact patch will be examined. The CSTATUS output from Abaqus is shown in Fig. 5.7. This shows the regions in the model that are either stuck, slipping or not in contact. On the left is the contact patch for the flat FEM interface and on the right is the contact patch for the modified interface.

There is a dramatic difference in the area of the closed, or in contact, region of the joint. As a result, the maximum pressure in the contact (and in the micro-slip regime on the edges) will be much higher than was found for the nominally flat model. Figure 5.8 quantifies, the maximum contact pressure (CPRESS) of the flat interface (left) which is $17\times$ smaller than the pressure on the modified interface (right).

In the preload study in Sect. 5.4.2, very high pressures in the interface of the joint took the longest to solve. This is reinforced here as Abaqus took eight steps to solve the nonlinear preload step for the flat interface and twenty steps to solve the same step for the modified surface. Unfortunately, because the mesh was coarsened near the hole to speed up computation for the flat-on-flat model, there is now not a sufficient mesh density to accurately resolve the microslip in the joint. A finer mesh would need to be made to study this curved interface in more depth, and thus, the model with the modified interfaces will not be explored beyond a brief preload study. The damping and frequency vs. velocity plots are compared to experimental data below.

The models with the modified surface geometry show lower damping for the same preload, which makes sense considering that the contact pressure is higher. As was the trend for the bolt preload cases in Sect. 5.4.2, a higher contact pressure decreased the damping in the joint. The lack of mesh quality is apparent in the damping curve, which now deviates from power-law behavior at low amplitudes, presumably because the mesh density is insufficient to resolve the small changes that occur near the periphery of the contact.

As was the case previously, the simulations do not agree with the experimentally measured damping curves for reasonable values of the contact pressure, as shown in Fig. 5.9. However, the mesh of the model is known to be insufficient, and so the fact that the model moves in the correct direction (towards lower damping for the higher preload) is promising (Fig. 5.10).

The effect for the natural frequency is now reversed and the linear natural frequency moved closer to the experimental measurement with higher pressure. This is expected since the curved interfaces now provide a Hertzian-type contact [16] where the area of the contact increases with increasing pressure.

Comparing the natural frequency versus amplitude to the experimental data, we see that the models with a modified surface have natural frequencies that are about 4 Hz lower. Hence, the uncertainty in the interface shape may account for the shift in linear frequencies that was noted earlier; it is probable that the modulus value used is accurate but the surface geometry accounts for any discrepancies in the linear natural frequencies.

One reason for the modified surfaces not bringing the model into better agreement, especially for natural frequency, could be due to poor quality measurements or the method for extrapolating a surface as described in Sect. 5.3. The biggest takeaway from these surface measurements is that implementing a realistic surface contour for a nominally flat model can produce a

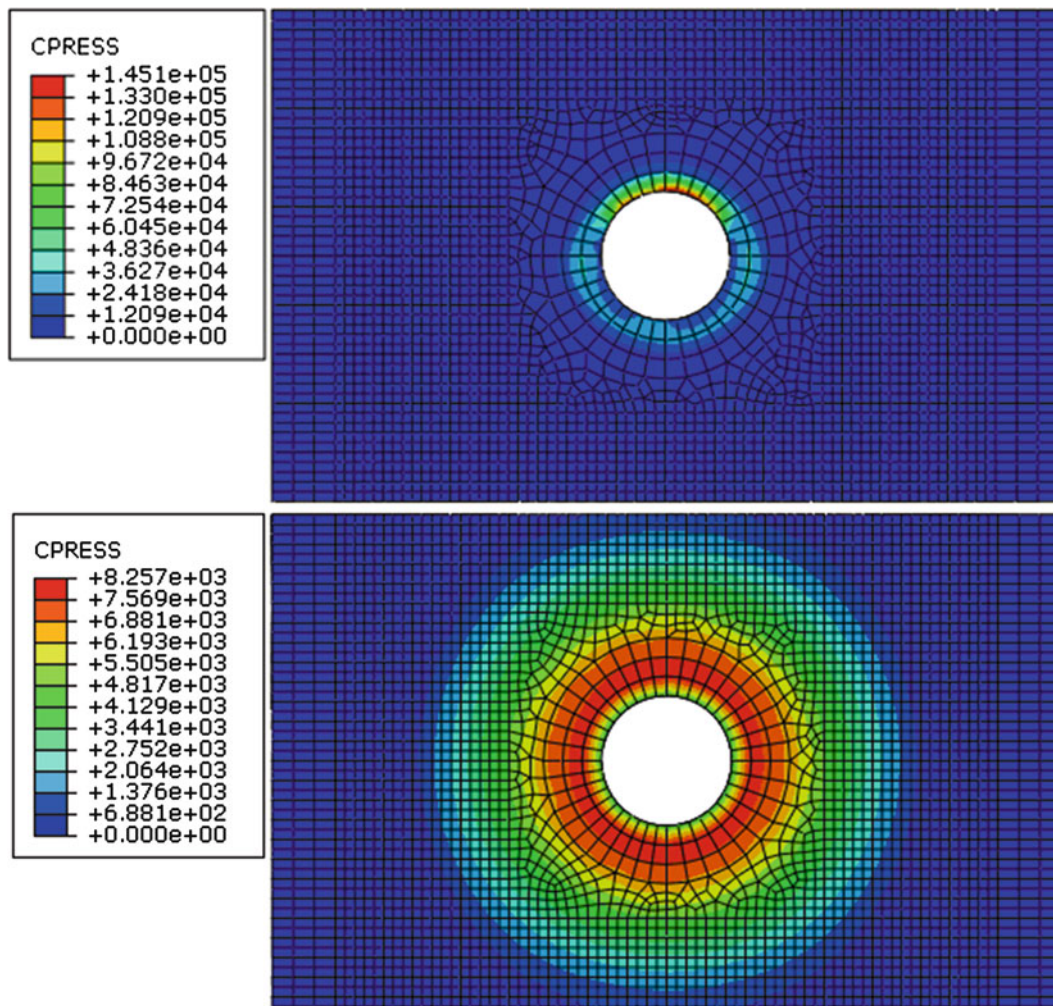


Fig. 5.8 Abaqus CPRESS for flat surface vs. modified surface, 21.2 Kn. Preload

large effect on the dynamic behavior of the joint. It seems that it will be critical to measure the surface geometry accurately and implement that into the FEM in order to obtain better agreement in the future..

5.5 Conclusion and Future Work

This paper has summarized work to date using quasi-static modal analysis (QSMA) to model nonlinearity due to micro-slip in the S4 Beam. The current model included about one million DOF, and was the smallest model that our group has been able to create to date that can capture the joints in this structure in sufficient detail while coarsening the mesh as much as possible in areas away from the joints. While it is probably possible to create a smaller model with additional effort, models of approximately this size are probably typical when seeking to describe a few joints in detail. With this model, a dynamic transient analysis would take several decades (extrapolating based on the static analysis that was performed), while with QSMA one could estimate the behavior that would be observed when the structure vibrates in one mode in 5–24 h. While it was not demonstrated here, from the QSMA results one could reconstruct the dynamic transient response until the amplitude of vibration decayed to zero (tens of seconds in the experimental results).

This work sought to use QSMA to correlate the FEM with measurements from a real S4 Beam, in which impact testing was used to extract the nonlinear behavior of a few modes. Our initial results were qualitatively very similar to the measurements, though they over-predicted damping by about an order of magnitude. A parameter study revealed that the model could not be made to agree with the measurements unless the preload was increased far beyond the yield strength of the bolts. An

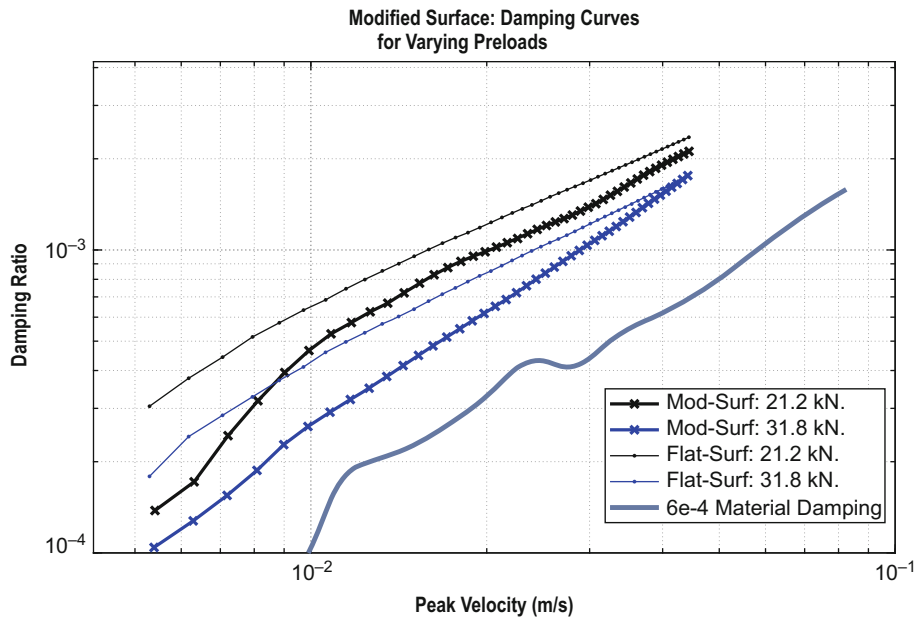


Fig. 5.9 Damping plots for modified surface and flat surface. $1\times$ and $1.5\times$ nominal preloads shown against experimental data with $\zeta = 0.0006$ linear damping subtracted off

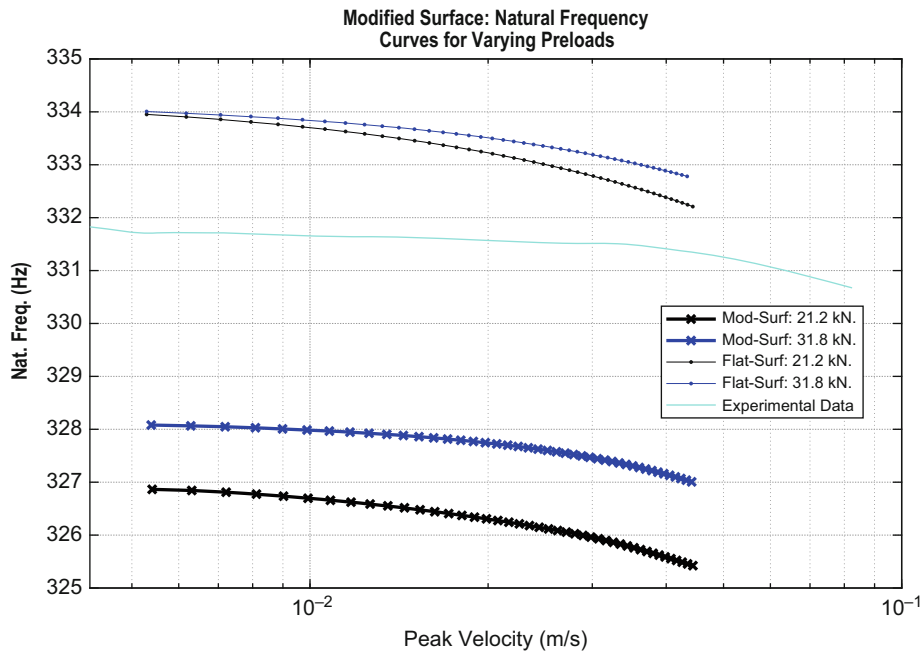


Fig. 5.10 Natural frequency plots for modified surface and flat surface. $1\times$ and $1.5\times$ nominal preloads shown against experimental data

investigation was performed in which the actual measured curvature of the surfaces was included in the FEM, and even though the geometry only changed by a few thousandths of an inch (about $100\ \mu\text{m}$), this had a dramatic effect on the contact pressure and on the predicted stiffness and damping of the joint. We expect that even larger differences may be observed once the FE mesh is refined to better capture the surface geometry. In retrospect, considering how stiff the structure/material is, it should have been obvious that the surface geometry would be so important.

Moving forward, the existing FE Model is also being used to compute the nonlinearity in the sixth mode of vibration, which was experimentally found to exhibit even stronger nonlinearity than Mode 2, which is the mode that was studied here. New profilometry measurements will be obtained and used to create a new FE model, whose mesh will be tailored to capture

the contact more accurately. It is hoped that these investigations will reveal whether it is possible to reproduce the physics (amplitude dependent damping and stiffness) that were observed in these experiments using an FE model with Coulomb friction at the interface. If this succeeds, this tool could be used to predict the effect that joints in a wide variety of structures have on the dynamics of their fundamental modes of vibration.

Acknowledgments This material is based in part upon work supported by the National Science Foundation under Grant Number CMMI-1561810. Any opinions, findings, and conclusions or recommendations expressed in this material are those of the author(s) and do not necessarily reflect the views of the National Science Foundation.

References

1. Berger, E.: Friction modeling for dynamic system simulation. *Appl. Mech. Rev.* **55**(6), 535 (2002)
2. Hartwigsen, C.J., Song, Y., McFarland, D.M., Bergman, L.A., Vakakis, A.F.: Experimental study of non-linear effects in a typical shear lap joint configuration. *J. Sound Vib.* **277**(1–2), 327–351 (2004)
3. Groper, M.: Microslip and macroslip in bolted joints. *Exp. Mech.* **25**(2), 171–174 (1985)
4. Groper, M., Hemmye, J.: The dissipation of energy in high strength friction grip bolted joints. In: Presented at the SESA Spring Conference, Cleveland, OH (1983)
5. Hartwigsen, K.: *Handbook of Lubrication, II—Theory and Design, Part I—Friction*. CRC Press Inc., Boca Raton, FL (1983)
6. Festjens, H., Chevallier, G., Dion, J.: A numerical tool for the design of assembled structures under dynamic loads. *Int. J. Mech. Sci.* **75**, 170–177 (2013)
7. Quinn, D.D.: Modal analysis of jointed structures. *J. Sound Vib.* **331**(1), 81–93 (2012)
8. Segalman, D.J.: A Modal Approach to Modeling Spatially Distributed Vibration Energy Dissipation. Sandia National Laboratories, Albuquerque, NM.” SAND2010-4763, 993326, Aug (2010)
9. Allen, M.S., Lacayo, R.M., Brake, M.R.: Quasi-Static Modal Analysis Based on Implicit Condensation for Structures with Nonlinear Joints, p. 15. Sandia National Laboratories, Albuquerque, NM (2016)
10. Segalman, D.J.: A four-parameter Iwan model for lap-type joints. *J. Appl. Mech.* **72**(5), 752 (2005)
11. Deaner, B.J., Allen, M.S., Starr, M.J., Segalman, D.J.: Investigation of modal Iwan models for structures with bolted joints. In: *Topics in Experimental Dynamic Substructuring*, vol. 2, pp. 9–25 (2014)
12. Lacayo, R.M., Allen, M.S.: Updating structural models containing nonlinear Iwan joints using quasi-static modal analysis. *Mech. Syst. Signal Process.* **118**, 133–157 (2019)
13. Jewell, E.A., Allen, M.S., Lacayo, R.: Predicting damping of a cantilever beam with a bolted joint using quasi-static modal analysis. V008T12A019 (2017)
14. Zare, I., Allen, M.S., Jewell, E.: *An Enhanced Static Reduction Algorithm for Predictive Modeling of Bolted Joints*. Springer International Publishing, Cham (2019)
15. Zare, I., Allen, M.S.: A Block-Gauss Seidel algorithm with static reduction to predict damping in bolted joints. In: Presented at the International Seminar on Modal Analysis (ISMA), p. 12. Leuven, Belgium (2018)
16. Ahn, Y.J., Barber, J.R.: Response of frictional receding contact problems to cyclic loading. *Int. J. Mech. Sci.* **50**(10–11), 1519–1525 (2008)
17. Flicek, R.C., Hills, D.A., Barber, J.R., Dini, D.: Determination of the shakedown limit for large, discrete frictional systems. *Eur. J. Mech. – A/Solids.* **49**, 242–250 (2015)
18. Masing, G., Mauksch, W.: *Eigenspannungen und Verfestigung des plastisch gedehnten und gestauchten Messings*. In: *Wissenschaftliche Veröffentlichungen aus dem Siemens-Konzern: IV. Band. Zweites Heft*, pp. 244–256. Springer, Berlin, Heidelberg (1925)
19. Singh, A., et al.: Experimental characterization of a new benchmark structure for prediction of damping nonlinearity. *Nonlinear Dynam.* **1**, 57–78 (2019)
20. Jewell, E., Allen, M.S., Zare, I., Wall, M.: Application of quasi-static modal analysis to a finite element model with experimental correlation. *J. Sound Vib.* Submitted for Publication (2019)
21. Lyndon, B.: *Criteria for Preloaded Bolts*, p. 38. NASA, Houston, TX (1998)
22. Motosh, N.: Development of design charts for bolts preloaded up to the plastic range. *J. Eng. Ind.* **98**(3), 849 (1976)
23. Fronk, M., et al.: Inverse methods for characterization of contact areas in mechanical systems. *Nonlinear Dynam.* **1**, 45–56 (2019)
24. Ames, N.M., et al.: *Handbook on Dynamics of Jointed Structures*. Sandia National Laboratories, Albuquerque, NM.” SAND2009-4164, 1028891 (2009)



Chapter 6

The Best Linear Approximation of MIMO Systems: First Results on Simplified Nonlinearity Assessment

Péter Zoltán Csurscia, Bart Peeters, and Johan Schoukens

Abstract Many mechanical structures are nonlinear and there is no unique solution for modeling nonlinear systems. When a single-input, single-output system is excited by special signals, it is easily possible to decide whether the linear framework is still accurate enough to be used, or a nonlinear framework must be used. However, for multiple-input, multiple-output (MIMO) systems, the design of experiment is not a trivial question since the input and output channels are not mutually independent. This paper shows the first results of an ongoing research project and it addresses the questions related to the user-friendly processing of MIMO measurements with respect to the design of experiment and the analysis of the measured data.

When the proposed framework is used, it is easily possible (a) to decide, if the underlying system is linear or not, (b) to decide if the linear framework is still accurate (safe) enough to be used, and (c) to tell the unexperienced user how much it can be gained using an advanced nonlinear framework. The proposed nonparametric industrial framework is illustrated on a ground vibration testing of an electrical airplane.

Keywords MIMO systems · Nonlinearity · Nonparametric estimation · System identification · Ground vibration testing

6.1 Introduction

In this paper we focus on nonparametric vibration analysis. Many mechanical and civil structures are inherently nonlinear. The problem lies in the fact that there are many different types of nonlinear systems, each of them behaves differently, therefore modelling is very involved, and universally usable design and modelling tools are not available. For these reasons the nonlinear systems are often approximated with linear systems, because its theory is user friendly and well understood.

Since the development of advanced digital signal processing algorithms and the increased computational capability, it became possible to use complex input signals such that a large variety of shaker excitation signals can be used to experimentally determine the broadband FRFs, which are required to obtain parametric models (e.g. resonance frequencies, modes shapes, etc.). One of the (best) possibilities is the usage of special multisines (known as pseudo random signal as well) because they can avoid spectral leakage, inconsistency, non-persistence, and they provide a handy, robust solution to build linear models (FRFs) and to detect the level and type of nonlinearities. The state-of-the-art knowledge known as the Best Linear Approximation (BLA) (best in mean square error sense) framework is already available for single-input, single-output (SISO) systems [1–4].

The aim of the paper is to introduce the BLA framework of multiple input-multiple output (MIMO) systems based on industrial vibrational measurements. The proposed BLA provides a user-friendly interpretation of the measurement data by extracting the user relevant information. The procedure consists of two main steps.

In the design of experiment step (step 1), systems are excited by multisine signals. The excitation signal consists of independent series of periodic multisines that are mutually independent over the experiments.

P. Z. Csurscia (✉)
Siemens Industry Software NV, Leuven, Belgium

Department of Engineering Technology (INDI), Vrije Universiteit Brussel, Elsene, Belgium
e-mail: pcsurcsi@vub.ac.be

B. Peeters
Siemens Industry Software NV, Leuven, Belgium

J. Schoukens
Department of Engineering Technology (INDI), Vrije Universiteit Brussel, Elsene, Belgium

The analysis of the measured signals (step 2) differs from the classical H1 Frequency Response Function (FRF) estimation process. The key idea is to make use of some statistical properties of the excitation signal such that it becomes possible to split up the classical coherence function of the FRF measurement into noise and nonlinearity information.

The proposed nonparametric industrial framework is illustrated on the ground vibration testing (GVT) measurement of a battery operated electrical airplane.

This paper is organized as follows. Section 6.2 briefly describes the considered systems and assumptions applied in this work. Section 6.3 addresses questions related to the experiment design. Section 6.4 discusses the estimation framework in detail. In Sects. 6.5 and 6.6 the description of the GVT measurement and its analysis are given. Conclusions can be found in Sect. 6.7.

6.2 Basics

The dynamics of a linear MIMO system can be nonparametrically characterised in the frequency domain by its Frequency Response Matrix (FRM) [5] G at a discrete frequency index k , which relates the inputs U to outputs Y as follows:

$$Y(k) = G(k)U(k) \quad (6.1)$$

In this work arbitrary number of input and output channels are considered and the underlying systems are BIBO stable physical systems [6]. For the sake of simplicity, the frequency indices will be omitted, and it is assumed to understand each quantity at frequency index k .

This system represented by the G is linear when the superposition principle is satisfied in steady-state, i.e.:

$$Y = G(a + b)U = aGU + bGU = (a + b)GU \quad (6.2)$$

where a and b are scalar values. If G is constant, for any a, b (and excitation), then the system is called linear-time invariant (LTI). On the other hand, when G varies with a and b (and the variation depends also on the excitation signal—e.g. level of excitation, distribution, etc.) then the system is called nonlinear.

Because time-varying systems are often misinterpreted as nonlinear systems, it is important to mention that when G varies over the measurement time, but at each time instant the principle of superposition is satisfied, then the system is called linear time-varying (LTV) [7].

In this work we consider nonlinear time-invariant stable (damped) mechanical (vibrating) systems where the linear response of the system is still present and the output of the underlying system has the same period as the excitation signal (i.e. the system has PISPO behaviour: period in, same period out [8]).

Further, it is assumed that the excitation signal is known (measured precisely). The actuator of the system is linear.

6.3 Design of Experiment

6.3.1 Multisine Excitation and Detection of Nonlinearities

In modern system identification special excitation signals are available to assess the underlying systems in a user-friendly, time efficient way [9]. To avoid any spectrum leakage, to reach full nonparametric characterization of the noise, and to be able to detect nonlinearities, a periodic signal is needed. Many users prefer noise excitations, because they are simple to implement, but in this case nonlinearities are not identifiable, and there is a possible leakage error. The best signal that satisfies the desired properties is the user-friendly multisine signal (see Fig. 6.1) which looks like Gaussian white noise, behaves like it but it is not a noise. The random phase (uniformly distributed) multisine is a sum of harmonically related sinusoids. The amplitude distribution of a random phase multisine is approximately normal (it approaches a Gaussian distribution as the number of harmonics tend to infinity).

In this work, random phase multisines are used and generated in the frequency domain such that the magnitude characteristic is set by the user, and the phases of the cosines are chosen randomly from a uniform distribution [8]. Note that this signal is also known as pseudo-random (multisine) signal.

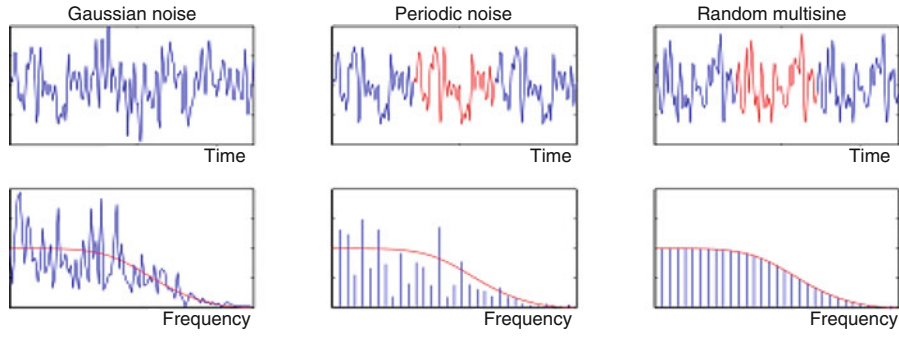


Fig. 6.1 Different excitation signals in time and in frequency domain

6.3.2 Multisines for Multiple Input Measurements

For the sake of simplicity—without loss of generality—we will focus on systems with two inputs and two outputs. This allows to illustrate the additional problems that appear when moving from SISO to MIMO for a minimal increase of the complexity. The straightforward extension of the SISO excitation case can be formulated in the frequency domain as follows:

$$Y = GU \iff \begin{bmatrix} Y_1 \\ Y_2 \end{bmatrix} = \begin{bmatrix} G_{11} & G_{12} \\ G_{21} & G_{22} \end{bmatrix} \begin{bmatrix} U_1 \\ U_2 \end{bmatrix} \quad (6.3)$$

where the indices of the input and output data refer to channel number.

The above-mentioned set of linear equations suffers from the degrees of freedom: there are 4 unknown parameters and only 2 independent equations. In order to overcome the issue with the degrees of freedom, the number of independent equations has to be increased. In this work this has been done by increasing the number of experiments by expanding the number of columns in U (and hence the number of columns in Y). Each column in U (Y) represents an experiment. In case of 2 inputs there are at least 2 experiments needed.

The solvability of the above-mentioned linear algebraic equation strongly depends on the condition number (i.e. the randomness) of the excitation signal's matrix U . In classical MIMO identification, one of the most often applied solution to this problem is the use of Hadamard decorrelation technique: a square matrix (whose entries are either +1 or -1) is elementwise multiplied with one realization of signal. The restriction here is that the order of the matrix must be 1, 2, or multiples of 4.

In order to overcome the issue with the limited possible orders of the Hadamard matrix, and to improve the estimation properties [10, 11] proposed to use orthogonal random multisines, extending the idea of the orthogonal inputs proposed for linear MIMO measurements in [12]. In this work the proposed procedure is to generate independent random excitation for every input channel such that we have (more) randomness in the measurement with respect to the Hadamard's technique. This sequence of signals will be placed in the first blocks of experiments (i.e. first column of U) and they will be shifted orthogonally for the subsequent experiments (i.e. the next columns in U) with the following weighting-shifting matrix:

$$W_{cn} = e^{-j2\pi(c-1)(n-1)/N_{input}} \quad (6.4)$$

where c refers to input channel number (i.e. the row number in U), n refers to the experiment number (column number in U), and N_{input} stands for the number of inputs. In case of 2 input/output channels, for one set of realization of the multisine signal, the following equation is given:

$$\begin{bmatrix} Y_{11} & Y_{12} \\ Y_{21} & Y_{22} \end{bmatrix} = \begin{bmatrix} G_{11} & G_{12} \\ G_{21} & G_{22} \end{bmatrix} \begin{bmatrix} U_{11} & U_{12} \\ U_{21} & U_{22} \end{bmatrix} = \begin{bmatrix} G_{11} & G_{12} \\ G_{21} & G_{22} \end{bmatrix} \begin{bmatrix} U_1 W_{11} & U_1 W_{12} \\ U_2 W_{21} & U_2 W_{22} \end{bmatrix} = \begin{bmatrix} G_{11} & G_{12} \\ G_{21} & G_{22} \end{bmatrix} \begin{bmatrix} U_1 & U_1 \\ U_2 & -U_2 \end{bmatrix} \quad (6.5)$$

6.4 Best Linear Approximation

The Best Linear Approximation (BLA) has been widely used in the last decades to efficiently estimate FRFs [9]. The BLA of a nonlinear system is an approach of modelling that minimizes the mean square error between the true output of a nonlinear system and the output of the linear model.

The proposed BLA technique makes use of the knowledge that the excitation signal has both stochastic and deterministic properties. In this work the excitation signal is a random phase multisine signal and it is assumed to be measured precisely. In each measurement there are m different random realizations of multisines (orthogonally shifted number of input channels times) and each of the realization is repeated p times.

From the philosophical point of view there are two main differences between the proposed BLA and the classical H1 (cross-power spectral density) estimate [13] frameworks. First, in the BLA case the FRM is estimated from the discrete Fourier transformed data instead of using the cross-power and auto-power matrices. Second, instead of directly using the averaged input and output data, a partial BLA estimate is calculated for each period of the excitation. A BLA FRM estimate, for a given signal, is then calculated via the average of partial BLA estimates. In this case we can easily estimate the noise levels and standard deviations on each frequency line. Using this information, the coherence function will be virtually split into (1) noise level and (2) nonlinear contribution estimates.

6.4.1 Theoretical Structure and the Basic Assumptions

As aforementioned, the BLA of a nonlinear system is an approach of modelling that minimizes the mean square error between the true output of a nonlinear system and the output of the linear model [8]. In the proposed robust BLA framework, multiple repeated realizations of the random phase multisine excitation are needed. The BLA estimate consists of several components. Figure 6.2 shows the theoretical structure of the considered BLA estimator.

G_{Linear} is the linear (transfer function) component of BLA. This component is phase coherent: random phase rotation in the input excitation would result in a proportional phase rotation at the output.

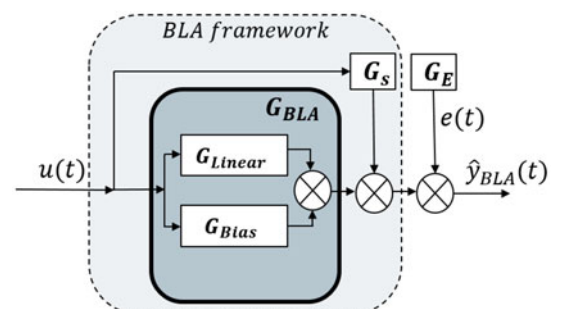
In case of non-coherent behaviour, the input phase rotation would result in a random phase rotation at the output. Please note that significant part of the nonlinearities is non-coherent. When many input phase rotations are performed, the random output rotations can be seen as an additional (nonlinear) noise source (G_S) next to the ordinary measurement noise (G_E)—assumed to be additive i.i.d. normal distributed with zero mean with a finite variance. The usage of periodic excitation reduces the effects of the measurement noise G_E . The usage of multiple random phase realizations reduces the level of non-coherent nonlinearities.

The (coherent) nonlinearities remaining after multiple realizations of the excitation signal result in a bias error of the BLA (denoted by G_{Bias}). The next section discusses a possibility to reduce the effects of G_S , G_E .

6.4.2 Two-Dimensional Averaging

When the BLA estimation framework is applied, the observed system is excited by random phase multisines (assumed to be measured precisely). In this work there are (N_{input} times phase-rotated) m different realization of the multisine excitation signal, each realization is repeated p period times. The considered steady-state model in the frequency domain at frequency bin index k is given by:

Fig. 6.2 The theoretical structure of the best linear approximation



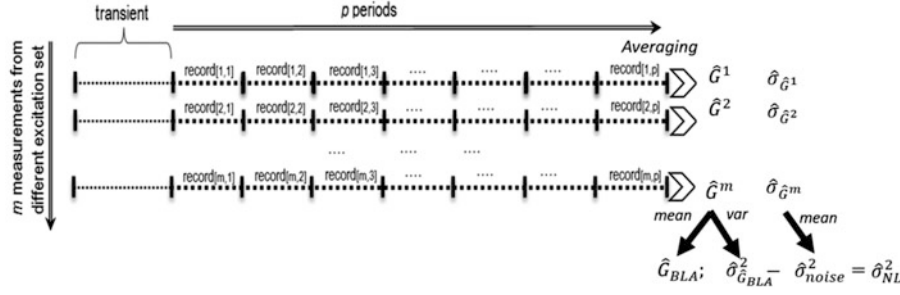


Fig. 6.3 Evaluation of BLA estimate with the help of 2D averaging

$$\widehat{G}^{[m][p]} = \widehat{Y}_{measured}^{[m][p]} \mathbf{U}^{[m]-1} = \widehat{G}_{BLA} + \widehat{G}_S^{[m]} + \widehat{G}_E^{[m][p]} \quad (6.6)$$

The steady state signals are obtained in this work by discarding some periods at the beginning of each realization block. In order to estimate the underlying system one has to average over p periods of repeated excitation signal, and over the m different realizations of the excitation signal [8] (see Fig. 6.3).

First, let us average over the p periods of a realization. If p is sufficiently large then (considering the law of large numbers and the distribution properties the observation noise) the expected value of $\widehat{G}_E^{[m][p]}$ converges to zero, so that term is eliminated. In other words, averaging over repeated blocks results in an improvement of the SNR. Because the stochastic nonlinear contribution $\widehat{G}_S^{[m]}$ does not vary over the repetition of the same realization we have to average over the m different realizations. If m is sufficiently large, then $\widehat{G}_S^{[m]}$ nonlinear noise source converges to zero, so that term is eliminated. After the 2D averaging the BLA estimate is obtained.

The estimate of the noise sample variance $\widehat{\sigma}_{G_E}^2$ is calculated from the averaged sample variance of each FRM realization and it is normalized by m . The total variance of the FRM $\widehat{\sigma}_{G_{BLA}}^2$ is calculated from the sample variance of each different partial BLA estimates $\widehat{G}^{[m]}$ and is normalized by m . The additional m normalization helps to show the average noise and nonlinearity effects on the FRF measurement.

The difference between the total variance and the noise variance is an estimate of the variance of the stochastic nonlinear contributions $\widehat{\sigma}_{NL}^2 \approx (\widehat{\sigma}_{G_{BLA}}^2 - \widehat{\sigma}_{G_E}^2)$. When the user intends to see how much nonlinearity is present on an arbitrary block (period) of the measurement, one has to consider m -times σ_{NL}^2 such that $\sigma_{NL}^2 m \sigma_{NL}^2$, and the noise variance term mp -times $\sigma_{G_E}^2 mp \sigma_{noise}^2$.

Using the proposed 2D averaging technique the influence of the noise and nonlinear contribution can be decreased, and the final result is BLA FRF estimate. In [5] it has been suggested to choose the number of periods more than one ($p \geq 2$) and the different realizations are more than six ($m \geq 7$). Detailed calculations of the proposed 2D approach can be found in [14].

6.5 Measurement

This section provides a brief overview of the GVT measurement of a battery operated small aircraft. The measurement took place at Magnus testing facility in Kecskemét, Hungary in 2017. The eFusion aircraft (see Fig. 6.4) is a two-seat, all-electric, low-wing monoplane, based on the piston engine. The light sport aircraft has a symmetric wing profile, a titanium firewall, and a centre section made of chrome molybdenum alloys. The fuselage is attached with a non-retractable tricycle landing gear. It has a length of 6.7 m, height of 2.4 m, and a wingspan of 8.3 m including winglet, whereas the wing area is 10.59 m². The aircraft is powered by a 60 kW electric drive system. The electric propulsion system including motor and batteries is designed by Siemens. The aircraft has an endurance of approximately one hour. The aircraft has an empty weight of 410 kg and a maximum take-off weight of 600 kg. It requires a landing roll from 150 to 200 m.

The measurement setup (see Fig. 6.5) consists of 2 shakers–2 force cells, and various 91 acceleration channels. The shaker reference (Volt) signals are random phase multisine signals. The sampling frequency is 200 Hz. The period length is 1024 resulting in a frequency resolution of 0.1953 Hz. The smallest excited frequency is 1.1719 Hz, the highest excited frequency is 50.7813 Hz.

There are eight different multisine realizations for each input channel per experiment. Each multisine realization is repeated 3 times. As explained earlier, the extra experimental blocks (necessary to solve the MIMO equations) are obtained by orthogonal phase shift. Thus, there are in total $m \cdot p \cdot N_{input} = 8 \cdot 3 \cdot 2 = 48$ blocks.



Fig. 6.4 The eFusion battery operated small aircraft



Fig. 6.5 The measurement setup and instrumentation

6.6 Analysis

This section concerns the analysis the random phase multisine GVT measurement. The GVT measurement has been executed at three different levels. Figure 6.6 shows the lowest and highest level excitation signals in the frequency domain. The excitation force is measured with approximately 65 dB SNR. This SNR is sufficiently good to fulfil the assumption on the precise excitation signal measurement. However, it is interesting to point out that the high level excitation signal is 10 dB higher than the low level excitation signal but the SNR improvement is only around 2 dB: the noise level estimate moved together with the excitation signal estimate. This indicates the presence of (low level) nonlinearities at the excitation system. The analysis of this phenomenon is out of the scope of this paper. Further, in order to simplify the analysis, the output and FRF are shown at the driving points only. The output (acceleration) measurement is shown in Fig. 6.7. As can be seen, the

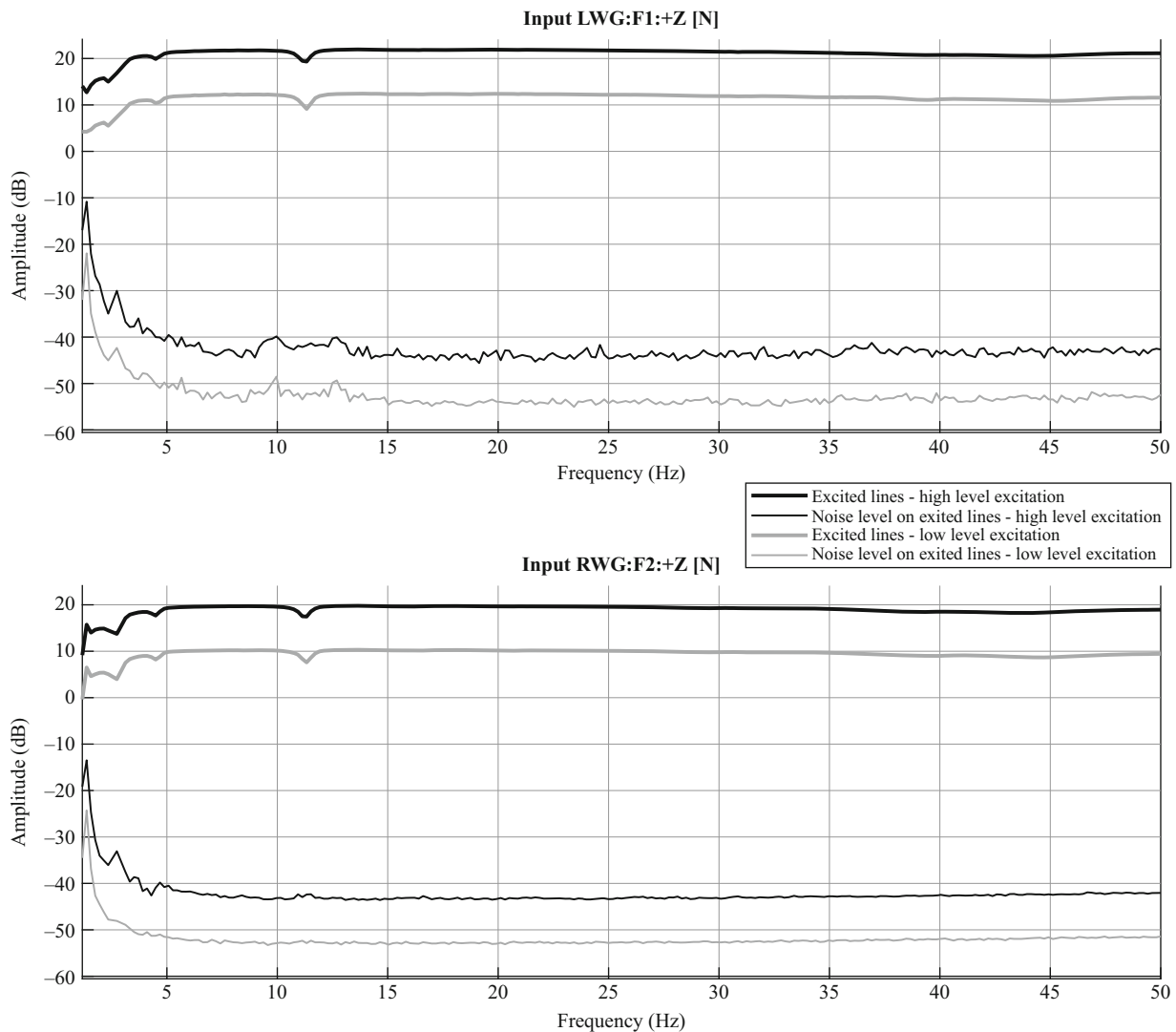


Fig. 6.6 The input (force) signal measured in frequency domain at the low and high amplitude levels

SNR dropped a little resulting around 60 dB SNR at the resonances. At the higher excitation level, the right wing SNR decreased with approximately 4 dB. This is a further indication of nonlinearities being present at the measurement.

In order to ensure that the measured signals are in the steady-state, a simple transient check-up is performed. Figure 6.8 shows the first realization of one of the output channels (with the slowest decay) in time domain. In order to determine the length of the transient (i.e. the number of delay blocks), the last block (period) of the first realization—assumed to be in steady-state—is subtracted from every block in that realization. As can be seen on the right side of Fig. 6.8, only the first block is disturbed by the transient. In this work, each first block (period) is discarded.

Figure 6.9 shows the FRFs at the driving points at low and high level excitation. It can be clearly observed that FRFs at different levels differ a lot from each other. This clearly indicated the presence of nonlinearities. The interesting point here is to tell the inexperienced user from only one measurement if the system is linear or nonlinear—on that particular level of excitation.

The classical H1 framework suggest calculating the coherence function for each frequency line. When the coherence function gives one it means that there is 100% linear correlation between the measured output and input data. When the coherence is lower than one it indicates the presence of (among others) high level noise and/or transient and/or leakage and/or nonlinearities. Since we have used periodic excitation with discarding the delay blocks (transient), we made sure that the lack of coherence stands only for the noise and nonlinearities. In the following part we focus on the first FRF in FRM at high level excitation.

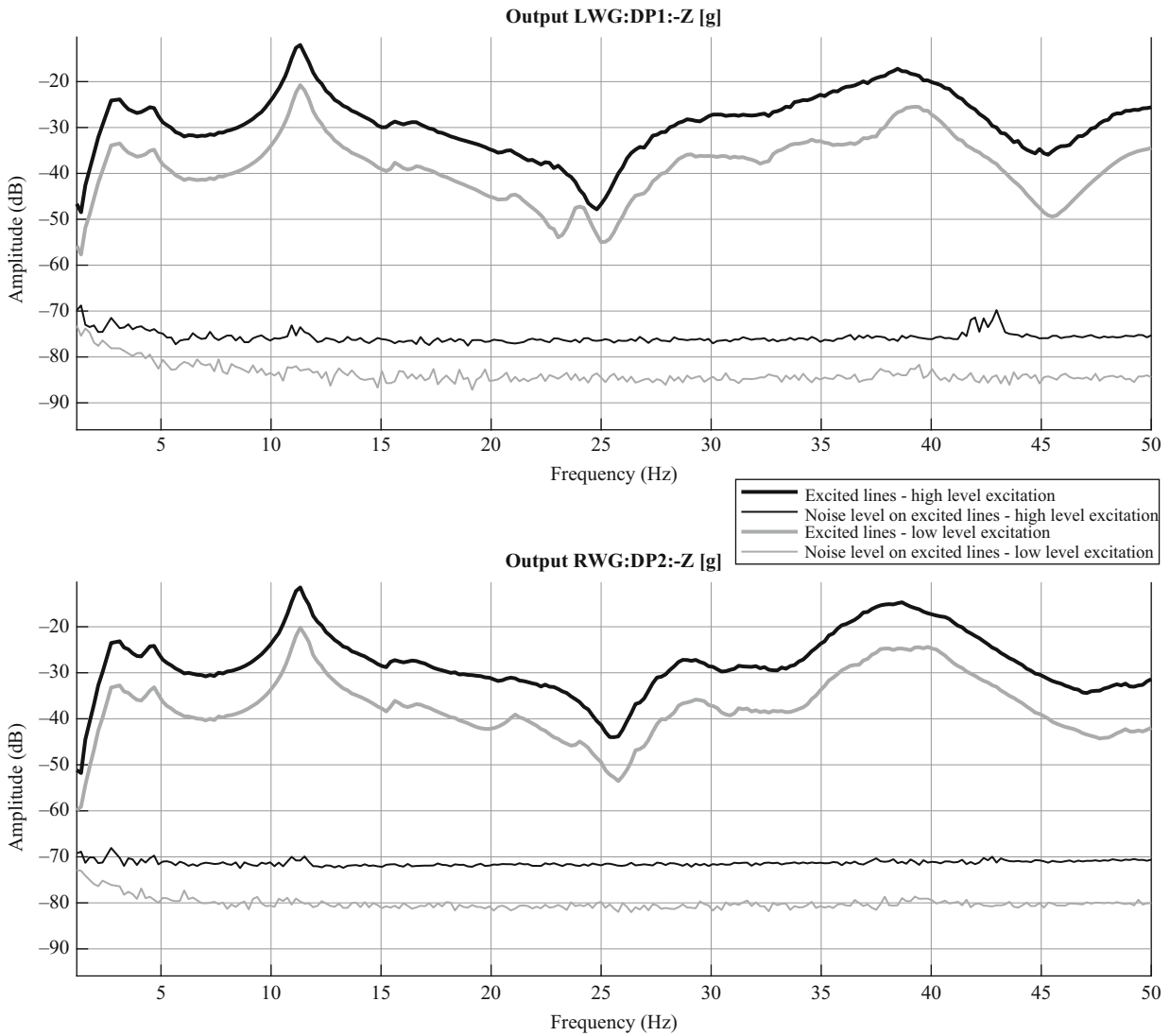


Fig. 6.7 The output (acceleration) signal measured in frequency domain at the low and high amplitude levels

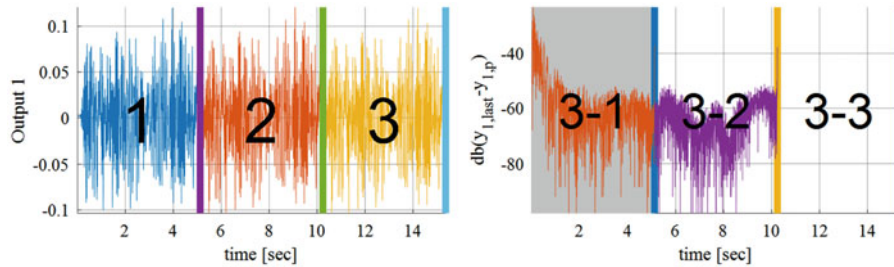


Fig. 6.8 Periodicity of the output measurement at high level in time domain. Left figures shows the block repetitions in one realization. The right figure shows the difference between the last block minus every block

In the classical H1 framework the coherence function (pink thick line in Fig. 6.10) is used to estimate the FRF measurement’s standard deviation (pink thin line in Fig. 6.10). For the numerical computation of coherence function in MIMO case we refer to [15]. Please note that by the use of the proposed BLA framework we can directly estimate the standard deviation and split it to into noise level estimation (black thin line in Fig. 6.10) and nonlinearity level estimation (red thin line in Fig. 6.10) as explained in the 2D averaging section of this paper.

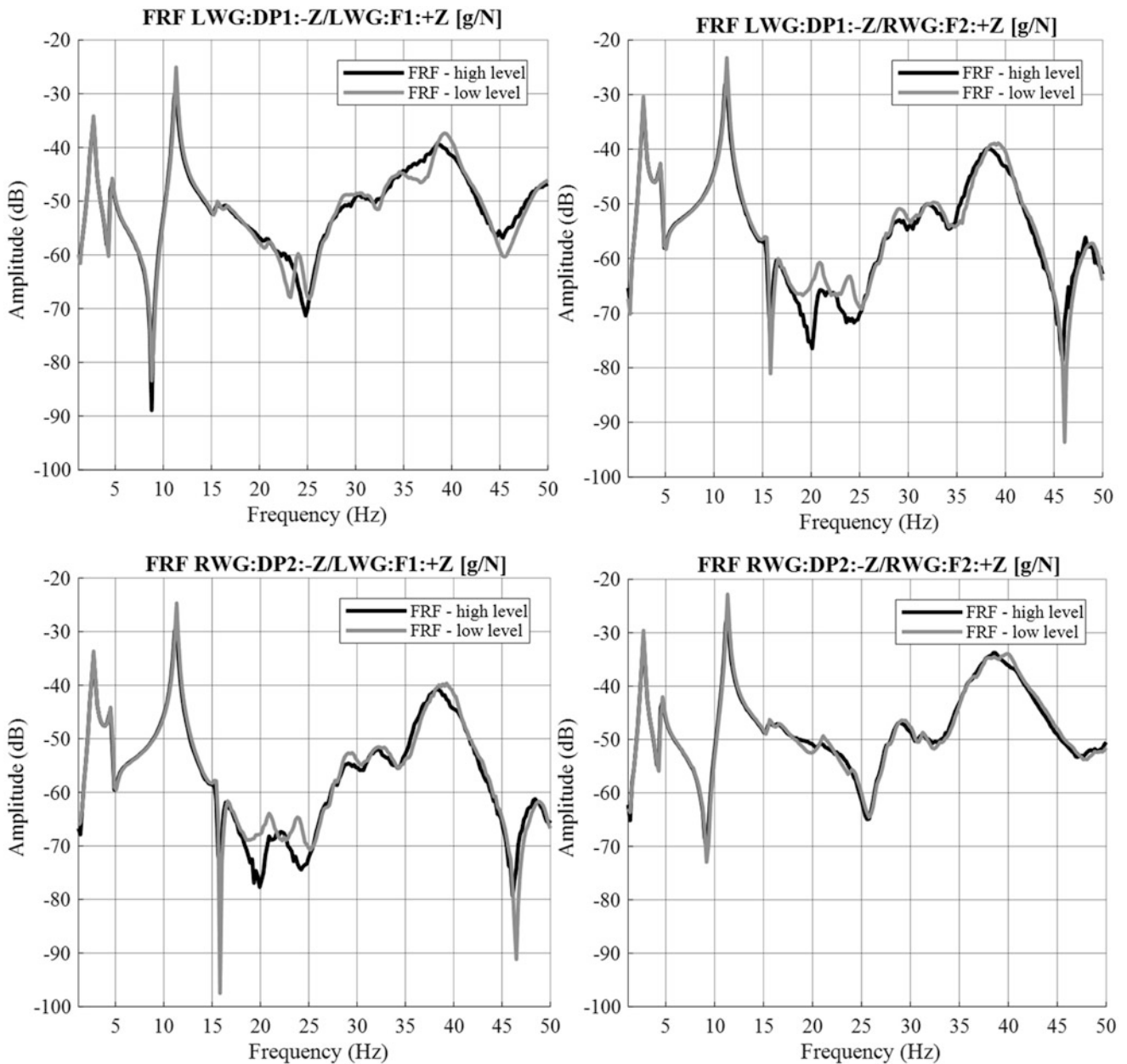


Fig. 6.9 FRFs at driving points estimated at the low and high excitation levels

With the help of these curves it is possible to tell how much is from the lack of coherence accounts for the noise and nonlinearity. For instance, the first resonance (around 3 Hz) has an SNR of 35 dB and an SNLR (signal-to-nonlinearity ratio) of 40 dB. This means that at this resonance the main error source is the noise. Looking at the largest resonance (fourth resonance at around 12 Hz) one can read that the SNR is around 60 dB and the SNLR is around 30 dB. At this resonance the dominant error source is the nonlinearity.

A further interesting point is to highlight that periodic excitation is used, therefore it is possible to estimate the standard deviation directly from the data instead. A standard deviation comparison between BLA and H1 is shown in Fig. 6.11. This comparison indicates that the BLA estimate is indeed more robust — the BLA's standard deviation can reach lower values than the standard deviation of H1.

The figures above show the improved FRM, noise and nonlinearity estimates by taking into account all the different realizations and experiments. The question arises: what would be the noise and nonlinearity level on an arbitrary chosen measurement block (period) without using the BLA technique. In this case one has to correct for the number of experiments

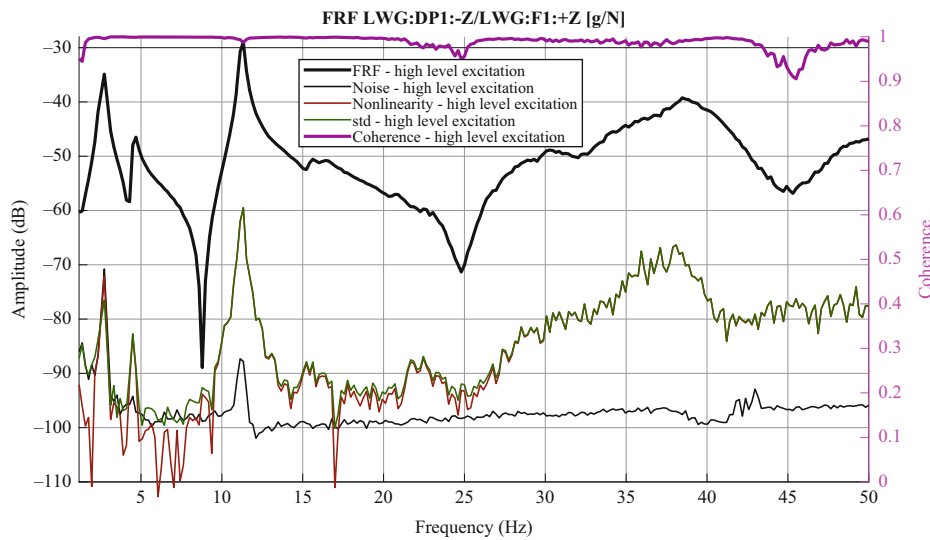


Fig. 6.10 The BLA FRF estimation at high level excitation using the proposed technique—taking into account all data

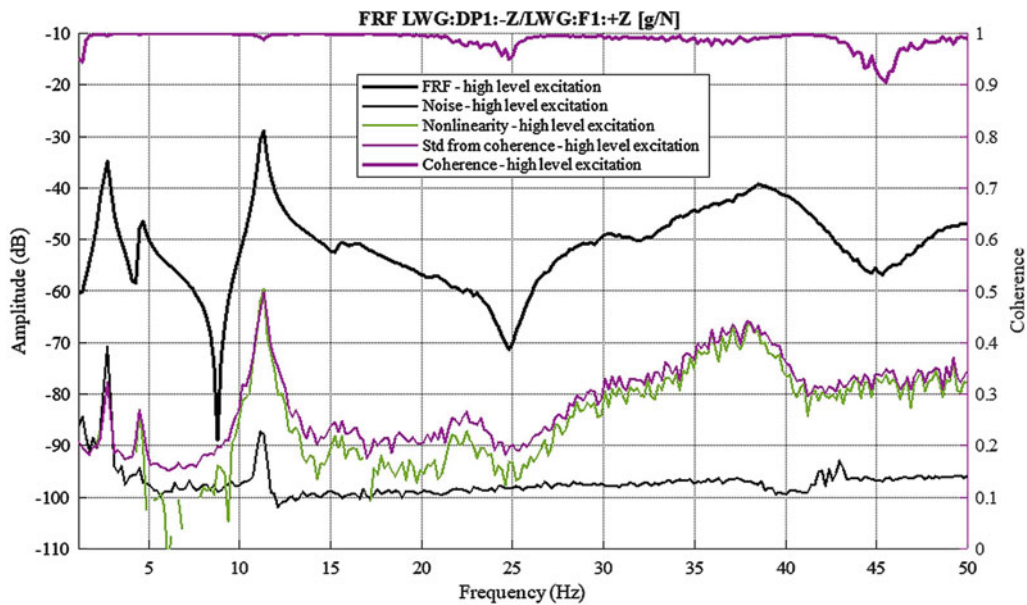


Fig. 6.11 Comparison of standard deviation estimation of BLA estimate (green line) and H1 (pink thin line)

(multiply the noise estimate by $\sqrt{p \cdot m}$, nonlinearity estimates by \sqrt{m}). This is shown in Fig. 6.12 for both low (lighter colors) and high (darker colors) level excitation. In this case, if the end-user decides the use a simple linear model in his application the error levels would be in order of SNLR. If the end-user decides to opt for an appropriate nonlinear model the error levels would be in order of SNR. The gain (improvement) by the use of an advanced nonlinear model would be approximately the difference between the SNR and SNLR.

A further interesting thing to mention is that the anti-diagonal FRFs have a significantly higher nonlinearity level then in the diagonal FRFs.

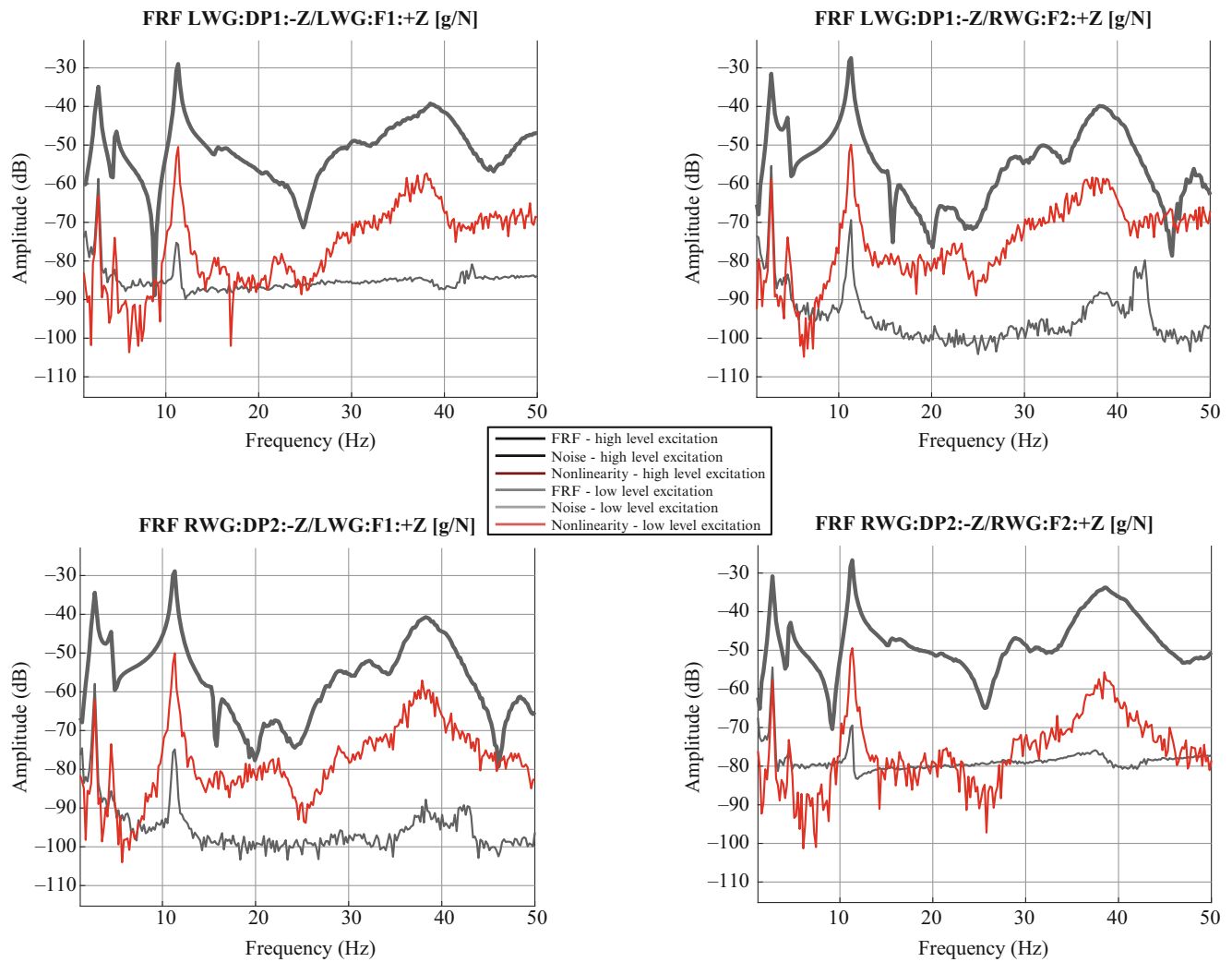


Fig. 6.12 Expected noise and nonlinearity levels at one measurement block (period)

6.7 Conclusion

In this work a MIMO Best Linear Approximation framework was developed to provide a user-friendly interpretation of the nonlinear behavior of MIMO measurement data by extracting user relevant information. The proposed framework turned to be useful for modelling FRFs because:

- orthogonal excitation signals have been provided (1) to improve the SNR, (2) to better characterize the underlying system, (3) to avoid spectral leakage, and (4) to overcome the issues with transient
- the input and output measurements were characterized,
- the frequency response matrix was estimated and characterized by virtually slitting up the coherence function into noise and nonlinearity level information
- at each amplitude level the noise and nonlinearity information can be retrieved.

Using the provided information potential users can decide if the usage of an advanced nonlinear framework is necessary.

Acknowledgments This work was funded by the VLAIO Innovation Mandate project number HBC.2016.0235.

References

1. Lauwers, L., Schoukens, J., Pintelon, R., Enqvist, M.: Nonlinear structure analysis using the best linear. In: Proceedings of International Conference on Noise and Vibration Engineering, Leuven (2006)
2. Esfahani, A., Schoukens, J., Vanbeylen, L.: Using the best linear approximation with varying excitation signals for nonlinear system characterization. *IEEE Trans Instrum Meas.* **65**, 1271–1280 (2016)
3. Wong, H.K., Schoukens, J., Godfrey, K.: Analysis of best linear approximation of a wiener–hammerstein system for arbitrary amplitude distributions. *IEEE Trans Instrum Meas.* **61**(3), 645–654 (2012)
4. Schoukens, J., Pintelon, R.: Study of the variance of parametric estimates of the best linear approximation of nonlinear systems. *IEEE Trans Instrum Meas.* **59**(12), 3156–3167 (2010)
5. Pintelon, R., Schoukens, J.: *System Identification: A Frequency Domain Approach*, 2nd edn. Wiley. ISBN: 978-0470640371, Hoboken, NJ (2012)
6. Ljung, L.: *System Identification: Theory for the User*, 2nd edn. Prentice-Hall., ISBN: 9780136566953, New Jersey (1999)
7. Csurcsia, P.Z., Lataire, J.: Nonparametric estimation of time-variant systems using 2D regularization. *IEEE Trans Instrum Meas.* **65**(5), 1259–1270 (2016)
8. Csurcsia, P.Z.: Static nonlinearity handling using best linear approximation: an introduction. *Pollack Periodica.* **8**(1), 153–165 (2013)
9. Schoukens, J., Pintelon, R., Rolain, Y.: *Mastering System Identification in 100 Exercises*. Wiley. ISBN: 978047093698, Hoboken, NJ (2012)
10. Solomou, M., Rees, D.: Measuring the best linear approximation of systems suffering nonlinear distortions: an alternative method. *IEEE Trans Instrum Meas.* **52**(4), 1114–1119 (2003)
11. Dobrowiecki, T., Schoukens, J.: Linear approximation of weakly nonlinear MIMO systems. In: *IEEE International Instrumentation and Measurement Technology Conference (I2MTC)*, pp. 1607–1612 (2004)
12. Guillaume, P., Pintelon, R., Schoukens, J.: Accurate estimation of multivariable frequency response functions. *13th World Congress of IFAC.* **29**(1), 4351–4356 (1996)
13. Priemer, R.: *Introductory Signal Processing*. World Scientific, Singapore. ISBN: 9971509199 (1991)
14. Alvarez Blanco, M., Csurcsia, P.Z., Janssens, K., Peeters, B., Desmet, W.: Nonlinearity assessment of mimo electroacoustic systems on direct field environmental acoustic testing. In: *International Conference on Noise and Vibration Engineering*, Leuven (2018)
15. Peeters, B., El-Kafafy, M., Guillaume, P., Van der Auweraer, H.: Uncertainty propagation in experimental modal analysis. In: *Conference Proceedings of the Society for Experimental Mechanics Series* (2014)



Chapter 7

Forced Response of Nonlinear Systems Under Combined Harmonic and Random Excitation

Alwin Förster, Lars Panning-von Scheidt, and Jörg Wallaschek

Abstract Mechanical systems are often subjected to different types of excitation. In addition to the commonly considered case of deterministic excitation, random excitation or a combination of both types can occur. The authors present a method to calculate periodic probability density functions of nonlinear mechanical systems under combined harmonic and random excitation. During the calculation, the non-stationary Fokker–Planck equation is solved with a Galerkin-type method. The method uses combined orthogonal, time dependent polynomial as well as harmonic correction terms to reshape an initial guess of the probability density function. It can be used to calculate the stochastic behavior of smaller multi-degree of freedom systems. The applicability is demonstrated using different nonlinear mechanical systems, whereby the results of Monte-Carlo simulations validate the method.

Keywords Random excitation · Probability density function · Combined excitation · In-stationary Fokker–Planck equation · Periodic

Nomenclature

a, b, \dots, z	Counting indices	ζ_i	Correction coefficient
\mathbf{B}	Diffusion matrix	μ_g	Friction coefficient
D	Spectral density	ξ	Gaussian white noise
f	Drift vector	σ	Standard deviation
F_N	Normal force	φ_i	One-dim. orthogonal correction functions
\mathbf{H}	Galerkin-matrix	Φ_i	Multi-dim. orthogonal correction functions
m, c, k, λ	Mass, damping, stiffness, cubic stiffness	$\ A\ $	Euclidean norm
m	Number of correction polynomials	$\mathbf{A} \otimes \mathbf{B}$	Kronecker-product
n	Number of state space dimensions	$A \oplus B$	Exclusive disjunction
N_{DOF}	Number of DOF's	DOF	Degree of freedom
$N_\varphi^{(b)}$	bth approximation order	FDM	Finite difference method
p	Probability density function	FEM	Finite element method
p_0	Weighting function	FFT	Fast Fourier transform
$P\{A\}$	Occurrence probability of case A	FPE	Fokker–Planck equation
q	Generalized coordinate	GWN	Gaussian white noise
${}_b\mathcal{S}_{k,l}$	Num. of factorized diffusion terms per $b_{k,l}$	IFFT	Inverse fast Fourier transform
${}_f\mathcal{S}_k$	Num. of factorized drift terms per f_k	JPDF	Joint probability density function
t	Time	MCS	Monte-Carlo Simulation
w	Wiener-process	MHBM	Multi-Harmonic Balance Method
x_k	State space variable	PDF	Probability density function
$\delta(y)$	Dirac delta function	RMS	Root mean square
$\delta_{i,j}$	Kronecker-delta	SDE	Stochastic differential equation

A. Förster (✉) · L. Panning-von Scheidt · J. Wallaschek
 Institute of Dynamics and Vibration Research, Faculty of Mechanical Engineering, Leibniz University Hannover, Hannover, Germany
 e-mail: foerster@ids.uni-hannover.de

7.1 Introduction

Most real mechanical systems are subjected to a variety of different forms of excitation. Starting with periodic/harmonic, over non-periodic to different types of random excitation. In literature commonly, one type of excitation is reviewed. Regarding nonlinear mechanical systems, the principle of superposition cannot be used to add the results of different excitation types. This paper describes a way to calculate the response of a nonlinear system to an additive noise-superimposed harmonic excitation.

The most important quantity when it comes to describing the random oscillations of a mechanical system is the probability density function (PDF). The probability density function is a function of the state space variables and time. The temporal evolution of the probability density function of a mechanical system is determined by the Fokker–Planck equation, also known as the Kolmogorov forward equation. Interested readers are referred to Risken [1].

In the last decades different methods were developed to describe oscillations in consequence of random excitation. This paper takes a special look at the field of turbine blade vibrations. One method is the Path Integral Method (PIM) which was investigated by Naess [2], Kumar [3, 4], Pirrotta [5] and Narayanan [6] (see [3] with regard to turbine blades). The method is suitable for determining non-Gaussian stationary probability density functions of low-dimensional systems. Further possibilities are offered by the Finite Difference Method (FDM) of Kumar [3] and the Finite Element Method (FEM) of Kumar [7] and Narayanan [6]. Both methods have been considered so far mainly for steady-state probability density functions, but could be extended to an additional harmonic excitation. The complex calculation, however, limits both methods to systems with one, maximum two, degrees of freedom. The equivalent linearization method, which was used by Caughey [8] and by Cha [9] for turbine blades, offers only the possibility to calculate stochastic stationary system responses. The calculated approximations are always Gaussian and stationary. With this method a linear system is determined whose Gaussian distributed response shows as small a deviation as possible from that of the nonlinear system. The simplest and most straightforward approach for calculating random oscillations is given by the Monte-Carlo Simulation (MCS) (see Pradlwarter [10], Higham [11]). It is a collective term for different numerical time step integration methods e.g. the Euler–Maruyama method.

This paper introduces an extension of a Galerkin-type method to determine the system response of nonlinear systems under noise superimposed harmonic excitation. The original method was presented by Wedig [12–14] and von Wagner [15–17] and applied in various ways by Martens [18–20] and Lentz [21]. The method can only be used for the calculation of stochastic steady-state probability density functions. The authors have applied this method in Förster [22] to a simple model of a friction damped bladed disk assembly.

This Galerkin-type method is now extended for the calculation of probability density functions of nonlinear mechanical systems under a well-defined deterministic excitation and an additive random excitation. The advanced method calculates coefficients for weighting orthogonal time-dependent polynomials and harmonic functions to correct an initial estimate for the transient but periodic probability density function of a nonlinear system. Since the method calculates coefficients of a function and not the function values at certain points in the state space (e.g. finite difference method), this method is not as limited in the number of degrees of freedom as the other methods mentioned above. The applicability of the method is demonstrated using various nonlinear exemplary systems.

7.2 The Fokker–Planck Equation

The Fokker–Planck equation is a second-order linear partial differential equation which describes the time evolution of the JPDF $p(\mathbf{x}, t)$ for a mechanical system under random excitation. Interested readers are referred to Risken [1]. The equation is

$$\frac{\partial p(\mathbf{x})}{\partial t} = - \sum_{k=1}^n \frac{\partial}{\partial x_k} [f_k(\mathbf{x}) p(\mathbf{x})] + \sum_{k=1}^n \sum_{l=1}^n \frac{\partial^2}{\partial x_k \partial x_l} [b_{k,l}(\mathbf{x}) p(\mathbf{x})], \quad (7.1)$$

where f_k are the components of the drift vector \mathbf{f} and $b_{k,l}$ are the components of the diffusion describing matrix \mathbf{B} . The drift vector and diffusion matrix are taken from the systems ITÔ SDE

$$d\mathbf{x} = \mathbf{f}(\mathbf{x}, t) dt + \mathbf{G}(\mathbf{x}, t) d\mathbf{w}, \quad (7.2)$$

which describes its stochastic behavior, whereby $\xi = \frac{dw}{dt}$ is the time derivative of a Wiener-process. A Wiener-process is an example of a Markov-process with normally distributed growth (see Gardiner [23]). In the multi-dimensional FPE, $\xi = \frac{dw}{dt}$ is a vector of uncorrelated Gaussian white noise (GWN) with $E[\xi_i \xi_j] = 2D\delta(t)$. The \mathbf{B} -matrix is calculated using $\mathbf{B} = \frac{1}{2}\mathbf{G}^T \mathbf{D} \mathbf{G}$, with the spectral density D and the diffusion matrix \mathbf{G} , which originate from the systems SDE.

The JPDF p obeys the normalization condition

$$\int_{-\infty}^{+\infty} p(\mathbf{x}, t) d\mathbf{x} = 1, \quad (7.3)$$

so that the total probability is always equal one

$$P\{-\infty \leq \mathbf{x} \leq +\infty\} = 1. \quad (7.4)$$

In the case that the left side of the FPE vanishes ($\frac{\partial p(\mathbf{x})}{\partial t} = 0$) one refers to it as the stationary FPE respectively a stationary PDF/JPDF.

7.3 Galerkin-Type Method for Combined Harmonic and Random Excitation

This section introduces a new Galerkin-type method to calculate the probability density function of nonlinear mechanical systems under harmonic and random excitation. The harmonic part of the external force has a distinct phase and is therefore not included in the random excitation.

The first step is to define an initial guess for the PDF respectively a multi-dimensional weighting function

$$p_0(\mathbf{x}, t) = p_0^{(t)}(t) \prod_{b=1}^n p_0^{(b)}(x_b, t), \quad (7.5)$$

which is a product of n one-dimensional weighting functions for every state space dimension and one function for the time. The weighting function is Ω -periodic, whereby Ω is the fundamental frequency of the harmonic excitation force. The initial PDF is corrected by orthogonal, multi-dimensional and time dependent correction functions

$$\Phi_i(\mathbf{x}, t) = \varphi_i^{(t)}(t) \prod_{b=1}^n \varphi_b^{(b)}(x_b, t), \quad (7.6)$$

which apply to the orthogonality condition

$$\int_{-\infty}^{+\infty} p_0^{(b)}(x_b, t) \varphi_{i_b}^{(b)}(x_b, t) \varphi_{j_b}^{(b)}(x_b, t) dx_b = \delta_{i_b, j_b} \quad (7.7)$$

respectively

$$\int_0^{\frac{2\pi}{\Omega}} p_0^{(t)}(t) \varphi_{i_t}^{(t)}(t) \varphi_{j_t}^{(t)}(t) dt = \delta_{i_t, j_t} \quad (7.8)$$

for the time. For the spacial dimensions time dependent normal distributions and orthogonal polynomials can be used, while the time only needs a correction factor as a weighting function and harmonic functions as correction functions. The ansatz for the time dependent JPDF is

$$p(\mathbf{x}, t) \approx p_0(\mathbf{x}, t) \sum_{i=1}^m \zeta_i \Phi_i(\mathbf{x}, t) = \sum_{i=1}^m \zeta_i \prod_{b=1}^{n+1} \begin{cases} p_0^{(b)}(x_b, t) \varphi_{i_b}^{(b)}(x_b, t) & \text{for } b \leq n \\ p_0^{(t)} \varphi_{i_t}^{(t)}(t) & \text{for } b = n + 1 \end{cases}. \quad (7.9)$$

It means, that the initial weighting function is reshaped by the correction functions, which are weighted by the factors ${}_t \zeta_i$. Inserting this ansatz into the weak form of the non-stationary FPE gains

$$\begin{aligned} & \sum_{i=1}^m {}_t \zeta_i \left[\sum_{k=1}^n \int_{-\infty}^{+\infty} \int_{-\infty}^{+\infty} p_0(\mathbf{x}, t) \Phi_i(\mathbf{x}, t) f_k(\mathbf{x}, t) \frac{\partial \Phi_j(\mathbf{x}, t)}{\partial x_k} d\mathbf{x} dt + \dots \right. \\ & \dots + \sum_{k=1}^n \sum_{l=1}^n \int_{-\infty}^{+\infty} \int_{-\infty}^{+\infty} p_0(\mathbf{x}, t) \Phi_i(\mathbf{x}, t) b_{k,l}(\mathbf{x}, t) \frac{\partial^2 \Phi_j(\mathbf{x}, t)}{\partial x_k \partial x_l} d\mathbf{x} dt + \dots \\ & \left. \dots + \int_{-\infty}^{+\infty} \int_{-\infty}^{+\infty} p_0(\mathbf{x}, t) \Phi_i(\mathbf{x}, t) \frac{\partial \Phi_j(\mathbf{x}, t)}{\partial t} d\mathbf{x} dt \right] = 0. \end{aligned} \quad (7.10)$$

Equation (7.10) is simplified written as

$$\sum_{i=1}^m {}_t \zeta_i \int_{-\infty}^{+\infty} \left[\sum_{k=1}^n \sum_{a=1}^{f_{S_k}} \prod_{b=1}^{n+1} {}_t \Theta_k^{i,j}{}^{a,b}(t) + \sum_{k=1}^n \sum_{l=1}^n \sum_{a=1}^{b_{S_{k,l}}} \prod_{b=1}^{n+1} {}_t \Gamma_{k,l}^{i,j}{}^{a,b}(t) + \sum_{a=1}^{n+1} \prod_{b=1}^{n+1} {}_t \Xi^{i,j}{}^{a,b}(t) \right] dt = 0 \quad (7.11)$$

with

$${}_t \Theta_k^{i,j}{}^{a,b}(t) = \begin{cases} p_0^{(t)} \varphi_{i_b}^{(t)} \varphi_{j_b}^{(t)} & \text{if } b = n+1 \\ \int_{-\infty}^{+\infty} p_0^{(b)} \varphi_{i_b}^{(b)} a f_k^{(b)} \frac{\partial \varphi_{j_b}^{(b)}}{\partial x_b} dx_b & \text{if } b = k \\ \underbrace{\int_{-\infty}^{+\infty} p_0^{(b)} \varphi_{i_b}^{(b)} a f_k^{(b)} \varphi_{j_b}^{(b)} dx_b}_{= a f_k^{(b)} \cdot \delta_{i_b, j_b} \vee a f_k^{(b)} = \text{const.}} & \text{if } b \neq k \wedge b \leq n \end{cases} \quad (7.12)$$

as well as

$${}_t \Gamma_{k,l}^{i,j}{}^{a,b}(t) = \begin{cases} p_0^{(t)} \varphi_{i_b}^{(t)} \varphi_{j_b}^{(t)} & \text{if } b = n+1 \\ \int_{-\infty}^{+\infty} p_0^{(b)} \varphi_{i_b}^{(b)} a b_{k,l}^{(b)} \frac{\partial \varphi_{j_b}^{(b)}}{\partial x_b} dx_b & \text{if } b = k \oplus b = l \\ \int_{-\infty}^{+\infty} p_0^{(b)} \varphi_{i_b}^{(b)} a b_{k,l}^{(b)} \frac{\partial^2 \varphi_{j_b}^{(b)}}{\partial x_b^2} dx_b & \text{if } k = l \wedge b = k \\ \underbrace{\int_{-\infty}^{+\infty} p_0^{(b)} \varphi_{i_b}^{(b)} a b_{k,l}^{(b)} \varphi_{j_b}^{(b)} dx_b}_{= a b_{k,l}^{(b)} \cdot \delta_{i_b, j_b} \vee a b_{k,l}^{(b)} = \text{const.}} & \text{if } b \neq k \wedge b \neq l \wedge b \leq n \end{cases} \quad (7.13)$$

and

$${}_{t}^{a,b}\Xi^{i,j}(t) = \begin{cases} p_0^{(t)} \varphi_{i_b}^{(t)} \varphi_{j_b}^{(t)} & \text{if } a \neq b \wedge b = n+1 \\ p_0^{(t)} \varphi_{i_b}^{(t)} \frac{\partial \varphi_{j_b}^{(t)}}{\partial t} & \text{if } a = b \wedge b = n+1 \\ \int_{-\infty}^{+\infty} p_0^{(b)} \varphi_{i_b}^{(b)} \frac{\partial \varphi_{j_b}^{(b)}}{\partial t} dx_b & \text{if } a = b \wedge b \leq n \\ \underbrace{\int_{-\infty}^{+\infty} p_0^{(b)} \varphi_{i_b}^{(b)} \varphi_{j_b}^{(b)} dx_b}_{=\delta_{i_b, j_b}} & \text{if } a \neq b \wedge b \leq n \end{cases} \quad (7.14)$$

for the spacial integrals. The time integral from $-\infty$ to $+\infty$ in Eq. (7.11) only vanishes if the zeroth Fourier-coefficient

$$\mathcal{F}^{(0)} \left[\sum_{k=1}^n \sum_{a=1}^f \sum_{b=1}^{s_k n+1} \prod_t {}_{t}^{a,b}\Theta_k^{i,j}(t) + \sum_{k=1}^n \sum_{l=1}^n \sum_{a=1}^{b s_{k,l} n+1} \prod_t {}_{t}^{a,b}\Gamma_{k,l}^{i,j}(t) + \sum_{a=1}^{n+1} \prod_{b=1}^{n+1} \prod_t {}_{t}^{a,b}\Xi^{i,j}(t) \right] \stackrel{!}{=} 0 \quad (7.15)$$

is zero. Therefore the integration limits can be changed from $(-\infty, +\infty)$ to $\left[0, \frac{2\pi}{\Omega}\right)$. So that Eq. (7.11) than changes to

$$\sum_{i=1}^m {}_t \zeta_i \int_0^{\frac{2\pi}{\Omega}} \left[\sum_{k=1}^n \sum_{a=1}^f \sum_{b=1}^{s_k n+1} \prod_t {}_{t}^{a,b}\Theta_k^{i,j}(t) + \sum_{k=1}^n \sum_{l=1}^n \sum_{a=1}^{b s_{k,l} n+1} \prod_t {}_{t}^{a,b}\Gamma_{k,l}^{i,j}(t) + \sum_{a=1}^{n+1} \prod_{b=1}^{n+1} \prod_t {}_{t}^{a,b}\Xi^{i,j}(t) \right] dt = 0. \quad (7.16)$$

Equation (7.16) generates a linear system of equation

$$\mathbf{0} = \mathbf{H} \cdot {}_t \zeta \quad (7.17)$$

to calculate the weighting factors ${}_t \zeta_i$. Where the entries of the \mathbf{H} -matrix are calculated by

$$h_{j,i} = \int_0^{\frac{2\pi}{\Omega}} \left[\sum_{k=1}^n \sum_{a=1}^f \sum_{b=1}^{s_k n+1} \prod_t {}_{t}^{a,b}\Theta_k^{i,j}(t) + \sum_{k=1}^n \sum_{l=1}^n \sum_{a=1}^{b s_{k,l} n+1} \prod_t {}_{t}^{a,b}\Gamma_{k,l}^{i,j}(t) + \sum_{a=1}^{n+1} \prod_{b=1}^{n+1} \prod_t {}_{t}^{a,b}\Xi^{i,j}(t) \right] dt. \quad (7.18)$$

Due to the fact, that every derivative of a zeroth order correction function—polynomial or harmonic—is going to be zero, Eq. (7.17) is reduced to

$$\mathbf{H}_{(2,\dots,m) \times (2,\dots,m)} \cdot {}_t \zeta_{(2,\dots,m)} = -\mathbf{H}_{(2,\dots,m) \times (1)} \cdot {}_t \zeta_1, \quad (7.19)$$

where ${}_t \zeta_1$ is chosen to be one. After solving Eq. (7.19), one can calculate approximations for time-dependent PDFs by

$$p^{(k)}(x_k, t_g) \approx \frac{2\pi}{\Omega} \sum_{i=1}^m \left[{}_t \zeta_i p_0^{(k)}(x_k, t_g) \varphi_{i_k}^{(k)}(x_k, t_g) \cdot \left[\prod_{\substack{b=1 \\ b \neq k}}^n \int_{-\infty}^{+\infty} p_0^{(b)}(x_b, t_g) \varphi_{i_b}^{(b)}(x_b, t_g) dx_b \right] \cdot p_0^{(t)}(t_g) \varphi_{i_t}^{(t)}(t_g) \right] \quad (7.20)$$

or time-independent PDF by integrating over one period

$$p^{(k)}(x_k) \approx \sum_{i=1}^m \left[{}_t \zeta_i \int_0^{\frac{2\pi}{\Omega}} p_0^{(k)}(x_k, t) \varphi_{i_k}^{(k)}(x_k, t) \cdot \left[\prod_{\substack{b=1 \\ b \neq k}}^n \int_{-\infty}^{+\infty} p_0^{(b)}(x_b, t) \varphi_{i_b}^{(b)}(x_b, t) dx_b \right] \cdot p_0^{(t)}(t) \varphi_{i_t}^{(t)}(t) dt \right]. \quad (7.21)$$

JPDFs for any sub-spaces $\mathbf{x}_{\mathbf{k}} \in \mathbb{R}^N$ with $\mathbf{k} \in \mathbb{R}^N$ and $N \leq n, N \in \mathbb{N}$ can be calculated with

$$p^{(\mathbf{k})}(\mathbf{x}_{\mathbf{k}}) \approx \sum_{i=1}^m \left[{}_t \zeta_i \int_0^{\frac{2\pi}{\Omega}} p_0^{(i)}(t) \varphi_{i_t}^{(i)}(t) \cdot \left[\prod_{b=1}^n \begin{cases} \int_{-\infty}^{+\infty} p_0^{(b)}(x_b, t) \varphi_{i_b}^{(b)}(x_b, t) dx_b & \text{for } b \notin \mathbf{k} \\ p_0^{(b)}(x_b, t) \varphi_{i_b}^{(b)}(x_b, t) & \text{for } b \in \mathbf{k} \end{cases} \right] dt \right]. \quad (7.22)$$

One can also calculate conditional probabilities for certain states ${}_u \mathbf{x} \leq \mathbf{x} \leq {}_o \mathbf{x}$ by

$$P\{{}_u \mathbf{x} \leq \mathbf{x} \leq {}_o \mathbf{x}\} \approx \sum_{i=1}^m \left[{}_t \zeta_i \int_0^{\frac{2\pi}{\Omega}} \left[\prod_{b=1}^n \int_{{}_u x_b}^{{}_o x_b} p_0^{(b)}(x_b, t) \varphi_{i_b}^{(b)}(x_b, t) dx_b \right] \cdot p_0^{(i)}(t) \varphi_{i_t}^{(i)}(t) dt \right]. \quad (7.23)$$

7.4 Orthogonal Time-Dependent Correction Functions

As mentioned above, the weighting function for the time is just a correction factor

$$p_0^{(i)} = \frac{\Omega}{2\pi} \quad (7.24)$$

and the solely time dependent correction functions are harmonic functions

$$\varphi_{i_t}^{(i)}(t) = \begin{cases} 1 & i_t = 0 \\ \sqrt{2} \cdot \cos\left(\frac{2i_t + (-1)^{i_t+1} + 1}{4} \Omega t\right) & \forall i_t \% 2 = 1 \\ \sqrt{2} \cdot \sin\left(\frac{2i_t + (-1)^{i_t+1} + 1}{4} \Omega t\right) & \forall i_t \% 2 = 0 \end{cases} \quad (7.25)$$

The factors in Eqs. (7.24) and (7.25) are chosen to hold the orthogonality condition from Eq. (7.8). The weighting functions $p_0^{(b)}$ for all spacial dimensions are chosen to be time-dependent normal distribution

$$p_0^{(b)}(x_b, t) = \frac{1}{\sqrt{2\pi \zeta_b^2(t)}} \exp\left[-\frac{(x_b - \mu_b(t))^2}{2\zeta_b^2(t)}\right] \quad (7.26)$$

with the mean value and the standard deviation being a function of time. All time-dependent orthogonal polynomials and their derivatives for such a function can be derived analytically from the time-independent orthogonal polynomials in Martens [20]. The zeroth order polynomial is given by

$$\varphi_0^{(b)}(x_b, t) = 1 \quad (7.27)$$

with its derivatives

$$\frac{\partial \varphi_0^{(b)}(x_b, t)}{\partial x_b} = 0, \quad \frac{\partial^2 \varphi_0^{(b)}(x_b, t)}{\partial x_b^2} = 0 \quad \text{and} \quad \frac{\partial \varphi_0^{(b)}(x_b, t)}{\partial t} = 0. \quad (7.28)$$

The first order polynomial is given by

$$\varphi_1^{(b)}(x_b, t) = \frac{x_b - \mu_b(t)}{\zeta_b(t)} \quad (7.29)$$

so that its derivatives are

$$\frac{\partial \varphi_1^{(b)}(x_b, t)}{\partial x_b} = \frac{1}{\varsigma_b(t)}, \quad (7.30)$$

$$\frac{\partial^2 \varphi_1^{(b)}(x_b, t)}{\partial x_b^2} = 0 \quad (7.31)$$

and

$$\frac{\partial \varphi_1^{(b)}(x_b, t)}{\partial t} = -\frac{\frac{\partial \mu_b(t)}{\partial t}}{\varsigma_b(t)} - \frac{[x_b - \mu_b(t)] \frac{\partial \varsigma_b(t)}{\partial t}}{\varsigma_b^2(t)}. \quad (7.32)$$

All higher order polynomials can be recursively calculated via

$$\varphi_{d+1}^{(b)}(x_b, t) = \frac{x_b - \mu_b(t)}{\varsigma_b(t) \sqrt{d+1}} \varphi_d^{(b)}(x_b, t) - \sqrt{\frac{d}{d+1}} \varphi_{d-1}^{(b)}(x_b, t). \quad (7.33)$$

All derivatives of these high order polynomials can be expressed analytically by

$$\frac{\partial \varphi_{d+1}^{(b)}(x_b, t)}{\partial x_b} = \frac{1}{\varsigma_b(t) \sqrt{d+1}} \varphi_d^{(b)}(x_b, t) + \frac{x_b - \mu_b(t)}{\varsigma_b(t) \sqrt{d+1}} \frac{\partial \varphi_d^{(b)}(x_b, t)}{\partial x_b} - \sqrt{\frac{d}{d+1}} \frac{\partial \varphi_{d-1}^{(b)}(x_b, t)}{\partial x_b} \quad (7.34)$$

for the first derivative with respect to the spacial dimension x_b and

$$\frac{\partial^2 \varphi_{d+1}^{(b)}(x_b, t)}{\partial x_b^2} = \frac{2}{\varsigma_b(t) \sqrt{d+1}} \frac{\partial \varphi_d^{(b)}(x_b, t)}{\partial x_b} + \frac{x_b - \mu_b(t)}{\varsigma_b(t) \sqrt{d+1}} \frac{\partial^2 \varphi_d^{(b)}(x_b, t)}{\partial x_b^2} - \sqrt{\frac{d}{d+1}} \frac{\partial^2 \varphi_{d-1}^{(b)}(x_b, t)}{\partial x_b^2} \quad (7.35)$$

for the second derivative. The first time-derivative is given by

$$\begin{aligned} \frac{\partial \varphi_{d+1}^{(b)}(x_b, t)}{\partial t} = & -\frac{1}{\varsigma_b(t) \sqrt{d+1}} \frac{\partial \mu_b(t)}{\partial t} \varphi_d^{(b)}(x_b, t) + \frac{x_b - \mu_b(t)}{\varsigma_b(t) \sqrt{d+1}} \frac{\partial \varphi_d^{(b)}(x_b, t)}{\partial t} - \dots \\ & \dots - \frac{x_b - \mu_b(t)}{\varsigma_b^2(t) \sqrt{d+1}} \frac{\partial \varsigma_b(t)}{\partial t} \varphi_d^{(b)}(x_b, t) - \sqrt{\frac{d}{d+1}} \frac{\partial \varphi_{d-1}^{(b)}(x_b, t)}{\partial t}. \end{aligned} \quad (7.36)$$

For this ansatz the functions $\mu_b(t)$ and $\varsigma_b(t)$ have to be known approximately. To gain these functions, methods like the multi-Harmonic Balance Method (MHBM, see Urabe [24], Cameron [25] and Cardona [26, 27]) and the Monte-Carlo simulation can be used.

7.5 Application

This section demonstrates the application of the method described above to various nonlinear systems. As this is a numerical study, no units are used for all parameters and variables of the systems under consideration. All calculations were performed using MatLab 2018a. In order to improve the weighting functions, the calculations were carried out several times, whereby the weighting functions are improved iteratively. In this procedure, low correction functions are used and only replaced by higher orders in the last calculation step.

7.5.1 Duffing-Oscillator

The Duffing-oscillator is a simple and often used nonlinear one degree of freedom system with a cubic stiffness. The associated differential equation is

$$m\ddot{q} + c\dot{q} + kq + \lambda q^3 = f_{ex} \quad (7.37)$$

with the cubic stiffness λ . In the case of a harmonic excitation superimposed with GWN, the external force has the form $f_{ex} = \hat{f}_{ex} \cos(\Omega t) + \sigma \frac{dw}{dt}$ with $\frac{dw}{dt}$ being GWN. The corresponding SDE is

$$dx = \underbrace{\begin{pmatrix} x_2 \\ -\frac{c}{m}x_2 - \frac{k}{m}x_1 - \frac{\lambda}{m}x_1^3 + \frac{\hat{f}_{ex}}{m} \cos(\Omega t) \end{pmatrix}}_f dt + \underbrace{\begin{pmatrix} 0 & 0 \\ 0 & \frac{\sigma}{m} \end{pmatrix}}_G dw \quad (7.38)$$

where f is the drift vector and G is the diffusion matrix. The B -matrix

$$B = \frac{1}{2} \cdot \begin{pmatrix} 0 & 0 \\ 0 & \frac{\sigma^2}{m^2} \end{pmatrix} \quad (7.39)$$

can be calculated from the diffusion matrix G . The system parameters are $m = 0.2$, $c = 0.425$, $k = 40$ and $\lambda = 150$. It is excited with a harmonic force amplitude of $\hat{f}_{ex} = 2.5$ at the angular frequency $\Omega = 15$ and additionally with GWN with a standard deviation of $\sigma = 0.075$.

The initial functions for the time-dependent mean value $\mu_b(t)$ and the standard deviation curve $\sigma_b(t)$ can be determined in different ways. The standard deviation $\varsigma_b(t)$ can either be roughly estimated or taken from a short MCS. The mean value progression $\mu_b(t)$ can be estimated using the MHBM, the shooting method or the time step integration of the deterministic system. If these time-dependent functions are approximated with harmonic functions, it is advisable not to select the maximum order of the harmonic correction functions smaller than the one used in the approach. In this case, the MHBM and a short MCS were used to determine the time progression. These functions can then be used for a Gaussian approach. The harmonic order used is $N_{h,\mu} = 5$ respectively $N_{h,\sigma} = 10$ and the orders of the correction functions are $N_\varphi^{(1)} = 6$, $N_\varphi^{(2)} = 6$ and $N_\varphi^{(t)} = 20$. In order to improve the quality of the results, the calculation is carried out several times, whereby the approach is repeatedly adapted to the results. The correction orders are low for the first computations and only increased in the last step.

Figure 7.1 shows the one-dimensional PDFs for the displacement x_1 and velocity x_2 . The red curve represents the results of a MCS and the blue curve shows the results of the Galerkin-type method. Both PDFs are time-integrated over N periods and are calculated with Eq. (7.21). The black lines indicate the value of the amplitude of the deterministic system. The results of the MCS and the Galerkin-type method show only minor deviations. In Fig. 7.2 one can see a time-integrated two-dimensional JPDP [left] calculated with Eq. (7.22). On the right side the PDF for the displacement at $t = N\frac{2\pi}{\Omega}$ is shown. The dotted black and blue lines show the temporal progression of the maximum of the PDF, where black stands for the ansatz function and blue for the Galerkin solution. The green curve is the result of a MCS, while the blue curve shows

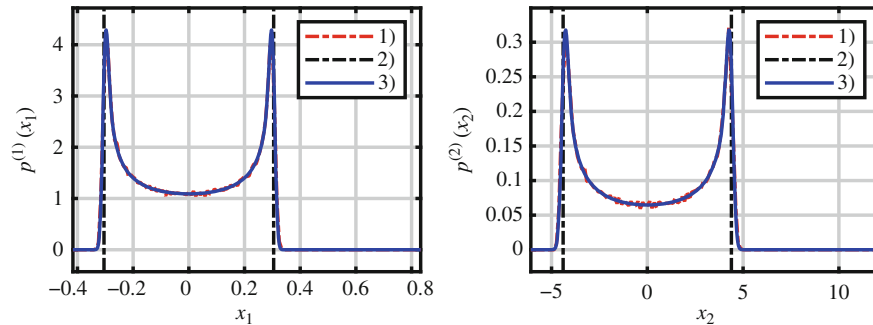


Fig. 7.1 Galerkin-approximation of $p^{(1)}$ and $p^{(2)}$ with (1) MCS-results, (2) $\hat{x}_{b,det}$, (3) $p_{Galerkin}^{(b)}$

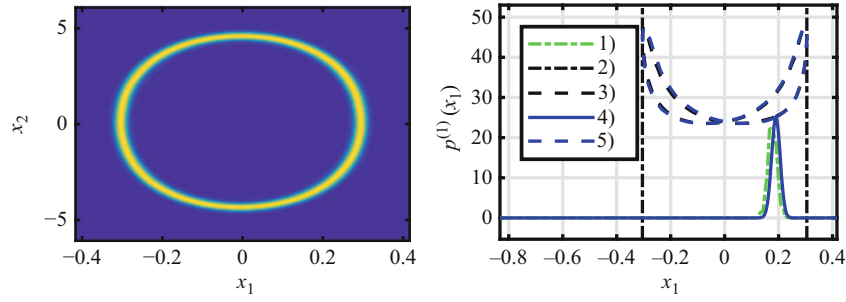


Fig. 7.2 Galerkin-approximation of $p^{(1,2)}(x_1, x_2)$ [left] and $p^{(1)}\left(x_1, t = \frac{2\pi}{\Omega}\right)$ with (1) MCS-results, (2) $\hat{x}_{1,\text{det}}$, (3) $\hat{p}_0^{(1)}(x_1)$, (4) $p_{\text{Galerkin}}^{(1)}\left(x_1, t = \frac{2\pi}{\Omega}\right)$ and (5) $\hat{p}_{\text{Galerkin}}^{(1)}(x_1)$ [right]

the Galerkin solution. One can see a small difference between the course of the maxima of the weighting function and the Galerkin solution. This means that the weighting function could be chosen even better or that there is a deviation from a purely Gaussian distribution due to the non-linearity. There is also a small difference between the PDF from the MCS and the Galerkin-type method. This can be primarily explained by different time discretization, but also partly by the general inaccuracy of the MCS. Other than that, the results of the MCS and the Galerkin-type method also agree very well in the individual time steps.

The calculation took around 10 s with low approximation orders and around 2 min for the final high quality results. An MCS of comparable quality would take much longer.

7.5.2 Duffing-van der Pol-Oscillator

The Duffing-van der Pol-oscillator is a combination of the Duffing-oscillator and the van der Pol-oscillator. Its differential equation is

$$m\ddot{q} + c\dot{q} + kq + \lambda q^3 + \nu q^2\dot{q} = f_{ex} \quad (7.40)$$

with the cubic stiffness λ and the van der Pol-coefficient ν . The external force f_{ex} is identical with the one used before, so that the corresponding stochastic differential equation is as follows

$$dx = \underbrace{\begin{pmatrix} x_2 \\ -\frac{c}{m}x_2 - \frac{k}{m}x_1 - \frac{\lambda}{m}x_1^3 - \frac{\nu}{m}x_1^2x_2 + \frac{\hat{f}_{ex}}{m}\cos(\Omega t) \end{pmatrix}}_f dt + \underbrace{\begin{pmatrix} 0 & 0 \\ 0 & \frac{\sigma}{m} \end{pmatrix}}_G dw \quad (7.41)$$

with the drift vector f and diffusion matrix

$$B = \frac{1}{2} \cdot \begin{pmatrix} 0 & 0 \\ 0 & \frac{\sigma^2}{m^2} \end{pmatrix} \quad (7.42)$$

resulting from the matrix G . The system is characterized by its parameters $m = 0.2$, $c = 0.425$, $k = 40$, $\lambda = 150$, $\nu = 120$. The external force is given by $\sigma = 0.075$, $\hat{f}_{ex} = 2.5$ and $\Omega = 14$.

The harmonic order used is $N_{h,\mu} = 5$ as well as $N_{h,\sigma} = 5$ and the orders of the final correction functions are $N_\varphi^{(1)} = 6$, $N_\varphi^{(2)} = 6$ and $N_\varphi^{(t)} = 10$. In order to improve the quality of the results, the calculation is also carried out several times in this case, whereby the approach is always adapted to the intermediate results

Figures 7.3 and 7.4 show the results for the Duffing-van der Pol-oscillator, for which there is also a large similarity between the results of MCS and the Galerkin-type method.

Due to the strong damping of the Duffing-van der Pol-oscillator, the Galerkin-type method is able to calculate the temporal course of the PDF for any excitation frequency Ω using Gaussian ansatz functions. If the solutions calculated for adjacent

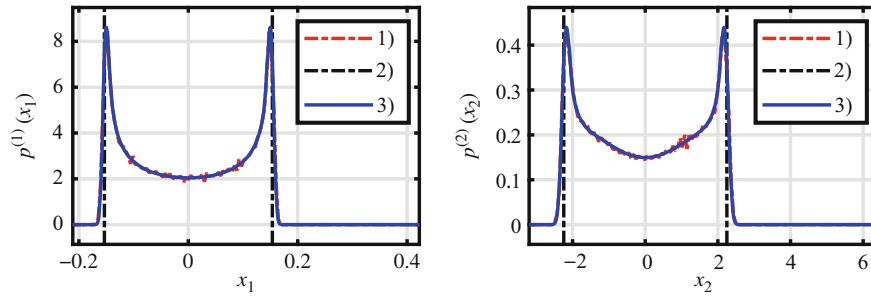


Fig. 7.3 Galerkin-approximation of $p^{(1)}$ and $p^{(2)}$ with (1) MCS-results, (2) $\hat{x}_{b,det}$, (3) $p_{Galerkin}^{(b)}$

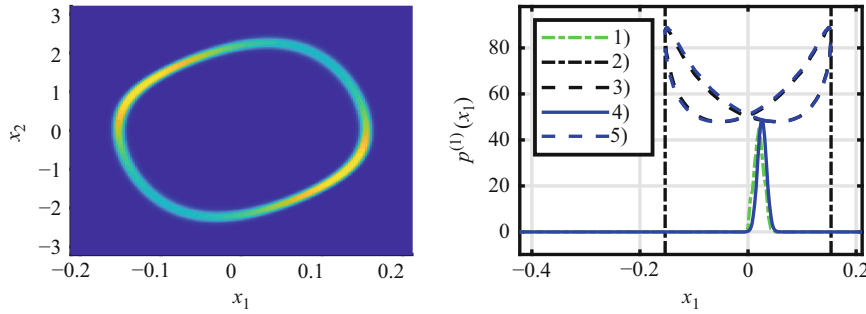


Fig. 7.4 Galerkin-approximation of $p^{(1,2)}(x_1, x_2)$ [left] and $p^{(1)}\left(x_1, t = \frac{2\pi}{\Omega}\right)$ with (1) MCS-results, (2) $\hat{x}_{1,det}$, (3) $\hat{p}_0^{(1)}(x_1)$, (4) $p_{Galerkin}^{(1)}\left(x_1, t = \frac{2\pi}{\Omega}\right)$ and (5) $\hat{p}_{Galerkin}^{(1)}(x_1)$ [right]

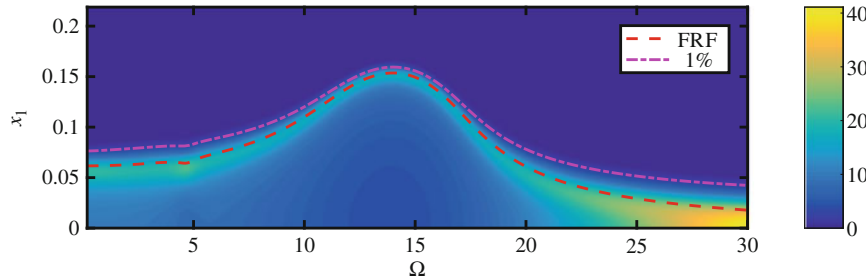


Fig. 7.5 Galerkin-approximation of $p^{(1)}(x_1, \Omega)$, deterministic FRF and curve of 1% probability

frequencies are used as approaches for the next frequency, the PDFs for entire FRFs can be calculated relatively quickly. For each frequency the calculation is carried out several times, whereby the approaches are always adapted to the intermediate results and the order of approximation is increased step by step. The result of such a calculation can be seen in Fig. 7.5, where the red curve is the FRF of the entirely deterministic system. The magenta curve represents the 1% limit for x_1 . This means that the probability of occurrence for displacements greater than this line is equal to 1%. Figure 7.5 can be calculated in high resolution within 1 h on a state of the art desktop computer.

A calculation of the PDF for almost all frequencies of harmonic excitation is, however, usually only possible for small systems without overhanging branches in the frequency response. With overhanging branches or isolated areas, several stable, deterministic oscillation states can occur. In the case of a disturbance, e.g. by a noise excitation, several stable states into which the drift vector could pull the system would in principle be present. However, the current Gaussian approach only allows one stable state at a time, which is why the method has only limited applicability so far. The calculation time is about 10 s for low and 1 min for the final high approximation orders. The calculations were performed on a state-of-the-art desktop computer. An MCS with comparable or even lower quality takes more time, from several seconds to minutes or even hours depending on the quality.

7.5.3 3-DOF-System

The next system to be considered is a 3-DOF system with friction elements as shown in Fig. 7.6. The system consists of three identical masses, which are connected to each other and to the environment by a spring, a damper and a cubic spring. In addition, all masses are connected to the environment via a sliding friction element. The force $F_N = 0.25$ is a constant contact force, which is converted into a friction force by the friction coefficient $\mu = 0.01$. The other parameters are chosen to be mass $m = 0.25$, stiffness $k = 140$, cubic stiffness $\lambda = 1330$ and damping $c = 1.47$. The external forces are $f_{ex,1} = f_{ex,2} = f_{ex,3} = 5 \cos(\Omega t) + \sigma \frac{dw}{dt}$ with $\Omega = 27.5$ and $\sigma = 0.25$. The system is described by its differential equation

$$\underbrace{\begin{pmatrix} m & 0 & 0 \\ 0 & m & 0 \\ 0 & 0 & m \end{pmatrix}}_{\mathbf{M}} \cdot \ddot{\mathbf{q}} + \underbrace{\begin{pmatrix} 2c & -c & 0 \\ -c & 2c & -c \\ 0 & -c & 2c \end{pmatrix}}_{\mathbf{C}} \cdot \dot{\mathbf{q}} + \underbrace{\begin{pmatrix} 2k & -k & 0 \\ -k & 2k & -k \\ 0 & -k & 2k \end{pmatrix}}_{\mathbf{K}} \cdot \mathbf{q} + \underbrace{\begin{pmatrix} \lambda q_1^3 + \lambda (q_1 - q_2)^3 + \mu F_N \frac{2}{\pi} \arctan(\gamma \dot{q}_1) \\ \lambda (q_2 - q_1)^3 + \lambda (q_2 - q_3)^3 + \mu F_N \frac{2}{\pi} \arctan(\gamma \dot{q}_2) \\ \lambda q_3^3 + \lambda (q_3 - q_2)^3 + \mu F_N \frac{2}{\pi} \arctan(\gamma \dot{q}_3) \end{pmatrix}}_{\mathbf{f}_{nl}} = \dots$$

$$\dots = \underbrace{\begin{pmatrix} 5 \\ 5 \\ 5 \end{pmatrix}}_{\mathbf{f}_{ex,det}} \cos(\Omega t) + \underbrace{\begin{pmatrix} \sigma & 0 & 0 \\ 0 & \sigma & 0 \\ 0 & 0 & \sigma \end{pmatrix}}_{\mathbf{\Sigma}} \cdot \frac{d\mathbf{w}}{dt}, \quad (7.43)$$

where $\frac{2}{\pi} \arctan(\gamma \dot{q}_i)$ is an approximation of the signum-function $\text{sgn}(\dot{q}_i)$ with $\gamma = 10^4$. The drift vector of the corresponding SDE is

$$\mathbf{f}(\mathbf{x}, t) = \mathbf{E}_1 \cdot \mathbf{x} + \mathbf{E}_2 \cdot \frac{1}{m} [\mathbf{f}_{ex,det} - \mathbf{f}_{nl}(\mathbf{x}) - \mathbf{C} \cdot \mathbf{E}_3 \cdot \mathbf{x} - \mathbf{K} \cdot \mathbf{E}_4 \cdot \mathbf{x}] \quad (7.44)$$

with the matrices $\mathbf{E}_1 = \mathbf{I}_3 \otimes \begin{pmatrix} 0 & 1 \\ 0 & 0 \end{pmatrix}$, $\mathbf{E}_2 = \mathbf{I}_3 \otimes \begin{pmatrix} 0 \\ 1 \end{pmatrix}$, $\mathbf{E}_3 = \mathbf{E}_2^T$ and $\mathbf{E}_4 = \mathbf{I}_3 \otimes (1 \ 0)$. The diffusion matrix is

$$\mathbf{B} = \frac{1}{2} \left[\left[\mathbf{\Sigma} \otimes \begin{pmatrix} 0 & 0 \\ 0 & 1 \end{pmatrix} \right]^T \cdot \left[\mathbf{\Sigma} \otimes \begin{pmatrix} 0 & 0 \\ 0 & 1 \end{pmatrix} \right] \right]. \quad (7.45)$$

The calculation was performed using the harmonic orders $N_{h,\mu} = 3$ and $N_{h,\sigma} = 3$ as well as the correction function orders $N_\varphi^{(b)} = 2 \forall \mathbf{b} \in [1, \dots, n]$ and $N_\varphi^{(t)} = 6$.

In Fig. 7.7 one can see calculation results for the second DOF. There is a large agreement between the results of the MCS and those of the Galerkin-type method. The results for a single point in time shown in Fig. 7.8 also show a good agreement between the MCS and the Galerkin-type method. Also the two-dimensional projection on the location and velocity of the second degree of freedom seems plausible. In other projections, e.g. onto the subspace x_1-x_3 , it can be seen that second order

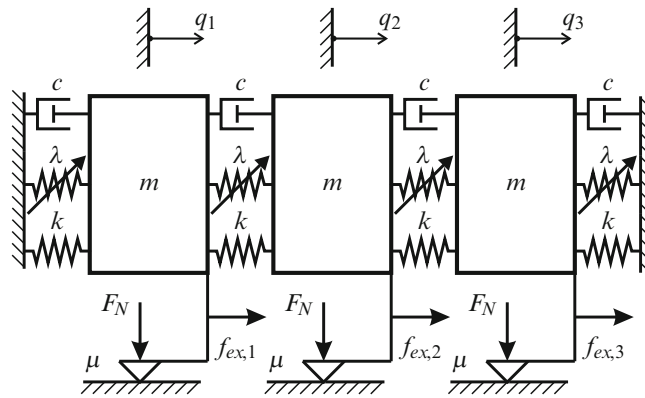


Fig. 7.6 3-DOF-system with friction

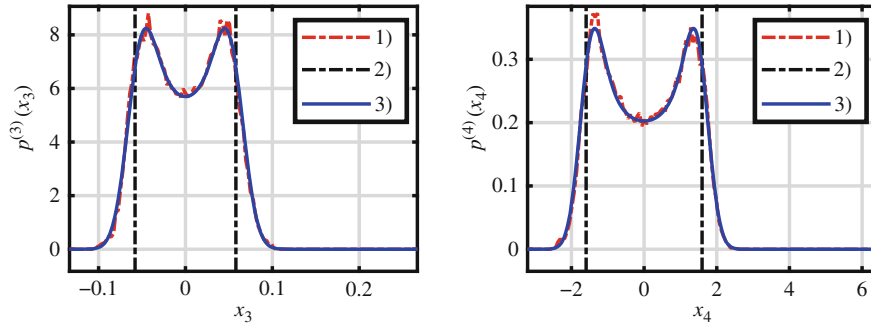


Fig. 7.7 Galerkin-approximation of $p^{(3)}$ and $p^{(4)}$ with (1) MCS-results, (2) $\hat{x}_{b,det}$, (3) $p_{Galerkin}^{(b)}$

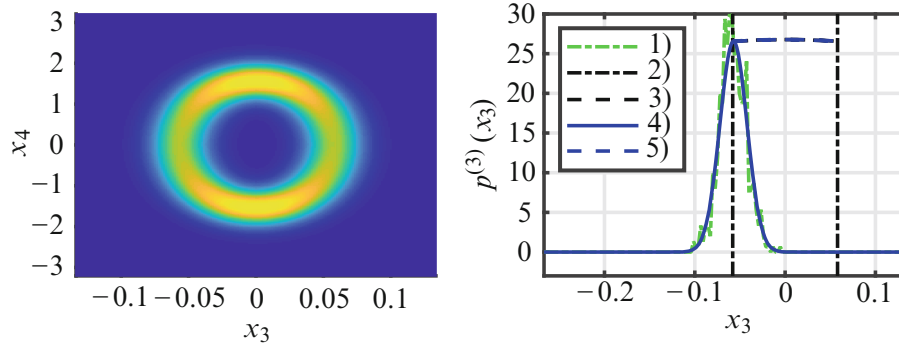


Fig. 7.8 Galerkin-approximation of $p^{(3,4)}(x_3, x_4)$ [left] and $p^{(3)}(x_3, t = \frac{2\pi}{\Omega})$ with (1) MCS-results, (2) $\hat{x}_{3,det}$, (3) $\hat{p}_0^{(3)}(x_3)$, (4) $p_{Galerkin}^{(3)}(x_3, t = \frac{2\pi}{\Omega})$ and (5) $\hat{p}_{Galerkin}^{(3)}(x_3)$ [right]

polynomials are not suitable in this case to correct the one-dimensional Gaussian approach sufficiently. In this projection, which is not shown here, slightly negative values would occur in some areas.

The calculation time in this case is about 30 min. The long calculation time is due to the large number of multi-dimensional correction functions, which result from the large number of combinations of one-dimensional polynomials and harmonic functions. In this case, an MCS would probably be faster with acceptable quality of the results.

7.5.4 20-DOF Model of a Bladed Disk Assembly

The last exemplary system considered in this paper is a cyclic 20-DOF system as a model of a bladed disk assembly. This system can be seen in Fig. 7.9. The system is excited with engine order (EO) 30, so that the harmonic force has the form

$$f_{ex,i,det} = \hat{f}_{ex,i} \cdot \cos(\Omega t - \chi_i), \quad (7.46)$$

where $\hat{f}_{ex,i} = 5$, $\Omega = 9.5$ and $\chi_i = (i - 1) \frac{2\pi \cdot EO}{N_{DOF}}$. The drift vector components $2i - 1 \forall i \in [1, \dots, N_{DOF}]$ are

$$f_{2i-1} = x_{2i} \quad (7.47)$$

and the components $2i \forall i \in [1, \dots, N_{DOF}]$ are

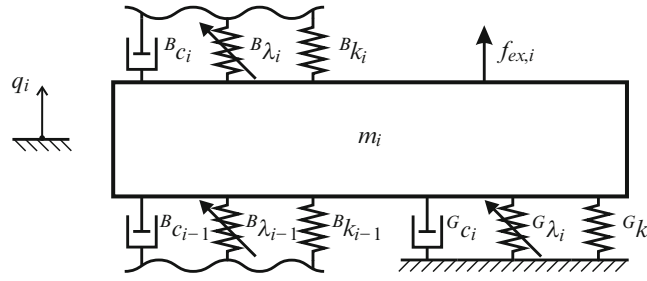


Fig. 7.9 M-DOF-model of a bladed disk assembly

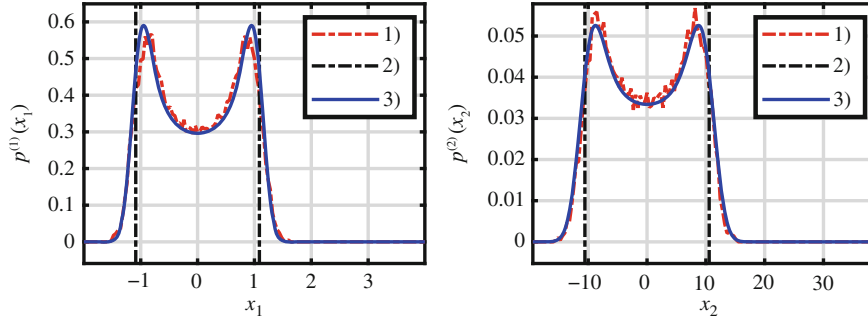


Fig. 7.10 Galerkin-approximation of $p^{(1)}$ and $p^{(2)}$ with (1) MCS-results, (2) $\hat{x}_{b,det}$, (3) $p_{Galerkin}^{(b)}$

$$\begin{aligned}
 f_{2i} = & -\frac{G_{c_i}}{m_i} x_{2i} - \frac{G_{k_i}}{m_i} x_{2i-1} - \frac{G_{\lambda_i}}{m_i} x_{2i-1}^3 - \frac{B_{c_i}}{m_i} (x_{2i} - x_{2i+2}) - \frac{B_{k_i}}{m_i} (x_{2i-1} - x_{2i+1}) - \frac{B_{\lambda_i}}{m_i} (x_{2i-1} - x_{2i+1})^3 - \dots \\
 & \dots - \frac{B_{c_{i-1}}}{m_i} (x_{2i} - x_{2i-2}) - \frac{B_{k_{i-1}}}{m_i} (x_{2i-1} - x_{2i-3}) - \frac{B_{\lambda_{i-1}}}{m_i} (x_{2i-1} - x_{2i-3})^3 + \frac{\hat{f}_{ex,i}}{m_i} \cdot \cos(\Omega t - \chi_i)
 \end{aligned} \quad (7.48)$$

The entries of the diffusion describing matrix are $b_{2i,2i} = \frac{1}{2} \frac{\sigma_i}{m_i} \forall i \in [1, \dots, N_{DOF}]$ and $b_{k,l} = 0$ for $k \neq 2i \wedge l \neq 2i$. The individual blade has the mass $m_i = 1.2$, the stiffnesses $G_{k_i} = 80$ and $B_{k_i} = 30.5$, the damping values $G_{c_i} = 0.08$ and $B_{c_i} = 0.03$, and the cubic stiffnesses $G_{\lambda_i} = 1.5$ and $B_{\lambda_i} = 10.2$. The standard deviation of the additive excitation with uncorrelated GWN is $\sigma_i = 1$ for each blade. The final correction orders used are $N_{\varphi}^{(1)} = 6$, $N_{\varphi}^{(2)} = 6$ and $N_{\varphi}^{(b)} = 0 \forall b \in [3, \dots, n]$ as well as $N_{\varphi}^{(t)} = 10$. Before the final calculation, two calculations with lower approximations were performed. In Fig. 7.10 one can see the one-dimensional PDFs for the first DOF. Especially in the PDF for the displacement one can see that there are some differences between the results of the MCS and those of the Galerkin-type method. These differences probably occur because the correlation between the DOFs with the selected correction polynomials cannot be sufficiently mapped. Although the information about a correlation is taken into account during the calculation, the equilibrium to be solved is only correct on average. This is why the result is only as good as the available polynomials. Figure 7.11 shows the two-dimensional JPDF of the first DOF after the correction and the PDF of the displacement of the first DOF at $t = \frac{2\pi}{\Omega}$.

As this is a cyclic system, the other DOFs can be derived comparatively well from the results of the first DOF. This allows the representation in Fig. 7.12. Even if the most DOFs are not improved with correction functions, different JPDFs can be calculated approximately.

7.6 Problems and Limitations

Although the presented method offers some possibilities, it is subject to several restrictions. On the one hand, the ability to break down the drift vector into one-dimensional functions is a basic prerequisite for being able to apply the method. However, this is not the case, for example, if there is a simple friction contact between two DOFs. In this case, the signum function would depend on the velocities of both DOFs. If, as in this case, only two dimensions are connected, a two-dimensional integration could be carried out in the state space, followed by the time integration. For more complex

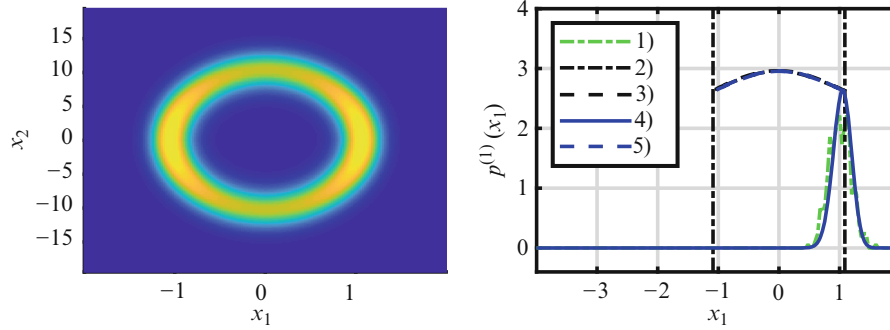


Fig. 7.11 Galerkin-approximation of $p^{(1,2)}(x_1, x_2)$ [left] and $p^{(1)}(x_1, t = \frac{2\pi}{\Omega})$ with (1) MCS-results, (2) $\hat{x}_{1,det}$, (3) $\hat{p}_0^{(1)}(x_1)$, (4) $p_{Galerkin}^{(1)}(x_1, t = \frac{2\pi}{\Omega})$ and (5) $\hat{p}_{Galerkin}^{(1)}(x_1)$ [right]

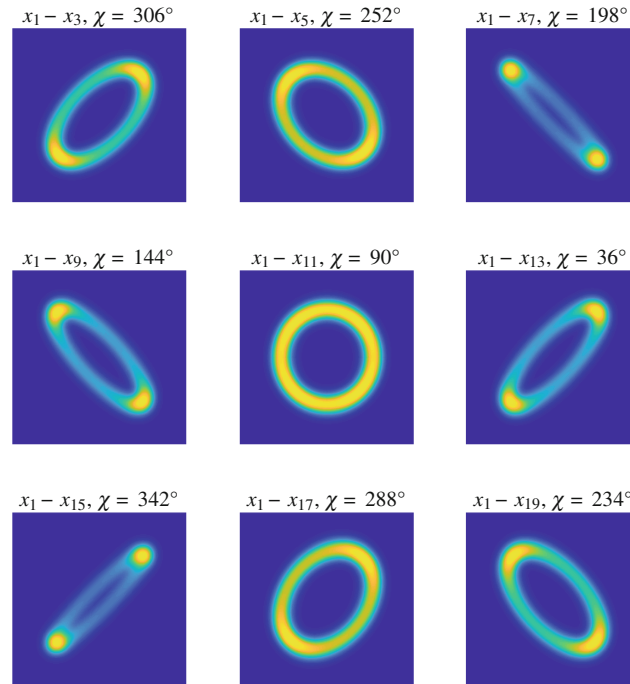


Fig. 7.12 JPDFs between x_1 and different dimensions; x_1 is always on the abscissa; additionally the phase shift of the excitation between the dimensions is indicated

connections, such as a stick-slip element, even higher dimensional integrations would be necessary. Thus, the method would at least be inefficient or no longer applicable. A further limitation results from the number of dimensions to be corrected. It is possible to provide only individual degrees of freedom with correction functions. However, this only provides satisfactory results as long as there is no particularly strong correlation between the state space dimensions at individual points in time. However, this can occur with a stiffer connection between the degrees of freedom or in the resonance case. The number of correction functions cannot simply be increased for all dimensions, because otherwise the size of the system of equations to be solved increases with

$$m = \prod_{b=1}^{n+1} (N_\varphi^{(b)} + 1). \quad (7.49)$$

The effort to calculate all entries of the matrix \mathbf{H} (see Eq. (7.18)) is then, from one point, no longer justifiable. While the resonance case may not be represented by one-dimensional Gaussian approaches, it is certainly not possible to calculate areas with overhanging branches in the deterministic FRF. The only exception could be if at most one branch represents a

stable equilibrium. However, if several stable equilibria occur, this should also be reflected in the PDF by the fact that it has several local core areas. Such a form cannot be represented by either one- or multi-dimensional Gaussian approaches.

7.7 Conclusion and Outlook

In this paper a new method for obtaining approximate solutions of the Fokker–Planck equation for nonlinear mechanical systems in the case of periodic probability density functions as a result of combined harmonic and stochastic excitation is presented. In addition to the basic method, suitable weighting functions and both proper time-dependent orthogonal polynomial and harmonic correction functions are provided. As a proof of feasibility, the Galerkin-type method is verified with various nonlinear mechanical systems.

It is shown that the method is fully applicable to smaller nonlinear systems of one to three degrees of freedom. The basic requirement is that the stochastic part of the excitation is Gaussian. For one and two degree of freedom systems, the method offers a clear speed advantage over Monte-Carlo simulations. Starting from three degrees of freedom this advantage ends, if all degrees of freedom are to be provided with correction functions. For larger systems, the method can only be used to a limited extent. Thus, it is only possible to correct the probability density in the dimensions of one to three degrees of freedom simultaneously. Here, a possibly existing correlation can be considered only with restrictions. Nevertheless, the application in the 20 degrees of freedom system shown leads to acceptable results, which can be calculated in considerably shorter time than with a Monte-Carlo simulation. Limitations also result from the fact that the components of the drift vector must be separable into one-dimensional functions. This is no longer the case with a simple friction contact between two degrees of freedom. Furthermore, the selected approaches cannot be used if the system has several stable states into which it tends despite the noise superposition. This is one of the points that must be investigated in further work. The authors see possible approaches to overcome the weaknesses of the method in the choice of other weighting functions. For example, the use of coordinate transformed multi-dimensional weighting functions is an area of investigation for future work. In this context, but also with regard to the decomposability of the drift vector, integration methods such as the quasi-Monte-Carlo method (see Dick [28]) could possibly be useful. A further possibility to calculate higher dimensional systems in a short time with high approximations without neglecting the correlation between several degrees of freedom could be to choose the polynomials skilfully. This could considerably reduce the size of the equation system to be calculated and solved. In spite of the still existing limitations and weaknesses, the Galerkin-type method offers a good possibility to calculate smaller nonlinear systems which are under a noise superimposed harmonic excitation. In most cases the calculation time remains considerably shorter than in the Monte-Carlo simulation, which to the best knowledge of the author's is the only other method that can be used for this purpose.

References

1. Risken, H., Haken, H.: *The Fokker–Planck Equation: Methods of Solution and Applications*. Springer Series in Synergetics, vol. 18, 2nd edn. Springer, Berlin (1989)
2. Naess, A., Moe, V.: Efficient path integration methods for nonlinear dynamic systems. *Probab. Eng. Mech.* **15**(2), 221–231 (2000)
3. Kumar, P., Narayanan, S.: Nonlinear stochastic dynamics, chaos, and reliability analysis for a single degree of freedom model of a rotor blade. *J. Eng. Gas Turbines Power* **131**(1), 012506 (2009)
4. Kumar, P., Narayanan, S.: Efficient path integral solution of Fokker–Planck equation: response, bifurcation and periodicity of nonlinear systems. *Int. J. Adv. Eng. Sci. Appl. Math.* **3**(1–4), 111–125 (2011)
5. Pirrotta, A., Santoro, R.: Probabilistic response of nonlinear systems under combined normal and Poisson white noise via path integral method. *Probab. Eng. Mech.* **26**(1), 26–32 (2011)
6. Narayanan, S., Kumar, P.: Numerical solutions of Fokker–Planck equation of nonlinear systems subjected to random and harmonic excitations. *Probab. Eng. Mech.* **27**(1), 35–46 (2012)
7. Kumar, P., Narayanan, S.: Response statistics and reliability analysis of a mistuned and frictionally damped bladed disk assembly subjected to white noise excitation. In: *Volume 6: Structures and Dynamics, Parts A and B*, pp. 649–658. ASME, New York (2010)
8. Caughey, T.K.: Nonlinear theory of random vibrations. In: *Advances in Applied Mechanics*, vol. 11, pp. 209–253. Elsevier, Amsterdam (1971)
9. Cha, D., Sinha, A.: Statistics of responses of a mistuned and frictionally damped bladed disk assembly subjected to white noise and narrow band excitations. *Probab. Eng. Mech.* **21**(4), 384–396 (2006)
10. Pradlwarter, H.J., Schuëller, G.I.: On advanced Monte Carlo simulation procedures in stochastic structural dynamics. *Int. J. Non-Linear Mech.* **32**(4), 735–744 (1997)
11. Higham, D.J.: An algorithmic introduction to numerical simulation of stochastic differential equations. *SIAM Rev.* **43**(3), 525–546 (2001)
12. Wedig, W.V.: Generalized hermite analysis of nonlinear stochastic systems. *Struct. Saf.* **6**(2–4), 153–160 (1989)
13. Wedig, W., Krée, P. (eds.): *Probabilistic Methods in Applied Physics*. Lecture Notes in Physics, vol. 451. Springer, Berlin (1995)

14. Wedig, W.V., von Wagner, U., Spanos, P.D., Brebbia, C.A. (eds.): *Extended Laguerre Polynomials for Nonlinear Stochastic Systems*. Springer, Dordrecht (1999).
15. von Wagner, U.: Zur Berechnung stationärer Verteilungsdichten nichtlinearer stochastisch erregter Systeme. In: *Fortschritt-Berichte VDI Reihe 11, Schwingungstechnik*, VDI-Verl., Düsseldorf, als ms. gedr. edn. (1999)
16. von Wagner, U., Wedig, W.V., On the calculation of stationary solutions of multi-dimensional Fokker–Planck equations by orthogonal functions. In: *Zinc Industry*, vol. 21, pp. 289–306. Woodhead Publishing, Cambridge (2000)
17. von Wagner, U.: On double crater-like probability density functions of a duffing oscillator subjected to harmonic and stochastic excitation. In: Lipka, M. (ed.) *Xenophon’s Spartan Constitution*, vol. 28, pp. 343–355. De Gruyter, Berlin (2002)
18. Martens, W., von Wagner, U., Mehrmann, V.: Calculation of high-dimensional probability density functions of stochastically excited nonlinear mechanical systems. *Nonlinear Dyn.* **67**(3), 2089–2099 (2012)
19. Martens, W., von Wagner, U.: Calculation of probability density functions for nonlinear vibration systems. *Proc. Appl. Math. Mech.* **11**(1), 923–926 (2011)
20. Martens, W.: *On the solution of the Fokker-Planck-Equation for multi-dimensional nonlinear mechanical systems*. Zugl., Berlin, Techn. Univ., Diss., 2013, *Berichte aus dem Maschinenbau*, 1st edn. Shaker, Aachen (2014)
21. Lentz, L., Martens, W.: On the solution of the Fokker-Planck equation on infinite domains using problem-specific orthonormal basis functions in a Galerkin-type method. *PAMM* **14**(1), 767–768 (2014)
22. Förster, A., Panning-von Scheidt, L., Wallaschek, J.: Approximate solution of the Fokker–Planck equation for a multidegree of freedom frictionally damped bladed disk under random excitation. *J. Eng. Gas Turbines Power* **141**(1), 011004 (2019)
23. Gardiner, C.W.: *Handbook of Stochastic Methods for Physics, Chemistry, and the Natural Sciences: For Physics, Chemistry and the Natural Sciences*. Physics and Astronomy Online Library, vol. 13, 3rd edn. Springer and Springer-Verlag, Berlin (2004). isbn 978-3540208822
24. Urabe, M.: Galerkin’s procedure for nonlinear periodic systems. *Arch. Ration. Mech. Anal.* **20**(2), 120–152 (1965)
25. Cameron, T.M., Griffin, J.H.: An alternating frequency/time domain method for calculating the steady-state response of nonlinear dynamic systems. *J. Appl. Mech.* **56**(1), 149 (1989)
26. Cardona, A., Coune, T., Lerusse, A., Geradin, M.: A multiharmonic method for non-linear vibration analysis. *Int. J. Numer. Methods Eng.* **37**(9), 1593–1608 (1994)
27. Cardona, A., Lerusse, A., Gérardin, M.: Fast Fourier nonlinear vibration analysis. *Comput. Mech.* **22**(2), 128–142 (1998)
28. Dick, J., Kuo, F.Y., Sloan, I.H.: High-dimensional integration: the quasi-Monte Carlo way. *Acta Numer.* **22**, 133–288 (2013)



Chapter 8

Gerrymandering for Interfaces: Modeling the Mechanics of Jointed Structures

T. Dreher, Nidish Narayanaa Balaji, J. Groß, Matthew R. W. Brake, and M. Krack

Abstract Recent experiments with the Brake-Reuß-Beam (BRB), a three-bolt lap-jointed benchmark system, have shown that neither the contact pressure nor the contact area are constant within the interface during oscillation, two traditional assumptions made for modeling bolted structures. Thus, it is important to preserve interfacial kinematics and represent the underlying physics in a consistent fashion to develop consistent computational models. Most consistent formulations tend to result in large model sizes and thus make computations for large structures nearly intractable. However, there have been multiple efforts at interface reduction. Most of these formulations though, have the disadvantage of having to deal with large number of points for the nonlinear force calculations. The current study proposes an interfacial reduction approach that is both consistent with the kinematics and at the same time does not require transformations to the original coordinates. Based upon this framework, the current work also compares different criteria for the reduction procedure. The method is demonstrated to improve the efficiency of nonlinear simulations (conducted using two different approaches), with little to no sacrifice in accuracy.

Keywords Interface reduction · Rough surface contact · Zero Thickness Elements (ZTEs) · Quasi Static Modal Analysis (QSMA) · Hyper-reduction

8.1 Introduction

The presence of jointed structures in nearly every mechanical assembly demonstrates the necessity of creating reliable contact models and the significance of understanding the underlying physics. The common practice of modeling a jointed structure is to assume that the contact pressure and area are constant during dynamic excitation. However, recent experiments with the Brake-Reuß-Beam (BRB) benchmark system [2, 9] have shown that neither the contact pressure nor the contact area are constant within the interface during oscillation. These observations are incongruent with traditionally used approaches for modeling jointed interfaces, as e.g. a low number of Iwan Elements are used to represent the interfacial properties. In this research a new modeling approach that considers the physical effects during oscillation and reduces the model order of the interface is investigated. Contact patches that are

1. uniformly distributed over the interface
2. based on the salient physical phenomena

are analyzed with zero thickness elements [6] in combination with a rough contact constitutive model [4]. A perfectly elastic unilateral spring and a 2D coupled elastic dry friction formulation are used in normal and tangential directions.

T. Dreher · J. Groß · M. Krack
Institute of Aircraft Propulsion Systems, University of Stuttgart, Stuttgart, Germany

N. N. Balaji · M. R. W. Brake (✉)
Department of Mechanical Engineering, William Marsh Rice University, Houston, TX, USA
e-mail: brake@rice.edu

8.2 Model Description

An Abaqus Finite Element (FE) Model with a structured mesh serves as basis for the study. Each bolt of the three-bolt lap joint is pre-stressed to extract the mass and stiffness matrix of the assembly using Abaqus substructuring, whose theory can be found in the user manual [3], with 20 fixed-interface modes. All nodes on both contact surfaces of the structure are retained. In a second reduction step the matrices obtained from Abaqus were transformed into relative coordinates between the coincident nodes of the two contact interfaces. Thus, the number of Degrees of Freedom (DOFs) is reduced to the number of interface nodes (680×3) plus the 20 generalized coordinates. To the reduced model, a segment to segment contact with Zero Thickness Elements (ZTEs) is applied [6], which introduces a new mesh of surface elements with new nodes. For this purpose a transformation between the original nodes and the new nodes of the ZTEs can be established. This reduction allows that the contact model can be evaluated in the reduced coordinates, which is often called hyper-reduction. The number of generalized coordinates is reduced to three times the number of nodes of the ZTE Mesh plus modal degrees of freedom.

8.2.1 ZTE Meshes

A Zero Thickness Element Mesh, which is similar to the interfacial mesh of the Abaqus Model, serves as reference for all investigations and is shown at top of Fig. 8.1. Against this reference model, two different reduction methods are compared against each other. One of them is an uniformly distributed mesh shown in the middle of Fig. 8.1. It is deduced from the original mesh by combining adjacent elements. The second mesh is shown in the bottom of Fig. 8.1 and is generated based on the interface's static pressure distribution due to the pre-load and the mode shape of the first mode. The pressure distribution and mode shape are normalized and weighted equally to create a 3D surface, which is used to seed new nodes on different contour lines. Ensuring that element quality standards are fulfilled, re-meshing of the seeded nodes results in the shown mesh. Taking the static pressure and the mode shape for the mesh generation into consideration accounts for the salient physics, as

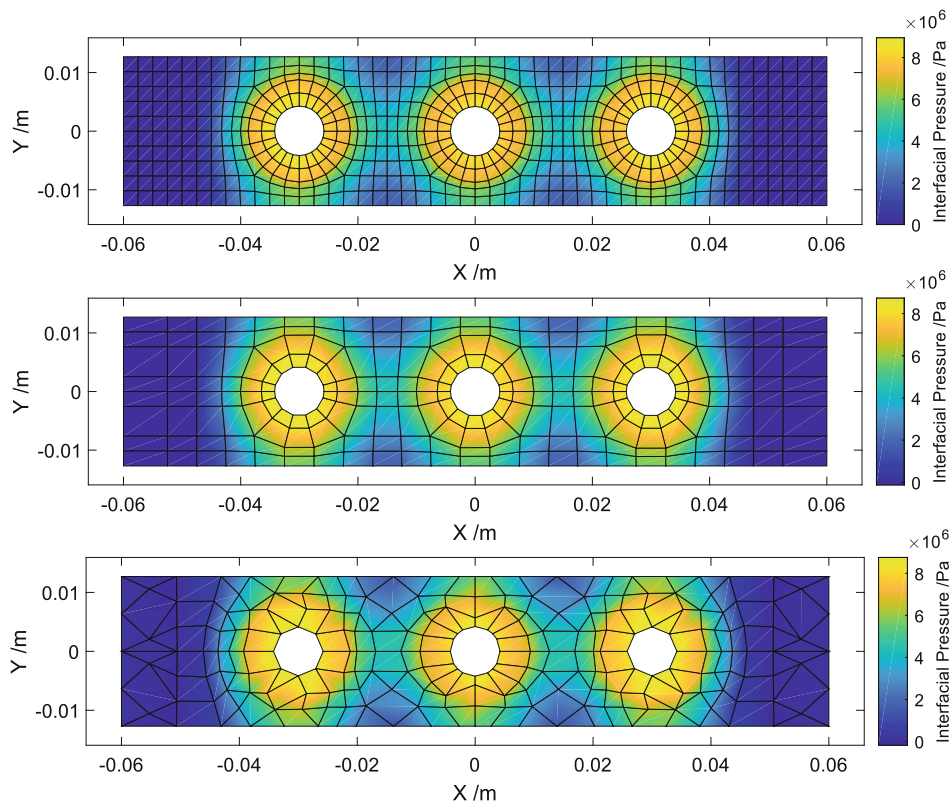


Fig. 8.1 Investigated meshes and the corresponding interpolated pressure distribution for: mesh of the original Abaqus FE model (top), uniformly distributed mesh (middle), and physics based mesh (bottom)

e.g. regions with higher static pressure gradient are finer resolved. The uniformly distributed mesh consists of 232 elements (282 nodes) and the pressure based mesh of 240 elements (240 nodes). Both three and four node linear triangular and quadrilateral ZTEs are used.

For all meshes the pressure distribution in the interface is shown as a contour plot. The pressure (and displacement) distribution are obtained by interpolating the nodal pressures from the Abaqus model. Nodal element forces are computed by integration of the interpolated pressure distribution.

8.2.2 Quasi Static Modal Analysis

Quasi Static Modal Analysis (QSMA) is conducted on the resulting system matrices for the different meshes after applying the ZTEs. It is assumed that the modal deflection shape, obtained by linear modal analysis for a contact in sticking conditions, remains constant for all vibration levels, which allows that the theory for an uncoupled system as per [1] is used. A rough contact constitutive model as proposed by Greenwood in [4] is applied to model the nonlinear behavior of the interface. For this purpose the contact model is evaluated at the 25 integration points of each element and weighted with the shape function to obtain the nonlinear force at the nodes. The contact model takes as input: interpolated pressure values extracted from the pre-stressed Abaqus model (as shown in Fig. 8.1), the tangential stiffness value of the interface k_t estimated by [7], the normal stiffness k_n obtained with k_t and the Mindlin relationship between k_t and k_n [5, 8], and a friction coefficient of $\mu = 0.1$ (the effect of μ is considered in a later study). The standard deviation of the roughness in the equation for k_t was tuned to match the measured natural frequency for low excitation amplitudes for the reference mesh (see Fig. 8.1 (top)). The tuned value for the standard deviation of roughness is approximately three and a half times larger than measured. As the formula assumes an exponential asperity peak distribution, that might not represent the reality sufficiently, the deviation between the measured and tuned parameter can be justified.

The QSMA hysteresis loops for different modal excitation forcing levels are predicted and natural frequency and damping are extracted to determine the backbone curves of the nonlinear system. The secant of the quasi-statically traced hysteresis loop is used to calculate the natural frequency, ω_r , as

$$\omega_r(\alpha_n) = \sqrt{\frac{2 \cdot \alpha_n}{\max(q_r(\alpha_n)) - \min(q_r(\alpha_n))}} \quad (8.1)$$

Here, α_n represents the modal excitation force of the n th loading level and q_r the modal displacement for the r th mode. The modal damping ratio due to the nonlinearity in the interface is calculated as

$$\zeta_r(\alpha_n) = \frac{D(\alpha_n)}{2\pi (q_r(\alpha_n)\omega_r(\alpha_n))^2}, \quad (8.2)$$

with $D(\alpha)$ as energy dissipation per cycle, which is equal to the area of the hysteresis loop defined in [1]. In addition 0.5% linear modal damping are added to account for the material damping of the system. Results of the numerical analysis are presented in the following section.

8.3 Results

In Fig. 8.2, the natural frequency ω_r (left) and the modal damping ratio ζ_r (right) are shown over the modal acceleration amplitude for the BRB's first bending mode. The model for this analysis was pre-stressed with a force to the effect of a 6.8 Nm bolt torque. Comparing the natural frequency for all curves, a softening behavior is observed, as the natural frequency decreases with increasing modal response amplitude. The convergence towards a limit value—the linear natural frequency—for low response amplitudes can be observed. However, the limit value differs for the different reduction methods. Both reduced meshes overestimate the natural frequency, i.e. the stiffness of the system. For the pressure based mesh a deviation of about 2 Hz is seen, and the uniformly distributed meshes' linear natural frequency is about 1.4 Hz higher, compared to the reference solution. The increased frequency for the reduced meshes is explained by the coarser mesh in the interface, which stiffens the system. It is supposed that for the pressure based mesh especially the triangular elements stiffen the system, making the observed difference plausible. With increasing amplitude the solution for both types of mesh converge towards the

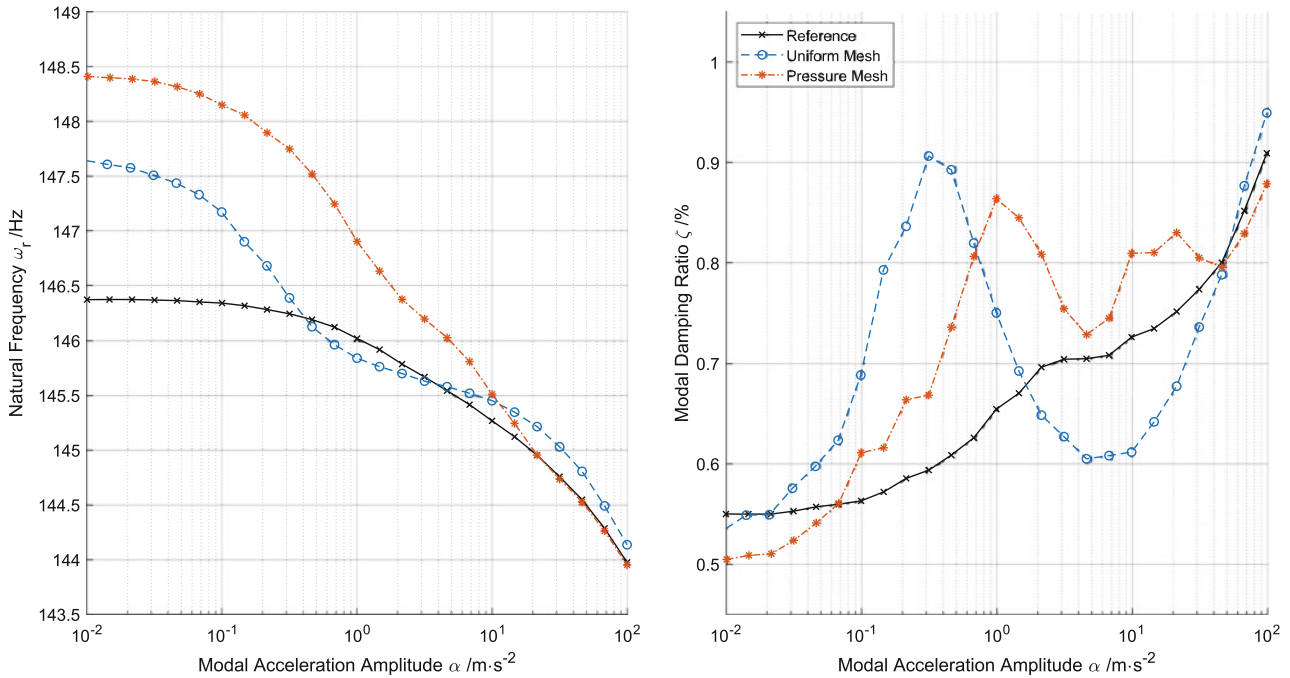


Fig. 8.2 Backbone curves for natural frequency ω_r (left) and modal damping ratio ζ_r (right) over modal acceleration amplitude for different meshes

reference. While the analysis for the pressure based mesh shows a higher natural frequency compared to the reference within the whole response range, the curve for the uniformly distributed mesh converges faster towards the reference solution and oscillates around it. The results for the pressure based mesh show no deviation for amplitudes higher than $10^1 m/s^2$, whereas the curve for the uniformly distributed shows comparable low deviation for a wider range (above $2 \cdot 10^{-1} m/s^2$).

The modal damping ratio for the reference system, shown on the right side of Fig. 8.2, increases with the response as expected. For low amplitudes the damping due to nonlinear effects is small, as ζ is only slightly greater than the added linear damping of 0.5%. For a response level of $10^2 m/s^2$ the nonlinear damping increases up to about 0.9%. The damping prediction with the reduced meshes are similar for the low and the high end of the response range, but show different behavior in-between. Compared to the reference, peaks in the damping curve are present for the response at about $10^0 m/s^2$ for the pressure based, and at about $2 \cdot 10^{-1} m/s^2$ for the uniformly distributed mesh. The peaks are suspected to be induced by macro slip behavior in the interface, which emerges only for the reduced interface meshes as the resolution is lower. For the pressure based mesh the overall prediction of the modal damping is better compared to the uniformly distributed mesh, as the maximal deviation is lower (about 0.2% compared to 0.3%) and the absolute difference for a wider response range is smaller.

8.4 Conclusion

Both interface reduction approaches have the ability to predict the trend of the backbone curve. However, the reduced number of elements leads to stiffening of the system and therefore an overestimation of the linear natural frequency. For the studied case with an uniformly distributed mesh the nonlinear frequency behavior is predicted to be more accurate. For both approaches additional peaks in nonlinear damping behavior are seen. The total deviation is lower for the pressure based mesh. However, between the two mesh approaches no significant difference is observed. Further analysis with different meshes and contact models is needed to come to a final conclusion. This hyper-reduction method allows an efficient calculation of the nonlinear forces in the reduced domain.

References

1. Allen, M.S., Lacayo, R.M., Brake, M.R.W.: Quasi-static modal analysis based on implicit condensation for structures with nonlinear joints. In: International Conference on Noise and Vibration Engineering, Leuven (2016)
2. Brake, M.R.W.: Round robin systems. In: Brake, M.R.W. (ed.) *The Mechanics of Jointed Structures: Recent Research and Open Challenges for Developing Predictive Models for Structural Dynamics*, pp. 45–58. Springer, Berlin (2018)
3. Dassault Systèmes: SIMULIA User Assistance 2018. Simulia (2017)
4. Greenwood, J.A., Williamson, J.B.P.: Contact of nominally flat surfaces. *Proc. R. Soc. Lond. A* **295**, 300–319 (1966)
5. Królikowski, J., Szczepek, L.: Assessment of tangential and normal stiffness of contact between rough surfaces using ultrasonic method. *Wear* **160**(2), 253–258 (1993)
6. Mayer, M.H., Gaul, L.: Segment-to-segment contact elements for modelling joint interfaces in finite element analysis. *Mech. Syst. Signal Process.* **21**(2), 724–734 (2007)
7. Medina, S., Nowell, D., Dini, D.: Analytical and numerical models for tangential stiffness of rough elastic contacts. *Tribol. Lett.* **49**(1), 103–115 (2013)
8. Mindlin, R.D.: Compliance of elastic bodies in contact. *J. Appl. Mech.* **16**, 259–268 (1949)
9. Seeger, B., Butaud, P., Baloglu, M.V., Du, F., Brake, M.R.W., Schwingshackl, C.W.: In situ measurements of interfacial contact pressure during impact hammer tests. In: Kerschen, G. (ed.) *Nonlinear Dynamics, Volume 1: Proceedings of the 36th IMAC, a Conference and Exposition on Structural Dynamics 2018*, pp. 225–236. Springer, Berlin (2018)



Chapter 9

An Analysis of the Gimballed Horizontal Pendulum System for Use as a Rotary Vibrational Energy Harvester

D. Sequeira, J. Little, and B. P. Mann

Abstract This paper examines a gimballed horizontal pendulum for use as an energy harvester. It can be designed for threshold escape behavior rather than the conventional method of matching frequencies. A nonlinear electromechanical model is developed to study the system's equilibrium states as a function of tilt angle. Bifurcation diagrams are generated to illustrate these equilibria and their associated stability. A bifurcation point is solved for analytically and the implications for an energy harvester, one that can be designed to jump across stable attractors based on forcing amplitudes, are discussed.

Keywords Nonlinear energy harvester · Bifurcation analysis · Bistable system · Electromechanical · Attractors

9.1 Introduction

Vibratory energy harvesting has grown increasingly popular in recent years as battery technology has been unable to keep pace with the rapid advancements in the field of micro-electronics [1]. This motivation has led to a significant amount of research on novel ways to scavenge energy from environmental excitations where the majority of studies focus on designing harvesters to match their natural frequencies with the environmental excitation frequency [2]. This paper investigates a new type of rotary vibrational energy harvester with unique tuning capabilities that allow for designing to the excitation amplitude rather than its frequency. This approach can be useful when the excitation amplitude is significantly more predictable than the excitation frequency as is the case in numerous environmental excitations. The proposed system resembles an inclined pendulum with an additional gimbal-like rotational degree of freedom that introduces complex dynamics into the system which can be leveraged for improved energy harvesting under various conditions.

To analyze this system, multiple steps are taken. First, the system is described geometrically by breaking it into its component pieces and allowing for three degrees of rotation, where one of the rotations powers an electromechanical transducer. The electromechanical equations of motion are derived using Lagrange's equations under the assumption that the harvester uses electromagnetic inductance. Next, a bifurcation analysis of the system is performed to investigate the system behavior at various orientations in absence of external forcing. An analytical expression is derived for the transition point as a function of the system's geometric parameters and bifurcation diagrams are generated that unveil the presence of non-trivial equilibrium solutions for certain tilt angles. Finally, the implications of these bifurcation diagrams is discussed to bridge the gap between understanding how the system behaves in a static setting and how it would respond to dynamic excitations with an emphasis on how interaction across stable attractors could be encouraged [3].

9.2 Analysis

Figure 9.1 illustrates both the electrical circuit and corresponding mechanical system that this paper will study. As shown, three rotations have been defined to describe the system's position at any given time: a rotation of the entire system ψ out of the page, another rotation θ about the gimballed axis, and a third rotation ϕ about the horizontal pendulum's axis. This paper will assume that the whole system is driven in ψ by an external forcing function which results in prescribed motion, $\psi(t) = A \sin(\omega t)$ where A is the amplitude of rotation in radians and ω is the frequency of rotation in rad/s. This assumption defines the system using two rotational degrees of freedom (θ and ϕ) being driven by a prescribed rotational motion (ψ).

D. Sequeira (✉) · J. Little · B. P. Mann

Department of Mechanical Engineering and Material Science, Pratt School of Engineering, Duke University, Durham, NC, USA
e-mail: dane.sequeira@duke.edu

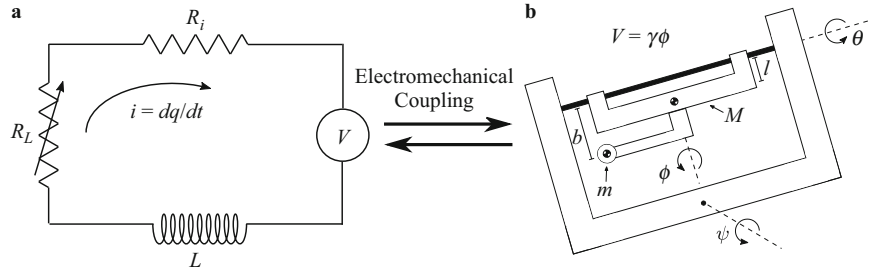


Fig. 9.1 (a) Illustration showing the electrical circuit that could be used to harvest energy from the mechanical system through electromagnetic induction. (b) Drawing of the gimballed horizontal pendulum which identifies the three rotations

The analysis that follows will investigate how these two degrees of freedom respond to various external forcings with a particular focus on how the system responds for different amplitudes.

Equations of motion can be obtained for this system by applying Lagrange's equations and assuming that energy is transferred from the mechanical system into the electrical circuit through electromagnetic inductance. Once equations of motion have been obtained, equilibrium solutions are determined by putting the system into state space form, setting all time dependent terms equal to zero, and solving for the resulting equilibria as a function of the tilt angle ψ . The corresponding stability of these equilibria can be determined from the state space equation by evaluating the Jacobian at its equilibria and calculating the resulting eigenvalues. In particular, if the real part of the eigenvalues is greater than zero, the associated equilibrium position is unstable. Otherwise, they represent stable equilibria.

Using these methods, bifurcation diagrams can be generated for this system by solving for the equilibria and their associated stability as a function of a changing parameter. For this study, ψ was chosen as the control parameter for its implications on the forced dynamic system. To do this, ψ was treated as a static value rather than a time varying one and the system characteristics were studied as a function of different fixed values of ψ . Figure 9.2 shows multiple different interpretations of the equilibrium solutions for both $\tilde{\theta}$ and $\tilde{\phi}$ as the fixed value for ψ is varied where solid lines correspond to stable solutions and dashed lines represent unstable solutions. Figure 9.2a, b show the bifurcation diagrams for the system as they exist in two-dimensional space where only non-trivial equilibrium solutions are included for clarity. When analyzing these results, it is worth noting that these equilibrium solutions repeat themselves periodically every 2π radians in each variable. This makes intuitive sense because the system is characterized by three rotations so should look mathematically identical for a full revolution in any direction. Further inspection shows that the non-trivial solutions for $\tilde{\theta}$ trace out a circle with a characteristic radius. The value of this radius can be determined analytically by solving for $\tilde{\theta}$ when $\psi = 0$ as

$$\xi_s = \cos^{-1} \left[\left(\frac{lm + bM}{mr} \right) \sin \xi_s \right] \quad (9.1)$$

where l and b represent distances from the rotating mass and disc to the gimballed pivot, respectively, m and M are the masses of the point mass and disc (shown in Fig. 9.1), respectively, and ξ_s is the radius of the circle traced out on the bifurcation diagram. This value represents an important transition at $\psi = \pm \xi_s$ where non-trivial bistable equilibrium solutions converge onto a single trivial equilibrium solution. This bifurcation point can be determined numerically by solving the implicit Eq. 9.1 for a given set of geometric parameters. This value represents a particularly interesting characteristic of the system because it signifies both the angle $\tilde{\theta}$ that the system comes to rest at when $\psi = 0$ which is the same as the minimum displacement angle ψ that is required for the system to equilibrate at $\tilde{\theta} = 0$. These angles are important because they act as transition points between trivial and non-trivial solutions. If ψ is within one of the periodically repeating intervals $\psi = (n\pi \pm \xi_s)$, then the system is in a non-trivial state where small changes in ψ correspond to a change in both θ and ϕ . If ψ is outside of this range, however, the system equilibrates at $(\tilde{\theta}, \tilde{\phi}) = (n\pi, k\pi)$ and remains there throughout small changes in ψ . This trivial solution is interesting because it connects symmetrically opposing branches of non-trivial equilibrium solutions and consequently offers a smooth avenue for the system to travel along either branch. This avenue could be exploited in a dynamic setting to encourage interaction across stable attractors, which is desirable for energy harvesters.

Figure 9.2c combines these previous two plots to create a three-dimensional bifurcation diagram to illustrate how $\tilde{\theta}$ and $\tilde{\phi}$ vary together as a function of ψ . This figure also includes the trivial equilibrium solutions which have been superimposed onto the plane, $\tilde{\theta} = 0$, that they exist on. These solutions overlap one another in a two-dimensional plot due to their periodicity

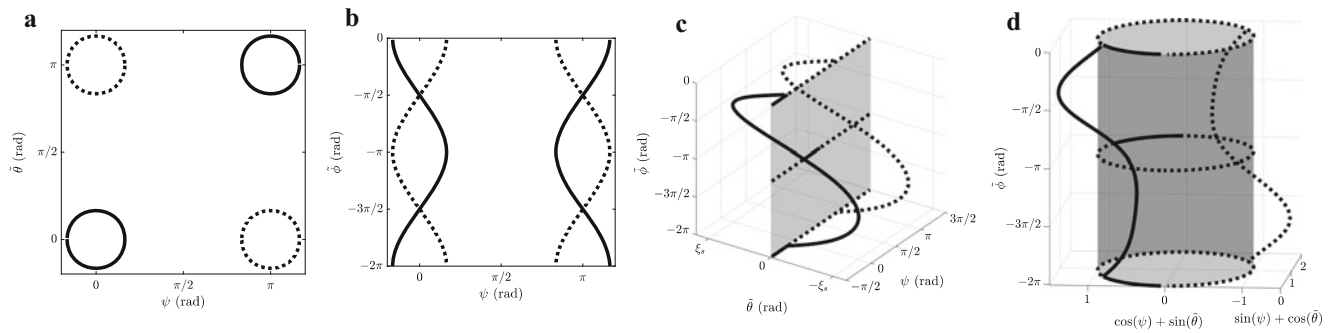


Fig. 9.2 (a, b) Bifurcation diagrams showing non-trivial solutions for θ and ϕ as functions of ψ where solid lines indicate stable solutions and dotted lines indicate unstable solutions. (c) Three-dimensional bifurcation which includes trivial solutions as the exist on the plane $\psi = 0$. (d) Three-dimensional bifurcation diagram where results have been wrapped around a cylinder to illustrate the system's periodicity

which is the reason they were excluded from Fig. 9.2a, b. Finally, Fig. 9.2d shows the results obtained by converting Fig. 9.2c from cartesian into cylindrical coordinates where the trivial solutions now exist on the edge of a cylinder to illustrate the system's periodicity.

9.3 Conclusion

This paper investigated using a gimballed horizontal pendulum as an energy harvester. In doing this, a static stability analysis was conducted that revealed the development of non-trivial equilibria occurring at a critical tilt angle which was a function of the system's geometric parameters. By altering these parameters to match expected forcing characteristics, desirable energy harvesting outcomes can be realized with applications ranging from ocean energy harvesting to monitoring structural integrity.

Acknowledgments This research was supported by both the Link Foundation and Duke University. We thank both of these organizations for the invaluable funding and resource contributions they provided.

References

1. Baerta, K., Gyselinckxa, B., Torfsa, T., Leonova, V., Yazicioglu, F., Brebelsa, S., Donnaya, S., Vanfleteren, J., Beyna, E., Van Hoof, C.: Technologies for highly miniaturized autonomous sensor networks. *Sensors Actuators A*. **135**, 881–888 (2007)
2. Stanton, S.C., McGehee, C.C., Mann, B.P.: Nonlinear dynamics for broadband energy harvesting: investigation of a bistable piezoelectric inertial generator. *Physica D*. **239**, 640–653 (2010)
3. Virgin, L.N., Plaut, R.H., Cheng, C.C.: Prediction of escape from a potential well under harmonic excitation. *Int. J. Non-lin. Mech.* **27**(3), 357–365 (1992)



Chapter 10

On the Dynamic Response of Flow-Induced Vibration of Nonlinear Structures

Banafsheh Seyed-Aghazadeh, Hamed Samandari, and Reza Abrisham Baf

Abstract Fundamentals of Fluid-Structure Interaction (FSI) of a nonlinear structure placed in the wake of a prismatic bluff body is studied, experimentally. Elastically mounted prismatic structures placed in flow can undergo Flow-Induced Vibration (FIV). Flow forces acting on these structures consist of a main frequency, close to the natural frequency of the system, as well as its higher harmonic components. Mostly in FIV studies, the structural stiffness is provided through linear springs. The linearity of the structure limits occurrence of potential large amplitude oscillations at higher harmonics of the main frequency. In this study, an inherently nonlinear structure is implemented in FIV study of a prismatic structure. The results show that large amplitude, low frequency galloping type oscillation is accompanied by large contributions from the higher harmonics in the frequency content of the oscillations. Numerical simulation using Differential Quadrature Method was conducted to identify the optimum structural configurations for coupling between the higher harmonics and natural frequencies of the system.

Keywords Flow-induced vibration · Fluidic energy harvester · Nonlinear structure · Fluid-structure interactions · Higher harmonics

10.1 Introduction

Converting vibrations to usable form of electrical energy has been the subject of several studies over the past few years [1–3]. Research into energy harvesting started with the fundamental efforts for converting simple harmonic vibrations into electricity. However, in the last couple of years, research efforts have focused on converting other forms of mechanical energy, such as random ambient vibrations, surface strain energy of civil engineering structures and vibration induced by wind and water flow. On this basis, energy harvesters from vibration induced by flow energy have been proposed to operate self-powered devices including micro-electro-mechanical systems and wireless sensors. They are also designed to replace small batteries that have a finite life span or would require expensive and time-consuming maintenance.

When a flexible or flexibly mounted structure is placed in fluid flow, it can deform or oscillate. The deformation or oscillation of the structure will result in the change of flow forces, which in turn will result in the change of the structure's deformation or oscillation. This oscillation is called Flow-Induced Vibration (FIV). The most common fluidic energy harvester works based on Flow-Induced Vibration that can harvest energy from external sources available in the environment such as wind or marine currents. There are several studies on FIV with applications in wind energy with novel energy extraction ideas [4–8].

Most common fluidic energy harvesters consist of a piezoelectric cantilevered beam, clamped at one end, connected to a rigid prism with a specific cross-section at the free end, placed in flow. When the vortex formation frequency in the wake of the prism is relatively close to the beam's modal frequencies (usually the first), FIV will occur. The oscillation will cause large strain near the clamped end. The strain produces a voltage difference in the piezoelectric patches and a circuit converts the electric potential to a current. Flow forces acting on the structure undergoing FIV consists of the main frequency, close to

B. Seyed-Aghazadeh (✉)
Department of Engineering Technology, Miami University, Middletown, OH, USA
e-mail: seyedab@miamioh.edu

H. Samandari
Department of Mechanical and Manufacturing Engineering, Miami University, Oxford, OH, USA

R. Abrisham Baf
Department of Engineering Technology, Miami University, Hamilton, OH, USA

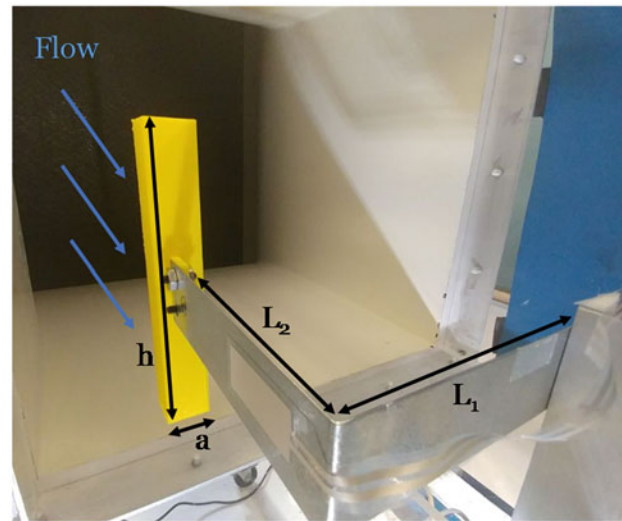


Fig. 10.1 Experimental setup consisting on an L-shaped beam carrying a square prism at its tip, placed in the test-section of the wind tunnel

the NF of the system, as well as its higher harmonic components [9, 10]. In previous studies of FIV based energy harvesters, while linear structures are widely used to provide structural stiffness, the structure could only experience oscillations at frequency values close to its natural frequencies. Despite the existence of such high frequency flow forces, contributions from higher harmonic components of the flow forces are not observed in the frequency content of the oscillation.

In this study, we propose implementing an inherently nonlinear structure in FIV study of a prismatic structure. The system is designed such that the structural nonlinearity, coupled with the aerodynamic nonlinearity allows generation of higher harmonics in the frequency content of the oscillation. Dynamics of Fluid-Structure Interaction of this configuration is studied, experimentally. This configuration will be able to extract energy from the incoming flow, and potentially improve the electrical outputs in fluidic energy harvesters by employing the nonlinear features of the beam. Through numerical simulations, we will investigate how the geometric parameters of the L-shaped beam will influence the internal resonance of the nonlinear beam and how that in return will affect the FSI response of the system.

10.2 Experimental Setup

The experiments were performed in a subsonic wind tunnel, with a test section of $1.27 \text{ m} \times 0.5 \text{ m} \times 0.38 \text{ m}$. An L-shaped beam, holding a square cross-section prism at the tip was tested. Figure 10.1 shows the experimental setup which consists of an L-shaped beam, clamped to a fixture at one end, which fixed the structure to the frame of the wind tunnel. The square cross-section prism was attached to the free end of the beam, where its flat side was facing the incoming flow. For each test, the wind speed was increased from its minimum to its maximum in small steps. The beam was subjected to uniform air-flow with mean flow speed, U . When the mean speed, U , exceeds a critical speed, the beam underwent steady-state oscillations. At each step, the steady-state tip displacements of the beams was measured, using a laser displacement sensor running in tandem with a piezo sensor attached closed to the clamped end of the beam. The prism's displacement in the crossflow direction were measured in the flow velocity range of $U = 0.5\text{--}12.9 \text{ m/s}$, and Reynolds number range of $Re = 4270\text{--}12,800$.

10.3 Results

Figure 10.2a, b shows the dimensionless amplitudes and frequencies of oscillations versus flow velocity for a square prism. To shed light on different types of response observed in Fig. 10.2a, three representative points at three wind velocities of $U = 1.4 \text{ m/s}$, 4.3 m/s , 10.5 m/s have been selected (shown with highlighted columns in Fig. 10.2a). Figure 10.2c–e shows the frequency contents (FFT plots) of the flow-induced vibration response for the sample wind speeds.

The FFT plots exhibit distinct frequency contents: while the main peak in all of these FFT plots corresponds to a frequency close to the natural frequency of the system, contributions of the second and third harmonics, i.e. with twice and three times

the frequency of oscillations, are observed in these cases. The contribution from the third harmonics of the main frequency got larger as the flow velocity was increased. High frequency flow forces at odd integers of the main harmonics has been previously observed in the galloping response of an elastically mounted square prism [11]. These measurements are the first evidence of existing high frequency oscillations in the galloping response of a nonlinear structure.

A series of numerical simulations were also conducted to study the structural dynamics of the L-shaped beam in absence of the fluid flow. The goal was to calculate the natural frequencies of the system and the corresponding higher harmonics under external excitation. The numerical simulations used to determine the nonlinear multi-modal dynamics of L-shaped beams are based on Differential Quadrature Method (DQM), a higher order finite element solution approach. Differential Quadrature Method (DQM) has the capability of producing highly accurate results with minimum computational effort compared to conventional finite element and finite difference methods. This technique enables one to monitor the tuning of the first two bending mode frequencies of the L-shaped beam by studying the influence of each of following geometric parameters: the length of L-shaped beam, width, structural elasticity and the tip prismatic structure mass and mass moment of inertia. Studying the amplitudes and frequencies of oscillations, one can investigate the interplay between the internal resonance of the first two bending modes of the beam, the higher harmonics of the main resonance and high frequency flow forces matching the vibrational modes of the beam. Each line in Fig. 10.3 represents the ratio between the second to the first mode frequency in an L-shaped beam with varying geometrical parameters. The first two bending mode frequencies in the current study are tuned such that the structure has a 3:1 internal resonance. On the other hand, with such frequency tuning, the second bending mode frequency matches the high frequency flow forces resulting from high frequency vortex shedding in the wake of the prismatic structure. These phenomena would affect the FSI response of the system, which in turn can change the level of the energy harvested in the proposed device.

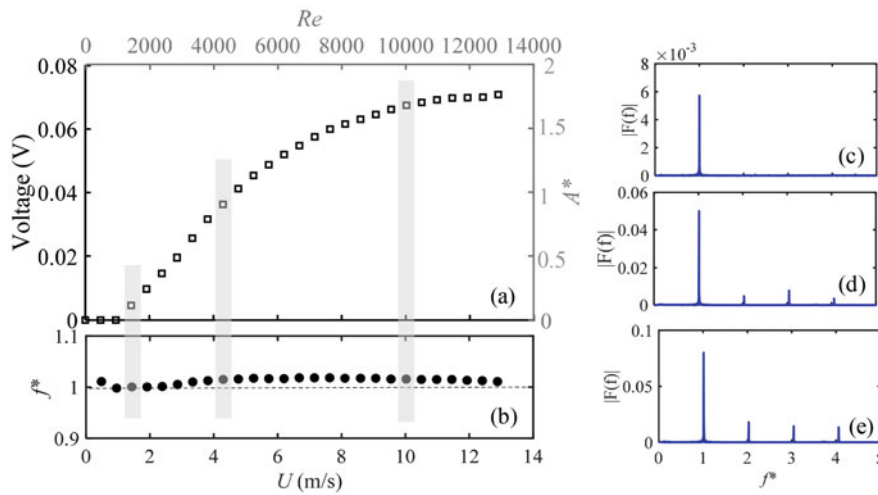


Fig. 10.2 (a, b) Dimensionless amplitudes and frequencies of oscillations versus wind velocity for a square prism, (c–e) frequency contents (FFT plots) for the sample wind speeds of $U = 1.4$ m/s, 4.3 m/s, 10.5 m/s

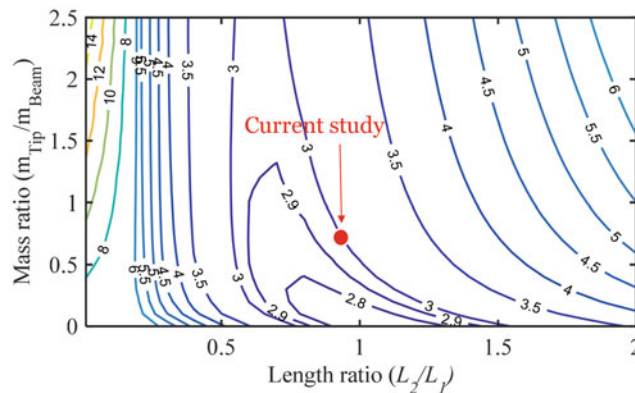


Fig. 10.3 The ratio between the second to the first mode frequency in an L-shaped beam with varying geometrical parameters

10.4 Conclusion

Flow-Induced Vibration of an inherently nonlinear beam with prismatic bluff-body attached at the tip was studied, experimentally. The existence of high frequency flow-induced vibrations as a result of the existing high frequency flow forces was investigated. Large contributions of the higher harmonics in the oscillations of the nonlinear L-shaped beam with a prismatic tip oscillator were observed. In addition, through numerical simulations it was shown that the bending mode frequencies for an L-shaped beam can be tuned to have integer ratios. This tuning cannot be achieved for classical energy harvesters using conventional cantilevered beam configuration. Through this unique design, energy exchange between the first two modes is possible. This could potentially affect the FSI response of the system, which in turn will change the level of the energy harvested in the proposed device.

References

1. Elvin, N., Erturk, A.: *Advances in Energy Harvesting Methods*. Springer Science & Business Media, New York (2013)
2. Anton, S.R., Sodano, H.A.: A review of power harvesting using piezoelectric materials (2003–2006). *Smart Mater. Struct.* **16**(3), R1 (2007)
3. Erturk, A., Renno, J.M., Inman, D.J.: Modeling of piezoelectric energy harvesting from an L-shaped beam-mass structure with an application to UAVs. *J. Intell. Mater. Syst. Struct.* **20**(5), 529–544 (2009)
4. Bryant, M., Garcia, E.: Modeling and testing of a novel aeroelastic flutter energy harvester. *J. Vib. Acoust.* **133**(1), 011010 (2011)
5. Abdelkefi, A.: Aeroelastic energy harvesting: a review. *Int. J. Eng. Sci.* **100**, 112–135 (2016)
6. Akaydin, H.D., Elvin, N., Andreopoulos, Y.: Energy harvesting from highly unsteady fluid flows using piezoelectric materials. *J. Intell. Mater. Syst. Struct.* **21**(13), 1263–1278 (2010)
7. Peng, Z., Zhu, Q.: Energy harvesting through flow-induced oscillations of a foil. *Phys. Fluids.* **21**(12), 123602 (2009)
8. Barrero-Gil, A., Alonso, G., Sanz-Andres, A.: Energy harvesting from transverse galloping. *J. Sound Vib.* **329**(14), 2873–2883 (2010)
9. Seyed-Aghazadeh, B., Budz, C., Modarres-Sadeghi, Y.: The influence of higher harmonic flow forces on the response of a curved circular cylinder undergoing vortex-induced vibration. *J. Sound Vib.* **353**, 395–406 (2015)
10. Seyed-Aghazadeh, B., Carlson, D.W., Modarres-Sadeghi, Y.: Vortex-induced vibration and galloping of prisms with triangular cross-sections. *J. Fluid Mech.* **817**, 590–618 (2017)
11. Nemes, A., et al.: The interaction between flow-induced vibration mechanisms of a square cylinder with varying angles of attack. *J. Fluid Mech.* **710**, 102–130 (2012)



Chapter 11

Potential and Limitation of a Nonlinear Modal Testing Method for Friction-Damped Systems

Maren Scheel, Tobias Schulz, and Malte Krack

Abstract Experimental nonlinear modal analysis has been applied successfully, mainly on structures with stiffness nonlinearities. However, it remains a challenge to experimentally extract a nonlinear modal model of structures with nonlinear damping, such as friction. To systematically investigate a modal testing method for friction-damped structures, we introduce a new test specimen. The specimen is a beam that is clamped on one side and offers six possible locations to induce friction. Changing the friction location varies the significance of the non-linear effects, that is, frequency shift, increase in damping and change of mode shapes. We apply experimental modal analysis with one excitation point to track the properties of one mode from full stick to macro slip. To assess the quality and validity of the extracted modal model, we compare predicted steady-state vibrations with frequency response measurements close to resonance. Based on these results, we discuss the potential and limitation of the applied modal testing approach.

Keywords Nonlinear modes · Modal analysis · Force appropriation · Jointed structures · Nonlinear system identification

11.1 Introduction and Method

In lightweight structures, the dry sliding friction in mechanical joints is often the main dissipation mechanism (friction damping). The strongly nonlinear frictional interactions cause a dependence of the joint's effective stiffness and damping on the vibration level. Contact interactions are commonly described by empirical laws involving parameters that have to be identified from suitable measurements. Moreover, measurements are required to properly verify simulation approaches. Nonlinear (normal) modes capture the vibration signature of a nonlinear system and are therefore an interesting basis both for contact parameter identification and for verification of simulation approaches.

We use the extended periodic motion concept (EPMC) which defines a nonlinear mode as family of periodic motions of an autonomous system [1]. In the non-conservative case, the motions are *made* periodic by an artificial negative damping term. This concept is consistent with the conservative case and the linear case with modal damping. The concept allows to determine how modal frequency, damping ratio and deflection shape (including higher harmonics) for a given mode depend on the vibration level. With these properties one can define a single degree of freedom nonlinear modal oscillator. The agreement of the response of this model with the initial one measures the significance of the modal properties. The above defined nonlinear modes accurately represent steady-state periodic oscillations if the vibration energy is mainly confined in a single nonlinear mode, which is typically the case under harmonic forcing near primary resonances, or self-excited vibrations under negative damping of a particular mode [1].

To experimentally realize the EPMC, we apply the method proposed in [2], where the negative damping is replaced by a phase resonant external forcing. By varying the forcing amplitude and measuring the steady-state response, one effectively tracks the system's backbone curve. Scheel et al. [2, 3] considered systems with well-spaced modes, moderate damping level and only a few percent nonlinear variation of modal frequency and damping ratio. A focus was placed on structures with bolted joints. It was shown that reasonable results can already be achieved with only a single-point, single-frequency phase resonant forcing. Once the nonlinear mode is isolated in a periodic state, the modal frequency can be easily determined and the mode shape (including higher harmonics) measured. The modal damping ratio is obtained using the active power

M. Scheel (✉) · M. Krack
Institute of Aircraft Propulsion Systems, University of Stuttgart, Stuttgart, Germany
e-mail: scheel@ila.uni-stuttgart.de

T. Schulz
MesH Engineering GmbH, Stuttgart, Germany

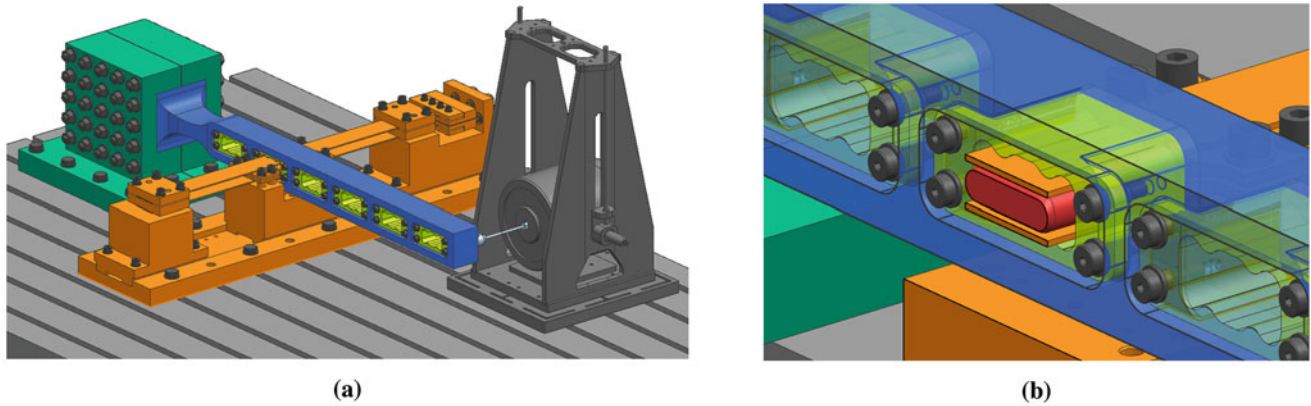


Fig. 11.1 Experimental setup: (a) One-sided clamped beam. (b) Zoom of the friction nonlinearity

provided by the fundamental harmonic component of the excitation force and the experimentally identified modal mass of the deflection shape.

Up to this point, it has not been assessed if the proposed single-point, single-frequency phase resonant excitation force is sufficient for systems with highly nonlinear damping or significant changes in mode shape. Therefore, the experimental realization of the extended periodic motion concept is applied in this work to a test rig with a friction nonlinearity, ranging from (nearly) full stick to macro slip. To assess the mode isolation quality, we also investigate how sensitive the extracted modal properties are with respect to the excitation location.

11.2 Beam Test Rig with Friction Nonlinearity

The test rig [4] consists of a one-sided clamped beam (see Fig. 11.1). The beam has six pockets, each equipped with an inlet (green). To introduce friction, two metal plates (orange) are inserted in one of the pockets. The contact interfaces between inlet and plates are ideally lines, two on the top plate and two on the bottom plate. An air tube (red) inserted between the plates applies normal load to the contact, which can be set through the air pressure in the tube. By design, the location of the nonlinearity can be varied in the test rig, thus varying severeness of nonlinearity, e. g., change in frequency, damping and deflection shape.

11.3 Experimental Nonlinear Modal Analysis

The nonlinear modal analysis described in [2] is applied to the setup shown in Fig. 11.1. Here, the force appropriation is ensured using a phase-locked loop controller implemented on a dSPACE MicroLabBox with successively decreasing excitation level. The mode under investigation is the first horizontal bending mode at about 115 Hz for low vibration levels (contact interfaces presumably in full stick).

For low amplitudes, the extracted modal frequency is nearly constant (see Fig. 11.2a) which supports that contact interfaces are in full stick. As the amplitude increases, the modal frequency drops significantly, and the system shows the expected softening behavior. For high amplitudes, the frequency-amplitude curve flattens which suggests that the joint is in macro slip. Note that the frequency is normalized with the modal frequency at small amplitudes. The damping ratio is low for small amplitudes and increases to a maximum value of about 17% with a subsequent decrease.

To assess the amplitude dependence of the deflection shape, the first harmonic component of the nonlinear deflection shape is projected onto linear modes to determine the amplitudes of the linear modal coordinates. First, the first three linear bending modes identified for low amplitudes (full stick) are used as basis. The magnitude of the modal amplitudes are indicated with solid lines in Fig. 11.2b. Note that the values are normalized such that they sum up to one. For low amplitudes, the nonlinear deflection shape resembles the linear first bending mode with a fully stuck joint. With increasing amplitude, the nonlinear deflection shape changes such that the other two linear modes contribute significantly. To further understand the change in shape, the nonlinear deflection shape is also projected onto modes identified for the beam without contact between beam and

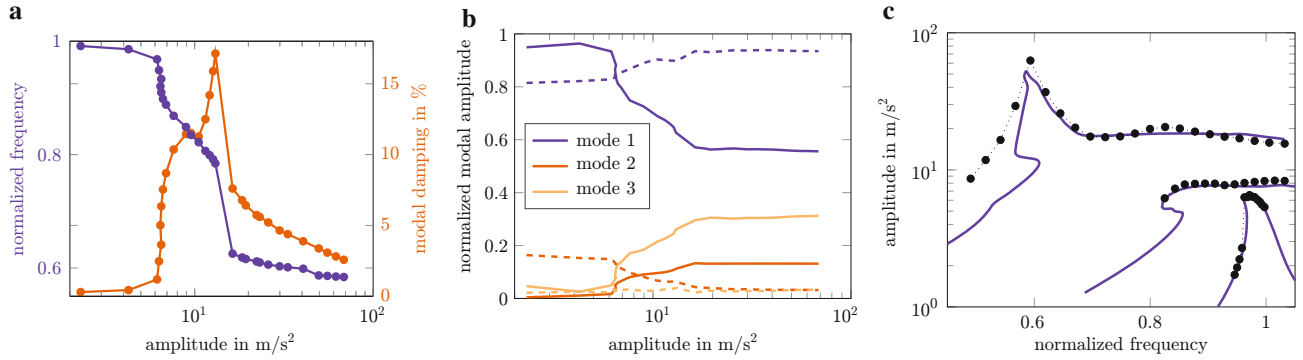


Fig. 11.2 (a) Normalized resonant frequency and damping ratio over drive point amplitude. (b) Normalized modal amplitudes of linear full stick modes (*solid line*) and linear modes of beam without contacting plates (*dashed line*) over drive point amplitude. (c) Measured (*dots*) and synthesized (*solid line*) frequency responses for the drive point at three forcing levels

plates (dashed lines in Fig. 11.2b). For high amplitudes, when the joint is in macro slip, the deflection resembles the first bending mode of a beam without joint. For the regime at moderate amplitudes (high damping ratio), however, the deflection shape cannot be explained by a single mode of either modal basis. The shape is in fact a combination of three linear modes. At this point, it is unclear if this is a property inherent to the structure or if it is induced by the imperfect excitation.

For validation of the extracted modal properties, frequency responses are synthesized with the associated nonlinear modal model for three forcing levels (0.5 N, 4.3 N, and 19.4 N). As reference, frequency responses are measured using force-controlled stepped sine excitation at the same forcing levels (see Fig. 11.2c). Note that the excitation location is the same as for the backbone measurement. The predicted frequency responses match the measurements well for lower amplitude levels. For the highest excitation level, the prediction differs significantly from the measurement, underestimating the maximum amplitude. The difference can be accounted to imperfect phase control during the backbone measurement and moderate measurement repeatability. The dynamics for frequencies lower than the resonance are not captured well. This work will be presented in more detail at the conference, analyzing the amplitude-dependent modal properties in more depth. Furthermore, the influence of the excitation location will be addressed [5].

11.4 Conclusion

With the suggested experimental realization of the extended periodic motion concept, amplitude-dependent modal properties can be extracted from full stick to macro slip regime. The tested beam structure exhibits strong nonlinearity: modal frequency, damping ratio and deflection shape change significantly with amplitude. Vibration predictions near the first resonance based on the extracted modal model are deemed satisfactory. However, the excitation location in this work was the same for backbone and frequency response measurements. Therefore, further work is required to assess the validity of the model with respect to changes in the exciter and friction contact location.

References

1. Krack, M.: Nonlinear modal analysis of nonconservative systems: extension of the periodic motion concept. *Comput. Struct.* **154**, 59–71 (2015)
2. Scheel, M. et al.: A phase resonance approach for modal testing of structures with nonlinear dissipation. *J. Sound Vib.* **435**, 56–73 (2018)
3. Scheel, M. et al.: System identification of jointed structures: nonlinear modal testing vs. state-space model identification. In: *Nonlinear Dynamics*, vol. 1, pp. 159–161. Springer, Cham (2019)
4. Schulz, T.: Konzeption, Auslegung und Konstruktion eines Versuchsstandes für die Untersuchung dissipativer Strukturen (Design and construction of a test rig for the investigation on dissipative structures) Master's thesis. University of Stuttgart, Germany (2018)
5. Scheel, M. et al.: Nonlinear Modal Testing of a Strongly Friction-damped Beam (in preparation)

Chapter 12

Dynamics of a Magnetically Excited Rotational System



Xue-She Wang and Brian P. Mann

Abstract This extended abstract investigates the dynamics of a non-contact linear-to-rotary magnetic transmission system. Equations of motion were derived using a Dipole Model. An equilibria and stability analysis revealed coexisting solutions exist as magnets are close, and experimental studies were conducted to verify this trend. Simulation results gave the system's dynamic response under forward and reverse frequency sweeps, which show good agreement with experimental studies.

Keywords Dipole model · Equations of motion · Equilibria and stabilities · Dynamics

12.1 Introduction

Harvesting energy from vibration has been broadly discussed in recent decades [1, 2]. Among various energy conversion methods (piezoelectric transduction, electromagnetic induction, electrostatic transduction, etc.), harvesting energy from rotational movement has advantages of high efficiency, easy implementation and space-saving [3]. However, most types of environmental vibration are translational. Traditionally, translation can be converted to rotation with connecting rods but friction in the transmission process oftentimes consume lots of energy thus impairing conversion efficiency. This extended abstract will introduce a novel design of transmission system, which achieves the conversion from translation to rotation and utilize non-contact magnetic interaction to avoid energy consuming from friction. In the following sections, mathematical modeling of this transmission system will be formulated, and its static property and dynamic responses will be investigated.

12.2 System Description

Figure 12.1 shows a shaker provides translational motions of the drive magnet, which applies magnetic force to the rotary driven magnet. The mass center of the driven magnet is pinned at a non-moving potentiometer, thus limiting to pure rotation. A rotary circular plate is attached to the driven magnet and wrapped around by two strings, which connect springs to provide linear restoring torque. The potentiometer was used to measure the angle of the driven magnet, and a laser tachometer was used to measure the displacement of the drive magnet.

The equation of motion for the driven magnet could be written as a linear mass-spring-damper system driven by magnetic torque $T(\theta, x)$:

$$I\ddot{\theta} + c\dot{\theta} + k(\theta - \theta_0) = T(\theta, x) \quad (12.1)$$

where I , c , k and θ_0 are the driven magnet's moment of inertia, torsional damping coefficient, torsional spring coefficient and offset bias angle respectively. Dipole Model was used to describe the magnetic torque and the equation of motion becomes:

$$I\ddot{\theta} + c\dot{\theta} + k(\theta - \theta_0) = \alpha \left\{ \frac{\sin \theta}{[(b + A \cos(\Omega t))^2 + h^2]^{3/2}} - 3 \frac{[b + A \cos(\Omega t)][h \cos \theta + (b + A \cos(\Omega t)) \sin \theta]}{[(b + A \cos(\Omega t))^2 + h^2]^{5/2}} \right\} \quad (12.2)$$

X.-S. Wang (✉) · B. P. Mann

Department of Mechanical Engineering and Materials Science, Pratt School of Engineering, Duke University, Durham, NC, USA
e-mail: xueshe.wang@duke.edu

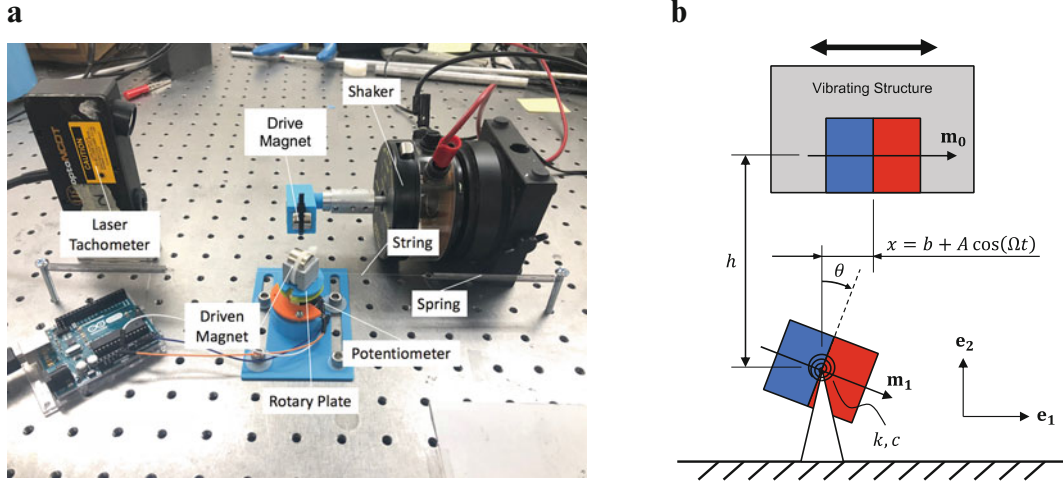


Fig. 12.1 (a) Experimental setup and (b) schematic diagram of the non-contact linear-to-rotary magnetic transmission system

where $\alpha = \mu_0 M_0 V_0 M_1 V_1 / (4\pi)$, μ_0 is the permeability of free space, M_0 , V_0 are the drive magnet's magnetization and volume respectively, and M_1 , V_1 are the driven magnet's magnetization and volume respectively.

12.3 Equilibria and Stabilities

Dipole Model gives the expression of the system's potential energy as follow:

$$U = \alpha \left[\frac{\cos \theta}{(h^2 + b^2)^{3/2}} + 3 \frac{b(h \sin \theta - b \cos \theta)}{(h^2 + b^2)^{5/2}} \right] + \frac{1}{2} k (\theta - \theta_0)^2 \quad (12.3)$$

Taking the first derivative of the total potential energy U , with respect to the generalized coordinate θ , and setting it equal to zero gives the equilibria of the static rotary system $\tilde{\theta}$:

$$\frac{k}{\alpha} (\tilde{\theta} - \theta_0) (h^2 + b^2)^{5/2} + (2b^2 - h^2) \sin \tilde{\theta} + 3hb \cos \tilde{\theta} = 0 \quad (12.4)$$

The Lagrange-Dirichlet theorem states that the stability of a single degree-of-freedom system's equilibria can be determined by evaluating the sign of the second derivative of the potential energy function with respect to the generalized coordinate at the equilibrium position. Therefore, stability is determined by the sign of the following expression:

$$\left. \frac{d^2 U}{d\theta^2} \right|_{\theta=\tilde{\theta}} = k + \alpha (h^2 + b^2)^{-5/2} \left[(2b^2 - h^2) \cos \tilde{\theta} - 3hb \sin \tilde{\theta} \right] \quad (12.5)$$

where $d^2 U/d\theta^2 > 0$ indicates a stable equilibrium and $d^2 U/d\theta^2 < 0$ indicates an unstable equilibrium. Figure 12.2 shows the trend of equilibrium and stability with a varying bias, b . When the bias is small, i.e. two magnets are close, multiple equilibria were found. As shown in Fig. 12.2b, a non-zero θ_0 breaks the symmetry of the bifurcation diagram. Especially for $\theta_0 = \pi/4$, the remote solution indicates that the magnetic torque here is extremely strong to balance the large restoring force.

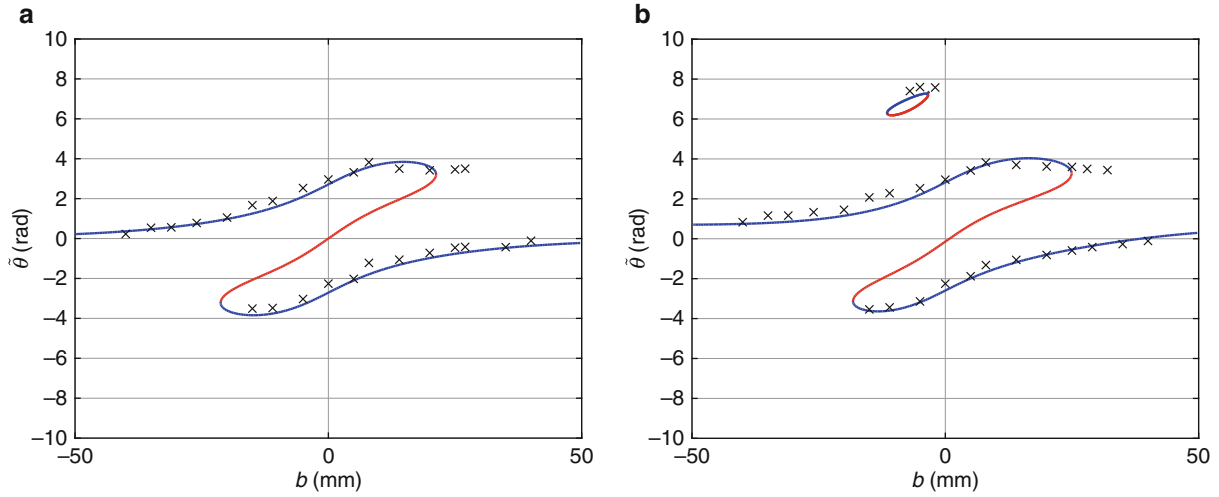


Fig. 12.2 Bifurcation diagrams showing the equilibria and their stabilities. (a) shows the case with an offset bias angle $\theta_0 = 0$, while (b) shows the case with an offset bias angle $\theta_0 = \pi/4$. Equilibrium angle of the driven magnet were found by sweeping a control parameter of bias b , where blue lines represent stable equilibria while red lines represent unstable equilibria. Cross points are the experimental data

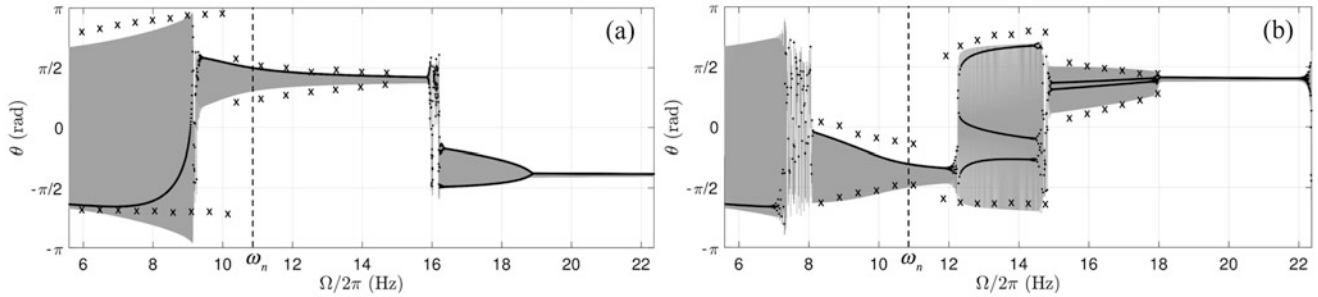


Fig. 12.3 The responses of the driven magnet under (a) forward frequency sweep and (b) reverse frequency sweep. The excitation has an amplitude of 3 mm and frequencies ranging from $0.5\omega_n$ to $2\omega_n$, where ω_n is the natural frequency of the driven magnet. Grey areas represent time series responses, black dots represent stroboscopic samples, and black crosses represent the envelope of responses experimentally measured

12.4 Dynamic Response

Simulation were performed using Eq. (12.2) along with the parameters measured from the experiments. Figure 12.3 shows the simulation result of the transmission system's frequency responses. In Fig. 12.3a, b, excitation frequency is linearly increasing and decreasing with time respectively, thus making horizontal axis represent frequency as well as time. The shaded gray line therefore shows the time series for the driven magnet's angle and the amplitude of each steady state driven by a given frequency. Stroboscopic samples (black dots and lines) were also used to illustrate the periodicity of the response with respect to the excitation frequency [4].

As shown in Fig. 12.3, the forward and reverse frequency sweeps result in coexisting solutions. Multiple periodicities of response were found by observing the stroboscopic samples, including harmonic, sub-harmonic and chaotic responses. Compared with the forward sweep, the reverse sweep yields larger responses of amplitude near the natural frequency. However, the forward sweep gives larger and more stable (non-chaotic) responses far away from natural frequency. Experimental studies were performed to obtain the envelopes of responses under forward and reverse sweep, which show good agreement with simulation results.

12.5 Conclusion

This extended abstract derived the equation of motion for the non-contact linear-to-rotary magnetic transmission system. The good agreement of theoretical equilibria with experimental studies proves the applicability of Dipole Model for describing the magnetic force in this prototype. For the system's dynamic response, simulations show multiple periodicities, coexisting solutions of steady states, and a broadening in the frequency response. Experimental studies verify the simulation results by comparing the amplitude of responses under forward and reverse frequency sweeps.

References

1. Bernard, B.P., Mann, B.P.: Increasing viability of nonlinear energy harvesters by adding an excited dynamic magnifier. *J. Intell. Mater. Syst. Struct.* **29**(6), 1196–1205 (2018)
2. Mann, B.P., Barton, D.A.W., Owens, B.A.M.: Uncertainty in performance for linear and nonlinear energy harvesting strategies. *J. Intell. Mater. Syst. Struct.* **23**(13), 1451–1460 (2012)
3. Wang, X.-S., Mazzoleni, M.J., Mann, B.P.: Dynamics of unforced and vertically forced rocking elliptical and semi-elliptical disks. *J. Sound Vib.* **417**, 341–358 (2018)
4. Sequeira, D., Wang, X.-S., Mann, B.: Analytical method for stroboscopically sampling general periodic functions with arbitrary frequency sweep rates. *J. Vib. Acoust.* **140**(6), 061008 (2018)



Chapter 13

Experimental Nonlinear Dynamics of a Post-buckled Composite Laminate Plate

John I. Ferguson, Stephen M. Spottswood, David A. Ehrhardt, Ricardo A. Perez, Matthew P. Snyder, and Matthew B. Obenchain

Abstract Composite laminate materials are prevalent in the aerospace industry as programmable high-strength structural options. An increased focus on high-speed and space flight demands an understanding of composite materials subject to extreme combined thermal, aeroelastic and acoustic loading. Under such conditions constrained composite panels may buckle, thus exhibiting nonlinear structural behavior. This study focuses on a unidirectional carbon fiber epoxy composite laminate plate, a surrogate for more complex composite structures, with four stable static equilibria under fixed-fixed, free-free boundary conditions. The experiment includes pre- and post-buckled modal analysis as well as characterization of the nonlinear response due to transverse excitation. An electrodynamic shaker excites the plate at varying frequencies and loading amplitudes. The dynamic response of the post-buckled plate is measured with the 3D dynamic digital image correlation (DIC) technique combined with a laser vibrometer. The results show single-well and coexisting responses for the four stable equilibria along with chaotic snap through between equilibria. The experimental results of the pre-buckled plate modal analysis are compared to an analytical solution based on classical laminate plate theory (CLPT) and the equation of motion for transverse vibration of laminated plates. Future efforts include modeling and analyzing carbon fiber laminates with respect to damage initiation and material degradation due to high-stress snap through response.

Keywords Composite plates · Post-buckled plates · Snap-through · Experimental mechanics · Digital image correlation

13.1 Introduction

The aerospace industry has become reliant on composite materials due to the high strength to weight ratio and programmable stiffness of composite components. The structural applications of these materials range from micro air vehicles to Lockheed Martin's JCM missile to the future SpaceX Big Falcon Rocket (BFR). A primary concern during high-speed flight is that constrained panels will buckle due to the substantial temperature variation within a flight regime [1, 2]. A thermally buckled panel, simultaneously excited by large aeroelastic and acoustic loads, can exhibit nonlinear dynamic behavior, to include snap-through between stable equilibria [3]. Post-buckled behavior of aircraft skin panels has been observed in both the X-15 (Fig. 13.1a) and SR-71 Blackbird (Fig. 13.1b). The large amplitude deformation of a snap-through event results in a significant compressive load that can threaten the structural life of the component. Specifically, delamination of composite ply layers may be accelerated by the large instantaneous compressive load [4, 5]. The delamination of composite plies within a component can rapidly reduce the structural integrity and lead to catastrophic failure of the system. Therefore, knowledge of the post-buckled dynamic behavior of composite panels is critical to the development and safety of high-speed aerospace structures.

This study focuses on experimentally characterizing the dynamic behavior of a unidirectional carbon fiber epoxy laminate plate, a surrogate for more complex composite structures. A linear modal analysis is conducted on the pre-buckled laminate with fixed-fixed, free-free boundary conditions as well as in a cantilever configuration. The modal behavior is compared to an analytical model based on the classical laminated plate theory (CLPT) and fundamental mode shapes of beams [6, 7]. The composite plate is then buckled under fixed-fixed, free-free boundaries to exhibit four stable states. The post-buckled analysis includes linear modal experimentation as well as an investigation of the nonlinear response under transverse excitation. The

J. I. Ferguson (✉) · M. P. Snyder · M. B. Obenchain

Department of Engineering Mechanics, United States Air Force Academy, U.S. Air Force Academy, CO, USA
e-mail: c19john.ferguson@usafa.edu

S. M. Spottswood · D. A. Ehrhardt · R. A. Perez

Air Force Research Laboratory, Wright-Patterson Air Force Base, Dayton, OH, USA

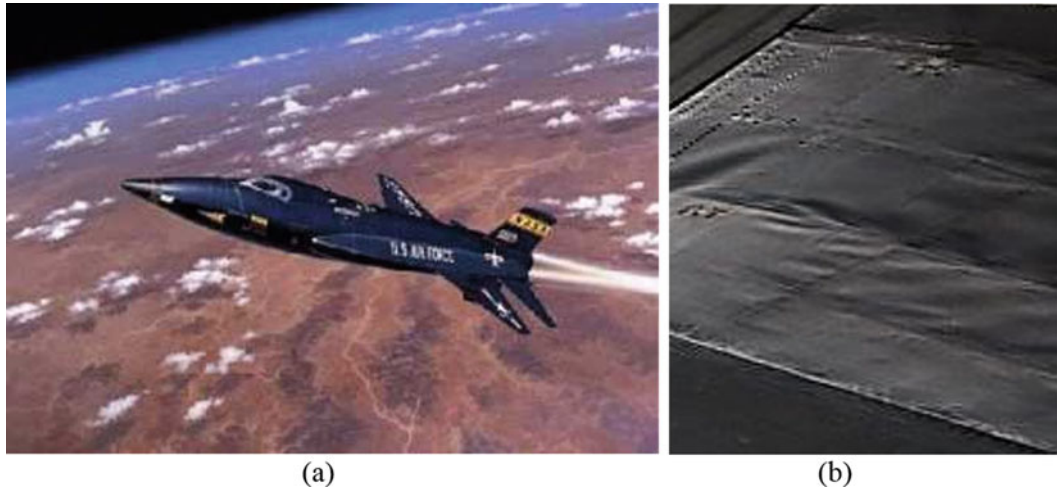


Fig. 13.1 High-speed vehicles with observed nonlinear behavior of skin panels. (a) North American X-15 [8] (b) Buckled skin panel on the underside of the fuselage of an SR-71 [9]

post-buckled plate is excited by an electrodynamic shaker to investigate the transition to chaotic snap-through and coexisting response between equilibria. The dynamic response is measured using the 3D digital image correlation technique (DIC) and a laser vibrometer.

13.2 Pre-buckled Analysis

13.2.1 Analytical Solution

Development of the equation of motion for the free transverse vibration of a plate follows the methods found in many composite mechanics texts [6, 10]. The differential equations of motion based on the stress resultants and external loads are:

$$\frac{\partial^2 N_x}{\partial x^2} + \frac{\partial N_{xy}}{\partial y} = \rho_0 \frac{\partial^2 u}{\partial t^2} \quad (13.1)$$

$$\frac{\partial^2 N_y}{\partial y^2} + \frac{\partial N_{xy}}{\partial x} = \rho_0 \frac{\partial^2 v}{\partial t^2} \quad (13.2)$$

$$\frac{\partial^2 M_x}{\partial x^2} + 2 \frac{\partial^2 M_{xy}}{\partial x \partial y} + \frac{\partial^2 M_y}{\partial y^2} = \rho_0 \frac{\partial^2 w}{\partial t^2} \quad (13.3)$$

In Eqs. 13.1–13.3, N and M represent the load and moment resultants, respectively. The load and moment resultants are assumed to relate to the mid-plane strains and curvatures of the plate based on classical laminated plate theory, as shown in Eq. 13.4 [6].

$$\begin{bmatrix} N \\ M \end{bmatrix} = \begin{bmatrix} A & B \\ B & D \end{bmatrix} \begin{bmatrix} \epsilon^0 \\ \kappa \end{bmatrix} \quad (13.4)$$

In this study, the formulation is restricted to isotropic plates and symmetric laminates, thus the substitution of the relationships in Eq. 13.4 decouples the three equations of motion, and the governing equation for transverse vibration becomes:

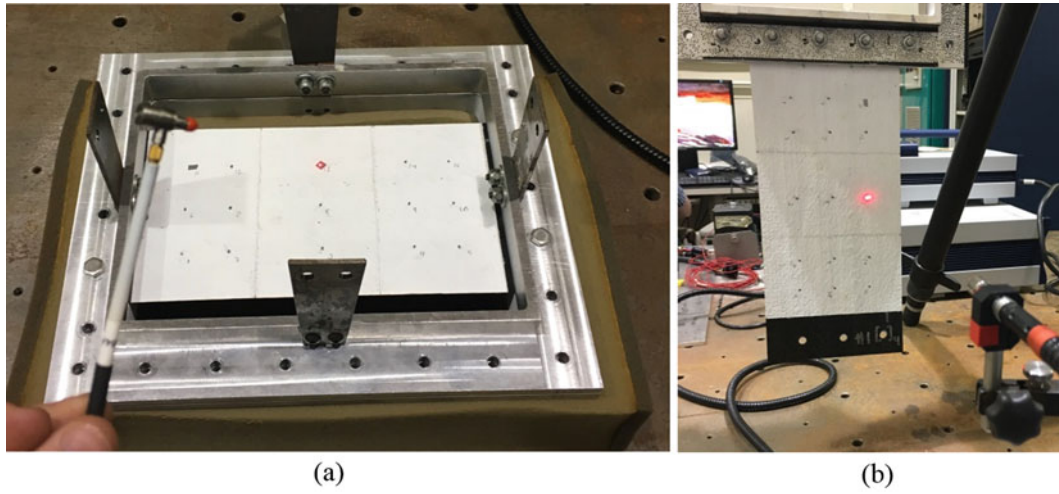


Fig. 13.2 Experimental modal analysis of unidirectional composite plate. (a) Clamped-clamped, free-free boundary conditions (CCFF). (b) Cantilever boundary conditions (CFFF)

$$D_{11} \frac{\partial^4 w}{\partial x^4} + 2(D_{12} + 2D_{66}) \frac{\partial^4 w}{\partial x^2 \partial y^2} + D_{22} \frac{\partial^4 w}{\partial y^4} + \rho_0 \frac{\partial^2 w}{\partial t^2} = 0 \quad (13.5)$$

The D coefficients in the equation of motion are components of the plate's bending stiffness matrix, which are readily obtained using classical laminated plate theory.

This analysis assumes the solution to the transverse vibration of the plate is harmonic, according to:

$$w(x, y, t) = W(x, y) e^{i\omega t} \quad (13.6)$$

where $W(x, y)$ is a mode shape function for the plate's given boundary conditions. The solution is in the form:

$$W(x, y) = X(x) Y(y) \quad (13.7)$$

where $X(x)$ and $Y(y)$ are the fundamental beam mode shapes of the plate in each direction. This analysis utilizes a series of shape functions published by Leissa [7]. The substitution of the modal $W(x, y)$ shape functions results in the analytical solution to the composite laminates natural frequencies, in the form:

$$\omega = \sqrt{\frac{1}{\rho_0 W} \left[D_{11} \frac{\partial^4 W}{\partial x^4} + 2(D_{12} + 2D_{66}) \frac{\partial^4 W}{\partial x^2 \partial y^2} + D_{22} \frac{\partial^4 W}{\partial y^4} \right]} \quad (13.8)$$

The first four analytically determined natural frequencies and mode shapes are validated against the experimental results for the pre-buckled unidirectional carbon fiber epoxy laminate plate.

13.2.2 Experimentation

The pre-buckled modal experimentation focused on a unidirectional composite plate with clamped-clamped, free-free boundary conditions (Fig. 13.2a) as well as a cantilever configuration (Fig. 13.2b). The geometric and material properties of the composite specimen are shown Table 13.1.

In this experiment, a roving input was used to excite the fundamental modes of the plates, while a fixed-point laser vibrometer output measured the dynamic response. The response was measured at Point 13 ($x = 4.5$ in, $y = 3.75$ in) at a 6000 Hz sampling frequency. A fast Fourier transform converted the response to the frequency domain to determine the natural frequencies and subsequently the mode shapes of the unidirectional carbon fiber plate.

Table 13.1 Geometric and material properties of specimen

Property	Specimen
Layup	[0] ₄
Length (in.)	9
Width (in.)	5
Thickness (in.)	0.026
E ₁₁ (Msi)	15
E ₂₂ (Msi)	0.6
G ₁₂ (Msi)	0.8
Poisson's Ratio, ν_{12}	0.3
Density, ρ_0 (lb/in. ³)	0.0503

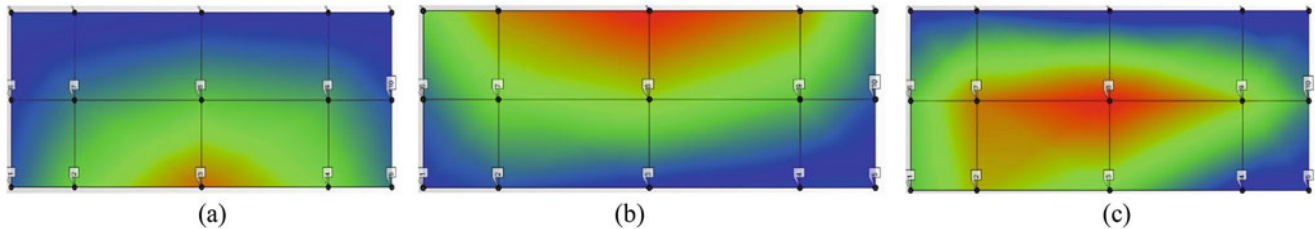


Fig. 13.3 Clamped-clamped, free-free experimental modal results. (a) Bottom torsional mode $\omega_1 = 116$ Hz (b) Top torsional mode – $\omega_2 = 184$ Hz (c) Bending mode – $\omega_3 = 221$ Hz

13.2.3 Comparison of Analytical Solution and Experimental Results

The clamped-clamped, free-free experimental modal results (Fig. 13.3) and the analytical solution (Fig. 13.4) exhibited largely different mode shapes at different frequencies. The low transverse stiffness (E_{22}) and incongruities in the composite matrix due to the room temperature lay-up technique resulted in independent torsional modes. The top half of the composite plate was stiffer, causing the top torsional mode to occur at 184 Hz versus the bottom torsional mode at 116 Hz. The stiffness differential is also apparent in the first bending mode at 221 Hz in which the mode shape is asymmetric, skewing toward the bottom half of the plate. Figure 13.4 illustrates the analytically determined first bending and torsional modes. The analytical model assumes a perfectly orthotropic plate, without material incongruities. Also, the analytical solution does not account for pre-stress in the material due to the clamping procedure. These simplifying assumptions result in disparity between the analytical and experimental natural frequencies and shapes. The model does not predict the two independent torsional modes and the experimental modes are higher likely due to tensioning of the material while the fixed ends are clamped.

The inaccuracy of the analytical solution in the clamped-clamped, free-free analysis motivated an investigation of cantilever boundary conditions to eliminate the pre-stress in the material. The shape functions in the analytical solution were altered to model a single clamped edge in a cantilever configuration. Figure 13.5 illustrates the experimental first two modes of the cantilevered composite laminate. The experimental fundamental mode exhibits a nearly symmetric bending mode at 13.7 Hz (Fig. 13.5a), while the second mode occurring at 41.1 Hz is an asymmetric torsional mode, favoring the top half of the plate (Fig. 13.5b). Figure 13.6 displays the model results for the first two cantilever modes. The analytical fundamental mode (Figure 13.6a) at 13.7 Hz has a 16% error in comparison to the experimental first bending mode result. The correlation between the model and experimental results is significantly improved by eliminating the pre-stress in the material. The second mode approximation does not correlate as well with the experimental results due to the incongruities of the material causing an asymmetric mode shape. The model will continue to be improved by accounting for pre-stress and material inconsistency.

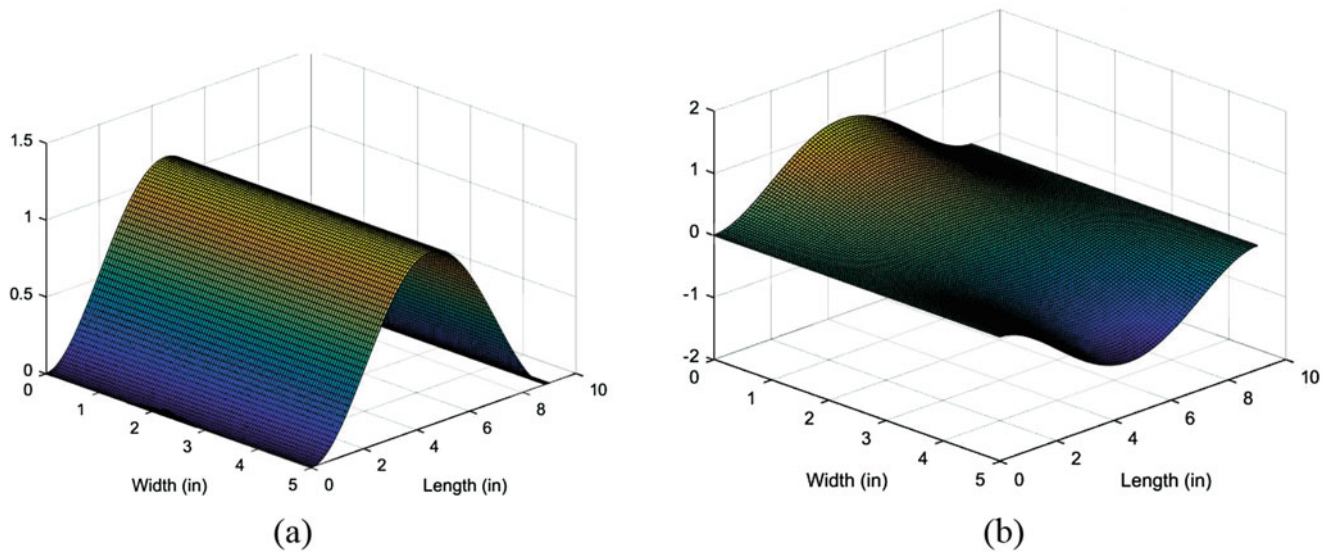


Fig. 13.4 Clamped-clamped, free-free analytical solution modal results. (a) Bending mode – $\omega_1 = 99.47$ Hz (b) Torsional mode – $\omega_2 = 147.1$ Hz

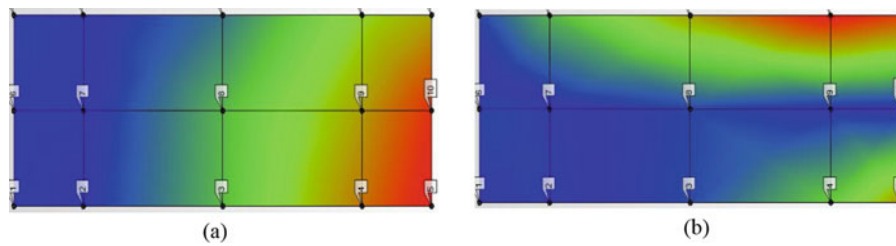


Fig. 13.5 Cantilever experimental modal results. (a) Bending mode – $\omega_1 = 13.7$ Hz (b) Torsional mode – $\omega_2 = 41.1$ Hz

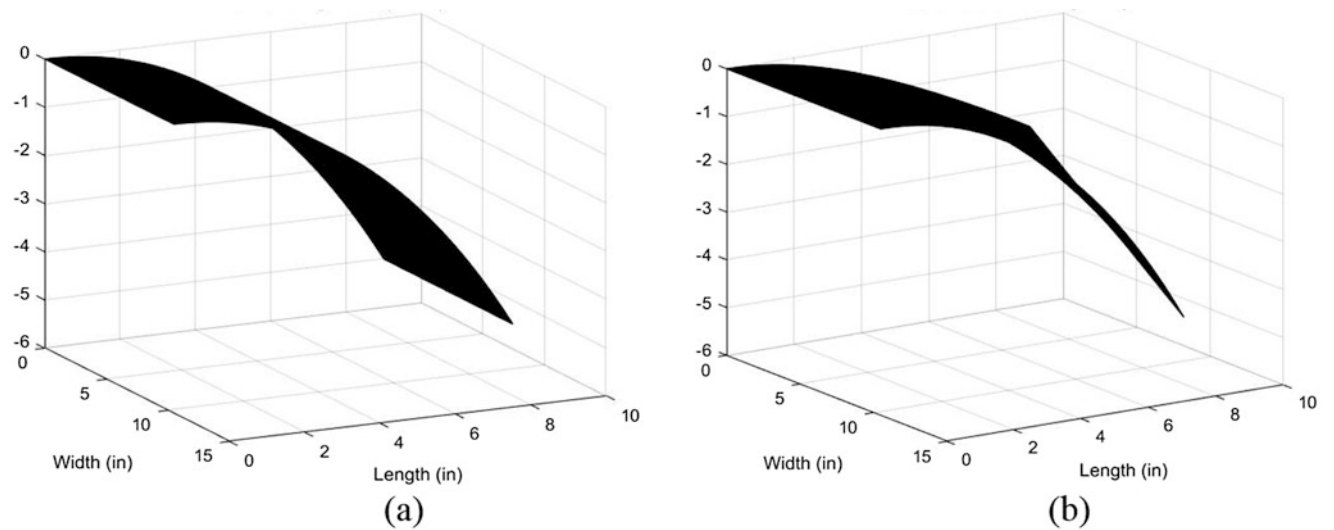


Fig. 13.6 Cantilever analytical solution modal results. (a) Bending mode – $\omega_1 = 11.5$ Hz (b) Torsional mode – $\omega_2 = 71.97$ Hz

13.3 Post-buckled Analysis

13.3.1 Experimentation

In the post-buckled experiment, the digital image correlation (DIC) technique is used to obtain full-field measurements of the dynamic response of the unidirectional plate specimen. The three-dimensional specimen is reconstructed using the binocular stereovision technique [11]. The two FASTCAM SA5 high-speed cameras (Fig. 13.7a) are positioned with intersecting fields, to capture the full-field dynamic response of the specimen. The cameras trace the speckle pattern (Fig. 13.7b) at a 2000 Hz sampling frequency, with laser vibrometers measuring the out of plane response at a 6000 Hz sampling frequency. Figure 13.8 shows the sampling points for the DIC measurement. The cameras captured 111 sampling points on the plate and 4 sampling points on the fixture in order to obtain the displacement of the plate relative to the motion of the clamp.

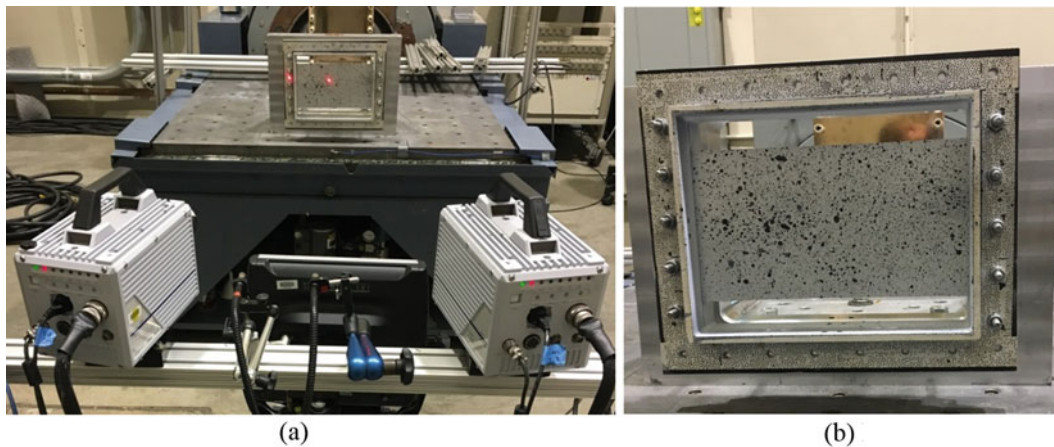


Fig. 13.7 DIC Experimental Setup. (a) Two laser vibrometers and two FASTCAM SA5 cameras (b) DIC speckle pattern on specimen

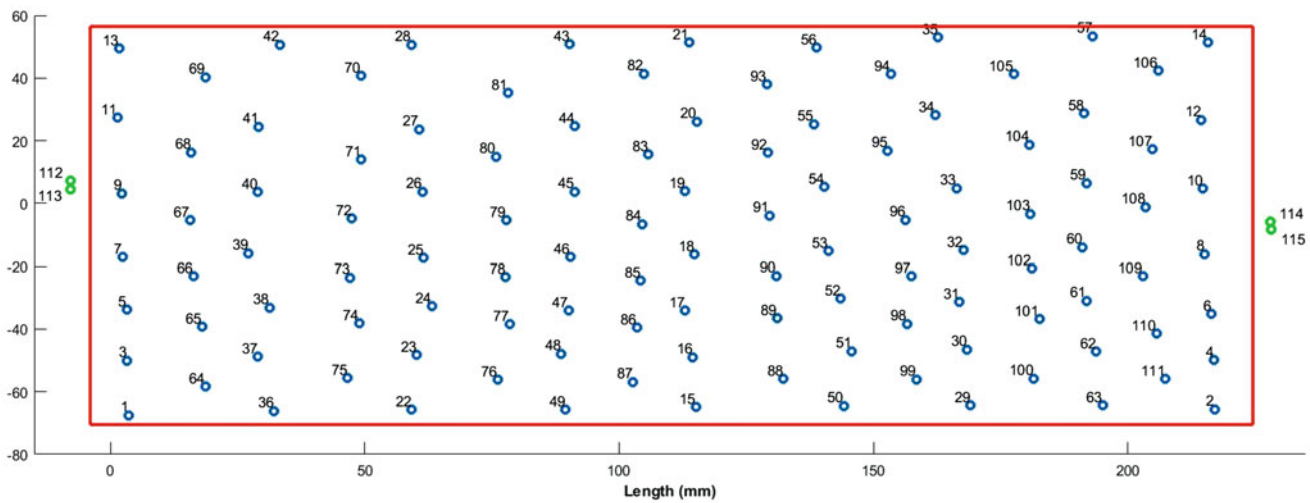


Fig. 13.8 Superposition of the plate (red line), 111 sampling points on the plate (blue circles), and 4 sampling points on the clamp (green circles) for DIC measurement

13.3.2 Asymmetric Buckle

The unidirectional composite laminate plate was mechanically buckled with clamped-clamped, free-free boundary conditions. The resulting buckle was largely asymmetrical due an imprecise buckling technique and a low transverse stiffness along the width of the plate. Figure 13.9 shows the four independent statically stable equilibria of the post-buckled laminate. The interpolated surface plots, viewed along the clamped width, show the buckled shape of the specimen reconstructed by the static measurements from DIC with 111 sampling points before the specimen was subjected to transverse loading [12]. Table 13.2 lists the transverse displacement of the critical points of each static equilibria (named P_1 to P_4).

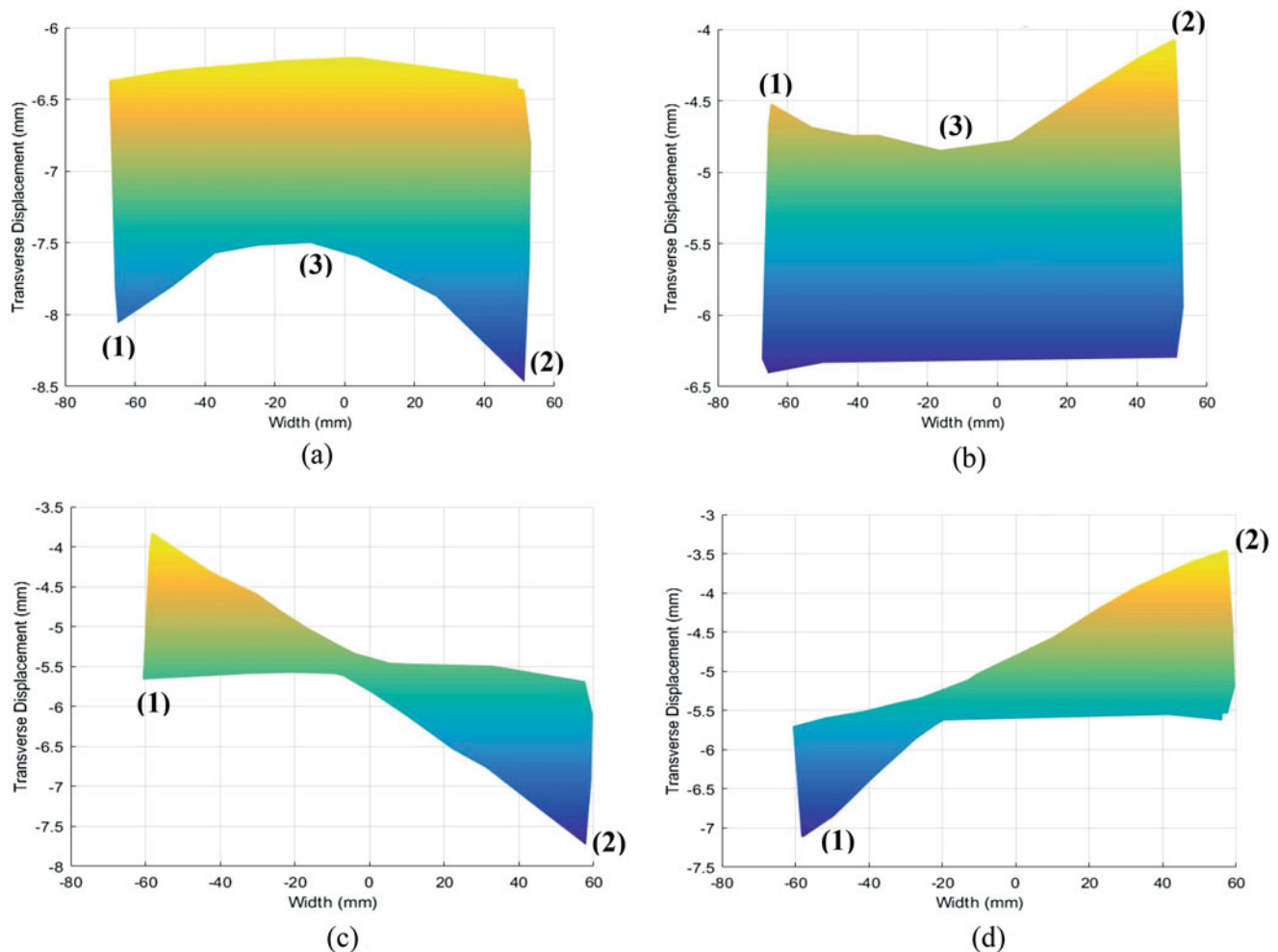


Fig. 13.9 Post-buckled stable equilibria. (a) Initial P_1 Configuration (b) Initial P_2 Configuration (c) Initial P_3 Configuration (d) Initial P_4 Configuration

Table 13.2 Post-buckled critical points transverse displacement

	P_1 (mm)	P_2 (mm)	P_3 (mm)	P_4 (mm)
1	(-) 1.61	(+) 1.78	(+) 1.85	(-) 1.42
2	(-) 2.02	(+) 2.32	(-) 2.07	(+) 2.20
3	(-) 1.01	(+) 1.46		

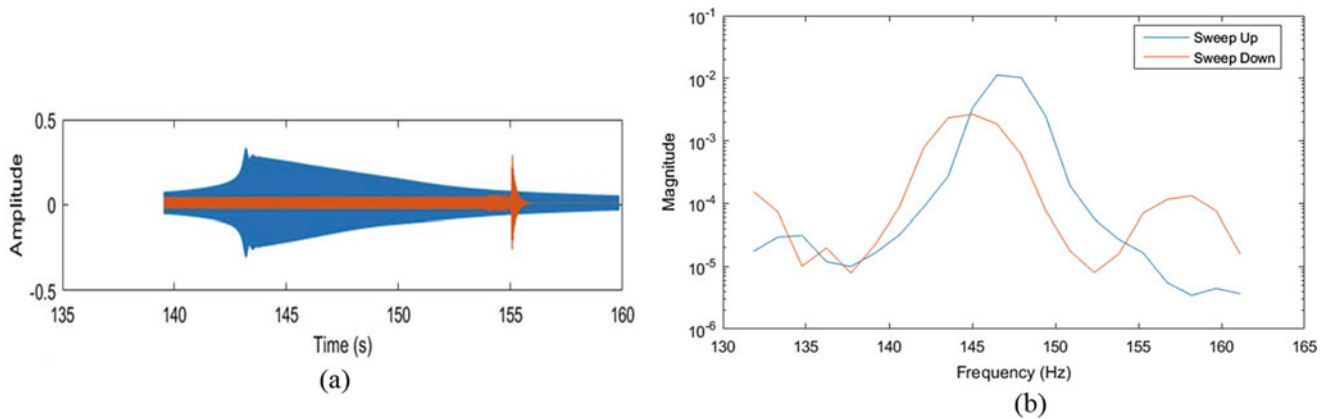


Fig. 13.10 P_4 Snap to P_2 at 0.4 g loading at peak response frequency of 145 Hz. (a) Time history of snap-through (b) DFT of response at snap-through

13.3.3 Chaotic Snap Through

The identification of chaos in the dynamic response of the specimen was achieved with the heuristic approach of identifying regions of excessive noise in the data [13]. The P_4 configuration (Fig. 13.9d) was qualitatively determined to be the least stable equilibrium state and the most readily excited to respond chaotically. The shallow buckle of the bottom half of the plate in the P_4 state was excited to snap through to the P_2 configuration at a 0.4g sine sweep from 40 to 180 Hz. Figure 13.10 shows the single snap-through event (measured by the laser vibrometers) at a peak response frequency of approximately 145 Hz during the sweep up and sweep down.

The bottom half of the plate in the P_4 configuration realized chaotic snap-through response at loading amplitudes as low as 1.3 g (Fig. 13.13). Figure 13.11 illustrates a segment of the chaotic response between the P_2 and P_4 states during an amplitude sweep from 0.5 to 3.5 g at a frequency dwell of 135 Hz. The chaotic response initiated at 2.0 g, continued to the peak 3.5 g, and continued down to 1.8 g. Figure 13.11a exhibits the time history of point 86 in Fig. 13.8. This is the nominal midpoint of the bottom half of the plate. The large amplitude oscillations favor the P_2 state as seen in Fig. 13.11b as the plate chaotically snaps to the P_4 configuration of Fig. 13.11d. Figure 13.11e, f show the path of the snap-through event. The path is asymmetric, favoring the same region illustrated in the plate's first bending mode (Fig. 13.3c). The modal shape and dynamic response may favor the lower edge of the plate due to a material incongruity resulting in a more compliant section.

Unlike the P_4 configuration, the P_3 state (Fig. 13.9c) illustrated coexisting snap-through response between the independently bistable top and bottom sections of the laminate. Figure 13.12 illustrates the coexisting response of the P_3 configuration during a frequency sweep from 100 to 140 Hz at 4.5 g. Under the large amplitude load of 4.5 g, the plate exhibits large single well response until a single snap event to the P_2 configuration (Fig. 13.12d, e). The bottom section of the specimen then responds chaotically (Fig. 13.12f), and finally settles into an equilibrium at its original P_3 configuration (Fig. 13.12g). The large amplitude chaotic cross-well response exists between an excitation frequency of 116 and 135 Hz.

An investigation into the P_4 configuration snap boundary was conducted as it was the least stable state. Figure 13.13 shows the presumed snap boundary for chaotic snap-through of the bottom half of the plate. This figure illustrates that the lowest amplitude chaos occurred at 1.3 g at 140 Hz. This was a qualitative analysis; Fig. 13.13 is schematic in nature.

13.3.4 Low Amplitude Modal Sweeps

The first tests conducted on each day of testing were low amplitude (0.5 g) random transverse excitation (50–850 Hz) to determine the state of the plate. The plate was manually transitioned between each state to excite and measure the response of each static equilibria individually. Figure 13.14 illustrates the results of the frequency domain analysis of the laser vibrometer data collected from each modal sweep. The power spectral density (PSD) plots exhibit the variation of the plate's state throughout the testing. The P_2 equilibrium, the plate buckled toward the cameras, realized the most significant variation throughout testing with a variation of 64 Hz between the fundamental peaks of the morning and afternoon tests on 19 June. Also, the least stable state (P_4) became statically unstable toward the end of several days. The primary cause of the

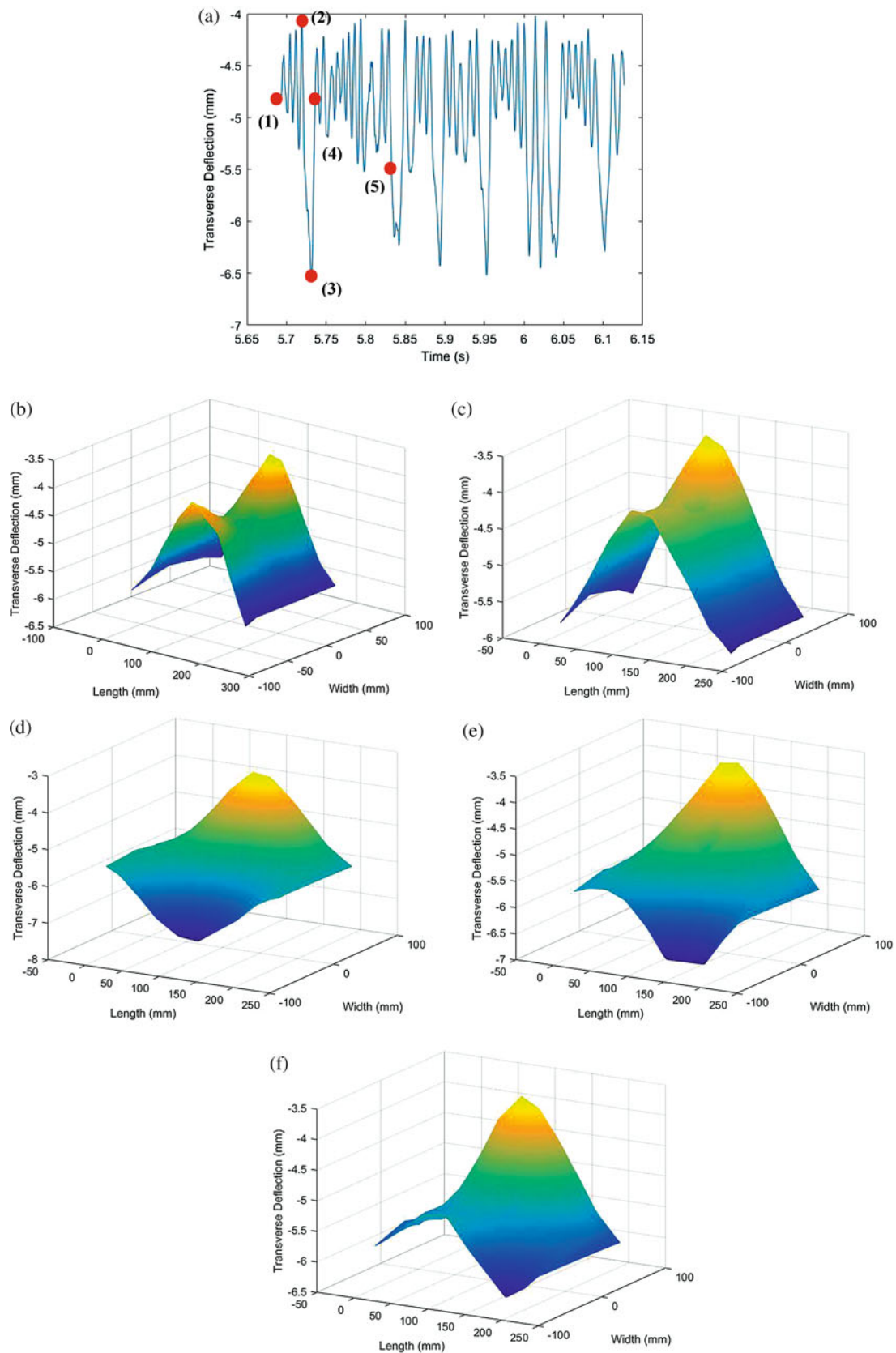


Fig. 13.11 Chaotic dynamic response of bottom half of plate originally in P_4 configuration and deflected shapes of specimen. (a) Part of chaotic response of point 86 in Fig. 13.8 (b) Interpolated deflected shape at (1). (c) Interpolated deflected shape at (2) (d) Interpolated deflected shape at (3) (e) Interpolated deflected shape at (4). (f) Interpolated deflected shape at (5)

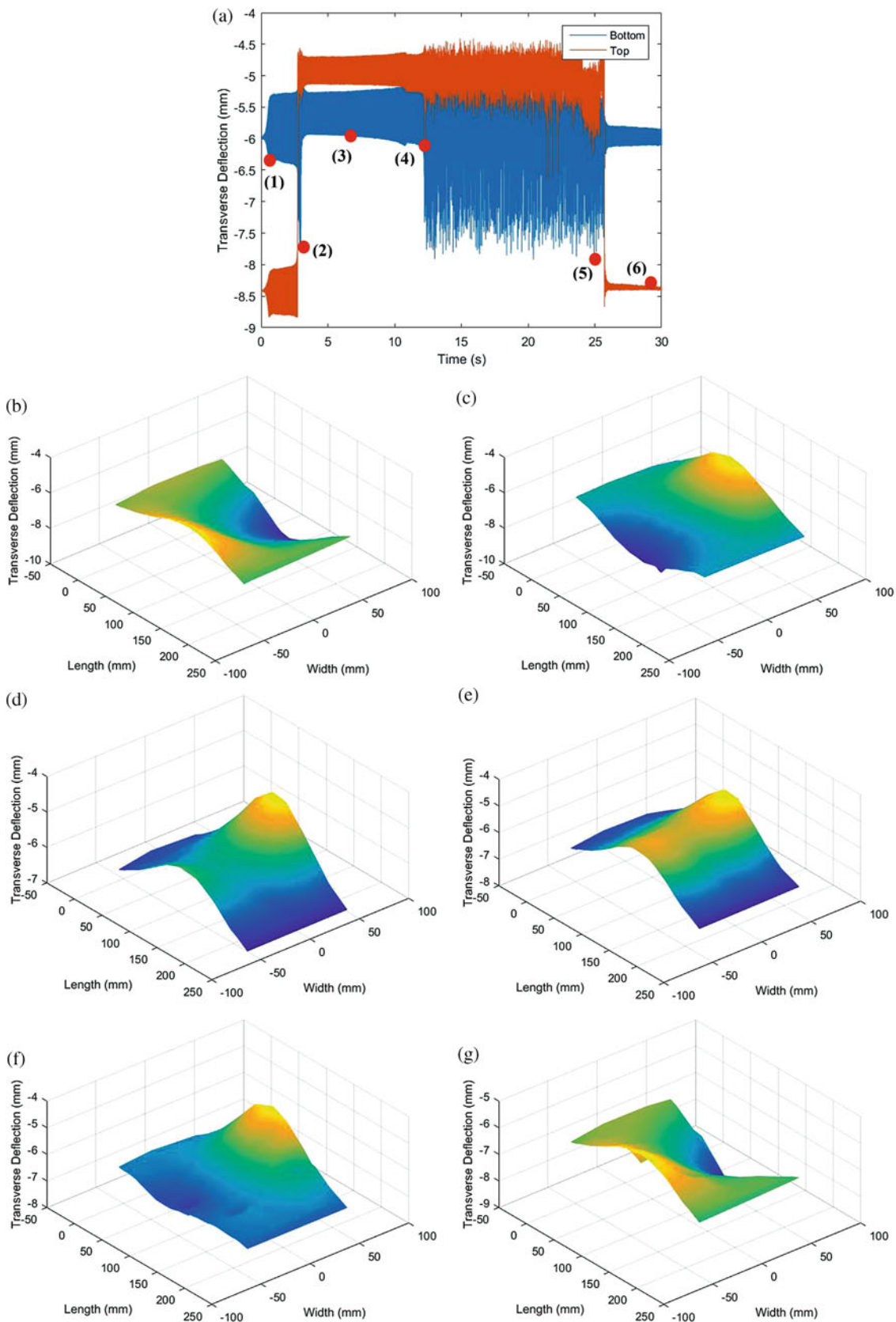


Fig. 13.12 Coexisting snap-through response originally in P_3 configuration and deflected shapes of specimen. (a) Chaotic response of point 86 (blue) and point 82 (red) (b) Interpolated deflected shape at (1). (c) Interpolated deflected shape at (2) (d) Interpolated deflected shape at (3) (e) Interpolated deflected shape at (4). (f) Interpolated deflected shape at (5) (g) Interpolated deflected shape at (6)

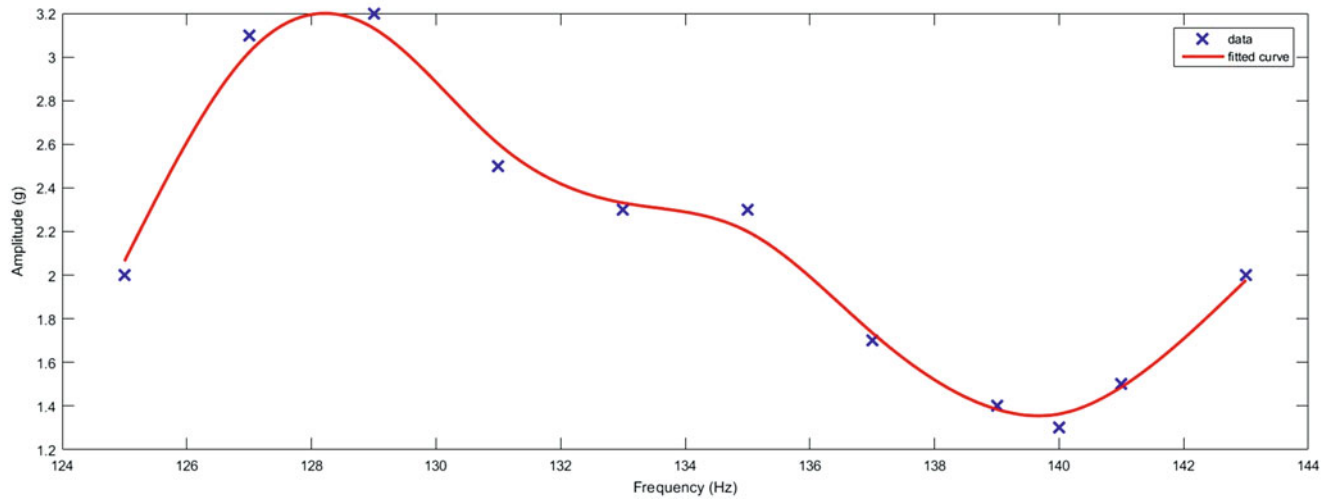


Fig. 13.13 P_4 chaotic snap boundary schematic

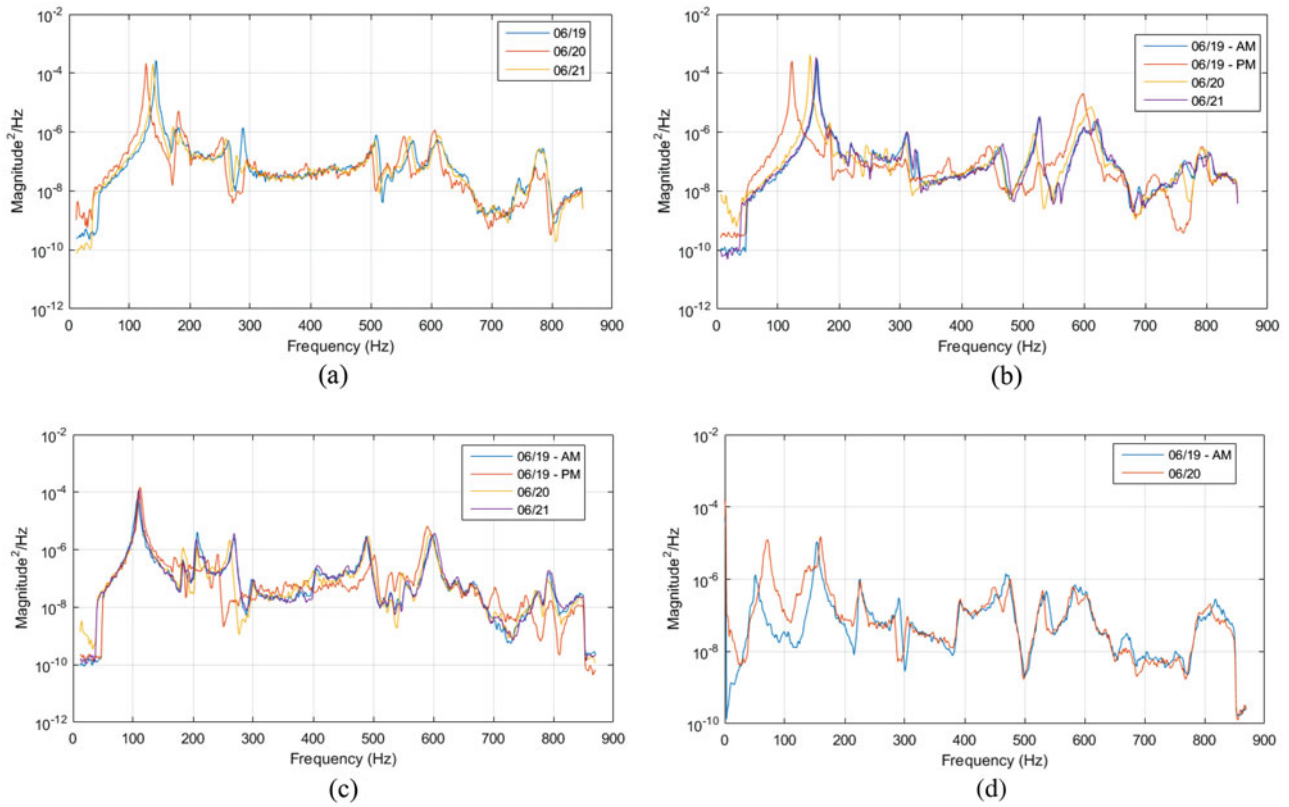


Fig. 13.14 (a and b) Power spectral density for the P_1 and P_2 states at low amplitude, random transverse excitation. (a) P_1 power spectral density (b) P_2 power spectral density. Power spectral density for the P_3 and P_4 states at low amplitude, random transverse excitation. (c) P_3 power spectral density (d) P_4 power spectral density

state change was the variation of the temperature of the testing environment. The plate was originally buckled with a frame temperature of 66.4 °F. The temperature of the room peaked at 72.9 °F in the afternoon of 19 June. This temperature variation was due to external factors such as no overnight air conditioning, outside air temperature increasing throughout the day, as well as large halogen overhead lights emitting heat. The temperature increase resulted in expansion of the aluminum plate fixture (the coefficient of thermal expansion of aluminum is significantly greater than that of the composite plate), which reduced the compressive buckling load, and produced a shallower post-buckled configuration. The change of state could also be attributed to material degradation, as the plate was subject to continuous large transverse loads and snap-through events; however, the results do not indicate a continuous state change as if caused by crack propagation.

13.4 Summary and Future Work

The pre- and post-buckled dynamic response of a composite plate was collected using a laser vibrometer and the digital image correlation technique and presented in this paper. The pre-buckled dynamic response was compared to an analytical solution based on the classical laminated plate theory. The analytical solution was not precise in modeling the plate under clamped-clamped, free-free boundary conditions because the pre-stress of the material was not modeled. In future work, the analytical solution will be modified to include the material pre-stress and material incongruities.

The post-buckled experimental results illustrated single-well and snap-through response between the statically stable equilibria. In future work, a focus on control of the testing environment will ensure minimal post-buckled state change. Also, the snap-through boundaries will be further investigated along with efforts to numerically model snap-through phenomena and damage propagation caused by the in-plane compressive loading during a snap-through event.

Acknowledgments The authors wish to thank the Air Force Research Laboratory for sponsoring this research in the Structural Sciences Center.

References

1. Meyers, C., Hyer, M.: Thermally-induced, geometrically nonlinear response of symmetrically laminated composite plates. In: 33rd Structures, Structural Dynamics and Materials Conference, Structures, Structural Dynamics, and Materials and Co-located Conferences
2. Che, L.-W., Chen, L.-Y.: Thermal postbuckling behaviors of laminated composite plates with temperature-dependent properties. *Compos. Struct.* **19**(3), 267–283 (1991)
3. Kim, H.-G., Wiebe, R.: Experimental nonlinear dynamics and snap-through of post-buckled composite plates. *Nonlinear Dynam.* **1**. Conference Proceedings of the Society for Experimental Mechanics Series, 21–35 (2017). https://doi.org/10.1007/978-3-319-54404-5_3
4. Kim, H.-G.: Nonlinear structural dynamics and delamination growth in laminated composite structures subjected to mode II fatigue loading
5. Andrews, M.G., Massabò, R., Cox, B.N.: Elastic interaction of multiple delaminations in plates subject to cylindrical bending. *Int. J. Solids Struct.* **43**(5), 855–886 (2006)
6. Gibson, R.F.: *Principles of Composite Material Mechanics*. CRC Press, Taylor & Francis Group, Boca Raton (2012)
7. Leissa, A.W.: *Vibration of Plates*, p. SP-160. National Aeronautics and Space Administration, Washington, DC (1969)
8. North American X15 | Aircraft | fiddlersgreen.net, www.fiddlersgreen.net/models/aircraft/North-American-X15.html
9. Pokrycie: SR-71a Blackbird. gamek.pl, img2.gamek.pl/a.gamek.pl/019/577/19577669_800.0.jpg/sr-71a-blackbird-pokrycie.jpg
10. Jones, R.M.: *Mechanics of Composite Materials*. McGraw-Hill, New York, NY (1975)
11. Grediac, M., Hild, F.: *Full-Field Measurements and Identification in Solid Mechanics*. Wiley, Weinheim (2012)
12. MATLAB R2015b. The MathWorks, Inc. (2015)
13. Wiebe, R., Virgin, L.N.: A heuristic method for identifying chaos from frequency content. *Chaos.* **22**, 013136 (2012)

Chapter 14

Simulation of a Self-Resonant Beam-Slider-System Considering Geometric Nonlinearities



Florian Müller and Malte Krack

Abstract Self-adaptive systems have the special ability to adjust their dynamical characteristics depending on certain operating conditions. In previous research a clamped-clamped beam with an attached slider has shown self-resonant behavior in experiments. However, the physical mechanisms producing this self-adaptivity are not yet fully understood. Here, we present a numerical model in which the beam is described by its lowest-frequency normal modes and taking into account geometric nonlinearities. Additionally, a clearance between beam and slider allows for unilateral and dry frictional contact interactions between the respective bodies. We demonstrate that the contact interactions are the key to explain the self-adaptive behavior. Moreover, we illustrate that the beam's geometric nonlinearity is essential to simulate jumps to significantly higher amplitude levels.

Keywords Self-resonant · Self-adaptive · Non-smooth dynamics · Geometric nonlinearities · Midplane stretching

14.1 Introduction

Self-adaptive systems provide the potential to act in energy harvesting applications or as broadband vibration absorbers passively, so that no electrical power is needed for adaptation. A self-adaptive system consisting of a clamped-clamped beam with moveable slider was investigated by several groups in the past. In [1, 2], the self-adaptive process of this system was demonstrated experimentally. Hereby the vibrational amplitude was initially small, but enlarged after the slider has passively achieved a certain position on the beam. The self-adaptive process could be reproduced successfully for a broad range of exciting frequencies and size scales of the system. However, no conclusive theory explaining this behavior was provided. Different kinds of unsuccessful adaptation processes were reported in [3]. Hereby the slider's gap size was identified as crucial parameter. In [4], a numerical model of the system was developed. The beam was described in terms of its linear bending modes. A gap between beam and slider was introduced to allow for unilateral and frictional contact interactions. The contact interactions turned out to be crucial for the adaptation process. However, the jumps to significantly higher vibrational amplitudes known from experiments couldn't be reproduced.

In this work, the model proposed in [6] is used to consider geometric nonlinearities of the beam. Simulations with free and axially fixed slider are performed and compared in order to understand the self-adaptive process. Additionally, an approximation for the system's first natural frequency is provided. The system specification is mostly adopted from [2]. More precisely, a steel beam of length $L = 130$ mm, thickness $2r = 1$ mm and a slider of mass $m = 25$ g is considered, see Fig. 14.1a.

14.2 Natural Frequency of Clamped-Clamped Beam with Bonded Slider

In this work, the beam's deformation is described in terms of its bending modes. Considering the N lowest-frequency bending modes, the equations of motion without slider read

F. Müller (✉) · M. Krack
Institute of Aircraft Propulsion Systems, University of Stuttgart, Stuttgart, Germany
e-mail: mueller@ila.uni-stuttgart.de; florian.mueller@ila.uni-stuttgart.de

$$\ddot{q}_n + 2D_n\omega_n\dot{q}_n + \omega_n^2q_n + \sum_{j=1}^N \sum_{k=j}^N \sum_{l=k}^N b_{j,k,l}^{(n)} q_j q_k q_l = \gamma_n \ddot{w}_0(t) \quad \text{with } n = 1, 2, \dots, N, \quad (14.1)$$

where q_n are the modal coordinates of the mass-normalized bending modes $\varphi_n(x)$ determined in accordance with linear Euler-Bernoulli theory. The terms on the left hand side represent forces due to inertia, damping (modal damping ratio D_n , natural frequency ω_n), linear restoring forces and nonlinear restoring forces respectively. The nonlinear restoring forces account for coupling between bending and stretching of the midplane and cause a coupling between the equations. Their coefficients $b_{j,k,l}^{(n)}$ can be found analytically according to [5]. The right hand side accounts for base excitation of the system, where γ_n is the modal excitation coefficient and $\ddot{w}_0(t)$ the acceleration of base, see Fig. 14.1a.

In previous research [1, 2, 4], the frequency range around the system's first natural frequency was investigated. To identify the relevant frequency range, the first natural frequency of the beam with bonded slider was approximated as a function of the slider's position x_C using the Rayleigh quotient [4]. However, the influence of vibrational amplitude due to geometric nonlinearities was neglected. In [6], we propose an approach for estimating the system's first natural frequency $\tilde{\omega}_1$ as a function of modal amplitude \hat{q}_1 and slider position x_C ,

$$\tilde{\omega}_1^2(\hat{q}_1, x_C) := \frac{\omega_1^2 + \frac{3}{4}b_{1,1,1}^{(1)}\hat{q}_1^2}{1 + m(\varphi_1(x_C))^2 + J_{yy}^{(C)}(\varphi_1'(x_C))^2}. \quad (14.2)$$

Considering the first bending mode only ($N = 1$), Eq. (14.1) reduces to the classical Duffing equation. The amplitude dependent natural frequency of this oscillator can be approximated by Harmonic Balance with the single-term ansatz $q_1 = \hat{q}_1 \cos(\tilde{\omega}_{1,\text{HB}}t)$. This approximation provides the numerator of Eq. (14.2). The denominator accounts for the influence of mass m and inertia $J_{yy}^{(C)}$ of the slider as proposed in [4]. Herein φ_1 denotes the shape of the first bending mode and φ_1' its first derivative with respect to x .

14.3 Self-Resonant Process

To simulate the self-resonant process, we extend the model proposed in [4] by the nonlinear terms in the beam's equation of motion [6]. We account for unilateral and frictional contact interactions between beam and slider applying the set-valued Signorini's and Coulomb's laws. To this end, the equation of motion is converted to a measure differential inclusion. Numerical integration of this equation is performed using Moreau's time stepping scheme. For more details on the numerical model see [4].

A result of the time integration is given in Fig. 14.1b. Here, the gap size is chosen to be $R/(2r) = 1.05$ and harmonic base excitation with $\hat{w}_0 = 20 \text{ m/s}^2$ and $f_{\text{ex}} = 180 \text{ Hz}$ is applied. Initially, the slider moves toward clamping (red line). At $t \approx 66 \text{ s}$, the beam's vibrational amplitude (gray line) jumps to a higher level, however decreases slowly after that, while

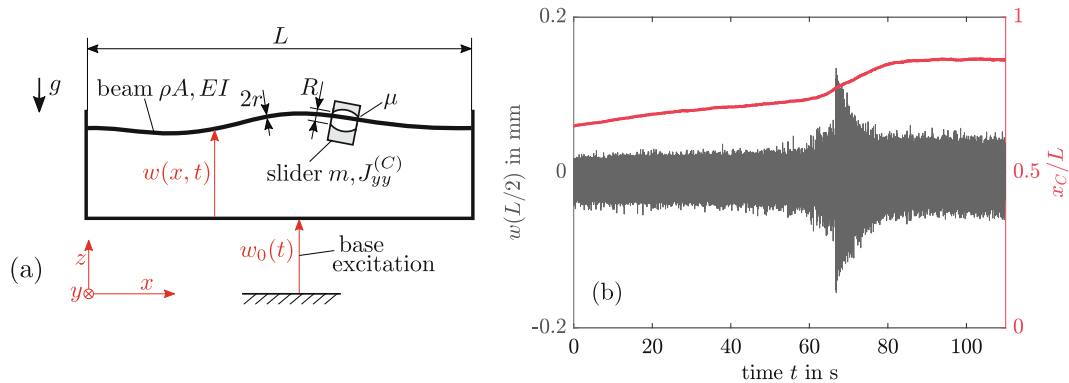


Fig. 14.1 (a) Two dimensional model of self-adaptive system. (b) Simulation of unsuccessful process. Gray: Beam's deformation at center. Red: position of slider

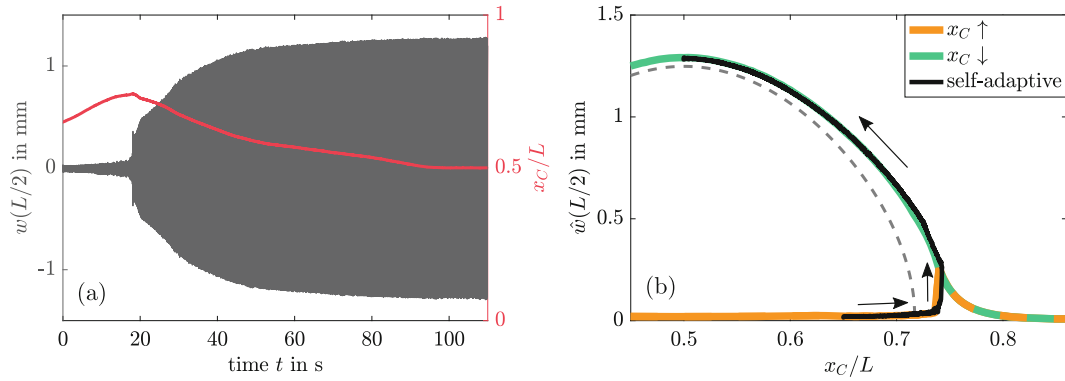


Fig. 14.2 (a) Simulation of self-resonant process. Gray: Beam's deformation at center. Red: position of slider. (b) Vibrational amplitude versus slider position. Orange/Green: increasing/decreasing prescribed slider position. Black: self-resonant process, arrows indicate direction. Dashed gray: relation between amplitude and slider position for resonance according to Eq. (14.2)

the slider keeps moving toward clamping. The same behavior was observed in experiments [3], whereby a too large gap size was identified to be crucial for the failure of adaptation.

Considering a smaller gap size ($R/(2r) = 1.02$) yields successful adaptation within the simulation as shown in Fig. 14.2a. Firstly, the beam's vibration level is small and the slider moves toward clamping. At $t \approx 17$ s, the vibrational amplitude jumps to a higher level and the slider starts moving back toward beam's center. The vibrational amplitude grows further until the slider reaches the beam's center. Now, the system maintains the slider position and a high vibrational amplitude in the steady state. This simulation result is in good accordance with previous experimental observations [1, 2].

To get more insight in the adaptive process, we now consider a modified system, in which the slider position x_C is no longer a free variable but a prescribed parameter. Based on this model, a diagram showing the beam's amplitude vs. x_C is given in Fig. 14.2b. Steady state is achieved via time integration until the vibrational amplitude doesn't change anymore. The system's state at the end of the simulation is used as initial condition for the next calculation for a slightly changed x_C ($\Delta x_C/L = 0.004$). This sequential continuation procedure is done for increasing (orange line) and decreasing (green line) x_C . For increasing x_C , the steady state amplitude is initially small, but jumps to a higher level at $x_C/L \approx 0.72$ and merges with the branch for decreasing x_C . For decreasing x_C , the steady state amplitude grows until $x_C = 0.5L$. The result of the simulation with free slider is also plotted into this diagram (black line). Here, the slider is initially placed at $x_C/L = 0.65$. First, the black curve follows the orange curve. After the jump to higher amplitude it follows the green curve until the slider stays at the center, where the non-adaptive system exhibits a maximum amplitude. Therefore the adaptive process is *self-resonant*. To complete the picture, one can approximate the relation of amplitude and slider position for which the system is at resonance according to Eq. (14.2). To this end, Eq. (14.2) is solved for \hat{q}_1 and resonance condition $\tilde{\omega}_1 = 2\pi f_{ex}$ is applied. To visualize the deformation at beam's center instead of the modal coordinate, the result is multiplied by $\varphi_1(L/2)$ and plotted in Fig. 14.2b (dashed gray line). Simulations with free and prescribed slider position both are approaching this curve as the slider's position gets closer to beam's center.

14.4 Conclusion

In this work, the self-resonant behavior of a clamped-clamped beam with a sliding mass is investigated. The models proposed in [6] are used to consider kinematic nonlinearities describing the coupling between bending and stretching of the beam. For the system with bonded slider, an approximation of the first natural frequency dependent on vibration level and slider position is derived. For the system with free slider, simulation results are in good accordance with experimental observations, both successful and unsuccessful adaptation processes can be reproduced. For the system with prescribed slider position, the illustration of steady state amplitude versus slider position exhibits coexisting stable states with different amplitudes and a certain point after that both solution branches are merging. This point marks the position, where the slider turns back toward the beam's center and the amplitude jumps to a higher level. The amplitude of the system with free slider closely follows the different steady-state response branches of the system with prescribed slider position. This explains why the slider has to initially move away from its final position and turn at a certain point to bring the system into resonance.

References

1. Miller, L.M.: Micro-scale piezoelectric vibration energy harvesting: from fixed-frequency to adaptable-frequency devices. Doctoral dissertation, UC Berkeley (2012)
2. Aboulfotouh, N. et al.: Experimental study on performance enhancement of a piezoelectric vibration energy harvester by applying self-resonating behavior. *Energy Harvest. Syst.* **4**(3), 131–136 (2017)
3. Gregg, C.G., Pillatsch, P., Wright, P.K.: Passively self-tuning piezoelectric energy harvesting system. *J. Phys. Conf. Ser.* **557**(1), 012123 (2014)
4. Krack, M. et al.: Toward understanding the self-adaptive dynamics of a harmonically forced beam with a sliding mass. *Arch. Appl. Mech.* **87**, 699–720 (2017)
5. Nayfeh, A.H., Mook, D.T.: *Nonlinear Oscillations*. Wiley, London (1979)
6. Müller, F., Krack, M.: The role of geometric nonlinearities on the self-resonant behavior of a beam-slider-system. (in preparation)



Chapter 15

Reinforcement Learning for Active Damping of Harmonically Excited Pendulum with Highly Nonlinear Actuator

James D. Turner, Levi H. Manring, and Brian P. Mann

Abstract Active vibration dampers can reduce or eliminate unwanted vibrations, but determining a good control policy can be challenging for highly nonlinear systems. For these types of systems, reinforcement learning is one method to optimize a control policy with only limited prior knowledge of the system dynamics. An experimental system was constructed by attaching a permanent magnet to the end of a pendulum and positioning an electromagnetic actuator below the resting position of the pendulum. The pendulum was excited with a sinusoidal force applied horizontally at the pivot point, and the control input was the applied voltage across the electromagnet. Due to the geometric arrangement and the strong dependence of magnetic force on distance, the relationship between the position of the pendulum and the actuation torque for any control input was highly nonlinear. A generalized version of the PILCO reinforcement learning algorithm was used to optimize a control policy for the electromagnet with the objective of minimizing the distance between the end of the pendulum and the downward position. After 16 s of interaction with the experimental system, the resulting learned policy was able to substantially reduce the amplitude of oscillation. This experiment illustrates the applicability of reinforcement learning to highly nonlinear active vibration damping problems.

Keywords Reinforcement learning · Active damping · Nonlinear dynamical system · Nonlinear control · Vibration

15.1 Introduction

Vibration in mechanical structures such as machines, buildings, and vehicles can reduce user comfort and damage the structure due to high stresses or fatigue. One approach to reduce vibration amplitude is to add an active damper that provides controlled force inputs to the structure. Applications of active vibration dampers include helicopters, optical systems such as cameras, and manufacturing machinery [1]. Reinforcement learning (RL) provides an approach for controlling active dampers when traditional techniques are insufficient. For example, RL can handle cases where developing an analytical model of the system dynamics is difficult. Additionally, RL can handle optimal control problems such as minimizing total actuation energy to reach and maintain a desired amplitude of oscillation. RL does not require prior knowledge of the system dynamics; the control policy is improved based on information collected while interacting with the system.

Interacting with an experimental system can be time-consuming or expensive, so an important characteristic of RL algorithms is their sample efficiency, i.e. how much experience is required to learn a good policy. One RL algorithm known for its sample efficiency is the probabilistic inference for learning control (PILCO) algorithm [2, 3]. PILCO approximates the system dynamics with a Gaussian process (GP) model learned from data collected while interacting with the system, and then improves the policy by simulating the system with the GP model.

An experiment was conducted to determine the applicability of an extended version of the PILCO algorithm to the system illustrated in Fig. 15.1 with the goal of reducing the amplitude of oscillation of the pendulum. The pivot was fixed to a shaker table, a permanent magnet was attached to the end of the pendulum, and an electromagnet was placed directly under the pivot. The pendulum was driven by a 1 Hz sinusoidal force applied to the shaker table, and the system was controlled by applying voltage v across the electromagnet. Due to the geometric configuration and strong dependence of magnetic force on distance, the electromagnet could apply a noticeable torque on the pendulum only in a narrow band on either side of the downward position. The objective was to minimize the angle of the pendulum over an episode of 4 s, with the system starting from steady-state forced oscillation at $t = 0$. The control frequency was 20 Hz, and the applied voltage was constrained to $-v_{\max} \leq v \leq v_{\max}$.

J. D. Turner (✉) · L. H. Manring · B. P. Mann

Department of Mechanical Engineering and Materials Science, Pratt School of Engineering, Duke University, Durham, NC, USA
e-mail: jim.turner@duke.edu

15.2 Methods

The PILCO algorithm optimizes the parameters for a control policy for an iterative dynamical system given no prior knowledge of the system dynamics. The PILCO algorithm assumes that the system is fully observable, the next state depends solely on the state \mathbf{x}_t and control \mathbf{u}_t , and the dynamics are continuous and smooth. The objective is to find the parameters $\boldsymbol{\psi}$ for a control policy $\mathbf{u}_t = \boldsymbol{\pi}(\mathbf{x}_t, \boldsymbol{\psi})$ that minimize the total expected cost $J^\pi(\boldsymbol{\psi}) = \sum_{t=0}^T \mathbb{E}_{\mathbf{x}_t} [c(\mathbf{x}_t)]$ of controlling the system for an episode of T time steps, where $c(\mathbf{x}_t)$ is a function of the difference between \mathbf{x}_t and a target state $\mathbf{x}_{\text{target}}$. Briefly, the PILCO algorithm works by learning an approximate GP model of the dynamics from data, evaluates the policy by simulating the system with the GP and policy, and then improves the policy based on the simulation. The process of applying the policy to the system to collect data, updating the GP, simulating the system, and improving the policy repeats until convergence [2, 3].

For the forced pendulum problem, however, this approach is inadequate: the next state of the system depends not only on the state and control but also on the forcing \mathbf{f}_t . Assuming the forcing is the same for each episode such that $\mathbf{f}_t = \mathbf{f}(t)$, the PILCO algorithm can handle this type of problem with two modifications: (1) incorporate \mathbf{f}_t as inputs to the GP model and policy, and (2) when simulating with the GP and policy, use the sequence of forcing $(\mathbf{f}_0, \dots, \mathbf{f}_T)$ recorded during the most recent episode.

For the experimental system in Fig. 15.1, the state, forcing, and control were $\mathbf{x} = \{\theta \dot{\theta} x \dot{x} i\}^\top$, $\mathbf{f} = \{f\}^\top$, and $\mathbf{u} = \{v\}^\top$, respectively, where θ and $\dot{\theta}$ were the angle and angular velocity of the pendulum, x and \dot{x} were the position and velocity of the shaker table, i was the current in the electromagnet, f was the external force applied to the shaker table, and v was the applied voltage across the electromagnet. However, the mass of the shaker table in the experimental system was so much larger than the mass of the pendulum that its motion could be approximated as being independent of the motion of the pendulum. This simplified the problem because the position and velocity of the shaker table could be handled as forcing terms. The new state and forcing vectors were then $\mathbf{x}_0 = \{\theta \dot{\theta} i\}^\top$ and $\mathbf{f}_i = \{f x \dot{x}\}^\top$. It was also useful to split the angle into components for input to the GP and policy, so this state vector was $\mathbf{x}_i = \{\sin \theta \cos \theta \dot{\theta} i\}^\top$. The GP model \mathcal{GP} was then $\mathbf{x}_{0,t+1} - \mathbf{x}_{0,t} = \mathcal{GP}(\mathbf{x}_{i,t}, \mathbf{f}_{i,t}, \mathbf{u}_t)$, and the policy function $\boldsymbol{\pi}$ was $\mathbf{u}_t = \boldsymbol{\pi}(\mathbf{x}_{i,t}, \mathbf{f}_{i,t}, \boldsymbol{\psi})$. The target was $\theta = 0$.

15.3 Results

Figure 15.2 shows the steady-state response of the system with $v = 0$. The amplitude was 0.27 rad, and the frequency was the same as the forcing frequency, 1 Hz. Figures 15.6, 15.3, 15.4 and 15.5 show the results of experimental episodes with various control policies, where each episode started at $t = 0$ at the point of the steady-state response with maximum θ .

Figure 15.3 shows the result of applying a constant voltage $v = -v_{\text{max}}$. This corresponds to always attracting the pendulum to the electromagnet with as much force as possible. This policy immediately reduced the response amplitude to 0.18 rad. Then, the transient response gradually died out with damping, reaching a new steady-state response with amplitude

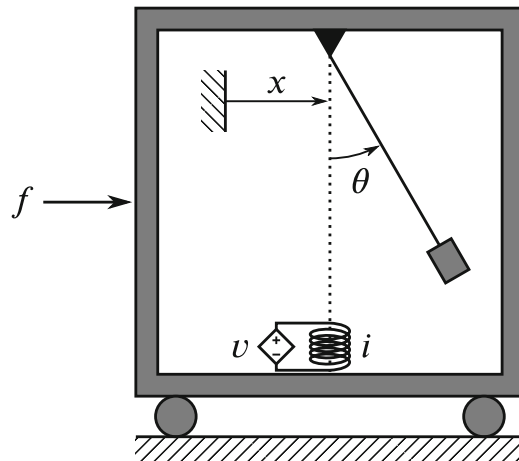


Fig. 15.1 Schematic of experimental system

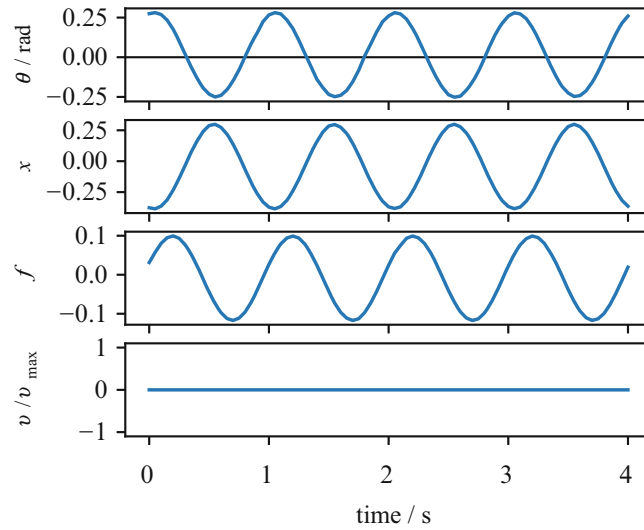


Fig. 15.2 Steady-state response with $v = 0$

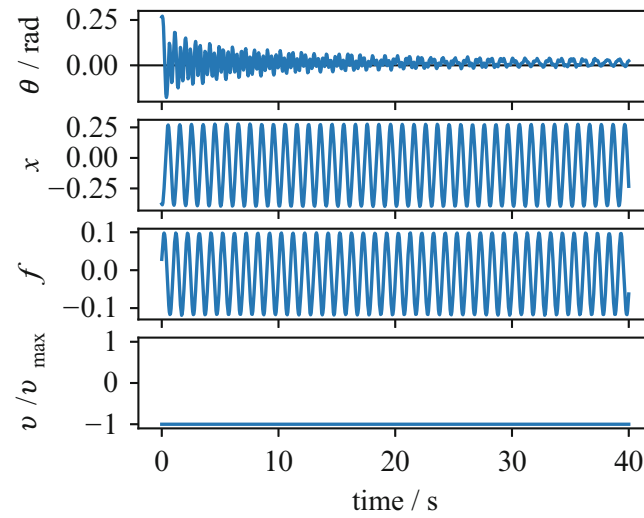


Fig. 15.3 Experimental episode when applying a constant $v = -v_{\max}$. Note that the time duration shown in the figure is longer than a single episode in order to illustrate the long-term behavior of this policy

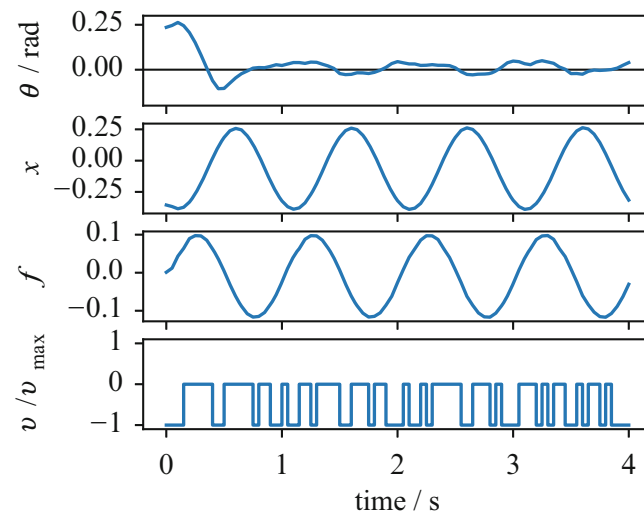


Fig. 15.4 Experimental episode when applying bang-bang control with control values $v \in \{-v_{\max}, 0\}$

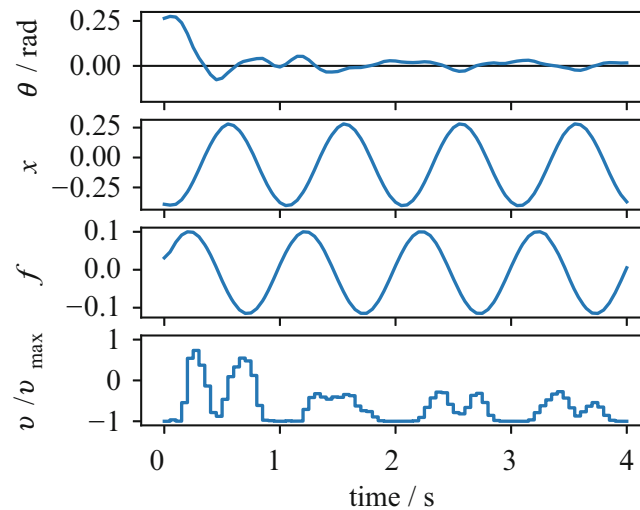


Fig. 15.5 Experimental episode when applying optimized policy generated by PILCO after 16 s of experience

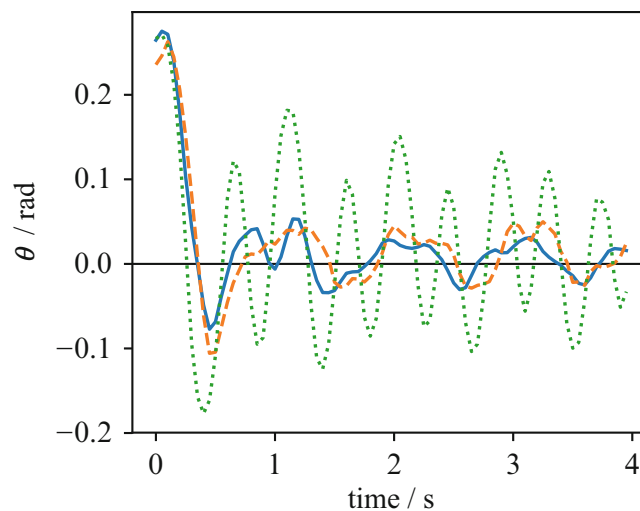


Fig. 15.6 Comparison of policy performance: $v = -v_{\max}$ (dotted green), bang–bang (dashed orange), PILCO-generated (solid blue)

0.02 rad. This demonstrated that the amplitude could be kept small after dissipating as much energy as possible, but simply applying $v = -v_{\max}$ required the inherent damping of the system to reduce the amplitude to this level.

Given prior knowledge of the dynamics, another approach was a bang–bang policy. This policy applied $v = 0$ while the pendulum was moving towards the target and $v = -v_{\max}$ while it was moving away from the target. Figure 15.4 shows that this policy rapidly brought the pendulum near the target and kept it there, substantially outperforming the constant voltage policy.

Figure 15.5 shows the result of a policy generated by the extended PILCO algorithm after 4 episodes of experience. The series of control values is more interesting than those of the other two policies. This policy repelled the pendulum as it moved toward the target in order to reduce overshoot, then mostly attracted it to keep its amplitude small.

Figure 15.6 shows a comparison of the pendulum angle for the episodes of all three policies. Both non-constant policies performed substantially better than the constant $v = -v_{\max}$ policy. The difference between the bang–bang and PILCO-generated policies was less significant, but the PILCO-generated policy exhibited less overshoot and overall 15% lower cost. Unlike the bang–bang policy, which was developed from intuition of the system’s behavior, the PILCO-generated policy was based solely on 16 s of experience, with no prior knowledge of the dynamics.

15.4 Conclusion

A pendulum subject to sinusoidal external forcing and controlled by an electromagnet positioned below its pivot was constructed. An extended version of the PILCO reinforcement learning algorithm was used to optimize a policy with the goal of minimizing the angle of the pendulum from the downward position for a 4 s episode. The policy generated after 16 s of experience, with zero prior knowledge of the system dynamics, outperformed a simple human-generated bang–bang policy. This experiment demonstrated the applicability of the extended PILCO algorithm to highly nonlinear forced vibration problems.

Acknowledgements Funding was provided by Army Research Office (ARO) grant W911NF-17-0047 and the National Defense Science & Engineering Graduate (NDSEG) Fellowship.

References

1. Takács, G., Rohal'-Ilkiv, B.: Model Predictive Vibration Control: Efficient Constrained MPC Vibration Control for Lightly Damped Mechanical Structures. Springer, London (2012). <https://doi.org/10.1007/978-1-4471-2333-0>
2. Deisenroth, M.P., Rasmussen, C.E.: PILCO: a model-based and data-efficient approach to policy search. In: Proceedings of the International Conference on Machine Learning (2011)
3. Deisenroth, M.P., Rasmussen, C.E.: A practical and conceptual framework for learning in control. Technical report. UW-CSE-10-06-01. Department of Computer Science and Engineering, University of Washington, June 2010



Chapter 16

Investigation of Nonlinear Dynamic Phenomena Applying Real-Time Hybrid Simulation

Markus J. Hochrainer and Anton M. Puhwein

Abstract Real-time hybrid simulation techniques have developed significantly in the last decades, driven by scientific research and steady progress in simulation and modeling techniques together with powerful automatic code generation tools. In engineering applications, hybrid simulation is mainly used for physical testing of critical components, while the remaining rest of the system is incorporated as computer model and properly coupled to the elements being tested. The focus of this research is to connect virtual nonlinear components with arbitrary characteristics to an existing mechanical model. This approach allows experimental verification of almost any classical nonlinear dynamic phenomena. The methodology can be applied for both, the optimal design of nonlinear components as well as testing of complex elements or materials based on experimental data, respectively. The laboratory setup comprises of standard hardware components used in modal testing including electrodynamic shakers, force, displacement and acceleration sensors and furthermore a real-time processing unit with feedback control for proper system coupling. For periodic forcing, the efficiency of the proposed method is demonstrated in a laboratory setup consisting of a rigid mass attached to a virtual nonlinear spring-damper element. All tests performed confirm the efficiency of the proposed system because nonlinear oscillations are reproduced with a very high level of accuracy.

Keywords Real-time hybrid testing · Hardware in the loop · Nonlinear vibrations · Periodic forcing · Experimental substructuring

16.1 Introduction

The concepts of substructuring, real-time hybrid testing (RTHT) or real-time hybrid simulation (RTHS) have become well accepted and established in engineering since their first introduction many decades ago, see e.g. [1–3]. Consequently, real-time substructuring is widely used in research and development because of its salient features, including the reduction of development costs, a reduced time to market, the availability of virtual prototypes during the development process and the outstanding possibilities in product testing. Driven by the steady development of simulation techniques and the permanent increase of computer performance, hybrid simulations have become popular in almost any field of engineering. The technique is particularly attractive because it allows testing of physical components under most realistic conditions, by coupling them to a virtual model simulated in a real-time environment. The appeal of RTHT, also known as hardware in the loop (HIL) or cyber physical testing, is to use the benefits of both, experimental techniques and numerical simulations, respectively. Consequently, the physical model under test can often remain isolated and at component level without the need to embed it into its adjacent subsystems during experimental testing. However, when designing a RTHS experiment, the boundaries of the virtual and the physical system must be chosen carefully, since their selection determines the coupling/interface conditions, which generally predefine the complexity and feasibility of an experiment. Although real-time hybrid testing and simulation have reached a high level of reliability and acceptance, they only reduce the amount of full scale testing at the moment, but are still no substitute. Another important aspect of the increasing acceptance of the hybrid techniques is the availability of a wide range of real-time hardware. Popular low-cost embedded systems can be used in the same way as high performance assemblies, because most simulation environments support the development of virtual models by graphical design tools and model based design methodologies. Furthermore, automatic code generation is provided by most development tools. In a modern environment the real-time target platform can be changed or even remain undefined up to the last development steps.

M. J. Hochrainer (✉) · A. M. Puhwein
University of Applied Sciences, Wiener Neustadt, Austria
e-mail: markus.hochrainer@fhwn.ac.at

Starting from first applications in civil engineering RTHT has become established in many other areas, including automotive and aerospace industry, mechanical engineering, chemical industry or automation technology. The complexity of RTHS applications is varying accordingly, beginning from rather simple small scale laboratory setups, to full scale testing of individual components as well as high fidelity testing of complete systems. There is no doubt, that the technique has become wide spread and very attractive to the engineering community.

16.2 Nonlinear Vibrations in Hybrid Simulation

When designing real-time hybrid testing experiments, the most critical step is the separation of the physical and the virtual components. Proper coupling is straightforward at interfaces requiring only the transmission of digital or analog signals, but it is significantly more difficult if a component is physically separated from its adjacent (linked) elements, because all kinematic and dynamic boundary conditions must be fulfilled at the newly created physical interface, see Fig. 16.1a. When replacing a physical component by its virtual substitute, all interaction forces and displacements must be provided by an auxiliary system denoted “transfer system”. In a minimum configuration it consists of a feedback controlled actuator as well as force and motion sensors for every degree of freedom. In vibration experiments, the actuation force is commonly provided by electrodynamic or hydraulic shakers which have been proven in vibration testing for many decades. Nevertheless, the authors are not aware of a universal transfer system that reliably fulfills different boundary conditions without the need for reconfiguration, reparametrization or other adaptations for a specific testing task. Typical challenges comprise nonlinear dynamic effects, limited frequency ranges, actuator saturation and most critical the presence of delays [4–6]. A fundamental property of force controlled physical systems is, that most disturbances remain unobserved until they deteriorate the actuator output. One common way to circumvent this difficulty is to assume periodicity and restrict the RTHT to periodic vibrations. In the work presented, this approach is pursued, because the length of a period can be chosen according to the dynamic phenomenon of interest. This even allows the investigation of transient phenomena, if the experiment can be repeated periodically.

It is demonstrated, that RTHT is an adequate, comparatively simple and efficient technique for studying and testing nonlinear oscillations. Therefore, a typical low order mechanical system with lumped parameter will be considered, and consequently, Duffing’s equation, see e.g. [7, 8].

$$m\ddot{x} + F_d(\dot{x}) + F_k(x) = F_0\sin(\omega t), \tag{16.1}$$

describing a well researched single degree of freedom nonlinear oscillator with displacement x , is studied in this work. To keep the interface conditions simple, the physical model consists only of the lumped mass m , whereas all other components

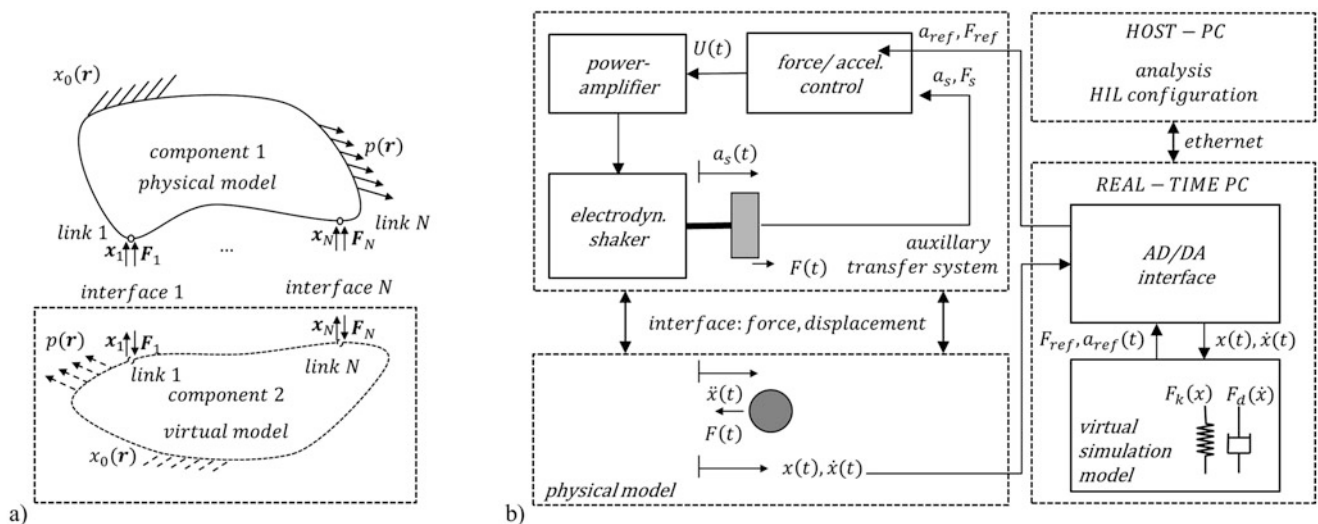


Fig. 16.1 Real-time hybrid simulation/testing (a) separation of a mechanical system into physical and virtual (simulation) components (b) schematics of the nonlinear vibration experiment

are collected in the virtual system. A simulated damper dissipates energy by the damping force $F_d(\dot{x})$ and a nonlinear elastic spring model renders the restoring spring force $F_k(x)$. The excitation is described by a harmonic driving term of amplitude F_0 and angular frequency ω . The RTHT schematics and the model separation is illustrated in Fig. 16.1b. Rearranging Eq. (16.1) according to the separation into a virtual and a physical model, the interaction force $F_s(x, \dot{x}, t)$ provided by the transfer system becomes

$$F_s(x, \dot{x}, t) = F_0 \sin(\omega t) - F_d(\dot{x}) - F_k(x). \quad (16.2)$$

At any physical system boundary, it is possible to prescribe either the flow or the potential quantity. Thus, it would also be possible to determine the reference displacement (or velocity) from the real-time simulation and measure the required interaction force, see e.g. [9] for such an application in dynamic vibration absorption. During testing, the physical model displacements and/or their derivatives are measured and transmitted to the simulation model for immediate processing. Finally, the computer simulation calculates the required interaction force F_s which is applied to the physical model, instantaneously, thereby closing the feedback loop. Since the entire (nonlinear) system dynamics is determined by F_s an extremely precise control of the interaction force it is obligatory. Within the scope of this work, all investigations are restricted to periodic processes, because this simplifies the control of the transfer system's actuator. All relevant control parameter are adapted by a learning algorithm until steady state equilibrium conditions are reached.

The separation of the mass m at the proposed interface, see Fig. 16.1b, has the advantage that spring and damping components can be selected without any limitations or restrictions. Theoretically, any nonlinear spring or damper characteristics can be implemented as long as the actuator of the transfer system can provide the required force. Therefore, smooth non-linearities described by polynomials or piecewise linear functions are easy to implement, whereas limits stops and similar elements causing impulsive loading are rather difficult to include in a RTHT experiment.

16.3 Control of Transfer System

Although the idea of RTHT seems surprisingly simple and straightforward for mechanical systems, its major challenge is to fulfil the dynamic boundary/interface conditions at the highest possible level of accuracy. Therefore, a feedback controlled actuator with excellent tracking performance and good disturbance rejection is inevitable. Since the control of actuators is very common in vibration testing, there is a vast literature available on actuator control see, e.g. [10–13]. Shakers like most other actuators, behave nonlinear, show complicated friction effects, deliver limited forces, have restricted stroke and power supply and most important, the control-structure interaction force is often difficult to predict and thus hard to include in the force control. Consequently, the supply of a desired forcing is very demanding. If, however, the system dynamics is periodic and the same trajectory are repeated, iterative learning control (ILC) or repetitive type control (RC) schemes have proven to work effective in many applications [14, 15]. Those algorithms update the control input based the errors of the previous iterations. From a control point of view the performance enhancing method is classified as a feedforward control, which can be added to any existing (feedback) controlled system, see Fig. 16.2. For an acceptable learning process, it is vital to converge after several iteration cycles. Therefore, a suitable feedback controller $R(z^{-1})$ with excellent tracking properties is obligatory as inner control loop in the transfer system.

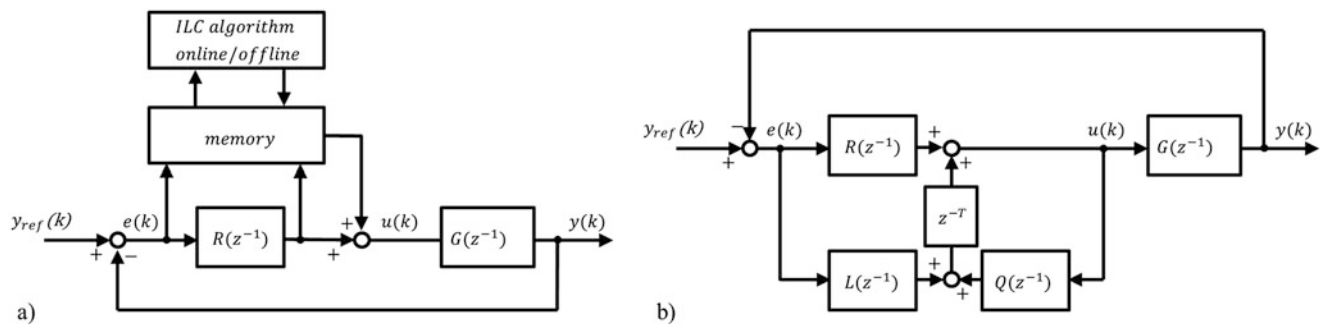


Fig. 16.2 Iterative learning/repetitive control (a) typical setup [modified from 15] (b) structure implemented in control of transfer system $G(z^{-1})$ for period T

Although the implementation of ILC finally turned out as the key technology for successful hybrid testing of nonlinear oscillators, the first design task is the setup of the transfer system, and the characterization of the actuator and sensor dynamics. Consequently, the identification of the plant model $G(z^{-1})$ is fundamental. It is, in essence, determined by the electrodynamic shaker and the power amplifier dynamics in the appropriate frequency and amplitude range. For further analysis, a plant model of output error type was identified from voltage input and acceleration output measurements. It is used for the design of a fairly robust, linear output feedback control $R(z^{-1})$ based on Nyquist's stability criterion. Surprisingly, it turned out that a simple time discrete integral control law renders a favorable closed loop behavior in the considered frequency range. Although this I-type controller guaranteed a stable closed loop performance with an acceptable frequency response amplitude, the phase shift, equivalent to a delayed actuation force, was not acceptable in the project. Additionally, a second order high pass filter had to be added to remove undesired low frequency actuator motion. Even though the transient behavior of the closed loop dynamics was not sufficient for a direct application in RTHT, it formed a suitable and robust foundation for an ILC algorithm of the form

$$u_i(k) = R(z^{-1})e_i(k) + L(z^{-1})e_{i-1}(k) + Q(z^{-1})u_{i-1}(k), \quad (16.3)$$

with i and k denoting the iteration number and the discrete time index, respectively. In the control update $u_i(k)$, the filter $Q(z^{-1})$ can be adjusted to limit the learning bandwidth. In controller used for RTHT, the learning filter L is set $L = 0$ and the filter $Q(z^{-1})$ which limits the learning bandwidth to the highest expected actuator frequency ω_{max} is implemented as a non-causal low pass zero phase FIR filter with a cut off frequency of $\omega_{max} = 10\omega$. The closed loop tracking behavior of the transfer system is shown in Fig. 16.3. Apparently, the output feedback control (I-control) is not able to follow the reference signal without significant errors, but the developed ILC algorithm shows perfect tracking behavior without any delay, and a negligible steady state error bound in the considered frequency range, see Fig. 16.3b for a detailed view of the outstanding control performance. Another benefit of the implemented ILC algorithm is the relatively fast convergence of typically much less than 50 iterations. Hence, the developed ILC control algorithm meets all expectations and is adequate for RTHS experiments. All further results presented, were obtained with a real-time operating system (Simulink Real-Time) running at a sampling frequency of $f_s = 5000$ Hz. The analog/digital IO is done using a multi function I/O card of type Humusoft MF624 with 14-bit AD/DA conversion. Acceleration is measured by IEPE transducers (BK4507) with proper signal conditioning and possible displacement measurements are carried out using a single point Laser Doppler Vibrometer (LDV) with controller OMV-5000 and sensing head OMV505. Finally, an electrodynamic shaker (LDS V406) with the matching amplifier (LDS P100E) were used as actuator in the transfer system.

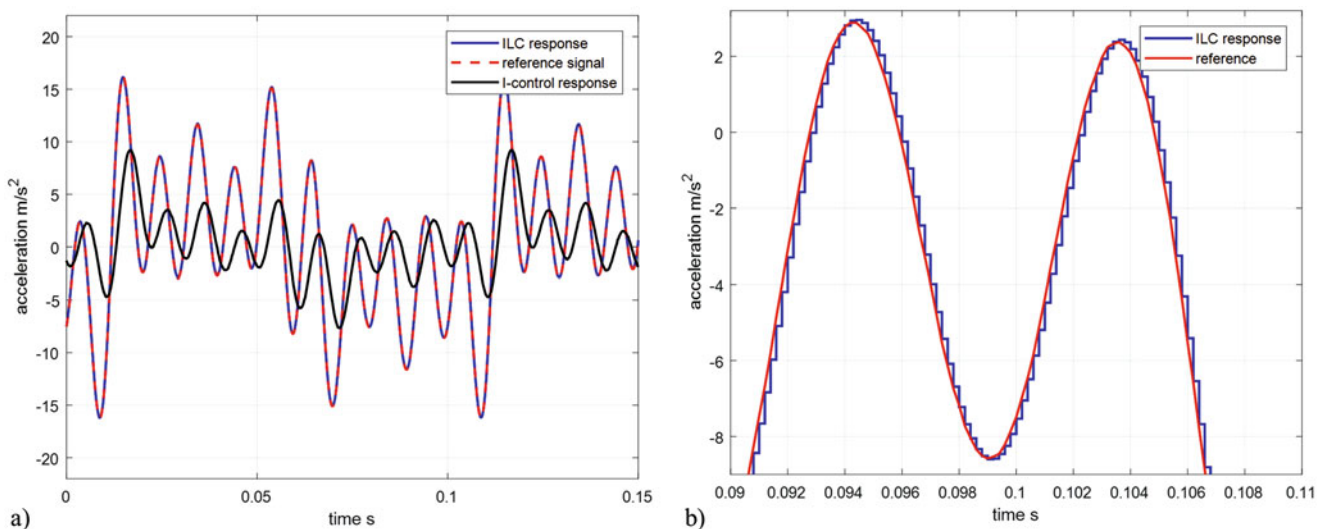


Fig. 16.3 Signal following of feedback controlled transfer system (a) comparison of ILC and output feedback (I-control) (b) detail of dynamic signal tracking

16.4 Real-Time Hybrid Testing of a Duffing Oscillator

The effectiveness of RTHT for nonlinear oscillations is illustrated by comparing experimental data of the Duffing oscillator with numerical simulations. Since the physical system consists of the lumped mass m rigidly attached to the transfer system's actuator, Newton's law renders the mass-shaker interaction force $F_s = m\ddot{x}$ directly. Thus, the need for an additional force measurement is eliminated assuming that \ddot{x} is already measured. During the RTHT the damping and spring forces are described by

$$\begin{aligned} F_d &= d\dot{x}, \\ F_k &= k(x + \alpha x^3) \end{aligned} \quad (16.4)$$

with d , k and α denoting the linear viscose damping constant, the linear elastic spring constant and the coefficient describing the cubic spring hardening effect, respectively. Since the acceleration of the physical system \ddot{x} is identical to the shaker acceleration a_s the mass normalization of nonlinear equation of motion, Eq. (16.1), renders

$$\ddot{x} = a_s = a_F \sin(\omega t) - 2\zeta\omega_0\dot{x} - \omega_0^2(x + \alpha x^3), \quad (16.5)$$

with $\omega_0 = \sqrt{k/m}$, $\zeta = d/2m\omega_0$ describing the undamped natural frequency and the damping coefficient of the corresponding linear oscillator, respectively. $a_F = F_0/m$ represents the equivalent acceleration of the external forcing. In RTHT, the transfer system accelerates the mass according to the respective forcing, and the velocity \dot{x} and displacement x are obtained or derived from measurements. This is in contrast to a simulation, where the displacements are obtained from a numerical solution of the nonlinear equation of motion, Eq. (16.5). A comparison between the RTHT results and those obtained from pure numerical simulations show almost perfect agreement. Figure 16.4 compares displacement and acceleration responses of a linear ($\alpha = 0$) SDOF oscillator at resonance for both, RTHT and simulation, respectively. By visual inspection it is difficult to detect any deviations, and therefore the time responses are averaged over several periods to determine the mean vibration amplitude. This additional data processing renders a corresponding relative displacement and acceleration error of $e_{disp} = 0.36\%$ and $e_{accel} = -0.87\%$, respectively. The small variance in the relative error can be traced back to the different transducers used for displacement and acceleration measurements.

Next, the virtual spring model is chosen nonlinear with cubic stiffening by setting $\alpha = 10^8$. The RTHT steady state vibrations responses are given in Fig. 16.5. Again, there is an excellent correspondence with the simulated system, and when compared to the linear system response, see Fig. 16.4, the high order harmonics are clearly perceptible. The responses also show that the nonlinear system has significantly smaller vibration amplitudes due to a resonance shift at larger displacement amplitudes. Very similar results have been obtained for other nonlinearities, e.g. turbulent damping forces or a bilinear spring

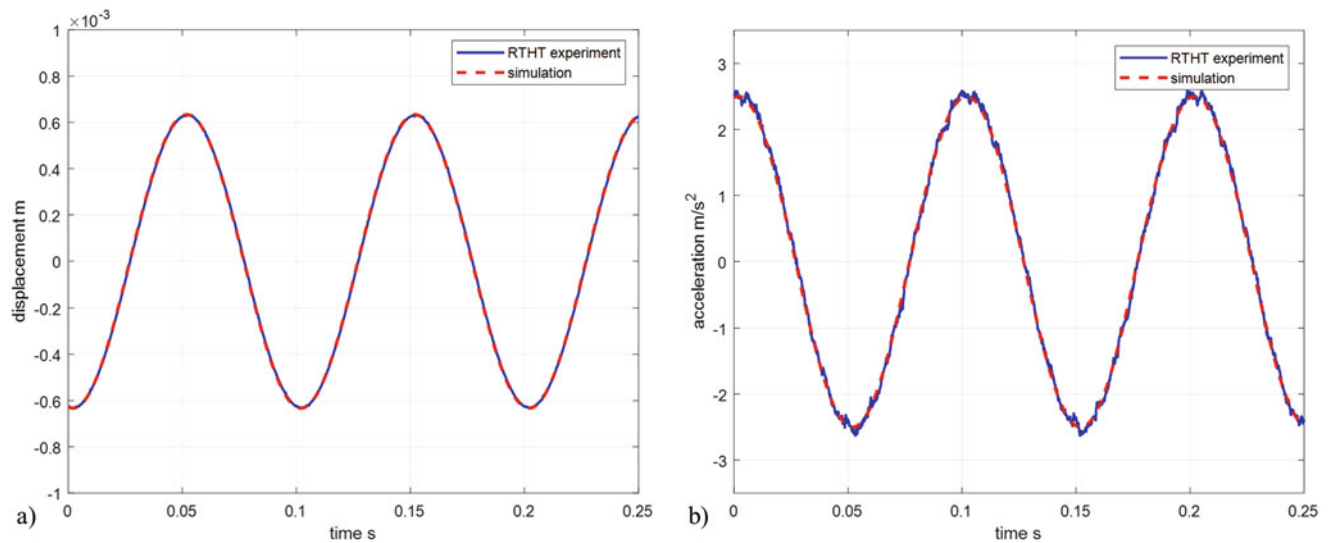


Fig. 16.4 Comparison between RTHT and simulation: steady state response for linear system with $\alpha = 0$, $a_F = 1 \text{ m/s}^2$, $\omega_0 = \omega = 20\pi \text{ rad/s}$, $\zeta = 0.2$ (a) measured (LDV) and simulated displacement x (b) measured (accelerometer) and simulated acceleration \ddot{x}

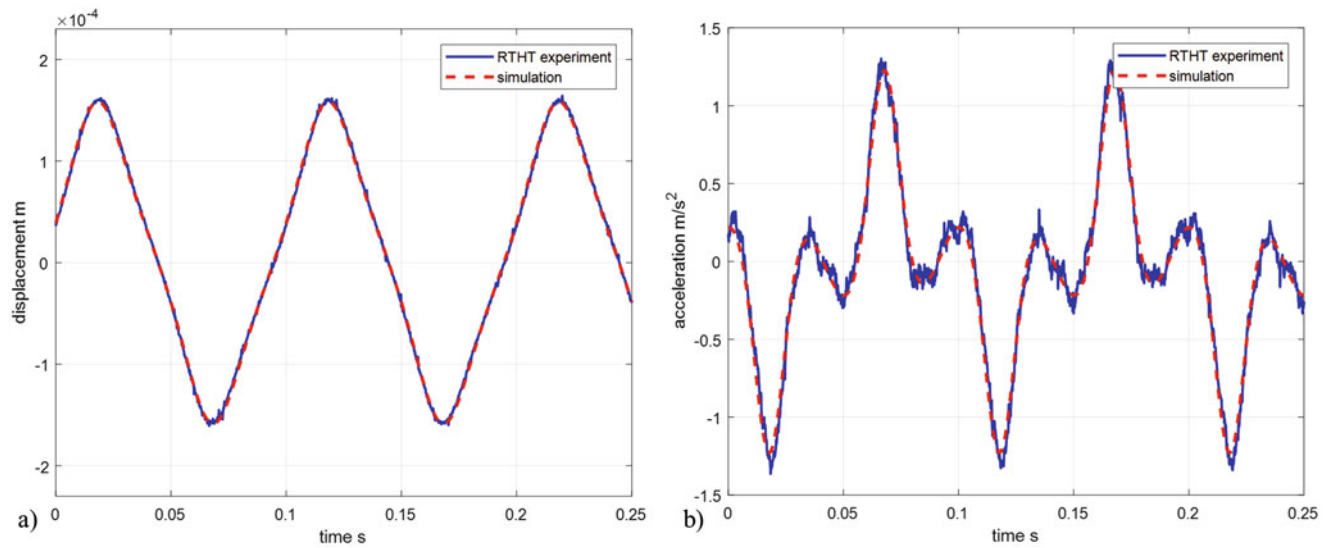


Fig. 16.5 Comparison between RTHT and simulation: steady state response for nonlinear system with $\alpha = 10^8$, $a_F = 1 \text{ m/s}^2$, $\omega_0 = \omega = 20\pi \text{ rad/s}$, $\zeta = 0.2$ (a) measured (LDV) and simulated displacement x (b) measured (accelerometer) and simulated acceleration \ddot{x}

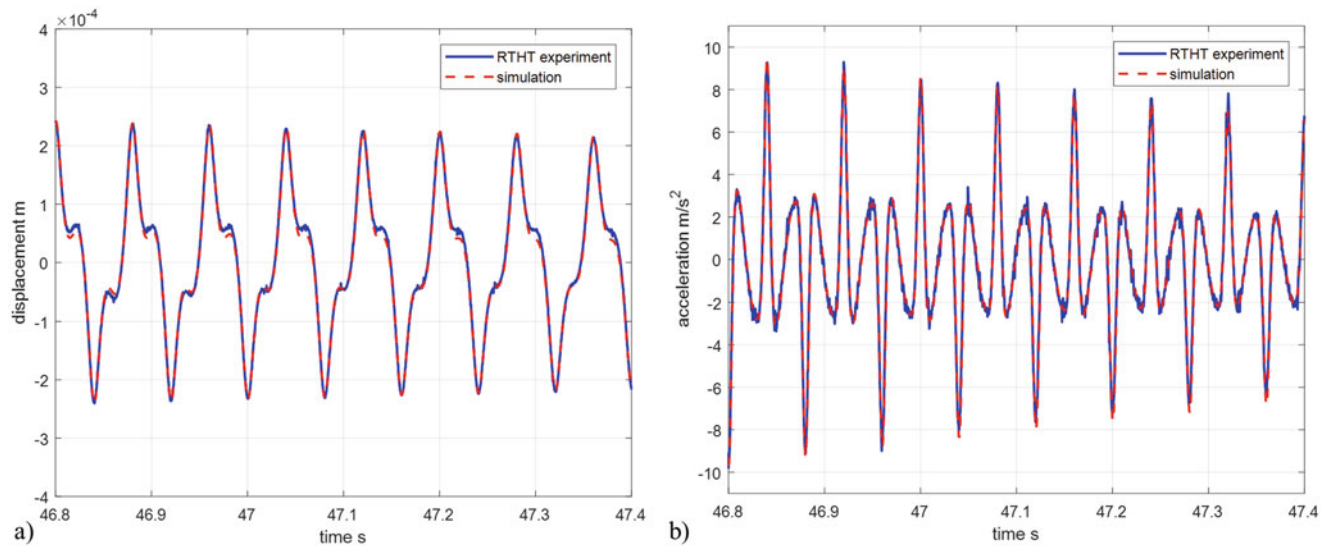


Fig. 16.6 Comparison between RTHT and simulation: transient response during decay of external forcing for $\alpha = 10^8$, $\omega = 25\pi \text{ rad/s}$, $\omega_0 = 30\pi \text{ rad/s}$, $\zeta = 0.2$ (a) measured (LDV) and simulated displacement x (b) measured (accelerometer) and simulated acceleration \ddot{x}

characteristics. The steady state T -periodic results and a comparison to their corresponding numerical simulations clearly demonstrate that the setup is adequate for RTHT of nonlinear dynamic systems.

Although designed for periodic processes, the setup turned out to perform satisfactorily under weakly nonstationary conditions, e.g. the moderate decay of oscillations, see Fig. 16.6. The results confirm that the possible application to transient vibrations is only limited by the transfer system's dynamics. Once again, this underlines, that the development of a flexible, reliable and robust transfer system is the most important requirement for successful RTHT applications.

16.5 Conclusion

In this work, the idea of real-time hybrid testing has been applied to the investigation of nonlinear vibrations. Although known for many decades, RTHT has become popular about 20 years ago, because of the availability of a broad spectrum

of real-time hardware and software necessary for simulation and control. For an engineer, RTHT is attractive, because an isolated physical component can be tested under realistic conditions, since all components eliminated from physical tests are collected in a virtual model. This model is running in a real time simulation and is interacting with the physical component. For a fundamental demonstration of the practicability of RTHT of nonlinear dynamic systems, both, the physical and the simulation model are kept simple. The former consists of a rigid mass, the latter of a nonlinear spring damper element. If the models are coupled in accordance with all boundary conditions, a nonlinear single degree of freedom oscillator of Duffing type is obtained. Although the Duffing oscillator can be used to demonstrate several nonlinear effects, all experiments are restricted to time periodic forcing. This restriction results from limitations of the developed transfer system, which must possess a highly accurate tracking performance for reliable results. The transfer system's main components are an electrodynamic shaker and an iterative learning control algorithm, which is particularly appropriate for periodic processes. The hybrid simulation technique presented allows easy modification of the simulation model's nonlinearities and shows excellent agreement with all simulations. The efficiency of the proposed system is confirmed for different periodic forcings, and all results underline that the method presented enables developments, which are hardly possible with traditional methods, or only at the price of a significantly greater effort.

References

1. Saouma, V., Sivaselvan, M.: Hybrid Simulation: Theory, Implementation and Applications. Taylor & Francis Ltd., London (2008)
2. Bursi, O.S., Wagg, D.: Modern testing techniques for structural systems. In: Dynamics and Control, CISM International Centre for Mechanical Sciences, vol. 502. Springer-Verlag Wien, New York (2008)
3. Hochrainer, M.J.: Real-time hybrid testing: challenges and experiences from a teaching point of view. In: Mains, M., Dilworth, B. (eds.) Topics in Modal Analysis & Testing, Conference Proceedings of the Society for Experimental Mechanics Series, vol. 9. Springer, New York (2019)
4. Ahmadizadeh, M., Mosqueda, G., Reinhorn, A.M.: Compensation of actuator delay and dynamics for real-time hybrid structural simulation. *Earthq. Eng. Struct. Dyn.* **37**(1), 21–42 (2008)
5. Chen, C., Ricles, J.M.: Analysis of actuator delay compensation methods for real-time testing. *Eng. Struct.* **31**(11), 2643–2655 (2009)
6. Bartl, A., Mayet, J., Karamooz Mahdiabadi, M., Rixen, D.J.: Multi-DoF interface synchronization of real-time-hybrid-tests using a recursive-least-squares adaption law: a numerical evaluation. In: Proceedings of the 34th IMAC, A Conference and Exposition on Structural Dynamics, 2016
7. Virgin, L.N.: Introduction to Experimental Nonlinear Dynamics. Cambridge University Press, Cambridge (2000)
8. Ziegler, F.: Mechanics of Solids and Fluids, 2nd edn. Springer, New York, Vienna (1998)
9. Hochrainer, M., Schattovich, P.: Real-time hybrid simulation of an unmanned aerial vehicle. In: Dynamics of Coupled Structures, Conference Proceedings of the Society for Experimental Mechanics Series, https://doi.org/10.1007/978-3-319-54930-9_4, 2017
10. Maghareh, A., Silva, C.E., Dyke, S.J.: Servo-hydraulic actuator in controllable canonical form: identification and experimental validation. *Mech. Syst. Signal Process.* **100**, 398–414 (2018)
11. Guan, F.-G., Xiong, W., Wang, H.-T.: Adaptive random control of a two-axis redundantly actuated electro-hydraulic shaking table. *J. Vib. Control.* **22**(16), 3455–3469 (2014)
12. Zhang, R., Lauenstein, V., Phillips, B.: Substructure real-time hybrid simulation with a small-scale uni-axial shake table. In: 6th International Conference on Advances in Experimental Structural Engineering, August 1–2, 2015, University of Illinois, Urbana-Champaign, USA (2015)
13. Plummer, A.R.: Model-based motion control for multi-axis servohydraulic shaking tables. *Control. Eng. Pract.* **53**, 109–122 (2016)
14. Wang, Y., Gao, F., Doyle, F.J.: Survey on iterative learning control, repetitive control, and run-to-run control. *J. Process Control.* **19**, 1589–1600 (2009)
15. Bristow, D.A., Baron, K.L., Alleyne, A.G.: Iterative learning control. In: Levine, W.S. (ed.) The Control Handbook. CRC Press, Boca Raton, FL (2010)



Chapter 17

Experimental and Numerical Aeroelastic Analysis of Airfoil-Aileron System with Nonlinear Energy Sink

Claudia Fernandez-Escudero, Miguel Gagnon, Eric Laurendeau, Sebastien Prothin, Annie Ross, and Guilhem Michon

Abstract Recent studies on nonlinear passive absorbers present high control efficiency for broadband frequency range with low added mass. This work presents a configuration of an airfoil typical section where the flap is considered as a Nonlinear Energy Sink (NES), which adds zero mass and has a cubic stiffness. An aeroelastic test-bench was created and characterized for linear and nonlinear structural configurations and tested in a subsonic wind-tunnel experimental campaign. The strongly nonlinear hardening stiffness is obtained by using linear springs and geometric nonlinearities. For the nonlinear tests, several Limit Cycle Oscillation (LCO) and subcritical and supercritical Hopf bifurcations were observed. Numerical analysis was also carried out for both linear and nonlinear cases using: Unsteady Vortex Lattice Method (UVLM) and Theodorsen theory (both low fidelity), Euler (medium fidelity) and Reynolds-Averaged Navier Stokes (high fidelity) methods. The numerical methods present good agreement, within the limits of each approach, and correspond with the experimental data. Using the NES, a gain of flutter speed is reached compared to the linear flap restoring force configuration.

Keywords Aeroelasticity · Unsteady aerodynamics · Flutter · LCO · Nonlinear dynamics

17.1 Present Work

An important phenomenon encountered in dynamic aeroelasticity is flutter. If there are no sources of nonlinearities the system can only experience classic flutter which is defined as self-excited vibration of the structure due to energy extraction of the incident airflow. This generally results from the coalescence of two structural modes: pitch and plunge, which reach the same vibration frequency. If the speed becomes greater than the flutter speed, the amplitude of the movement grows exponentially causing structural failure [1].

The presence of nonlinearities can change dramatically the observed behaviour as other phenomena, such as limit cycle oscillations (LCOs), can appear in the system's response. During a LCO, the vibration reaches a finite amplitude which remains constant unless the wind speed changes. LCOs can be observed in subcritical or in supercritical regime once flutter speed is exceeded [2].

In order to increase the systems flutter speed, active methods (energy input) are very efficient but can be obsolete in emergency cases (ie. lack of power). Tuned Vibration Absorbers (TVA) are a good alternative and are already widely used in civil engineering [3]. The classic linear TVA is simple and efficient but only close to a single frequency. The main drawback is the inefficiency to control an oscillator whose natural frequencies changes with the wind speed (ie. aeroelastic wing). Semi-active strategies could solve this problem but the energy dependency is still present. This is the reason why some research studies focus on Nonlinear Tuned Vibration Absorber (NLTVA) [4]. The Nonlinear Energy Sink (NES) [5] is a NLTVA with

C. Fernandez-Escudero
ISAE-Supaero, Toulouse, France

Polytechnique Montreal, Montreal, QC, Canada

S. Prothin
ISAE-Supaero, Toulouse, France

M. Gagnon · E. Laurendeau · A. Ross
Polytechnique Montreal, Montreal, QC, Canada

G. Michon
Université de Toulouse, ICA, CNRS, ISAE-Supaero, Toulouse, France

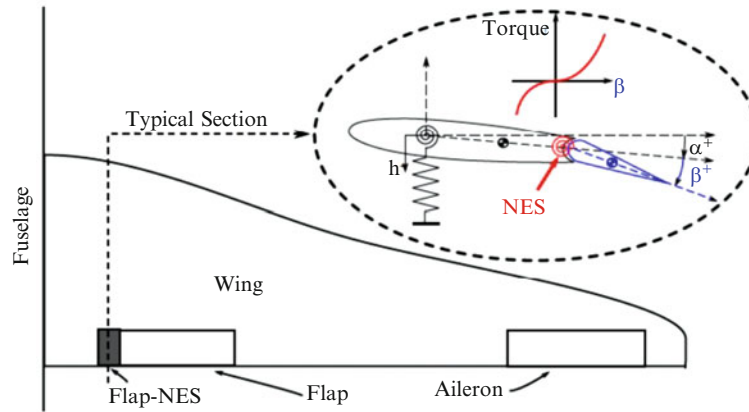


Fig. 17.1 Configuration of wing with NES with zero added mass

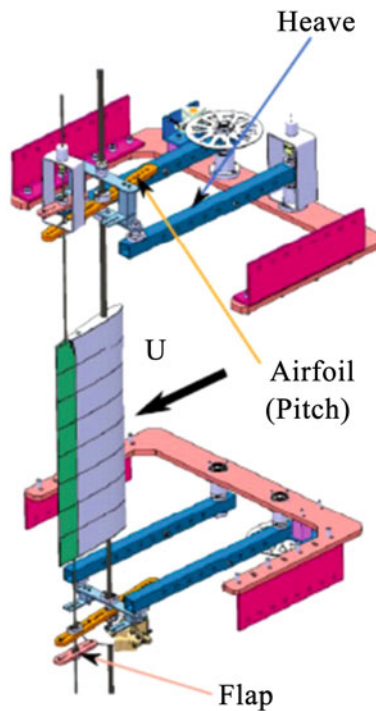


Fig. 17.2 CAD of 3DOF mechanism [6]

a purely nonlinear stiffness that presents high vibration absorption characteristics for a broadband frequency range and a low added mass.

With the objective of controlling passively flutter of a wing for a minimum added mass, the idea of this work is to design one of the wing's flaps as a NES (Fig. 17.1). In this respect, the work continues on the fundamental observations of Amar [6]. For a better understanding of the system, an experimental campaign was carried on a 2 degrees of freedom (DOF) and 3DOF aileron/airfoil typical section with a strongly nonlinear stiffness in the control surface. Similarly, pertinent numerical analysis is carried out. The aerodynamic forces acting on the airfoil are computed and these forces together with the equations of motion enable the computation of the fluid-structure interaction and, therefore, the resolution of the aeroelastic system. Different numerical methods are used for this purpose: Theodorsen theory, UVLM, unsteady Euler and URANS.

The experimental setup was designed to enable the number of degrees of freedom to be varied to enable, firstly, the stiffness of each DOF to be calculated and, secondly, the 2DOF and 3DOF cases to be tested. In order to enable the movement of the wing, a mechanism is placed above and below the wind tunnel test section so that it has no influence on the airflow. The mechanical system can be divided into three subsystems each responsible for one of the DOF (see Fig. 17.2). Also, the stiffness of each DOF can be modified by changing the springs so nonlinearities can easily be introduced. The inlet velocity of

the wind tunnel was varied in order to see the change in the response of the system. Flutter and subcritical and supercritical LCOs were encountered.

Regarding the aeroelastic analysis, the linear flutter speed is identified for a 2DOF and a 3DOF typical section. Non-linearities through freeplay and cubic stiffness in the pitching DOF for the 2DOF case and aileron freeplay for the 3DOF are added to the system to evaluate its response. Both Theodorsen and UVLM are able to capture subcritical LCOs similar to those identified in the literature. Since they are low fidelity methods which include several simplifications, the computational time and cost of Theodorsen and UVLM are lower by several orders of magnitude than those of URANS or even unsteady Euler method.

Acknowledgements The authors would like to acknowledge the Natural Sciences and Engineering Research Council of Canada and ISAE-Supaero for the funding. The work benefited from the advices of Simon Bourgault-Côté and Matthieu Parenteau regarding the software NSCODE and UVLM, respectively.

References

1. Bisplinghoff, R.L.: Aeroelasticity. Dover, New York (1996)
2. Strogatz, S.H.: Nonlinear Dynamics and Chaos with Application in Physics, Biology, Chemistry and Engineering. Addison-Wesley Publishing Company, Boston, MA (1994)
3. Mesenguer, J., et al.: Aerodinamica Civil: Efectos del Viento en Edificaciones y Estructuras. Ibergarceta Publicaciones, SL, Madrid (2013)
4. Habib, G., Kerschen, G.: Suppression of limit cycle oscillations using the nonlinear tuned vibration absorber. Proc. R. Soc. A. The Royal Society. **471**, 20140976 (2015)
5. Lee, Y.S., et al.: Passive non-linear targeted energy transfer and its applications to vibration absorption: a review. Proc. Inst. Mech. Eng. K J. Multi-body Dyn. **222**, 77–134 (2008)
6. Amar, L.: Nonlinear Passive Control of an Aeroelastic Airfoil, Simulations and Experimentations. PhD Thesis, Toulouse University (2017)

Chapter 18

On the Modal Surrogacy of Joint Parameter Estimates in Bolted Joints



Nidish Narayanaa Balaji and Matthew R. W. Brake

Abstract The Surrogate system hypothesis for jointed mechanics proposes that the influence of a jointed interface on an otherwise linear system is identical irrespective of the structural features of the so-called far-field linear structure. The implication, if the hypothesis finds support, is that the characterization of a joint in a single structural context can be used for developing predictive models of completely different structures, albeit with identical joint configurations. In critical applications such as aerospace, this can potentially lead to a more cost-effective design flow enabling tighter design optimization. In order to evaluate the hypothesis, the major influences on the nonlinear behavior of a jointed structure has to be delineated and studied individually as well as in combinations. Proceeding in the spirit of previous investigations where the effect of far-field structures and joint interface modeling approaches have been tackled, the current investigation studies the so-called “modal surrogacy” of a structural system. The investigation serves to understand the sufficiency of modeling the nonlinear behavior in lower modes to make high-modal nonlinear predictions. The Brake-Reuß Beam (BRB), which is an assembly of two monolithic beams connected together using a bolted lap joint with three bolts, is used as a test specimen for the current investigations. Due to the presence of regions with zero static pre-stress in the interface, considerable separation combined with stick & slip has been numerically as well as experimentally observed. This leads to significant nonlinear effects in the response of the system and thus serves as a convenient benchmark for the current work.

Keywords Joint mechanics · Multi-objective optimization · Interface modeling · Friction · Parameter identification · Nonlinear modal response

18.1 Introduction

Predictive dynamic modeling for bolted joints has been a persisting challenge for the joint mechanics community due to gaps in the understanding of the fundamental physics governing the interfacial mechanics leading to nonlinear macro-level behavior [10]. Although highly resolved as well as kinematically consistent approaches have been reported (see, for example [6, 7, 11]), there is still not much consensus about contact-constitutive modeling. However, experimental as well as numerical efforts have demonstrated that experimentally identified models of joints can be used to make meaningful predictions in a limited sense. But the classical idea of the context-independence of system identification has to be scrutinized for nonlinear systems.

The surrogate system hypothesis for joint mechanics [1, 2] provides a framework for assessing the robustness of parameter estimations across multiple “structural contexts”. The hypothesis proposes that the influence of a jointed interface on an otherwise linear system is identical irrespective of the structural features of the so-called far-field linear structure. The implication, if the hypothesis finds support, is that the characterization of a joint in a single structural context can be used for developing predictive models of completely different structures, albeit with identical joint configurations, or in the very least develop an estimator for the confidence of the same. In order to evaluate the hypothesis, the major influences on the nonlinear behavior of a jointed structure has to be delineated and studied individually as well as in combinations. Proceeding in the spirit of previous investigations where the effect of far-field structures and joint interface modeling approaches have been tackled, the current investigation studies the so-called “modal surrogacy” of a structural system. The investigation serves to understand the sufficiency of modeling the nonlinear behavior in lower modes to make high-mode nonlinear predictions. The Brake-Reuß Beam (BRB), which is an assembly of two monolithic beams connected together using a three-bolt lap joint, is used as the test structure for the current investigations. Due to the presence of regions with zero static pre-stress in the

N. N. Balaji · M. R. W. Brake (✉)
Department of Mechanical Engineering, Rice University, Houston, TX, USA
e-mail: brake@rice.edu

interface, considerable separation combined with stick & slip has been numerically as well as experimentally observed. This leads to significant nonlinear effects in the response of the system and thus serves as a convenient benchmark for the current work.

While the principles developed [1, 2] are applicable in a general system identification context, the current study focuses on interfaces modeled with simplified kinematics but detailed constitutive models. This simplification, coupled with the modal quasi-static simulation approach QSMA [5], makes it possible to conduct modal feature extraction in a highly efficient manner.

In [2] the authors investigated the surrogacy confidence between physically perturbed configurations of the BRB and the developed metric is shown to be robust across different contact constitutive models. The main implication is that the confidence metric can be thought of to be independent of the contact constitutive model and can be used just to study the similarity of structural behavior. In the present work, the relationship between contact parameters tuned for three different structural modes of the BRB are studied in the same context. The computational efficacy enabled partly by the kinematic simplification and by the simulation strategy is exploited in order to conduct a large number of random simulations for empirical extraction of the surrogacy confidence.

18.2 Methodology

A finite-element model is developed for the BRB and five patches are defined on the interface which are independently constrained to five virtual nodes. The nonlinear element is then applied across pairs of these nodes on an extracted substructure. For QSMA, the system is subjected to a forcing in the shape of the mode shapes. Since the contact models do not model separation, the frictional elements obey Masing's rules, i.e., their hysteresis loops preserve certain symmetries enabling one to predict the complete hysteresis using just the backbone. The solution at each load step is transformed back to modal coordinates (following the assumption that the mode shape is not modified too much by the presence of the nonlinearity) and the natural frequency & effective damping factor are extracted using the modal secant stiffness and the hysteretic dissipation (area) respectively. Specifically, the current investigation uses Segalman's four-parameter Iwan model [9] in the tangential direction and linear springs in the normal direction. With 5 parameters for each patch, the estimation problem has a total of 15 parameters to be estimated (3 unique patches out of 5 by symmetry). Since the model itself is a tuned model, no further assumptions are made.

Experimentally, the transient responses of the system subjected to hammer impacts are passed through a modal filter and processed using the Hilbert Transform to obtain the ring down envelope and the time varying phase. Since the envelope corresponds to a much longer time-scale than the change in the system's phase, it is assumed that the system is quasi-linear, i.e., instantaneously being governed by a linear system defined by the current response amplitude (envelope). This leads to a time dependent estimate of the instantaneous natural frequencies and damping factors as the system rings down. Thus, the experimentally derived dependence of the linear modal characteristics to the modal displacement may be compared with numerical predictions from QSMA. For the following analysis the root-mean-squared error between the prediction and the experiment are used to evaluate the error in the prediction by a contact model.

Since the main objective of refining contact parameters is to reduce the above error in terms of both the frequency and damping factor, the estimation procedure is cast as a bi-objective optimization problem. Defining an "acceptability region" in the error-space for each structure, it becomes possible to define a surrogacy metric based on the percentage overlap between the pre-images of the acceptability regions in the error space mapped back to the parameter-space. In [2] this region was defined based on maximal error bounds on the predicted quantities. In the current study however, the region is defined using the ranks of non-dominated sets in the error-space.

A non-dominated set, sometimes referred to as a Pareto set, is defined as a set of designs in which no design performs better than any other design in terms of both the objectives [4]. Furthermore, the Pareto rank of a non-dominated set is defined as the number of non-dominated sets that perform at least as good as the best designs in this set in terms of both the objectives. For a bi-objective minimization problem, the highest ranked (rank 1) Pareto set, will be at the bottom left in a normed error plot. The shape of the Pareto set can be used to further classify the problem into convex and non-convex. From Fig. 18.1a it can be observed that while the rank 1 set is clearly non-convex, higher ranked sets become progressively convex. Intuitively, convexity in the Pareto front indicates that it is possible, by appropriate choice of parameters, to make either of the objectives arbitrarily small at the expense of the other.

Figure 18.1 depicts the error-space plots for the different modes considered. Different ranks of Pareto designs are highlighted in each subfigure. For the Pareto sets, it was first constrained that the maximal RMS error in frequency can not exceed 1% of deviation. The error-space performance of the population was sorted using a free and open-sourced

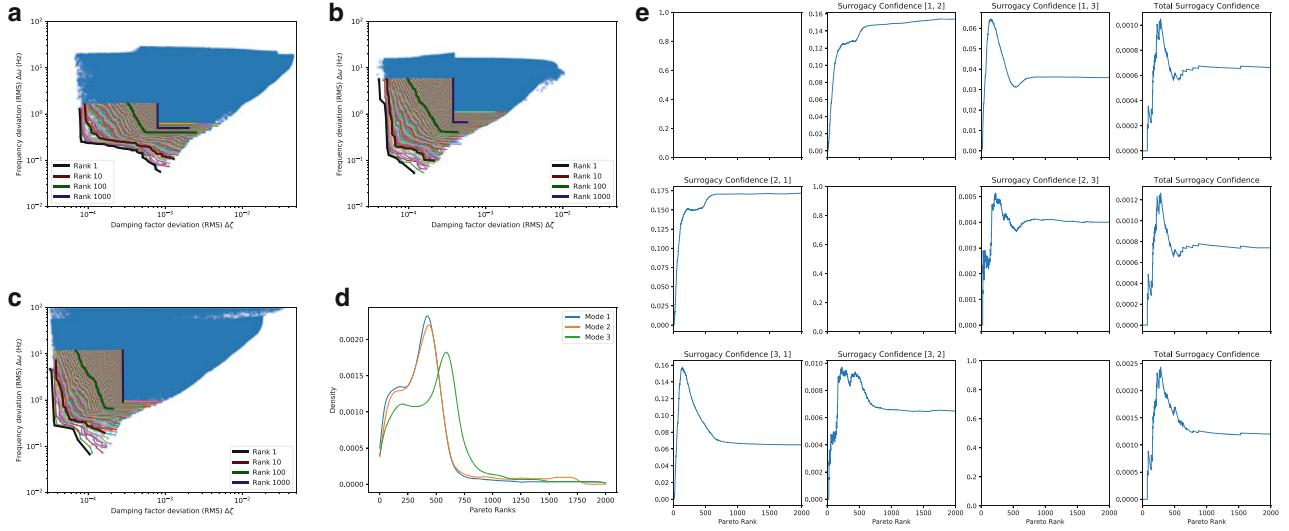


Fig. 18.1 Error-space plots for (a) Mode 1; (b) Mode 2; (c) Mode 3; (d) Pareto population distribution; (e) Evolution of the surrogacy confidence metric with the Pareto ranks

implementation of non-dominated sorting.¹ The distribution of the number of designs lying on each Pareto rank for the three modes are depicted in Fig. 18.1d. It can be seen here that most of the designs are concentrated around the higher Pareto ranks (until around 750). The low density near rank 1 can be corroborated to the “data sparsity” effects expected for high dimensional random populations [8]. It may be observed that the Pareto sets are no longer non-convex in the tail region.

The empirical surrogacy confidence metric for a given Pareto rank p considering mode i as surrogate to mode j is calculated as the ratio between the number of designs ranked higher than p for both the modes and the number of total designs of mode i ranked higher than p . This is a Bayesian statistic evaluating the predictive capability of parameter identification on mode i for mode j . In order to test the robustness of the estimate, the functional dependence of the metric to the rank p is studied. Mathematically the surrogacy confidence can be expressed as

$$SC[i, j](p) = P(\mathcal{A}_p^j | \mathcal{A}_p^i) = E[P(X \in \mathcal{M}_p^j | X \in \mathcal{M}_p^i)], \quad (18.1)$$

where the event \mathcal{A}_p^i is defined as the event of the Pareto rank of a design for predicting the i th mode being at least p , and \mathcal{M}_p^i is the “acceptability region” defined by the Pareto rank p . The last part of Eq. (18.1) offers an alternative definition as the expectation of a given design X to be acceptable for mode j given that it is acceptable for mode i . After applying Bayes’ theorem, the following empirical estimator is used for the calculations:

$$E[P(X \in \mathcal{M}_p^j | X \in \mathcal{M}_p^i)] = E \left[\frac{P(X \in \mathcal{M}_p^i \cap \mathcal{M}_p^j)}{P(X \in \mathcal{M}_p^i)} \right] \approx \frac{\sum_n I_p^i(x_n) I_p^j(x_n)}{\sum_n I_p^i(x_n)} \quad (18.2)$$

$$\text{with, } I_p^i(x_n) = \begin{cases} 1 & x_n \in \mathcal{M}_p^i \\ 0 & \text{otherwise} \end{cases}$$

The sums over the function $I_p^i(x_n)$ represents counts of the number of designs from a simulation that lie in the region \mathcal{M}_p^i .

¹<https://github.com/matthewjwoodruff/pareto.py>.

18.3 Results and Conclusions

Figure 18.1e depicts the surrogacy confidence metric evaluated empirically by an LHS-sampled simulation with 5,000,000 designs in total. Surrogacy Confidence $[i, j]$ denotes the confidence one can place on parameter estimates conducted by tuning mode i for predicting mode j . More rigorously, the confidence metric may be understood as the conditional probability of a random design lying in the acceptable region for mode j given that the design lies in the acceptable region for mode i . Along with these, the total surrogacy, i.e., the confidence of estimations on one mode alone being accurate for all modes, is also plotted in the last column. It can be seen that a little after rank 750, the confidence metric converges to a constant value in all cases. This demonstrates that the metric is indeed asymptotically independent of the definition of the error-space acceptability region used for the estimation.

It is known that the first and third mode shapes are similar in nature on the interface. However, the surrogacy pairs $[1, 3]$ & $[3, 1]$ seem to converge to a much lower value than the pair $[1, 2]$ & $[2, 1]$. This, being counter-intuitive to the physical argument, may be due to the kinematic inaccuracies inherent to the whole-joint modeling approach. This is further indicated by the fact that the total surrogacy for all the modes is very low. However, the fact that it is indeed possible to obtain an acceptable design for each mode shows that the whole-joint model can be tuned for a given (modal) response. Therefore, once tuned, the whole-joint model can be sufficient for modeling a given joint in different structures but the same does not apply for making accurate predictions about the higher modes of the structure.

Although the empirical estimator used here is technically unbiased, population of the parameter-space need not be. Though there must be a continuous region in the parameter-space with designs which map onto a particular rank in the error space, due to finite sampling, one will end up with just a portion of this region, which need not be unbiased (evolutionary algorithms, for example, are known to show clustering). Thus any estimator averaging over the finite population is bound to have bias. Nevertheless, it is used as a first-pass estimator. In order to investigate the dimensionality of the acceptable design parameters, its principal component variances were calculated. This revealed that the component variance contributions seem to be distributed rather uniformly and thus no dimension reduction can be carried out using classical PCA methods. The authors are currently investigating the suitability of generalized statistical distances [3] and estimators based on kernel density estimates of the acceptable regions as alternatives to the estimator in Eq. (18.2).

Acknowledgements The authors thank the participants of the Nonlinear Mechanics and Dynamics (NOMAD) Research Institute of 2016 for the experimental data and Robert M. Lacayo for helpful discussions.

Funding: This material is based upon work supported by the National Science Foundation under Grant Number 1744327.

References

- Balaji, N.N., Brake, M.R.W.: The surrogate system hypothesis for joint mechanics: statement and evaluation through empirical parameter estimation. In: Proceedings of ISMA-USD 2018 (2018)
- Balaji, N.N., Brake, M.R.W.: The surrogate system hypothesis for joint mechanics. *Mech. Syst. Sig. Process.* **126**, 42–64 (2019). ISSN 0888-3270, <https://doi.org/10.1016/j.ymsp.2019.02.013>
- Cha, S.-H.: Comprehensive survey on distance/similarity measures between probability density functions. *Int. J. Math. Model. Methods Appl. Sci.* **4**, 300–307 (2007)
- Deb, K.: *Multi-Objective Optimization Using Evolutionary Algorithms*, vol. 16. Wiley, Hoboken (2001)
- Lacayo, R.M., Allen, M.S.: Updating structural models containing nonlinear Iwan joints using quasi-static modal analysis. *Mech. Syst. Sig. Process.* **118**, 133–157 (2019). <https://doi.org/10.1016/j.ymsp.2018.08.034>
- Mayer, M., Gaul, L.: Modeling of contact interfaces using segment-to-segment-elements for FE vibration analysis. In: 23rd International Modal Analysis Conference (IMAC XXIII), Bethel, CT (2005)
- Mayer, M.H., Gaul, L.: Segment-to-segment contact elements for modelling joint interfaces in finite element analysis. *Mech. Syst. Sig. Process.* **21**(2), 724–734 (2007). <https://doi.org/10.1016/j.ymsp.2005.10.006>
- Scott, D.W.: *Multivariate Density Estimation: Theory, Practice, and Visualization*. Wiley, New York (2015)
- Segalman, D.J.: A four-parameter Iwan model for lap-type joints. *J. Appl. Mech.* **72**(5), 752–760 (2005)
- Segalman, D.J., Gregory, D.L., Starr, M.J., Resor, B.R., Jew, M.D., Lauffer, J.P., Ames, N.M.: *Handbook on Dynamics of Jointed Structures*. Technical report SAND2009-4164. Sandia National Laboratories, Albuquerque, NM (2009)
- Siewert, C., Panning, L., Wallaschek, J., Richter, C.: Multiharmonic forced response analysis of a turbine blading coupled by nonlinear contact forces. *J. Eng. Gas Turbines Power* **132**(8), 082501 (2010). <https://doi.org/10.1115/1.4000266>

Chapter 19

Vehicle Escape Dynamics on an Arbitrarily Curved Surface



Levi H. Manring and Brian P. Mann

Abstract This paper derives a planar model for a vehicle on an arbitrarily curved surface. The goal is to investigate different strategies that may be used to free a vehicle from a ditch. More specifically, extricating a modern vehicle typically requires someone to get behind the vehicle and assist in pushing it out of the ditch. Due to human limitations in power output, the individual learns to rhythmically time their push, or applied force, to build momentum and achieve escape.

Numerical simulations were used to explore different strategies, or forcing functions, on this system. For example, this paper considers forcing the system at its linear natural frequency and a forcing strategy more akin to human behavior. Comparisons are made to determine the safest and most efficient strategy to achieve an escape. This paper will show the effectiveness of human intuition in pushing a vehicle out of a ditch.

Keywords Vehicle dynamics · Nonlinear dynamical system · Unknown terrain · Arbitrary surface · Escape

19.1 Introduction

The experience of having a vehicle stuck in a ditch is one that likely resonates with many automobile owners. In such a scenario, the driver and any potential passengers may get out and try to dislodge the vehicle by pushing. This research seeks to examine the vehicle dynamics associated with this scenario and consider different control strategies for achieving escape from the ditch.

The motivation for this research is directly related to the development of autonomous vehicle technology. As the demand for autonomous vehicles continues to grow, there is a need for adaptive control for hazardous situations. It would be useful, in the lodged vehicle scenario, for the vehicle to have a predictive model of the system dynamics surrounding its predicament and be able to intuitively maneuver an escape without driver intervention. One problem to overcome in developing a robust control strategy for escape is the fact that ditches are all unique in shape. Thus, a dynamics model is needed for an arbitrary surface profile.

In addition to a dynamics model, there are issues to overcome in creating a robust control system for achieving escape. Like humans pushing a vehicle, applying high torque to the wheels has power limitations and the possibility of slipping. In many dynamic systems, one way to generate a large amplitude response is to force the system at its linear natural frequency. Since the end goal is to generate a large enough response to achieve escape, this open-loop control strategy seems feasible for this system. Additionally, forcing the system in a way that is comparable to human behavior is a useful control strategy to model. The reason for this is that humans can push vehicles out of ditches despite their power limitations.

This paper will consider the problem of a vehicle escaping a ditch with an arbitrary profile by (1) developing a model of the system dynamics, (2) detailing two methods for escape: linear natural frequency forcing and human-behavioral forcing, and (3) comparing the results from these two control strategies to gain further insight into the dynamics of this system.

19.2 Background

There is a vast amount of literature on the topic of vehicles and so it is unsurprising there are many models of vehicle dynamics. Many of these vehicle models seek to understand complex problems such as steering, tire deformation, suspension systems, and braking and involve many degrees of freedom (DOF). A comprehensive survey of different vehicle dynamics

L. H. Manring (✉) · B. P. Mann

Department of Mechanical Engineering and Materials Science, Pratt School of Engineering, Duke University, Durham, NC, USA

e-mail: levi.manring@duke.edu

applications is presented in [1]. This survey focuses primarily on automotive suspension systems, worst-case maneuvering, minimum-time maneuvering, and driver modeling, while citing 185 references. However, in the minimum-time maneuvering problem these applications are more focused on minimum track time for the purposes of racing, whereas this work is focused on getting a vehicle out of a ditch with minimum effort and time. Another article summarizes advancements in the study of vehicle dynamics across a range of vehicle, tire, and driver models [2], and identifies a need for further development of comprehensive nonlinear dynamic models for vehicles. In [3], several benchmarks for vehicle dynamics problems are considered for both rail and road vehicles, particularly focusing on studying wheel sticking/slipping and lateral dynamics.

As mentioned previously, the demand for vehicle automation and innovative optimal control solutions has been a strong motivation for further understanding of vehicle dynamics. A vehicle motion prediction module utilizing vehicle dynamics is presented in [4]. Multi-body simulation software (ADAMS-car) was used for vehicle dynamic analysis and for simulation of precalculated maneuvers on public roads. A vehicle is modeled as a 6 DOF system composed of two rigid bodies in [5] to develop a nonlinear robust control design for an interconnected set of H_∞ control problems. However, the authors only model vertical motion of the vehicle, ignoring translational motions. Some researchers have sought to develop vehicle control strategies that perform well in hazardous scenarios. In [6], a modified fixed-point control allocation scheme is implemented in a Simulink CarSim simulation to test braking during high-speed double lane changing on slippery roads and hard braking with an actuator failure. A gyroscope is used in [7] to enhance vehicle handling in strenuous control situations. The authors used a 10 DOF linear vehicle model as a basis for developing an LQR control framework. In [8], a coordinate control system involving electronic stability control, active roll control, and engine torque control is used to maximize driver comfort. However, the authors do not present their nonlinear dynamics model that is used to simulate the response of their controller. A linearized 2 DOF dynamics model is used in [9] to develop an adaptive optimization based second-order sliding mode controller. For modeling the controller, the authors assume the vehicle velocity while turning is pseudoconstant and the steering and side-slip angles are small. In [10], Chebyshev series expansions were used to approximate analytical solutions for nonlinear ODEs modeling tire dynamics and the steering mechanism.

While most vehicle dynamics models in the literature seek to include some combination of steering, suspension, and tire dynamics, few seek to address anything like the problem of a vehicle moving on an arbitrary curved surface. A model of a cart moving on a smooth surface is presented in [11, 12], but the author provides an insufficient mathematical derivation and no validation of the model through simulation or experiment. Cart dynamics are considered in [13] as well, where the authors derive the dynamics of a cart that is being excited by a moving base using Lagrange's method. They include results from an earthquake response simulation. A similar dynamics problem of a ball rolling on a 2-dimensional potential surface is shown in [14], with a resulting dynamic model that appears similar in form to the dynamics model presented in this paper, without the effect of additional rigid bodies.

In addition to modeling the dynamics of a vehicle moving on an arbitrary surface, this paper seeks to consider the effect of a human pushing this system. While the literature does not discuss this effect, there have been some studies on humans pushing carts, particularly as they relate to ergonomics and risk of injury [15–18]. There is also a study on the metabolic demands of pushing a vehicle as a form of exercise [19], which provides the rather obvious result that pushing a vehicle for exercise imposes high levels of metabolic and neuromuscular stress on a human.

19.3 Models

This paper presents a planar model of a vehicle moving on a surface $y(x)$. In developing a model for a vehicle moving on an arbitrary surface, the wheels were assumed to roll without slipping and to maintain contact with the surface. This planar model consists of three rigid bodies: two wheels and the main body of the vehicle.

Figure 19.1 provides a visual description of how this system was modeled. The coordinate x is the contact point between the wheel A and the surface $y(x)$. For this research, a Gaussian function of the form $y(x) = -\beta e^{-(\mu x)^2}$ was used for a surface profile. Torques τ_A and τ_B are control inputs that can be applied at wheels A and B of radius R respectively. The main body of the vehicle is represented by rigid body M, which forms an angle θ_M with the horizontal and has a center of mass located at (x_c, y_c) relative to the center of wheel A. Since the vehicle does not leave the surface, $\theta_M = f(x)$, where $f(x)$ is the solution to a transcendental equation dependent on the length l of rigid body M. This system was modeled using three equations for

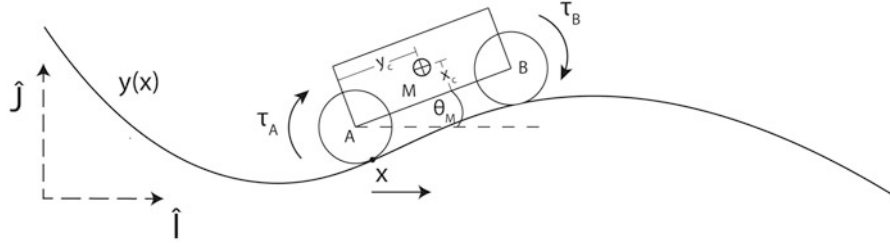


Fig. 19.1 A diagram of a vehicle composed of three rigid bodies moving on a surface $y(x)$

each rigid body: $\sum F_k(\hat{i}) = M_k \ddot{r}_k(\hat{i})$, $\sum F_k(\hat{j}) = M_k \ddot{r}_k(\hat{j})$, and $\sum T_k = I_k \ddot{\theta}_k$, where M_k is the mass, \ddot{r}_k is the acceleration of the center of mass, θ_k is the orientation, and I_k is the moment of inertia for each rigid body denoted by subscript k . The position vectors for each rigid body are shown in Eq. (19.1). In the following derivation, subscript x denotes derivatives with respect to the system coordinate and subscripts A and B the contact point between each wheel and surface $y(x)$.

$$\begin{aligned} \mathbf{r}_A &= \left(x - \frac{R y_{A,x}}{\sqrt{1 + y_{A,x}^2}} \right) \hat{i} + \left(y(x) + \frac{R}{\sqrt{1 + y_{A,x}^2}} \right) \hat{j} \\ \mathbf{r}_B &= \mathbf{r}_A + (l \cos \theta_M) \hat{i} + (l \sin \theta_M) \hat{j} \\ \mathbf{r}_M &= \mathbf{r}_A + (x_c \cos \theta_M - y_c \sin \theta_M) \hat{i} + (y_c \cos \theta_M + x_c \sin \theta_M) \hat{j} \end{aligned} \quad (19.1)$$

The corresponding acceleration vectors necessary to develop the equations for the rigid bodies are shown in Eq. (19.2)

$$\begin{aligned} \ddot{\mathbf{r}}_A &= (\ddot{x} P_A + \dot{x}^2 P_{A,x}) \hat{i} + (\ddot{y}_{A,x} P_A + \dot{x}^2 (y_{A,xx} P_A + y_{A,x} P_{A,x})) \hat{j} \\ \ddot{\mathbf{r}}_B &= \ddot{\mathbf{r}}_A - l \left[\ddot{x} \theta_{M,x} \sin \theta_M + \dot{x}^2 (\theta_{M,xx} \sin \theta_M - \theta_{M,x}^2 \cos \theta_M) \right] \hat{i} \\ &\quad + l \left[\ddot{x} \theta_{M,x} \cos \theta_M + \dot{x}^2 (\theta_{M,xx} \cos \theta_M - \theta_{M,x}^2 \sin \theta_M) \right] \hat{j} \\ \ddot{\mathbf{r}}_M &= \ddot{\mathbf{r}}_A - x_c \cos \theta_M \left[\ddot{x} \theta_{M,x} (\tan \theta_M + \sigma) + \dot{x}^2 ((\theta_{M,xx} - \sigma \theta_{M,x}^2) \tan \theta_M + \theta_x^2 + \sigma \theta_{M,xx}) \right] \hat{i} \\ &\quad + x_c \cos \theta_M \left[\ddot{x} \theta_{M,x} (1 - \sigma \tan \theta_M) - \dot{x}^2 ((\sigma \theta_{M,xx} + \theta_{M,x}^2) \tan \theta_M + \sigma \theta_{M,x}^2 - \theta_{M,xx}) \right] \hat{j} \end{aligned} \quad (19.2)$$

where

$$P_A = 1 - \frac{R y_{A,xx}}{(1 + y_{A,x}^2)^{3/2}}, \quad P_B = 1 - \frac{R y_{B,xx}}{(1 + y_{B,x}^2)^{3/2}}, \quad \sigma = \frac{y_c}{x_c}. \quad (19.3)$$

The rotational acceleration for each rigid body is defined in Eq. (19.4). The rotational accelerations for wheels A and B were developed by applying a roll without slip constraint.

$$\begin{aligned} \ddot{\theta}_M &= \ddot{x} \theta_{M,x} + \dot{x}^2 \theta_{M,xx} \\ \ddot{\theta}_A &= \frac{1}{R} \left(\ddot{x} \sqrt{1 + y_{A,x}^2} + \dot{x}^2 \frac{y_{A,x} y_{A,xx}}{\sqrt{1 + y_{A,x}^2}} \right) \\ \ddot{\theta}_B &= \frac{\sqrt{1 + y_{B,x}^2}}{R P_B^2} \left(\ddot{x} P_B (P_A - l \theta_{M,x} \sin \theta_M) + \dot{x}^2 \left((P_A - l \theta_{M,x} \sin \theta_M)^2 \frac{y_{B,x} y_{B,xx}}{1 + y_{B,x}^2} \right. \right. \\ &\quad \left. \left. + P_B (P_{A,x} - l \theta_{M,xx} \sin \theta_M - l \theta_{M,x}^2 \cos \theta_M) - P_{B,x} (P - l \theta_{M,x} \sin \theta_M) \right) \right) \end{aligned} \quad (19.4)$$

Using Eqs. (19.1–19.4), a 1 DOF model was developed, where g is the gravitational constant:

$$\begin{aligned}
& \frac{(I_M + M_M(x_c^2 + y_c^2))(y_{B,x} - y_{A,x})}{l \cos \theta_M} \ddot{\theta}_M \\
& - (y_{B,x} - y_{A,x})(M_M(\ddot{j}) + g) + M_A(\ddot{i}_A + g) \\
& + \tan \theta_M (y_{B,x} - y_{A,x})(M_M \ddot{i}_M + M_A \ddot{i}_A) \\
& + (1 + y_{A,x} \tan \theta_M) \left[\begin{aligned} & M_A \ddot{i}_A + M_B \ddot{i}_B + M_M \ddot{i}_M \\ & + y_{B,x} (M_A \ddot{j}_A + M_B \ddot{j}_B) + M_M \ddot{j}_M + (M_A + M_B + M_M)g \end{aligned} \right] \\
& + \left[(y_{A,x} - \tan \theta_M)(y_{B,x} - y_{A,x}) + (1 + y_{A,x} \tan \theta_M)(y_{A,x} y_{B,x} - 1) \right] \frac{I_A \ddot{\theta}_A + \tau_A}{R \sqrt{1 + y_{A,x}^2}} \\
& - (1 + y_{A,x} \tan \theta_M)(1 - y_{B,x}^2) \frac{I_B \ddot{\theta}_B + \tau_B}{R \sqrt{1 + y_{B,x}^2}} + (y_{B,x} - y_{A,x})(x_c - y_c \tan \theta_M) \frac{M_M g}{l} = 0
\end{aligned} \tag{19.5}$$

which can be simplified to

$$G(x)\ddot{x} + H(x)\dot{x}^2 + J(x)g + Q_A(x)\tau_A + Q_B(x)\tau_B = 0 \tag{19.6}$$

where $G(x)$, $H(x)$, $J(x)$, $Q_A(x)$, and $Q_B(x)$ are all nonlinear functions of x . The results shown in this paper only consider torques applied to wheel A, so $Q_B(x)$ is set to be zero.

19.4 Methods

This paper considers two forcing or open-loop control strategies for achieving escape: (1) forcing at the linear natural frequency for this system and (2) forcing in a human-behavioral pattern. For control strategy 1, the linear natural frequency was obtained using a variational method. By perturbing this system about the equilibrium position with $\tau_A, \tau_B = 0$, a variational equation in terms of the perturbation is obtained:

$$f(\xi) = \frac{J(\bar{x} + \xi) - J(\bar{x})}{G(\bar{x} + \xi)} g = 0 \tag{19.7}$$

where \bar{x} is the equilibrium position and ξ is the perturbation. By numerically solving for $f(\xi)$ and fitting a polynomial $f(\xi) \approx a_0 + a_1\xi + \dots + a_n\xi^n$ to the resulting curve, $\omega = \sqrt{a_1} = 1.85$ rad/s. This result was confirmed in simulation.

For control strategy 2, we introduce and apply a model for human-behavioral forcing. People usually attempt to get a vehicle out of a ditch by pushing hard until the vehicle achieves a maximum velocity (i.e., at the bottom of the ditch), releasing, then waiting for the vehicle to rock backwards toward them, and then repeating. Additionally, they start pushing at some initial force value and then increase force until they release the vehicle. Thus human-behavioral forcing is a function of vehicle position since it is applied over some length of the ditch, but it is also a function of vehicle velocity since it is only applied when velocity is positive. It should be noted that this contrasts with forcing this system at its linear natural frequency, which involves continuously applying force in two directions due to the nature of a sinusoidal function. A sketch of the human-behavioral forcing can be seen in Fig. 19.2.

Figure 19.2 illustrates the human-behavioral forcing pattern. As the vehicle moves in one direction, denoted by the large arrow, the human will push by starting at an initial force value and ramping up to a maximum force value as the vehicle crosses the bottom of the ditch. The shape of this forcing function looks like the first integral of a sawtooth, which is the function used in this paper to generate results for this control strategy.

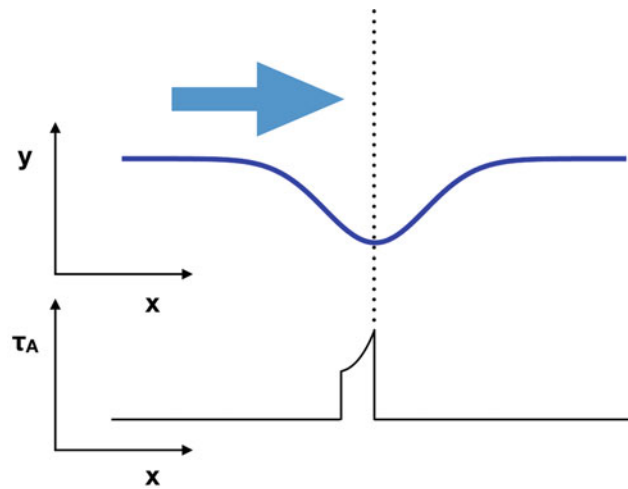


Fig. 19.2 A diagram of human-behavioral forcing

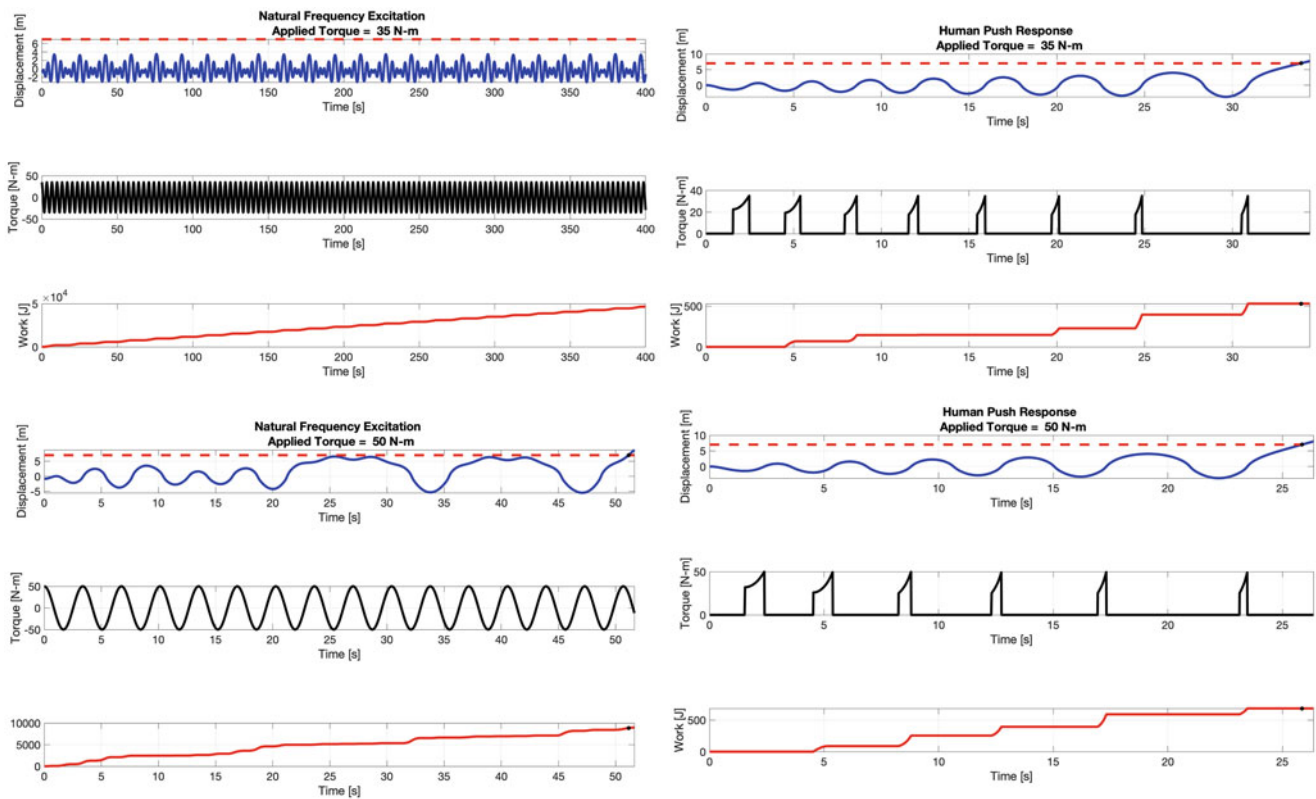


Fig. 19.3 A comparison of forcing at linear natural frequency and human-behavioral forcing showing displacement, torque, and work done on the system. *Top row:* with a maximum applied torque of 35 N-m. *Bottom row:* with a maximum applied torque of 50 N-m. The dashed line denotes the escape criteria

19.5 Results

The results from this research were obtained by applying the control strategies presented in the Methods section to the dynamics model presented in Eq. (19.6). Two benchmarks were used to compare the results from the two control strategies: achieving escape from the ditch and total work done on the system. The key results of this research can be seen in Fig. 19.3.

In the upper left corner of Fig. 19.3, the natural frequency excitation with a maximum torque of 35 N-m does not result in the vehicle escaping. Instead, the vehicle develops a steady-state periodic motion that never grows in amplitude. In contrast,

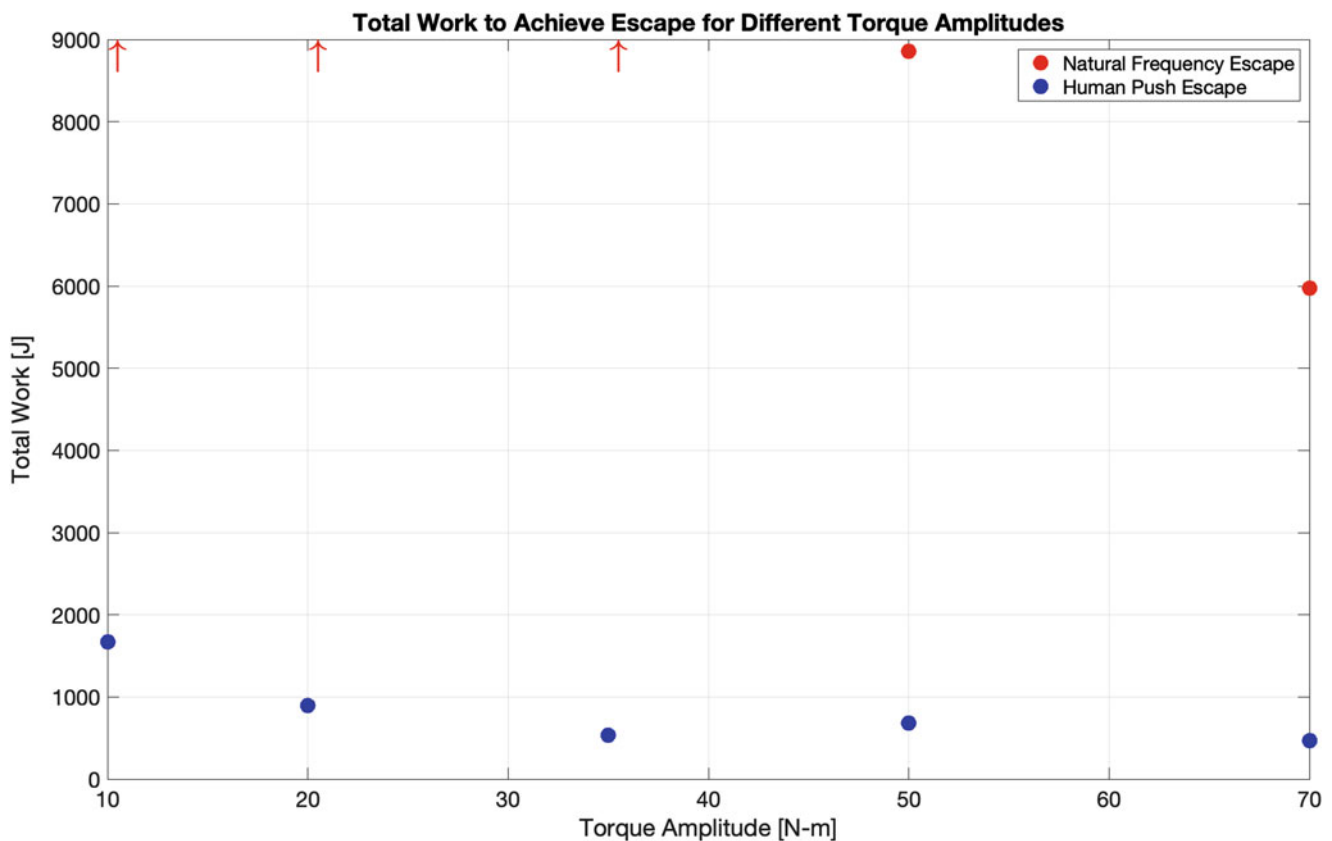


Fig. 19.4 A comparison of the total work done on the vehicle to achieve escape (dots indicate escape was achieved, arrows indicate was not achieved)

using human-behavioral forcing at the same maximum torque (see upper right corner of Fig. 19.3), achieves escape in ~ 34 s. Forcing the system at its linear natural frequency does result in escape for a maximum torque of 50 N-m (bottom left of Fig. 19.3) but the human-behavioral forcing achieves escape in half the time (bottom right of Fig. 19.3). The two maximum torque examples shown in Fig. 19.3 are indicative of the overall performance difference between these two control methods. Across the board, using human-behavioral forcing outperforms forcing the system at its linear natural frequency. Figure 19.4 shows that human-behavioral forcing uses less energy as well.

The results shown in Fig. 19.4 clearly indicate that in every instance, human-behavioral forcing consumes less energy than forcing at the linear natural frequency. In addition, for small torque amplitudes, linear natural frequency forcing does not result in escape at all (also shown in the upper left corner of Fig. 19.3), which means infinite work can be done on the system without any escape. One of the reasons for the disparity between these two control strategies is that humans intuitively know how to build momentum in this system, and with every well-timed push are increasing the energy of the system. Thus, the human-behavioral method will always result in escape, provided the forcing is sufficient to overcome damping.

The primary reason that the linear natural frequency method has less success than the human-behavioral method is that this system is highly non-linear. While this is known analytically from Eq. (19.6), the degree of nonlinearity is difficult to quantify without producing some simulated results. One method for understanding the nonlinearity of this system is to determine its stiffening/softening characteristics.

From Fig. 19.5, the static torque to keep the vehicle stationary is a complex function, illustrating that the dynamics for this system are softening, stiffening, and then softening again for different parts of the ditch profile. These are characteristics of a highly nonlinear system in contrast to the linear stiffness for this system denoted by the linear dashed line. It should be noted that the reason the equilibrium point is not directly over $x = 0$ is because the coordinate is not measured from the center of the vehicle, but from the contact point of wheel A with the surface.

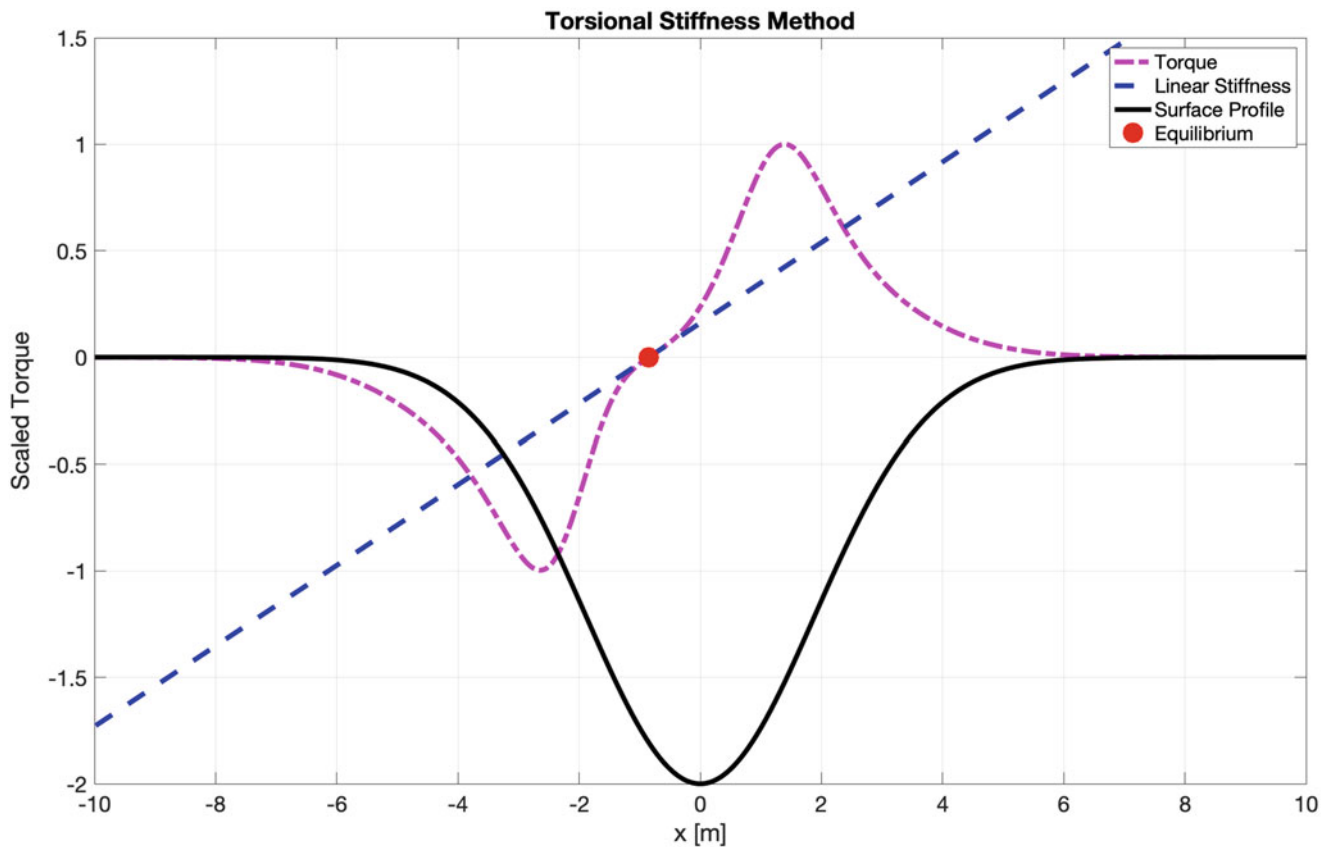


Fig. 19.5 Stiffening/softening illustrated by the static torque to maintain equilibrium

Another method for understanding the performance of the linear natural frequency method is to understand how the linear natural frequency changes across the ditch profile. To simulate this, the vehicle was released from a range of initial conditions along the ditch profile to determine the natural frequency.

From Fig. 19.6, the linear natural frequency obtained in the Methods section (~ 1.85 rad/s) is only valid for two perturbations (equilibrium and 2.3 m). As the system builds amplitude, the linear natural frequency approximation becomes invalid, and a different linear natural frequency more accurately represents this system. It is possible that creating a closed-loop control strategy which involves an amplitude-dependent forcing frequency may produce better results, since such a control strategy would always be forcing the system at its linear natural frequency.

19.6 Conclusion

This paper has presented an investigation of a vehicle stuck in a ditch. To understand the dynamics of this system, a dynamic model was developed using Newtonian mechanics. This model treated the vehicle as a system of three rigid bodies moving on a arbitrarily curved surface. Additionally, two control strategies to achieve escape were put forward: forcing the system at its linear natural frequency and human-behavioral forcing. Using the dynamics model, these control strategies were examined and the results conclusively showed that the human-behavioral method outperforms the linear frequency method both in terms of achieving escape and lower energy consumption. It was shown that the linear natural frequency varies across the surface of the ditch, meaning that a single approximation of the linear natural frequency is insufficient to achieve good control. Thus, for this highly nonlinear system, a nonlinear control strategy, such as human-behavioral forcing, is a good method for achieving escape.

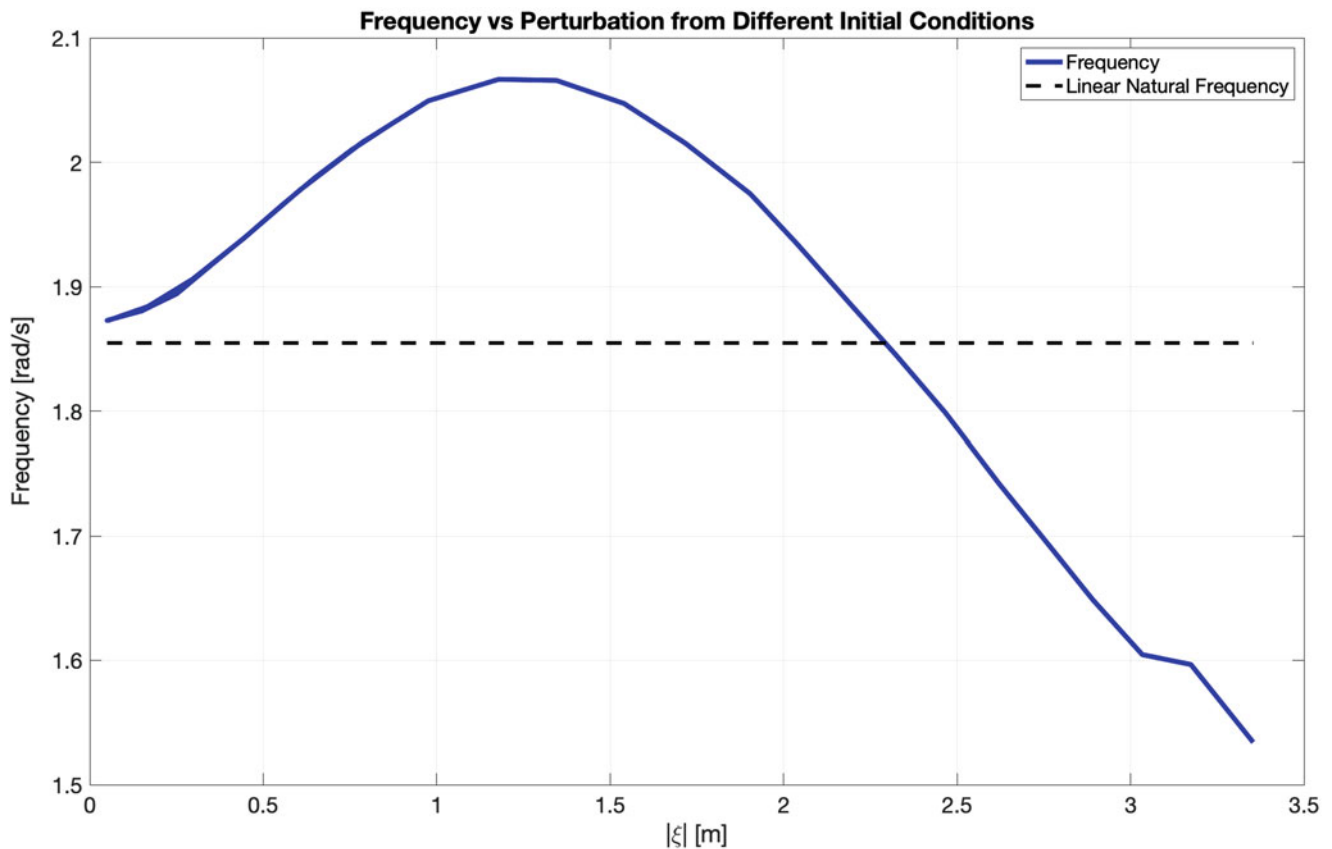


Fig. 19.6 Illustrating the linear natural frequency variation across the ditch profile by a plot of frequency vs. perturbation magnitude. The horizontal black line indicates the linear natural frequency value obtained from equilibrium (see Methods)

19.7 Future Work

In the future, we would like to expand the model and results to include the complexity that arises from introducing stick/slip friction into the system. This model could be further developed to include a 3D surface profile and rigid bodies. The control system for this could be expanded to include models for control of wheel B in conjunction with wheel A.

Acknowledgments The research is funded by Army Research Lab Grant W911NF-17-2-0047.

References

1. Sharp, R.S., Peng, H.: Vehicle dynamics applications of optimal control theory. *Veh. Syst. Dyn.* **49**(7), 1073–1111 (2011)
2. Yang, S., Lu, Y., Li, S.: An overview on vehicle dynamics. *Int. J. Dynam. Control.* **1**(4), 385–395 (2013)
3. Schiehlen, W.: Benchmark problems from vehicle dynamics. *J. Mech. Sci. Technol.* **29**(7), 2601–2606 (2015)
4. Leoro, J., Krutitskiy, S., Tarasov, A., Borovkov, A., Aleshin, M., Kylavin, O.: Vehicle dynamics prediction module. *Mater. Phys. Mech.* **34**(1), 82–89 (2017)
5. He, Z., Ji, X.: Nonlinear robust control of integrated vehicle dynamics. *Veh. Syst. Dyn.* **50**(2), 247–280 (2012)
6. Wang, J., Longoria, R.G.: Coordinated and reconfigurable vehicle dynamics control. *IEEE Trans. Control Syst. Technol.* **17**(3), 723–732 (2009)
7. Mashadi, B., Gowdini, M.: Vehicle dynamics control by using an active gyroscopic device. *J. Dyn. Syst. Meas. Control.* **137**(12), 121007 (2015)
8. Velardocchia, M.: Control systems integration for enhanced vehicle dynamics. *Open Mech. Eng. J.* **7**(1), 58–69 (2013)
9. Ferrara, A., Incremona, G.P., Regolin, E.: Optimization-based adaptive sliding mode control with application to vehicle dynamics control. *Int. J. Robust Nonlinear Control.* (2018). <https://doi.org/10.1002/rnc.4105>

10. Lopez, A., Moriano, C., Olazagoitia, J.L., Paez, F.J.: Fast computing on vehicle dynamics using Chebyshev series expansions. *IEEE/ASME Trans. Mechatronics*. **20**(5), 2563–2574 (2015)
11. Yavin, Y.: Modelling of the motion of a cart on a smooth rigid surface. *Math. Comput. Model.* **36**(4–5), 525–533 (2002)
12. Yavin, Y.: Modelling and control of the motion of a cart moving on a plane with a time-dependent inclination. *Math. Comput. Model.* **37**(3–4), 293–299 (2003)
13. Chatzis, M.N., Smyth, A.W.: Three-dimensional dynamics of a rigid body with wheels on a moving base. *J. Eng. Mech.* **139**(4), 496–511 (2013)
14. Virgin, L.N., Lyman, T.C., Davis, R.B.: Nonlinear dynamics of a ball rolling on a surface. *Am. J. Phys.* **78**(3), 250–257 (2010)
15. Nimbarte, A.D., Sun, Y., Jaridi, M., Hsiao, H.: Biomechanical loading of the shoulder complex and lumbosacral joints during dynamic cart pushing task. *Appl. Ergon.* **44**(5), 841–849 (2013)
16. Hoozemans, M.J.M., Slaghuis, W., Faber, G.S., van Dieën, J.H.: Cart pushing: the effects of magnitude and direction of the exerted push force, and of trunk inclination on low back loading. *Int. J. Ind. Ergon.* **37**(11–12), 832–844 (Nov 2007)
17. Glitsch, U., Ottersbach, H.J., Ellegast, R., Schaub, K., Franz, G., Jäger, M.: Physical workload of flight attendants when pushing and pulling trolleys aboard aircraft. *Int. J. Ind. Ergon.* **37**(11–12), 845–854 (2007)
18. Ciriello, V.M., Maikala, R.V., Dempsey, P.G., OBrien, N.V.: Cart pushing capabilities for males and females: an update. *Proc. Hum. Factors Ergonomics Soc. Annu. Meet.* **53**(14), 897–901 (2009)
19. Berning, J.M., Adams, K.J., Climstein, M., Stamford, B.A.: Metabolic demands of “junkyard” training: pushing and pulling a motor vehicle. *J. Strength Cond. Res.* **21**(3), 853 (2007)

Chapter 20

Nonlinear Dynamical Analysis for Coupled Fluid-Structure Systems



Q. Akkaoui, E. Capiez-Lernout, C. Soize, and R. Ohayon

Abstract The present research concerns the numerical dynamical analysis in elasto-acoustics, taking into account the geometrical nonlinearities induced by the large displacements/deformations of the structure and assuming the internal acoustic fluid occupying an internal cavity coupled to the structure to remain in a linear range of vibration. More particularly, the modeling includes sloshing and capillarity effects on the free surface. A numerical application is presented.

Keywords Fluid-structure interaction · Sloshing · Capillarity · Reduced-order model · Geometric nonlinearities

20.1 Introduction

The structural-acoustic system under consideration is made up of a tank structure filled with a linear inviscid compressible fluid. Gravity effects and surface-tension effects of the free surface and corresponding coupling terms are taken into account as described in [1]. A linear elastic constitutive equation is considered for the structure. It is also assumed that the structure undergoes sufficiently large deformations and large displacements in order to consider the geometrical nonlinear effects [2], but also sufficiently moderate so that the fluid behavior remains linear [3]. A total Lagrangian formulation around a static equilibrium state taken as a reference configuration is used.

20.2 Description of the Computational Model

Let $\mathbf{U}(t)$, $\mathbf{P}(t)$, and $\mathbf{H}(t)$ be the \mathbb{R}^{n_s} , \mathbb{R}^{n_f} , and \mathbb{R}^{n_h} -vectors corresponding to the finite element discretization of the structural displacement, fluid pressure, and free-surface elevation fields. The computational model is then written [3] as,

$$[M_S]\ddot{\mathbf{U}}(t) + [D_S]\dot{\mathbf{U}}(t) + [K_S]\mathbf{U}(t) + \mathbf{F}^{\text{NL}}(\mathbf{U}) + [C_{pu}]\mathbf{P}(t) + [C_{\eta u}]^T \mathbf{H}(t) = \mathbf{F}^S(t), \quad (20.1)$$

$$-[C_{pu}]^T \ddot{\mathbf{U}}(t) + [M]\ddot{\mathbf{P}}(t) + [D]\dot{\mathbf{P}}(t) + [K]\mathbf{P}(t) - [C_{p\eta}]^T \ddot{\mathbf{H}}(t) = \mathbf{0}, \quad (20.2)$$

$$[C_{\eta u}]\mathbf{U}(t) + [C_{p\eta}]\mathbf{P}(t) + [K_{gc}]\mathbf{H}(t) = \mathbf{0}, \quad (20.3)$$

in which $[M_S]$, $[D_S]$, $[K_S]$ and $[M]$, $[D]$, $[K]$ are the mass, dissipation and stiffness matrices for the structure and the corresponding one for the acoustic fluid, where $[C_{pu}]$, $[C_{\eta u}]$, and $[C_{p\eta}]$ are coupling matrices, and where $[K_{gc}]$ is the stiffness matrix of the free surface induced by the gravitational and the capillarity effects [1, 3, 4]. The \mathbb{R}^{n_s} -vector $\mathbf{F}^{\text{NL}}(\mathbf{U})$ is the nonlinear term issued from the large displacements/deformations induced by the geometrical nonlinearities. An adapted numerical nonlinear reduced-order model of order N requiring the numerical computation of the elastic modes of the structure with fluid added mass effect, of the acoustic modes of the fluid, and of the sloshing modes of the free surface [1] is proposed in [3]. Such computation on mid-power computers can be very challenging when large finite element meshes are involved. The original computational strategy [5] that allows for circumventing these difficulties is used in this analysis.

Q. Akkaoui · E. Capiez-Lernout (✉) · C. Soize

Laboratoire Modélisation et Simulation Multi-Echelle, MSME UMR 8208 CNRS, Université Paris-Est, Marne-La-Vallée, Marne-la-Vallée Cedex 2, France

e-mail: evangeline.capiez-lermout@u-pem.fr

R. Ohayon

Structural Mechanics and Coupled System Laboratory, Conservatoire National des Arts et Métiers (CNAM), Paris, France

The nonlinear reduced-order model is then written as

$$\mathbb{X}(t) = \begin{bmatrix} \mathbf{U}(t) \\ \mathbf{P}(t) \\ \mathbf{H}(t) \end{bmatrix} = [\Phi] \mathbf{Q}, \quad [\Phi] = \begin{bmatrix} [\Phi^S] & \mathbf{0} & \mathbf{0} \\ \mathbf{0} & [\Phi^F] & [\Phi^{FH}] \\ \mathbf{0} & \mathbf{0} & [\Phi^H] \end{bmatrix} \quad (20.4)$$

in which \mathbf{Q} is the \mathbb{R}^N -vector of the generalized coordinates, solution of the nonlinear dynamical equation

$$[\mathcal{M}_{FSI}] \ddot{\mathbf{Q}} + [\mathcal{D}_{FSI}] \dot{\mathbf{Q}} + [\mathcal{K}_{FSI}] \mathbf{Q} + \mathcal{F}^{\text{NL}}(\mathbf{Q}) = \mathcal{F}, \quad (20.5)$$

in which $[\mathcal{M}_{FSI}]$, $[\mathcal{D}_{FSI}]$, and $[\mathcal{K}_{FSI}]$ are the reduced mass, damping, and stiffness matrices of the coupled fluid-structure system, where \mathcal{F} and $\mathcal{F}^{\text{NL}}(\mathbf{Q})$ are the \mathbb{R}^N -vectors of the reduced external force and of the reduced nonlinear force that is obtained numerically from the explicit construction of the quadratic and cubic reduced stiffness terms with the finite element method [2].

20.3 Numerical Application

The coupled fluid-structure system under consideration is made up of a cylindrical tank with external radius $R_e = 3.06 \times 10^{-2}$ m, thickness $e = 2.79 \times 10^{-4}$ m, and height $h = 7.97 \times 10^{-2}$ m, partially filled with an acoustic fluid with height $h_f = 3.05 \times 10^{-2}$ m. It is described in a global cartesian coordinate system $(O, \mathbf{e}_1, \mathbf{e}_2, \mathbf{e}_3)$, where O is the center of the cylinder basis, and where the cylinder axis is defined along \mathbf{e}_3 . The structure is composed of a linear isotropic homogeneous elastic material for which the Young modulus, the Poisson ration, and the mass density are $E = 2.05 \times 10^{11}$ N m $^{-2}$, $\nu = 0.29$, and $\rho_S = 7800$ kg m $^{-3}$. The fluid has mass density $\rho_F = 1000$ kg m $^{-3}$ and sound velocity $c_F = 1460$ m s $^{-1}$. A fixed boundary condition is applied at the bottom of the cylinder. Furthermore, capillarity effects are added in the numerical model with surface tension coefficient $\sigma_\Gamma = 0.0728$ and contact angle $\alpha = 83^\circ$. The main curvature radii R_1 and R_2 of the free surface and the numerical coefficients that characterize the triple line are computationally obtained in each node of the mesh according [4].

The finite element model of the coupled fluid structure system is constructed using $m_S = 111,746$ and $m_F = 133,719$ three dimensional solid finite elements with 10 nodes for the structure and for the acoustic fluid (tetrahedral finite elements), $m_H = 3392$ bi-dimensional finite elements with 6 nodes for the free-surface and $m_\gamma = 144$ one-dimensional finite elements with 3 nodes for the triple line. Thus, there are $n_S = 658,209$ dofs, $n_F = 194,354$ dofs and $n_H = 6929$ dofs corresponding to the displacement unknowns of the structure, to the pressure unknowns of the fluid, and to the normal displacement unknowns of the free surface. The damping matrices of the acoustic fluid and of the structure are defined as $[D] = \tau_F [K]$ and $[D_S] = \tau_S [K_S]$ in which $\tau_F = 10^{-5}$ and $\tau_S = 10^{-6}$. A small patch located on one side of the structure is subjected to a transverse load. Such load is of intensity $s_0 = 0.001$ N and uniformly excites the frequency band $\mathbb{B}_e = [2000, 4000]$ Hz. In such excitation frequency band, it should be noted that 11 structural modes and no acoustic modes neither sloshing modes are excited. The computations are carried out with a nonlinear reduced-order model whose optimal order, issued from a convergence analysis is set to $\{N_S, N_F, N_H\} = \{100, 40, 1000\}$. Let ν be the frequency in Hz. Figures 20.1 and 20.2 display the graph $\nu \mapsto |\widehat{u}(2\pi\nu)|$ of the structural displacement and the graph $\nu \mapsto \widehat{h}(2\pi\nu)$ of the normal displacement of the free surface located on the triple line for both linear and nonlinear cases. It can be seen that the presence of geometrical nonlinearities modifies the nonlinear behavior of the fluid-structure system and that non-expected resonances do appear outside \mathbb{B}_e .

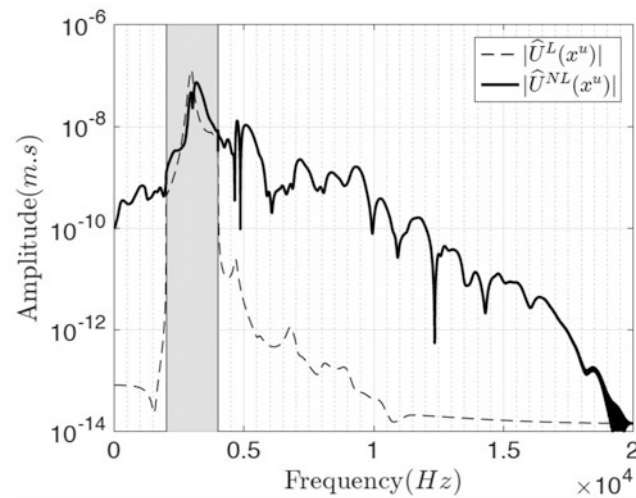


Fig. 20.1 Graph $\nu \mapsto |\hat{u}(2\pi\nu)|$ of the structural displacement for both linear (dashed line) and nonlinear (full line) cases

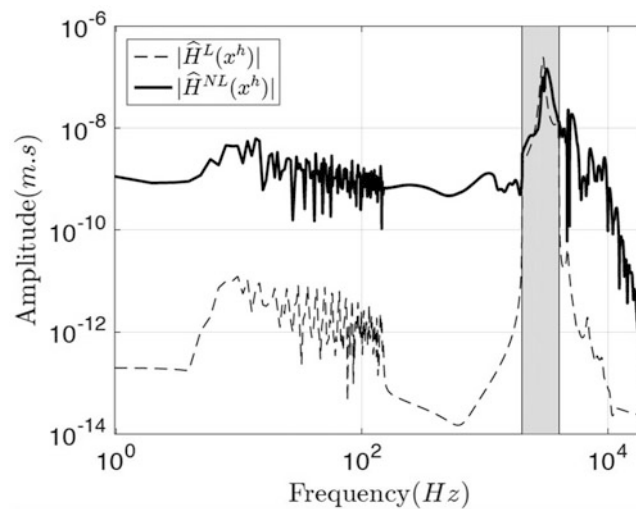


Fig. 20.2 Graph $\nu \mapsto \hat{h}(2\pi\nu)$ of the normal elevation for both linear (dashed line) and nonlinear (full line) cases

20.4 Conclusions

The nonlinear dynamical analysis of a coupled fluid-structure system taking into account both sloshing and capillarity effects has been investigated. Its efficiency is demonstrated through a numerical application.

Acknowledgements This work is fully supported by the DGA (French Defense Agency), which is gratefully acknowledged.

References

1. Ohayon, R., Soize, C.: Vibration of structures containing compressible liquids with surface tension and sloshing effects. Reduced-order model. *Comput. Mech.* **55**(6), 1071–1078 (2015)
2. Capiiez-Lernout, E., Soize, C., Mignolet, M.-P.: Computational stochastic statics of an uncertain curved structure with geometrical nonlinearity in three-dimensional elasticity. *Comput. Mech.* **49**(1), 87–97 (2012)
3. Ohayon, R., Soize, C.: Nonlinear model reduction for computational vibration analysis of structures with weak geometrical nonlinearity coupled with linear acoustic liquids in the presence of linear sloshing and capillarity. *Comput. Fluids* **141**, 82–89 (2016)
4. Morand, H.J.-P., Ohayon, R.: *Fluid Structure Interaction*. Wiley, New York (1995)
5. Akkaoui, Q., Capiiez-Lernout, E., Soize, C., Ohayon, R.: Solving generalized eigenvalue problems for large scale fluid-structure computational models with mid-power computers. *Comput. Struct.* **205**, 45–54 (2018)



Chapter 21

Experimental Nonlinear Vibration Analysis of a Shrouded Bladed Disk Model on a Rotating Test Rig

Ferhat Kaptan, Lars Panning-von Scheidt, and Jörg Wallaschek

Abstract The optimization of the mechanical design process of turbomachinery has already been subject of research for decades. In this context, many researchers developed efficient numerical methods to calculate the vibration response of bladed disks. In particular, shrouded bladed disks with frictional contacts present a major challenge in the design process. Beside efficient simulations, the validation process plays an important role in most recent studies. The quality of the comparison depends directly on the system's boundary conditions in the simulation as well as in the experiment. For instance, the estimation of the excitation forces should be as precise as possible, because the vibration response, in particular in the nonlinear case, depends strongly on the excitation forces.

In this paper, a newly developed rotating test rig for bladed disks is introduced. The test rig consists of a rotating shaft mounted in a vacuum chamber, in order to avoid any aerodynamic loadings and damping, and an excitation with multiple permanent magnets. Here, a large number of permanent magnets is applied to approximate a continuous force distribution along the circumference. To estimate the overall force distribution, magnetic field simulations are performed and compared to the measurements with a very good agreement. Compared to other excitation methods such as a single ac-magnet or air jet excitation, the presented method manages a high energy input at a specific engine order or frequency with modest complexity. The nonlinear vibration response is measured by strain gauges for various numbers of magnets and excitation force amplitudes. The presented results are characterized by an excellent repeatability and precise measurements of resonance passages. Especially, the nonlinear behavior of the structure such as rotational speed and excitation force dependent resonance amplitudes and frequencies as well as jumping phenomena can be shown. The developed rotating test rig proves to be particularly suitable for the vibration analysis of rotating bladed disks considering nonlinearities.

Keywords Nonlinear dynamics · Bladed disk · Shroud contact · Rotating test rig

21.1 Introduction

During operation of turbomachinery, the streaming unsteady airflow causes dynamic excitation of the rotating turbine blades. Actually, the airflow is a chaotic distributed dynamic pressure field. Due to a certain number of preconnected guide vanes or other parts in the flow channel, the pressure field contains periodic components leading to a stationary harmonic excitation of the rotating system. To avoid High Cycle Fatigue (HCF) failure, a good prediction of the vibration response at the operating range of the system is necessary. Friction damping, e.g. through underplatform dampers or tip shrouds, is commonly used to reduce the vibration amplitudes by energy dissipation. The design process of friction damped blades is still subject of research due to the strongly nonlinear characteristics. The calculation of the nonlinear forced response is generally based on the well-known Multiharmonic Balance Method (MHBM) [1, 2]. Beside calculations, the experimental validation of the numerical results plays an important role in current research projects. For an accurate comparison between simulations and experiments, a clear modeling of the system's boundary conditions is required. In particular, the excitation forces have a significant influence on the force response, thus, it is essential to estimate and to predict the excitation forces as precisely as possible. Several excitation techniques are used in the literature as non-contact excitation, e.g. magnets [3, 4] or air jets [5], or piezoelectric excitation [6–9]. All methods have their benefits as well as drawbacks and depend on the specific application. For the excitation of a rotationally periodic structure, a traveling wave type excitation is necessary [10]. This can be achieved by a rotating excitation mechanism and a non-rotating test setup, and vice versa. In most studies, a so-called blisk (bladed integrated disk) without any joints is investigated to estimate for example the structural damping [6, 11] or to characterize

F. Kaptan (✉) · L. Panning-von Scheidt · J. Wallaschek

Institute of Dynamics and Vibration Research, Faculty of Mechanical Engineering, Leibniz University Hannover, Hannover, Germany
e-mail: kaptan@ids.uni-hannover.de

mistuning induced mode localizations [7, 9]. Also frictionally coupled structures, for instance by underplatform dampers [3, 8], shroud contacts [12], friction rings [13] or root contacts [14], are analyzed in several studies. Due to the considerable complexity of the nonlinear vibration response of coupled rotating systems, there is still a great demand concerning this subject.

In this context, a new rotating test rig is designed and developed at the *Institute of Dynamics and Vibration Research* to measure the vibration response of bladed disks. Basically, excitation is achieved by ac-/permanent magnets, piezo patches or air jets. However, due to the high global stiffness of the investigated bladed disk model, a sufficient excitation force amplitude is needed. Thus, a large number of permanent magnets is used in this study. In particular, the blades are coupled with each other to the tip shroud and at multiple locations with the disk to the root. To analyze the nonlinear characteristics of the system, a variable excitation level is essential. Here, quasi-static ANSYS Maxwell simulations are performed and compared to an experimental setup to estimate the excitation force potential. The rotating experiments are carried out at different excitation levels in a wide rotational speed range. It should be noted that the main focus of this paper is the experimental study of a bladed disk model. However, numerical results of a linearized modal analysis will be shown in the next chapter. A detailed description of the numerical nonlinear vibration response is given in [15].

21.2 Bladed Disk Model

The investigated bladed disk model consists of 60 single blades and a comparatively rigid disk, see Fig. 21.1. The blades are statically prestressed at the tip shroud by an interference fit and coupled at multiple locations with the disk to the root. During operation, centrifugal forces cause a deformation of the system leading to a change of the contact forces. As a result, the dynamic behavior of the structure is highly nonlinear and depends on the rotational speed. To characterize the linear dynamic behavior, a numerical linear modal analysis, under the assumption of a perfectly tuned system, is applied. The symmetric properties of rotationally periodic structures can be exploited to compute the dynamic behavior of the full system by only one sector model [16]. In this study, ANSYS Mechanical is used to discretize a sector model of the system and to compute the nonlinearly prestressed cyclic modal parameters. The computational procedure is divided into two parts. First, a quasistatic nonlinear analysis is applied by considering an interference fit at the shroud contact and by preloading the structure with centrifugal forces. Subsequently, the system is linearized by considering the computed contact areas. In a second step, a modal analysis of the linearized system is applied. Here, the modal parameters, such as natural frequencies and eigenvectors, depend on the so-called nodal diameter, which corresponds to the phase relation between the cyclic edges. For instance, at

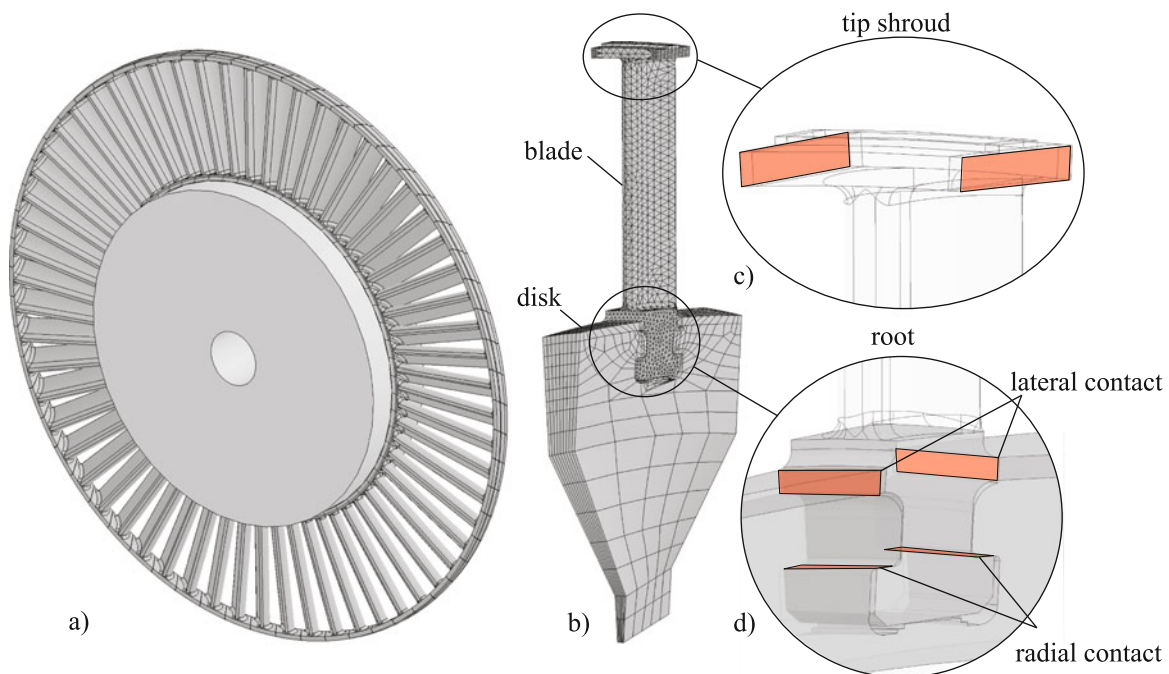


Fig. 21.1 Bladed disk model (a), finite element segment model (b), tip shroud contact area (c), root contact areas (d)

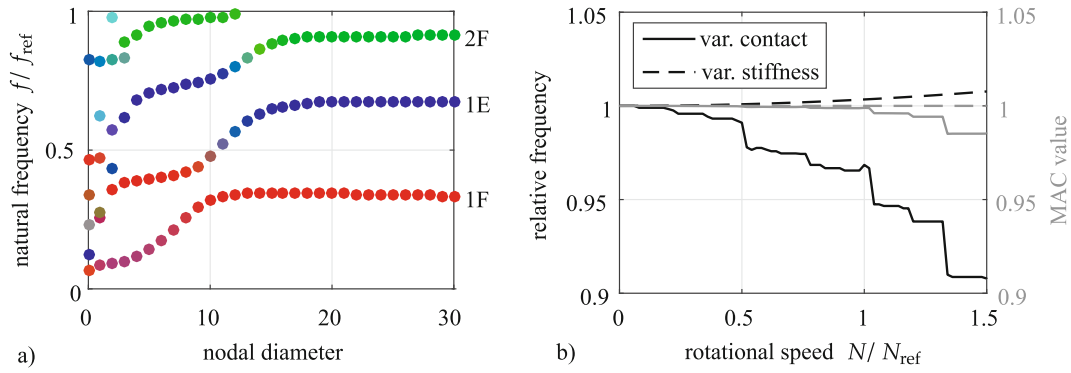


Fig. 21.2 Nodal diameter map of the linear system at zero rotational speed $N = 0$ (a), rotational speed dependent natural frequency and MAC value of 1F-ND15-mode (b)

nodal diameter zero, all blades oscillate in phase and at nodal diameter 30 (i.e. half of the amount of blades) in antiphase. The nodal diameter map is given in Fig. 21.2a at zero rotational speed. Note that the color of the dots corresponds to a mode family, i.e. red for the first flapwise (1F) mode, blue for the first edgewise (1E) mode and green for the second flapwise (2F) mode. The color scaling is based on the modal assurance criterion (MAC) value at nodal diameter 30 and illustrates nodal diameter dependent veering regions, for instance at nodal diameter 10. Veering is a well-known phenomenon regarding bladed disks, see [17]. It is caused by disk-dominated modes and, here, indicated by the color of the dots and the low correlation to the blade modes. The nodal diameter map in Fig. 21.2a is only valid for one specific rotational speed. Increasing the rotational speed leads to a change of the modal properties of the system. On the one hand, centrifugal forces increase due to the stress stiffening effect of the system's natural frequencies. On the other hand, the contact area depends on the rotational speed. To quantify the influence of both phenomena independently, the rotational speed dependent natural frequency and MAC value of the 1F-ND15-mode is shown in Fig. 21.2b. It can be seen that the natural frequency is highly sensitive to a variable contact area. The relative decrease of the natural frequency amounts to 9%, while the increase due to stress stiffening effects is approximately 1%. Regarding the MAC value, a decrease by 2% in case of a variable contact area can be noted, while a variable stiffness shows no change. Even a decrease of the MAC value by 2% is marginal, a change of the MAC value leads to a slightly different mode shape and thus to a different stress condition of the blades.

21.3 Rotating Test Rig

The experimental study is performed on the rotating test rig shown in Fig. 21.3. An electric motor is used to drive the bladed disk model up to 3600 rpm. To avoid any aerodynamic effects, such as damping or ventilation, the tests are performed in a vacuum chamber at low pressure level $p_{\text{vacuum}} < 1$ mbar. The vacuum chamber is connected to a foundation with a high mass of $m_f > 8$ tons and is dynamically isolated by air bearings. In addition, the vacuum chamber has several connection possibilities in radial direction and a glass window at the top of the chamber for optical measurement systems. However, in this study, strain gauges are used to measure the vibration response of the blades. The electric signals are amplified on a circuit board and transferred by a slip ring to the data acquisition. As an excitation unit, up to 45 permanent magnets are used to approximate a continuous magnetic field distribution along the circumference. A particular part of this study is the estimation of the resulting force amplitudes during operation, thus, the excitation mechanism is considered in detail in the following chapter.

21.4 Excitation Mechanism

The aim of the developed excitation unit is to excite a desired mode by a specific engine order. Due to the comparatively rigid disk and the blade coupling by shrouds, a high energy input is necessary to sufficiently excite the system. In addition, a large number of magnets is essential to excite the system at its resonance frequency in the considered rotational speed range. Regarding nonlinear systems, an accurate estimation of the excitation spectrum is particularly important. For this purpose, an ANSYS Maxwell model is set up to calculate the applying forces by magnetostatic analysis, see Fig. 21.4a. The magnetic

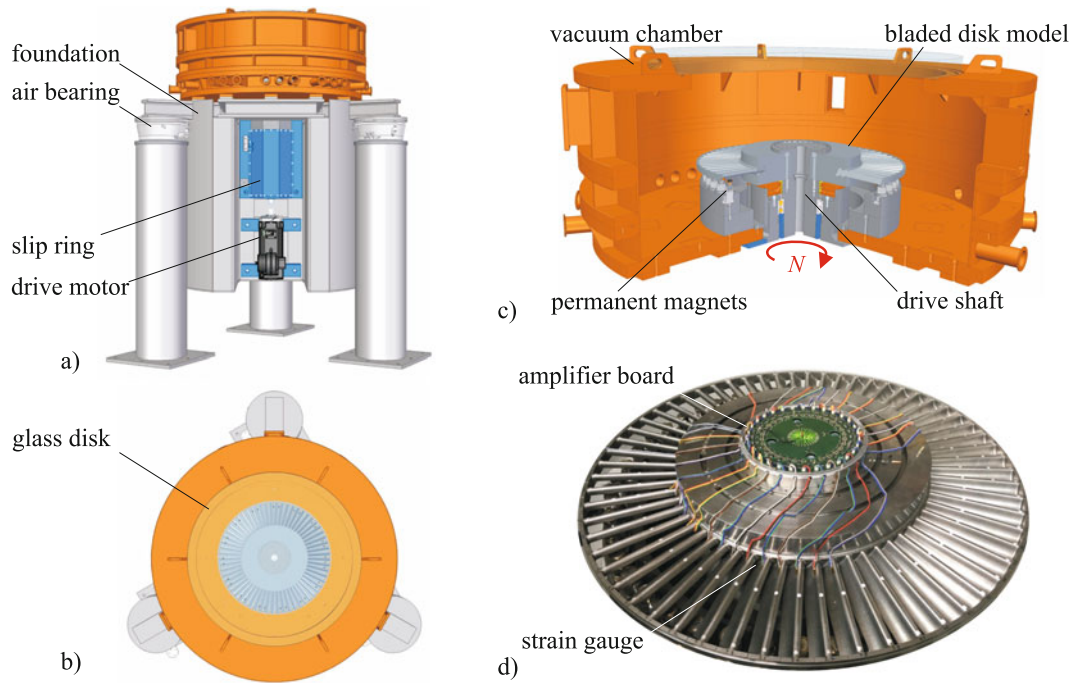


Fig. 21.3 Scheme of the rotating test rig: front view (a), top view (b), interior view (c), image of the bladed disk model (d)

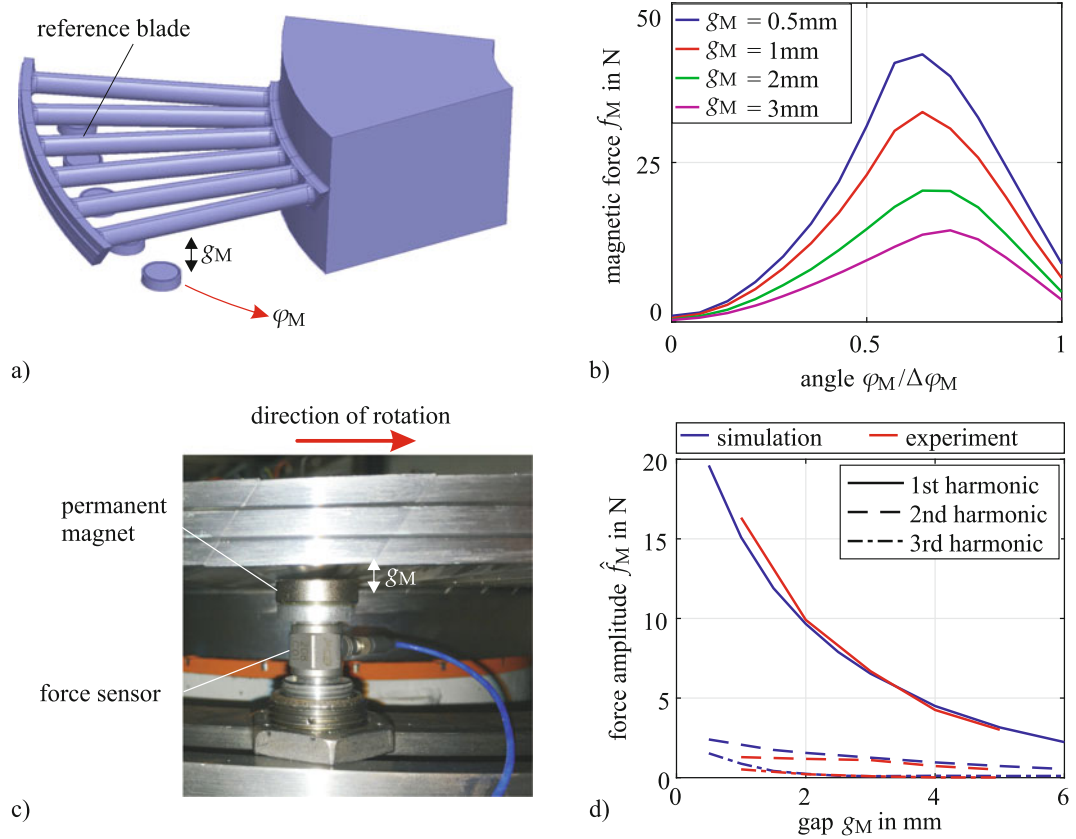


Fig. 21.4 ANSYS Maxwell simulation model (a), results of magnetostatic simulations (b), experimental setup for magnetic force measurements (c), comparison of simulation and experimental results (d)

forces are evaluated at the reference blade for various magnet gap values g_M and angles $\varphi_M/\Delta\varphi_M$, whereby $\Delta\varphi_M = 2\pi/N_M$ is defined by the number of magnets $N_M = 45$, see Fig. 21.4b. It can be noted that the static magnetic forces are highly sensitive to gap variation. The magnetic force increases up to 45 N at $g_M = 0.5$ mm and shows a sinusoidal progression over the rotation angle φ_M . However, for the rotational operation only the dynamic components of the excitation unit are crucial, which can be obtained by a decomposition of the spatial magnetic force distribution in its harmonic coefficients by FOURIER series. For the verification of the results, the magnetic forces are also measured by an experimental setup shown in Fig. 21.4c. A piezoelectric force sensor is used to measure the magnetic forces during rotation for various gap values g_M . The results of the comparison between simulation and experiment of the first three harmonic coefficients are given in Fig. 21.4d. The agreement of the comparison is remarkable. In particular, the first two harmonics are perfectly suitable for a gap variation in the rotational experiments due to a very marked gradient of the force amplitude. The third harmonic is rather unsuitable because of an approximately constant force level over the gap distance g_M . The slight deviation for $g_M < 2$ mm is caused by a mistuning of the gap between each blade and the magnet unit in the experiment. It should be noted that during the rotational experiments the magnetic forces will not be measured. To sum up, the developed permanent magnet unit is excellently suitable for the excitation of rotating bladed disks due to a high energy input in a desired engine order and an exceptional variability with respect to excitation amplitude and frequency.

21.5 Experimental Results

All measurements performed and presented in this paper are summarized in Table 21.1. The measurement series are defined by the number of magnets and by the gap value g_M . All measurements are carried out under technical vacuum conditions ($p_{\text{vacuum}} < 1$ bar) in the rotational speed range $0 \leq N \leq N_{\text{ref}}$. The vibration response is measured under steady-state conditions, meaning that the stationary vibration response of the strain gauges is recorded for each rotational speed step in the time domain. Based on this data, the mean value of the results are visualized in a Campbell diagram.

The functionality of the excitation mechanism as well as the data acquisition are investigated first. For this purpose, the Campbell diagrams of the measurement sets 1–3 are compared in Fig. 21.5. Without any magnet excitation, Fig. 21.5a, b, the structure is only excited by a dynamic imbalance of the system. Due to an adjustment of the bearings of the shaft, the imbalance of the system also has an effect in axial direction and, consequently, can excite blade modes. The vibration response shows a very low signal-to-noise ratio (SNR) but regarding the 2D Campbell diagram in Fig. 21.5b, it can clearly be seen that the response at a low order is dominant. It should be noted that the color scaling of each 2D Campbell diagram always refers to its maximum value. The rotational speed independent amplitude at $f/f_{\text{ref}} \approx 0.8$ is caused by the cut-off frequency of the amplifier board. Considering one permanent magnet, Fig. 21.5c, the SNR is still very low, proving that a large number of magnets is necessary for the excitation of a comparatively stiff system. It is interesting to note that in this case, dominant orders can be figured out regarding the spectrum in Fig. 21.5d. Due to the 1F mode at the frequency $f/f_{\text{ref}} \approx 0.35$, see Fig. 21.2, increased amplitudes at $N/N_{\text{ref}} > 0.5$ occur. It is also notable that the spectrum shows increased amplitudes at $f/f_{\text{ref}} \approx 0.1$ over a wide rotational speed range. This frequency corresponds clearly to the system's nodal diameter 0 mode, also known as the umbrella mode, and is mainly excited by the ball pass frequency of the bearings. Increasing the number of magnets to 45, it can be recognized that the SNR significantly increases and that the engine order 45 as well as its harmonics appear mainly in the Campbell diagram, see Fig. 21.5e, f. Again, the umbrella mode appears at $f/f_{\text{ref}} \approx 0.1$, which is in this case negligible compared to the amplitudes at engine order 45 and 90. The results of the first experimental study show that the rotating test rig and, in particular, the developed excitation mechanism work as intended. In addition, the reproducibility of the measurement results is of great importance and is investigated in the following within the scope of an order analysis

Table 21.1 Overview of the measurement series

Set	Number of magnets	Gap g_M in mm	Rotational speed range
1	0	–	$0 - N_{\text{ref}}$
2	1	5	$0 - N_{\text{ref}}$
3	45	5	$0 - N_{\text{ref}}$
4	45	4	$0 - N_{\text{ref}}$
5	45	3	$0 - N_{\text{ref}}$
6	33	5	$0 - N_{\text{ref}}$
7	33	4	$0 - N_{\text{ref}}$
8	33	3	$0 - N_{\text{ref}}$

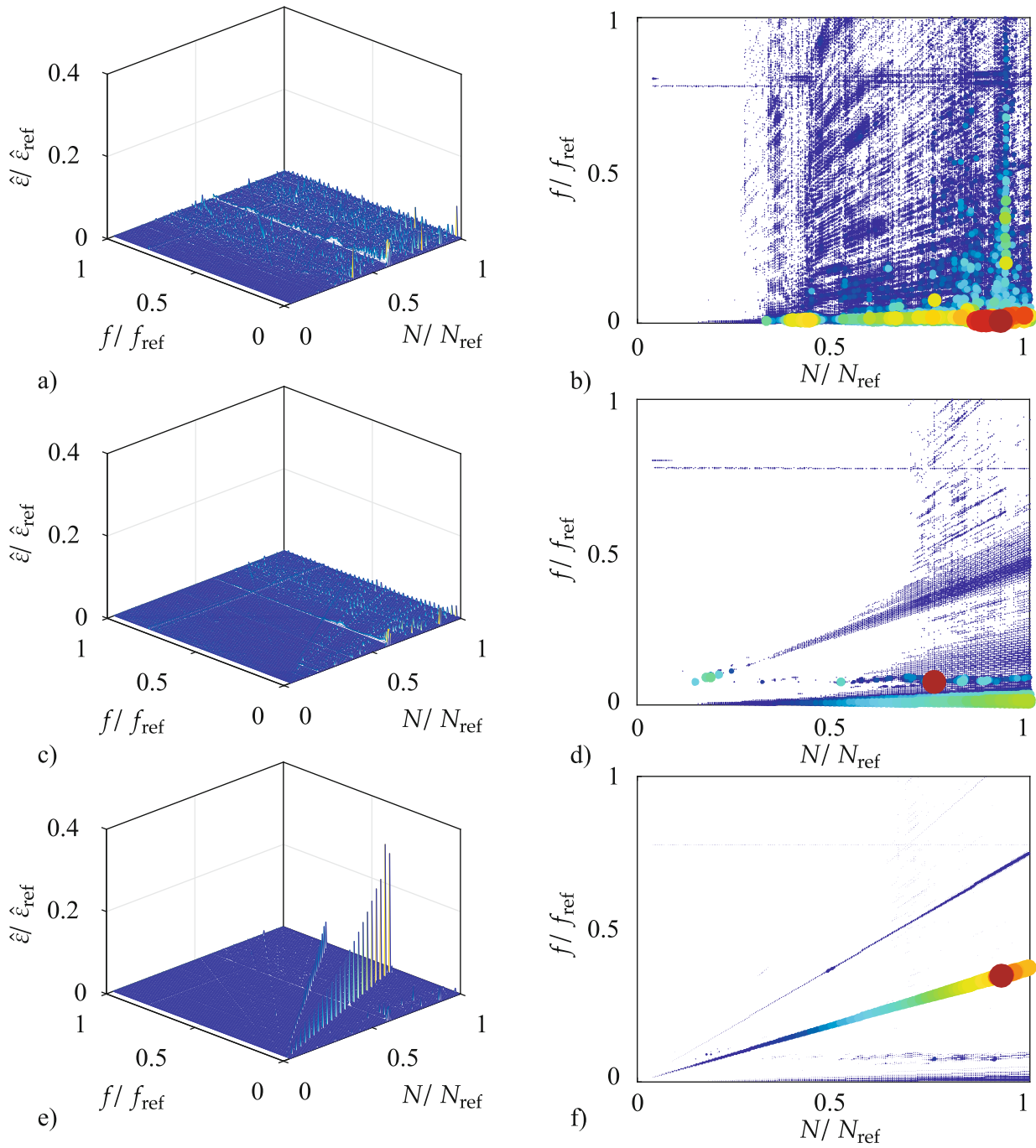


Fig. 21.5 Measured Campbell diagrams of the measurement sets 1–3: without magnet excitation (a, b), using one magnet (c, d), using 45 magnets (e, f)

of measurement set 3. For this purpose, the frequency responses along the first three orders, i.e. engine order (*EO*) 45 (red), 90 (blue) and 135 (green), are analyzed in detail, see Fig. 21.6a. The relation between the engine order *EO* and the nodal diameter *ND* is

$$EO = kN_s \pm ND, \quad (21.1)$$

where N_s denotes the number of segments and $k = 0(1)\infty$. Thus, the nodal diameter 15 is excited by the engine order 45 and 135, and the nodal diameter 30 by the engine order 90. The frequency response of 5 repeated measurements is presented

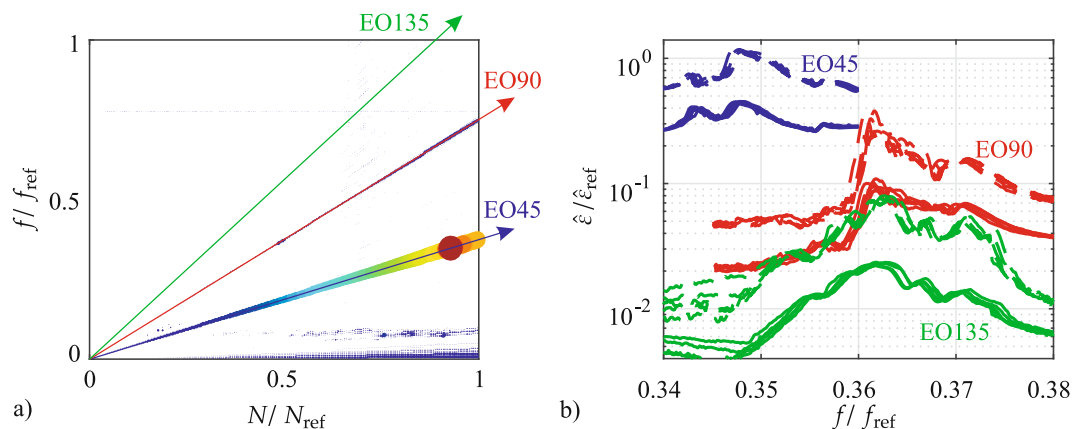


Fig. 21.6 Order analysis of measurement set 3 considering 5 repeated measurements: Campbell diagram with marked order numbers (a), mean (solid line) and maximum (dashed line) value of the vibration response at the orders 45, 90 and 135 (b)

in Fig. 21.6b, whereby the solid line represents the mean value and the dashed line the maximum value of all strain gauges. The obtained results are characterized by an excellent reproducibility as well as a high accuracy. The measured resonance frequencies at engine order excitation 45 and 90 clearly belong to the 1F-mode with nodal diameter 15 and 30, respectively. In particular, a resonance frequency shift of 5% between the engine order 45 and 135 is remarkable, even though it is theoretically the same mode shape, i.e. 1F-mode-ND15. This phenomenon is caused by the nonlinear structural mechanical behavior of the system and depends highly on the system's rotational speed. The rotational speed obtained by an engine order 45 excitation is three times larger as by an engine order 135 excitation. According to Fig. 21.2b, increasing the rotational speed leads—due to a change of the contact pressures at the joints—to lower natural frequencies.

In addition, the excitation level of the first harmonic, see Fig. 21.4d, is significantly larger than of the third harmonic leading to an additional frequency shift due to sliding processes at the joints. It is also noticeable that additional local maxima occur at engine order 135. This is caused by the gap mistuning of the excitation setup and the low energy input in this specific engine order. The nodal diameter 30 is excited by the engine order 90 (red lines) that corresponds to an antiphase mode shape of the blades. In this case, the resonance magnification shows an asymmetric, strongly nonlinear behavior. The unsteady curve progression implies local separation at the joints. Regarding the dynamic behavior of the whole system, it can be noted that the bladed disk model is highly mistuned. Due to manufacturing tolerances, material inhomogeneities and, in case of coupled bladed disks, installation conditions, the cyclic symmetry is highly disturbed leading to a mode and frequency splitting of the system, see [18]. As a result, the system's response consists of a superposition of standing and traveling waves despite a traveling wave excitation. With increasing the intensity of the mistuning, the amount of standing waves increases, while the travelling wave component decreases. Thus, localization effects can occur, such that some blades can show increased vibration amplitudes. This situation explains the differences between the maximum and the mean value in Fig. 21.6b.

To quantify the nonlinear structural mechanical effects, a gap variation and, thus, an excitation level variation is performed, see Fig. 21.7. It should be noted that for each gap value the mean value of 5 measurements is shown. For the sake of comparison, the results are normalized by a reference amplitude for each measurement set separately. Note that in the linear case, all frequency responses would lie on top of each other. Here, decreasing the gap between the magnets and blades leads to higher excitation forces and further to a decrease of the resonance frequencies. This is based on the frictional joints of the system. Increased excitation amplitudes lead to higher relative motion in the joints and, consequently, to more sliding and separation. In particular, the mode shapes of shrouded blades depend highly on the contact situation, as seen for instance in Fig. 21.2b. Regarding the 1F-ND15 mode, the maximum of the normalized response increases by increasing the excitation forces. This is obviously caused by a changing contact situation producing a slight change of the mode shape, see Fig. 21.7a. At off-resonance, the normalized response roughly shows a linear behavior. The 1F-ND30-mode shows a nonlinear jumping phenomenon, see Fig. 21.7b. An increase of the excitation level leads to lower frequencies and higher maximum amplitudes of the normalized vibration response. This is basically caused by the antiphase vibration between the blades with nodal diameter 30. Due to a high relative motion in normal direction of the shroud contact, local separation leads to a jumping phenomenon.

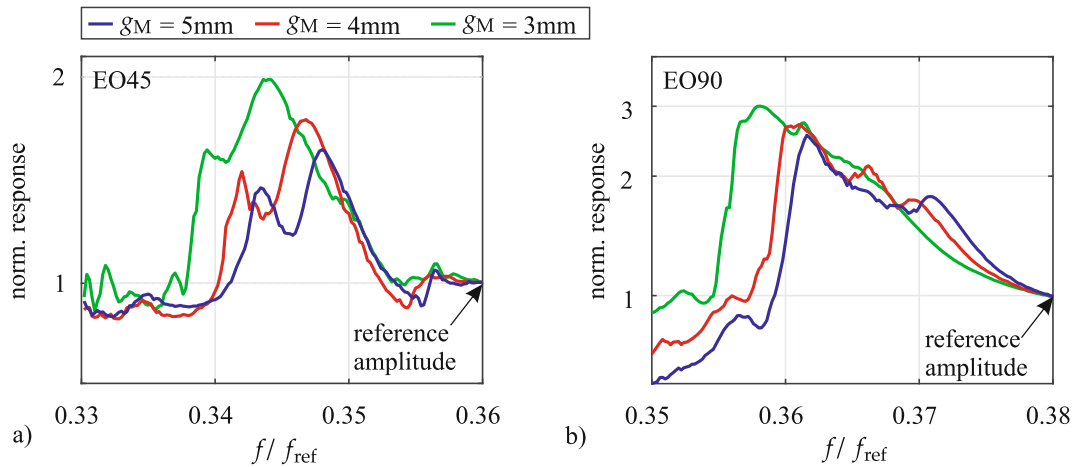


Fig. 21.7 Normalized vibration results by magnet gap variation: 1F-ND15-mode (a), 1F-ND30-mode (b)

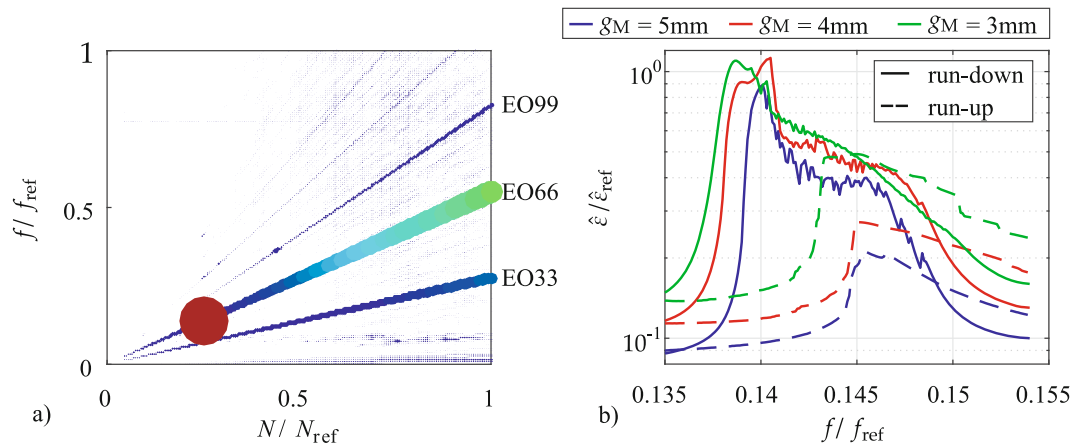


Fig. 21.8 Results of measurement sets 6–8: Campbell diagram (a), vibration results by an engine order 66 excitation (b)

In the last experimental study, the number of magnets is reduced to 33. According to Eq. (21.1), the nodal diameter 6 can be excited by the second harmonic of the excitation, i.e. EO66. In comparison to the nodal diameter 15, the nodal diameter 6 is isolated to other nodal diameters and is obviously a disk-dominated mode, see Fig. 21.2a. The Campbell diagram in Fig. 21.8a shows a resonance passage at the frequency $f/f_{\text{ref}} \approx 0.14$ with the engine order 66. In addition, a resonance passage appears at the frequency $f/f_{\text{ref}} \approx 0.37$ with the engine order 99, which corresponds to the nodal diameter 21. The amplitude level is comparatively low. Therefore, this mode is not considered further. Here, the order analysis is only applied to the engine order excitation 66, see Fig. 21.8b. Again, the mean value of 5 repeated measurements is considered. It is interesting to note that the vibration response shows significant differences between a run-up and a run-down measurement. A frequency difference of up to 4% can be noted. This phenomenon suggests that high contact separation occurs, which is, for instance, well-known for a prestressed mechanical gap oscillator. Due to high relative vibrations in normal direction of the contact, the contact separates leading to a spontaneous loss of stiffness and further to a reduction of the resonance frequency. The amplitude response is characterized by a hanging branch with multiple solutions at specific frequencies. The idealized model of a gap oscillator can be transferred only to a limited extent to the investigated bladed disk system. Due to the highly mistuned system, the contacts at the 60 blades do not separate simultaneously. Contact mistuning is still largely unexplored and should be investigated in future research to improve the understanding of shrouded bladed disks.

21.6 Conclusions

In this paper, a shrouded bladed disk model is investigated experimentally. A newly developed rotating test rig is used to measure the nonlinear vibration response for various excitation levels and engine orders. The developed excitation system, consisting of up to 45 permanent magnets, is analyzed in detail by means of a magnetostatic analysis and a validation of the excitation spectrum by an experimental test setup. The developed excitation system can be used to excite a specific engine order with a high energy input. It has been shown that the vibration response, i.e. resonance frequency as well as amplitude, strongly depends on the excitation and rotational speed level. In particular, the mode shapes of shrouded blades highly depend on the pressure distribution of the shroud contact. Increasing the excitation level leads to more local separation and, thus, to an increase of the vibration response at resonance condition. It could be noted that the system is highly mistuned, which, in this case, is mainly induced by the installation conditions leading to different contact pressures at the shrouds. Future work will be the numerical validation of the experimental results based on the computational methodology described in [15].

Acknowledgements The investigations were conducted as a part of the joint research program COOREFlex-turbo in the frame of AG Turbo. The work was supported by the Bundesministerium für Wirtschaft und Technologie (BMWi) as per resolution of the German Federal Parliament under grant number 03ET7020K. The authors gratefully acknowledge AG Turbo and MAN Energy Solutions SE for their support and permission to publish this paper. The responsibility for the content lies solely with its authors.

References

- Petrov, E.P., Ewins, D.J.: Analytical formulation of friction interface elements for analysis on nonlinear multi-harmonic vibrations of bladed discs. In: Proceedings of ASME Turbo Expo 2002. American Society of Mechanical Engineers, New York (2002)
- Siewert, C., Panning-von Scheidt, L., Wallaschek, J., Richter, C.: Multiharmonic forced response analysis of a turbine blading coupled by nonlinear contact forces. In: Proceedings of ASME Turbo Expo (2009)
- Sever, I.A., Petrov, E.P., Ewins, D.J.: Experimental and numerical investigation of rotating bladed disk forced response using underplatform friction dampers. *J. Eng. Gas Turbines Power* **130**(4), 042503 (2008)
- Firrone, C.M., T. Berruti.: An electromagnetic system for the non-contact excitation of bladed disks. *Exp. Mech.* **52**(5), 447–459 (2012)
- Chang, J.Y., Wickert J.A.: Measurement and analysis of modulated doublet mode response in mock bladed disks. *J. Sound Vib.* **250**(3), 379–400 (2002)
- Kielb, J.J., Abhari, R.S.: Experimental study of aerodynamic and structural damping in a full-scale rotating turbine. In: Proceedings of ASME Turbo Expo (2001)
- Judge, J., Pierre, C., Mehmed, O.: Experimental investigation of mode localization and forced response amplitude magnification for a mistuned bladed disk. In: Proceedings of ASME Turbo Expo (2000)
- Szwedowicz, J., Gibert, C., Sommer, T.P., Kellerer, R.: Numerical and experimental damping assessment of a thin-walled friction damper in the rotating setup with high pressure turbine blades. *J. Eng. Gas Turbines Power* **130**(1), 012502 (2006)
- Gibert, C., Kharyton, V., Thouverez, F., Jean, P.: On forced response of a rotating integrally bladed disk: predictions and experiments. In: Proceedings of ASME Turbo Expo (2010)
- Wildheim, S.J.: Excitation of rotationally periodic structures. *J. Appl. Mech.* **46**(4), 878–882 (1979)
- Kammerer, A., Abhari, R.S.: Experimental study on impeller blade vibration during resonance—part II: blade damping. *J. Eng. Gas Turbines Power* **131**(2), 022509 (2009)
- Szwedowicz, J., Sextro, W., Visser, R., Masserey, P.A.: On forced vibration of shrouded turbine blades. In: Proceedings of ASME Turbo Expo (2003)
- Laxalde, D., Gibert, C., Thouverez, F.: Experimental and numerical investigations of friction rings damping of blisks. In: Proceedings of ASME Turbo Expo (2008)
- Charleux, D., Gibert, C., Thouverez, F., Dupeux, J.: Numerical and experimental study of friction damping blade attachments of rotating bladed disks. *Int. J. Rotating Mach.* (2006). <http://dx.doi.org/10.1155/IJRM/2006/71302>
- Kaptan, F., Panning-von Scheidt, L., Wallaschek, J.: Numerical and experimental study of shrouded blade dynamics considering variable operating points. In: ASME Turbo Expo 2018: Turbomachinery Technical Conference and Exposition. American Society of Mechanical Engineers, New York (2018)
- Thomas, D.L.: Dynamics of rotationally periodic structures. *Int. J. Numer. Methods Eng.* **14**, 81–102 (1979)
- Kenyon, J.A., Griffin, J.H., Kim, N.E.: Sensitivity of tuned bladed disk response to frequency veering. In: ASME Turbo Expo 2004: Power for Land, Sea, and Air. American Society of Mechanical Engineers, New York (2004)
- Castanier, M.P., Pierre, C.: Modeling and analysis of mistuned bladed disk vibration: current status and emerging directions. *J. Propul. Power* **22**(2), 384–396 (2006)

Chapter 22

The Measurement of Tangential Contact Stiffness for Nonlinear Dynamic Analysis



C. W. Schwingshackl and D. Nowell

Abstract Nonlinear dynamic models for frictional interfaces require a number of input parameters to allow a realistic representation of the contact interface. Interface geometry and static pressure distributions can be obtained reliably from numerical analysis. However, it is also necessary to measure the friction coefficient, and the tangential and normal contact stiffness. The tangential contact stiffness plays a significant role in the dynamic response, but is very challenging to measure. In this paper quasi-static and dynamic experiments developed at the University of Oxford and at Imperial College London respectively, will be compared and discussed. Of particular interest is the dependence of the stiffness on the static normal load and the overall contact area.

Keywords Tangential contact stiffness · Measurement · Nonlinear dynamics

22.1 Introduction

Most mechanical engineering systems consist of an assembly of individual components with frictional interfaces which transfer load between the parts. In order to accurately predict the vibration performance of the system it is necessary to know the properties of each interface. Surface roughness will mean that each interface has a finite stiffness in both the normal and tangential directions. Imperial College and the University of Oxford have independently developed test rigs capable of measuring contact stiffness, but starting from quite different initial requirements. Hence the two rigs differ in contact geometry, frequency of loading, measurement systems, etc., but they should be capable of measuring the same underlying parameters. The purpose of this paper is to compare the two rigs, focussing particularly on the measurement of tangential contact stiffness, which is found to be the most difficult of the three parameters to measure.

22.2 Oxford Rig

The rig developed at the University of Oxford was originally intended to assess friction coefficients for different coating materials under conditions representative of those in the dovetail root of an aero-engine fan blade. Figure 22.1a shows a schematic of the contact configuration. An opposing pair of pads, each of 80 mm² nominal contact area are pressed against a flat specimen by a hydraulic cylinder. The threaded end of the specimen is attached to the piston of a servo-hydraulic test machine, and may be moved up and down relative to the pads to create relative tangential motion at the interfaces. Tangential load is measured by the load cell in the test machine, and it is assumed that an equal load is carried at each contact. An LVDT is used to give a measurement of relative tangential motion between the pads and the specimen, but since the measurement points are somewhat remote from the contact, this is insufficient to provide reliable measurement of contact stiffness. Hence, digital image correlation is employed local to the interface. A ‘Questar’ log-range microscope is used to focus on an area approximately 0.65 × 0.50 mm at the centre of one of the contacts using a digital camera. This allows production of a force-displacement hysteresis loop for two points very close to the interface. The rig is essentially designed to investigate quasi-static conditions, and a loading frequency of 1 Hz was employed in the experiment. The rig is more fully-described in [1] and the overall arrangement of the rig is shown in Fig. 22.1b.

C. W. Schwingshackl (✉) · D. Nowell
Imperial College London, London, UK
e-mail: C.schwingshackl@imperial.ac.uk

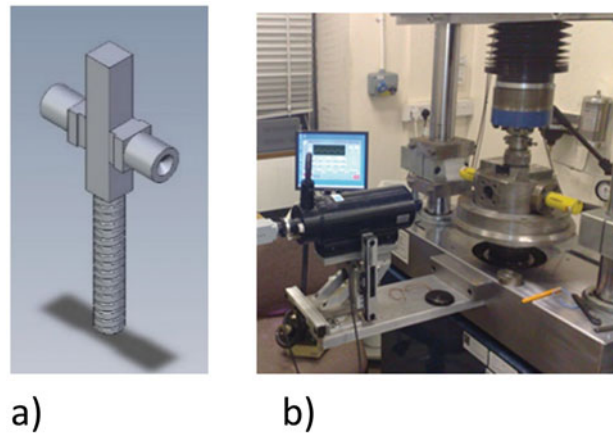


Fig. 22.1 (a) schematic contact configuration, (b) general view of the apparatus

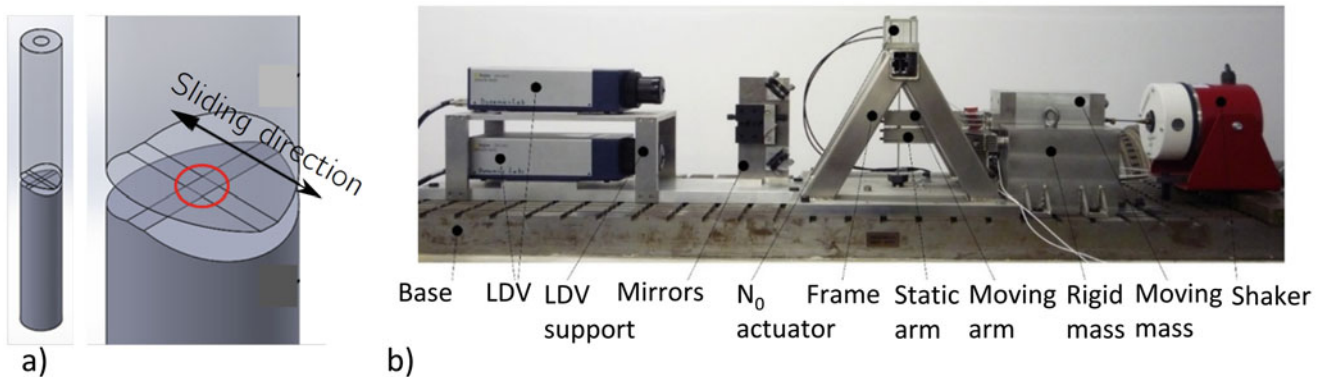


Fig. 22.2 Imperial College London 1D friction rig, (a) the specimen configuration and (b) the general setup

22.3 Imperial College Rig

The 1D friction test rig at Imperial College London [2] has been designed to measure friction interface parameters (friction coefficient, μ , and the tangential contact stiffness, k_t) under realistic operational conditions for under-platform dampers, providing a flat-on-flat contact interface with a nominal area of 1 mm^2 , a maximum mean contact pressure of 500 MPa, frequencies from 20 to 200 Hz, interface motion from 0 to 100 μm (covering stuck, micro-, and macro-slip regimes), and temperatures up to 1000 °C. The main concept of the test rig shown in Fig. 22.2b is based on a unidirectional motion of a moving mass and specimen, against a static specimen. The system is excited via an electrodynamic shaker and the variable normal contact load is applied with a pneumatic loading system. The specimens in Fig. 22.2a consist of two cylindrical rods, each with a flat top that leads to a square contact area once they are mounted 90° rotated to each other. A contactless measurement of the relative displacement between the two test specimens is achieved by two LDVs [3] and the transmitted friction forces are measured via three force transducers at the static side of the rig. A combination of the measured friction forces and the relative displacement between the two specimens leads to a hysteresis loop from which the tangential contact stiffness, k_t , is extracted from the slope of the ‘fully stuck’ section of the loop, immediately after load reversal, while the friction coefficient, μ , can be obtained from the macro-slip zone.

22.4 Comparison of Tangential Contact Stiffness

Results for the Imperial rig are presented in Fig. 22.3a, which shows the variation of tangential contact stiffness with mean contact pressure taken with the initial ‘as machined’ surfaces. Results for a single specimen with five newly refurbished contact areas ranging consecutively from 2.15 to 2.96 mm^2 are presented where the stiffness values were extracted under

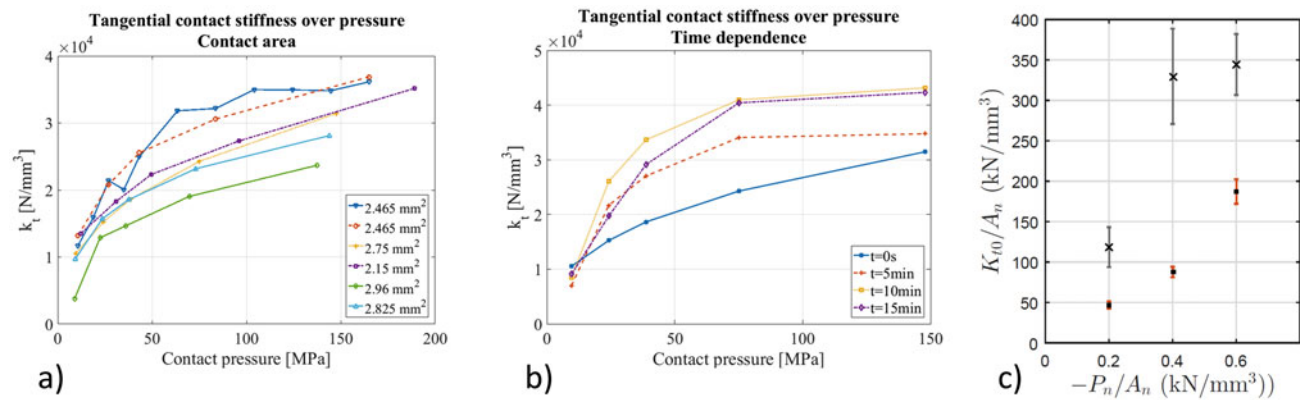


Fig. 22.3 Variation of tangential contact stiffness with pressure for (a) different contact areas and (b) different numbers of cycles (time) in the Imperial rig; (c) variation with pressure in the Oxford rig (rough and smooth specimens) from [5]

stuck conditions. It can be seen that for each contact pair, the stiffness increases with load, more rapidly at first, before reaching an approximately linear variation. There is no clear correlation with contact area, although the range of areas considered is limited. The first contact pair was then run in sliding contact for a total of 15 min, to allow wear to take place at the interface. In 5 min intervals the k_t vs. pressure measurements were repeated leading to the results in Fig. 22.3b. It can be seen that the stiffness increases with wear, most noticeably between 0 and 10 min. The curves for 10 and 15 min are similar, suggesting that the roughness profile of the surfaces had reached a steady state. It would be expected that the initial wear process would remove the high points on each surface, and therefore reduce the overall surface roughness. The results are therefore consistent with the predictions of [4], which suggest that stiffness should vary inversely with rms peak height. Figure 22.3c shows recent results from the Oxford rig, which show the variation of normalised tangential stiffness with mean pressure. Two sets of results are shown: crosses for a ‘smooth’ pair of contacts, and dots for a ‘rough’ pair. It will be seen that similar trends to the Imperial results are obtained.

22.5 Discussion and Conclusions

The results presented for the Oxford and Imperial rigs show broadly similar trends, despite being very different in concept and in measurement methods. Tangential contact stiffness is found to increase with mean contact pressure in both cases. Further, smooth interfaces (either worn in the case of the Imperial rig or prepared by a different process (Oxford rig)) are found to have higher tangential stiffness than rough interfaces. Both these trends are as predicted by simple elastic models of surface roughness. Absolute values of the stiffness from the Oxford rig appear to be about 10 times larger than the Imperial one, when normalised for contact area, but it should be borne in mind that both surface roughness and normal pressure are different in the two cases. The presentation will discuss these results and will draw conclusions relevant to the design of future rigs.

References

1. Kartal, M.E., Mulvihill, D.M., Nowell, D., Hills, D.A.: Determination of the frictional properties of Titanium and Nickel alloys using the digital image correlation method. *Exp. Mech.* **51**, 359–371 (2011)
2. Schwingshackl, C.W.: Measurement of Friction Contact Parameters for Nonlinear Dynamic Analysis. In: *Proceedings of the International Modal Analysis Conference XXX*, Jacksonville, FL, 2012
3. Kreider, M., Schwingshackl, C.W.: Experimental Evaluation of Pressure Dependent Tangential Contact Stiffness. In: *Proceedings of ISMA 2018*, Leuven, Belgium, 2018
4. Medina, S., Nowell, D., Dini, D.: Analytical and numerical models for tangential stiffness of rough elastic contacts. *Tribol. Lett.* **49**(1), 103–115 (2013)
5. Parel, K.: An Analysis of Contact Stiffness and Frictional Receding Contacts, D.Phil. Thesis, University of Oxford (2018)



Chapter 23

Investigating Nonlinearity in a Bolted Structure Using Force Appropriation Techniques

Benjamin R. Pacini, Daniel R. Roettgen, and Daniel P. Rohe

Abstract Understanding the dynamic response of a structure is critical to design. This is of extreme importance in high-consequence systems on which human life can depend. Historically, these structures have been modeled as linear, where response scales proportionally with excitation amplitude. However, most structures are nonlinear to the extent that linear models are no longer sufficient to adequately capture important dynamics. Sources of nonlinearity include, but are not limited to: large deflections (so called geometric nonlinearities), complex materials, and frictional interfaces/joints in assemblies between subcomponents. Joint nonlinearities usually cause the natural frequency to decrease and the effective damping ratio to increase with response amplitude due to microslip effects. These characteristics can drastically alter the dynamics of a structure and, if not well understood, could lead to unforeseen failure or unnecessarily over-designed features.

Nonlinear structural dynamics has been a subject of study for many years, and provide a summary of recent developments and discoveries in this field. One topic discussed in these papers are nonlinear normal modes (NNMs) which are periodic solutions of the underlying conservative system. They provide a theoretical framework for describing the energy-dependence of natural frequencies and mode shapes of nonlinear systems, and lead to a promising method to validate nonlinear models. In and, a force appropriation testing technique was developed which allowed for the experimental tracking of undamped NNMs by achieving phase quadrature between the excitation and response. These studies considered damping to be small to moderate, and constant. Nonlinear damping of an NNM was studied in using power-based quantities for a structure with a discrete, single-bolt interface. In this work, the force appropriation technique where phase quadrature is achieved between force and response as described in is applied to a target mode of a structure with two bolted joints, one of which comprised a large, continuous interface. This is a preliminary investigation which includes a study of nonlinear natural frequency, mode shape, and damping trends extracted from the measured data.

Keywords Nonlinear normal modes · Force appropriation · Nonlinear structural dynamics · Experimental techniques · Modal analysis

23.1 Approach

The tested structure is referred to as the Cylinder-Plate-Beam (CPB) and has been used in previous nonlinear studies. The goal of the nonlinear testing is to excite the CPB such that the response of the target NNM (mode 7) is isolated, allowing for the extraction of the amplitude-dependent characteristics of frequency, mode shape, and damping. This was accomplished using the force appropriation technique developed in. The general concept is, for sinusoidal excitation of a NNM, the input force will be 90 degrees out of phase with the acceleration, i.e. the input and response will be in phase quadrature. While the theory states that this phase quadrature criterion must be satisfied for all degrees of freedom and each harmonic (requiring an input at each degree of freedom), Peeters showed that NNM isolation can be approximately achieved using single-point excitation. Several mode indicator functions (MIFs) have also been developed for appraising the quality of NNM isolation. However, given the preliminary nature of this work, these were not used. Instead, NNM isolation was judged by the quadrature between the excitation force and the highest responding point of the target mode while using single-point excitation provided by a modal shaker. Closed loop control was utilized to isolate the NNM as indicated by this phase quadrature criterion. Once this was satisfied for a given excitation level, a 2 s frame of data was recorded, the force level increased, and the control sequence repeated. Phase resonance was achieved at 95 different excitation levels.

B. R. Pacini (✉) · D. R. Roettgen · D. P. Rohe
Department of Structural Dynamics, Sandia National Laboratories, Albuquerque, NM, USA
e-mail: brpacin@sandia.gov

23.2 Results

Figure 23.1 shows the fundamental frequency for each measurement frame where a 13% decrease is seen between low and high-level response. Figure 23.2 shows the magnitudes of the fundamental frequency and its harmonics for the control accelerometer. Note that the amplitude of the ninth harmonic begins to increase near frame 45 and eventually becomes larger than the fundamental near frame 69. This response is due to the nonlinearity produced by the target mode and indicates a potential modal interaction. More detail will be given in the conference presentation. Other topics that will be covered include: assessment of NNM isolation purity via two different MIFs, mode shape analysis, evidence supporting a modal interaction, and computation of an amplitude-dependent damping coefficient for the target mode.

Notice: This manuscript has been authored by National Technology and Engineering Solutions of Sandia, LLC, under Contract No. DE-NA0003525 with the U.S. Department of Energy/National Nuclear Security Administration. The United States Government retains and the publisher, by accepting the article for publication, acknowledges that the United States Government retains a non-exclusive, paid-up, irrevocable, world-wide license to publish or reproduce the published form of this manuscript, or allow others to do so, for United States Government purposes.

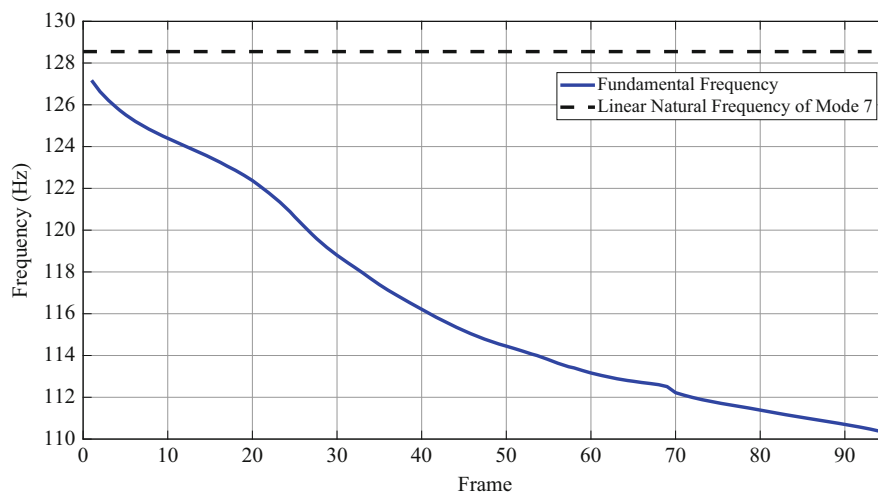


Fig. 23.1 Fundamental frequency for each frame

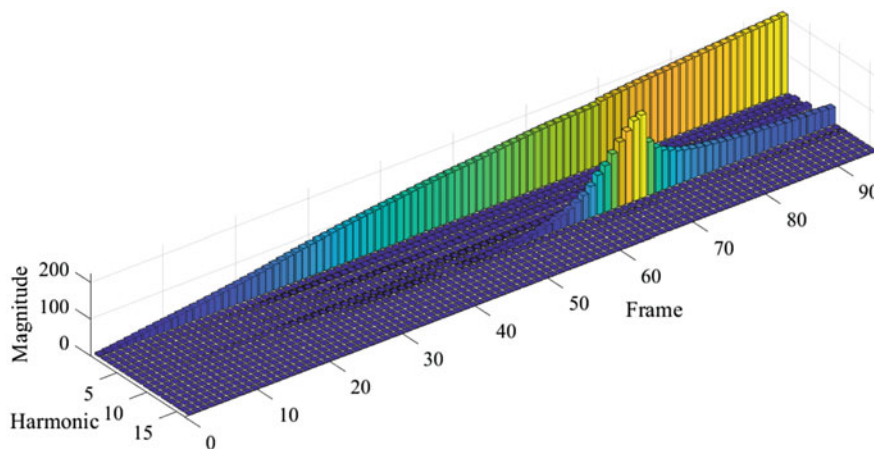


Fig. 23.2 Fundamental and harmonic frequencies for each frame of control accelerometer response

References

1. Kerschen, G., Worden, K., Vakakis, A.F., Golinval, J.-C.: Past, present and future of nonlinear system identification in structural dynamics. *Mech. Syst. Signal. Process.* **20**, 505–592 (2006)
2. Noel, J.-P., Kerschen, G.: Nonlinear system identification in structural dynamics: 10 more years of progress. *Mech. Syst. Signal. Process.* **83**, 2–35 (2017)
3. Peeters, M., Kerschen, G., Golinval, J.: Dynamic testing of nonlinear vibrating structures using nonlinear normal modes. *J. Sound Vib.* **330**, 486–509 (2011)
4. Kuether, R.J., Allen, M.S., Hollkamp, J.J.: Evaluation of geometrically nonlinear reduced-order models with nonlinear normal modes. *AIAA J.* **53**(11), 3273–3285 (2015)
5. Peeters, M., Kerschen, G., Golinval, J.: Modal testing of nonlinear vibrating structures based on nonlinear normal modes: experimental demonstration. *Mech. Syst. Signal. Process.* **25**, 1227–1247 (2011)
6. Scheel, M., Peter, S., Leine, R.I., Krack, M.: A phase resonance approach for modal testing of structures with nonlinear dissipation. *J. Sound Vib.* **435**, 56–73 (2018)
7. Mayes, R.L., Pacini, B.R., Roettgen, D.R.: A modal model to simulate typical structural dynamics nonlinearity. In: *Proceedings of the 34th International Modal Analysis Conference, Orlando, FL, 2016*
8. Pacini, B.R., Mayes, R.L., Owens, B.C., Schultz, R.: Nonlinear finite element model updating, part I: experimental techniques and nonlinear modal model parameter extraction. In: *Proceedings of the 35th International Modal Analysis Conference, Garden Grove, CA, 2017*
9. Roettgen, D.R., Pacini, B.R., Mayes, R.L., Schoenherr, T.F.: Experimental-analytical substructuring of a complicated jointed structure using nonlinear modal models. In: *Proceedings of the 36th International Modal Analysis Conference, Orlando, FL, 2018*
10. Peter, S., Leine, R.I.: Excitation power quantities in phase resonance testing of nonlinear systems with phase-locked-loop excitation. *Mech. Syst. Signal. Process.* **96**, 139–158 (2017)
11. Mayes, R.L., Johansen, D.D.: A modal parameter extraction algorithm using best-fit reciprocal vectors. In: *Proceedings of the 16th International Modal Analysis Conference, Santa Barbara, CA, 1998*
12. Hensley, D.P., Mayes, R.L.: Extending SMAC to multiple references. In: *Proceedings of the 24th International Modal Analysis Conference, 2006*
13. Carne, T.G., Dohrmann, C.R.: Support conditions, their effect on measured modal parameters. In: *16th International Modal Analysis Conference, Santa Barbara, CA, 1998*
14. Slonim, M.A.: Distortion power in linear and non-linear systems. *Int. J. Electron. Theor. Exp.* **68**(5), 769–778 (1990)
15. Ginsberg, J.H.: *Mechanical and Structural Vibrations*, pp. 130–134. John Wiley & Sons, Inc., New York (2001)

Chapter 24

Techniques for Nonlinear Identification and Maximizing Modal Response



D. Roettgen, B. R. Pacini, and R. Mayes

Abstract Recent research has shown that weakly nonlinear structures can be modeled as a combination of nonlinear pseudo-modal models. These modal models consist of a linear spring, mass, and damper with the addition of a nonlinear element often identified using a restoring force surface technique. This approach is limited by force level achieved when exciting the system for identification. Extrapolation leads to poor results when predicting the nonlinear response; thus, there is a need to maximize the modal amplitude excited in these weakly nonlinear structures. Previous works have compared hammer testing to shaker testing using windowed sinusoidal input forces. This appeared to be a promising technique to increasing the excited modal amplitude. In this work the windowed sinusoidal technique is further investigated to understand how window parameters (such as window width) can be optimized to maximize the modal amplitude obtained during the identification process.

Keywords Nonlinear system identification · Experimental techniques · Structural dynamics · Modal analysis · Nonlinear testing methods

24.1 Introduction

Many industries design and manufacture mechanical structures with bolted joints. The frictional interfaces that occur due to these joints often introduce nonlinearity into an otherwise linear system. Two main approaches exist to account for these nonlinearities: local physical models and pseudo-modal modeling [1–3]. Local physical modeling attempts to capture the physics happening at each local joint. While physically insightful, this method can be computationally expensive, and the constitutive models require expensive calibration for every structural joint. Nonlinear pseudo-modal modeling is computationally inexpensive, and nonlinear parameters can be identified from a quick experiment focused on each nonlinear mode. In this work, a weakly nonlinear system is studied which exhibited small shifts in frequency with large changes in damping. In previous works [4, 5] pseudo-modal modeling was found to be a practical approach for this type of nonlinear system.

Nonlinear pseudo-modal models take a form analogous to a standard modal model except augmenting a single degree-of-freedom (DOF) system with a nonlinear forcing element. This element has taken many forms, from an Iwan element [6] to simple polynomial springs and dampers [5]. This approach relies on two primary assumptions. First, the modes of the system must remain uncoupled in the amplitude range of interest. Second, the mode shapes of the system must not change with amplitude. These assumptions allow for the use of a modal filter to obtain single degree-of-freedom signals in order to identify a nonlinear model. Like most nonlinear modeling techniques, the model is only accurate in the amplitude range used in parameter identification, so maximizing this amplitude range is of great interest.

In previous works [4, 7], the achievable structural response was not limited by mechanical factors but by the maximum allowable voltage output by the shaker amplifier. The objective of this work is to maximize the modal response using the

Sandia National Laboratories is a multimission laboratory managed and operated by National Technology and Engineering Solutions of Sandia, LLC., a wholly owned subsidiary of Honeywell International, Inc., for the U.S. Department of Energy's National Nuclear Security Administration under contract DE-NA-0003525. This paper describes objective technical results and analysis. Any subjective views or opinions that might be expressed in the paper do not necessarily represent the views of the U.S. Department of Energy or the United States Government.

D. Roettgen (✉) · B. R. Pacini · R. Mayes
Department of Structural Dynamics, Sandia National Laboratories, Albuquerque, NM, USA
e-mail: droett@sandia.gov

windowed sinusoidal approach first presented in [4] by investigating the influences of two factors of the input signal: frequency of the sine wave and the window width. An experimental bolted assembly was utilized in order to obtain linear and nonlinear response. Using a given shaker-amplifier configuration, the structure was tested with various windowed sinusoidal loadings to observe which properties of the input signal resulted in increased modal response amplitude, thus increasing the range for which the identified nonlinear model is valid.

This paper is organized as follows. Section 2 contains a brief description of the nonlinear pseudo-modal modeling technique, the modal filter, and a windowed sinusoidal excitation method. Section 3 shows the experimental system of interest and Sect. 4 details a standard nonlinear modal model fit to a baseline windowed sinusoidal excitation as performed in [4]. Section 5 shows the different experimental loading cases investigated and Sect. 6 compares the models obtained from select load cases. Finally, Sect. 7 contains conclusions from this study along with questions for future investigations.

24.2 Theory

This section provides an overview of the pseudo-modal model method used in this work to extract experimentally observed nonlinearity. The objective of this study is to compare the modal amplitude levels and models fit from different loading cases. Thus, this section also contains a summary of the modal filter and a detailed look at the arbitrary source excitation technique employed.

24.2.1 Nonlinear Pseudo-Modal Model

This work focuses on weakly nonlinear mechanical systems, which can be modeled as nonlinear pseudo-modal models. A nonlinear pseudo-modal model retains the assumptions of a linear modal model and acts similarly with a modal mass connected to ground by a spring and damper, but with the addition of an unknown nonlinear forcing element. Note that this technique assumes that the modes remain uncoupled and shapes do not change with amplitude. In [8], Eriten has shown a rigorous theoretical foundation for these assumptions in the presence of weak nonlinearities.

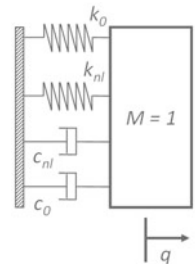
For this work, the nonlinear forcing element are parameterized with polynomial springs and dampers as shown in Fig. 24.1. In order to identify these polynomial stiffness and damping coefficients a Restoring Force Surface [9] technique was implemented. A classical linear modal equation of motion is written as shown in Eq. (24.1), where \ddot{q} , \dot{q} , and q are the modal acceleration, velocity, and displacement, c_0 and k_0 are the linear modal damping and stiffness, and $\phi^T F$ is the modal excitation force.

$$\ddot{q} + c_0 \dot{q} + k_0 q = \phi^T F \quad (24.1)$$

The nonlinear elements are added to this equation of motion as seen in Eqs. (24.2) and (24.3). In Eq. (24.2), F_{nl} is a generic nonlinear functional form, while in Eq. (24.3) this is parameterized with quadratic and cubic springs and dampers, a form which has worked well in previous studies.

$$\ddot{q} + c_0 \dot{q} + k_0 q + F_{nl} = \phi^T F \quad (24.2)$$

Fig. 24.1 Schematic of single degree-of-freedom nonlinear pseudo-modal model



$$\ddot{q} + c_0\dot{q} + k_0q + c_1\dot{q}|\dot{q}| + c_2\dot{q}^3 + k_1q|q| + k_2q^3 = \phi^T F \quad (24.3)$$

The mode shapes and linear coefficients (c_0 and k_0) are defined from low-level linear testing and the modal acceleration (\ddot{q}), velocity (\dot{q}), displacement (q), and force (F) are measured during a high-level test. Thus the procedure from [5] is implemented to obtain the nonlinear spring and damper coefficients c_1 , c_2 , k_1 , and k_2 . This procedure involves gathering terms with known or measured coefficients on one side of the equations and terms with unknown coefficients on the other as shown in Eq. (24.4).

$$\bar{U} = \phi^T F - \ddot{q} - c_0\dot{q} - k_0q = \begin{bmatrix} \dot{q}|\dot{q}| & \dot{q}^3 & q|q| & q^3 \end{bmatrix} \begin{bmatrix} c_1 \\ c_2 \\ k_1 \\ k_2 \end{bmatrix} = P \begin{bmatrix} c_1 \\ c_2 \\ k_1 \\ k_2 \end{bmatrix} \quad (24.4)$$

Note, the best parameters were obtained by transforming these quantities to the frequency domain, and stacking the real and imaginary parts of the signals as described in [5]. A least-squares estimate of these unknown coefficients are obtained by pre-multiplying \bar{U} by the pseudo-inverse of experimental derived values P as in Eq. (24.5). Using these polynomial coefficients, the nonlinear forcing element can now be used to predict the nonlinear response of this mode to several different loading cases.

$$\begin{bmatrix} c_1 \\ c_2 \\ k_1 \\ k_2 \end{bmatrix} = P^+ \bar{U} \quad (24.5)$$

24.2.2 Modal Filter Theory

The nonlinear pseudo-modal model technique described in Sect. 2.1 relies on obtaining a single degree of freedom modal response. Thus, modal filtering is an essential step in the nonlinear modal modeling process. In this study, a spatial filter referred to here as the full-modal filter [5, 10] was used to isolate the single degree-of-freedom response for the target mode of the system.

In linear modal analysis, physical and modal accelerations are related through the linear mode shape matrix, Φ , as shown in Eq. (24.6).

$$\Phi \ddot{q} = \ddot{x} \quad (24.6)$$

By premultiplying the physical domain measurements with the Moore-Penrose pseudo-inverse of the mode shape matrix, measured modal responses can be obtained (see Eq. 24.7). This filtering is key to the nonlinear pseudo-modal modeling process and thus sufficient instrumentation must be used in order to properly filter the modes.

$$\ddot{q} = \Phi^+ \ddot{x} \quad (24.7)$$

24.2.3 Experimental Applied Force

Hammer and shaker excitation techniques were studied and compared in [4]. For this study, the windowed sinusoid approach discussed in [4] was used to excite an experimental structure to high excitation levels. This has been found to be a practical way to obtain high amplitude response of a single mode. The windowed sinusoid approach takes a sine wave at a designated center frequency, f_e , and applies a window to modulate the amplitude. This signal is used as the input voltage to the amplifier that powers the modal shaker. Because of the window, the frequency content of the signal is not contained solely at f_e , but spread over the frequency band $f_e \pm \Delta f_r$, where Δf_r is the excitation bandwidth determined by the window function.

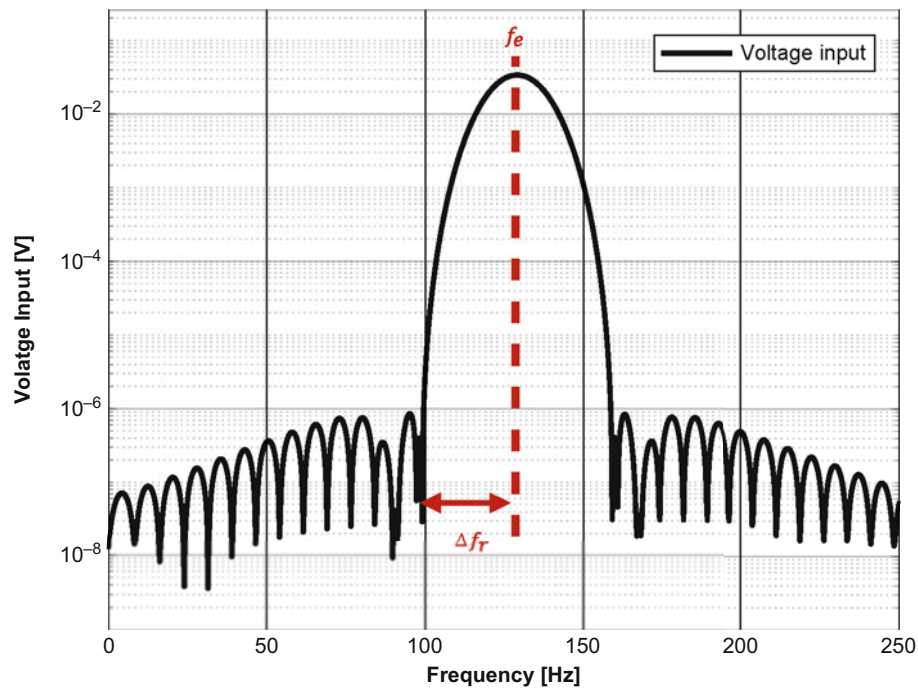


Fig. 24.2 Arbitrary voltage input for a windowed sinusoidal excitation

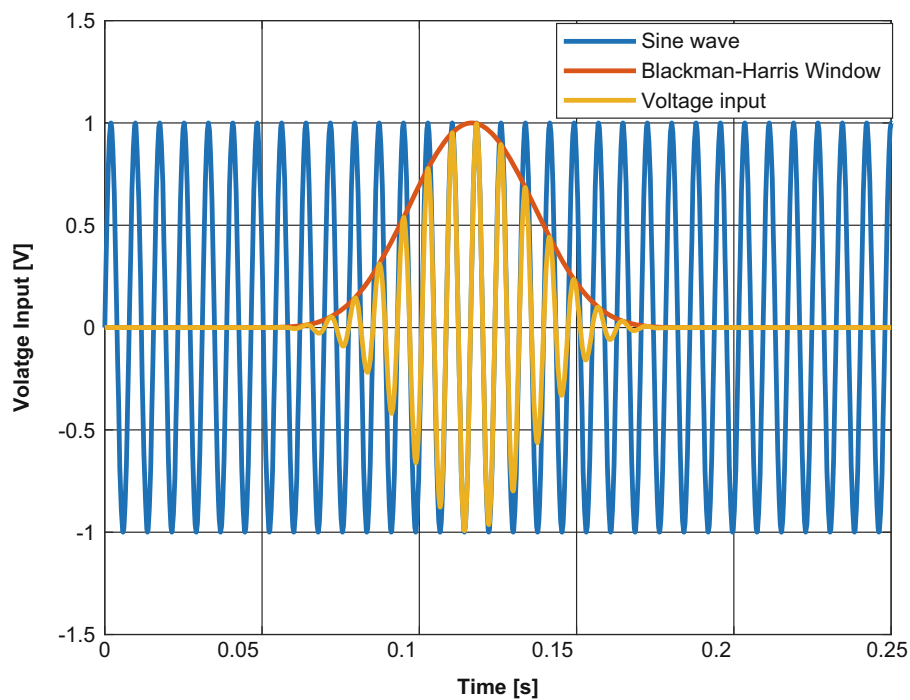


Fig. 24.3 Example windowed sinusoidal input

Figure 24.2 shows this input voltage in the frequency domain, while Fig. 24.3 shows the input voltage, sine wave, and window in the time domain.

Spreading of the frequency content is ideal for nonlinear investigations. Often, a weakly nonlinear system contains a small shift in resonant frequency as amplitude is increased. Therefore, a single tone sine wave may not input sufficient energy into a nonlinear mode as the system softens or hardens unless the frequency is constantly updated to match the shifting resonance.

The windowed sinusoid spreads the frequency content to help ensure the system has some excitation energy at resonance regardless of shifting due to nonlinearity. In past studies, windows with large Δf_r were used to ensure energy was input at resonance. Signals with large Δf_r in the frequency domain correspond to short pulses in the time domain, which reduces the excitation of the target mode. During testing, amplifier voltage limits were typically reached, reducing the achievable response amplitude of the mode. It was theorized that concentrating the input energy over a narrower band and shifting it near where the nonlinear resonance of the mode is expected to transition to at higher response levels would result in larger responses without exceeding the electrical limits of the amplifier. For example, if preliminary tests show that the target mode softens at high amplitude, then f_e is set to be lower than the linear natural frequency. However, if the band is too narrow, the mode may soften or harden past the input energy band and fall off-resonance, therefore, a balance must be achieved such that a high response level is achieved while also continuously exciting the mode's resonance. This study iterates on the center frequency, f_e , and excitation bandwidth, Δf_r , in order to optimize the response of a target mode of a jointed structure. Note that in previous works [4, 7], a triangle window was used on the sinusoid, but in more recent works and this study, a Blackman-Harris [11] window was utilized. The latter is preferred as it has lower side lobes in the frequency domain which allows for more energy input in the frequency band of interest.

24.3 Experimental Set-Up

24.3.1 Hardware Description

A picture of the experimental set-up is shown in Fig. 24.4. The hardware consists of an aluminum beam and plate connected with two bolts and a layer of epoxy. This subassembly is connected to an aluminum cylinder with eight bolted joints along a large continuous interface. This system is referred to as the Cylinder-Plate-Beam (CPB) and has been the focus of many nonlinear studies including [4, 5, 7].

The system was instrumented with 26 triaxial accelerometers in the same configuration as tested in [4]. These were selected using mode shapes from a finite element model to ensure independent shapes below 1600 Hz. The CPB was suspended using two bungee cords to approximate a free-free boundary condition. For all testing, a force transducer and shaker set-up were attached at the rear of the cylinder. This shaker was used to perform low-level burst random testing as well as high-level arbitrary source excitations.

24.3.2 Linear Model Extraction

A low-level burst random test was performed in order to obtain linear modal parameters. The linear shapes from this test were used to filter high-level accelerometer measurements into single degree-of-freedom modal responses while the linear natural frequencies and damping ratios were used as known quantities during the nonlinear identification process. The linear natural frequencies and damping ratios of the system are shown in Table 24.1.

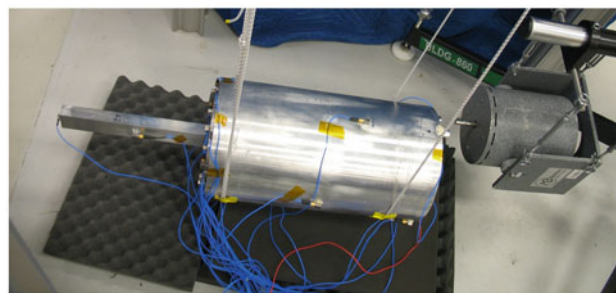
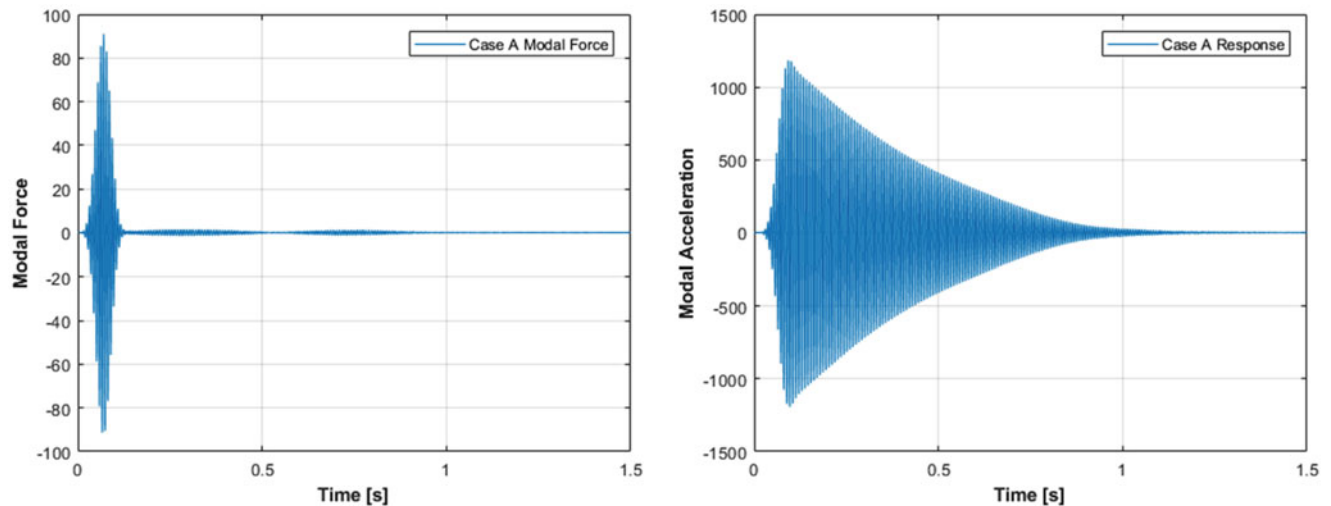


Fig. 24.4 Physical CPB hardware configuration

Table 24.1 Linear modal parameters

Mode	f_n (Hz)	ζ (% cr)	Shape description
7	129.6	0.397%	1st soft bending of Beam
8	172.6	0.322%	1st stiff bending of Beam
9	385.8	0.069%	(2,0) Ovaling model
10	391.9	0.083%	(2,0) Ovaling model
11	551.6	0.278%	Axial mode
12	945.4	0.413%	(3,0) Ovaling model
13	1025.7	0.076%	2nd soft bending of Beam

Fig. 24.5 Model process overview**Fig. 24.6** Time domain modal force and acceleration

24.4 Nonlinear Modal Model Extraction Overview

In this section, the results from a traditional windowed sinusoid excitation are analyzed resulting in a nonlinear pseudo-modal model.

The procedure used to identify nonlinear pseudo-modal models from experimental data as described in Sect. 2.1 can be broken into three main steps. First, a high-level excitation must be applied, such as the windowed sinusoid discussed in Sect. 2.3. Next, a single degree-of-freedom modal response must be obtained, often with the use of a spatial modal filter. Finally, using this modal response the restoring force surface technique described in Sect. 2.1 can be used to identify a nonlinear pseudo-modal model that best fits the measured data in a least squares sense (Fig. 24.5).

For a baseline, the CPB was tested using a wide-bandwidth windowed sinusoid. For this initial test, the structure was excited using a windowed sinusoid where the center frequency, f_e , was the first linear natural frequency of 130 Hz, and the excitation bandwidth, Δf_r , was ± 30 Hz. This provides a wide pulse of energy in the frequency domain near the first bending resonance of the structure. The voltage level was tuned to maximize the voltage output of the amplifier without exceeding the electrical limits. After applying the modal filter, the accelerometer measurements were transformed into a single DOF response of the first bending mode. Figure 24.6 shows the applied modal force and response in the time domain, while Fig. 24.7 shows the data in the frequency domain.

Following the RFS procedure from Sect. 2.1, a nonlinear modal model was extracted using a cubic and quadratic polynomial spring and damper as the nonlinear forcing elements. A simulation of the model was performed and obtained good agreement with the measured response data as shown in Fig. 24.8. Early in time, at high amplitude levels, the signals have great correlation, while later in time the measurement has more damping and the model begins to overpredict. This wide bandwidth windowed sinusoid is similar to those applied to the system in recent works [4], where results with similar

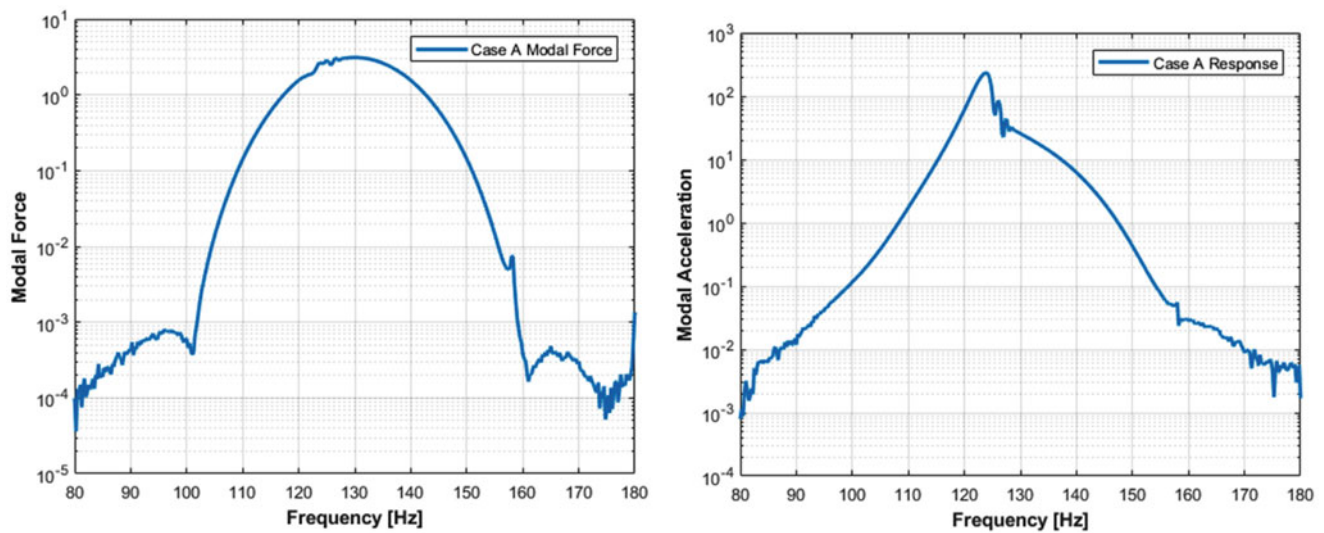


Fig. 24.7 Frequency domain modal force and response

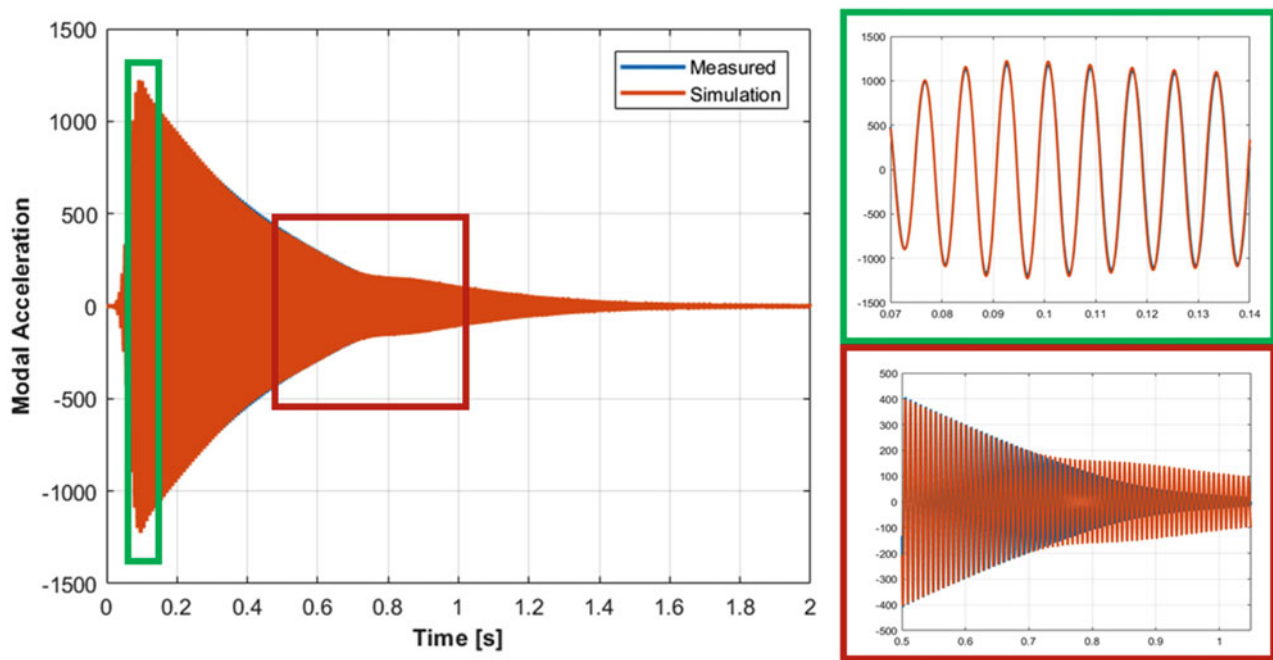


Fig. 24.8 Simulated response for baseline case

accuracy were obtained. The slight degradation in the prediction late in time is believed to be a result of the least-squares fitting since this method biases the coefficients to minimize the error at the high amplitude responses.

24.5 Experimental Results to Modified Windowed Sinusoidal Inputs

In order to optimize modal amplitude, the values of f_e and Δf_r were adjusted from this baseline case to observe the impact of these input parameters on the modal amplitude achieved for the mode of interest. These test cases are summarized in Tables 24.2, 24.3, and 24.4. First, the center frequency was held constant and the excitation bandwidth, Δf_r , was narrowed from 30 Hz to 20, 10 and 5 Hz respectively. By narrowing Δf_r but maintaining the same maximum voltage, the applied force

Table 24.2 Windowed sinusoidal signal parameters Cases A–D

Test case	f_e (Hz)	Δf_r (Hz)	Amplifier level	Description
A	130	± 30	70	Baseline
B	130	± 20	70	–
C	130	± 10	70	–
D	130	± 5	70	–

Table 24.3 Windowed sinusoidal signal parameters Cases E–G

Test case	f_e (Hz)	Δf_r (Hz)	Amplifier level	Description
E	129	± 30	70	Second Baseline
F	119	± 30	70	–
G	119	± 5	70	–

Table 24.4 Windowed sinusoidal signal parameters Cases E and H

Test case	f_e (Hz)	Δf_r (Hz)	Amplifier level	Description
E	129	± 30	70	Second Baseline
H	119	± 5	43	Matched Amplitude

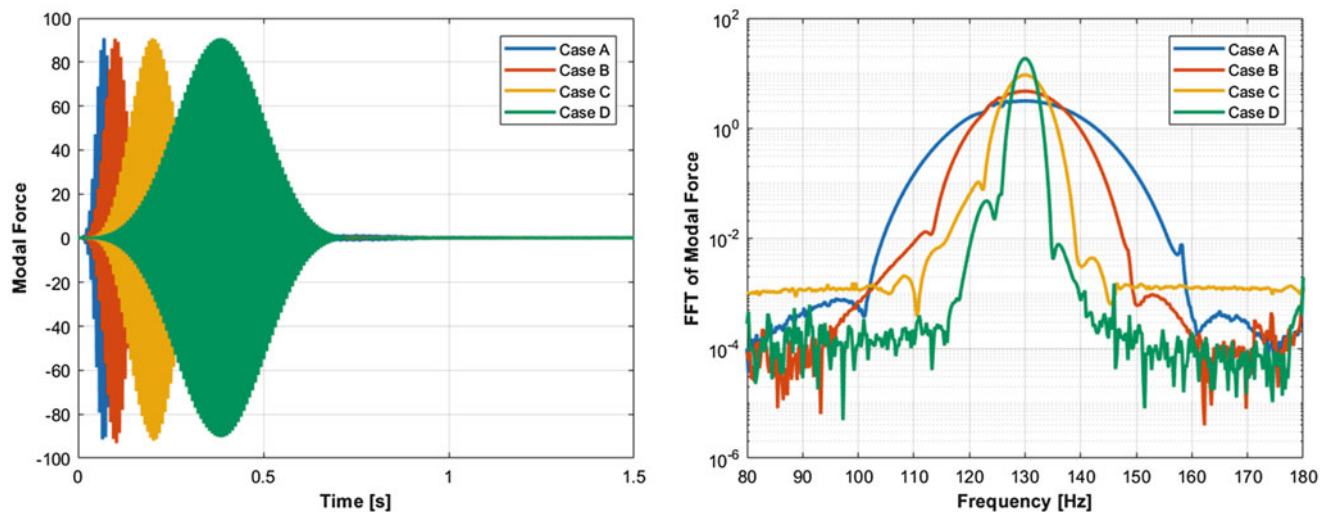


Fig. 24.9 Cases A–D modal response time and frequency response

provided additional margin to the shakers electrical limits, allowing the applied force to be increased. These are represented in Test Cases A–D.

Next the system was excited with a windowed sinusoid with a shifted center frequency. Note that the testing was conducted over a period of two days, during which the linear natural frequency of the target mode shifted. Thus, a new baseline case is contained in Test Case E, and Test Cases F–H contain correspond to experiments with shifted center frequencies. From preliminary testing and previous studies conducted on this structure, the target mode is known to soften, so Cases F–H have center frequencies lower than the linear natural frequency. Case F retained the baseline 30 Hz window width. Case G applied a force with a center frequency of 119 Hz but narrows the excitation bandwidth to ± 5 Hz. Finally, Case H lowers the input voltage of Case G to obtain approximately the same modal amplitude as the second baseline case.

24.5.1 Experimental Results from Cases A–D

The results of Experimental Cases A–D are shown in Figs. 24.9 and 24.10, where Fig. 24.10 shows the modal response obtained from the excitation inputs displayed in Fig. 24.9. The frequency band from ± 30 to ± 5 Hz to see the effect on the resulting modal amplitude. The windowed sinusoid signal parameters are summarized in Table 24.2.

As shown in Fig. 24.10, the broadband frequency input of Case A does apply a smaller force in the frequency domain than the narrower window Cases B–D. In a linear system, the higher modal forces would be expected to obtain higher modal response but the opposite is seen in Case D where the forcing is concentrated in a narrow band around the linear natural frequency. Recall the nonlinearity for this mode results in a softening effect. The lower modal amplitude at a higher force implies that, as the mode achieved higher response levels, its resonant frequency decreased out of the excitation bandwidth. Conversely, loading from Case B provided the highest modal response without applying the highest modal force, so there is an optimal excitation bandwidth for exciting a high modal response.

The instantaneous frequency of each of the above cases was computed as the inverse of the oscillation period as determined from the zero crossings in the respective responses, see Fig. 24.11. The initial timeframes, t_i , begin near 130 Hz which was the selected forcing frequency for these experiments. As the amplitude increases, each of the experimental cases follows a different trajectory as the frequency traces through the response transient. Eventually, Cases A–C converge onto the same curve and end at the final time, t_f . Note that as the signals become smaller, the calculated instantaneous frequency becomes very noisy, so only a certain amplitude range of data was considered which is why the curves do not end at the linear natural frequency of 130 Hz. Cases A and B lay on the same curve as the frequency shifts from ~ 122 Hz back to ~ 128 Hz. Case D never falls onto this curve because by the time the force response ends the signal is almost fully decayed. This is confirmed in the time histories shown in Figs. 24.9 and 24.10. These case studies show that an optimal window width can be selected to maximize modal amplitude but a balance must be achieved such that the excitation envelopes the shift in the

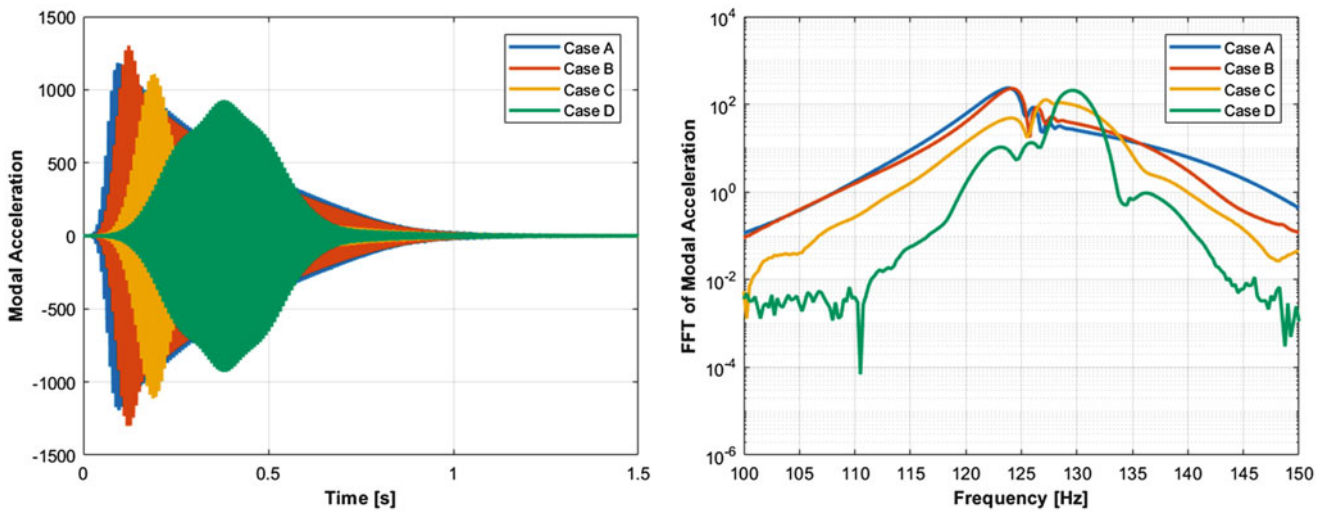


Fig. 24.10 Cases A–D acceleration time and frequency response

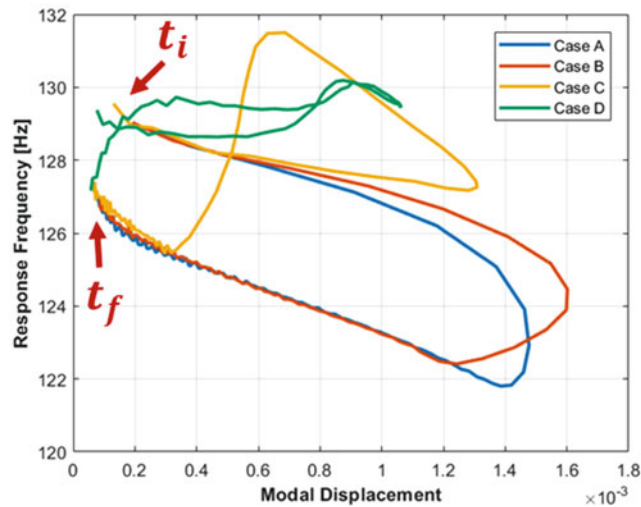


Fig. 24.11 Cases A–D frequency tracking

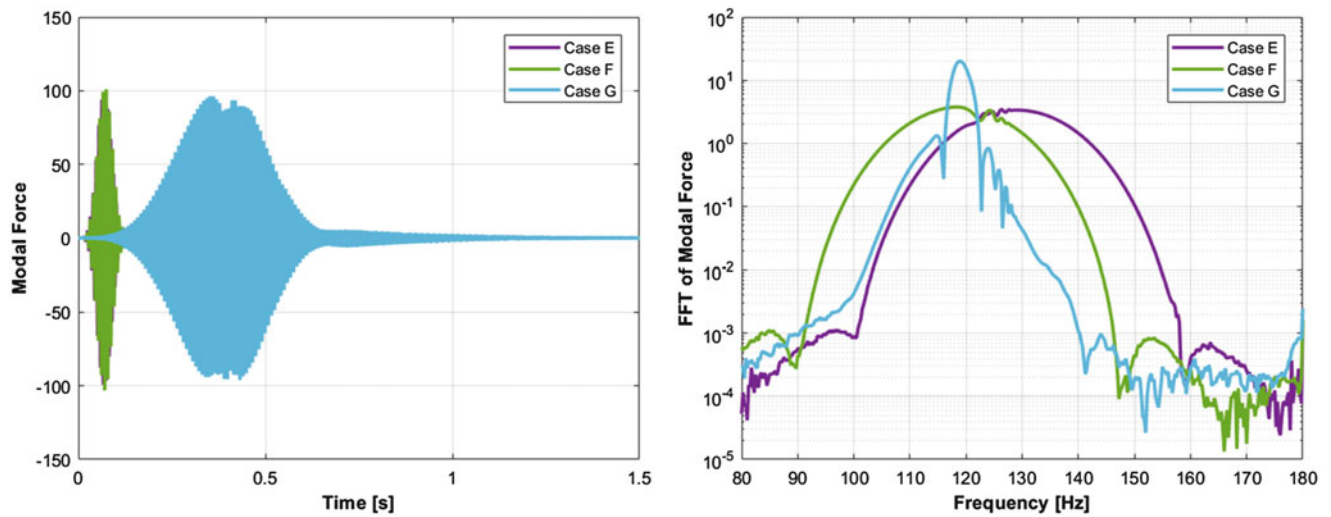


Fig. 24.12 Cases E–G modal response time and frequency response

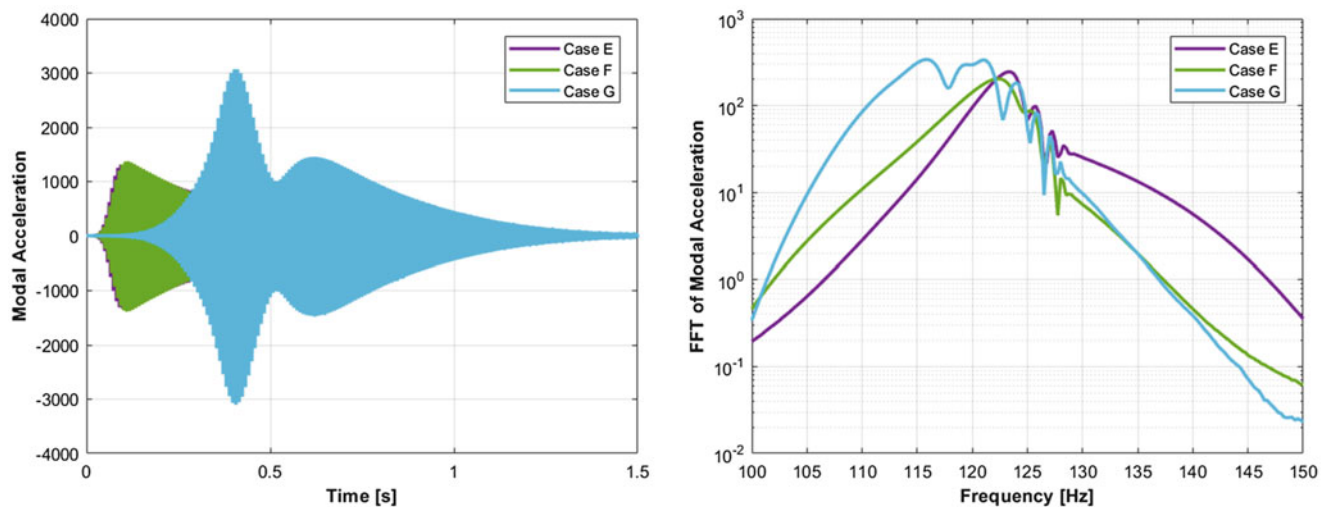


Fig. 24.13 Cases E–G modal acceleration time and frequency response

nonlinear resonance Ideally, a quality nonlinear pseudo-modal model would match all time responses as it should be able to accommodate complicated, potentially off-resonance loadings.

24.5.2 Experimental Results from Cases E–F

With the insight gained from Cases A–D, another series of tests were conducted with the center frequency of the windowed sinusoid shifted from the linear natural frequency of the target mode. This was accomplished by adjusting f_e in the input voltage signal. These new loading signals, Cases E–G, are summarized in Table 24.3.

This shifted resonance study consists of Case E–G shown in Figs. 24.12 and 24.13. Cases E and F provide nearly identical results, with both reaching around the same modal amplitude while Case G magnifies the modal amplitude by over a factor of 2 in the time domain. With more optimization on center frequency shift and excitation bandwidth, this magnification could be even higher. The modal response also has a second pulse as can be observed in Fig. 24.13.

Figure 24.14 shows the frequency tracking plot for Cases E–G. Here, the responses of Case E and F begin near their respective forcing frequencies. Both cases eventually converge to the same backbone during the free decay portion of the transient. Case G begins at the forced natural frequency of around 119 Hz, then softens as it reaches peak modal amplitude

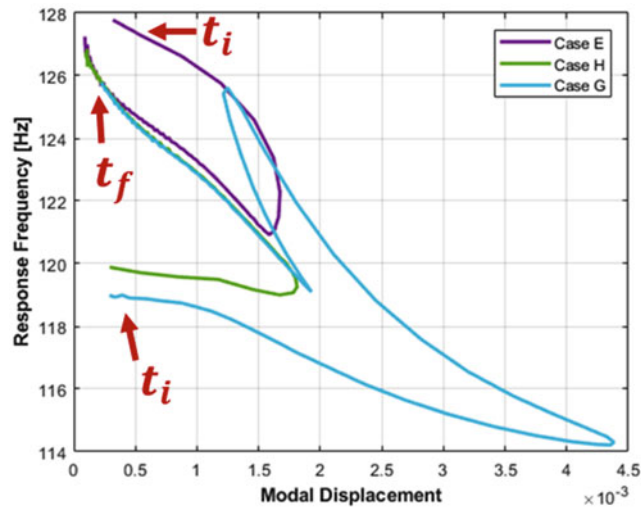


Fig. 24.14 Cases E–G frequency tracking

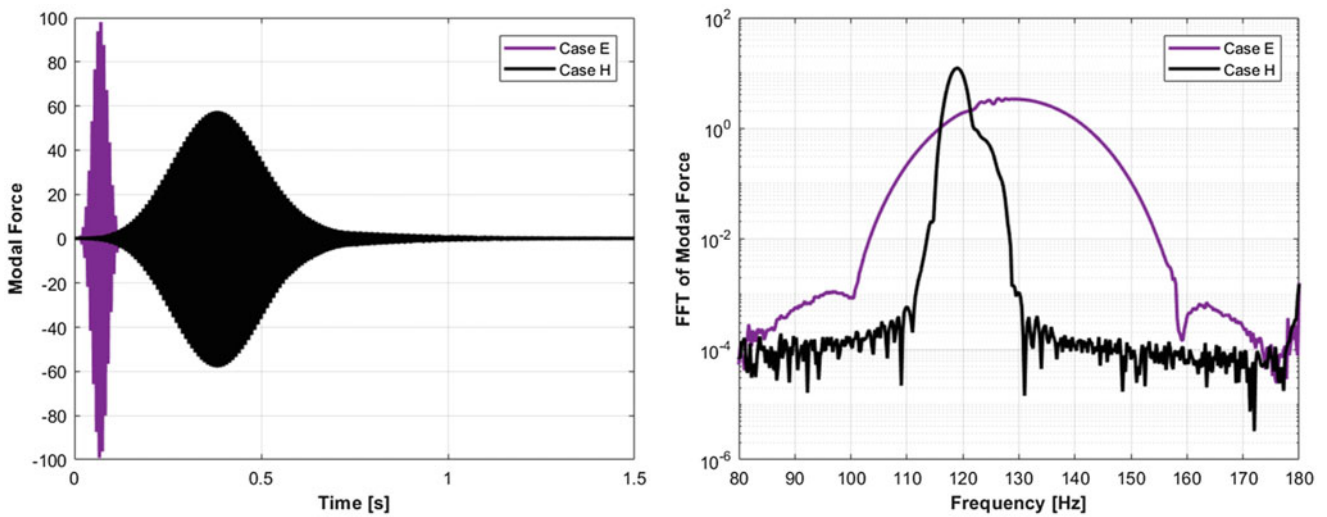


Fig. 24.15 Cases E and H modal force time and frequency response

down to around 114 Hz before hardening to around 125 Hz. The signal of the response, while under forced response conditions, appears to be semi-bounded by the excitation bandwidth Δf_r set of ± 5 Hz.

24.6 Experimental Results from Cases E and H

In order to evaluate the nonlinear models extracted from varying inputs, the voltage input from Case G was scaled until it excited the same modal amplitude as Case E. The second baseline and the new loading signal, Case H, are shown in Table 24.4.

This new loading case is shown as Case H in Figs. 24.15, 24.16, and 24.17. While the modal amplitudes are similar, the peak modal force required for Case H is much smaller. Figure 24.17 shows the frequency tracking for these two cases which behave as expected: the initial frequency of each response is near their corresponding forcing frequencies and then the free-decay portions overlay near the end of the transient. In the next section, models fit from these two cases are compared in order to understand how shifting f_e influences the model obtained from a restoring force surface identification process.

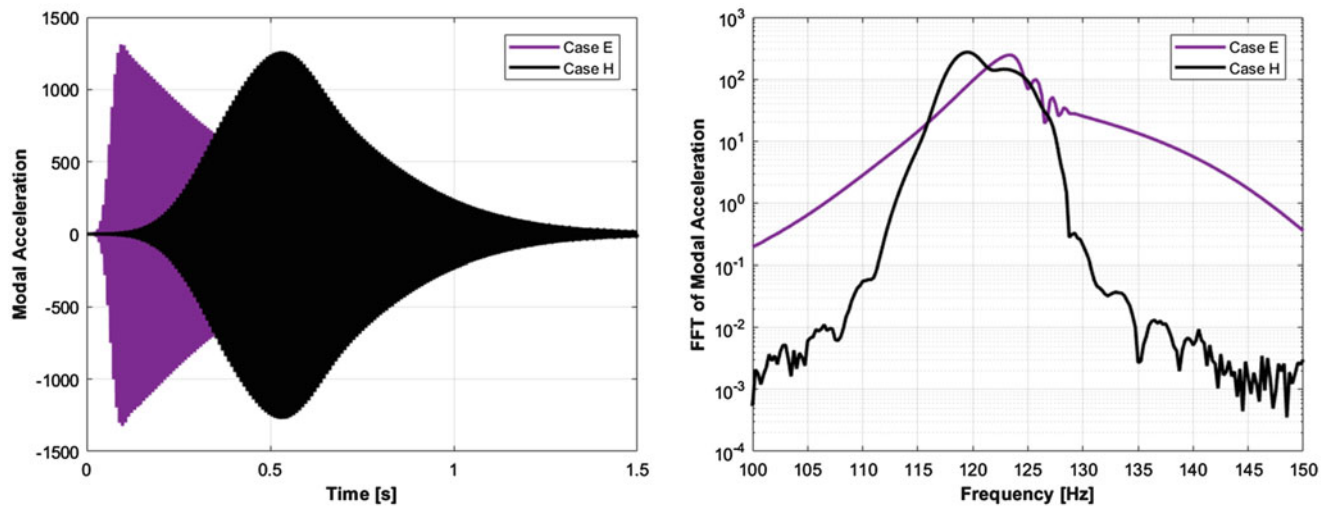


Fig. 24.16 Cases E and H modal acceleration time and frequency response

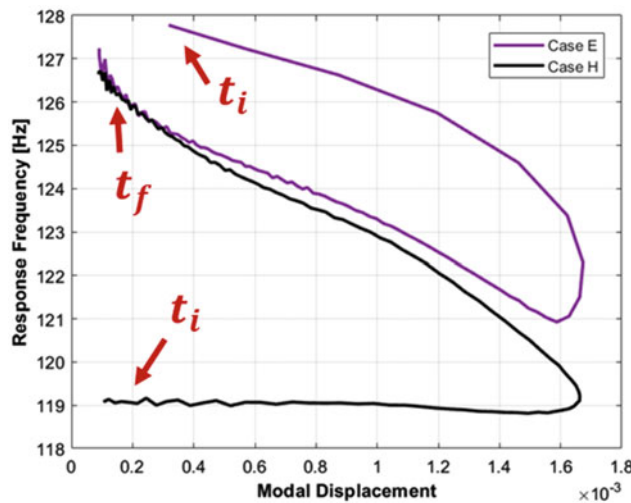


Fig. 24.17 Cases E and H frequency tracking

Table 24.5 Windowed sinusoidal signal parameters Cases E, G, and H

Test case	f_e (Hz)	Δf_r (Hz)	Amplifier level	Description
E	129	± 30	70	Second Baseline
G	119	± 5	70	–
H	119	± 5	43	Matched Amplitude

24.7 Model Comparison

The restoring force surface technique outlined in Sect. 2.1 was implemented in order to find nonlinear modal models for Cases E, G and H. For convenience, the loading parameters for these simulations, Cases E, G and H, are shown in Table 24.5.

The cubic and quadratic polynomial stiffness and damping coefficients obtained are displayed in Table 24.3. Note, the value of these coefficients are drastically different for Cases E and G. This is expected as these two tests reached different modal amplitude levels and used the same model order to fit this different range of amplitudes. Comparing the coefficients from Cases E and H is more useful as these two cases reached nearly the same modal amplitude level but used different values of f_e and Δf_r . The models obtained for these two cases are nearly identical showing that peak modal amplitude is more influential in the model than the center frequency and/or window width (Table 24.6).

The response of the target mode was simulated using two different models: one identified from the Case E measurements and the other from Case G measurements. The forcing for both of these simulations is that from Case E. The results are shown in Fig. 24.18. Both simulations compare to measured data favorably with the Case E model performing slightly better, as it overlays with the measured in late time. The error in the late time simulation using the Case G model is similar to the error seen in previous studies [4]. Even with different coefficient values for the nonlinear models, the two models exhibited similar nonlinear effects in the response range achieved with Case E forcing. Figure 24.19 displays the effective stiffness and damping for each of these models where $k_{eff} = k_0 + k_1|q| + k_2q^2$ and $c_{eff} = c_0 + c_1|\dot{q}| + c_2\dot{q}^2$. These show good agreement between the two models but the Case G model goes to a higher modal amplitude. There is a slight discrepancy in modal effective dissipation, potentially due to the nature of the forced response of Case G model but this is a topic for future study.

Next, the Case G loading was applied to the same two models. Here, the Case G model vastly outperforms the Case E system. This is expected as the Case E simulation has to extrapolate to reach the modal response levels of the Case G excitation (Fig. 24.20).

Finally, models identified from Case E and Case H were used to simulate the response of the target mode to the Case H loading, see Fig. 24.21. The results of the two simulations are very similar which is to be expected given that they had very little difference in their nonlinear coefficient values. so they are expected the perform similarly. As shown in Fig. 24.21, the Case E model can capture the milder second pulsing of this loading case and the effective stiffness and damping curves overlay as shown in Fig. 24.22. Neither model matches the measured response for the entire transient like the baseline loading presented in Sect. 4 and this should be a topic for further study.

Table 24.6 Nonlinear coefficients for cases E, G and H

Test Case	Case E	Case G	%diff. EG	Case H	%diff. EH
k_1	-7.50E+07	-5.63E+07	-25%	-7.28E+07	-3%
k_2	1.54E+10	4.73E+09	-69%	1.37E+10	-11%
c_1	-1.489	-1.186	-20%	-1.403	-6%
c_2	-0.025	0.109	-536%	-0.034	36%

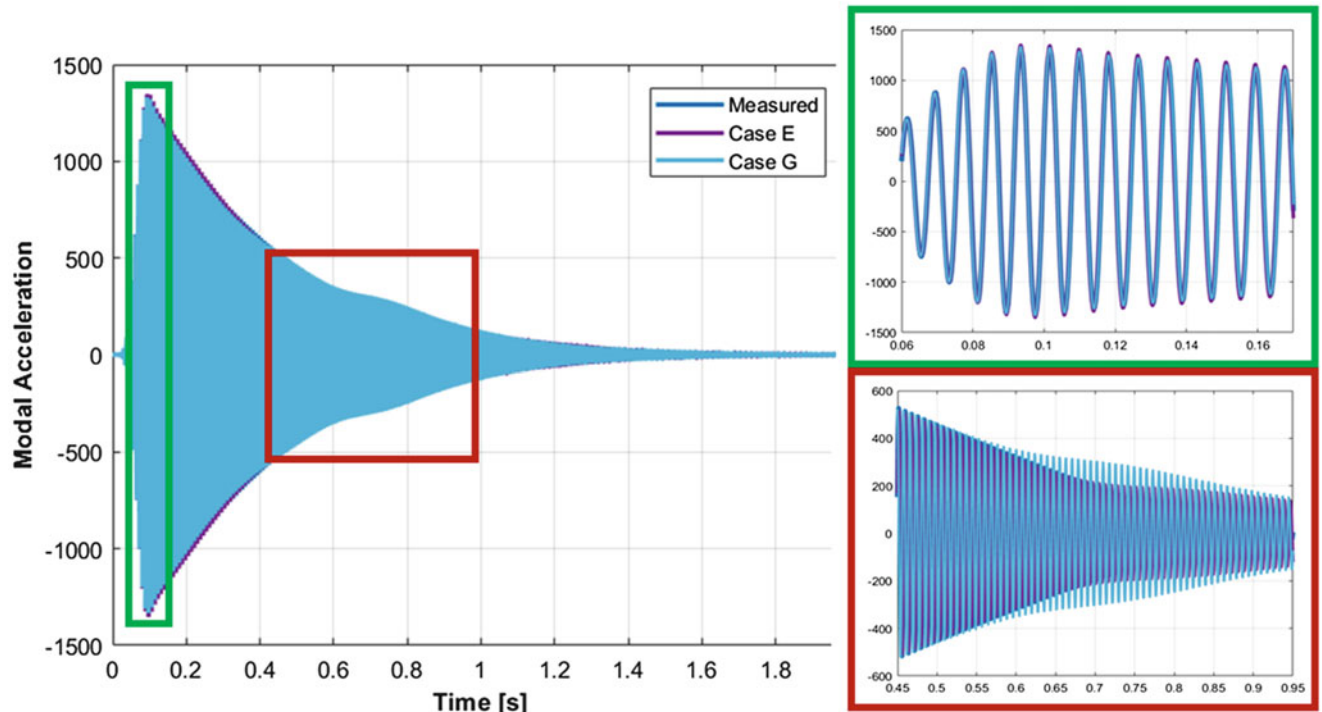


Fig. 24.18 Cases E and G simulations to Case E forcing

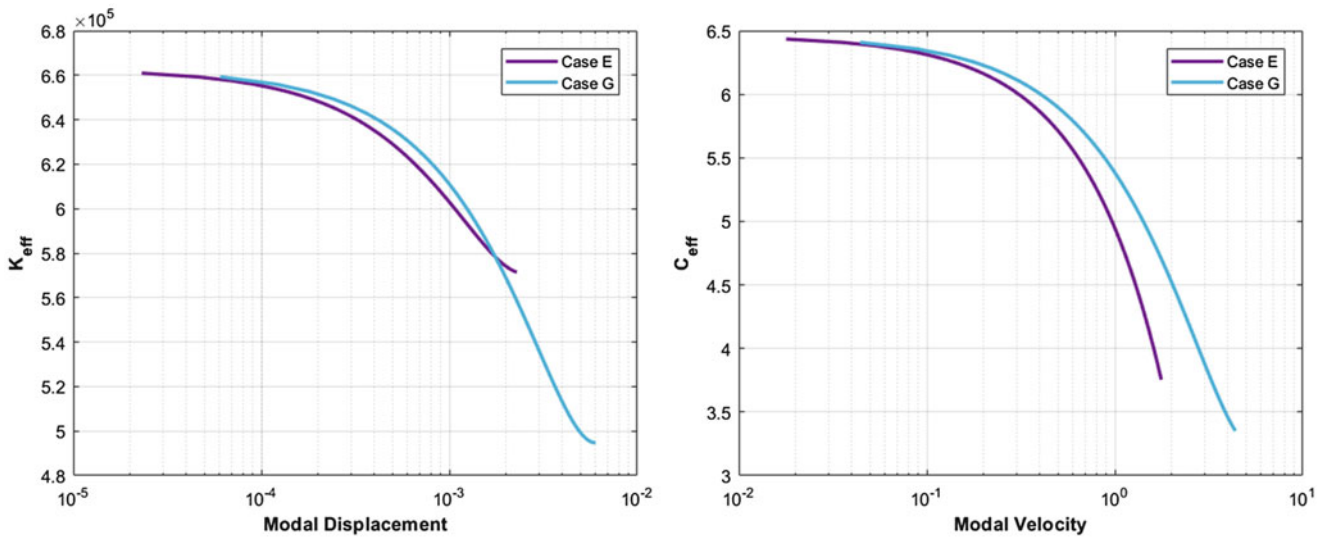


Fig. 24.19 Effective stiffness and damping for Cases E and G

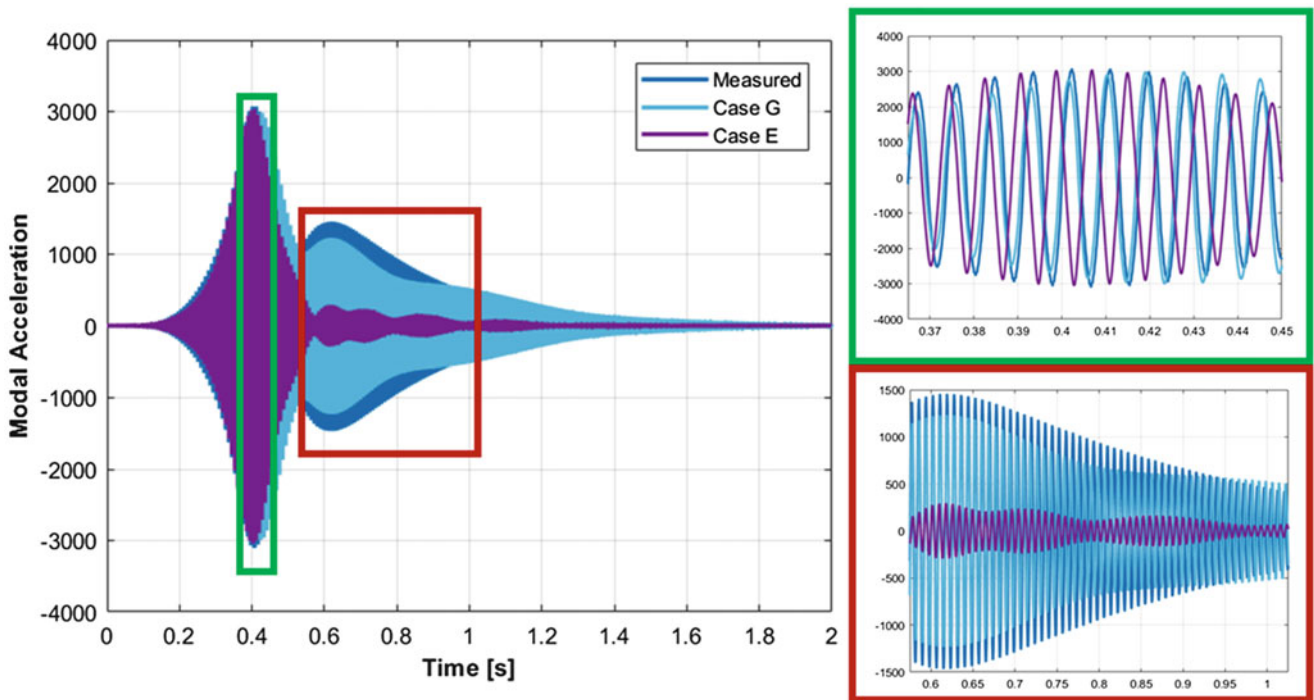


Fig. 24.20 Cases E and G simulation to Case G

24.8 Conclusions and Future Work

Nonlinear models identified from experiments are only accurate to the response amplitudes achieved during testing, thus obtaining higher modal amplitudes during experiments is very important to the versatility of the identified models. This work demonstrated new innovative techniques for optimizing modal amplitude given a specific shaker and amplifier configuration. These techniques were implemented on a bolted assembly consisting of an aluminum cylinder, plate, and beam. In previous studies, windowed sinusoidal inputs proved to be a useful excitation technique when attempting to reach high modal amplitudes in a jointed structure. In previous studies, this sinusoidal pulse was centered around the linear natural frequency. In this work, the windowed sinusoidal technique was implemented with varied window widths and center frequencies with the goal of placing more energy near the expected resonance of the structure which softened due to nonlinearity. By applying

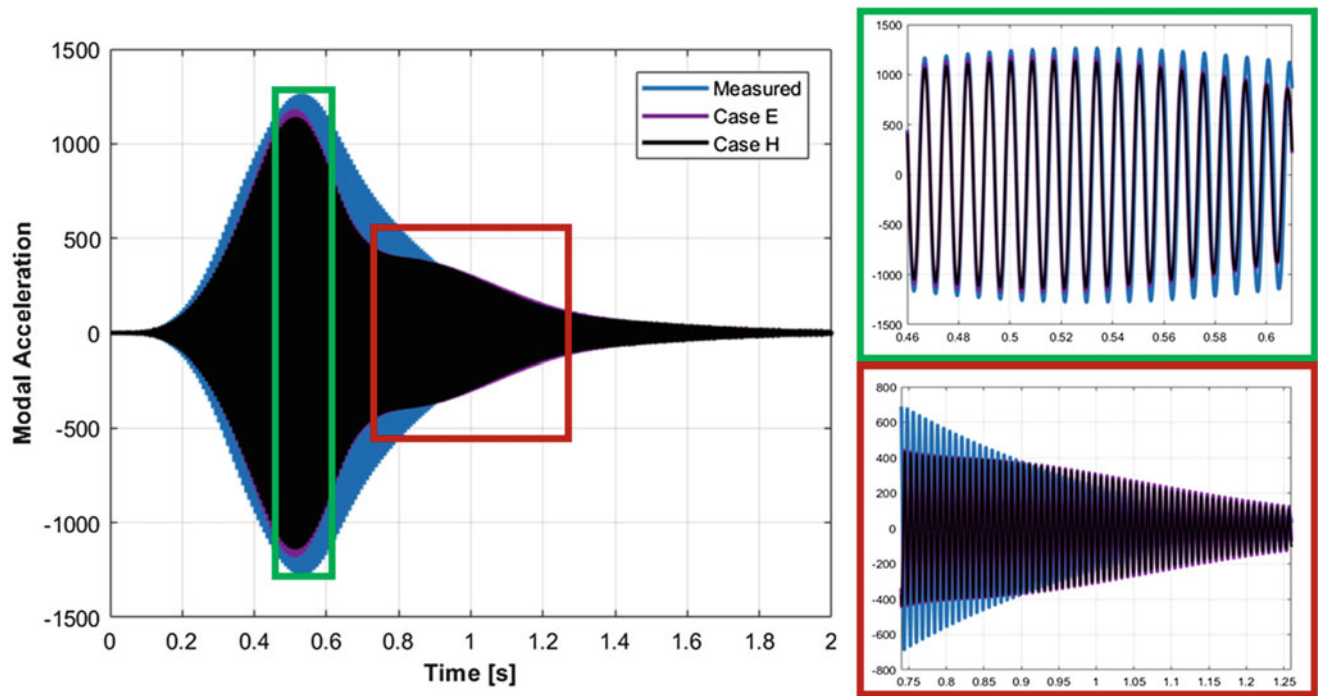


Fig. 24.21 Cases E and H simulation to Case H

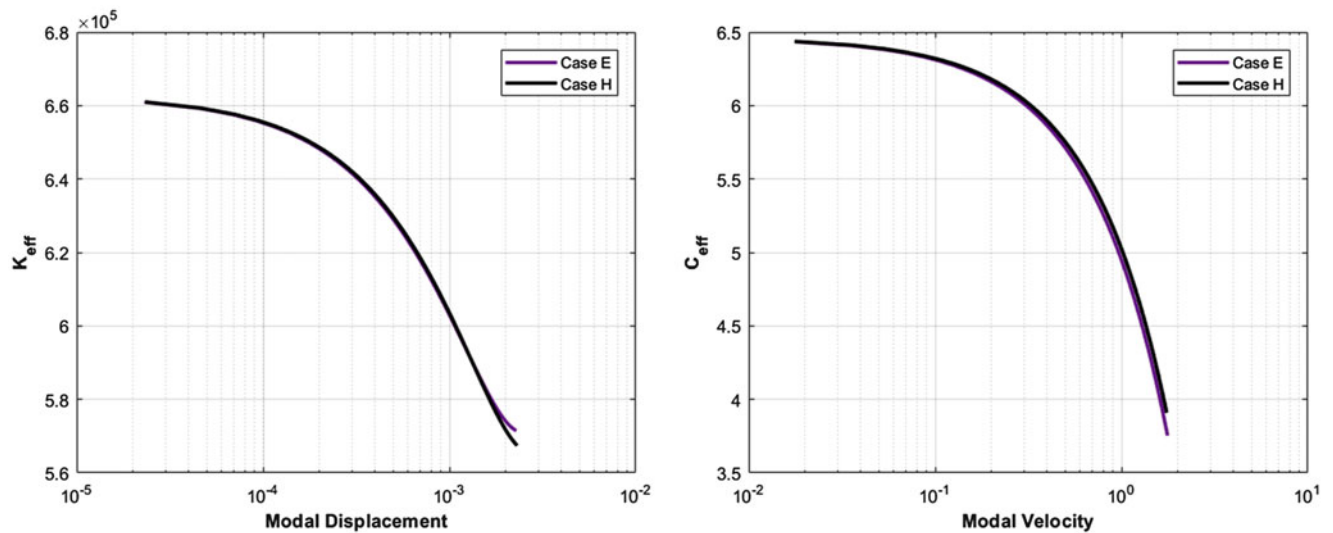


Fig. 24.22 Effective stiffness and damping for Cases E and H

a narrow window at an offset frequency, the modal amplitude achieved double that of previous tests using the same set-up. Additional optimization could be performed to increase the amplification to even higher levels and is of interest for future work. This amplification is significant as it means natural excitations slightly off of linear resonance can still lead to large response due to a nonlinearity in the structure.

A restoring force surface technique was applied to identify several nonlinear models from experiments with different load cases to capture the nonlinearity of the structure for the mode of interest. It was shown that the model identified from a standard windowed sinusoidal excitation was equivalent to that of the new technique, provided, they both excite the system to the same modal amplitude. Additionally, a model identified from a data set with even higher modal amplitude provided a quality fit for the standard excitation providing a model more versatile of multiple excitation configurations.

Notice: This manuscript has been authored by National Technology and Engineering Solutions of Sandia, LLC, under Contract No. DE-NA0003525 with the U.S. Department of Energy/National Nuclear Security Administration. The United States Government retains and the publisher, by accepting the article for publication, acknowledges that the United States Government retains a non-exclusive, paid-up, irrevocable, world-wide license to publish or reproduce the published form of this manuscript, or allow others to do so, for United States Government purposes.

References

1. Segalman, D.: A Modal Approach to Modeling Spatially Distributed Vibration Energy Dissipation. Sandia National Labs SAND2010-4763, Albuquerque, NM (2010)
2. Deaner, B.J.: Modeling the Nonlinear Damping of Jointed Structures Using Modal Models. Masters of Science Thesis: University of Wisconsin, Madison (2013)
3. Roettgen, D., Allen, M.: Nonlinear characterization of a bolted, industrial structure using a modal framework. *Mech. Syst. Signal Process.* **84**, 152 (2016)
4. Pacini, B.R., Mayes, R.L., Owens, B.C., Schultz, R.: Nonlinear Finite Element Model Updating, Part I: Experimental Techniques and Nonlinear Modal Model Parameter Extraction. In: International Modal Analysis Conference XXXV, Garden Grove, CA (2017)
5. Mayes, R.L., Pacini, B.R., Roettgen, D.R.: A Modal Model to Simulate Typical Structural Dynamic Nonlinearity. In: International Modal Analysis Conference XXXIV, Orlando, FL (2016)
6. Segalman, D.J.: A Four-Parameter Iwan Model for Lap-Type Joints. *J. Appl. Mech.* **72**, 752–760 (2005)
7. Roettgen, D., Pacini, B., Mayes, R., Schoenherr, T.: Experimental-Analytical Substructuring of a Complicated Jointed Structure Using Nonlinear Modal Models. In: International Modal Analysis Conference XXXVI, Orlando, FL (2018)
8. Eriten, M., Kurt, M., Luo, G., Vakakis, A.: Nonlinear system identification of frictional effects in a beam with a bolted joint connection. *Mech. Syst. Signal Process.* **39**, 245–264 (2013)
9. Kerschen, G., Worden, K., Vakakis, A., Golinval, J.C.: Past, present and future of nonlinear system identification in structural dynamics. *Mech. Syst. Signal Process.* **20**(3), 505–592 (2006)
10. Spottswood, S., Allemang, R.: On the investigation of some parameter identification and experimental modal filtering issues for nonlinear reduced order models. *Exp. Mech.* **47**, 511–521 (2007)
11. Harris, F.: On the use of windows for harmonic analysis with the discrete fourier transform. In: Proceedings of the IEEE (1978)



Chapter 25

Influences of Modal Coupling on Experimentally Extracted Nonlinear Modal Models

Benjamin J. Moldenhauer, Aabhas Singh, Phil Thoenen, Daniel R. Roettgen, Benjamin R. Pacini, Robert J. Kuether, and Matthew S. Allen

Abstract Research has shown that mechanical structures can be modeled as a combination of weakly nonlinear uncoupled modal models. These modal models can take many forms such as a basic cubic stiffness and damping force model, or a modal Iwan model. This method relies on two assumptions: (1) the mode shapes of the structure are not amplitude dependent, and (2) the modes of the structure do not couple or interact in the amplitude range of interest. Recently, a hypothesis was proposed that when multiple modes are excited that exercise the same nonlinear joint, the modes begin to couple. This hypothesis is tested on a physical system using a series of narrow-band excitation techniques via a modal shaker and broad-band excitation from a modal hammer. The resulting amplitude dependent stiffness and damping from the various excitation types are used to characterize the degree of modal coupling. Significant modal coupling is observed between three of the low order modes of a cylindrical structure with a beam connected to a plate on its end, which exhibits nonlinearity due to micro-slip in bolted joints.

Keywords Modal coupling · Nonlinear modal model · Iwan model · Nonlinear simulation · Hilbert analysis · Nonlinear reduced order models

25.1 Introduction

Mechanical structures with jointed interfaces are common in modeling and design due to ease of assembly and the difficulty in producing single part structures. These jointed interfaces introduce nonlinearity to structural dynamic response in the form of frictional energy dissipation caused by microslip in low pressure contact regions. This behavior affects the frequency and damping characteristics observed in the mechanical response of the global system, which is difficult to model and requires advanced computational and experimental techniques to characterize.

Modal analysis is the most utilized approach for non-destructive experimental testing to determine natural frequencies and damping ratios of built-up systems. For linear analysis, it is proven that the modes of vibration are amplitude independent and can be superimposed due to their orthogonality properties. For pseudo—nonlinear modal analysis, it is assumed that the nonlinearity primarily affects damping and does not alter the mode shapes; thus, the linear modes are assumed to remain uncoupled and can be used to decouple nonlinear data, as shown by Eriten et al. [1]. However, recent studies have demonstrated that the coupling between modes is nonnegligible and can lead to inaccurate nonlinear models [2]. This work drives to challenge the uncoupled mode assumption by experimentally measuring modal coupling behavior in a controlled testing environment. Multimodal structural response is passed through a modal filter to approximate a single degree of

Sandia National Laboratories is a multimission laboratory managed and operated by National Technology and Engineering Solutions of Sandia, LLC., a wholly owned subsidiary of Honeywell International, Inc., for the U.S. Department of Energy's National Nuclear Security Administration under contract DE-NA-0003525.

B. J. Moldenhauer (✉) · A. Singh · M. S. Allen
Department of Engineering Physics, University of Wisconsin, Madison, WI, USA
e-mail: bmoldenhauer@wisc.edu

P. Thoenen
Department of Mechanical Engineering, University of Southern California, Los Angeles, CA, USA

D. R. Roettgen · B. R. Pacini · R. J. Kuether
Sandia National Laboratories, Albuquerque, NM, USA

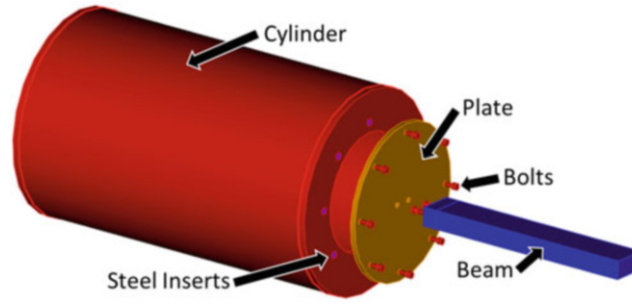


Fig. 25.1 A schematic of the Cylinder – Plate – Beam (CPB)

freedom response, which is then analyzed with the Hilbert Transform, as described by Feldman [3], to extract the amplitude dependent natural frequency and damping ratio for each mode. These modal characteristics serve as the metrics for evaluating the influence of modal coupling.

The structure of interest is the Cylinder–Plate–Beam (CPB) benchmark structure, which consists of an aluminum cylinder with an end plate and a cantilever beam, as shown in Fig. 25.1. The small joint interface between the plate and beam is presumed to be essentially bonded, as the beam is attached via two steel bolts and an adhesive. Thus, most nonlinearity in the system is assumed to be frictional damping in the large, continuous interface between the plate and cylinder flange.

To capture the modal coupling within this system, the first three elastic modes, the soft and stiff cantilever beam modes and the first drum mode of the end plate, are excited both independently and simultaneously. In this work, windowed sinusoids from a modal shaker [4] and modal hammer impacts are used to excite these CPB modes. By comparing the nonlinear response from each, the degree of coupling can be quantified, as detailed in the results that follow.

25.2 Experimental Theoretical Background

25.2.1 Pseudo – Modal Models

Linear motion in structural dynamics implies that the response of the system is linearly proportional to the excitation amplitude and the modal frequency and damping is constant with respect to response amplitude. A typical linear system can be denoted by Eq. (25.1) where M , C , and K are the mass, damping and stiffness matrices, respectively, F is the physical input force vector, and $x(t)$ is the physical motion of the system.

$$[M]\ddot{x}(t) + [C]\dot{x}(t) + [K]x(t) = \{F\} \quad (25.1)$$

A modal filter can transform the physical motion to a set of single degree of freedom (SDOF) modal systems as shown in Eqs. (25.2) and (25.3), where $q(t)$ is the modal response as described in [5–7]. The modal filter consists of the system linear mass normalized mode shapes.

$$\ddot{x}(t) = \Phi\ddot{q}(t) \rightarrow \ddot{q}(t) = \Phi^\dagger\ddot{x}(t) \quad (25.2)$$

$$\ddot{q}_r(t) + 2\zeta_r\omega_r\dot{q}_r(t) + \omega_r^2q_r(t) = \Phi^T\{F\} \quad (25.3)$$

A nonlinear pseudo–modal model introduces a nonlinear term into Eq. (25.3) as shown in the following equation.

$$\ddot{q}_r(t) + 2\zeta_r\omega_r\dot{q}_r(t) + \omega_r^2q_r(t) + F_{nl}(\dot{q}_r, q_r) = \Phi^T\{F\} \quad (25.4)$$

This model assumes:

1. The mode shapes of the structure are amplitude independent
2. Mode shapes do not couple or interact, and no energy is transferred between modal DOF

Using these assumptions, the linear mode shapes can decouple nonlinear response of the system into a modal response. However, if significant interactions between modes are introduced, i.e. modal coupling, these assumptions fail and cannot accurately capture the nonlinear behavior of the system. The nonlinear terms added to the linear equations of motion (EOM) could incorporate additional stiffness and damping that are functions of the response of other modes.

25.2.2 Hilbert Analysis

Linear modal analysis is used to capture the modal parameters (i.e. mode shapes, frequencies, and damping) of a time invariant system. However, for systems that depict nonlinearities, Hilbert Analysis is widely used to depict the amplitude dependent frequency and damping behavior [8–10] of a SDOF response. If the modes can be sufficiently uncoupled to yield SDOF modal equations for the r^{th} mode, the response envelope can be described as a sum of the decaying harmonic response and its Hilbert transform as governed by

$$Q_r(t) = q_r(t) + i\tilde{q}_r(t) \quad (25.5)$$

where $\tilde{q}_r(t)$ is the Hilbert transform of the signal $Q_r(t) = A(t) \exp(i\psi(t))$, $A(t)$ is the magnitude of the envelope and $\psi(t)$ is the instantaneous phase of the modal response.

Using that equation, the nonlinear amplitude dependency can be described through the modal damping and stiffness as a function of amplitude. As a result, the instantaneous damped natural frequency and the instantaneous damping ratio can be described as derivatives of the phase and amplitude, respectively, where $\omega_r = \omega_{r,damped}/\sqrt{1 - \zeta_r^2}$.

$$\omega_{r,damped} = \frac{d\psi(t)}{dt} \quad (25.6)$$

$$-\omega_r \zeta_r = \frac{dA(t)}{dt} \quad (25.7)$$

An extended overview of the Hilbert transformation and its application to modal analysis can be found in Feldman [3]. In this work, the Hilbert transformation is used to determine the amplitude dependent modal parameter behavior of experimental system response from windowed sinusoid shaker testing and modal hammer impacts.

25.3 Experimental Methodology

25.3.1 Test Structure

The Cylinder – Plate – Beam (CPB) structure, depicted in Fig. 25.2, is manufactured from 6061-T6 aluminum and anodized for aesthetic reasons. The structure consists of an 18// long, 11// diameter hollow cylinder in which eight steel inserts are press-fit into the flange on each end. The interior of the cylinder was lined with foam to mitigate any acoustic resonances of



Fig. 25.2 A side view of the Cylinder – Plate – Beam (CPB)

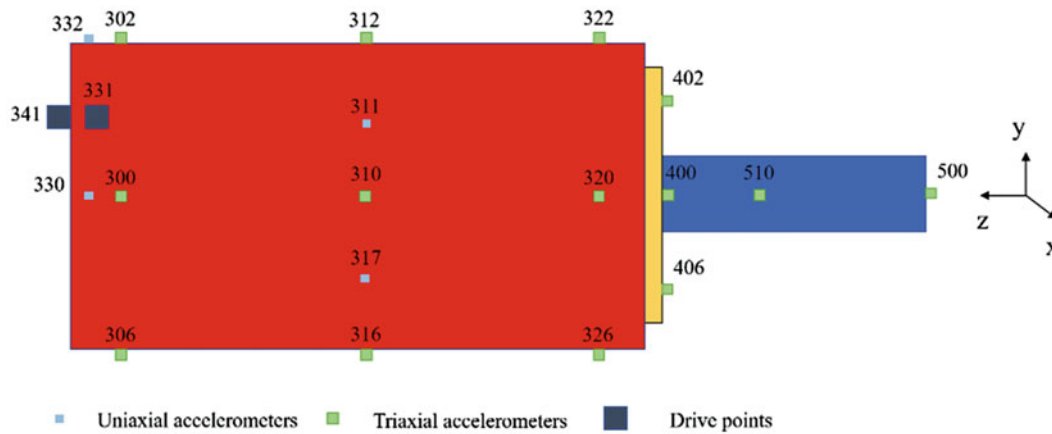


Fig. 25.3 CPB Accelerometer Layout. Green denotes triaxial, blue are uniaxial, and black are uniaxial accels underneath a force transducer to serve as shaker drive points

Table 25.1 Experimental natural frequencies and damping ratios

	Mode 1	Mode 2	Mode 3
Natural frequency (Hz)	121.2	155.7	548.8
Damping ratio (%)	0.206	0.325	0.247

the cylinder that could interfere with the recorded responses. An 8.5// diameter \times 0.25// thick plate is attached to the cylinder flange using eight steel bolts, threaded into the steel inserts to a torque of 50 in-lbs. A 1// \times 2// \times 12// beam is bolted to the plate using two bolts as well as bonded with dental cement to minimize contact nonlinearities at this particular interface. The intent of this was to localize any nonlinear behavior in the response to the large contact area between the plate and cylinder flange.

Twenty-six accelerometers, eighteen triaxial and eight uniaxial, are placed on the structure according to engineering judgement, as shown in Fig. 25.3. Accelerometers on flat faces were attached with superglue while those on the curved wall of the cylinder were mounted with dental cement to better bond to the non-flat surface. Point 341, on the cylinder flange and in the axial direction, was selected as the shaker drive point since the first three modes of the CPB, the target modes, could all be easily excited from this location. The accelerometer response data was recorded in LMS Test.Lab™ software with an 88 channel LMS SCADAS frontend. In order to achieve a fine time domain resolution, a bandwidth of 12,800 Hz was used with 65,536 frequency lines, leading to a time sample increment of 39.0625 μ s.

25.3.2 Linear Testing

To collect the linear modal parameters for the CPB, low level burst random excitation from the shaker was utilized to avoid exciting any nonlinearity in the cantilevered beam modes and drum mode of the end plate. The resultant linear FRFs, a composite of which is shown below in Fig. 25.4, were curve fit using the Algorithm of Mode Isolation (AMI) [11] in MATLAB, producing the natural frequencies and damping ratios contained in Table 25.1, and mass normalized mode shapes, representations of which are given in Fig. 25.5.

25.3.3 Nonlinear Shaker Testing

To obtain nonlinear response data, the shaker was used to excite the CPB via the setup shown in Fig. 25.6. The aluminum stinger connecting the shaker to the CPB was set to have a free length of 1.5// to maximize separation between the CPB and the shaker while keeping the first stinger buckling mode above the frequency range of interest.

To excite the CPB, the shaker was supplied with signal traces to create windowed sinusoidal inputs, or a sine beat [12]. These signals are a sine wave of specified frequency and sample rate passed through a Blackman-Harris window [13], resulting in a signal of definable width in the frequency domain. For example, the signal used to excite the first mode is

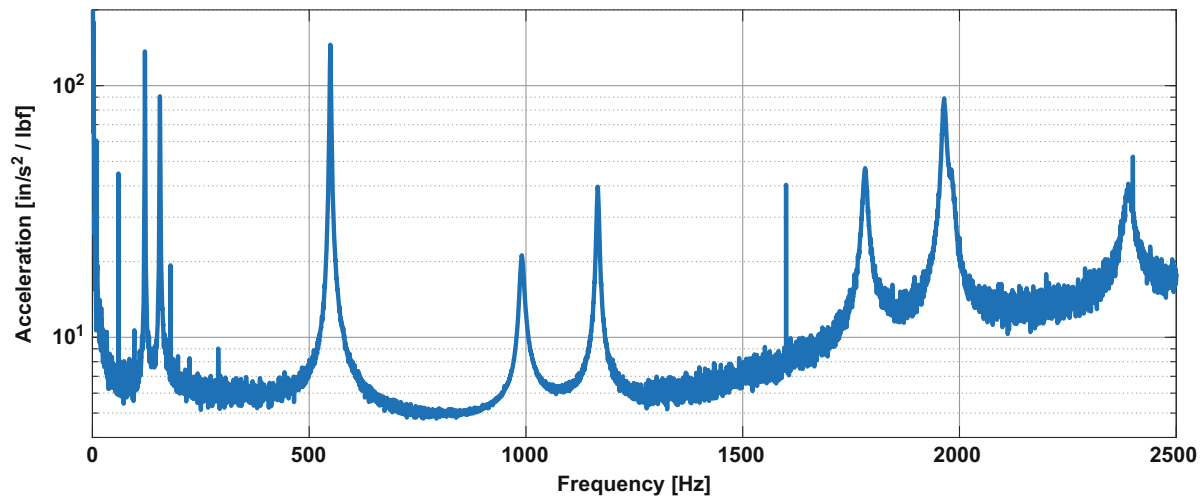


Fig. 25.4 Composite FRF from a low level burst random shaker test of the CPB

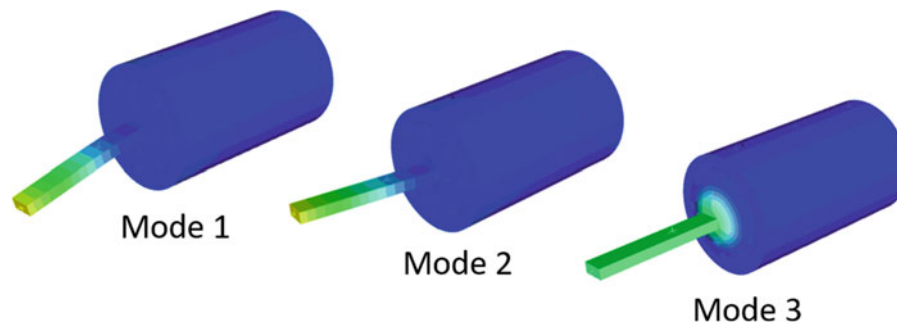


Fig. 25.5 The first three elastic modes of the CPB

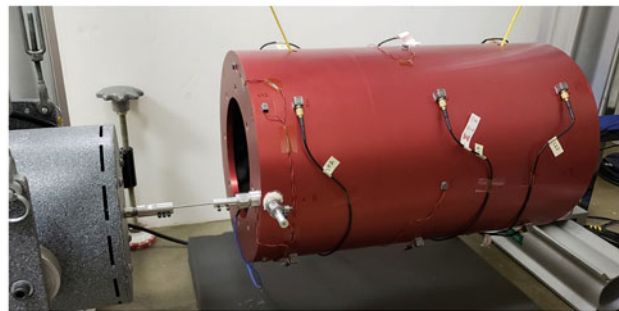


Fig. 25.6 Experimental Setup, showing the shaker, CPB, and the stinger connecting them

shown in Fig. 25.7. The time trace on the left shows the windowed sine wave, while its FFT on the right shows that the frequency content contained in the signal is centered at the natural frequency and has a maximum width of 60 Hz. A 30 Hz roll off to either side of the natural frequency was chosen to produce a peak wide enough to continually excite the mode as the natural frequency shifts due to nonlinear effects, while narrow enough to only significantly excite the mode of interest.

The goal of this work is to study whether the test specimen exhibits a different nonlinear response when a single mode is excited versus when multiple modes are excited. To excite two modes simultaneously, the same process was completed on each mode, with the windowed signals then added and superimposed. To exemplify this, the signal created to excite mode 1 and mode 2 is shown in Fig. 25.8.

Windowed sine excitations were defined for each mode individually and for each pairing between the first three modes, or modes 1 & 2, 1 & 3, and 2 & 3. For the individual modes, peak voltages of 7.0, 5.6, 3.5, and 1.4 volts were used. A maximum of 7 volts was set due to the shaker amplifier at predetermined settings being unable to accept above this level

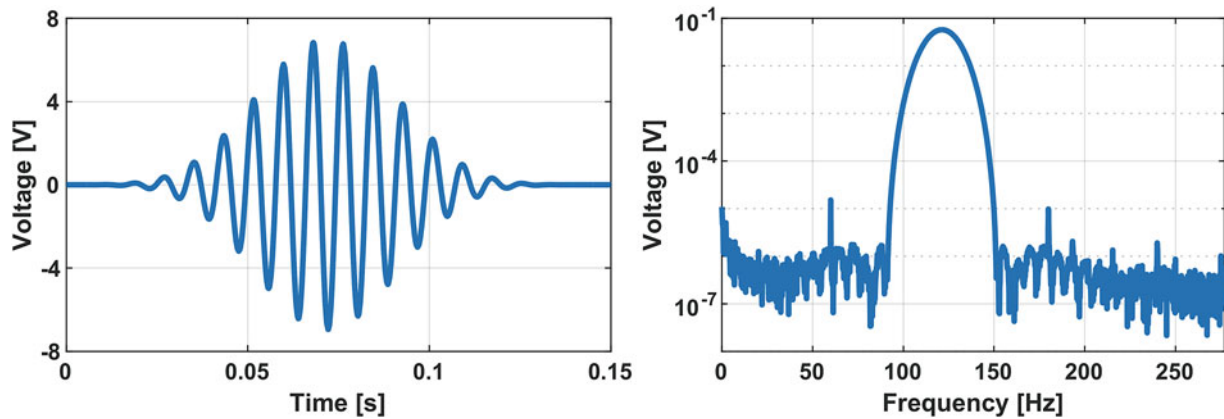


Fig. 25.7 Voltage signal sent to produce a windowed sine centered on mode 1

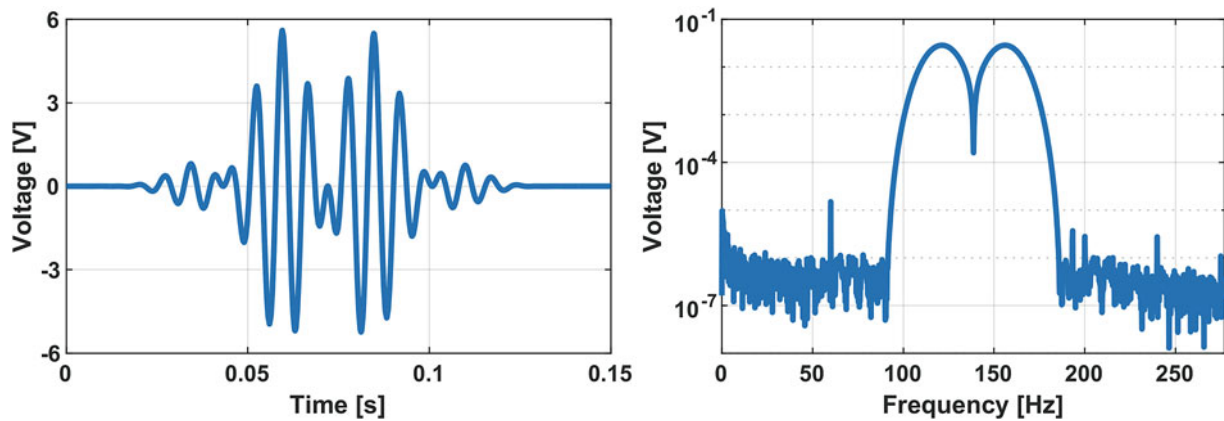


Fig. 25.8 Voltage trace used to simultaneously excite modes 1 and 2

Table 25.2 Test Matrix showing all the test cases and voltages used

Mode 1	Mode 2	Mode 3	Modes 1 & 2		Modes 1 & 3		Modes 2 & 3	
1.4 V	1.4 V	1.4 V	1.4 V	1.4 V	1.4 V	1.4 V	1.4 V	1.4 V
3.5 V	3.5 V	3.5 V	3.5 V	1.4 V	3.5 V	1.4 V	3.5 V	1.4 V
5.6 V	5.6 V	5.6 V	1.4 V	3.5 V	1.4 V	3.5 V	1.4 V	3.5 V
7.0 V	7.0 V	7.0 V	3.5 V	3.5 V	3.5 V	3.5 V	3.5 V	3.5 V
			5.6 V	1.4 V	5.6 V	1.4 V	5.6 V	1.4 V
			1.4 V	5.6 V	1.4 V	5.6 V	1.4 V	5.6 V

without clipping the signal. The subdivisions below 7 V were set to provide several intermediary excitation levels to compare the response from each. The mode pairs were performed with various combinations of these voltage levels, as shown in Table 25.2. This was done to collect data with modes at different relative excitation levels, which could cause varying degrees of modal coupling.

25.3.4 Shaker Experimental Results

After performing all the necessary windowed sine excitations, the recorded time responses from the accelerometers were imported into MATLAB. This physical domain data was transferred to the modal domain by a modal filter, using the mass normalized mode shapes from the linear tests. This produces an approximately SDOF response for each mode, which can then be analyzed via the Hilbert Transform to acquire the amplitude dependent natural frequency and damping ratio. For the isolated modes 2 and 3, excited at various voltage levels, the Hilbert curves for damping ratio and natural frequency versus

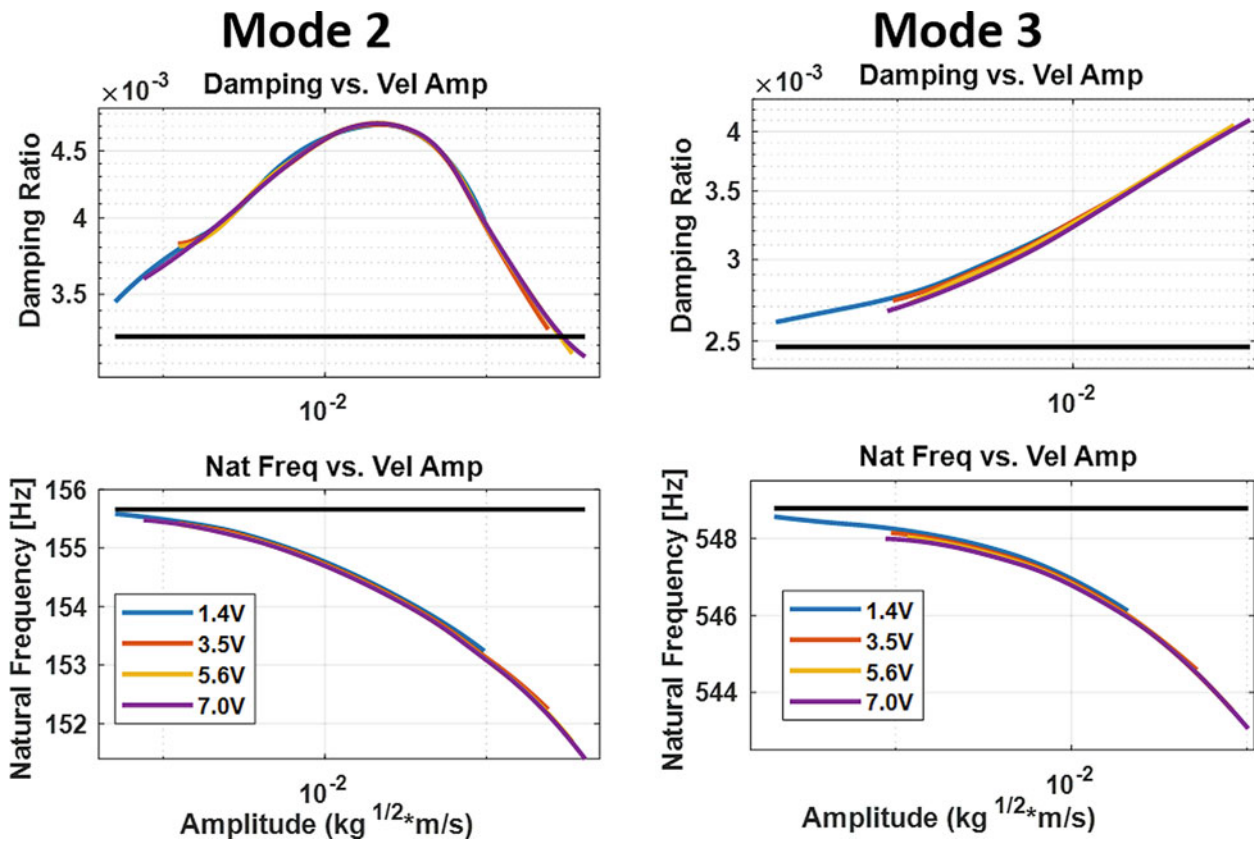


Fig. 25.9 Damping Ratio & Natural Frequency vs. Velocity Amplitude for (Left) Mode 2 and (Right) Mode 3 at various excitation levels. The horizontal black line represents the linear value

modal velocity amplitude are shown in Fig. 25.9; mode 1 results closely resemble mode 2 and are consigned to Appendix A, Fig. 25.15, for brevity.

In these figures, the horizontal black line represents the linear modal value, as determined from curve fitting a low level burst random test performed immediately prior to the windowed sinusoid tests. This value was found to agree with results from a curve fit of an additional low level burst random performed immediately after the windowed sines, signifying that the linear system did not significantly change during the test. At low amplitude, the Hilbert curves converge toward the expected linear value, while as amplitude increases, the natural frequency gradually decreases for all three modes. For mode 3, damping is observed to continually increase, while modes 1 and 2 experience an initial increase and then decrease in damping value, which may be indicative of macro-scale slip in the joint. However, all three modes follow their same trend in frequency and damping over all four excitation levels, in that the curves overlay. This signifies that, while the modes exhibit clearly nonlinear attributes, these effects are consistent and repeated excitations at various levels do not alter the system characteristics.

When exciting two modes simultaneously, the modally filtered response results in two SDOF responses that can be analyzed with the Hilbert Transform. Figure 25.10 shows the response of mode 2 when it is excited together with mode 1. The dashed line represents the response of an isolated mode 2, while the other lines represent the various combinations of mode 1 and 2 excitation. In the legend, the numbers are the voltage level of the mode with respect to the order given at the beginning of the entry. As the excitation of mode 1 increases relative to the mode 2 excitation, the Hilbert curves deviate further from the isolated baseline. The decrease in natural frequency becomes much more prominent and the damping curves seem to shift to the left, where the damping is increasing at lower amplitudes. These changes can be interpreted as follows: mode 2 has a certain damping nonlinearity when it is excited in isolation, which comes about because a larger fraction of the joint area slips as mode 2's amplitude increases. When mode 1 is also excited, this apparently puts the joints into a state of slip that is greater than what they would experience if mode 2 was excited alone, and so mode 2's apparent stiffness decreases and its damping increases. A similar trend is visible in the mode 1 response when mode 2 is excited, as shown in Fig. 25.16. Specifically, when mode 2 is excited to a higher level than mode 1, the mode 1 response deviates away from the isolated baseline.

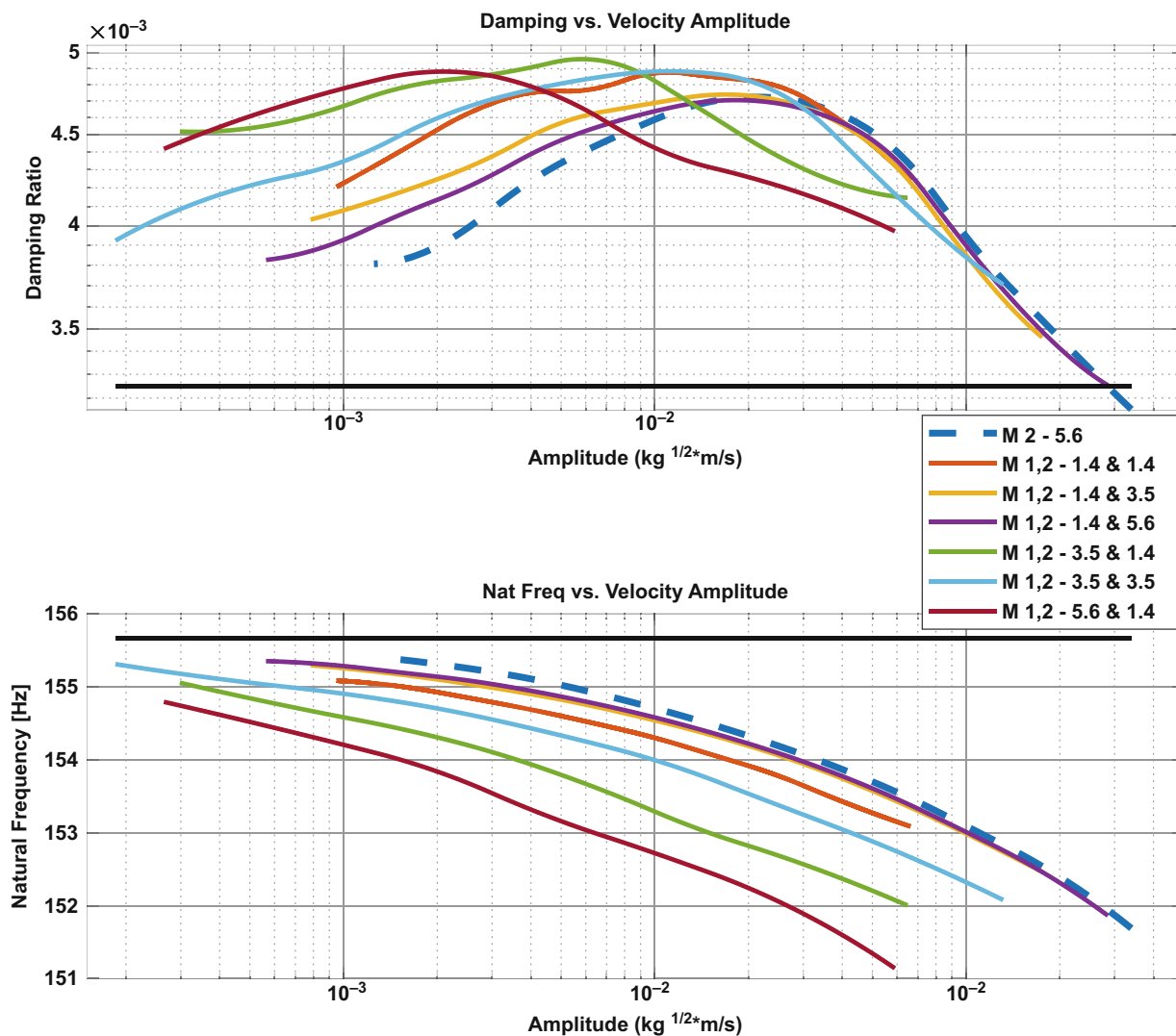


Fig. 25.10 Mode 2 response when modes 1 and 2 are excited simultaneously

Figure 25.11 shows the mode 2 response when mode 3 is also excited. This case does not show any significant change in natural frequency while also displaying a very slight decrease in damping for all the mode pair levels. This reveals that modes 2 and 3 are not significantly coupled, and perhaps arises because these modes exercise the joints in a way such that they do not influence the stiffness/damping of the other mode. Mode 1 also does not exhibit any reaction to mode 3 excitation, as shown in Fig. 25.17. These results indicate that modes 1 and 2, the first two cantilevered beam modes of the CPB, have some degree of modal coupling, while both seem to be independent of Mode 3, the drum mode of the plate.

Seemingly contrary to the previous statement, large deviations in the mode 3 response are observed when mode 2 is simultaneously excited, as seen in Fig. 25.12. Any degree of mode 2 excitation causes the mode 3 response to deviate from its isolated state, again given by the dashed line. Also, the various cases with the same mode 2 voltage level are grouped together, as in all three 1.4 V and both 3.5 V cases show very similar responses. A comparable scenario is observed when mode 1 is also excited, as shown in Fig. 26.18. As the mode 1 or 2 excitation increases, the mode 3 response exhibits consistently decreasing natural frequency and increasing damping.

Thus, while modes 1 and 2 both affect the response of the other, mode 3 seems to have little to no effect on modes 1 and 2, while mode 3 is greatly affected by modes 1 and 2. This would indicate that there is some degree of modal coupling present between all three modes, but to varying degrees. An explanation for this could simply be the dynamics of the physical motion associated with each mode. As seen in Fig. 25.5, modes 1 and 2 are first cantilever beam modes acting in perpendicular directions, but with the same mass. For both modes to be simultaneously excited, each must act against the inertia associated with the other. This will produce some degree of diagonal motion, changing how to beam contacts the plate at the root, thus

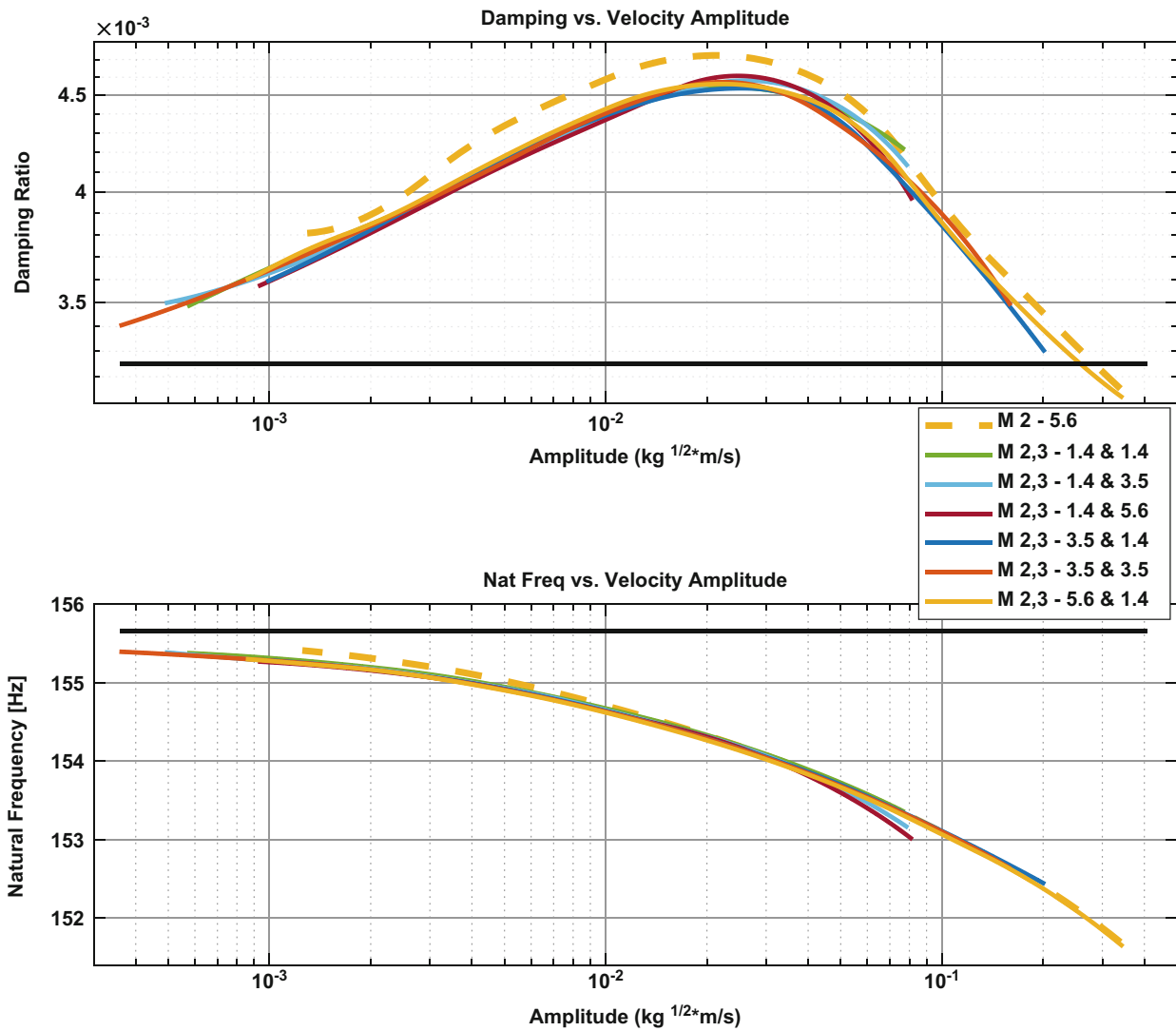


Fig. 25.11 Mode 2 response when modes 2 and 3 are excited simultaneously

slightly altering the characteristics of the modes. For mode 3, it likely doesn't affect the beam modes because the beam is rooted at the center of the plate. This location is a nodal point in the plate drum mode shape; the cantilevered motion of modes 1 and 2 are unperturbed by the root of the beam translating axially. However, it is the transverse motion of the beam in modes 1 and 2 that causes the drastic shifts in mode 3. As the beam oscillates, the plate flexes and warps under it, distorting the shape of the drum mode and thus how the plate contacts the cylinder flange. This range of dynamic interaction could be the cause of the modal coupling observed in the experimental data shown above.

25.3.5 Nonlinear Hammer Testing

Immediately following the shaker testing, a modal hammer was used to excite the CPB under the same boundary conditions, i.e. the same environment and with the shaker still attached. The CPB was impacted beside the shaker drive point to directly compare with the shaker results and at the tip of the beam in all three directions to directly excite each mode. As with the shaker data, the physical response was passed through a modal filter before performing Hilbert analysis. Figure 25.19 contains plots of typical hammer input, physical response, and modal response in the time and frequency domain. The resultant Hilbert curves for mode 2 due to the various impact cases are shown in Fig. 25.13, where the dashed line shows the response due to a windowed sinusoidal excitation from the shaker. In terms of natural frequency, all the impact responses

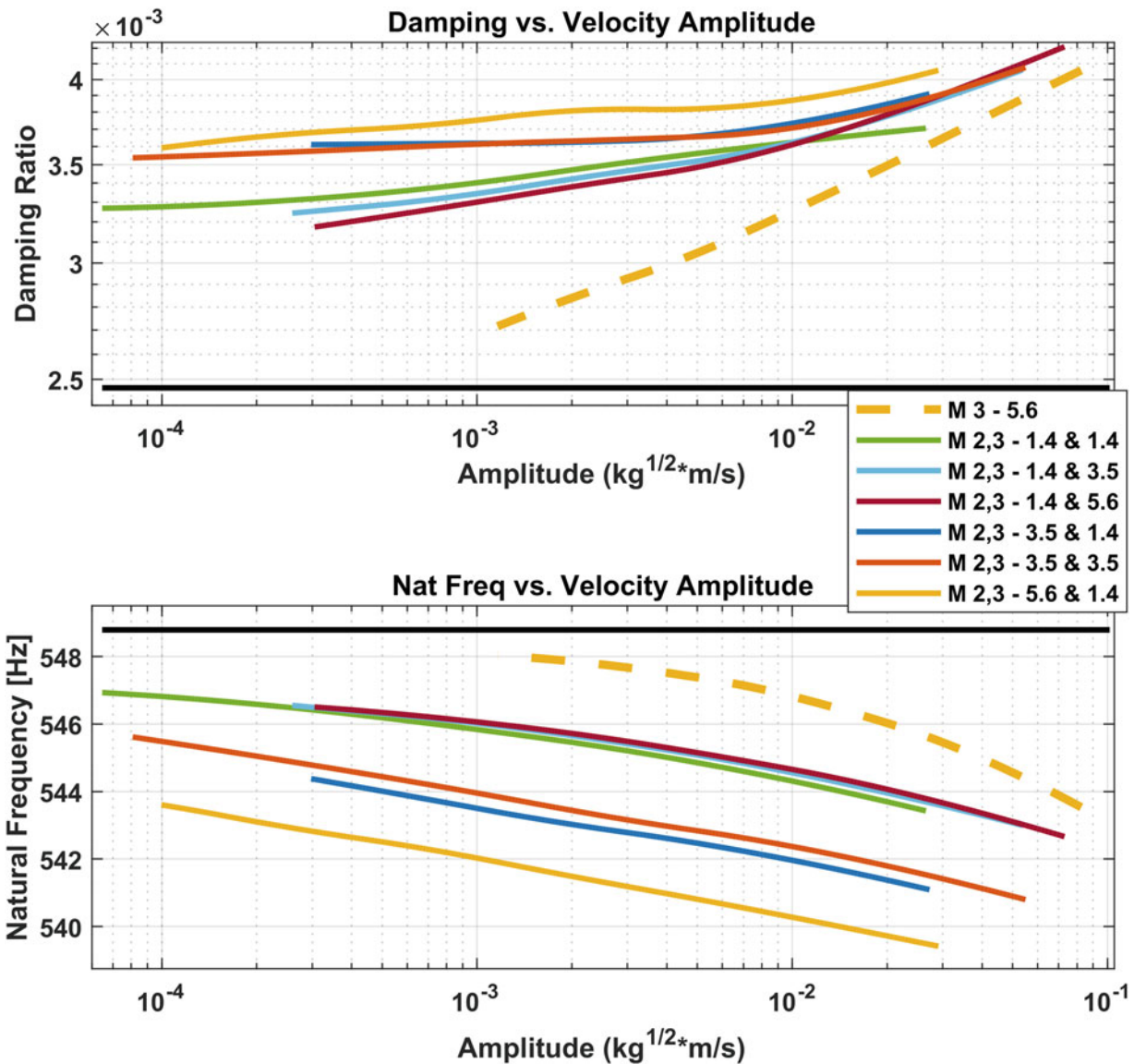


Fig. 25.12 Mode 3 response when modes 2 and 3 are excited simultaneously

overlay with the shaker results throughout the entire amplitude range. For damping, the impact excitation responses generally show the same curve profile as found in the shaker data, but at a lower magnitude. When impacting at the end of the beam, the damping converges toward the linear damping found in the low level burst random shaker data. Also, as the impact force level increases at the point near the shaker drive point, the damping curves seem to converge toward what is observed in the shaker response curve. The data for mode 1 again displays similar results to mode 2 and is shown in Fig. 25.20.

The Hilbert response curves for mode 3 are shown below in Fig. 25.14. In this case, only the very low force level impacts match the shaker results for natural frequency and show similar, or lower damping levels. As the excitation level increases, the response deviates further from the linear values and the shaker response curve. This agrees with what was observed in the shaker data when mode 3 was excited simultaneously with modes 1 or 2. The same is true here, as the broadband frequency content imparted by the modal hammer excites all modes up to several thousand Hertz, depending on the force level.

These results strongly correlate to those found from the shaker excitation. This shows that the effects of modal coupling can be observed under different excitation techniques, and thus, cannot be avoided by simply choosing a different excitation method.

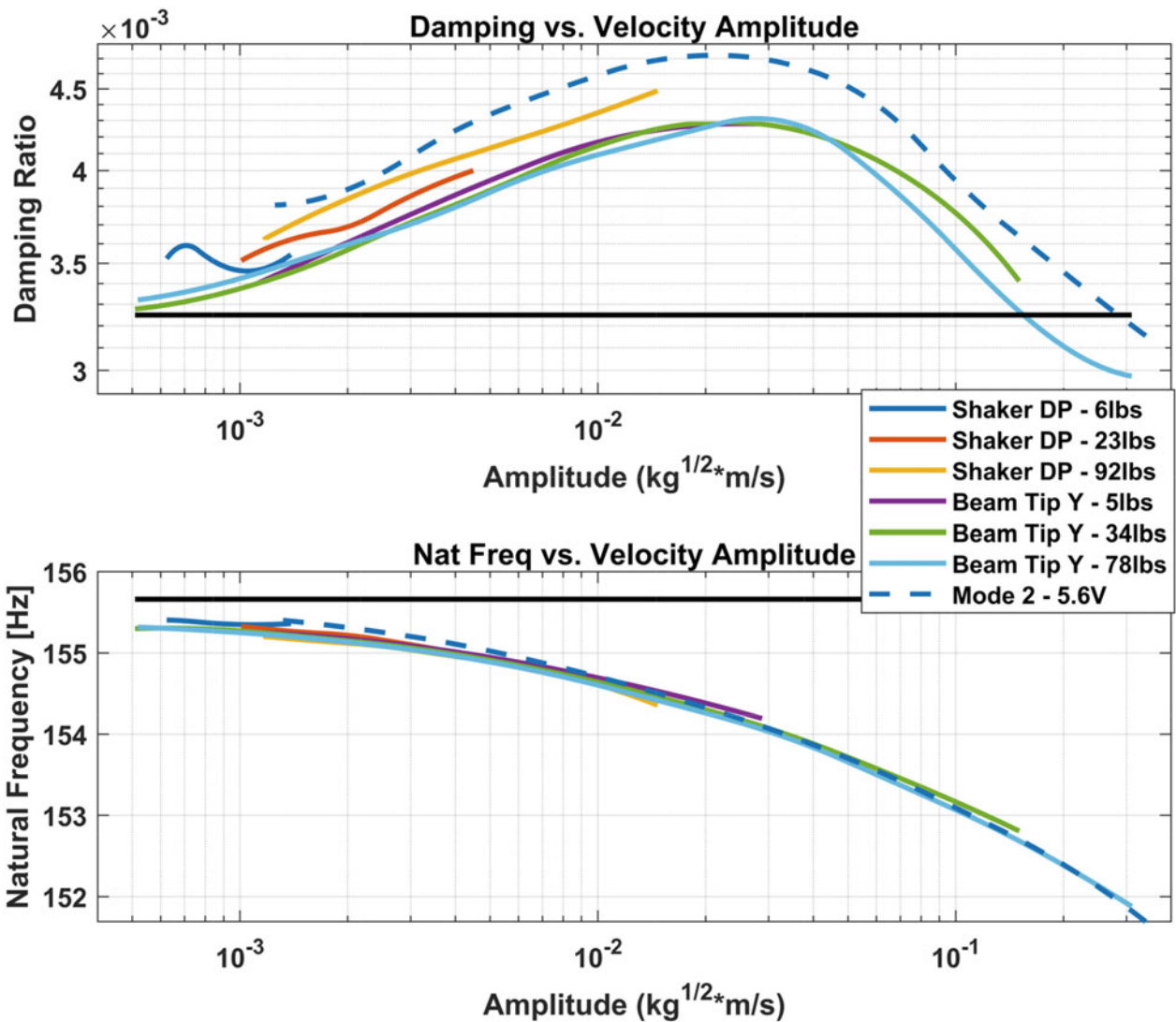


Fig. 25.13 Mode 2 response to various impact locations and force levels

25.4 Conclusions

The purpose of this work was to experimentally characterize a structure and establish a dataset that depicted modal coupling. To acquire this experimental data, a new Cylinder-Plate-Beam structure was manufactured and instrumented. Low-level shaker testing was done to identify baseline linear modal parameters, such as natural frequency, damping ratio, and mass normalized mode shapes. For nonlinear data, windowed sinusoidal excitations were completed at various excitation levels on each mode individually and on pairs of modes simultaneously. Modal hammer testing was also done at several locations and force levels to collect impact excitation response. After passing the physical response from each test case through a modal filter and performing Hilbert Analysis on the single degree-of-freedom modal responses, amplitude dependent natural frequency and damping ratio curves were found for each mode. For the isolated modes excited at various shaker levels, the curves were found to overlay, implying that while each is nonlinear, the corresponding response is consistent over the observed range and is independent of initial excitation. However, when Modes 1 and 2 are excited simultaneously, the Hilbert curves for each deviate from the isolated baseline as the relative excitation of the other increases. Such a relationship was not observed with either of these modes when Mode 3 was also excited. Conversely, Mode 3 was observed to vastly deviate from its isolated baseline when Modes 1 or 2 were also excited. Similar trends were also observed in the nonlinear modal hammer impact responses. Thus, the experimental data collected indicates that some degree of modal coupling is present and observable between the first three modes of the structure.

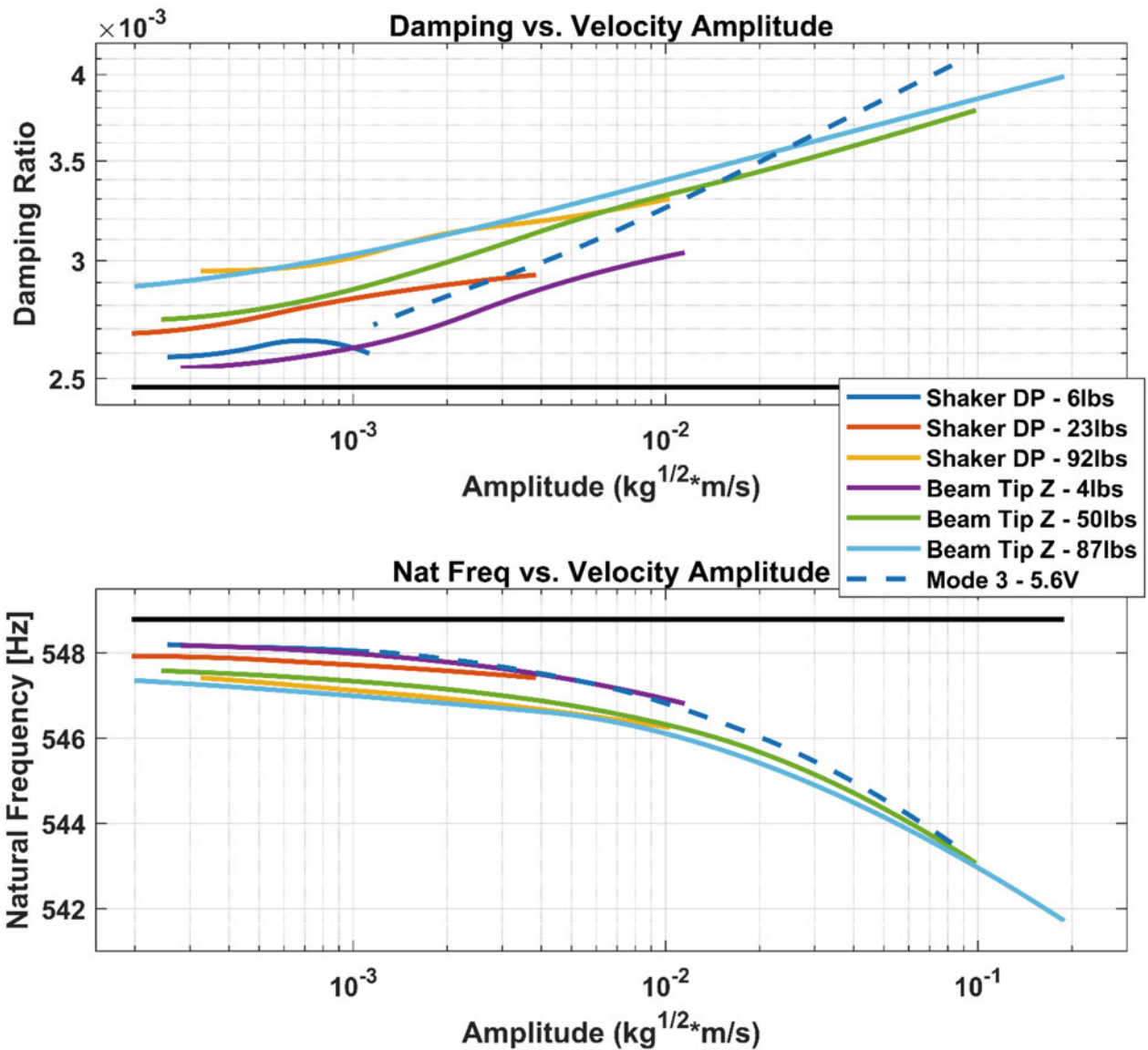


Fig. 25.14 Mode 3 response to various impact locations and force levels

Future work will seek to further understand these results by better quantifying the degree to which each mode was excited in the coupled responses and to understand what types of models can be used to capture the observed coupling. We have also begun to create a high-fidelity model that characterizes the interface using whole joint elements to represent each bolt. It also may be possible to create a model that reproduces the experimental data by using Restoring Force Surface Analysis Method [13–15] to fit quadratic/cubic stiffness and damping models to the measurements. Experimentally, additional mode pairings that include higher order modes could be examined. Expanding beyond pairs, groups of three or more modes could be excited simultaneously with windowed sinusoids.

Acknowledgments This research was conducted at the 2018 Nonlinear Mechanics and Dynamics (NOMAD) Research Institute supported by Sandia National Laboratories. Sandia National Laboratories is a multi-mission laboratory managed and operated by National Technology and Engineering Solutions of Sandia, LLC., a wholly owned subsidiary of Honeywell International, Inc., for the U.S. Department of Energy’s National Nuclear Security Administration under contract DE-NA-0003525. The authors would also like to thank Bill Flynn from Siemens Industry Software NV for supplying the data acquisition and testing systems used to collect the experimental measurements presented throughout this work.

Appendix A—Additional Shaker Hilbert Plots

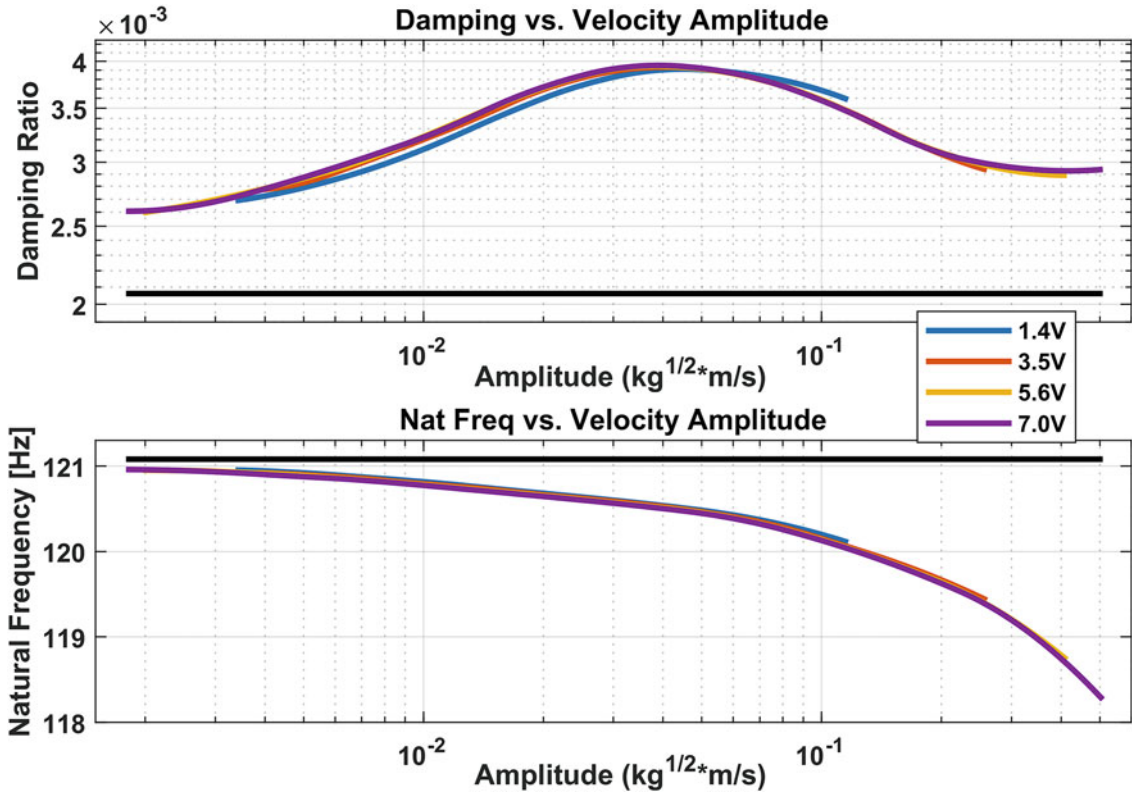


Fig. 25.15 Mode 1 response at various excitation levels

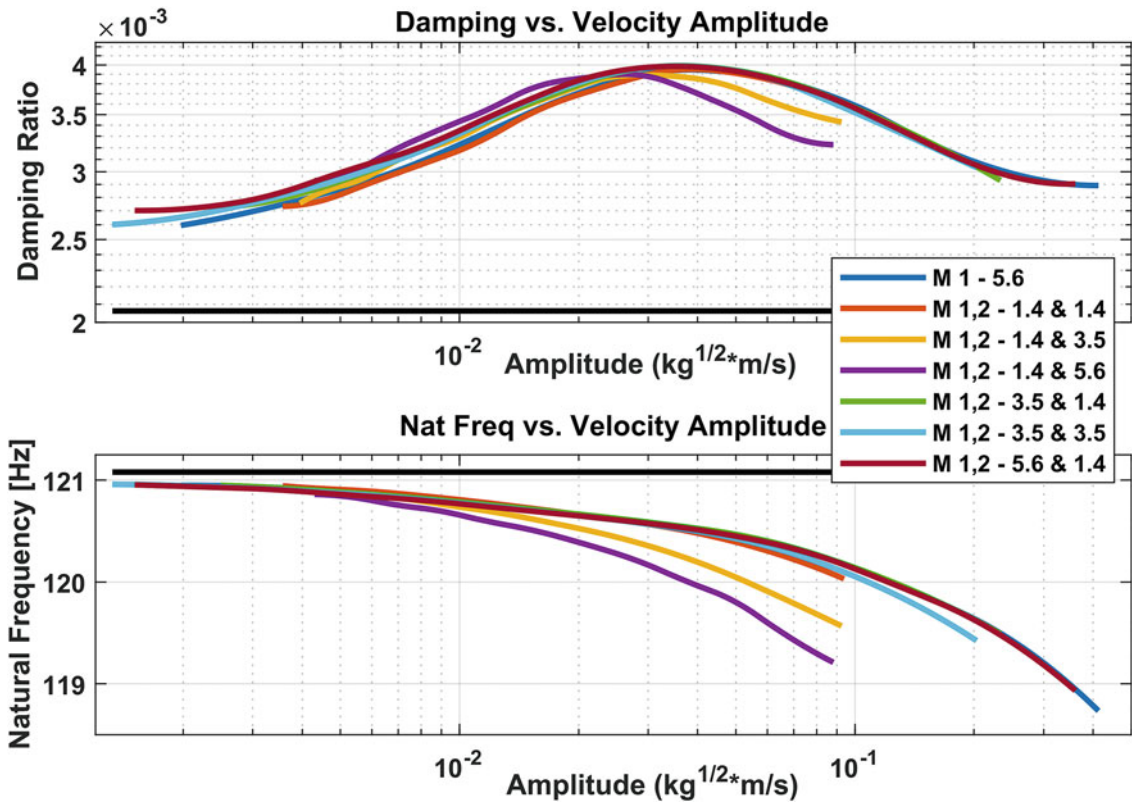


Fig. 25.16 Mode 1 response when modes 1 and 2 are excited simultaneously

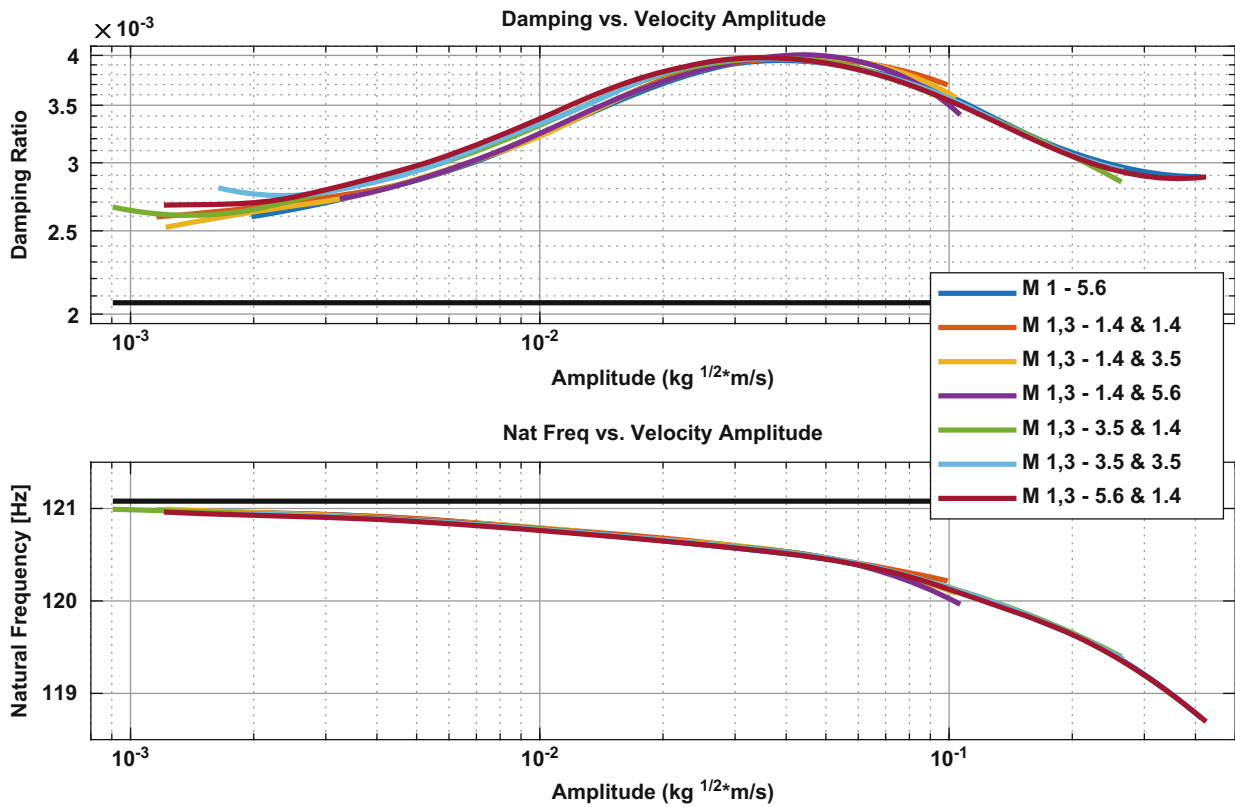


Fig. 25.17 Mode 1 response when modes 1 and 3 are excited simultaneously

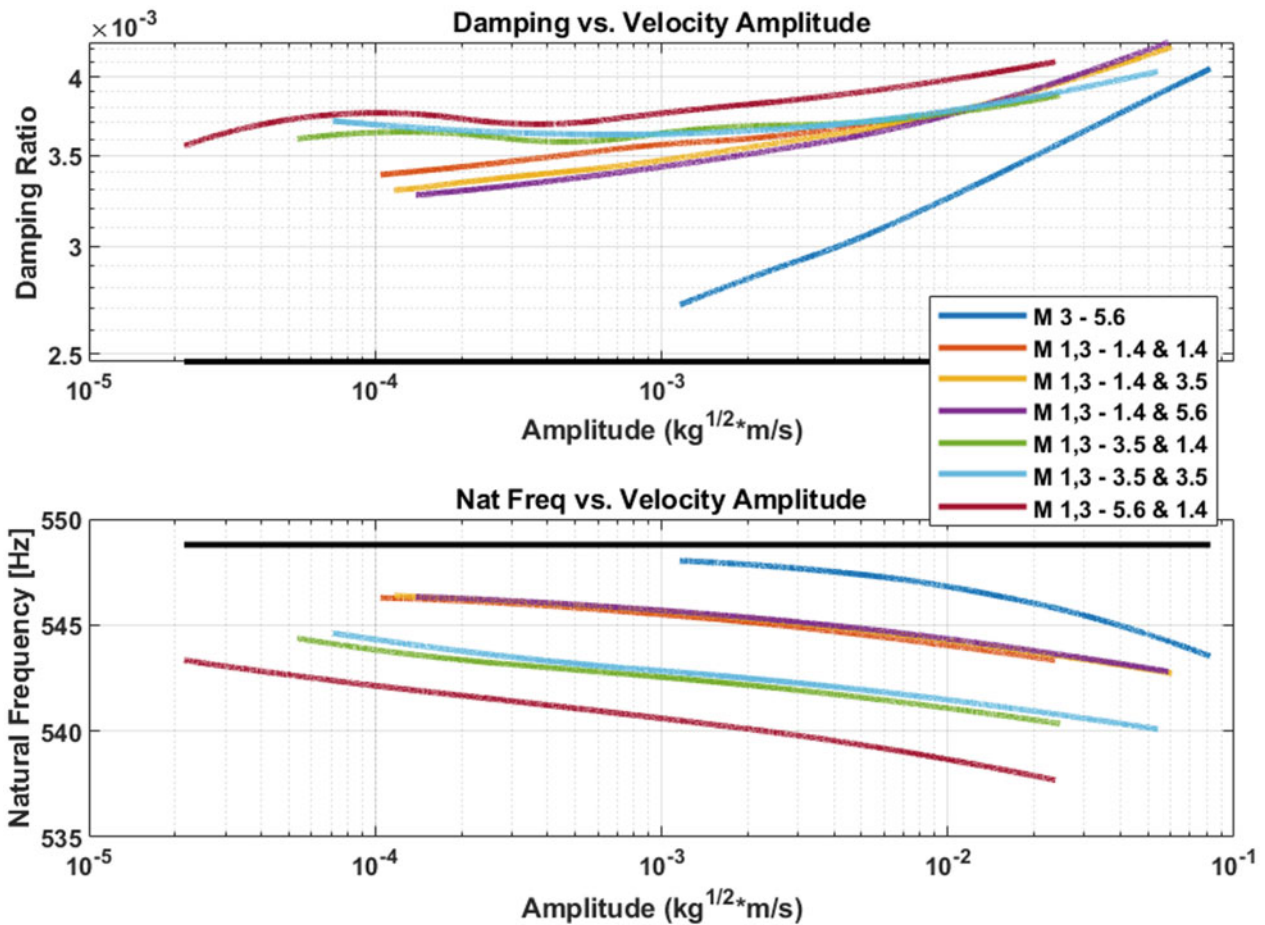


Fig. 25.18 Mode 3 response when modes 1 and 3 are excited simultaneously

Appendix B—Additional Hammer Data Plots

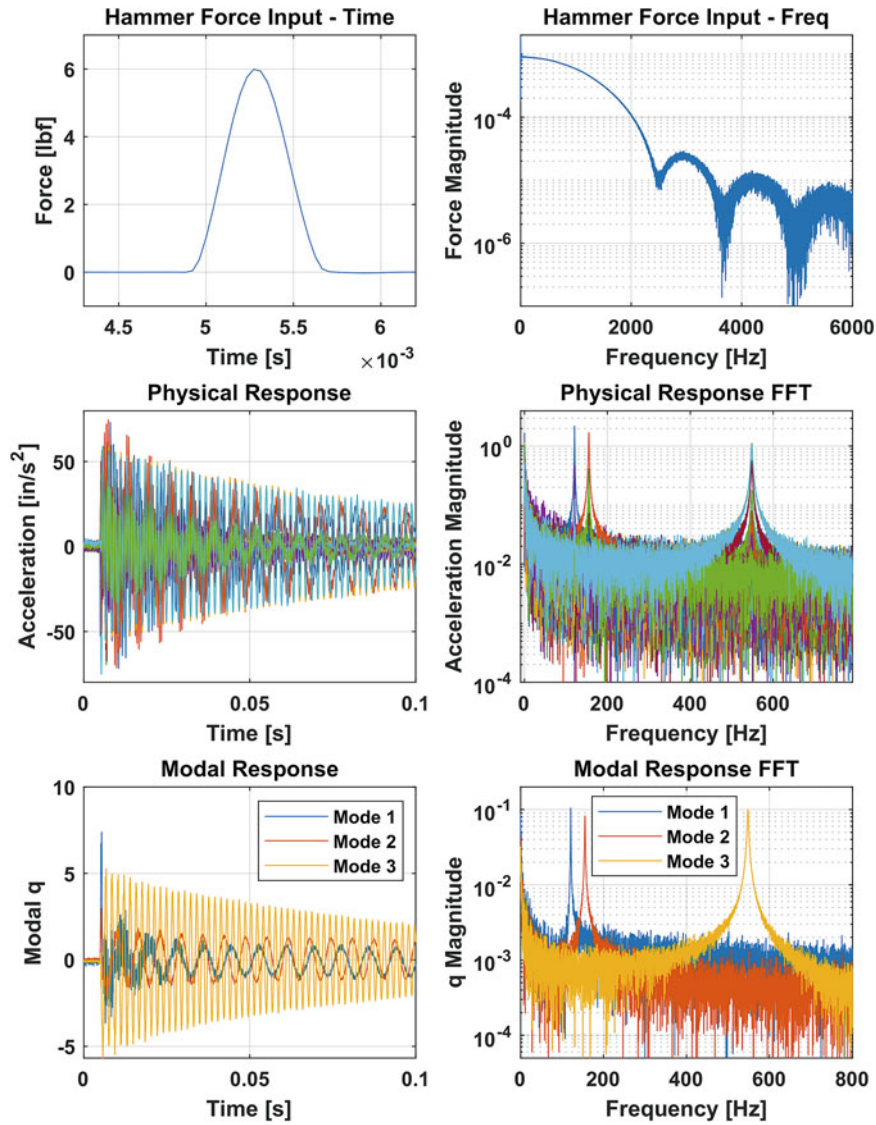


Fig. 25.19 Example of hammer, physical, and modal response in time and frequency domains

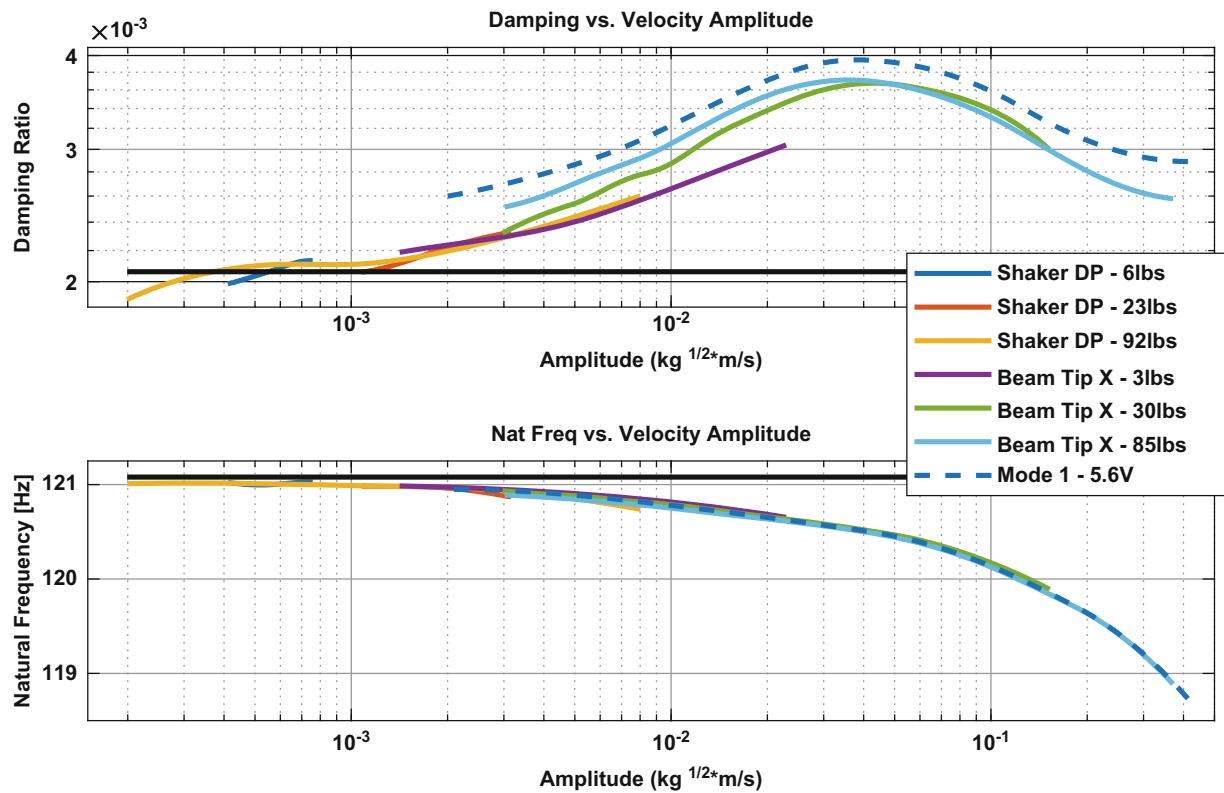


Fig. 25.20 Mode 1 response to various impact locations and levels

References

1. Eriten, M., Kurt, M., Luo, G., Michael McFarland, D., Bergman, L.A., Vakakis, A.F.: Nonlinear system identification of frictional effects in a beam with a bolted joint connection. *Mech. Syst. Signal Process.* **39**(1–2), 245–264 (2013)
2. Lacayo, R., Deaner, B., Allen, M.S.: A numerical study on the limitations of modal Iwan models for impulsive excitations. *J. Sound Vib.* **390**, 118–140 (2017)
3. Feldman, M.: Non-linear system vibration analysis using Hilbert transform–I. Free vibration analysis method ‘Freevib’. *Mech. Syst. Signal Process.* **8**(2), 119–127 (1994)
4. Pacini, B.R., Mayes, R.L., Owens, B.C., R. Schultz: Nonlinear Finite Element Model Updating, Part I: Experimental Techniques and Nonlinear Modal Model Parameter Extraction. In: Presented at the International Modal Analysis Conference XXXV, Garden Grove, CA, 2017
5. Phillips, A.W., Allemang, R.J.: Single Degree-of-Freedom Modal Parameter Estimation Methods. In: Presented at the 14th International Modal Analysis Conference (IMAC-14), 1996, pp. 253–260
6. Ginsberg, J.H.: *Engineering Dynamics*, 3rd edn. Cambridge University Press, Cambridge, MA (2005)
7. Kerschen, G., Worden, K., Vakakis, A.F., Golinval, J.-C.: Past, present and future of nonlinear system identification in structural dynamics. *Mech. Syst. Signal Process.* **20**, 505–592 (2006)
8. Singh, A. et al.: Experimental Characterization of a new Benchmark Structure for Prediction of Damping Nonlinearity. In: Presented at the 36th International Modal Analysis Conference (IMAC XXXVI), Orlando, Florida (2018)
9. Yang, J.N., Lei, Y., Pan, S., Huang, N.: System identification of linear structures based on Hilbert-Huang spectral analysis. Part 1: Normal modes. *Earthq. Eng. Struct. Dyn.* **32**(9), 1443–1467 (2003)
10. Feldman, M.: Time-varying vibration decomposition and analysis based on the Hilbert transform. *J. Sound Vib.* **295**(3–5), 518–530 (2006)
11. Allen, M.S.: Global and Multi-Input-Multi-Output (MIMO) Extensions of the Algorithm of Mode Isolation (AMI). Georgia Institute of Technology, Atlanta (2005)
12. Fischer, E.G.: Sine beat vibration testing related to earthquake resonance spectra. *Shock Vib. Bull.* **42**(2), 1–8 (1972)
13. Harris, F.: On the use of windows for harmonic analysis with the discrete Fourier transform. *Proc. IEEE.* **66**(1), 51–83 (1978)
14. Worden, K., Wright, J.R., Al-Hadid, M.A., Mohammad, K.S.: Experimental identification of multi degree-of-freedom nonlinear systems using restoring force methods. *Int. J. Anal. Exp. Modal Anal.* **9**(1), 35–55 (1994)
15. Allen, M., Sumali, H., Epp, D.S.: Restoring Force Surface Analysis of Nonlinear Vibration Data from Micro-Cantilever Beams. In: Presented at the 2006 ASME International Mechanical Engineering Congress and Exposition, 2006



Chapter 26

Dynamic Response of a Curved Plate Subjected to a Moving Local Heat Gradient

David A. Ehrhardt, B. T. Gockel, and T. J. Bebernis

Abstract Structures moving faster than the speed of sound will experience localized pressure and temperature gradients due to shockwave impingement. During in-flight maneuvers, these gradients will move across the surface of the structure, causing quasi-static thermal and mechanical strains. Loading conditions in these combined environments includes complicated aero-thermal-mechanical coupling, which is difficult to replicate in laboratory conditions. This work focuses on thermo-mechanical loading of a 12 inch \times 18 inch curved stainless-steel plate when subjected to a moving thermal gradient at a peak temperature of 200 °F and distributed white noise mechanical loading at 9 g 's from 100 to 800 Hz. The dynamic response of this plate is measured with high-speed 3D digital image correlation, and the temperature distribution is measured with a high-speed FLIR camera.

Keywords Combined loading · Nonlinear dynamics · Digital image correlation · IR camera

26.1 Introduction

Air vehicles operating in high-speed environments experience sharp pressure and temperature gradients in addition to extreme acoustic and mechanical loading [1, 2]. The complicated nature of such combined loading is difficult to reproduce in a laboratory environment. For simplicity, this work explores a repeatable thermal-mechanical laboratory scale experiment.

The two aspects of loading considered in this work are mechanical and thermal. While mechanical loading is provided with established electrodynamic shaker techniques, the thermal loading used in this work is provided inductively via a uniquely designed non-contacting coil. While a majority of previous work using inductive heaters [3, 4] aims to provide isothermal, or distributed, loading across a specimen, the coil of an inductive heater can be modified to apply any shape of thermal loading as done in this work. One additional benefit of inductive heating is the small time scale in which a structure will heat up allowing the application of a moving thermal gradient.

The localization of temperature distribution and structural responses require greater spatial measurement resolution since the exact location of the peak temperature or peak response is not known. Coupling full-field mechanical and thermal measurement techniques include additional challenges. In this work, full-field response measurements are optically obtained using high-speed stereo 3D digital image correlation (3D-DIC) techniques. The surface preparation is chosen to provide high contrast in the visible light range while maintaining consistent emissivity in the infrared range allowing full-field temperature measurements with Forward-looking Infrared cameras (FLIR).

This work examines the dynamic behavior of a cylindrically curved stainless steel plate, previously examined in [5], when subjected to a moving localized thermal load and distributed base excitation. Section 26.2 describes the experimental setup and Sect. 26.3 details the current results examining the quasi-static deformation and dynamic motion of the plate.

D. A. Ehrhardt (✉)
Ehrhardt Engineering LLC, Monticello, IL, USA

B. T. Gockel · T. J. Bebernis
Air Force Research Laboratory, Dayton, OH, USA

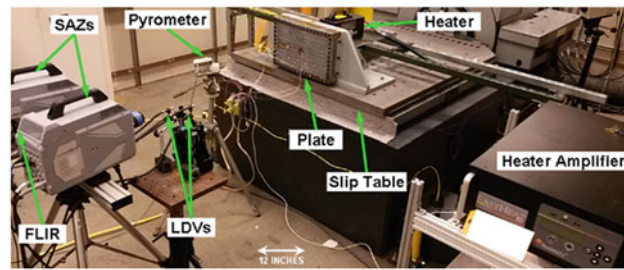


Fig. 26.1 Diagram of experimental setup

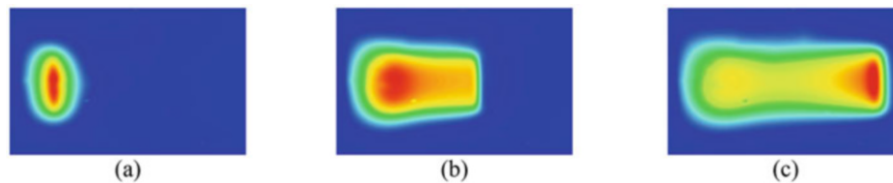


Fig. 26.2 Snapshot of the time dependent thermal gradient at (a) 0 s, (b) 33 s, and (c) 66 s

26.2 Experimental Setup

26.2.1 Introduction

The 12 inch \times 18 inch cylindrically curved stainless steel plate of interest was mounted to a slip table as shown in Fig. 26.1. This slip table, connected to a 20,000 lbf shaker, provided 100–800 Hz band limited white random noise base excitation at 9 g 's of acceleration. In addition to base excitation, a 6 kW inductive furnace was used to apply localized heating to the plate during excitation. The inductive heater was attached to a motorized linear stage which moved the heater head across the plate in 67 s. Images of the plate surface were measured at 1500 Hz using two Photron SAZ cameras and at 2 and 400 Hz using a forward looking infrared (FLIR) camera and provided full field coordinates and temperature measurements, respectively.

26.2.2 Thermal Loading

The inductive coil attached to a 6 kW furnace is placed behind the plate and suspended above the slip table as shown in Fig. 26.1. This furnace heats the article by inducing eddy currents in the material through a magnetic field via an oscillating current through a coil attached to the head of the furnace [3, 4]. For this series of tests, a coil is built to direct a magnetic field in a line along the plate and the head of the furnace is mounted to a linear stage to move the coil across the plate. The time dependent concentrated thermal gradient is controlled at 200 °F and set to traverse the plate in 67 s. However, there is lag in the controller during the temperature sweep due to the curvature of the plate and the temperature decreases to 167 °F at the center of the plate. This is demonstrated in Fig. 26.2 with snapshots of the temperature distribution presented at 0 s, 33 s, and 66 s where red to blue is high to low temperature, respectively.

26.3 Results

26.3.1 Quasi-Static Response

As the temperature gradient is moved across the plate, a quasi-static deformation is observed as shown in Fig. 26.3 at 0 s, 33 s, and 66 s. The traversing thermal gradient demonstrates the effect of simultaneous heat-up and cool-down. Prior to the heater traversing the plate, the localized steady-state deformation from the local thermal gradient (Fig. 26.2a) is shown in Fig. 26.3a. As the heater traverses the plate, the induced thermal gradient causes the quasi-static deformation of the plate to change as shown in Fig. 26.3a and b. Since the heat-up time scale of the inductive heater is shorter than the conduction/convection experienced in the plate, the final deformation (Fig. 26.3c) includes effects from the heater even though the coil has moved.

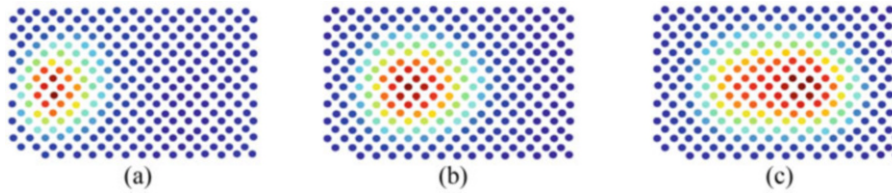


Fig. 26.3 Snapshot of the time dependent deformation of plate at (a) 0 s, (b) 33 s, and (c) 66 s

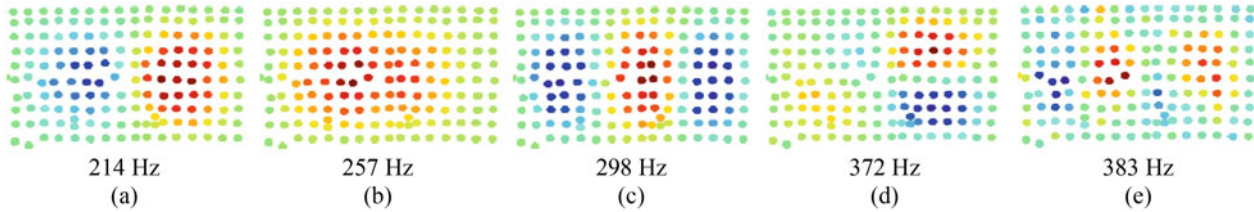


Fig. 26.4 First five linear modes of cold structure. (a) 214 Hz, (b) 257 Hz, (c) 298 Hz, (d) 372 Hz, and (e) 383 Hz

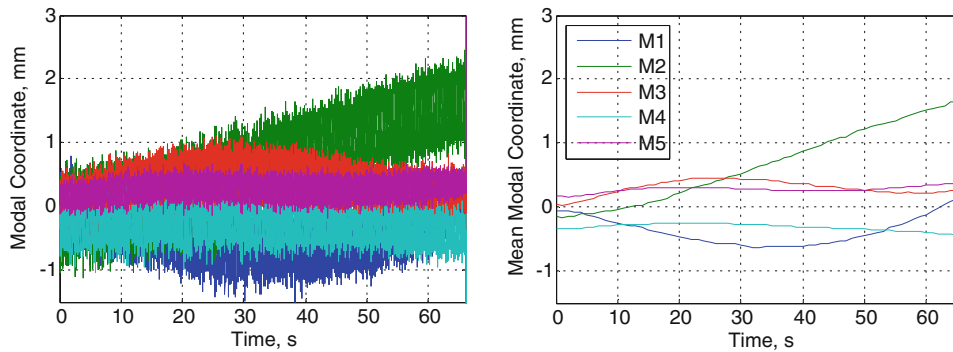


Fig. 26.5 The full-field response of the plate projected onto the first five resonance shapes of the cold structure (a) at each point in time and (b) averaged over 1 s intervals

26.3.2 Dynamic Response

Prior to heating, the curved plate is subjected to a low amplitude base excitation of $1 g$'s. Using single-value decomposition, the first five resonance shapes and frequencies are identified from the full-field displacement response measured with high-speed 3D-DIC. The first five linear resonances identified without heating correlates well with previous work [5] (Fig. 26.4).

After the initial linear tests, the base excitation is increased to $9 g$'s, which has been shown to result in nonlinear resonance behavior. The identified resonances shapes are used to project the full-field dynamic response of the hot-structure onto approximate modal coordinates as shown in Fig. 26.5a. For illustration, the mean value of the coordinate is taken at 1 s intervals and plotted in Fig. 26.5b. As the heater traverses the plate, these figures show a quasi-static change in dynamic equilibrium around which the structure vibrates (i.e. the thermal and mechanical loading affect the response of the plate at different time scales). Although the change in coordinate induced by the heater is slower than the dynamic response of the plate, the time dependent equilibrium of the plate with change the resonances of the plate.

The approximate modal coordinates shown in Fig. 26.5a are further decomposed into the frequency domain by calculating the power spectral density (PSD) of the Hanning windowed time series at 1 s intervals with 50% overlap. The resulting PSDs (Fig. 26.6) show how the approximate modal coordinates become coupled in the resonance behavior of the hot structure. Figure 26.6a shows that the first cold modal coordinate becomes coupled to the first three resonances of the hot structure as the heater traverses the plate. The level of coupling is relative to the approximate modal coordinate system and is shown from low (blue) to high (red). Each subsequent cold modal coordinate show coupling to multiple hot resonances. For example, the first hot resonance shows coupling between the first, second, and third cold modal coordinates.

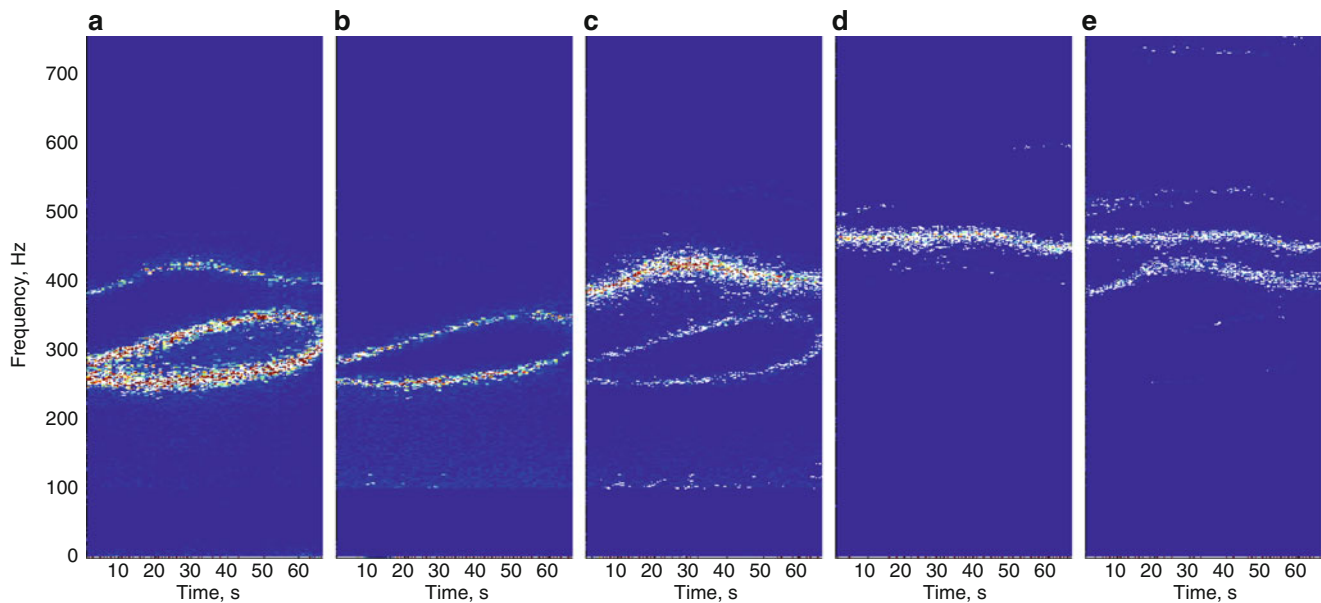


Fig. 26.6 Power spectral densities of the first five (a–e) approximate cold modal coordinates as the heater traverses the plate. The level of coupling between the cold coordinates is from low (blue) to high (red)

26.4 Future Work

Time dependent localized heating has shown a rich variation of dynamic response of the curved plate of interest. Full-field temperature and displacement measurements provide a complete picture of how the dynamic response of the plate changes throughout heating. A further examination of the appropriate modal basis is needed and additional high speed thermal effects will be explored.

References

1. Tzong, G., Jacobs, R., Liguore, S.: Predictive capability for hypersonic structural response and life prediction: phase I—identification of knowledge gaps. *Air Vehicle Integr. Technol. Res.* (2010)
2. Zuchowski, B.: Predictive capability for hypersonic structural response of life prediction: phase II—detailed design of hypersonic cruise vehicle hot-structure. *Air Vehicle Integr. Technol. Res.* (2012)
3. Zinn, S., Semiatin, S.L.: *Elements of induction heating: design, control, and applications*. ASM International, Metals Park, OH (1988)
4. Gockel, B.T., Kolesar, R.S., Rollett, A.D.: Experimental study of an aerospace titanium alloy under various thermal and tensile loading rate conditions. *Integr. Mater. Manuf. Innov.* **5**, 13 (2016)
5. Gordon, R.W., Hollkamp, J.J.: Reduced order models for acoustic response prediction. Air Force Res. Lab. (2011)



Chapter 27

A Test-Case on Continuation Methods for Bladed-Disk Vibration with Contact and Friction

Z. Saeed, G. Jenovencio, S. Arul, J. Blahoš, A. Sudhakar, L. Pesaresi, J. Yuan, F. El Haddad, H. Hetzler, and L. Salles

Abstract Bladed-disks in turbo-machines experience harsh operating conditions and undergo high vibration amplitudes if not properly damped. Friction at the blade-to-blade or blade-to-disk interfaces plays a key role in dampening the high amplitudes. Due to the inherent complexity of these structures and non-linearities introduced by the friction joints, accurate response prediction becomes very difficult. There are variety of methods in the literature to predict non-linear vibration due to contact friction. However, their application to the bladed-disks remains limited. Furthermore, there are not many 3D realistic test-cases in the open literature for testing those methods and serve as a benchmark. A bladed-disk representative of a real turbine is presented as an open numerical test-case for the research community. It is characterized by a blade root joint and a shroud joint. The bladed-disk sector is meshed in different ways along with component mode synthesis (CMS) model order reduction for onward non-linear computations. The steady-state solution is obtained by multi-Harmonic Balance method and then continuation method is employed to predict the non-linear frequency response. Thus, it can serve as a case for testing previous and new methods as well as a benchmark for comparative studies.

Keywords Bladed-disk · Cyclic symmetry · Nonlinear forced response · MHBM · Continuation method

27.1 Introduction

Turbo-machine components design is a great challenge in the presence of multitude of problems. High cycle fatigue of the rotating blades is one of those problems and requires that accurate modelling of the forced response is done including the damping from all the possible sources [1]. Contact friction at the blade-roots or shrouds (or under-platform dampers) provides some damping but it is highly non-linear. Different solution approaches in the literature have been presented in a period of over two decades, comprising of friction models as well as iterative solutions, for example [2–4].

In spite of various advanced models and methods developed for prediction of friction damping, their application to the bladed-disks remains limited due to their inherent complexity and large number of degrees of freedom (DOF). On the other hand, access to a real geometry with some experimental data also remains a big concern due to confidentiality and competitiveness of the industries. Sometimes, choosing a particular model is based on current practices of the institutions or as a call of faith, instead of the comparative knowledge basis. Therefore, a test-case geometry of blade assembly for the FUTURE project (2009–2012) [4] is used in this study and open-access modules are developed ranging from building the system matrices, model order reduction, harmonic balance method with continuation steps to penalty based friction models with a possibility to include fretting and wear. Such a modular framework might already be in a more advanced form with

Z. Saeed (✉)
Politecnico di Torino, Turin, Italy
e-mail: zeeshan.saeed@polito.it

G. Jenovencio
Technical University of Munich, Garching, Germany

S. Arul · A. Sudhakar
IT4I National Supercomputing Center, Ostrava, Czech Republic

J. Blahoš · L. Pesaresi · J. Yuan · F. El Haddad · L. Salles
Imperial College London, London, UK

H. Hetzler
University of Kassel, FG Technische Dynamik, Kassel, Germany

some industries and research institutions, but falls under confidentiality agreements. As a baseline work, modules on state-of-the-art methods have been developed and tested on simple cases.

27.2 Methodology and Analysis

The approach to solution of the aforementioned problem is followed using coupled static and dynamic multi-harmonic balance method [5]. Due to cyclic nature of the structure and excitation encountered by a bladed-disk, only a sector is considered for modelling using cyclic symmetry boundary conditions, as shown in Fig. 27.1a. The system matrices of the sector, discretized with finite elements (FE), undergoing subsequent refining for convergence of static and modal solutions up to a desired frequency range. The FE model is too large for non-linear response solution that it needs to be reduced. A Craig-Bampton reduction is applied to retain the interface, internal (for response) and cyclic DOFs and the modes of interest. The equation of motion of a single sector whose DOFs are condensed at the interface and response DOFs is

$$\bar{M}\ddot{u} + \bar{C}\dot{u} + \bar{K}u - \bar{f}_{\text{ext}} + \bar{f}_{NL}(u, \dot{u}) = 0 \quad (27.1)$$

where \bar{M} , \bar{C} , \bar{K} are the reduced mass, Rayleigh damping and prestressed stiffness matrices due to rotation, respectively, \bar{f}_{ext} is an external excitation harmonic force and $\bar{f}_{NL}(u, \dot{u})$ is a non-linear force due to contact friction. The reduced matrices are subsequently used in multi-harmonic balance method (MHBM) in which N nonlinear differential equations are converted to $N(2N_H + 1)$ nonlinear algebraic equations:

$$(-h^2\omega^2\bar{M} + ih\omega\bar{C} + \bar{K})\hat{u}^{(h)} = \hat{f}_{\text{ext}}^{(h)} - \hat{f}_{NL}^{(h)}(\hat{u}) \quad (27.2)$$

with $h = 0, \dots, N_H$ and at $h = 0$, only \bar{K} is considered for static balance. The non-linear forces are computed using a friction element in an alternate frequency time domain (AFT) fashion. The friction element is based on 3D Jenkins element with coupled tangential motion and variable normal load. The friction force is calculated in terms of contact parameters such as a tangential stiffness K_t , a normal stiffness K_n and a coefficient of friction μ . The Jacobian needed for Newton iteration within the continuation iteration is also computed analytically to save computational time and better convergence [3, 6]. The solution in the frequency domain is tracked by a parametric continuation procedure, such as pseudo arc-length [7]. A value for frequency ω_i is chosen and the residual of equation Eq. (27.1) is linearized based on the previous amplitude solution \tilde{u}_i

$$\left[\frac{\partial \tilde{R}(\tilde{u}_i; \omega_k)}{\partial \tilde{u}_i} \right] \delta \tilde{u}^{\text{pred}} = \tilde{R}(\tilde{u}_i) \quad (27.3)$$

where $\delta \tilde{u}^{\text{pred}} = \tilde{u}_{i+1}^{\text{pred}} - \tilde{u}_i$ is the amplitude predictor. The solution of Eq. (27.3) must be updated by an additional pseudo arc-length constraint, known as the corrector phase $C(\tilde{u}_{i+1}^{\text{corr}}, \omega_{i+1}) - \|\delta \tilde{u}^{\text{pred}}\| = 0$. A flow-chart of the above methodology with appropriate transformations is shown in Fig. 27.1b.

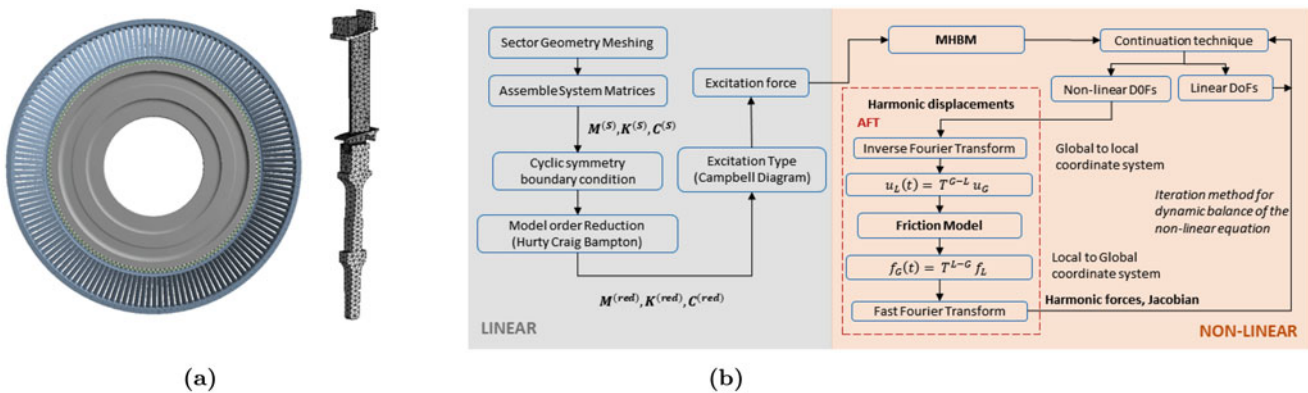


Fig. 27.1 (a) A bladed-disk with a meshed sector. (b) Flow chart for the framework

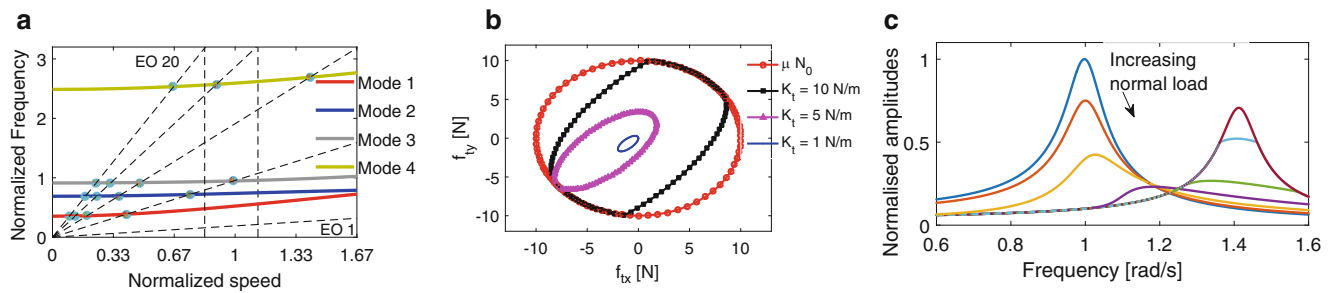


Fig. 27.2 (a) Campbell Diagram at $ND = 5$, (b) coupled tangential contact forces (x and y direction) over one period of oscillation and (c) first harmonic response of a mass and slider using pseudo arc-length continuation

27.2.1 Framework

The reduced system matrices are obtained in AMfe, an open source finite element library, are exported in an MHBM continuation code based on C++. This solves Eq. (27.3) iteratively using Trilinos library [8] and evaluates the nonlinear friction forces. The framework is modular with separate modules for friction model, continuation method, model order reduction, etc. The test-case blade assembly is used for verification of the solver and will be available as a benchmark. The framework and the geometry are available in open GIT repository: <http://github.com/jenovencio/NDCS14-2018>.

27.2.2 Preliminary Results

During testing of the modules, critical resonances of the cyclic sector are obtained by the Campbell diagram, see Fig. 27.2a. This is helpful in selecting the nodal diameter modes to be retained in the basis for non-linear iterative solution. The evolution of the tangential frictional forces is plotted in Fig. 27.2b with coupled behavior and Coulomb limit prescribed by a circle (for isotropic friction coefficient). Finally, the pseudo-arc length continuation scheme is plotted in Fig. 27.2c for a simple mass and slider with free and stick response and slipping in between for varying normal loads.

27.3 Conclusion

This work has aimed to develop individual modules for the bladed-disks subject to nonlinear friction forces with an open-access for all. All the modules have been individually tested on simple cases. This work can be used by the research community to compare different methods available in the research spectrum, along with their own work, against different parameters of interest. The present framework has two different platforms Python (AMfe library) and C++ (interface code and Trilinos library) which needs to be converted into one platform. Necessary interfacing between coding environments and inclusion of more models will be done in the future.

Acknowledgements This work is a part of the project EXPERTISE that received funding from the European Union's H2020 research and innovation program under the Marie Skłodowska-Curie grant agreement No 721865. The authors are grateful to the ND-CSI Non-linear Dynamics of Coupled Structures and Interfaces Summer School 2018 organizers.

References

- Seinturier, E.: Forced response computation for bladed disks industrial practices and advanced methods. Lecture Series - von Karman Institute for Fluid Dynamics 2 (2007)
- Petrov, E.P., Ewins, D.J.: Effects of damping and varying contact area at blade-disk joints in forced response analysis of bladed disk assemblies. *J. Turbomach.* **128**(2), 403–410 (2006)

3. Salles, L., Blanc, L., Thouverez, F., Gousskov, A.M., Jean, P.: Dynamic analysis of a bladed disk with friction and fretting-wear in blade attachments. In: ASME Turbo Expo 2009: Power for Land, Sea, and Air, pp. 465–476. American Society of Mechanical Engineers, New York (2009)
4. Afzal, M., Arteaga, I.L., Kari, L.: Numerical analysis of multiple friction contacts in bladed disks. *Int. J. Mech. Sci.* **137**, 224–237 (2018)
5. Charleux, D., Gibert, C., Thouverez, F., Dupeux, J.: Numerical and experimental study of friction damping blade attachments of rotating bladed disks. *Int. J. Rotating Mach.* **2006** (2006). <http://dx.doi.org/10.1155/IJRM/2006/71302>
6. Afzal, M., Arteaga, I.L., Kari, L.: An analytical calculation of the jacobian matrix for 3d friction contact model applied to turbine blade shroud contact. *Comput. Struct.* **177**, 204–217 (2016)
7. Sarrouy, E., Sinou, J.-J.: Non-linear periodic and quasi-periodic vibrations in mechanical systems-on the use of the harmonic balance methods. In: *Advances in Vibration Analysis Research*, InTech, Rijeka (2011)
8. Heroux, M.A., Willenbring, J.M.: Trilinos Users Guide. Tech. Rep. SAND2003-2952, Sandia National Laboratories, Albuquerque (2003)

Chapter 28

Dynamics of Geometrically-Nonlinear Beam Structures, Part 1: Numerical Modeling



D. Anastasio, J. Dietrich, J. P. Noël, G. Kerschen, S. Marchesiello, J. Häfele, C. G. Gebhardt, and R. Rolfes

Abstract The need of lightweight design in structural engineering is steadily growing due to economic and ecological reasons. This usually causes the structure to exhibit moderate to large displacements and rotations, resulting in a distributed nonlinear behavior. However, the characterization of geometrical nonlinearities is challenging and sensitive to structural boundaries and loading. It is commonly performed with numerical simulations, utilizing particularly finite element formulations. This study comprises simulations of a clamped-clamped beam with moderate to large amplitude oscillations. Four different (commercial and noncommercial) numerical approaches are considered: three finite element representations and one assumed-modes approach. A first comparison is conducted when the system is under a sine sweep excitation over one single mode. Subsequently, a modified model featuring nonlinear internal resonance is considered, to disclose differences in the modeling of the nonlinearity when coupling between modes occurs. The results show some expected features for geometrical nonlinearities in all methods, but also some important differences, especially when the modal interaction is activated.

Keywords Numerical methods · Distributed nonlinearity · Geometrical nonlinearity · Nonlinear beam · Internal resonances · Modal interaction

28.1 Introduction

Considering the last decades, the need of light and slender structures in structural engineering is steadily growing both for economic and ecological reasons [1]. Therefore, more structures exhibit moderate to large deflections and rotations causing strongly nonlinear system responses. For the characterization and the consideration of resulting geometrical nonlinearities, numerical simulations are commonly utilized. In comparison to linear simulations, incorporating nonlinearities is more challenging and complex, because there are particular nonlinear phenomena that have to be considered, such as modal interaction and resonance frequency shifts. There are different approaches for the formulation of the nonlinearities and the coupling between modes provided by both commercial or noncommercial codes. The aim of this study is to gain a better understanding of different approaches and their nonlinear simulations for engineering structures. For this purpose, four different (commercial and noncommercial) approaches are considered to perform simulations of a slender clamped-clamped beam featuring geometrical nonlinearities. Comparisons between the simulation results obtained by the considered codes are conducted for different load cases and simulation prerequisites.

D. Anastasio (✉) · S. Marchesiello
Department of Mechanical and Aerospace Engineering, Politecnico di Torino, Torino, Italy
e-mail: dario.anastasio@polito.it

J. Dietrich · J. Häfele · C. G. Gebhardt · R. Rolfes
Institute of Structural Analysis, Leibniz Universität Hannover, Hannover, Germany

J. P. Noël · G. Kerschen
Space Structures & Systems Lab., Bldg B52/3, Department of Aerospace and Mechanical Engineering, University of Liège, Liège, Belgium

28.2 Background

In order to obtain reasonable and reliable predictions for nonlinear structures, four commercial and noncommercial numerical codes are compared and discrepancies are analyzed. The comparison involves the two commercial codes Abaqus [2] (AB) and ANSYS [3] (AN). Noncommercial approaches like the geometrical local frame representation proposed by Sonnevile and Bruls [4] (LF) and the modal coordinates reduction [5] (MC) are considered as well. It should be noticed that the first three approaches rely on a finite element representation of the system, while the last one is based on a modal superposition principle with an expression of the nonlinearity by a modal coupling. Since the expression of the nonlinearity is analytic and in a closed-form in this case, it is also possible to compute the nonlinear response using the harmonic balance method [6], for the computation of stable and unstable paths. The setup contains a slender steel beam with the dimensions of $500 \times 1 \times 20$ mm (length \times thickness \times width). The first resonance frequencies are located at $f_1 = 20.75$ Hz, $f_2 = 57.21$ Hz, and $f_3 = 112.15$ Hz. For the modeling of the beam, a formulation with shear-deformable beam finite elements is used in Abaqus, ANSYS and the LF approach. Furthermore, the beam is modeled using Euler-Bernoulli beam theory in the analytical modal coordinates method. As it is a thin and slender beam, results from all approaches are comparable to each other. The time integration is performed according to the algorithms available for the different codes, which in any case belong to the Newmark family. No numerical damping was added in the approaches that allows such a control. Table 28.1 resumes the most important properties of the different approaches.

Five different forcing levels ranging from low to high amplitudes are taken into account. As an excitation signal, an upward linear sine sweep over the first mode is chosen, acting on a node close to one clamping. Based on this setup, a convergence study is performed and simulations settings are determined. In the next step, the simulation results obtained from the different codes are compared considering two scenarios: first, a single mode is responding to the excitation; second, an internal resonance is created to force a modal interaction between two different modes.

28.3 Results

The four simulation approaches generate simulation results differing in amplitudes and resonance frequencies. After the convergence study, the sampling frequency and the element discretization of the beam was set to 5000 Hz and 40 elements, respectively. In particular, the spatial discretization is an important parameter for the FE codes (AB, AN, LF), while it does not play any role in the accuracy of the response of the MC method, because it is based on a superposition of modes. Instead, the number of modes included in the response is crucial. Optimal results are obtained considering three modes.

Typical nonlinear behavior such as an increase of the resonance frequency and jumps can be detected for all the codes under moderate to large excitation amplitudes. Considering different levels of nonlinearity, the discrepancies between the codes increase for stronger nonlinear system responses. It is important to highlight that the implementation of the geometrical nonlinearity is done differently for the different codes, and in particular there might be some limitations in the assumptions made by each. For this reason, the final comparison is made in a moderately large amplitude setup, as shown in Fig. 28.1. Here, the results from LF and MC method are comparable using 40 elements for the discretization, while there is still a distinct difference to the results from Abaqus and ANSYS. The comparison shows that the simulations results from Abaqus are off. Neither can be stated, which computed response and, thus, which formulation is right. Even for the simple beam model without a modal interaction, the different approaches do not compute the same system responses considering the nonlinear case.

In a second part of the study, the beam model is modified by adding a mass close to the right boundary. The resonance frequencies vary with this modification in a way that the third harmonic of the first mode is in the vicinity of the second resonance frequency. Therefore, a 2-1 internal resonance is activated, meaning that also the second bending mode is responding when the first is excited. Internal resonances are very common in nonlinear systems, especially when a large

Table 28.1 Properties of the different approaches

Name		Type	Beam elements	Time integrator
Abaqus	AB	Nonlinear FEM	Timoshenko	HHT- α [7]
ANSYS APDL	AN	Nonlinear FEM	Timoshenko	Newmark [8]
Local Frames	LF	Nonlinear FEM	Timoshenko	Generalized- α [9]
Modal Coordinates	MC	Modes superposition	Euler-Bernoulli	Generalized- α

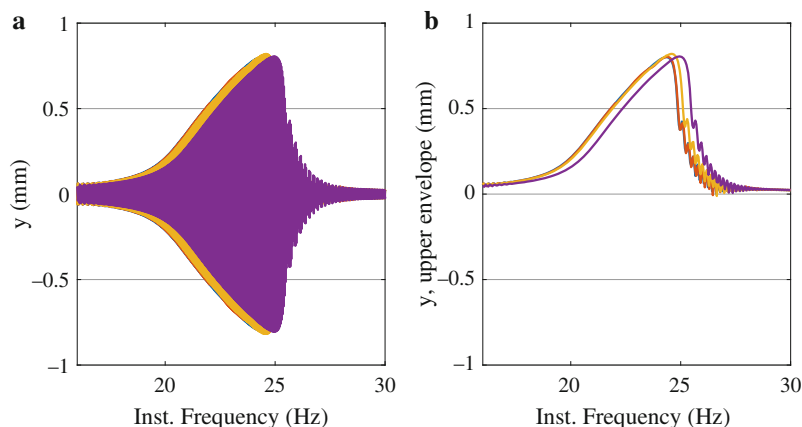


Fig. 28.1 Comparison of the system responses in the case of a single mode responding. Blue line: MC, red line: LF, yellow line: AN, purple line: AB. (a) Total response. (b) Upper envelope of the response

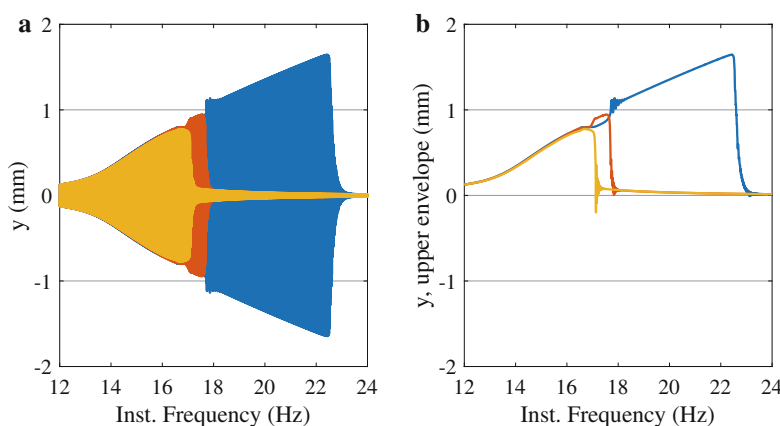


Fig. 28.2 Comparison of the system responses in the case of an internal resonance activated. Blue line: MC, red line: LF, yellow line: AN. (a) Total response. (b) Upper envelope of the response

number of modes is present. In this case the presence of such a phenomenon is a good test to see how the different methods behave when more than one mode is present in the response. Simulations are performed with MC, LF and AN approaches.

All the computed responses match up to a frequency of 16 Hz, which is the region where only the first mode dominates the response. For larger excitation frequencies, the codes differ strongly in the magnitude of the response and jump frequencies due to the interaction with the second mode (Fig. 28.2). In particular, for LF the jump occurs at noticeably higher frequencies compared to the other solutions accompanied by a distinctly larger displacement amplitude. The reason for this might be a convergence to an isolated solution in the LF simulation, that is not expected by the other methods. This causes the structure to feature a system response up to a higher resonance frequency with response amplitudes belonging to the isolated solution. On the contrary, results obtained by the ANSYS code seem to lead to an underestimation of the response amplitude in comparison to the other codes. From the comparison between all the approaches, it can be stated that a modal interaction evokes even greater differences between the simulation results, as dimensions of resonance amplitudes are noticeably different. The reason for this strong deviation between the simulation has not been determined yet. Especially for the commercial code ANSYS, it is unknown how the coupling between the modes is implemented.

28.4 Conclusion

Numerical simulations were conducted using different approaches for the simple model of a thin clamped-clamped beam. It was observed that the computed system responses differ. In particular, the two commercial codes ANSYS and Abaqus predict different system responses for strongly nonlinear cases. When an internal resonance is created, the simulation results

comprise significant differences in the response amplitudes and resonance frequencies of the system. Since the formulation of the nonlinearities is unknown for the commercial codes, the source of these differences cannot be determined exactly. From the results, it can be stated that the prediction of nonlinear system responses with numerical simulations is challenging and not necessarily reliable, even for simple models. It is not trivial to define, which approach leads to the most accurate solution compared to responses of real-life structures and circumstances.

References

1. Di Maio, D., delli Carri, A., Magi, F., Sever, I.A.: Detection of nonlinear behaviour of composite components before and after endurance trials. *Conf. Proc. Soc. Exp. Mech. Ser.* (2014). https://doi.org/10.1007/978-3-319-04522-1_8
2. Dassault Systems. Simulia, May 2018
3. ANSYS Mechanical APDL. Version Release 15
4. Sonnevile, V., Cardona, A., Brüls, O.: Geometrically exact beam finite element formulated on the special Euclidean group SE(3). *Comput. Methods Appl. Mech. Eng.* **268**, 451–474 (2014). <https://doi.org/10.1016/j.cma.2013.10.008>
5. Anastasio, D., Marchesiello, S., Noël, J.P., Kerschen, G.: Subspace-based identification of a distributed nonlinearity in time and frequency domains. Springer, Cham (2018). https://doi.org/10.1007/978-3-319-74280-9_30
6. Detroux, T., Renson, L., Masset, L., Kerschen, G.: The harmonic balance method for bifurcation analysis of large-scale nonlinear mechanical systems. *Comput. Methods Appl. Mech. Eng.* **296**, 18–38 (2015). <https://doi.org/10.1016/j.cma.2015.07.017>
7. Hilber, H.M., Hughes, T.J.R., Taylor, R.L.: Improved numerical dissipation for time integration algorithms in structural dynamics. *Earthq. Eng. Struct. Dyn.* **5**, 283–292 (1977). <https://doi.org/10.1002/eqe.4290050306>
8. Newmark, N.M.: A method of computation for structural dynamics. *J. Eng. Mech.* **85**, 67–94 (1959). <https://doi.org/10.1016/j.compgeo.2015.08.008>
9. Chung, J., Hulbert, G.M.: A time integration algorithm for structural dynamics with improved numerical dissipation: the generalized- α method. *J. Appl. Mech.* **60**, 371–375 (1993). <https://doi.org/10.1115/1.2900803>

Chapter 29

Dynamics of Geometrically-Nonlinear Beam Structures, Part 2: Experimental Analysis



D. Anastasio, J. Dietrich, J. P. Noël, G. Kerschen, S. Marchesiello, J. Häfele, C. G. Gebhardt, and R. Rolfes

Abstract System identification is a key tool to gather information about dynamical structures. In the last decades, important steps have been made to perform this task in the presence of localized nonlinearities. However, the continual interest in improving structural performance has created the need of designing light and flexible elements in several engineering fields. These elements are usually characterized by moderate and large deformations, exhibiting distributed nonlinearities. System identification of structures with distributed nonlinear features remains particularly challenging, especially when dealing with experimental data. This work proposes a method to perform such a task, relying on a convenient basis reduction of the measured signals. The identification is then performed using the nonlinear subspace identification method (NSI) in the reduced domain together with a closed-form nonlinear description. This methodology is validated on an experimental structure, consisting of a very thin steel beam that is clamped at both ends. Excited with a multisine, the beam undergoes large amplitude oscillations. A final objective of the identification is to exploit its response through the correct identification of the parameters that define the nonlinearity. Results show a high level of accuracy, which validates the effectiveness of the methodology and paves the way toward the identification of more complex real-life structures exhibiting large deformations.

Keywords Nonlinear system identification · Subspace identification · Geometrical nonlinearity · Nonlinear beam · Large deformation

29.1 Introduction

Large-amplitude vibrations of mechanical structures have been studied for decades, and many efforts have been made in order to mathematically represent their characteristics [1]. However, their importance has increased in the last years, driven by the need for designing flexible and light structures [2]. Generally, geometrical nonlinearity arises when a structure undergoes large amplitude vibrations, resulting in nonlinear strain-displacement relations. In this framework, a nonlinear model is very often obtained relying on a convenient basis reduction [3]. Linear normal modes (LNMs) are the most common choice when dealing with linear systems, but they have some limitations when nonlinearities are present [4]. Yet, their implementation is fairly easy especially when dealing with experimental data, and they are still capable of giving a nonlinear dynamical description when moderately large amplitude vibrations are considered [5].

In this work, a method is presented to identify a distributed nonlinear behavior from experimental data, relying on such a reduction. The identification is then performed using the nonlinear subspace identification (NSI) method [6–8] in the reduced domain using a closed-form nonlinear description. This approach has already been tested on numerical data [9], and it is now validated on experimental measurements acquired on a very thin clamped-clamped beam, undergoing large amplitude vibrations.

D. Anastasio (✉) · S. Marchesiello
Department of Mechanical and Aerospace Engineering, Politecnico di Torino, Torino, Italy
e-mail: dario.anastasio@polito.it

J. Dietrich · J. Häfele · C. G. Gebhardt · R. Rolfes
Institute of Structural Analysis, Leibniz Universität Hannover, Hannover, Germany

J. P. Noël · G. Kerschen
Space Structures & Systems Lab., Bldg B52/3, Department of Aerospace and Mechanical Engineering, University of Liège, Liège, Belgium

29.2 Beam Under Moderately Large Lateral Oscillations

A 2D Euler–Bernoulli beam with moderately large lateral deflection is considered. The governing equation is [1]:

$$\mu \frac{\partial^2 y}{\partial t^2} + EI \frac{\partial^4 y}{\partial x^4} - \frac{EA}{2L} \left(\int_0^L \left(\frac{\partial y}{\partial x} \right)^2 dx \right) \frac{\partial^2 y}{\partial x^2} = u(t) \delta(x - x_U) \quad (29.1)$$

where μ is the linear mass, E is the Young's Modulus, I is the moment of inertia, A is the section, L is the length, x_U is the forcing position and y is the lateral displacement. If LNMs $\boldsymbol{\phi}$ are used as a reduction basis, the solution to Eq. (29.1) can be found applying the modal transformation [9]. A set of N equations is obtained considering N modes, as expressed in Eq. (29.2):

$$m_j \ddot{\eta}_j + k_j \eta_j - \frac{EA}{2L} \sum_{r=1}^R \left(\alpha_r^{nl} \eta_r^2 \right) \beta_j^{nl} \eta_j = q_j, \quad j = 1, \dots, N, \quad R \leq N \quad (29.2)$$

where $q_j = \boldsymbol{\phi}_j^T u$ are the modal forces, m_j is the modal mass, k_j is the modal stiffness and $\alpha_r^{nl}, \beta_j^{nl}$ are the nonlinear coefficients. It should be noticed that the number of nonlinear terms per mode is $R \leq N$.

29.3 Nonlinear System Identification

Many methods can be found in the literature to perform nonlinear system identification [2, 10], and the procedure here presented can be adapted to many of them. Nonlinear Subspace Identification (NSI) method has already proved its effectiveness in several nonlinear structures with localized nonlinearities, and it is used in the following sections adapted to the distributed case. The method relies on the feedback interpretation of the nonlinearity, considered as a set of additional inputs to the underlying linear system. In this way it is possible to solve the state-space problem using subspace methods, either in the time domain (TNSI) [6] or in the frequency domain (FNSI) [7]. The outcome of the identification is the so-called extended state-space model, which includes both the underlying-linear and the nonlinear dynamics. The shape of the nonlinearity is needed as an a priori information together with the input-output data. In this case the identification is performed in the reduced-order domain, and the theoretical nonlinear shape for each mode is:

$$q_j^{nl} = \sum_{r=1}^R \eta_r^2 \eta_j \quad j = 1, \dots, N, \quad R \leq N \quad (29.3)$$

It should be noticed that even terms are not expected in this model. This is generally not the case when dealing with experimental data, as slight asymmetries in the structure can easily lead to even nonlinearities in the response. To account for this eventuality, second degree nonlinear couplings are also included in the nonlinear shape.

29.4 Experimental Tests and Results

A very thin steel beam of dimensions $479 \times 20 \times 0.75$ mm is considered. The ends of the beam are clamped, and the excitation source is a shaker positioned at 15 mm from one end, as can be seen in Fig. 29.1. The response is recorded with 7 accelerometers along the length of the beam. The chosen input is a full multisine signal [11] in the range 14–100 Hz, with 6 periods and 5 realizations.

Several tests have been performed increasing the input amplitude, from a linear regime to a highly nonlinear one. This can be observed in Fig. 29.2b, which shows the FRFs for the lowest and highest levels of amplitude. A distinctive hardening effect can be noticed on the three excited modes.

The nonlinear identification is performed on the highest level of amplitude, using the first four realizations as a test set. Outputs are then generated from the obtained nonlinear state-space model and compared with the validation set, consisting

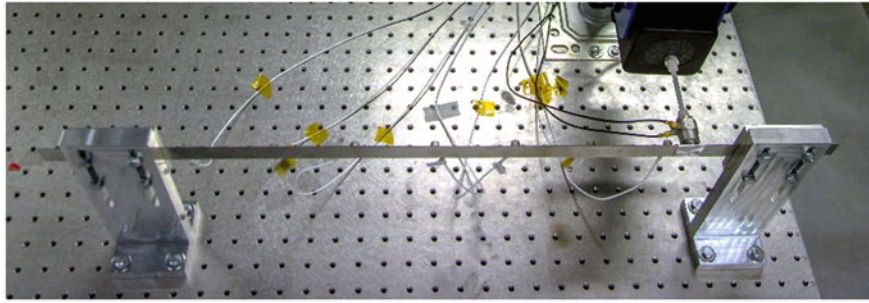


Fig. 29.1 Photo of the experimental setup

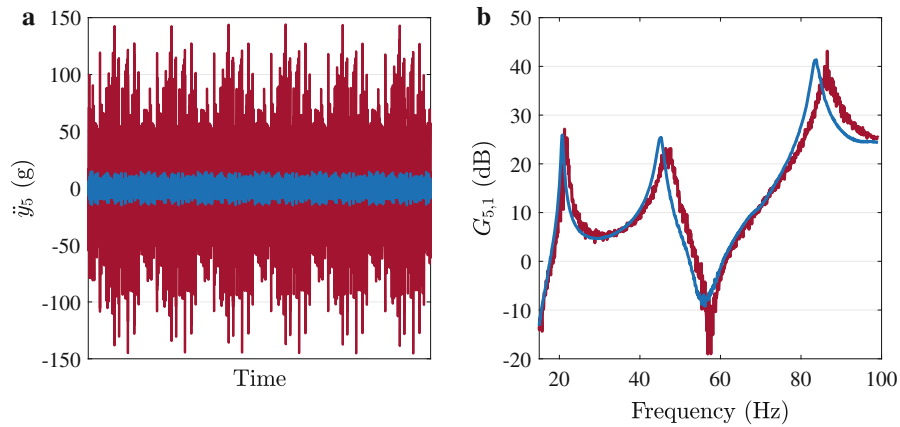


Fig. 29.2 (a) Recorded acceleration for one realization. Blue line: lowest level. Red line: highest level. (b) Inertance. Blue line: lowest level. Red line: highest level

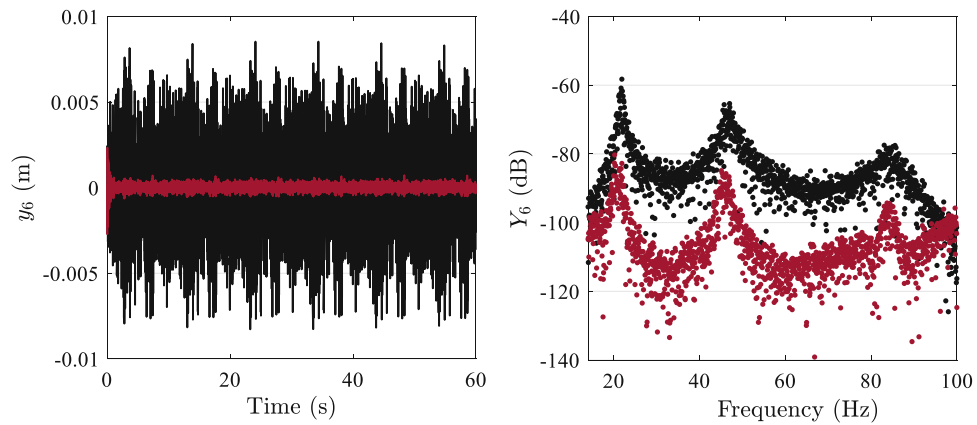


Fig. 29.3 Results of the identification - comparison between measured output and simulated one in time and frequency domains. Black line: measured signal. Red line: Residual with the simulated signal

of the last realization of the measured signal. The comparison is reported in Fig. 29.3 in both time and frequency domains. It can be seen that the residual between the measured output and the simulated one is very low, giving an averaged RMS error of 10%.

29.5 Conclusion

A methodology for performing nonlinear system identification of structures exhibiting distributed geometrical nonlinearities has been presented and validated on an experimental test bench. The results of the identification show a high level of accuracy, validating the effectiveness of the methodology and paving the way toward the identification of more complex real-life structures exhibiting large deformations.

References

1. Nayfeh, A.H., Pai, P.F.: Linear and nonlinear structural mechanics. *Meccanica*. **40**, 221–222 (2004). <https://doi.org/10.1007/s11012-005-0327-y>
2. Kerschen, G., Worden, K., Vakakis, A.F., Golinval, J.C.: Past, present and future of nonlinear system identification in structural dynamics. *Mech. Syst. Signal Process.* **20**, 505–592 (2006). <https://doi.org/10.1016/j.ymssp.2005.04.008>
3. Touzé, C., Thomas, O., Huberdeau, A.: Asymptotic non-linear normal modes for large-amplitude vibrations of continuous structures. *Comput. Struct.* **82**, 2671–2682 (2004). <https://doi.org/10.1016/j.compstruc.2004.09.003>
4. Sombroek, C.S.M., Tiso, P., Renson, L., Kerschen, G.: Numerical computation of nonlinear normal modes in a modal derivative subspace. *Comput. Struct.* **195**, 34–46 (2018). <https://doi.org/10.1016/j.compstruc.2017.08.016>
5. Claeys, M., Sinou, J.J., Lambelin, J.P., Alcoverro, B.: Multi-harmonic measurements and numerical simulations of nonlinear vibrations of a beam with non-ideal boundary conditions. *Commun. Nonlinear Sci. Numer. Simul.* **19**, 4196–4212 (2014). <https://doi.org/10.1016/j.cnsns.2014.04.008>
6. Marchesiello, S., Garibaldi, L.: A time domain approach for identifying nonlinear vibrating structures by subspace methods. *Mech. Syst. Signal Process.* **22**, 81–101 (2008). <https://doi.org/10.1016/j.ymssp.2007.04.002>
7. Noël, J.P., Kerschen, G.: Frequency-domain subspace identification for nonlinear mechanical systems. *Mech. Syst. Signal Process.* **40**, 701–717 (2013). <https://doi.org/10.1016/j.ymssp.2013.06.034>
8. Noël, J.P., Marchesiello, S., Kerschen, G.: Subspace-based identification of a nonlinear spacecraft in the time and frequency domains. *Mech. Syst. Signal Process.* **43**, 217–236 (2014). <https://doi.org/10.1016/j.ymssp.2013.10.016>
9. Anastasio, D., Marchesiello, S., Noël, J.P., Kerschen, G.: Subspace-based identification of a distributed nonlinearity in time and frequency domains. Springer, Cham (2018). https://doi.org/10.1007/978-3-319-74280-9_30
10. Noël, J.P., Kerschen, G.: Nonlinear system identification in structural dynamics: 10 more years of progress. *Mech. Syst. Signal Process.* **83**, 2–35 (2017). <https://doi.org/10.1016/j.ymssp.2016.07.020>
11. Schoukens, J., Swevers, J., Pintelon, R., Van Der Auweraer, H.: Excitation design for FRF measurements in the presence of non-linear distortions. *Mech. Syst. Signal Process.* **18**, 727–738 (2004). [https://doi.org/10.1016/S0888-3270\(03\)00084-0](https://doi.org/10.1016/S0888-3270(03)00084-0)



Chapter 30

Constructing Backbone Curves from Free-Decay Vibrations Data in Multi-Degrees of Freedom Oscillatory Systems

Mattia Cenedese and George Haller

Abstract Backbone curves are often the best representation of the nonlinear behavior for the vibrations of mechanical systems. Several approaches for obtaining them are present in literature, either analytical, numerical or experimental ones. However, they often make assumptions that unavoidably limit the range of applicability, such as the dynamics of the underlying conservative system and the modeling of damping terms. Here, we describe a mathematical theory and the corresponding numerical methodology that is able to rigorously extract backbone curves from free-decay vibrations data and that can overcome some of the main limitations of existing methods. We illustrate our findings with synthetic and real experiment vibration measurements.

Keywords Backbone curves · Nonlinear vibrations · Damped vibrations · Nonlinear system identification · Spectral submanifolds

30.1 Introduction

In the field of nonlinear structural dynamics, backbone curves often represent the most valuable information to be extracted, either from a model or an experimental setup. Indeed, these amplitude-frequency plots are able to properly characterize the dynamics quantifying the nonlinear behavior and also predicting eventual interactions. The original definition of backbone curve was proposed by Nayfeh and Mook in [1] that refer to it as the frequencies of amplitude maxima in frequency responses of different forcing amplitudes. In literature, the same name is also given to the relation between amplitude and frequency of conservative periodic orbits in *nonlinear normal modes* (NNMs) [2] or *Lyapunov subcenter manifolds* (LSMs) [3]. Even though fundamentally different, these two different objects are often observed to be close, in some cases even identical. However, rigorous results that establish a relation between forced-damped backbone curves and conservative ones are still missing [4].

In order to compute backbone curves, other than generic methods such as analytical techniques (e.g. method of multiple scales [1] and averaging [5]) or numerical ones like continuation (see the packages AUTO [6], MATCONT [7] and COCO [8]), several ad-hoc developments do exist. For conservative backbone curves, popular analytical techniques rely on the *normal form method* of [9], while several numerical ones have been established within the framework of nonlinear normal modes [10], like the shooting technique in [11]. The most common experimental method for backbone curve extraction is a two-step procedure [12]. First, one applies the *force appropriation method* [13] where the main underlying assumption is that introducing a periodic forcing with a 90° phase lag in a conservative system with a small linear damping term should preserve exactly a periodic orbit of the conservative part. Once this orbit is detected, the second step exploits the *nonlinear resonance decay method* [14, 15] in which excitation is turned off. Here, it is assumed that the decaying vibrations are close to conservative ones such that, by properly post-processing the signal, the instantaneous amplitude-frequency plot describes the backbone curve. Other approaches utilize experimental continuation [16], always starting from the assumptions of the force appropriation method. In spite of being considerably less expensive than generic techniques, all these ad-hoc methods make strong assumptions often limiting their range of applicability: small enough oscillations amplitude, accurate knowledge of the nonlinear normal mode manifold, small position independent linear damping and the yet unproven relation between forced-damped backbone curves and conservative ones [4].

In this contribution, we propose a data-driven method for extracting forced-damped backbone curves that, having its foundations on the work of Haller and Ponsioen [17], should overcome most of these limitations. In this work, they define

M. Cenedese (✉) · G. Haller
Institute for Mechanical Systems, ETH Zürich, Zürich, Switzerland
e-mail: mattiac@ethz.ch

the concept of *spectral submanifolds* (SSMs) for generic multi-degrees of freedom mechanical systems (even in case of small time-dependent terms) where two-dimensional autonomous SSMs, i.e. when they are tangent at a stable equilibrium to one related modal subspace in case of no forcing, have a very special role. Indeed, the reduced dynamics on a single-mode SSM gives an exact nonlinear extension of the modal linear dynamics associated with the SSM. Thus, as discussed in [4, 18], the first approximation forced-damped backbone curve is exactly the graph expressing the decaying instantaneous vibration amplitude as function of the instantaneous frequency along the SSM. So, without requiring any assumption on damping terms nor relying on the conservative limit, we can directly and rigorously extract the backbone curves from the freely decaying vibrations in the vicinity of the natural frequencies of the linearized system at the equilibrium. Here, we give an overview of the method, that is described in all its details in [4], also showing some results using synthetic data.

30.2 Method Overview and Numerical Example

In our method we assume to deal with a damped n -degree of freedom mechanical systems to which state of the art linear modal analysis is applied [19]. Thus, we know a priori natural frequencies and mode shapes of the linearization. Moreover, we fix a priori the number of modes contributing to the system response to be $n_c > 2$. At this point, we select the mode of interest, a sampling time T and a single generic scalar observable, for instance, a position or a velocity coordinate of a certain material point of the mechanical system. Then, we perform a number of tests to gain the necessary free-decay data about this latter quantity. Precisely, we need to excite the structure in the vicinity of the mode of interest and the excitation should be strong enough to trigger the nonlinear behavior. In order to verify the nonlinear quality of the signal, one can look at its Hilbert or wavelet transforms [12]. At this point, we fit on these data a Nonlinear Auto-Regressive (NAR) polynomial-based model [20] that, thanks to Theorems 5.2 and 6.3 in [4], allows us to compute the SSM parametrization, the reduced dynamics and, in the end, the backbone curve. As a numerical experiment, consider the three degree-of-freedom mechanical system:

$$\begin{cases} m\ddot{q}_1 + k(2q_1 - q_2) + c(2\dot{q}_1 - \dot{q}_2) + \kappa q_1^3 + \gamma q_1^2 \dot{q}_1 = 0 \\ m\ddot{q}_2 + k(2q_2 - q_1 - q_3) + c(2\dot{q}_2 - \dot{q}_1 - \dot{q}_3) = 0 \\ m\ddot{q}_3 + k(2q_3 - q_2) + c(2\dot{q}_3 - \dot{q}_2) = 0 \end{cases} . \quad (30.1)$$

By simulating 15 decay responses per mode with the dimensionless parameters $m = k = 1$, $\kappa = 1$, $c = 0.003$ and $\gamma = 0.03$, our data-driven SSM method truncated at order 5 returns the backbone curves depicted with the red lines in Fig. 30.1 related to the first two modes. These plots are completed with black lines representing frequency responses for different small forcing amplitudes obtained with the PO toolbox of the continuation package COCO [8] and we can notice that the extracted backbone curves suitably fit with their peaks.

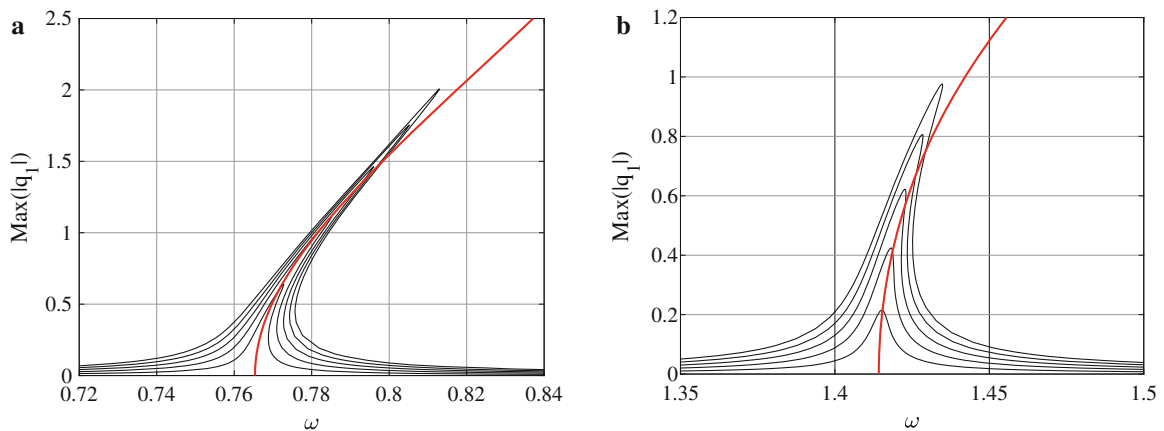


Fig. 30.1 Frequency-amplitude plots where the y-axis indicates the maximum in the first coordinate over one oscillation period around the first (a) and second (b) modes. The red lines represent the data-driven SSM backbone curves while black lines depict frequency responses computed with numerical continuation for different small amplitudes pure sinusoidal forcing applied to the first mass

30.3 Conclusion

We described a methodology that is able to rigorously extract the backbone curve from free-decay vibrations data. Relying on the powerful concept of spectral submanifolds, we do not need to make assumption on the underlying conservative system dynamics nor on the modeling of damping and our theoretical predictions have been verified with data coming either from numerical simulations and real experiment. Moreover, with respect to other experimental routines, our method only requires a limited amount of data that can be efficiently obtained by performing hammer impact tests on the structure of interest.

References

1. Nayfeh, A.H., Mook, D.T.: *Nonlinear Oscillations*. Wiley (2007)
2. Kerschen, G., Peeters, M., Golinval, J.C., Vakakis, A.F.: Nonlinear normal modes, part I: A useful framework for the structural dynamicist. *Mech. Syst. Signal Process.* **23**(1), 170–194 (2009)
3. Lyapunov, A.M.: The general problem of the stability of motion. *Int. J. Control.* **55**(3), 531–534 (1992)
4. Szalai, R., Ehrhardt, D., Haller, G.: Nonlinear model identification and spectral submanifolds for multi-degree-of-freedom mechanical vibrations. *Proc. Roy. Soc. Lond A.* **473**(2202), 32 (2017)
5. Sanders, J.A., Verhulst, F., Murdock, J.: *Averaging Methods in Nonlinear Dynamical Systems*, Volume 59 of Applied Mathematical Sciences, 2nd edn. Springer-Verlag, New York (2007)
6. Doedel, R.C., Paffenroth, E.J., Champneys, A.R., Fairgrieve, T.F., Kutnetsov, Y.A., Oldeman, B.E., Sandstede, B., Wang, X.J.: *Auto2000: Continuation and Bifurcation Software for Ordinary Differential Equations*
7. Dhooge, A., Govaerts, W., Kuznetsov, Y.A.: Matcont: a Matlab package for numerical bifurcation analysis of ODEs. *ACM Trans. Math. Softw.* **29**(2), 141–164 (2003)
8. Dankowicz, H., Schilder, F.: *Recipes for Continuation*. Society for Industrial and Applied Mathematics (2013)
9. Neild, S.A., Wagg, D.J.: Applying the method of normal forms to second-order nonlinear vibration problems. *Proc. Roy. Soc. Lond. A.* **467**(2128), 1141–1163 (2011)
10. Renson, L., Kerschen, G., Cochelin, B.: Numerical computation of nonlinear normal modes in mechanical engineering. *J. Sound Vib.* **364**, 177–206 (2016)
11. Peeters, M., Vigué, R., Sérandour, G., Kerschen, G., Golinval, J.C.: Nonlinear normal modes, part II: Toward a practical computation using numerical continuation techniques. *Mech. Syst. Signal Process.* **23**(1), 195–216 (2009). Special Issue: Nonlinear Structural Dynamics
12. Noël, J.P., Kerschen, G.: Nonlinear system identification in structural dynamics: 10 more years of progress. *Mech. Syst. Signal Process.* **83**, 2–35 (2017)
13. Peeters, M., Kerschen, G., Golinval, J.C.: Dynamic testing of nonlinear vibrating structures using nonlinear normal modes. *J. Sound Vib.* **330**(3), 486–509 (2011)
14. Peeters, M., Kerschen, G., Golinval, J.C.: Modal testing of nonlinear vibrating structures based on nonlinear normal modes: experimental demonstration. *Mech. Syst. Signal Process.* **25**(4), 1227–1247 (2011)
15. Londoño, J.M., Neild, S.A., Cooper, J.E.: Identification of backbone curves of nonlinear systems from resonance decay responses. *J. Sound Vib.* **348**, 224–238 (2015)
16. Renson, L., Gonzalez-Buelga, A., Barton, D.A.W., Neild, S.A.: Robust identification of backbone curves using control-based continuation. *J. Sound Vib.* **367**, 145–158 (2016)
17. Haller, G., Ponsioen, S.: Nonlinear normal modes and spectral submanifolds: existence, uniqueness and use in model reduction. *Nonlinear Dynam.* **86**(3), 1493–1534 (2016)
18. Breunung, T., Haller, G.: Explicit backbone curves from spectral submanifolds of forced-damped nonlinear mechanical systems. *Proc. Roy. Soc. Lond. A.* **474**(2213), (2018)
19. Avitabile, P.: *Modal Testing: A Practitioner's Guide*. Wiley (2017)
20. Billings, S.A.: *Nonlinear System Identification: NARMAX Methods in the Time, Frequency, and Spatio-Temporal Domains*. Wiley (2013)



Chapter 31

Nonlinear 3D Modeling and Vibration Analysis of Horizontal Drum Type Washing Machines

Cem Baykal, Ender Cigeroglu, and Yigit Yazicioglu

Abstract In this study, a nonlinear 3-D mathematical model for horizontal drum type washing machines is developed considering rotating unbalance type excitation. Nonlinear differential equations of motion are converted into a set of nonlinear algebraic equations by using Harmonic Balance Method (HBM). The resulting nonlinear algebraic equations are solved by using Newton's method with arc-length continuation. Several case studies are performed in order to observe the effects of orientation angles of springs and dampers between drum and the cabinet. In order to reduce the steady state vibration amplitude of the drum, suitable orientation angles of the springs and dampers and their implementation locations are identified. Moreover, in order to further reduce the vibration amplitude of the drum at high frequencies, instead of viscous dampers, dry friction dampers are introduced to the system. Effect of orientation angles and parameters of the dry friction damper and springs on the force transmitted to the cabinet are studied.

Keywords 3D washing machine model · Nonlinear vibrations · Harmonic balance method

31.1 Introduction

As the life standards are going up and customer expectations are going towards reduced noise and vibration, manufacturing of washing machines has been an important issue for the industry. To satisfy customers, design criterion of any machine, as well as washing machines, has tendency toward minimized vibration. Therefore, there have been many studies about minimizing vibration and noise amplitudes of both horizontal and vertical type washing machines during operation.

Türkay et al. [1, 2] worked on a 3D dynamic model of horizontal washing machines by neglecting gyroscopic effects and assuming inertia as time invariant. They solved the nonlinear equations with time integration and studied on minimization of sum of vertical-horizontal vibration amplitudes. Li and Yam [3] studied another model by assuming small deflections where they try to decrease the maximum vibration amplitude below the requirements of quality control. Papadopoulos and Papadimitriou [4] created another simplified model by just considering the four legs of horizontal type washing machines. Using a linear model, they analyzed walking and jumping conditions of washing machines. To reduce vibration amplitudes, authors introduced balancing masses around the drum of the washing machine.

Argentini et al. [5, 6] considered both finite element model (FEM) and 6-degrees of freedom (DOF) mathematical model by linearizing gyroscopic terms and neglecting time dependency of terms in the equation of motion. After linearizing the system around its equilibrium position, FEM is solved and a validated numerical model is constructed. By introducing dry friction dampers, additional masses and a secondary suspension system, vibration amplitudes are reduced.

Lim et al. [7] created a dynamical model for the drum by considering the effects of bearings in the washing machine. Rotor dynamics equations are solved by time integration to observe the effects of parameters of the washing machine. They validated their numerical model by comparing the results with experiments. Authors obtain Campbell diagram and forward whirling frequencies are also identified.

Nygårds and Berbyuk [8, 9] created another model utilizing dry friction and cubic stiffness as resilient elements. Pittner et al. [10–12] used another model by neglecting the translational motion of the mass center of the drum along the main rotation axis. By introducing two concrete blocks as extra masses and on-off dampers, vibration amplitudes are reduced.

Chen et al. [13, 14] mostly worked on stability analysis of the horizontal type washing machines using Poincaré mapping and by checking Floquet multipliers. Stability analysis is made in frequency domain by considering Torus bifurcation. In time domain, again, time integration is used to calculate vibration amplitude. Ball balancers are introduced to the system

C. Baykal · E. Cigeroglu (✉) · Y. Yazicioglu
Department of Mechanical Engineering, Middle East Technical University, Ankara, Turkey
e-mail: ender@metu.edu.tr

to reduce vibration amplitude. Generic algorithm is used to determine the amount of balls to be used in the gasket of the washing machine.

There are many studies aimed to reduce the vibration amplitude in horizontal type washing machines by using three dimensional dynamic models. Almost all of the studies consider the time response of the washing machine drum at a specific frequency. However, for washing machines working in a broadband frequency range, i.e. between 100 and 1000 rpm; it is to better analyze the vibration amplitude of the washing machine and obtain a frequency response function (FRF) to expedite the design procedure. In this work, a three dimensional dynamical model is introduced for horizontal-type washing machines without making any linearization. Resulting nonlinear differential equations of motion are converted into set of nonlinear algebraic equations utilizing Harmonic Balance Method (HBM). Newton’s method with arc-length is used to solve the resulting nonlinear equations. Effects of orientation positions and angles of the compliant elements, spring stiffness, damping constant and the type of the damper used on the vibration amplitude of the washing machine drum are studied under steady state conditions.

31.2 Analysis

3-D dynamic model for horizontal-type washing machines developed in this study including the drum, springs and dampers is shown in Fig. 31.1. Cabinet and cabinet side of the dampers and springs are assumed as fixed. A inertial reference frame F_0 and an non-inertial reference frame F_d are placed at the geometrical center of the washing machine. Initial Frame Based (IFB) 1-2-3 sequence is used to describe the transformation matrix between non-inertial and inertial reference frames. Transformation matrix can be written for IFB 1-2-3 sequence by using exponential transformation matrices [15] as follows:

$$\widehat{C}^{(0,d)} = e^{\tilde{u}_1\theta_3} e^{\tilde{u}_2\theta_2} e^{\tilde{u}_3\theta_1}, \tag{31.1}$$

$$e^{\tilde{u}_1\theta_3} = \begin{bmatrix} 1 & 0 & 0 \\ 0 & \cos(\theta_3) & \sin(-\theta_3) \\ 0 & \sin(\theta_3) & \cos(\theta_3) \end{bmatrix} \quad e^{\tilde{u}_2\theta_2} = \begin{bmatrix} \cos(\theta_2) & 0 & \sin(\theta_2) \\ 0 & 1 & 0 \\ \sin(-\theta_2) & 0 & \cos(\theta_2) \end{bmatrix} \quad e^{\tilde{u}_3\theta_1} = \begin{bmatrix} \cos(\theta_1) & \sin(-\theta_1) & 0 \\ \sin(\theta_1) & \cos(\theta_1) & 0 \\ 0 & 0 & 1 \end{bmatrix}. \tag{31.2}$$

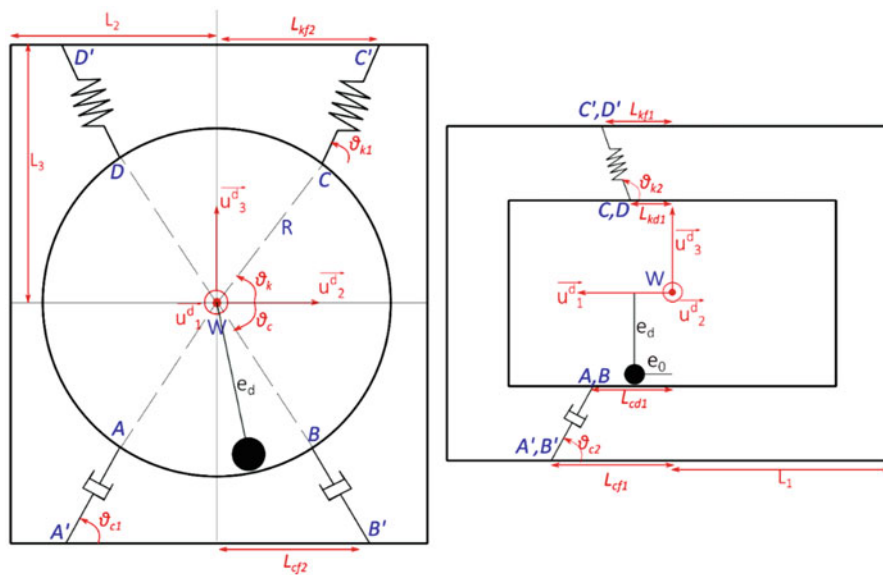


Fig. 31.1 Model of washing machine

At first, viscous dampers are introduced. Forces on springs and viscous dampers are calculated in the base frame, F_0 . The equation of motion is derived using Newton-Euler formulation as

$$\sum (\vec{F}_c + \vec{F}_s) = m \vec{a}, \quad (31.3)$$

$$\sum (\vec{M}_c + \vec{M}_s) = \dot{J} \cdot \vec{\alpha} + \vec{\omega} \times \dot{J} \cdot \vec{\omega}. \quad (31.4)$$

However, in order to simplify the calculations, column matrix representations of vectors and inertia tensors are used as follows

$$\sum (\overline{F}_c^{(0)} + \overline{F}_s^{(0)}) = m \overline{a}^{(0)}, \quad (31.5)$$

$$\sum (\overline{M}_c^{(0)} + \overline{M}_s^{(0)}) = \hat{J}^{(0)} \overline{\alpha}^{(0)} + \tilde{\omega}^{(0)} \hat{J}^{(0)} \overline{\omega}^{(0)}. \quad (31.6)$$

Overbars indicate the column matrix representations of vectors; where, supper scripts are used for the reference frames of which the vectors are resolved. Hats indicate matrix representation of the tensors and tilde represents the skew-symmetric form of the column matrices or simply cross product matrices. F_c & M_c are forces and moments coming from the viscous dampers, respectively; whereas, F_s & M_s represent the forces and moments of linear springs. Even though, it is preferred to work on the moving body frame, it is chosen to work in the inertial base frame, since, in eq. (31.6), to describe relative angular velocity and acceleration of the drum frame. Expressing relative angular velocity and acceleration in drum frame will lead lengthy equations; on the other hand, using inertial reference frame as the working frame, inertia matrices are needed to multiplied from both its left and right sides by transformation matrix and transpose of transformation matrix, respectively. Therefore, this decision is an engineering tradeoff, and base frame is selected as the working frame in this study.

Three dimensional, six degree of freedom, nonlinear differential equations of motions are converted into nonlinear algebraic equations utilizing HBM. In HBM, all nonlinear internal and external forces are represented by Fourier series. These representations are substituted in nonlinear differential equations and coefficients of similar harmonics are balanced to resolve all the displacements. Newton's method with arc-length continuation is used to obtain the steady state response of the system. The number of harmonics used in the solution is determined based on the accuracy desired in the calculations.

An example case, where all compliant elements and the mass center of laundry (the reason of rotating unbalance) are placed at the same fictitious y - z plane that includes the point W , is considered. After converting the system to a two dimensional, three degrees of freedom dynamical model, the results are compared with another study [16] to validate the model developed. Results are obtained by using 8 harmonics. It is observed from Fig. 31.2 that in order to accurately model the system, using three or four harmonics is sufficient.

As it seen from Fig. 31.2, at high frequencies excessive forces occur since force on the viscous dampers are directly proportional to the excitation frequency. To overcome this problem, dry friction dampers may be introduced instead of viscous dampers. Dry friction dampers are acting like springs for small deflections, which occur at every frequency, but around resonance. Due to this behavior, force transmitted to the cabinet will be much more small compared to viscous damper case.

31.3 Conclusion

A 3D nonlinear dynamical model of a horizontal type washing machines is developed in this study. HBM is used to obtain frequency response function (FRF) of the 6-DOF system. Multiple harmonics are used in order to accurately capture the steady-state vibration response. Several case studies are performed to see the effects of system parameters or geometrical orientations of compliant elements on system FRF.

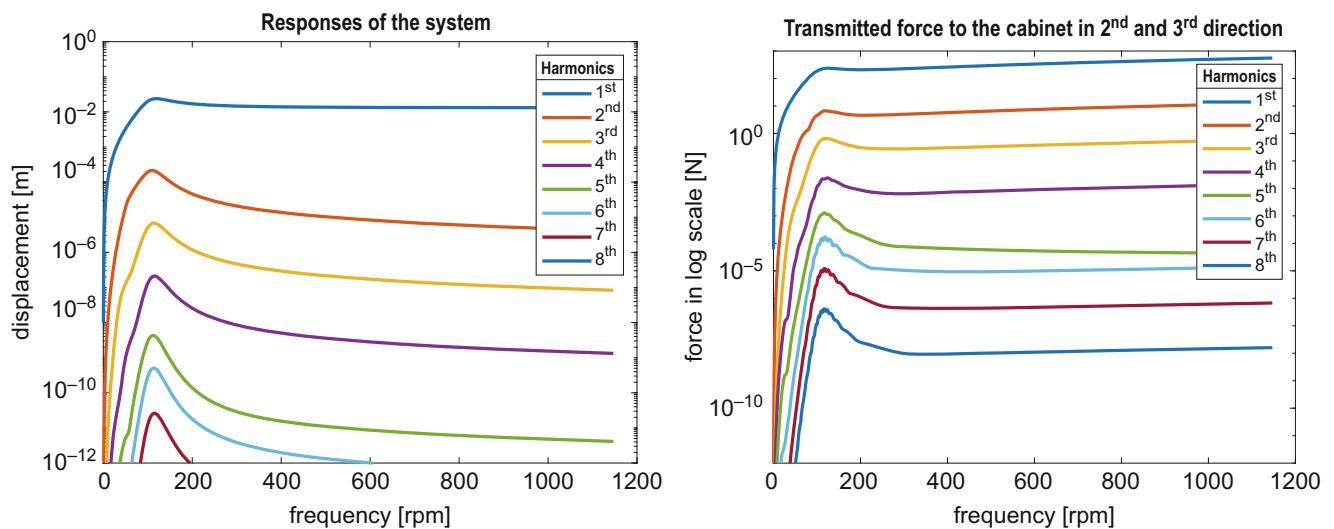


Fig. 31.2 Responses of the system and force transmitted to the cabinet in logarithmic scale

References

1. Türkay, O.S., Kiray, B., Tugcu, A.K., Sümer, T.: Formulation and implementation of parametric optimisation of a washing machine suspension system. *Mech. Syst. Signal Process.* **9**(4), 359–377 (1995)
2. Türkay, O.S., Sümer, I.T., Tuğcu, A.K., Kiray, B.: Modeling and experimental assessment of suspension dynamics of a horizontal-axis washing machine. *J. Vib. Acoust.* **120**(2), 534 (1998)
3. Li, D.B., Yam, L.H.: Modal synthesis method for vibration isolation design of massive rotating machines resiliently supported by an elastic structure. *J. Sound Vib.* **231**(1), 233–245 (2000)
4. Papadopoulos, E., Papadimitriou, I.: Modeling, design and control of a portable washing machine during the spinning cycle. In: *IEEE/ASME International Conference on Advanced Intelligent Mechatronics, AIM*, vol. 2, pp. 899–904 (2001)
5. Argentini, T., Belloli, M., Gaudiano, N., Fraternali, G., Panetta, F., Sabato, D., Vanali, M.: On a numerical model of a complete washing machine. In: *WIT Transactions on Modelling and Simulation*, vol. 46, pp. 723–733 (2007)
6. Argentini, T., Belloli, M., Robustelli, F. C., Martegani, L., Fraternali, G.: Innovative designs for the suspension system of horizontal-axis washing machines: secondary suspensions and tuned mass dampers. Volume 4B: Dynamics, Vibration and Control, 4 B, V04BT04A058 (2013)
7. Lim, H.-T., Jeong, W.-B., Kim, K.-J.: Dynamic modeling and analysis of drum-type washing machine. *Int. J. Prec. Eng. Manuf.* **11**(3), 407–417 (2010)
8. Nygård, T., Berbyuk, V.: Multibody modeling and vibration dynamics analysis of washing machines. *Multibody Syst. Dyn.* **27**(2), 197–238 (2012)
9. Nygård, T., Berbyuk, V.: Optimization of washing machine kinematics, dynamics, and stability during spinning using a multistep approach. *Optim. Eng.* **15**(2), 401–442 (2014)
10. Buśkiewicz, J., Pittner, G., Barczewski, R.: Numerical and experimental vibration analysis of domestic washing machine drum. *J. Appl. Mech. Eng.* **17**, 765–777 (2012)
11. Minorowicz, B., Stefański, F., Pittner, G., Regulski, R.: Share mode magnetorheological dampers for vibration attenuation in domestic washing machines. *Adv. Intell. Syst. Comput. Progr. Auto. Robot. Meas. Tech.*, 147–156 (2015)
12. Buśkiewicz, J., Pittner, G.: Reduction in vibration of a washing machine by means of a disengaging damper. *Mechatronics.* **33**, 121–135 (2016)
13. Chen, H.W., Zhang, Q.J., Wu, X.Q.: Stability and dynamic analyses of a horizontal axis washing machine with a ball balancer. *Mech. Mach. Theory.* **87**, 131–149 (2015)
14. Chen, H.W., Zhang, Q.: Design of horizontal axis washing machine with ball balancer and MR dampers. *Int. J. Prec. Eng. Manuf.* **18**(12), 1783–1793 (2017)
15. Özgören, M.K.: Kinematic analysis of spatial mechanical systems using exponential rotation matrices. *J. Mech. Design.* **129**(11), 1144 (2007)
16. Baykal C., Cigeroglu E., Yazicioglu Y.: Vibration Analysis of Washing Machines in the Drum Plane. *NODYCON 2019: First International Nonlinear Dynamics Conference*. February 17-20, 2019, Rome, Italy



Chapter 32

Comparison of Linear and Nonlinear Modal Reduction Approaches

Erhan Ferhatoglu, Tobias Dreher, Ender Cigeroglu, Malte Krack, and H. Nevzat Özgüven

Abstract Periodic vibration response of nonlinear mechanical systems can be efficiently computed using Harmonic Balance Method. However, computational burden may still be considerable and impede extensive parametric studies needed for, e.g., design optimization and prediction of vibration response especially when the degree of freedom is very large. In this work, the methods which had been previously developed by the authors for further model order reduction to one or a few coordinates are compared. The focus is placed mainly on modal approaches, namely Modal Superposition Method using Linear Modes (MSM-LM), Modal Superposition Method using Hybrid Modes (MSM-HM), and Modal Superposition Method using Nonlinear Modes (MSM-NM). Another method for vibration analysis of nonlinear structures is the Receptance Method (RM), in which the harmonic response of a nonlinear MDOF system is calculated from the receptances of the linear counterparts. This method exploits the sparsity of the nonlinear terms in frequency domain equations and therefore may be very efficient when the nonlinearity is local, which is the case in several applications. Performances and accuracies of these methods are compared with each other using the results of the direct analysis of the full order model as reference. The methods are applied to a benchmark system consisting of a finite element model of a beam with different nonlinear elements; but, only the results of dry friction elements are presented here. The focus is placed on periodic forced response regimes near resonances. Several conclusions and recommendations that may guide users are derived from the comparison studies.

Keywords Nonlinear vibration · Nonlinear normal modes · Hybrid modes · Harmonic balance · Nonlinear modal reduction

32.1 Harmonic Vibration Analysis of Nonlinear MDOF Systems

In this paper, the performances of four methods developed by the authors in previous studies for harmonic vibration analysis of nonlinear systems are compared. Some of these methods have been known for a while, but there was no thorough comparison of them. The first method, Modal Superposition Method using Linear Modes (MSM-LM), developed by Kuran and Özgüven [1] more than two decades ago, is one of the first methods for harmonic vibration analysis of nonlinear MDOF systems in modal domain. In the original formulation Describing Function Method (DFM) of Tanrikulu et al. [2] was used; here the same method is formulated with Harmonic Balance Method (HBM), as it is easier to express higher harmonic responses with this approach. The second method, Modal Superposition Method using Hybrid Modes (MSM-HM), is a very recent method proposed by Ferhatoglu et al. [3], which reduces model order down to one or a few modal coordinates and thus reduces computational effort. The third method, Modal Superposition Method using Nonlinear Modes (MSM-NM), is a method developed by Krack et al. [4], based on the extended periodic motion concept for defining a nonlinear (normal) mode [5]. In this method it is assumed that the vibration response of a nonlinear system is dominated by a single nonlinear mode, such that the system behaves like a single-degree-of-freedom nonlinear oscillator. These three methods use modal models, whereas the last method, Receptance Method (RM), is based on receptances. In RM, the harmonic response of a nonlinear system is calculated from the receptances of the linear counterparts which can easily be obtained by using linear modes. The receptance based method was developed by Menq et al. [6], in order to handle the nonlinear friction damping element located between two adjacent blades. It utilizes the partitioned receptance matrix to decrease the number of

E. Ferhatoglu · E. Cigeroglu · H. N. Özgüven
Middle East Technical University, Ankara, Turkey

T. Dreher · M. Krack (✉)
University of Stuttgart, Stuttgart, Germany
e-mail: krack@ila.uni-stuttgart.de

nonlinear algebraic equations to be solved to the number of nonlinear DOFs. Another receptance based approach developed by Tanrikulu et al. [2] uses the so-called “pseudo-receptance matrix” to determine the response of nonlinear systems with multiple nonlinear elements. This method exploits the sparsity of the nonlinear terms in frequency domain equations when nonlinearity is local, which is very often the case. Maliha et al. [7] re-formulated the receptance based method given in [2] similar to the one given in [6]. In this study, the receptance based solution method is referred to as Receptance Method (RM). The details of the formulation of RM used in this study can be found in [8].

Reducing the computational effort substantially without sacrificing accuracy significantly is of utmost importance, especially when extensive parametric studies are needed such as in design optimization and probabilistic analyses, the performances and accuracies of these methods are compared by applying all four methods to a benchmark system. The benchmark system consists of a finite element model of a beam with dry friction elements. Since the core attention in the design of nonlinear structures is mostly given to resonance regions, where the periodic vibration amplitudes and resonance frequencies determine the main dynamic characteristics, the main focus of this study is placed on periodic forced response regimes near resonances. A cantilever beam with different numbers of nonlinear elements and excited by different forcing levels is used for the comparison of these four methods in terms of computational time and accuracy. Several conclusions are derived from the case studies, the main objective being to provide guidelines to users in academia and industry about when to use which method for better accuracy and/or computational speed.

32.2 Case Study

The theories of all four methods compared here are given in previous works of the authors [1–4, 7, 8].

The application and the comparison of the methods are presented here by using a cantilever beam with different number of dry friction elements. The cantilever beam is divided into eight elements in which each node has transverse and rotational DOFs adding up to 16 DOFs. Firstly a single dry friction element is inserted between the transverse DOF of the free end and the ground; and then eight dry friction elements are placed between all transverse DOFs of the beam nodes and the ground. Two different force amplitudes, numerically $F = 10$ N and $F = 1$ N, are exerted on the system in turn. Transverse responses of the free end are calculated and compared with each other, as well as with the reference¹ responses obtained by using MSM-LM including all modes.

Performances of the methods in all cases are compared using three different criteria. The first one is the computational time comparison for about 250 solution points. For frequency response analyses, equidistant frequency points were specified in the depicted interval of interest. For the preliminary nonlinear modal analysis, the step length of the path continuation with respect to energy was adjusted to achieve 250 solution points as well. All methods are implemented in Matlab R2015 and the analyses are performed in the same computer whose properties are as Intel(R) Core(TM) i7 CPU 950 @ 3.07 GHz, 8.00 RAM and 64-bit operating system. Secondly, *amplitude error* is used, which is defined as the difference between the maximum amplitude obtained by using the method considered and the exact maximum amplitude in the frequency range of interest. The last one is *frequency error*, which is the difference between the resonance frequency value corresponding to the maximum amplitude obtained in each approach and the exact one. Mathematically, they are expressed as

$$Amplitude\ Error = \left| \frac{x_{max}^{exc} - x_{max}^{obt}}{x_{max}^{exc}} \right| \times 100 \quad , \quad Frequency\ Error = \left| \frac{\omega_{max}^{exc} - \omega_{max}^{obt}}{\omega_{max}^{exc}} \right| \times 100.$$

In Fig. 32.1, the forced responses are depicted for varying excitation levels utilizing one and eight nonlinear elements. For this specific case, using just one mode gives satisfactory results at resonance region in almost all modal methods. However, it is seen from Tables 32.1, 32.2, 32.3, and 32.4 that in this specific case study MSM-HM outperforms other methods in terms of response accuracy for almost all cases considered. It is interesting to note that the number of nonlinear elements directly affects the computational time. The maximum increase in computational time with the increase in the number of nonlinear elements is observed in RM. Further studies showed that when the contributions of all modes are considered, using RM is the most beneficial if nonlinearity is local, as the computational effort mainly depends on the number of nonlinear DOFs and therefore is almost independent of the number of remaining DOFs. When the total number of nonlinear DOFs increases, MSM-LM will require less computational time as can be seen from Tables 32.3 and 32.4. MSM-NM requires a Preliminary Modal Analysis (PMA) which is performed to determine the single mode where the energy is basically concentrated. This

¹In the following, the numerical results obtained by Harmonic Balance for this reference model are briefly referred to as ‘exact’ results.

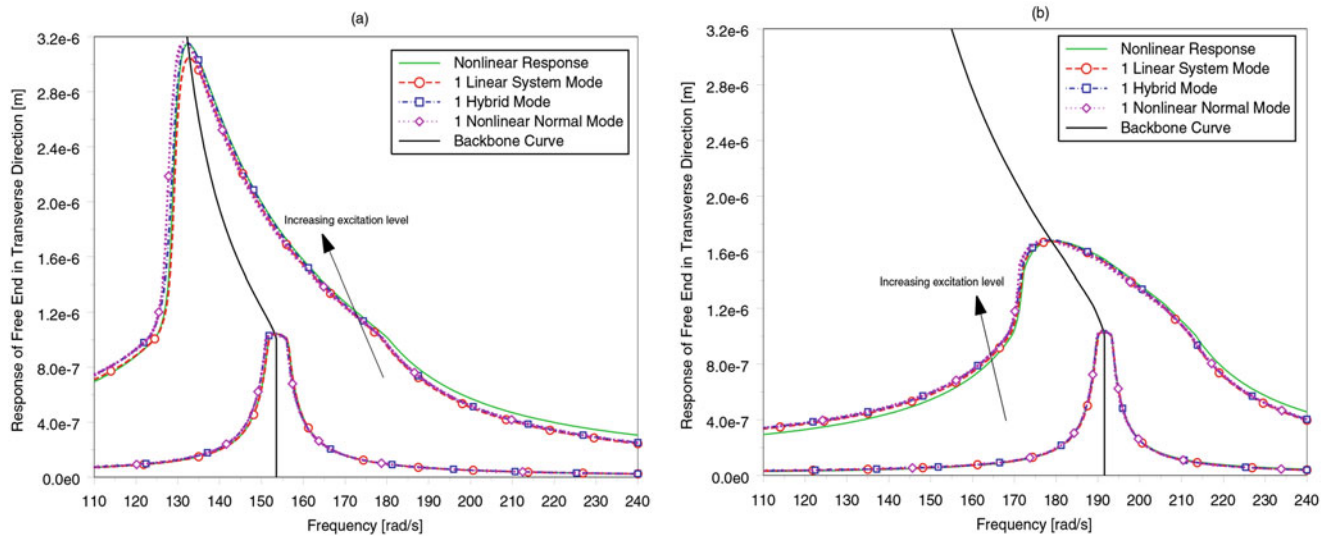


Fig. 32.1 Displacement amplitude of free end in transverse direction ((a) 1 nonlinear element attached, (b) 8 nonlinear elements attached)

Table 32.1 Error and time comparison of the methods for 1 dry friction element ($F = 10\text{ N}$)

Method used	Amp. error (%)	Freq. error (%)	Comp. time (s)		
			PMA	FRA	Total
MSM-LM (1Mode)	3.28	0.32	–	0.42	0.42
MSM-HM (1Mode)	0.13	0.08	–	0.61	0.61
MSM-NM (1Mode)	0.46	0.69	2.03	–	2.03
RM (1Mode)	3.28	0.32	–	0.57	0.57
RM (2Modes)	0.44	0.02	–	0.61	0.61

Table 32.2 Error and time comparison of the methods for 1 dry friction element ($F = 1\text{ N}$)

Method used	Amp. error (%)	Freq. error (%)	Comp. time (s)		
			PMA	FRA	Total
MSM-LM (1Mode)	0.33	0.33	–	0.47	0.47
MSM-HM (1Mode)	0.003	0	–	0.66	0.66
MSM-NM (1Mode)	0.0071	0.034	2.03	–	2.03
RM (1Mode)	0.33	0.33	–	0.58	0.58
RM (2Modes)	0.07	0	–	0.59	0.59

Table 32.3 Error and time comparison of the methods for 8 dry friction elements ($F = 10\text{ N}$)

Method used	Amp. error (%)	Freq. error (%)	Comp. time (s)		
			PMA	FRA	Total
MSM-LM (1Mode)	0.093	0.29	–	0.77	0.77
MSM-HM (1Mode)	0.43	0.48	–	0.98	0.98
MSM-NM (1Mode)	0.13	0.93	3.44	–	3.44
RM (1Mode)	0.093	0.29	–	1.69	1.69
RM (2Modes)	0.17	0.10	–	1.71	1.71

mode dominates the system response and is treated as nonlinear. This procedure introduces an extra computational cost which is in the order of calculating a single Frequency Response Analysis (FRA) for a given nonlinearity. It is carried out only once at the very beginning of the response calculations and therefore, when the response calculations at several excitation levels are of interest, the additional computational overhead becomes less important, making this method advantageous from the computational time point of view, compared to the other methods.

Table 32.4 Error and time comparison of the methods for 8 dry friction elements ($F = 1$ N)

Method used	Amp. error (%)	Freq. error (%)	Comp. time (s)		
			PMA	FRA	Total
MSM-LM (1Mode)	0.033	0.35	–	0.74	0.74
MSM-HM (1Mode)	0.003	0	–	0.97	0.97
MSM-NM (1Mode)	0.014	0.014	3.44	–	3.44
RM (1Mode)	0.033	0.35	–	1.81	1.81
RM (2Modes)	0.05	0	–	1.87	1.87

The precise computation times depend, among others, on the chosen resolution. Recall that our target was to have 250 solution points for both FRA and PMA. This is to some extent arbitrary, as a different resolution of the frequency axis might be appropriate than of the energy axis.

32.3 Conclusions

In this study, four methods developed in the previous studies of the authors [1–4, 7, 8] for periodic response analysis of nonlinear multi degree of freedom systems are compared. It is aimed to study the computational accuracy and speed of each method under different conditions (such as, different response levels and types of nonlinearity). Although many case studies with different types of nonlinear elements are conducted, only the results for dry friction nonlinearity are given here, because of space limitations. From these case studies it is concluded that RM is the most advantageous when the number of nonlinear DOFs are small as in the case of local nonlinearities, since its computational effort is basically determined by only the number of nonlinear algebraic equations—nonlinear DOFs—to be solved, not by the number of total DOFs. It should be noted that elements of receptance matrix used in RM are calculated by utilizing the linear modes of the system. Therefore, the number of modes used can be increased in order to improve response accuracy, since computational burden of RM is not strongly dependent on the number of modes used. As the number of nonlinear DOFs increases, on the other hand, MSM-LM performs much better than RM in terms of computational effort. It should also be noted that exactly the same accuracy level is obtained when the same number of linear modes are used in MSM-LM and in RM. Both methods can also deal with strong modal interactions. MSM-HM, which uses hybrid mode shapes, is able to capture the amplitude dependence of the deflection shapes, and can, thus, be more efficient than MSM-LM or RM, which use classical linear modes, in terms of accuracy for almost all cases. Additionally, in case of a highly nonlinear system, MSM-HM reduces the number of nonlinear equations to be solved further. Hence, it is also more advantageous than the other methods in terms of computational effort since one needs to increase the number of modes in MSM-LM or RM to attain a similar accuracy level of MSM-HM. However, MSM-HM is limited to regimes where single-term Harmonic Balance offers sufficient accuracy. MSM-NM also gives quite accurate responses in the neighborhood of resonance region for systems with well-separated modes. Since the method assumes the nonlinear response is dominated by a particular nonlinear mode, it cannot account for strong nonlinear modal interactions. Moreover, MSM-NM requires a preliminary modal analysis to compute nonlinear mode. After this, a closed-form expression is available for the frequency response, making the computation cost for the actual response analysis negligible. This makes MSM-NM well-suited when only excitation forces, linear damping properties and certain other properties are varied, since then the preliminary modal analysis does not have to be repeated. If other parameters are varied, or the response is of interest for only a single parameter set, the computation overhead of the preliminary analysis makes MSM-NM less attractive.

References

1. Kuran, B., Özgüven, H.N.: A modal superposition method for non-linear structures. *J. Sound Vib.* **189**(3), 315–339 (1996)
2. Tanrikulu, O., Kuran, B., Özgüven, H.N., Imregun, M.: Forced harmonic response analysis of nonlinear structures using describing functions. *AIAA J.* **31**(7), 1313–1320 (1993)
3. Ferhatoglu, E., Cigeroglu, E., Özgüven, H.N.: A new modal superposition method for nonlinear vibration analysis of structures using hybrid mode shapes. *Mech. Syst. Signal Process.* **107**, 317–342 (2018)
4. Krack, M., Panning-von Scheidt, L., Wallaschek, J.: A method for nonlinear modal analysis and synthesis: application to harmonically forced and self-excited mechanical systems. *J. Sound Vib.* **332**(25), 6798–6814 (2013)
5. Krack, M.: Nonlinear modal analysis of nonconservative systems: extension of the periodic motion concept. *Comput. Struct.* **154**, 59–71 (2015)

6. Menq, C.-H., Griffin, J.H., Bielak, J.: The forced response of shrouded fan stages. *J. Vib. Acoust. Stress Reliab.* **108**(1), 50–55 (1986)
7. Maliha, R., Doğruer, C.U., Özgüven, H.N.: Nonlinear dynamic modeling of gear-shaft-disk-bearing systems using finite elements and describing functions. *J. Mech. Des.* **126**(3), 534–541 (2004)
8. Koyuncu, A., Cigeroglu, E., Özgüven, H.N.: Localization and identification of structural nonlinearities using cascaded optimization and neural networks. *Mech. Syst. Signal Process.* **95**, 219–238 (2017)

Chapter 33

Reduced Order Modeling of Bolted Joints in Frequency Domain



Gokhan Karapistik and Ender Cigeroglu

Abstract Most of the structural systems assembled by using bolted joints. Therefore, bolted joint models have a critical importance to estimate the behavior of the overall assembled system. There are several linear bolted joint models which consist of spring and dashpot elements in literature. While they can estimate the resonant frequency of the overall system with a sufficient accuracy, linear bolted joint models are inadequate for approximating the damping which arises from the friction in the contact interface of assembled system. On the other hand, there are examples of nonlinear bolted joint models which utilize 3D contact models to account for the frictional damping behavior in the literature. However, modeling the structures with many bolted joints by using high fidelity 3D contact models is very time consuming. Therefore, reduced order bolted joint models with sufficient accuracy are in need. In this paper, a method for modeling bolted joints in frequency domain is introduced. The joint model consists of microslip friction elements each one of which is constructed by several Coulomb friction elements in parallel and located at both sides of bolt holes.

Keywords Joint model · Reduced joint model · Microslip friction · Multiple macroslip elements · Nonlinear vibrations

33.1 Introduction

Bolts are utilized to establish connection in many structural components. Fastening a structural component with bolts introduce complexity to the structural integrity in terms of both stiffness and damping characteristics. There are several studies to estimate the behavior of the bolted joints with linear springs and dashpots [1, 2]. However, inadequacy in capturing the energy loss of the structural system, especially with changing excitation levels, is a shortcoming of the linear joint models. To deal with the shortage of damping estimation, high fidelity models have been studied in the past few decades [3–5]. Nonetheless, computational cost of high fidelity models is considerable if a structural system with a lot of bolts is to be modeled. Main reason in this insufficiency of damping behavior in reduced order linear models is the absence of microslip friction model in the contact area. Structures with bolted joint have a complicated contact area exhibiting a variable contact force distribution. The contact forces near the bolt hole are sufficiently high; whereas, they become very low at some distant. Due to variability in contact forces, microslip like behavior arises. Hence, it is crucial to model the microslip friction present in the contact area. In order to model the microslip behavior, either specific microslip models [6–10] or distributed macroslip models are utilized [11, 12]. In macroslip models, entire surface associated with the friction model is either in slip state or in stick state. However, in microslip models, unlike macroslip models, partial slips in localized areas are allowed in the contact interface; hence, energy can be dissipated without the necessity of gross slip. In this study, the microslip friction element developed by Cigeroglu et al. [6] is used in modeling of bolted connections. However, since the variations of normal force in the bolted joints are relatively small, in this study, normal load variation is neglected. A reduced order joint model is introduced and it is compared with a representative high fidelity model obtained by utilizing multiple macroslip elements which is common in the modeling of friction contacts in bladed disks [11–13]. The Brake-Reuß beam [14] is considered for the comparison of the two different friction models. A nonlinear static analysis is performed in order to obtain the contact force distribution in the joint area which is used as the normal forces acting on the macroslip elements used in the high

G. Karapistik

Department of Mechanical Engineering, Middle East Technical University, Ankara, Turkey

ROKETSAN A.Ş., Kemalpaşa Mah. Şehit Yüzbaşı Adem Kutlu Sok. No:21, Ankara, Turkey

E. Cigeroglu (✉)

Department of Mechanical Engineering, Middle East Technical University, Ankara, Turkey

e-mail: ender@metu.edu.tr

fidelity model similar to [13]. For the reduced order joint modeling, macroslip friction elements are attached at both sides of bolt holes. Both systems are analyzed and the results obtained are compared with each other.

33.2 Theory

33.2.1 Nonlinear Static Analysis of Brake-Reuß Beam

Abaqus FEA software is used for the nonlinear static analysis of the Break-Reuß beam. In this model; bolts, washers and nuts are connected to each other so that they behave as a single part (tie constraint). Surface to surface contact algorithm with the penalty method is imposed between the contacting surfaces of beam structures in order to obtain the contact pressure distribution. 11500 N preload is applied from the center of the bolt shank to each bolt in the model. Finite element model (FEM) of Break-Reuß beam and the normal contact force distribution obtained through static analysis are shown in Fig. 33.1.

33.2.2 Representative High Fidelity Model

In this model all the nodes coincident to each other in the contact area are connected with one dimensional macroslip friction elements with constant normal loads. 1D macroslip friction elements consist of three parameters: tangential stiffness, normal load and coefficient of friction. In this model, tangential stiffness and coefficient of friction for all the friction elements are assumed to be 1000 N/mm and 0.12, respectively. Normal contact forces obtained from nonlinear static analysis are used as the normal loads acting on the friction elements. Locations of the contact nodes used in the high fidelity model are shown in Fig. 33.2 which are selected based on the normal contact force distribution given in Fig. 33.1b.

33.2.3 Reduced Order Joint Model

In the reduced order model, contact area is divided in to six regions, and two virtual nodes are placed at both sides of each bolt hole in the center of the divided regions as shown in Fig. 33.3. Hence, 12 virtual nodes are created in total for the six

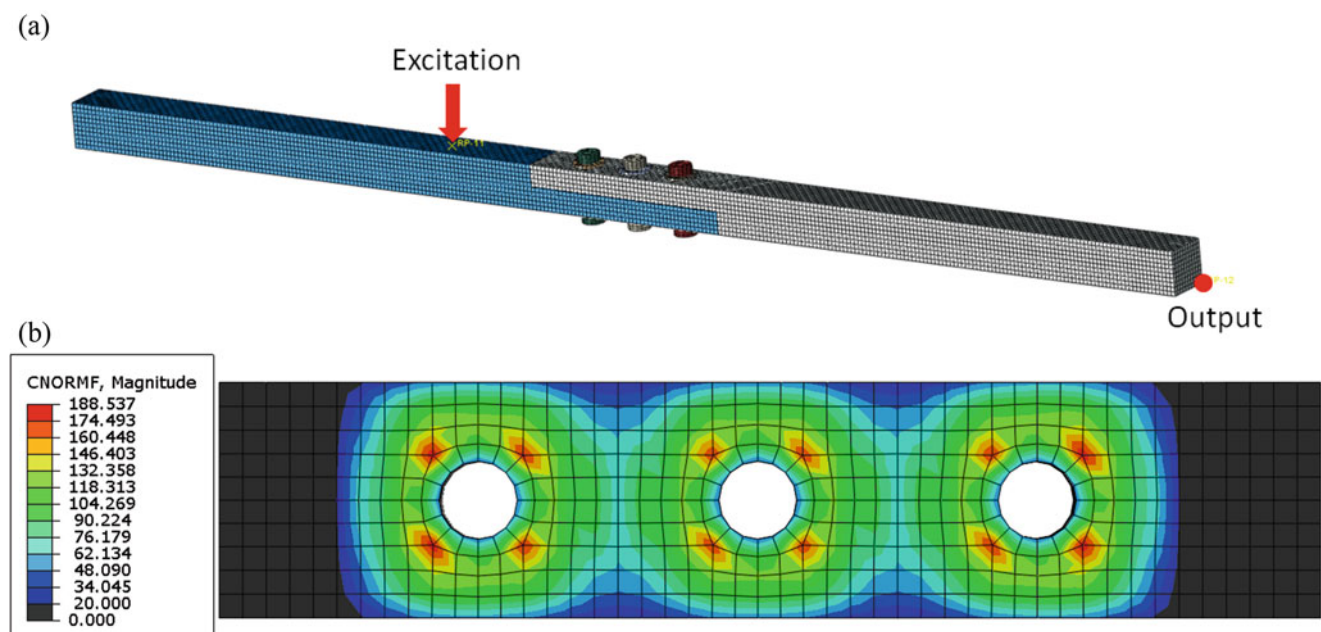


Fig. 33.1 (a) FEM of Break-Reuß beam and (b) normal contact force distribution [N]

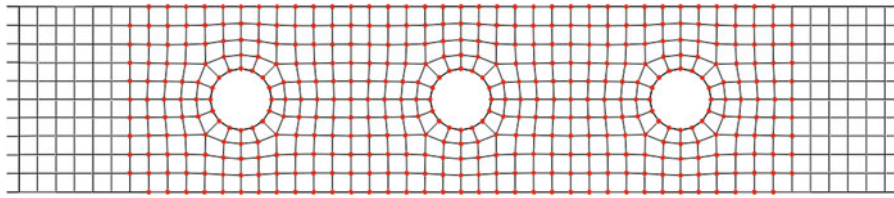


Fig. 33.2 Contact nodes used in the high fidelity model

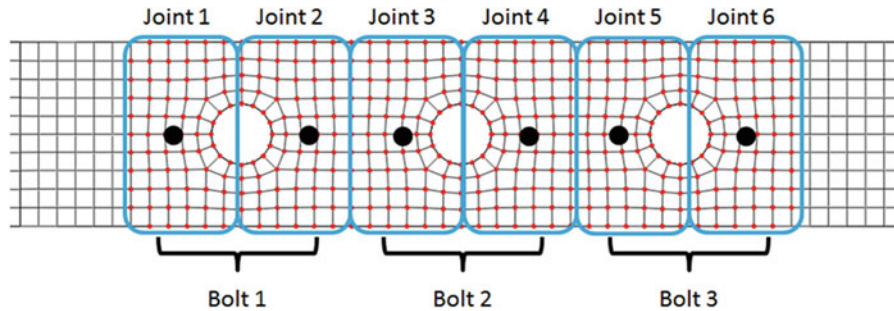


Fig. 33.3 Locations of the virtual nodes used for reduced joint model

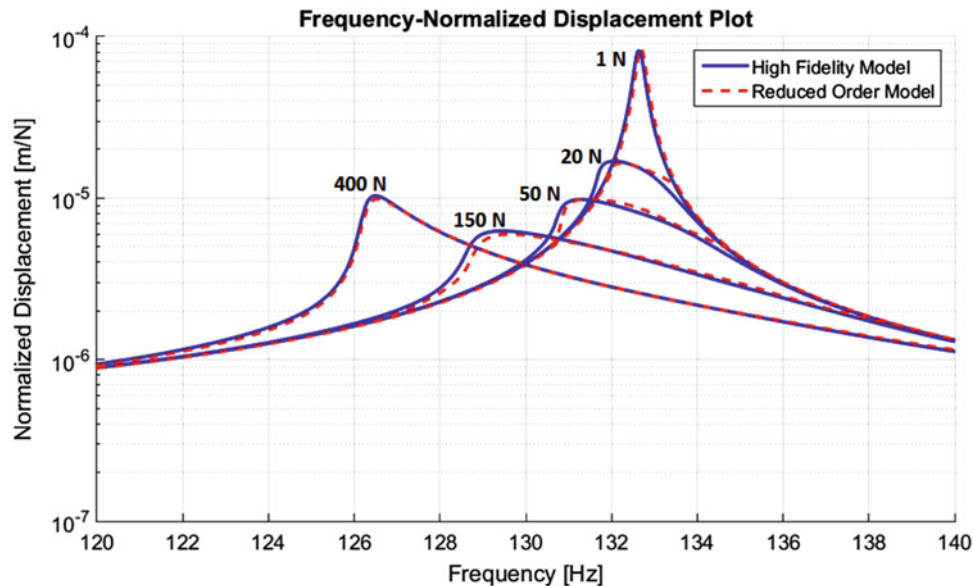


Fig. 33.4 Comparison of normalized displacement of high fidelity and reduced order joint models

contact pairs used. Virtual nodes coincident to each other form the contact pairs with reduced order joint elements created by utilizing the microslip friction model presented in [6]. Main idea of the reduced order joint element is to estimate the microslip behavior occurring in the joint contact area by utilizing less number of contact pairs. Parameters of the reduced order joint model are obtained by optimizing the summation of hysteresis loops of representative high fidelity model in the corresponding region of virtual nodes.

33.3 Results and Discussion

For high fidelity model and reduced order joint model, harmonic balance method with a single harmonic content is used for the frequency domain solution. Modal superposition method [15] is employed in order to reduce the number of nonlinear equations resulting from the use of FEM. Rigid body modes and first three bending modes of the system are included in the modal superposition. Excitation and output locations are shown in Fig. 33.1a. Both models are solved with free-free boundary conditions and 0.2% structural damping is imposed.

Normalized displacement for both high fidelity model and reduced order model are obtained for several excitation levels which are shown in Fig. 33.4. In the high fidelity model, 400 1D macroslip friction elements are used in total. However, in the reduced order joint model, 18 friction elements (6 reduced order joints and 3 1D macroslip friction elements for each joint) are used in total. Although there is a great difference in the number of friction elements utilized, results show that dynamic behavior of the jointed structure with the reduced order joint model can be estimated with similar accuracy as the one estimated from the high fidelity contact model.

Acknowledgments Authors would like to gratefully acknowledge the support provided by ROKETSAN A.Ş. through SAYP project no: 82202625-250.02-2016-O-17255.

References

1. Tsai, J.-S., Chou, Y.-F.: The identification of dynamic characteristics of a single bolt joint. *J. Sound Vib.* **125**(3), 487–502 (1988)
2. Mehrpouya, M., Graham, E., Park, S.S.: FRF based joint dynamics modeling and identification. *Mech. Syst. Signal Process.* **39**(1–2), 265–279 (2013)
3. Bograd, S., Reuss, P., Schmidt, A., Gaul, L., Mayer, M.: Modeling the dynamics of mechanical joints. *Mech. Syst. Signal Process.* **25**(8), 2801–2826 (2011)
4. Petrov, E.P.: Frequency-domain sensitivity analysis of stability of nonlinear vibrations for high-fidelity models of jointed structures. *ASME J. Turbomach.* **140**, 1–12 (2017)
5. Lacayo, R., Pesaresi, L., Groß, J., Fochler, D., Armand, J., Salles, L., Schwingshackl, C., Allen, M., Brake, M.: Nonlinear modeling of structures with bolted joints: a comparison of two approaches based on a time-domain and frequency-domain solver. *Mech. Syst. Signal Process.* **114**, 413–438 (2019)
6. Cigeroglu, E., An, N., Menq, C.H.: A macroslip friction model with normal load variation induced by normal motion. *Nonlinear Dyn.* **50**(3), 609–626 (2007)
7. Tworzydło, W.W., Cecot, W., Oden, J.T., Yew, C.H.: Computational micro- and macroscopic models of contact and friction: formulation, approach and applications. *Wear.* **220**, 113–140 (1998)
8. Menq, C.H., Bielak, J., Griffin, J.H.: The influence of macroslip on vibratory response, part I a new macroslip model. *J. Sound Vib.* **107**(2), 279–293 (1986)
9. Menq, C.H., Bielak, J., Griffin, J.H.: The influence of macroslip on vibratory response, part II a comparison with experimental results. *J. Sound Vib.* **107**(2), 295–307 (1986)
10. Cigeroglu, E., Lu, W., Menq, C.H.: One-dimensional dynamic macroslip friction model. *J. Sound Vib.* **292**(3–5), 881–898 (2006)
11. Cigeroglu, E., Menq, C.H.: A macroslip friction model for the analysis of frictionally damped turbine blades. In: *IMECHE Ninth International Conference on Vibrations in Rotating Machinery*, vol. 1, pp. 185–196 (2008)
12. Petrov, E.P., Ewins, D.J.: Analytical formulation of friction interface elements for analysis of nonlinear multi-harmonic vibrations of bladed disks. *J. Turbomach.* **125**(2), 364 (2003)
13. Cigeroglu, E., An, N., Menq, C.-H.: Forced response prediction of constrained and unconstrained structures coupled through frictional contacts. *J. Eng. Gas Turbines Power.* **131**(2), 022505 (2009)
14. Brake, M.R., Reuss, P., Segalman, D.J., Gaul, L.: Variability and repeatability of jointed structures with frictional interfaces. *Conf. Proc. Soc. Exp. Mech. Ser. 1*, 252 (2014)
15. Ferhatoglu, E., Cigeroglu, E., Özgüven, H.N.: A new modal superposition method for nonlinear vibration analysis of structures using hybrid mode shapes. *Mech. Syst. Signal Process.* **107**, 317–342 (2018)



Chapter 34

Comparison of ANM and Predictor-Corrector Method to Continue Solutions of Harmonic Balance Equations

Lukas Woiwode, Nidish Narayanaa Balaji, Jonas Kappauf, Fabia Tubita, Louis Guillot, Christophe Vergez, Bruno Cochelin, Aurélien Grolet, and Malte Krack

Abstract In this work we apply and compare two numerical path continuation algorithms for solving algebraic equations arising when applying the Harmonic Balance Method to compute periodic regimes of nonlinear dynamical systems. The first algorithm relies on a predictor-corrector scheme and an Alternating Frequency-Time approach. This algorithm can be applied directly also to non-analytic nonlinearities. The second algorithm relies on a high-order Taylor series expansion of the solution path (the so-called Asymptotic Numerical Method) and can be formulated entirely in the frequency domain. The series expansion can be viewed as a high-order predictor equipped with inherent error estimation capabilities, which permits to avoid correction steps. The second algorithm is limited to analytic nonlinearities, and typically additional variables need to be introduced to cast the equation system into a form that permits the efficient computation of the required high-order derivatives. We apply the algorithms to selected vibration problems involving mechanical systems with polynomial stiffness, dry friction and unilateral contact nonlinearities. We assess the influence of the algorithmic parameters of both methods to draw a picture of their differences and similarities. We analyze the computational performance in detail, to identify bottlenecks of the two methods.

Keywords Harmonic balance · Continuation · Alternating frequency-time scheme · Asymptotic numerical method · Nonlinear vibrations

34.1 Introduction

Harmonic Balance (HB) permits the efficient approximation of periodic solutions of nonlinear ordinary differential equations. Often, we want to determine the solution as a function of a free parameter. To this end, numerical path continuation is commonly applied. Continuation provides higher robustness and efficiency as compared to simply computing the solution for a sequence of equidistant parameter values. Perhaps more importantly, continuation allows us to overcome turning points and therefore to capture multiple solutions for a single parameter value. The purpose of this work is to enlighten the strengths and weaknesses of two popular methods for continuing solutions of the HB equations.

HB uses a truncated Fourier series as approximation ansatz. Substitution into the ordinary differential equation system gives a residual term, which is then made orthogonal to the Fourier basis function (Fourier–Galerkin projection). This corresponds to requiring that the Fourier coefficients of the residual are zero, for those harmonics retained in the ansatz.

L. Woiwode · M. Krack (✉)
University of Stuttgart, Stuttgart, Germany
e-mail: Lukas.Woiwode@ila.uni-stuttgart.de; Malte.Krack@ila.uni-stuttgart.de

N. N. Balaji
Rice University, Houston, TX, USA

J. Kappauf
University of Kassel, Kassel, Germany

F. Tubita
Ecole Centrale de Lyon, Lyon, France

L. Guillot · C. Vergez · B. Cochelin
École Centrale de Marseille, Marseille, France

A. Grolet
Ecole Nationale Supérieure d'Arts et Métiers Lille - LISPEN, Lille, France

When we apply this method to the equation of motion of a mechanical system, with generalized coordinates \mathbf{q} , subjected to periodic forcing, we obtain the algebraic equation system,

$$\hat{\mathbf{r}}(\hat{\mathbf{q}}, \Omega) := \mathbf{S}(\Omega) \hat{\mathbf{q}} + \hat{\mathbf{f}}_{\text{nl}}(\hat{\mathbf{q}}, \Omega) - \hat{\mathbf{f}}_{\text{ex}} \stackrel{!}{=} \mathbf{0}. \quad (34.1)$$

Herein, Ω is the angular excitation frequency, $\hat{\mathbf{q}}$ is the vector of Fourier coefficients of the approximation for $\mathbf{q}(t)$, and $\hat{\mathbf{f}}_{\text{nl}}$ and $\hat{\mathbf{f}}_{\text{ex}}$ are the Fourier coefficients of the nonlinear forces and the external forces, respectively. \mathbf{S} is dynamical stiffness matrix representing linear internal forces proportional to \mathbf{q} , $\dot{\mathbf{q}}$, and $\ddot{\mathbf{q}}$, where overdot denotes derivative with respect to time. \mathbf{S} is block diagonal (different harmonics are decoupled in the linear case).

34.1.1 Alternating-Frequency-Time Scheme with Predictor-Corrector Continuation (AFT-PreCo)

The AFT scheme approximates the Fourier coefficients $\hat{\mathbf{f}}_{\text{nl}}$ by sampling \mathbf{q} and $\dot{\mathbf{q}}$ at a certain number of equidistant time instants N along one period, evaluating $\mathbf{f}_{\text{nl}}(\mathbf{q}, \dot{\mathbf{q}})$ in the time domain, and applying the discrete Fourier transform to the samples of the nonlinear force. Hence, the nonlinear forces are represented by N samples. N affects the accuracy of the procedure and has to be selected properly. For polynomial forces, the sampling procedure is exact beyond a certain N . Otherwise, $\hat{\mathbf{f}}_{\text{nl}}$ is an approximation and contains aliasing errors. The great advantage of the AFT procedure is that it can be easily applied to smooth as well as non-smooth nonlinear forces. The downside of the AFT scheme is that it is not straight-forward to efficiently compute derivatives of order higher than one.

The AFT scheme is commonly combined with PreCo continuation. Suppose we want to determine $\hat{\mathbf{q}}$ for a range of the free parameter Ω . Starting from an initial solution \mathbf{X}^0 with $\mathbf{X} := [\hat{\mathbf{q}}^T \ \Omega]^T$, we can do a prediction,

$$\mathbf{X}_{\text{PreCo}}^{\text{pre}} = \mathbf{X}^0 + \alpha \mathbf{X}^1, \quad (34.2)$$

where \mathbf{X}^1 is the unit tangent to the solution path at the point \mathbf{X}^0 and α is the step length of the prediction. $\mathbf{X}_{\text{PreCo}}^{\text{pre}}$ will usually not satisfy Eq. (34.1). Hence, correction steps are necessary, commonly in the form of Newton iterations, to improve the estimate until $\|\hat{\mathbf{r}}(\mathbf{X})\| < \epsilon$ for a given tolerance ϵ . Note that the equation system is under-determined. This is often resolved by considering an additional equation that ensures that the new solution point lies at a certain distance α from \mathbf{X}^0 (arc-length continuation). In the PreCo, the step length is a crucial parameter: A too small step length leads to spurious computation effort, a too large step length may lead to many and costly correction iterations or even divergence. The step length is commonly adjusted automatically with the intent to achieve a desired number of correction iterations. However, it is advisable to choose reasonable upper and lower bounds, to avoid overlooking important features of the solution path and getting stuck near branching points, respectively. These bounds are usually chosen based on experience.

34.1.2 Classical Harmonic Balance with Asymptotic Numerical Method (cHB-ANM)

The ANM can be interpreted as high-order predictor (order p), which is a Taylor series expansion of the solution path, around \mathbf{X}^0 , in the arc length α ,

$$\mathbf{X}_{\text{ANM}}^{\text{pre}} = \mathbf{X}^0 + \alpha \mathbf{X}^1 + \dots + \alpha^p \mathbf{X}^p. \quad (34.3)$$

The step size α is determined such that the estimated error, based on the range of utility of the Taylor series, remains below the tolerance ϵ , with the intent to completely avoid correction iterations. For the ANM, the algebraic equation system is commonly recast into quadratic form, i.e., with only constant, linear and bilinear (quadratic) terms in the unknowns. The Fourier coefficients of the nonlinear terms can in this case be expressed analytically without having to resort to sampling, which corresponds to classical HB. Note that all variables, including the nonlinear forces are represented by $2H + 1$ Fourier coefficients. The quadratic form permits the successive computation of \mathbf{X}^k up to high order. Only a single Jacobian matrix

has to be factorized to determine all X^k , $k > 0$, per expansion point X^0 [1]. This contrasts the PreCo where several of such factorizations are required, one per Newton iteration, to get to the next point on the solution branch.

The cHB-ANM cannot directly deal with non-smooth nonlinearities. These have to be approximated by appropriate analytic functions (regularization). Moreover, the equations have to be brought into quadratic form, which generally requires introducing auxiliary variables and equations. For details on how the cHB-ANM can be implemented in a computationally efficient and user-friendly way, we refer to [2].

34.2 Results

Figure 34.1a depicts the frequency response of the Duffing oscillator. For the same H , both methods have the same number of unknowns (Fourier coefficients of q up to order H). However, the results differ as the nonlinear terms are represented in a different way. For the cubic term of the Duffing oscillator, it can be shown that the sampling procedure yields the Fourier coefficients of the nonlinear forces up to order H without aliasing error for $N \geq 4H + 1$. For Fig. 34.1a N was selected accordingly. For $2H_{\text{CHB}} + 1 = N_{\text{AFT}}$, the nonlinear terms are represented with the same number of Fourier coefficients in cHB as samples in the AFT, so that a similar accuracy can be expected. Hence, AFT $N_{\text{AFT}} = 5$ agrees well with cHB $H_{\text{ANM}} = 2$, $N_{\text{AFT}} = 13$ with $H_{\text{ANM}} = 6$ and so on.

Figure 34.1b shows the results for a single degree of freedom (SDOF) oscillator with elastic dry friction nonlinearity. Without regularization, only AFT can be applied, and a reasonable approximation is achieved with $H = 1$, $N = 45$. To regularize, an auxiliary variable describing the force had to be introduced, which is not well-represented with $H = 1$. Again, for $H = 22 = (45 - 1)/2$ both methods yield similar results for the regularized model. The remaining deviation to the reference is due to regularization. To compute the results depicted in Fig. 34.1b, AFT-PreCo $H = 1$, $N = 45$ (non-smooth) was about 25 times faster than cHB-ANM $H = 22$. We observed that as the regularization becomes steeper, the number of harmonics in the cHB-ANM has to be increased to continue the whole branch. Sometimes this value seems too high to be useful.

In Fig. 34.1c the computation effort is shown for a modal model (n modes) of a beam with geometric nonlinearity. The results suggest that cHB-ANM becomes more efficient for larger numbers of DOFs. The number of solution points was larger in the case of the cHB-ANM, which overall lead to approximately the same total number of Jacobian factorizations for the entire solution path. Apparently, the AFT calculation of the nonlinear forces and their derivatives is less efficient than

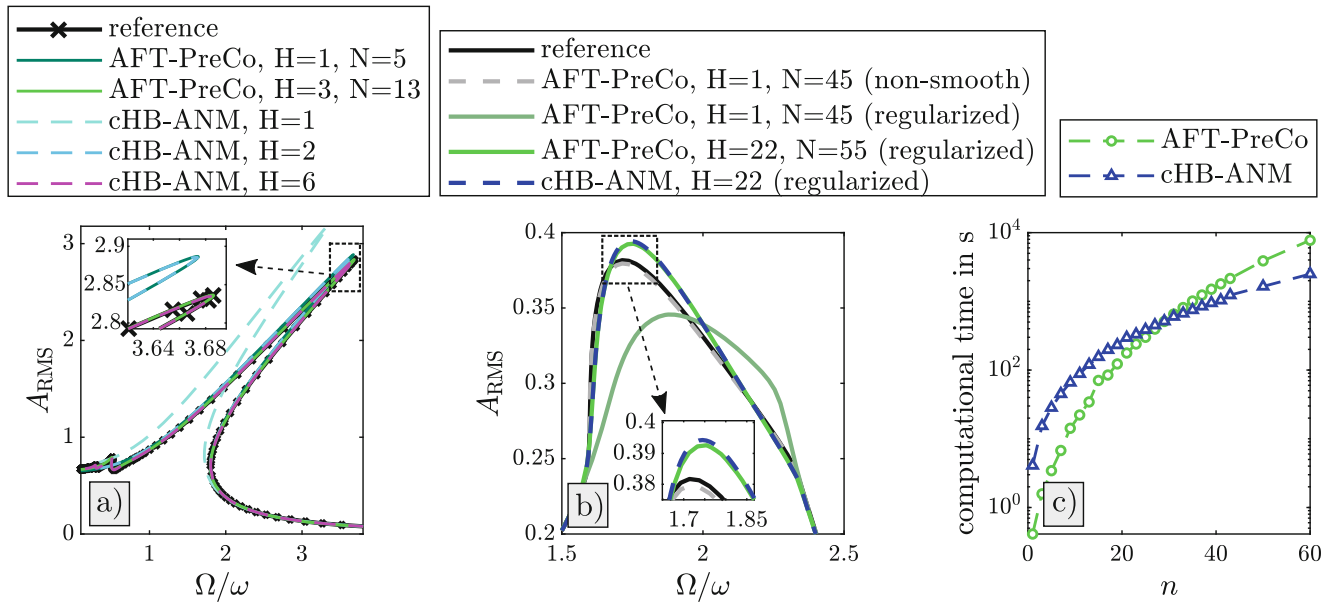


Fig. 34.1 Representative results: (a) Duffing oscillator; (b) SDOF system with elastic dry friction; (c) geometrically nonlinear beam with n coupled modal coordinates. A_{RMS} is the root-mean square of the generalized coordinate. More results on different benchmark systems and further analyses of opportunities and limitations of both methods will be published in a journal article

the evaluation of the nonlinear terms and calculation of higher-order Taylor series coefficients within the cHB-ANM. Further investigations are in progress to gain a better understanding of this.

34.3 Conclusions

The results indicate that the AFT-PreCo is better suited for non-smooth nonlinearities such as stick-slip friction or unilateral constraints. The cHB-ANM is highly efficient for low-order polynomial nonlinearities and problems with a large number of DOFs, as in the case of geometrically nonlinear finite element models. It is expected that the cHB-ANM would greatly benefit from selecting a separate, higher truncation order for the auxiliary variables.

References

1. Cochelin, B., Vergez, C.: A high order purely frequency-based harmonic balance formulation for continuation of periodic solutions. *J. Sound Vib.* **324**(1–2), 243–262 (2009)
2. Guillot, L., Cochelin, B., Vergez, C.: A generic and efficient Taylor series based continuation method using a quadratic recast of smooth nonlinear systems, *Numerical Methods in Engineering*, pp 1–20, (2018). doi:[10.1002/nme.6049](https://doi.org/10.1002/nme.6049)



Chapter 35

A Priori Methods to Assess the Strength of Nonlinearities for Design Applications

E. Rojas, S. Punla-Green, C. Broadman, Matthew R. W. Brake, B. R. Pacini, R. C. Flicek, D. D. Quinn, C. W. Schwingshackl, and E. Dodgen

Abstract One of the greatest challenges to the optimization of assembled systems is a lack of understanding of how jointed interfaces augment system dynamics. Thus, a design tool that can assess the nonlinearity of a joint prior to manufacturing and experimentation will lead to significant savings in qualification testing and improved performance in terms of dynamic properties and failure rates. This paper explores the *a priori* metric hypothesis for jointed structures, which states that the strength of a nonlinearity (SNL) can be estimated by a metric derived from both the magnitude and uniformity of contact pressure within an interface and the modal strain energy at an interface's location.

Keywords Jointed structures · Bolted joints · Nonlinear stiffness · Nonlinear damping · Interface dynamics

35.1 Introduction

The *a priori* metric hypothesis, stating that the SNL of a jointed system can be derived from the contact pressure and the modal strain energy at an interface's location, was based off four observations regarding the behavior of nonlinear systems:

1. Interfaces with high, uniform contact pressure yield system dynamics that appear linear [1].
2. Portions of interfaces that have a moderate contact pressure, which have previously been assumed to be time invariant during dynamic excitation, exhibit significant fluctuations during dynamic loading [2].
3. Portions of interfaces with low contact pressure are the source of energy dissipation within a jointed structure [1–3].
4. Modifications to the far-field structure around an interface affect how the interface is loaded, and thus affect the perceived strength of nonlinearity [4].

Sandia National Laboratories is a multimission laboratory managed and operated by National Technology and Engineering Solutions of Sandia, LLC., a wholly owned subsidiary of Honeywell International, Inc., for the U.S. Department of Energy's National Nuclear Security Administration under contract DE-NA-0003525.

E. Rojas
New Mexico State University, Las Cruces, NM, USA

S. Punla-Green
Rensselaer Polytechnic Institute, Troy, NY, USA

C. Broadman (✉) · M. R. W. Brake
William Marsh Rice University, Houston, TX, USA
e-mail: cwb6@rice.edu

B. R. Pacini · R. C. Flicek
Sandia National Laboratories, Albuquerque, NM, USA

D. D. Quinn
The University of Akron, Akron, OH, USA

C. W. Schwingshackl
Imperial College London, London, UK

E. Dodgen
Department of Energy's National Security Campus, Kansas City, MO, USA

This work attempts to validate this hypothesis by defining a SNL metric based on the reduction of natural frequency and the increase in energy dissipation as the response amplitude of a structure is increased. This metric will be developed by correlating numerically extracted contact pressure and modal strain from a finite element model (FEM) to experimentally extracted amplitude dependent frequency and damping.

35.2 Defining Strength of Nonlinearity

For the purposes of assessing the hypothesis, the SNL is defined here as Eq. (35.1).

$$S(\alpha, \beta, K_1, K_2) = \sqrt{(\alpha K_1)^2 + (\beta K_2)^2} + (\alpha K_1)^2 + (\beta K_2)^2 \quad (35.1)$$

$$\omega_p = \omega_l + K_1 A^{m-1} \quad (35.2)$$

$$\xi_p = \xi_l + K_2 A^{m-1} \quad (35.3)$$

Let Eq. (35.1) be the form of the SNL metric that was developed. This form was selected because a linear combination of a Euclidean norm and a sum of squares gave high resolution to a wide range of values. Equations (35.2) and (35.3) represent the theoretical behavior of amplitude dependent frequency and damping as derived through a perturbation analysis on a simplified 1 DOF mass-spring system with hysteretic damping. ω_p and ξ_p are the amplitude dependent natural frequency and damping of the examined system, ω_l is the linear natural frequency, ξ_l is the linear damping of the system, and A is the physical-space acceleration amplitude envelope of the system. Coefficients K_1 and K_2 enumerate the effect of the joint on the system, and m reflects how the interface of the joint influences the system. To focus on the effects of K_1 and K_2 , m is held constant at 1.25 across all systems; this value was selected to reflect the general shape of the amplitude dependent frequency and damping curves. Parameters α and β evenly weigh K_1 and K_2 so both frequency and damping nonlinearities equally impact the SNL.

35.3 Parameter Extractions

35.3.1 Amplitude Dependent Frequency and Damping

To investigate the universal applicability of the *a priori* metric hypothesis, experimental data from the Brake Reuss Beam [5], the S4-Beam [6], and the Four Bolt Interface (Fig. 35.1) were utilized. Amplitude dependent natural frequency and damping ratios for various modes of each structure were extracted from time responses measured from impact tests using the following process.

1. Impact structure and measure ring down time response.
2. Bandpass filter a single signal to isolate the response of a target mode as measured by that degree of freedom.
3. Hilbert transform this data and fit the amplitude dependent frequency and damping.
4. Repeat steps 1–3 at least 10 times for the target mode.



Fig. 35.1 The four bolt interface

5. Smooth and average the curves to generate a single amplitude dependent frequency curve and a single amplitude dependent damping curve for the targeted mode of the structure/configuration.
6. Scale measured response to the maximum response using FEM mode shape values as shown in Eq. (35.4).
7. Apply a least squares fit of Eqs. (35.2) and (35.3) to frequency and damping curves, extract the coefficients K_1 and K_2 , and calculate S using Eq. (35.1). Note: α and β were set to 20 and 1 respectively because these values most closely related the magnitudes of $\alpha[K_1]$ and $\beta[K_2]$ for all K_1 and K_2 , allowing frequency and damping to affect SNL equally.

$$A_{\max} = A_{\text{response}} \left(\frac{u_{\max}}{u_{\text{response}}} \right) \quad (35.4)$$

This process was repeated for each target mode for various assembled structures. For all configurations, bolt torque and impact force were altered to vary the contact pressure and to understand how force affects the behavior of systems. Due to modal coupling, the magnitude of change in frequency and dissipation increased with force. Modal coupling is still not well understood, so rather than normalize the response amplitude with respect to force levels, only trials with similar impact forces were compared. The post-processed data (S from step 7) was used as the training and validation sets to develop a correlation to contact pressure and modal strain (see Sect. 35.4).

35.3.2 Contact Pressure and Modal Strain

With emphasis on reducing the need for extensive computation, models of each configuration were created in Abaqus/CAE 2017 without rigorously tuning the model to the manufactured specimen nor defining the nonlinear characteristics of the joint. These models were run through the following analyses.

1. Linearized eigen analysis to obtain modal strain
2. Nonlinear frictionless interface contact pressure analysis

Based on these analyses, eleven statistics were calculated for each target mode of the various test structures: maximum, mean, standard deviation, skewness and kurtosis for both strain and contact pressure, and the contact area. These statistics were based on the strain and pressure values between individual elements in the joint interface and served as the independent variables for the model to determine SNL.

35.4 Correlation of Numerical and Experimental Parameters

The contact pressure and modal strain statistics data from Sect. 35.3.2 were input into MATLAB's built-in machine learning linear regression functions (*fitlm*, *step*, and *stepwiselm*) to establish a correlation with the measured SNL, S from Sect. 35.3.1. The results are shown in Eq. (35.5) with a determination of 70%. For all regression models, only statistically significant variables (p -value < 5%) were used.

$$S = 0.0658 + 1.74\mu_\varepsilon - 1.30\sigma_\varepsilon - 5.74 \left(10^{-9} \right) \sigma_{CP} - 41.3A_{CP} + 0.0413\beta_{2\varepsilon}^2 \quad (35.5)$$

where μ_ε = Mean strain, σ_ε = Standard deviation of strain, σ_{CP} = Standard deviation of contact pressure, A_{CP} = Area of contact pressure, $\gamma_{1\varepsilon}$ = Skewness of strain, $\beta_{2\varepsilon}$ = Kurtosis of strain.

This result is significant because this supports that the SNL of a beam can be mostly determined by evaluating contact pressure and the modal strain of a FEM. Using just five variables extracted through two non-rigorous numerical analyses, 70% of the SNL of a joint can be accounted for. To find the source of indeterminacy, SNL was split into frequency- and damping-based components by setting β and α to zero respectively. The strain and contact pressure parameters were correlated to frequency SNL (6) with 83% determination but were only correlated to damping SNL (7) with 52% determination. This indicates that just assessing variables pertaining to contact pressure and modal strain are not enough to describe the damping SNL; rather, another variable, such as surface roughness, must be used to better calculate SNL.

$$S_{\omega} = 0.00163 - 0.0777\mu_{\varepsilon} + 0.0634\sigma_{\varepsilon} - 0.00301\gamma_{1\varepsilon} + 1.28 \left(10^{-10}\right) \sigma_{CP} + 2.97 \left(10^{-4}\right) \beta_{2\varepsilon} + 0.516A_{CP} \quad (35.6)$$

$$S_{\zeta} = 0.0771 + 0.514\mu_{\varepsilon} - 4.18 \left(10^{-9}\right) \sigma_{CP} - 18.0A_{CP} - 0.0318 \text{Max}_{\varepsilon} \quad (35.7)$$

where μ_{ε} = Mean strain, σ_{ε} = Standard deviation of strain, σ_{CP} = Standard deviation of contact pressure, A_{CP} = Area of contact pressure, $\gamma_{1\varepsilon}$ = Skewness of strain, $\beta_{2\varepsilon}$ = Kurtosis of strain.

35.5 Conclusion

This work demonstrated the creation of a strength of nonlinearity metric to *a priori* predict the nonlinearity of a structure. A strength of nonlinearity metric was defined and then computed for different systems using experimentally extracted amplitude dependent natural frequency and damping curves. Along with this test data, modal strain and contact pressure from FEMs of the different test structures were used to create a model using machine learning that correlated contact pressure and modal strain statistics to SNL. This model identified the five variables needed to predict 70% of S , the six variables needed to predict 83% of S_{ω} , and the four variables needed to predict 52% of S_{ζ} . While these results are promising, the model could be improved by including variables such as surface roughness. Future research should focus on implementing this data into the metric, in addition to accounting for modal coupling and using different correlation methods to obtain a more accurate model.

Acknowledgments This research was conducted at the 2018 Nonlinear Mechanics and Dynamics (NOMAD) Research Institute supported by Sandia National Laboratories. Sandia National Laboratories is a multi-mission laboratory managed and operated by National Technology and Engineering Solutions of Sandia, LLC., a wholly owned subsidiary of Honeywell International, Inc., for the U.S. Department of Energy's National Nuclear Security Administration under contract DE-NA-0003525. The authors would also like to thank Bill Flynn from Siemens Industry Software NV for supplying the data acquisition and testing systems used to collect the experimental measurements presented throughout this work.

References

1. Dossogne, T., et al.: Experimental assessment of the influence of interface geometries on structural dynamic response. *Dyn. Coupled Struct.* **4**, 255–261 (2017)
2. Seeger, B., et al.: In situ measurements of interfacial contact pressure during impact hammer tests. *Nonlinear Dyn.* **1**, 225–236 (2018)
3. Goyder, H.G.D., Ind, P., Brown, D.: Development of a method for measuring damping in bolted joints. *Proc. ASME Design Eng. Tech. Conf.* **1**, 1253–1262 (2011)
4. Rosatello, M., et al.: Effect of far-field structure on joint properties. *Dyn. Coupled Struct.* **4**, 63–77 (2017)
5. Brake, M.R.W. (ed.): *The Mechanics of Jointed Structures*. Springer, Cham, Switzerland (2017)
6. Singh, A., et al.: Experimental Characterization of a new Benchmark Structure for Prediction of Damping Nonlinearity. *Nonlinear Dyn.* **1**, 57–78 (2018)



Chapter 36

Predictive Modeling of Bolted Assemblies with Surface Irregularities

Matthew Fronk, Gabriela Guerra, Matthew Southwick, Robert J. Kuether, Adam Brink, Paolo Tiso, and Dane Quinn

Abstract Bolted interfaces are a major source of uncertainty in the dynamic behavior of built-up assemblies. Contact pressure distribution from a bolt's preload governs the stiffness of the interface. These quantities are sensitive to the true curvature, or flatness, of the surface geometries and thus limit the predictive capability of models based on nominal drawing tolerances. Fabricated components inevitably deviate from their idealized geometry; nominally flat surfaces, for example, exhibit measurable variation about the desired level plane. This study aims to develop a predictive, high-fidelity finite element model of a bolted beam assembly to determine the modal characteristics of the preloaded assembly designed with nominally flat surfaces. The surface geometries of the beam interface are measured with an optical interferometer to reveal the amount of deviation from the nominally flat surface. These measurements are used to perturb the interface nodes in the finite element mesh to account for the true interface geometry. A nonlinear quasi-static preload analysis determines the contact area when the bolts are preloaded, and the model is linearized about this equilibrium state to estimate the modal characteristics of the assembly. The linearization assumes that nodes/faces in contact do not move relative to each other and are enforced through multi-point constraints. The structure's natural frequencies and mode shapes predicted by the model are validated by experimental measurements of the actual structure.

Keywords Modal analysis · Preload analysis · Bolted joints · Perturbed mesh · Interface stiffness

36.1 Introduction

The dynamic behavior of monolithic structures can be accurately modeled using conventional and well-established computational and analytical tools such as finite element analysis. However, the presence of joints and mechanical interfaces adds an appreciable degree of uncertainty to the dynamic behavior of a mechanical system and presents significant modeling challenges. Since the use of joints in design is ubiquitous, it is imperative to develop accurate models to predict the structural dynamic response of assembled systems that include bolted interfaces.

M. Fronk (✉)
Department of Mechanical Engineering, Georgia Institute of Technology, Atlanta, GA, USA
e-mail: mfronk3@gatech.edu

G. Guerra
Department of Mechanical and Aerospace Engineering, New Mexico State University, Las Cruces, NM, USA

M. Southwick
Department of Mechanical Engineering, University of Pittsburgh, Pittsburgh, PA, USA

R. J. Kuether (✉) · A. Brink
Sandia National Laboratories, Albuquerque, NM, USA
e-mail: rjkueth@sandia.gov

P. Tiso
ETH Zurich, Zurich, Switzerland

D. Quinn
The University of Akron, Akron, OH, USA

Many studies have investigated the uncertainty associated with the vibration of jointed structures. Paez et al. characterized the variability of the natural frequencies of a cantilever clamped beam with a bolt and washer using combined finite element analysis and experimental data [1]. Uncertainties in the parameters of non-ideal (i.e., flexible, non-rigid) boundary conditions have been investigated in [2, 3]. Fuzzy set theory has been applied to quantify the uncertainty of joint stiffness and damping [4, 5]. A review of the uncertainties in the prediction of dynamic response of jointed structures can be found in [6]. The literature, however, does not quantify the effect of surface waviness on the dynamic properties of a jointed structure or its associated uncertainty on experimental measurements. Bickford discusses that tightening joints composed of non-parallel or warped members hinders the accuracy of torque-preload relationships [7], but does not address its effect on the dynamic response of the assembly.

A common technique to improve the accuracy of computational models is model updating, wherein experimental test data is used to adjust—or update—model parameters. An overview of the model updating procedure applied to structural dynamics problems is found in [8]. When calibrating linearized models of jointed structures, prior studies have optimized the values of springs, masses, and dampers at the model’s interface to match modal characteristics measured from actual hardware [9–12]. Additional techniques include varying geometric parameters [13] as well as the material properties of a “doubly connective layer” [14]. Some of the authors recently published a study that proposed a model updating routine in which the contact definitions of elements at the nonlinear interface were varied (e.g. stuck, slipping or no contact) as a function of their normal contact pressure magnitude [15]. In comparison to modal test data, close agreement across six elastic modes was obtained for an optimal value of the model’s “cut-off pressure”, which was a single, scalar value used to assign the appropriate multi-point constraints. The current work expands on this study by performing model updating of individual beams to reduce the uncertainty of material properties, and evaluates the predictive capability of an FE model of the preloaded assembly when surface waviness at the interface is included.

A variety of techniques have been documented for modeling joint behavior in computational studies. In [16], two different multi-point constraint (MPC) configurations are compared in the calculation of the vibration modes of an automobile engine. The first confines member stiffness to be around each bolt hole and the second distributes member stiffness across the entire joint interface. The second configuration produces better agreement with the first two flexible modes of the actual engine. Four different approaches for modelling bolts in jointed structures were compared in [17]: a solid model of the bolt with solid elements, rigid spiders coupling the nodes around the bolt hole, a web of beam elements, and a constant preload force applied to the washer surfaces. While the most computationally expensive, the approach incorporating solid elements for the bolt produced the best agreement with static and dynamic test measurements. Other models characterizing the nonlinear effects of joints have been developed over recent years [18–21], but these studies are beyond the scope of this work since this work focuses on linear vibration responses at low excitation levels.

This paper presents the development of a high-fidelity finite element (FE) model of a jointed structure, with the aim of determining the effect of surface waviness at the interface on the assembled system’s natural frequencies. A benchmark structure consisting of two steel beams with nominally flat interfaces is studied, and a roving hammer impact test provides its linear natural frequencies and mode shapes for validation. Individual beams and fasteners are calibrated in isolation to obtain their material properties. In the FE model of the bolted assembly, nodes along the contact surfaces are perturbed based on measurements of surface heights on the actual beams. A brief outline of the paper is as follows: Sect. 36.2 describes the benchmark structure studied in this work. Section 36.3 outlines the model updating procedures carried-out on individual system components to minimize uncertainties due to material properties and interface geometry. Section 36.4 presents the results of the experimental modal analysis on the bolted assembly as well as the computational results of the model with the updated parameters and surface geometry from Sect. 36.3. The natural frequency predictions of the updated computational model are then compared to the measurements in the actual bolted assembly. Comparisons with the accuracy of other computational modelling approaches for the jointed structure are made.

36.2 System Description

Figure 36.1 depicts the bolted assembly considered in this study. The beams are manufactured from 4340 alloy steel and each are prescribed to have the same dimensions provided in Appendix A. The raised pads at the beams’ ends create well-defined regions of contact for the bolted interface. The assembled bolted structure uses two 5/16”-24 UNF-2B bolts and its associated nut and washer to fasten the individual beams at each end. Additionally, the beams were assigned serial numbers B9A and

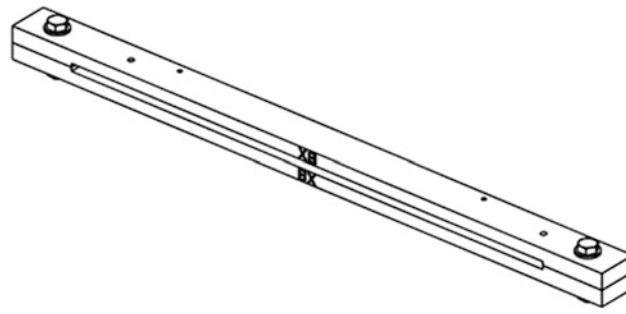


Fig. 36.1 Isometric view of bolted C-beam assembly

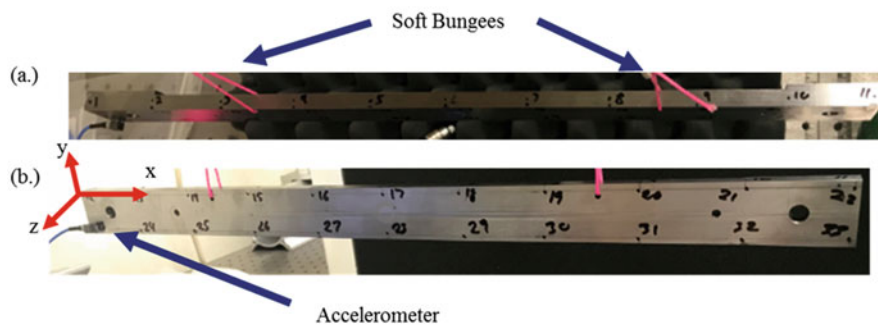


Fig. 36.2 Roving hammer impact test set-up for the single beam structure. (a) Top view, (b) Front view

Table 36.1 Natural frequencies [Hz] for the individual beams: experimental measurements compared to FE model with no updating

Mode	Natural frequency (Hz)		
	Beam 9A	Beam 9B	FE (nominal beams)
First y-bending	187.5	187.1	189.3
Second y-bending	526.3	525.1	523.3
Third y-bending	610.8	610.3	603.8
First z-bending	1042.7	1042.8	1037.9
First torsion	1545.5	1541.8	1530.7

B9B to facilitate the model updating process. A flatness tolerance of 0.001" was imposed on the manufacturing drawing to minimize the deviations from a nominally flat interface.

36.3 Single Beam Structure

The details of this experiment and model calibration of the individual beams are given in Sects. 36.3.1 and 36.3.2.

36.3.1 Experimental Modal Analysis

Roving impact hammer testing was performed on each of the individual beams to fit the natural frequencies and mode shapes. Figure 36.2 shows the test setup and reference coordinate grid for a single beam structure without any bolt hardware. The single beam was suspended by bungee cords to approximate free-free boundary conditions. Impacts from a roving hammer were carried out at a total of thirty-three input points in both the y and z directions. To maintain linearity of the response, the impacts were performed at low force levels around 11 lbf for all test points.

The natural frequencies and mode shapes for the first five elastic modes are presented in Table 36.1 for beam subcomponents B9A and B9B. The experimental modes were extracted using the LMS "PolyMAX" tool, a polyreference

least squares frequency domain modal parameter estimation method [22, 23]. Note the slight variation between the frequencies of B9A and B9B, which are likely due to small differences in their material properties. These results are compared to predictions from a high-fidelity FE model of the individual beams with nominal geometry and material properties (Young's modulus of 29,000 ksi, Poisson's ratio of 0.283, and density of 7.12E^{-04} slug/in³ [24]). Moderate agreement is obtained with these experimental measurements: the 3rd y-bending mode possessed the highest amount of error in its natural frequency of 1.2% whereas the 1st torsional mode possessed the lowest diagonal modal assurance criterion (MAC) value of 49.9%.

36.3.2 Model Updating

To further reduce the error between the model's predicted natural frequencies and those measured in the individual beams, model updating of the material properties of all subcomponents used in the final assembly was performed. As a result, sources of uncertainty outside of the mechanical interfaces were eliminated.

36.3.2.1 Density

The first material property updated in the FE model was mass density. Each individual beam and fastener were weighed to obtain the mass, and the density of each subcomponent was calculated by dividing each mass by its associated volume estimated from the FE model. It was assumed that the small deviations from nominal dimensions of the beams have a negligible effect on their overall volume and thus were not included in these calculations. The updated densities were used in the material property definitions of the linear elastic constitutive model. Furthermore, each bolt, nut, and washer were serialized to maintain consistency in the structure's configuration during assembly/reassembly and in the FE model. Table 36.2 lists the mass measurements and density calculations for all the components.

36.3.2.2 Young's Modulus

The elastic modulus of each beam was optimized in the FE model using the natural frequencies measurements from the roving hammer modal tests. The FE model included a point mass to account for the mass loading from the single accelerometer used during testing. The Young's modulus values that minimize the least squares error with the measured natural frequencies are 30,850 and 30,470 ksi for B9A and B9B, respectively. These values are approximately 6% and 5% larger than the nominal value of 4340 steel which is 29,000 ksi. Table 36.3 compares the experimental and material property-updated FE natural frequencies for B9A and B9B.

Table 36.2 Sub-component mass measurements and density calculations

	Beam		Bolt		Nut		Washer			
	B9A	B9B	Right	Left	Right	Left	Top right	Bottom right	Top left	Bottom left
Mass (Slug)	7.3E-03	7.3E-03	1.0E-04	1.0E-04	2.87E-05	2.8E-05	1.1E-05	1.2E-05	1.1E-05	1.2E-05
Density (Slug/in ³)	7.3E-04	7.4E-04	6.7E-04	6.7E-04	9.1E-04	9.0E-04	6.3E-04	6.4E-04	6.3E-04	6.4E-04

Table 36.3 Natural frequencies from the experiment and FE model with updated density and Young's modulus values

Mode	B9A		B9B	
	Natural frequency (Hz)		Natural frequency (Hz)	
	Experimental	Young's modulus updated FE	Experimental	Young's modulus updated FE
First y-bending	187.5	187.7 (+0.1%)	187.1	187.3 (+0.1%)
Second y-bending	526.3	527.4 (+0.2%)	525.1	526.4 (+0.2%)
Third y-bending	610.8	608.1 (-0.4%)	610.2	606.9 (-0.5%)
First z-bending	1042.7	1046.5 (-0.4%)	1042.9	1044.5 (+0.2%)
First torsion	1545.6	1541.8 (-0.2%)	1541.8	1538.8 (-0.2%)

Percent errors of the FE model predictions are listed in parenthesis

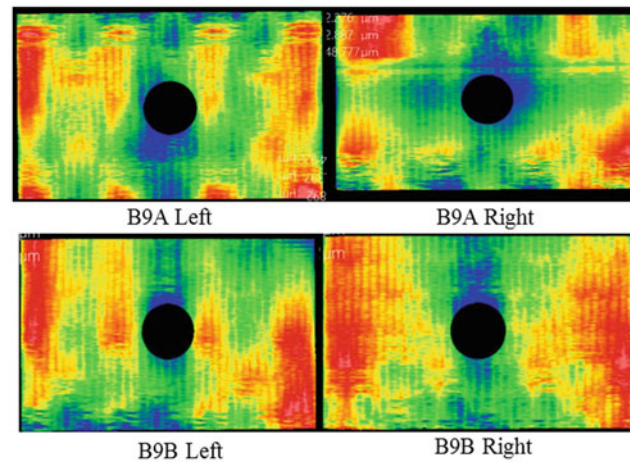


Fig. 36.3 Optical interferometer measurements of the beam surfaces. Hotter colors correspond to surface heights that are above the level plane while cooler colors correspond to surface heights below the level plane.

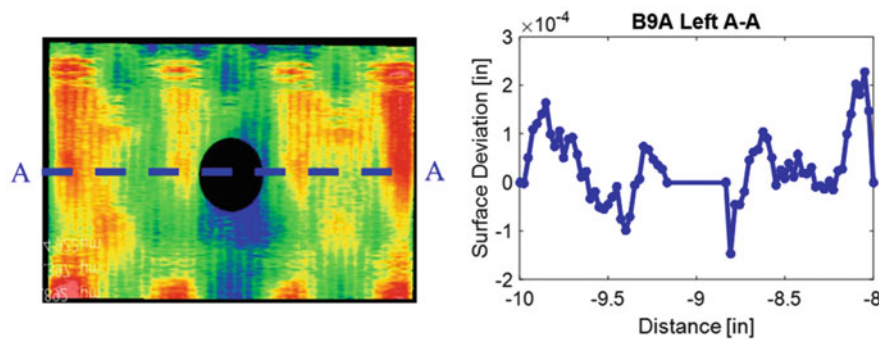


Fig. 36.4 Line scan of the surface displaying the magnitude of the deviation about the level plane from optical interferometer measurements

36.3.2.3 Surface Geometry

While tight tolerances were imposed on the fabricated beams, their geometry will inevitably deviate from the nominally flat design due to a number of factors during machining including vibration and deformation of the machine tools, insufficient clamping, and workpiece material inhomogeneities [25]. These deviations from the ideal flat surface were incorporated into the FE models of the beams to investigate their influence on the contact pressure distribution in the bolted assembly. Optical interferometer measurements generated high-resolution surface profile data for each of the four contact surfaces (two raised pads for each beam). Figure 36.3 presents images of the surface measurements in which hotter colors correspond to deviations above the level plane while cooler colors correspond to deviations below the level plane.

Figure 36.4 plots a line scan about the center of the raised pad to provide insight into the data of the surface deviation. For each node on the contact surfaces, the nearest coordinate, in the roughly 8000 by 5000 grid of measurements, was located and its corresponding surface height extracted. This array of deviated surface heights was used to update the nodal coordinates in the FE mesh. Each node was matched with a data point in the optical interferometer measurements with the closest coordinates and perturbed to have the corresponding amount of surface height deviation.

36.4 Bolted Beam Assembly

After minimizing the error between the computational model and experimental measurements of the individual beams, the bolted assembly was investigated to understand the influence of the interface geometry on the modes of the bolted assembly. Details of the experimental and computational analysis of the bolted assembly are provided here, concluding with a discussion of the predictive capability of different FE modelling approaches.

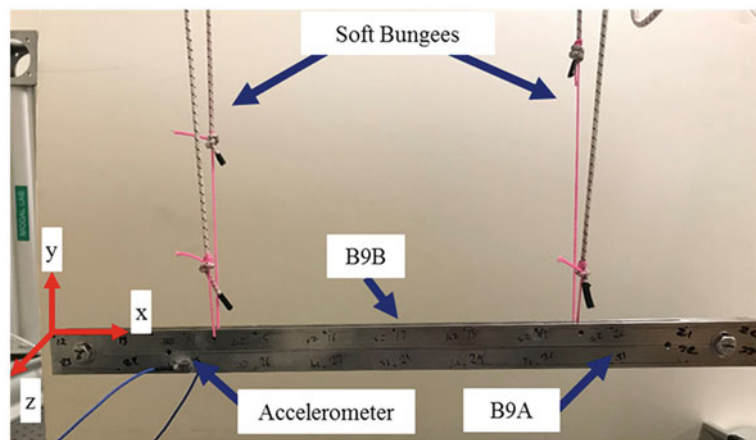


Fig. 36.5 Roving hammer impact test set-up for the bolted beam assembly

36.4.1 Experimental Modal Analysis

Modal testing was performed on the bolted assembly to extract linear natural frequencies and mode shapes at low excitation levels. Figure 36.5 depicts the experimental test setup. The assembly was supported with bungee cords to approximate free-free boundary conditions. Impact forces were applied in the y and z directions at sixty-six distributed points to accurately resolve the mode shapes along the length of the beam. Two triaxial accelerometers measured the accelerations for each impact point. Bolts were tightened to 110 in-lbf using a torque wrench and Table 36.4 provides a summary of the first eight elastic modes of the bolted beam assembly.



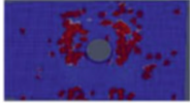
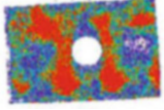

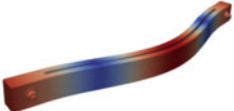
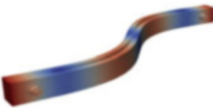





A linearity study was conducted to ensure the natural frequencies were extracted from hammer input levels known to excite linear vibration responses. The purpose of this study is to identify input forces that produce linear responses with little to no change in the system's measured frequency response function (FRF). The structure was impacted at a range of forces between 3 and 40 lbf and the measured FRF's from the different impact levels were visually compared. Figure 36.6 depicts the two forms of nonlinear responses observed in specific modes. The first type of nonlinear response is characterized by an opening/closing of the interface at higher input levels, which produced a shift in peak frequency and increase in FRF magnitude resulting from the apparent decrease in stiffness and damping during vibration. The 1st and 2nd out-of-phase y -bending modes exhibited this behavior. The second type of nonlinear response resulted from shear loads at the interface resulting in significant energy dissipation due to friction. Figure 36.6b shows how the 1st out-of-phase z -bending mode exhibits this behavior. Higher input levels produced a reduction in FRF magnitudes and an apparent decrease in peak frequency. The remaining results for the linearity study are provided in Appendix B.

In contrast to the behavior observed with the 1st out-of-phase z -bending mode, the 1st in-phase z -bending mode was inherently linear as evidenced by the FRF consistency across all input force levels. As apparent in its mode shape deformations, the 1st in-phase z -bending mode does not induce significant stresses at the interface when compared to the other modes. Between 3.5 and 14.2 lbf, the natural frequencies observed from the peak points of the FRF remain essentially unchanged with less than 1 Hz shifts. Only the damping levels seemed to be significantly affected by the input level. For all the results from the linearity study, it appeared that it was difficult to apply a low enough input force the excite the structure in such a way that linearity of the response can be confirmed via visual inspection of the FRF. The experimental modes used for validation purpose were fit from the FRFs obtained from the lowest possible input forces in hopes that these best approximate the linear response. This seemed reasonable since the natural frequencies were of most interest to understand the effect of surface geometry on the joint stiffness.

36.4.2 Computational Preload Analysis

The FE model was preloaded by applying an axial force along the bolt shank, then gluing the nut to the shank, thus locking in the preload. The conversion from torque to axial preload was determined using the Motosh equation [26]. This method produced the 2400 lbf preload used in the model. It should be noted that there is considerable uncertainty in the joint preload with a torque wrench. The preload force in an unlubricated bolt tightened with a torque wrench has been shown to possess a 35% uncertainty its predicted value [27].

Table 36.4 Comparison of natural frequency predictions from different FE models to experimental measurements

	Flat surface, fully stuck (Hz)	Flat surface, preloaded (Hz)	Perturbed surface, preloaded (Hz)	Experiment (Hz)
Mode shape				
	297.0 (+2.2%)	283.0 (-2.6%)	289.2 (-0.4%)	290.4
	359.2 (+1.5%)	354.5 (+0.2%)	355.5 (+0.5%)	353.8
	513.9 (+1.1%)	513.3 (+1.0%)	513.5 (+1.0%)	508.4
	597.0 (-0.3%)	597.0 (-0.3%)	597.1 (-0.3%)	598.6
	814.6 (+2.1%)	773.0 (-3.2%)	791.6 (-0.8%)	797.6
	982.9 (+2.8%)	925.9 (-3.2%)	948.7 (-0.7%)	955.6
	1183.7 (-0.2%)	1176.0 (-0.8%)	1178.9 (-0.6%)	1185.6
	1359.4 (+1.1%)	1353.0 (+0.6%)	1353.7 (+0.7%)	1344.4

Percent error between natural frequencies from the FE models and experimental measurements are displayed in parenthesis

Figure 36.7 presents the results of the preload analysis for the nominally flat surfaces. Note that the contact pressure is largest around the bolt hole and decreases further away from it, forming concentric rings of pressure. Such a contact area is characteristic of receding contact in which the area remains independent of the load while the pressures scale linearly with the load [28].

Figures 36.8 and 36.9 present the results of the preload analysis for the surfaces with irregularities. The resulting contact area is markedly different than that of the nominally flat case. Zones of high contact pressure loosely correspond to regions near the bolt hole with large surface deviations.

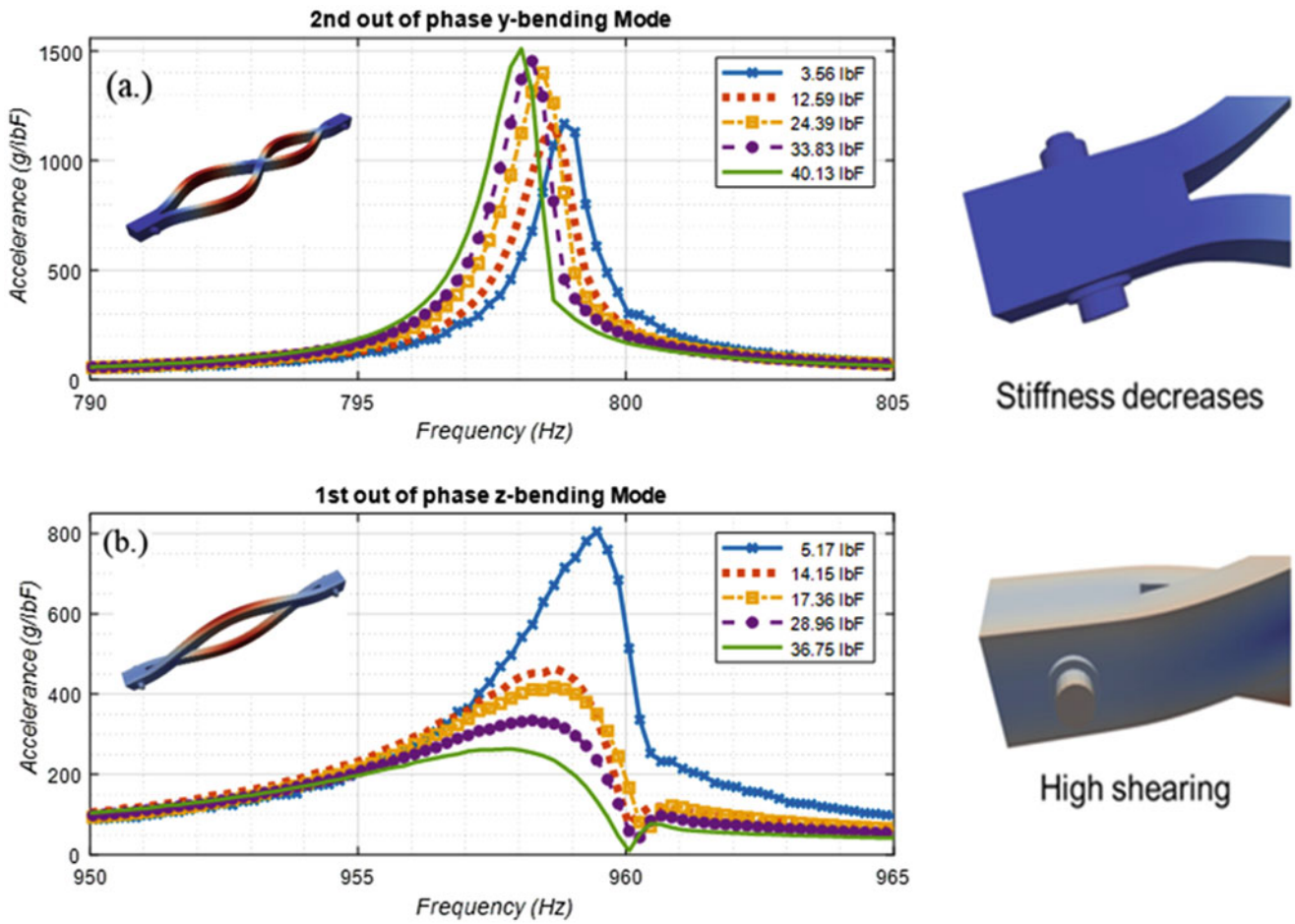


Fig. 36.6 Two classes of nonlinear behavior observed in the measured FRF's of the bolted assembly: (a) stiffness decrease due to opening of the interface (b) high dissipation due to shearing forces at the interface

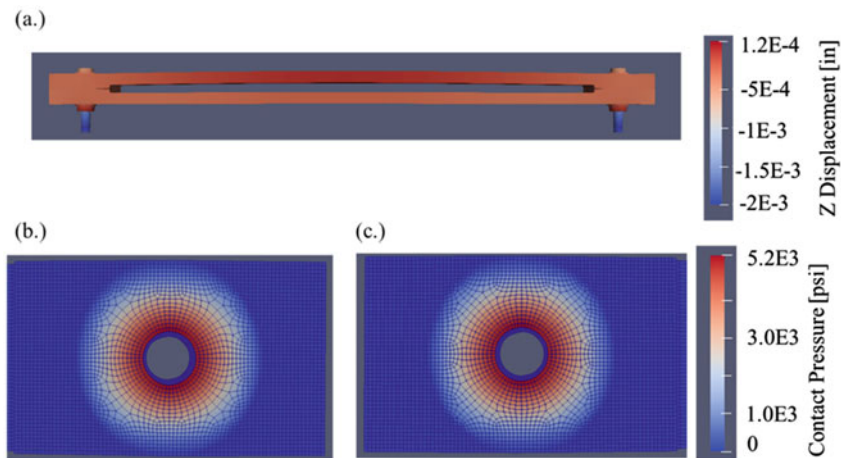


Fig. 36.7 Results of the static preload FE analysis for the flat beam assembly. (a) Z displacements in the structure. (b) Left side contact pressure at the beam/beam interface. (c) Right side contact pressure at the beam/beam interface

The results from the preload analysis on the non-flat geometry are compared to digitized pressure film measurements in the actual beam assembly. These films were inserted in the interface and output contact pressures between 350 and 1400 psi after applying the torque to the bolts. Figure 36.10 displays the results. While they are not in complete agreement, note that the model for the left side captures the two “strips” of high pressure to the left and right sides of the bolt hole. This agreement looks qualitatively better than the nominally flat results, which suggest the pressures are distributed in concentric rings around the bolt hole.

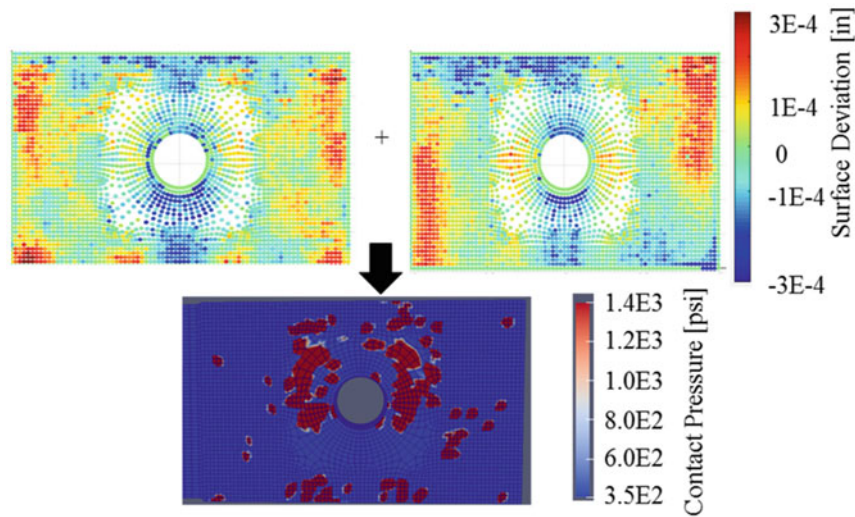


Fig. 36.8 Computationally-determined interface contact pressure for the left side of the bolted beam assembly

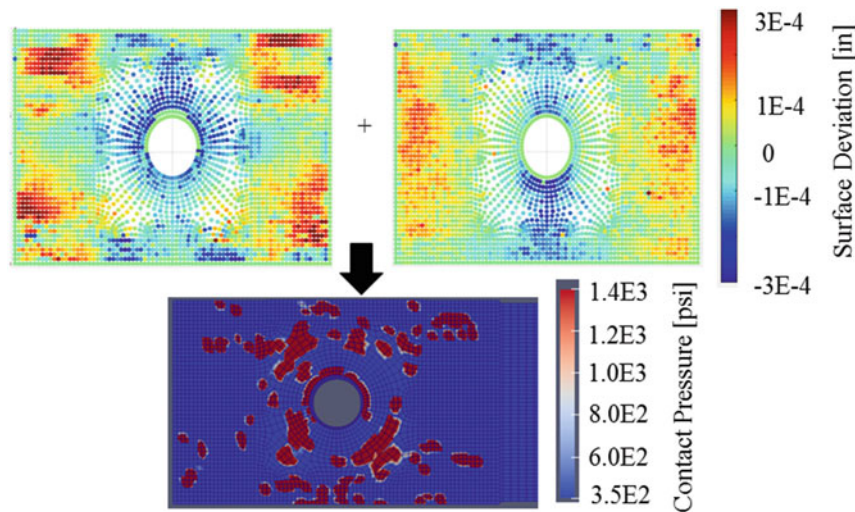


Fig. 36.9 Computationally-determined interface contact pressure for the right side of the bolted beam assembly

36.4.3 Modal Analysis Validation

The results from the preload analysis are transferred into the Sierra Structural Dynamics FE code [29] to perform modal analysis and calculate the linearized natural frequencies and mode shapes. It was assumed that the bolt preload was high enough such that regions in contact remained in contact during vibration. Thus, rigidly tied multi-point constraints were applied to all nodes surrounding elements in contact. Additionally, both structural damping and dissipation caused by relative motion at the interface were neglected. Free-free boundary conditions were prescribed to the model to match the approximate boundary conditions from test (Figs. 36.11 and 36.12).

Table 36.4 compares the natural frequency predictions of each of the computational models relative to the experimental measurements. Each computational model incorporates higher complexity in its description of contact and surface geometry. The percent error of each computational prediction of natural frequency relative to the experimental value is listed in parenthesis. The simplest modeling approach—flat surface, fully stuck—defined all nodes on the perfectly flat raised pads to be rigidly tied together, enforced by multi-point constraints. Such configuration overpredicts the natural frequencies as it has much larger stiffness than the actual structure. The second modelling approach—flat surface, preloaded—uses the static preload results on the flat beams to determine which nodes are tied together using the method described in Sect. 36.4.2. With this approach, a constant ring of stuck elements was formed around the bolt hole, which offers the most accurate natural

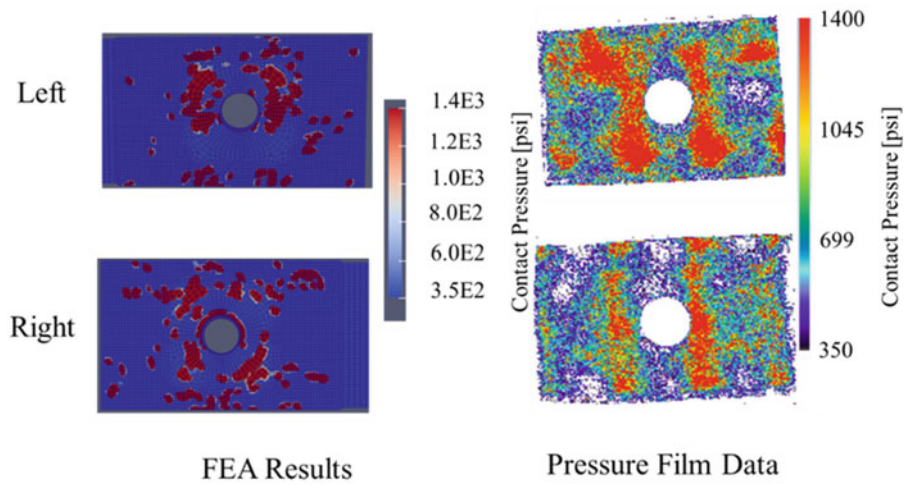


Fig. 36.10 Computationally-determined contact pressures compared to digitized pressure film measurements in the actual beam assembly

4. SURFACES SHALL BE FINISHED WITH PRECISION GRINDING.

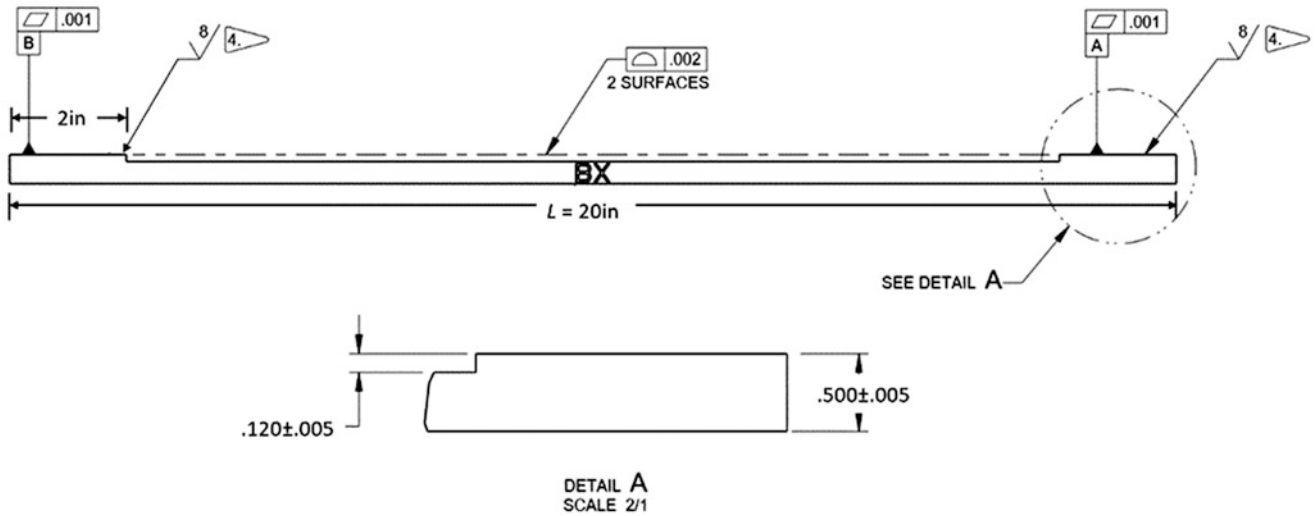


Fig. 36.11 Dimensions of the individual beams

frequency predictions for the in-phase y-bending modes. The most complicated modelling approach—perturbed surfaced, preloaded—updates the surface geometry based on the surface deviation data and then runs the static preload analysis to determine the distribution of struck and free nodes at the interface. This method offers an order of magnitude reduction in the error of its natural frequency predictions relative to the flat surface case for the out-of-phase y and z-bending modes.

For all the modes in which the perturbed surface model has a higher level of accuracy compared to the flat surface model, the stiffness of the structure increases to raise the natural frequency. Such trend may be due to the points far away from the bolt hole that have high surface deviation and therefore come into contact during the static preload. A receding contact model cannot capture these points and thus may under-predict the joint’s stiffness. If out-of-phase bending modes are desired to be predicted by a model, the perturbed surface approach may be the most attractive candidate in applications where a high-degree of accuracy is demanded. However, this modeling approach requires special equipment to measure surface deviations which may not be readily available or such measurements may not be easily carried-out for large and complex engineering structures.

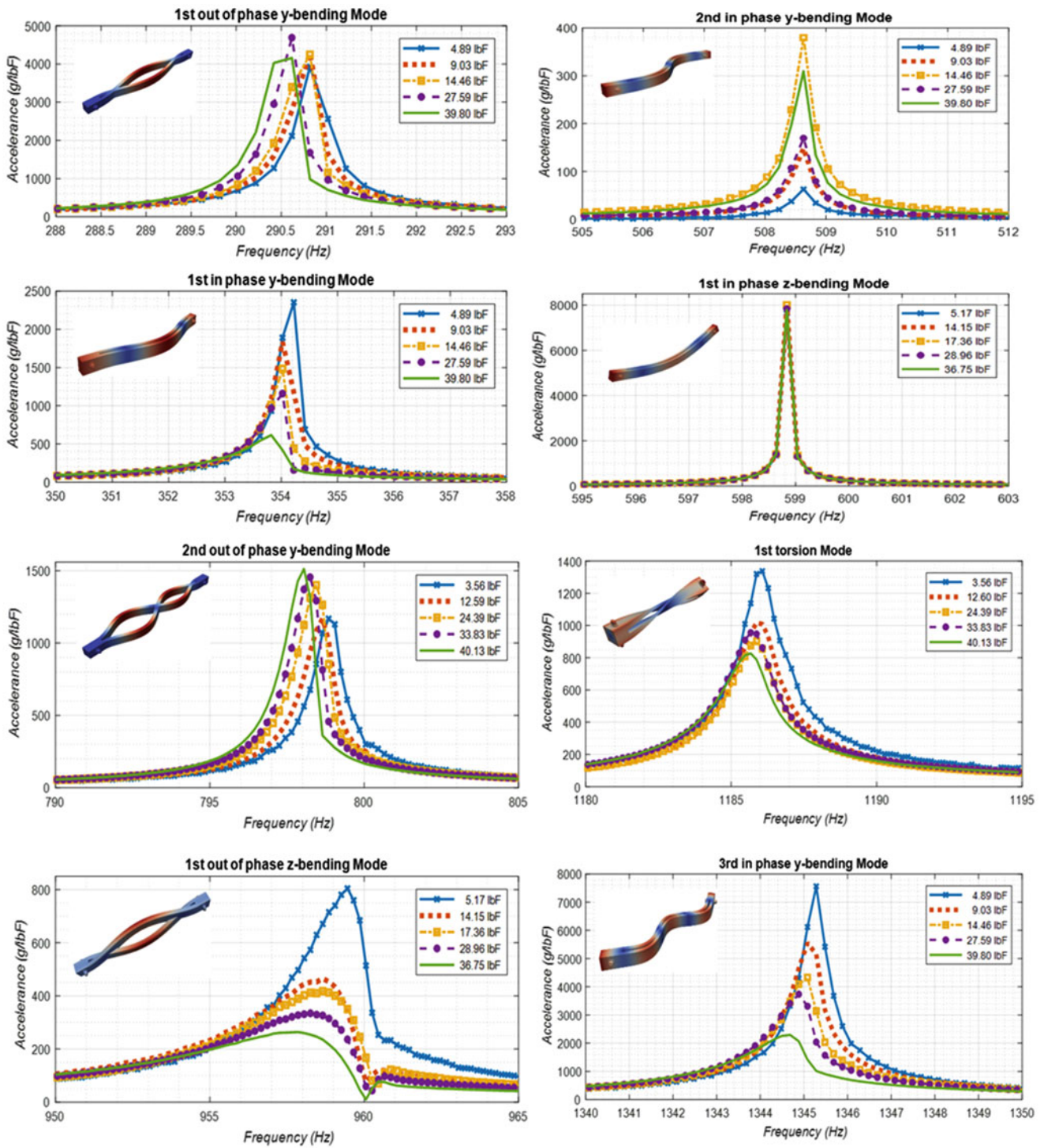


Fig. 36.12 Linearity study of the bolted beam assembly

36.5 Conclusions

A high-fidelity FE model of a bolted beam assembly was developed, calibrating the material properties of individual beams and fasteners with experimental measurements and perturbing nodal coordinates at the interface with surface height measurements from an optical interferometer. A preload analysis determines the distribution of contact pressure in the interface and consequently which nodes/faces are tied together. Significant improvements in the model’s predictions of natural frequency for the actual beam system are observed in out-of-phase bending modes, likely due to perturbed surface

heights coming into contact far away from the bolt hole, a phenomenon unable to be captured by a receding contact description for nominally flat surfaces. This high-fidelity modelling method could be implemented in applications where enhanced predictive capability is important.

While finer meshes capture more detail in the surface topographies, it is advised in future studies to employ an averaging method to the mesh perturbation such that a small neighborhood of points in the data file are averaged for each nodal coordinate. Doing so would account for outliers in the measured data from specks of dust or large angles in the surface (for low magnification lenses) or points located on edges. Additionally, it is suggested to consider surface geometries with a prescribed curvature instead of those that are nominally flat to investigate the robustness of this method.

Acknowledgments This research was conducted at the 2018 Nonlinear Mechanics and Dynamics (NOMAD) Research Institute supported by Sandia National Laboratories. Sandia National Laboratories is a multi-mission laboratory managed and operated by National Technology and Engineering Solutions of Sandia, LLC., a wholly owned subsidiary of Honeywell International, Inc., for the U.S. Department of Energy's National Nuclear Security Administration under contract DE-NA-0003525. The authors would also like to thank Bill Flynn from Siemens Industry Software NV for supplying the data acquisition and testing systems used to collect the experimental measurements presented throughout this work. SAND2018-11908 C

References

1. Paez, T.L., Branstetter, L.J., Gregory, D.L.: Modal randomness induced by boundary conditions, SAE Technical Paper No. 851930 (1985)
2. Fengquan, W., Shiyu, C.: A method to determine the boundary conditions of the finite element model of a slender beam using measured modal parameters. *J Vib Acoust.* **118**(3), 474–478 (1996)
3. Lee, U., Kim, J.: Determination of nonideal beam boundary conditions: a spectral element approach. *AIAA J.* **38**(2), 309–316 (2000)
4. Hanss M, Simulation and analysis of structural joint models with uncertainties. In: Proc. of the International Conference on Structural Dynamics Modeling-Test, Analysis, Correlation and Validation, Madeira Island, Portugal, 2002
5. Hanss, M., Oexl, S., Gaul, L.: Identification of a bolted-joint model with fuzzy parameters loaded normal to the contact interface. *Mech Res Commun.* **29**(2-3), 177–187 (2002)
6. Ibrahim, R.A., Pettit, C.L.: Uncertainties and dynamic problems of bolted joints and other fasteners. *J Sound Vib.* **279**(3), 857–936 (2005)
7. Bickford, J., An introduction to the design and behavior of bolted joints, Revised and Expanded, Routledge (2018)
8. Mottershead, J.E., Friswell, M.: Model updating in structural dynamics: a survey. *J Sound Vib.* **167**(2), 347–375 (1993)
9. Mottershead, J.E., Weixun, S.: Correction of joint stiffnesses and constraints for finite element models in structural dynamics. *J Appl Mech.* **60**(1), 117–122 (1993)
10. Kim, T., Wu, S., Eman, K.: Identification of joint parameters for a taper joint. *J Eng Ind.* **111**(3), 282–287 (1989)
11. Kim, T., Ehmann, K., Wu, S.: Identification of joint structural parameters between substructures. *J Eng Ind.* **113**(4), 419–424 (1991)
12. Nobari, A.S., Robb, D., Ewins, D.: Model updating and joint identification methods-applications, restrictions and overlap. *Int J Anal Exp Modal Anal.* **8**, 93–105 (1993)
13. Mottershead, J., Friswell, M., Ng, G., Brandon, J.: Geometric parameters for finite element model updating of joints and constraints. *Mech Syst Signal Process.* **10**(2), 171–182 (1996)
14. Adel, F., Shokrollahi, S., Jamal-Omidi, M., Ahmadian, H.: A Model updating method for hybrid composite/aluminum bolted joints using modal test data. *J Sound Vib.* **396**, 172–185 (2017)
15. Fronk, M., Eschen, K., Starkey, K., Kuether, R.J., Brink, A., Walsh, T., Aquino, W., Brake, M.: Inverse methods for characterization of contact areas in mechanical systems. In: Kerschen, G. (ed.) *Nonlinear Dynamics*, Volume 1. Springer (2019)
16. Langer, P., Sepahvand, K., Guist, C., Marburg, S.: Finite element modeling for structural dynamic analysis of bolted joints under uncertainty. *Procedia Eng.* **199**, 954–959 (2017)
17. Kim, J., Yoon, J.-C., Kang, B.-S.: Finite element analysis and modeling of structure with bolted joints. *App Math Model.* **31**(5), 895–911 (2007)
18. Allen, M.S., Lacayo, R.M., Brake, M.R.: Quasi-Static Modal Analysis Based on Implicit Condensation for Structures with Nonlinear Joints, SAND2016-5065C. Sandia National Laboratories, Albuquerque, NM (2016)
19. Flicek, R., Ramesh, R., Hills, D.: A complete frictional contact: the transition from normal load to sliding. *Int J Eng Sci.* **92**, 18–27 (2015)
20. Segalman, D.J.: A four-parameter iwan model for lap-type joints. *J Appl Mech.* **72**(5), 752–760 (2005)
21. Sellgren, U., Olofsson, U.: Application of a constitutive model for micro-slip in finite element analysis. *Comput Methods Appl Mech Eng.* **170**(1-2), 65–77 (1999)
22. Peeters, B., Auweraer, H., Guillaume, P., Leuridan, J.: The PolyMAX frequency-domain method: a new standard for modal parameter estimation? *Shock Vib.* **11**(3-4), 395–409 (2004)
23. The LMS Test.Lab Modal Analysis Manual, Rev12A, LMS International, pp. 30-31, 2012.
24. Bradley, R.: On the FEA Process via SNL Tools, SAND2018-6567 O. Sandia National Laboratories, Albuquerque, NM (2018)
25. Benardos, P.G., Vosniakos, G.C.: Predicting surface roughness in machining: a review. *Int J Mach Tool Manuf.* **43**(8), 833–844 (2003)
26. Motosh, N.: Development of design charts for bolts preloaded up to the plastic range. *J Eng Ind.* **98**(3), 849–851 (1976)
27. Brown, K., Morrow, C., Durbin, S., Baca, A.: Guideline for Bolted Joint Design and Analysis: Version 1.0, SAND2008-0371. Sandia National Laboratories, Albuquerque, NM (2008)
28. Dundurs, J.: Properties of elastic bodies in contact. In: de Pater, A.D., Kalker, J.J. (eds.) *The Mechanics of the Contact between Deformable Bodies*, pp. 54–66. Delft University Press, The Netherlands (1975)
29. Sierra Structural Dynamics Development Team: Sierra Structural Dynamics-User's Notes, SAND2017-3553. Sandia National Laboratories, Albuquerque, NM (2017)



Chapter 37

A Novel Computational Method to Calculate Nonlinear Normal Modes of Complex Structures

Hamed Samandari and Ender Cigeroglu

Abstract In this study, a simple and efficient computational approach to obtain nonlinear normal modes (NNMs) of nonlinear structures is presented. Describing function method (DFM) is used to capture the nonlinear internal forces under periodic motion. DFM has the advantage of expressing the nonlinear internal force as a nonlinear stiffness matrix multiplied by a displacement vector, where the off-diagonal terms of the nonlinear stiffness matrix can provide a comprehensive knowledge about the coupling between the modes. Nonlinear differential equations of motion are converted into a set of nonlinear algebraic equations using DFM under harmonic motion assumption. A matrix manipulation based on dynamic stiffness concept was used to localize nonlinearities and reduce the number of nonlinear equations improving the efficiency of the approach, which becomes important in solving large complex structures. The nonlinear algebraic equations are solved numerically by using Newton's method with Arc-Length continuation. The efficiency of proposed computational approach is demonstrated using a two-degree-of-freedom nonlinear system. The proposed approach has the potential to be applied to large-scale engineering structures with multiple nonlinear elements and strong nonlinearities.

Keywords Nonlinear normal modes · Describing function method · Nonlinear vibrations · Nonlinear numerical solver

37.1 Introduction

Nonlinear normal modes (NNMs) can be used to explain a wide class of nonlinear phenomena, mathematically and theoretically. However, the majority of structural engineers view it as a concept that is foreign to them. Recent studies show that the concept of NNMs can be used to describe nonlinear behaviors such as jumps, bifurcations, internal resonances, modal interactions, sub- and super-harmonic motions [1, 2]. Such potentials triggered the need to identify NNMs in engineering applications. In much of initial works to identify NNMs, analytical methods were commonly used [3]. However, analytical methods are not useful in analysis of complex high-dimensional structures, i.e. realistic systems, that led to the development of computational methods dedicated to NNMs.

Numerical algorithms to compute NNMs of conservative mechanical structures are rare and complex. Many of these algorithms require time integration of the equations of motion, combined with shooting and pseudo-arc-length continuation [4–6], which becomes computationally expensive with increasing number of degrees-of-freedom (DOF) in finite element models. Furthermore, computation of NNMs using shooting method is limited by the capabilities of used time integration algorithms. For example, these algorithms can hardly deal with nonsmooth systems with piecewise linear stiffness. Renson et al. [7] provides a summary of recent frameworks used in calculating NNMs based on time-integration methods. There have been also few recent attempts [8, 9] to experimentally isolate and identify NNMs, however the majority of these attempts are limited to simple structures.

Complexity of existed computational tools have prevented engineers from developing a practical nonlinear analog using the concept of nonlinear normal modes. This work focuses on developing a simple and efficient computational approach to identify nonlinear normal modes. The describing function method (DFM) is used to capture nonlinearities of the structure under periodic motion. Nonlinear differential equations of motion are converted into a set of nonlinear algebraic equations using DFM for periodic motion. Since the proposed approach works in frequency domain, it is free from typical challenges

H. Samandari (✉)

Department of Mechanical and Manufacturing Engineering, Miami University, Oxford, OH, USA
e-mail: samandh@miamioh.edu

E. Cigeroglu

Department of Mechanical Engineering, Middle East Technical University, Ankara, Turkey

confronted in time integration methods. A matrix manipulation based on dynamic stiffness concept is proposed in order to localize nonlinearities and reduce the number of nonlinear equations improving the efficiency of the approach even more.

37.2 Theory

Equations of motion of a nonlinear structure for free-vibration can be written as follows

$$\mathbf{M}.\ddot{\mathbf{x}} + \mathbf{C}.\dot{\mathbf{x}} + i\mathbf{H}.\mathbf{x} + \mathbf{K}.\mathbf{x} + \mathbf{f}_N(\mathbf{x}) = \mathbf{0}, \quad (37.1)$$

where \mathbf{M} , \mathbf{C} , \mathbf{H} , and \mathbf{K} represent the mass, viscous damping, structural damping, and stiffness matrices of the linear system, respectively. $\mathbf{f}_N(\mathbf{x})$ is the vector of internal nonlinear forcing and \mathbf{x} is the vector of displacements. *dot* denotes differentiation with respect to time and i is the unit imaginary.

37.2.1 Describing Function Method

Response of a nonlinear system to periodic excitation in general can be periodic, quasi-periodic or chaotic. Since the focus of this study is to find the steady-state solutions of the nonlinear system, only periodic solutions, which are of importance in the design of several mechanical systems, are considered. Using DFM, the nonlinear internal forcing vector can be written as a matrix multiplied by displacement vector as

$$\mathbf{f}_N(\mathbf{x}) = \Delta(\mathbf{x}).\mathbf{x} = [\Delta_{\text{re}}(\mathbf{x}) + i\Delta_{\text{im}}(\mathbf{x})].\mathbf{x}, \quad (37.2)$$

$\Delta(\mathbf{x})$ is a displacement or velocity dependent complex nonlinearity matrix. Elements of the complex nonlinearity matrix are pre-determined for each type of nonlinearity. Details of DFM and formulations to obtain $\Delta(\mathbf{x})$ for any given type of nonlinearity are given in [10–12]. For example using a single harmonic, describing function (DF) for cubic stiffness, for which the nonlinear internal force is $f_N(x) = k_N x^3$, is $3/4k_N x^2$. DFs for typical internal nonlinear forces such as piecewise linear stiffness nonlinearity, gap nonlinearity and dry friction nonlinearity can be found in [11] for single harmonic motion and can be calculated in a similar manner for multi-harmonic motions.

37.2.2 Dynamic Stiffness Formulation to Obtain NNMs

Assuming a harmonic motion ($\mathbf{x} = \mathbf{x}^* e^{i\omega t}$), the following set of nonlinear algebraic equations is obtained

$$\left[-\omega^2 \mathbf{M} + i\omega \mathbf{C} + i(\mathbf{H} + \Delta_{\text{im}}) + (\mathbf{K} + \Delta_{\text{re}}) \right] \mathbf{x}^* = \mathbf{0}. \quad (37.3)$$

A similar approach can be used to obtain the set of nonlinear algebraic equations if multiple harmonics are used. The real part of the nonlinearity matrix changes the overall stiffness matrix of the system; whereas, the imaginary part modifies the overall structural damping matrix.

Focusing on the undamped response of the system, the dynamic stiffness matrix, \mathbf{K}^D , of the linear counterpart is defined as

$$\mathbf{K}^D = \left[(\mathbf{K} + \Delta_{\text{re}}) - \omega^2 \mathbf{M} \right], \quad (37.4)$$

A similar approach as described in [13] is used to partition Eq. (37.3) localizing nonlinear DOFs as a result of which the following nonlinear equations for undamped response can be obtained

$$\left[\mathbf{K}_{\text{NN}}^D - \mathbf{K}_{\text{NL}}^D \left[\mathbf{K}_{\text{LL}}^D \right]^{-1} \mathbf{K}_{\text{LN}}^D \right] \mathbf{x}_N + \Delta_{\text{re}} \mathbf{x}_N = \mathbf{0}. \quad (37.5)$$

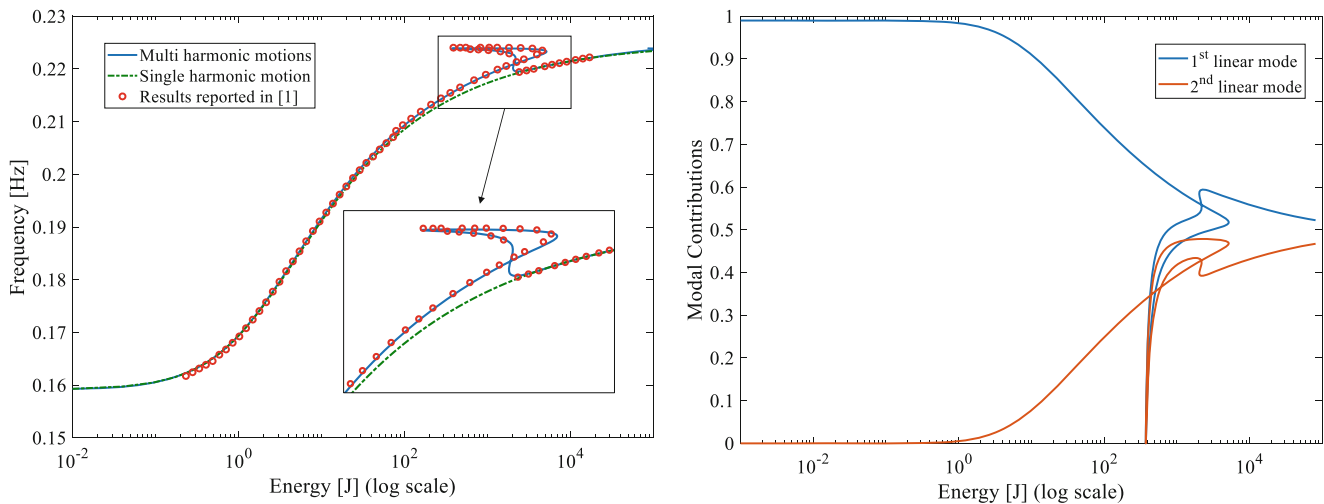


Fig. 37.1 Energy dependency (left panel) of 1st nonlinear natural frequency (circle denotes results reported in [1], dashed-line denotes single harmonic motion, and solid-line denotes multi-harmonic motions). Modal contributions (right panel) of mode shapes of the relevant linear system in the identified NNM at different energy levels calculated using Modal Assurance Criterion [13]

Above equation can be solved by using Newton's method with arc-length continuation as described in [11–13] to obtain the variation of nonlinear natural frequency with respect to the system's energy (i.e. sum of kinetic and potential energies).

37.3 Results

To demonstrate the approach, a two-degree-of-freedom system with a cubic nonlinearity is studied. The same parameters as reported in [1] are used for the comparison purpose. Equation of motion of the system in matrix form is given as follows

$$\begin{bmatrix} 1 & 0 \\ 0 & 1 \end{bmatrix} \begin{Bmatrix} \ddot{x}_1 \\ \ddot{x}_2 \end{Bmatrix} + \begin{bmatrix} 2 & -1 \\ -1 & 2 \end{bmatrix} \begin{Bmatrix} x_1 \\ x_2 \end{Bmatrix} + \begin{Bmatrix} 0 \\ 0.5x_1^3 \end{Bmatrix} = 0.$$

Figure 37.1 represents the backbone curve of the first natural frequency of the two-degree-of-freedom (DOF) system as a function of total energy. As it can be seen from the figure, the nonlinear natural frequency and the corresponding mode shape of the system depends on the total energy of the system. The proposed multi-harmonic approach is also successful in capturing other branches of harmonic motion detected in this system. These branches represent the realization of $n:m$ interactions between the in-phase and out-of-phase modes of the system. As discussed in [1], this two-DOF system is able to realize such modal interactions, since the frequency ratio between 1st and 2nd mode shapes varies with increasing energy level from its original value of $\sqrt{3}$ to ∞ .

37.4 Conclusion

The concept of NNMs has proven to be very effective in understanding complex behavior of nonlinear systems. This study has demonstrated an effective computational approach to identify nonlinear normal modes of such systems. The approach is demonstrated by using an easily understandable two-degree of freedom system. However, it can readily be extended to any large complex system. The used matrix manipulation based on Dynamic Stiffness has the advantage of reducing the number of nonlinear equations limiting it to the degrees of freedom only associated with nonlinearities.

References

1. Kerschen, G., Peeters, M., Golinval, J.C., Vakakis, A.F.: Nonlinear normal modes, part I: a useful framework for the structural dynamicist. *Mech. Syst. Signal Process.* **23**(1), 170–194 (2009)
2. Peeters, M., Viguié, R., Sérandour, G., Kerschen, G., Golinval, J.C.: Nonlinear normal modes, part II: toward a practical computation using numerical continuation techniques. *Mech. Syst. Signal Process.* **23**(1), 195–216 (2009)
3. Nayfeh, A.H., Nayfeh, S.A.: Nonlinear normal modes of a continuous system with quadratic nonlinearities. *J. Vib. Acoust.* **117**(2), 199–205 (1995)
4. Lee, Y.S., Kerschen, G., Vakakis, A.F., Panagopoulos, P., Bergman, L., McFarland, D.M.: Complicated dynamics of a linear oscillator with a light, essentially nonlinear attachment. *Physica D.* **204**(1–2), 41–69 (2005)
5. Jiang, D., Pierre, C., Shaw, S.W.: The construction of non-linear normal modes for systems with internal resonance. *Int. J. Non-Linear Mech.* **40**(5), 729–746 (2005)
6. Kuether, R.J., Allen, M.S.: A numerical approach to directly compute nonlinear normal modes of geometrically nonlinear finite element models. *Mech. Syst. Signal Process.* **46**(1), 1–15 (2014)
7. Renson, L., Kerschen, G., Cochelin, B.: Numerical computation of nonlinear normal modes in mechanical engineering. *J. Sound Vib.* **364**, 177–206 (2016)
8. Peeters, M., Kerschen, G., Golinval, J.C.: Modal testing of nonlinear vibrating structures based on nonlinear normal modes: experimental demonstration. *Mech. Syst. Signal Process.* **25**(4), 1227–1247 (2011)
9. Ehrhardt, D.A., Allen, M.S.: Measurement of nonlinear normal modes using multi-harmonic stepped force appropriation and free decay. *Mech. Syst. Signal Process.* **76**, 612–633 (2016)
10. Tanrikulu, O., Kuran, B., Ozguven, H.N., Imregun, M.: Forced harmonic response analysis of nonlinear structures using describing functions. *AIAA J.* **31**(7), 1313–1320 (1993)
11. Cigeroglu, E., Samandari, H.: Nonlinear free vibration of double walled carbon nanotubes by using describing function method with multiple trial functions. *Physica E.* **46**, 160–173 (2012)
12. Ferhatoglu, E., Cigeroglu, E., Özgüven, H.N.: A new modal superposition method for nonlinear vibration analysis of structures using hybrid mode shapes. *Mech. Syst. Signal Process.* **107**, 317–342 (2018)
13. Cigeroglu, E., Samandari, H.: Nonlinear free vibrations of curved double walled carbon nanotubes using differential quadrature method. *Physica E.* **64**, 95–105 (2014)



Chapter 38

Experimental-Numerical Comparison of Contact Nonlinear Dynamics Through Multi-level Linear Mode Shapes

Elvio Bonisoli, Domenico Lisitano, and Christian Conigliaro

Abstract An experimental nonlinear cantilever beam, including non-holonomic contacts, is experimentally tested. Time domain evolution is compared with simulated responses obtained by the proposed methodology, called Multi-Phi, which is based on piecewise linear mode shapes. The nonlinearities can be retained in a reduced model, using a linearisation in the configurations space. For each linearisation point a different base is used, consisting of a subset of linear mode shapes. The nonlinear system is globally approximated by a linear time variant system, described through a set of linear time invariant systems. The experimental time domain responses obtained from non-zero initial conditions are compared with the numerical simulation results. The comparison validates Multi-Phi method against non-smooth nonlinear piecewise systems behaviour in transient response.

Keywords Multi-Phi · Computational mechanics · Non-smooth nonlinearity

38.1 Introduction

Accurate simulations of a complex systems require high number of Degrees of Freedoms (DoFs) and therefore high computational cost. Computational effort further increases when the system requires the use of nonlinear models to describe its behaviour. In recent years, efforts have been made reduce the number of model DoFs, with a marginal loss of accuracy. Methods resulting from such activities are generically called Model Order Reduction (MOR) methods. These methods have been applied to several engineering fields, as summarized in [1, 2]. Examples of their application can be found in structural dynamics [3–6], systems and control [7, 8] and mathematics [9–11].

Two classes of MOR methods can be identified: Data-based and Model-based. The first class is based on a database of previous simulations of the full original nonlinear system. Proper Orthogonal Decomposition method (POD) [12, 13] is one of the examples of MOR method for nonlinear systems: a base of orthogonal modes is built to describe the system. The second class is based on the full nonlinear model itself and no preliminary simulations are required. The model is generically projected into a sub-manifold, whose definition depends on the method used. The reduced system has a lower computational cost and it is therefore useful for simulations, both in time or frequency domain. Methods of this class and aimed to nonlinear systems have been proposed, both retaining the nonlinearities [14, 15] and linearising them. Two interesting methods belonging to this last subclass are the Trajectory Piecewise Linear Approximation (TPWL) [16–18] and the Global Modal Parametrization (GMP) [19, 20].

In [21–23] the important topic of how to select a base is considered. Recently, classical model reduction techniques have been applied to contact problems [24], implementing linearised event-driven simulations that also address the problem of changing the reduced base.

Multi-Phi, the method proposed in this paper, is a linearisation method based on the projection of the original nonlinear system into the configuration space. Theoretically, it is possible to use any other space as long as it is possible to determine a univocal linear representation for each linearisation point. Since the span of the possible system states must be known before the simulation itself, the configuration space is the most predictable space and it is the one used in this paper. The nonlinear system is described by means of a set of linear systems (linearisation), and each one could be reduced by using a subset of its mode shapes.

Multi-Phi uses each base separately from the others, differently from TPWL: the bases are not orthonormal between each other, but they result to be orthonormal within themselves. With respect to GMP, the aim is not to transform Differential

E. Bonisoli (✉) · D. Lisitano (✉) · C. Conigliaro (✉)
Department of Mechanical and Aerospace Engineering, Politecnico di Torino, Torino, Italy
e-mail: elvio.bonisoli@polito.it; domenico.lisitano@polito.it; christian.conigliaro@polito.it

Algebraic Equations (DAEs) into nonlinear Ordinary Differential Equations (ODEs), but to build piecewise linear ODEs. In the proposed method, the off-line computation consists just in a series of linear modal analysis.

Nonlinearities in Multi-Phi are implied in the differences between the different bases. Non-holonomic constraints, such as contacts, or continuous nonlinear effects can be handled similarly. In the following, the proposed method is introduced and a simple application is provided.

Multhi-Phi methodology was presented in [25, 26], where it is applied to numerical nonlinear systems with localised nonlinearity. The method seems to be quite robust when the nonlinearities are both discrete or continuous. The potentiality in terms of accuracy and computational time reduction are shown through numerical simulations compared to classical integration. The aim of this work is to predict the time domain response of a non-smooth nonlinear system with a discrete nonlinearity and compare it to experimental results of the real system.

The paper is organised as follow: in Sect. 38.2 the experimental test-rig is shown with attention to the system equipment, in Sect. 38.3 the methodology for discrete system is explained. In Sect. 38.4 the results of a non-null initial condition case study are analysed and compared to the experimental results. Finally, some comments on this work are discussed in the conclusion.

38.2 Experimental Set-Up

The experimental laboratory test-rig is shown in Fig. 38.1. The nonlinear system is a flexible aluminium cantilever beam with an additional steel mass of 213 g in the free tip. The dimensions of the beam are shown in Fig. 38.2. A non-smooth nonlinearity is obtained though the addition of an ideally rigid support at 400 mm from the constraint, called Support constraint in Fig. 38.1, with a gap of 1.35 mm from the beam in its undeformed configuration. This is a non-holonomic constraint; therefore, the system is nonlinear because of the change of boundary conditions/stiffness matrix when the gap is closed. Three points of interest are selected along the beam: node 1 distant 95 mm from the clamped constraint and used for the excitation, node 2 that is the contact point of the non-smooth nonlinearity, and node 3 that is the free tip of the beam. A shaker is used to excite the system in node 1 during preliminary modal analysis tests. The response of the nonlinear beam is measured through three displacement laser sensors, monitoring node 1 (Keyence LK-H052), 2 (Keyence LK-H082) and 3 (Keyence LK-H152). The data are acquired using a LMS Scadas Mobile and Test.Lab software.

The characterisation of the beam natural frequencies and damping ratios is performed by sweeps from 2 to 250 Hz on the linear structure, i.e. with the support constraint removed. Only the bending modes in x - z plane are investigated. The natural frequencies of the bending modes inside the spanned frequency range are listed in Table 38.1.

A finite element model, shown in Fig. 38.3, is implemented to represent the beam. The model is made of one-dimensional Timoshenko beam with a total of 348 DoFs. The model was tuned on the experimental data; the resulting density ρ and Young Modulus E are respectively $\rho = 2700 \text{ kg/m}^3$ and $E = 43.5 \text{ GPa}$. The steel mass is modelled as a punctual mass in the DoF at 529 mm from the constraint, with the actual mass and inertia tensor of the steel cylinder.

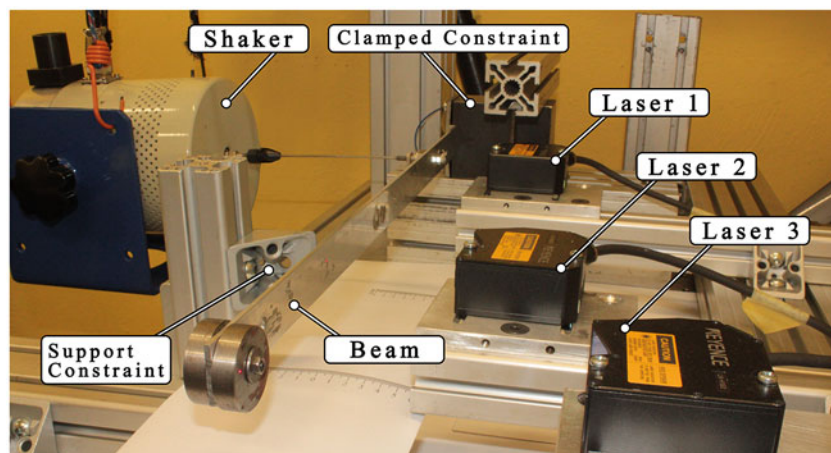


Fig. 38.1 Laboratory test-rig and experimental setup

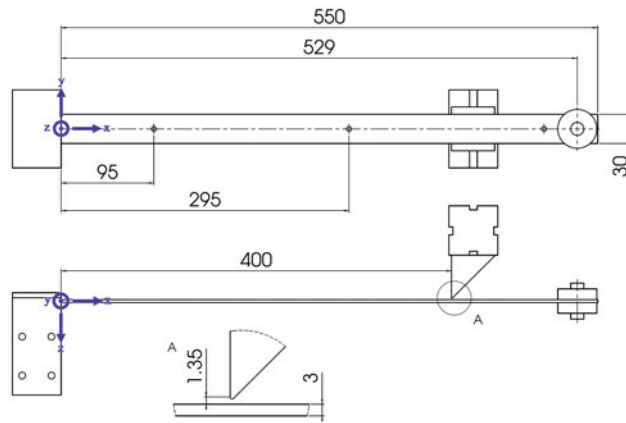


Fig. 38.2 Sketch of the non-linear system, relevant dimensions are in millimeters

Table 38.1 Experimental bending modes in $x-z$ plane

Mode	Clamped free (Hz)	Damping ratio (-) (%)	Description
1	3.99	4.340	First bending xz
2	37.00	1.670	Second bending xz
3	108.09	0.009	Third bending xz
4	205.29	0.240	Fourth bending xz

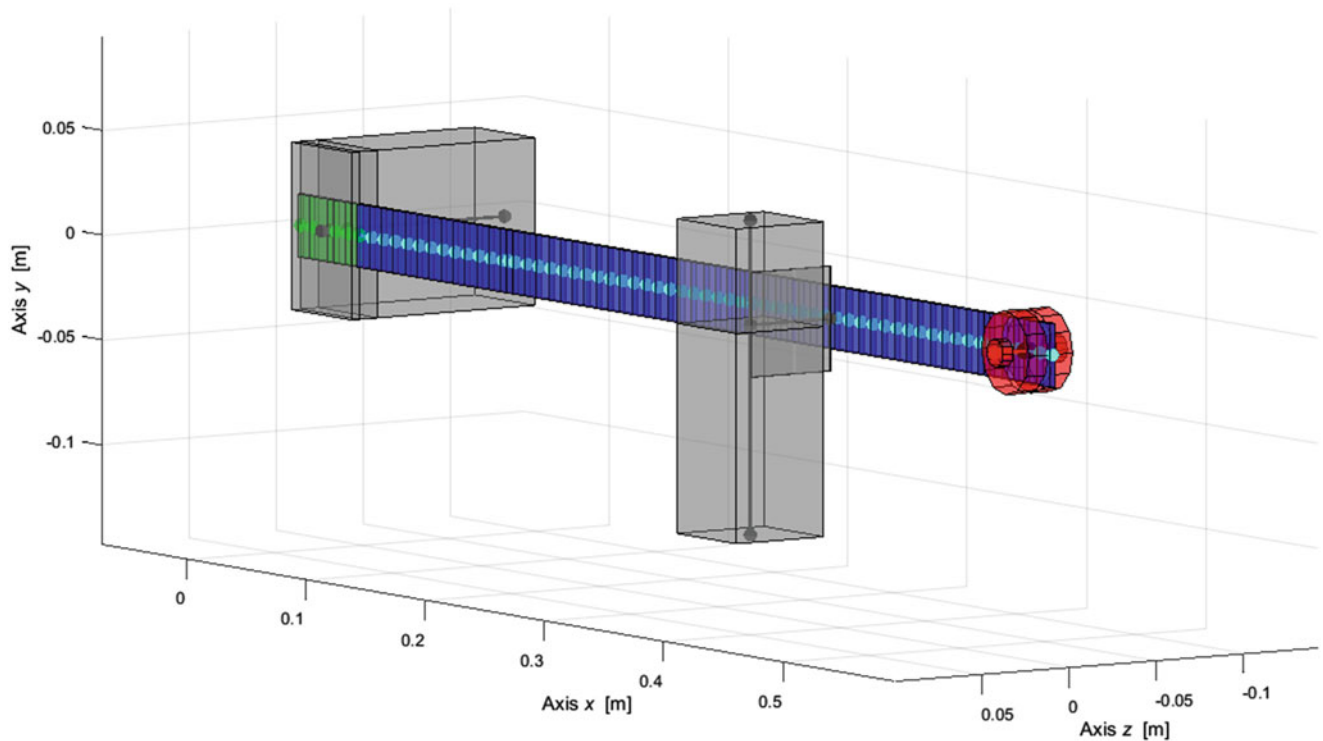


Fig. 38.3 One-dimensional finite element model

Several different tests are performed on the beam with non-null initial conditions. The initial conditions are obtained by the application of a static force in the three holes highlighted in Fig. 38.2, in both directions $\pm z$: the application of the force in different positions let to have different deformed initial conditions. If the force is applied in $-z$, the beam is in contact with the support constraint. The force is applied with a hanged weight linked to the beam by mean of a cable, which is cut to observe the free oscillations of the system.

38.3 Multi-Phi Method

Linear modal analysis allows to rewrite the equations of a linear dynamic system by means of diagonal matrices only, so uncoupling the problem. The proposal of Multi-Phi is to describe the nonlinearities through a limited number of parameters and to decompose the nonlinear system into a series of linear systems, each one characterised by a reference value of each parameter. In the following, the assumption of a single parameter α is made. It is considered a set of $l\nu$ linearised models characterised by a reference values α_l .

Linear modal analysis is performed on each linear system l , obtaining r_l modes, used to build a collection of $l\nu$ linear models. Each linear model can represent with a good approximation the system behaviour for $\alpha \approx \alpha_l$.

Considering a generic l linear system, the equations of motion are described by Eq. (38.1).

$$\mathbf{M}^{(l)} \ddot{\mathbf{x}} + \mathbf{C}^{(l)} \dot{\mathbf{x}} + \mathbf{K}^{(l)} \mathbf{x} = \mathbf{f}(t) \quad (38.1)$$

where $\mathbf{x}, \dot{\mathbf{x}}, \ddot{\mathbf{x}} \in \mathbb{R}^{n \times 1}$ are respectively displacements, velocities and accelerations of the system, $\mathbf{M}^{(l)}, \mathbf{C}^{(l)}, \mathbf{K}^{(l)}$ are respectively mass, damping and stiffness matrices of the l linear system and $\mathbf{f}(t)$ is the time depending external forcing function applied to the system.

Assuming a proportional damping matrix, the modal superposition results:

$$\mathbf{x} = \Phi^{(l)} \eta^{(l)} \quad (38.2)$$

where $\Phi^{(l)} \in \mathbb{R}^{n \times r_l}$ and $\eta^{(l)} \in \mathbb{R}^{r_l \times 1}$.

In Eqs. (38.1) and (38.2) the superscript (l) is referred to the modal coordinates of the l^{th} linear model.

If the eigenvectors are unitary modal mass normalised, Eq. (38.1) can be then expressed by means of modal coordinates as Eq. (38.3).

$$\mathbf{I} \ddot{\eta}^{(l)} + \text{diag}(2\zeta_l \omega_l) \dot{\eta}^{(l)} + \text{diag}(\omega_l^2) \eta^{(l)} = \Phi^{(l)T} \mathbf{f}(t) \quad (38.3)$$

where ω_l and ζ_l are the vector of natural frequencies and corresponding damping ratios vectors of the l^{th} linear model.

The state in terms of physical coordinates can be obtained using Eq. (38.4):

$$\begin{cases} \mathbf{x}(t) = \Phi(t) \eta(t) + \mathbf{x}_\infty(t) \\ \dot{\mathbf{x}}(t) = \Phi(t) \dot{\eta}(t) \\ \ddot{\mathbf{x}}(t) = \Phi(t) \ddot{\eta}(t) \end{cases} \quad (38.4)$$

In Eq. (38.4) the addition of \mathbf{x}_∞ , called asymptotic configuration, is necessary whenever the set of mode shapes used to simulate the system evolution cannot describe the system state because of non-null boundary conditions. It is considered function of time because it depends on the linearised system considered at each time instant.

To determine $\mathbf{x}_\infty^{(l)}$, the Guyan reduction is applied, by means of Eq. (38.5). In such equation, \mathbf{x}_k represents the boundary conditions (known DoFs) while \mathbf{x}_u represents the not constrained DoFs (unknown).

$$\begin{cases} \mathbf{x}_\infty = \begin{bmatrix} -(\mathbf{K}_{uu}^{(l)})^{-1} \mathbf{K}_{uk}^{(l)} \\ \mathbf{I} \end{bmatrix} \mathbf{x}_k \\ \dot{\mathbf{x}}_\infty = \mathbf{0} \end{cases} \quad (38.5)$$

The matrix $\Phi(t)$ is varying in time as a consequence of the transition between the linearised system: it is composed by the succession in time of the matrices Φ_l , with $l = 1, \dots, L$ if a number of linearised systems equal to L is considered.

In the following it will be referred to each linearised system as to a ‘‘level’’, so that at the level l it is associated the linearised system characterised by $\alpha = \alpha_l$, the set of reduced matrices $\text{diag}(2\zeta\omega)_l$, $\text{diag}(\omega_l^2)$, Φ_l and the asymptotic configuration $\mathbf{x}_{\infty, l}$.

When the nonlinearity is discrete, it is supposed that the parameter α can assume only discrete values. Therefore, during the simulation only one level at the time is considered, depending on the value of α . The evolution of the full system, during the span of time in which $\alpha = \alpha_l$, depends only by the linearised system l and the transition to another level m occurs whenever $\alpha = \alpha_m$.

The transition is governed by Eq. (38.6), in which the initial conditions of the modal coordinates of the level m are described by means of the final conditions of modal coordinates of the level l :

$$\begin{cases} \eta_{m,0} = \Phi_m^{-1} (\Phi_l \eta_{l,end} + \mathbf{x}_{\infty,l} - \mathbf{x}_{\infty,m}) \\ \dot{\eta}_{m,0} = \Phi_m^{-1} \Phi_l \dot{\eta}_{l,end} \end{cases} \quad (38.6)$$

The class of problem targeted is the one in which: (1) the external actions are potentially non-periodic; (2) the interest lies in the transient solution as well as in the steady state.

38.4 Comparison Between Prediction and Experimental Data

The case study discussed in this paragraph is the free oscillations of the system described in Sect. 38.2 due to non-null initial conditions. A force is applied in the hole closest to the free tip in $+z$ direction, as shown in Fig. 38.4, producing a deformation of the beam. The imposed deformation represents the displacement initial conditions of the free vibrations, while the velocity initial conditions are null. The observation of the free vibrations starts when the force is suddenly removed.

The evolution starts with a series of impacts of the beam on the support constraint, until the displacement oscillations of the beam contact point decreases under the gap level.

Time-frequency analysis of the evolution of the three measured points is shown in Fig. 38.5, through Wavelet [27] transformation. The time domain evolution presents 3–4 harmonics clearly identified related to the system natural frequencies when it is in contact with the support or not and some other natural frequencies that are the linear combination of those. The natural frequencies have an unexpected trend, in fact they are higher in the first second of oscillations and then they smoothly converge to the expected natural frequencies. This experimental behaviour is under further investigations, due to possible related geometric nonlinearity when the system presents large oscillations or non-ideal behaviour of the constraint.

The numerical model of the system has a discrete nonlinearity, the parameter is in this case the displacement of the contact point, $\alpha = x_2$. Two levels ($L = 2$) are used for the numerical prediction through Multi-Phi method. In particular, when the displacement of the contact point $x_2 > -g$ the corresponding linear system, shown in Fig. 38.6 (left), is a clamped free beam. On the other end when $x_2 < -g$ the boundary condition of the system changes and the displacement of the contact point along z is constrained, as shown in Fig. 38.6 (right). The modal properties used in the simulation are therefore related to these to linearised system. The natural frequencies of the bending modes of the two configurations are shown in Table 38.2.

The initial condition of all the degrees of freedom of the system is required for the numerical simulation. The initial conditions are obtained by imposing a static load in the same node on which it was applied in the experimental test (Fig. 38.7), in order to have the displacement of the contact point as in the experimental case.

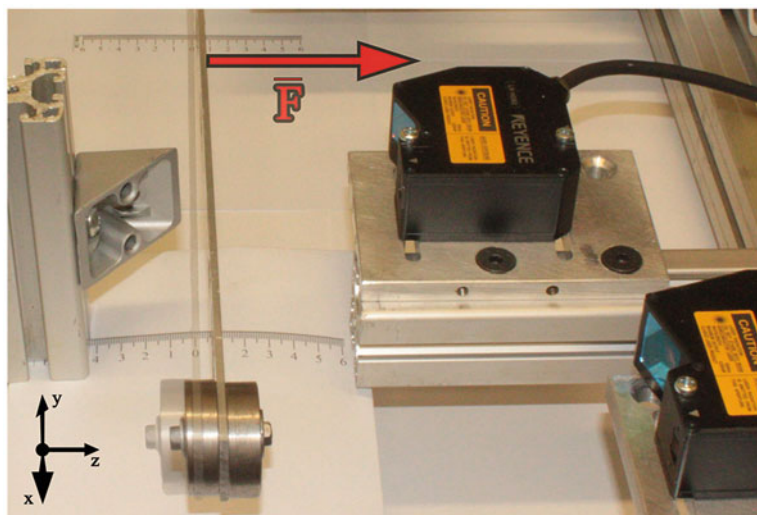


Fig. 38.4 Non-null initial condition imposed displacements (undeformed state is overlapped in transparency)

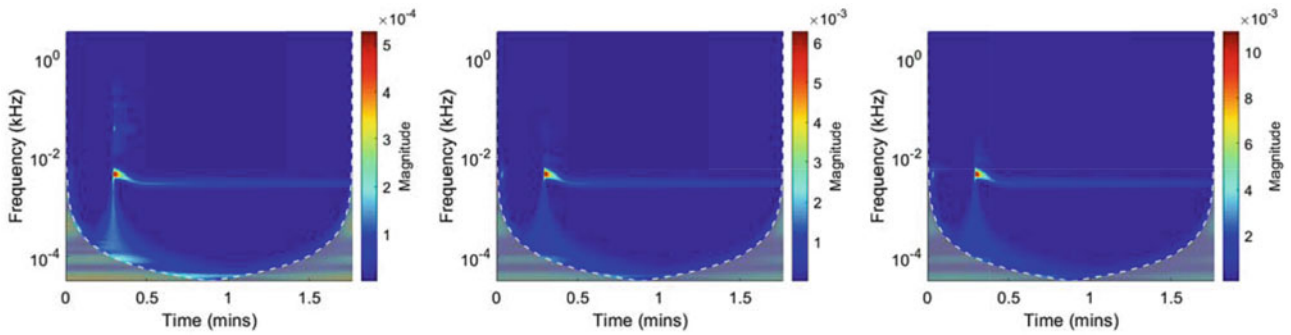


Fig. 38.5 Time-frequency analysis of the measured points: node 1 (left), node 2 (middle) and node 3 (right)

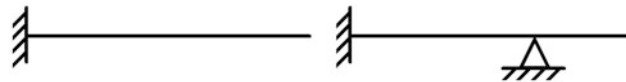


Fig. 38.6 Discrete levels used in the simulation: clamped-free (left) and clamped-pinned (right)

Table 38.2 Natural frequencies of each level

Mode	Clamped-free (Hz)	Clamped-pinned (Hz)	Description
1	3.99	14.43	First bending xz
2	37.00	85.56	Second bending xz
3	108.09	228.10	Third bending xz
4	205.29	287.90	Fourth bending xz

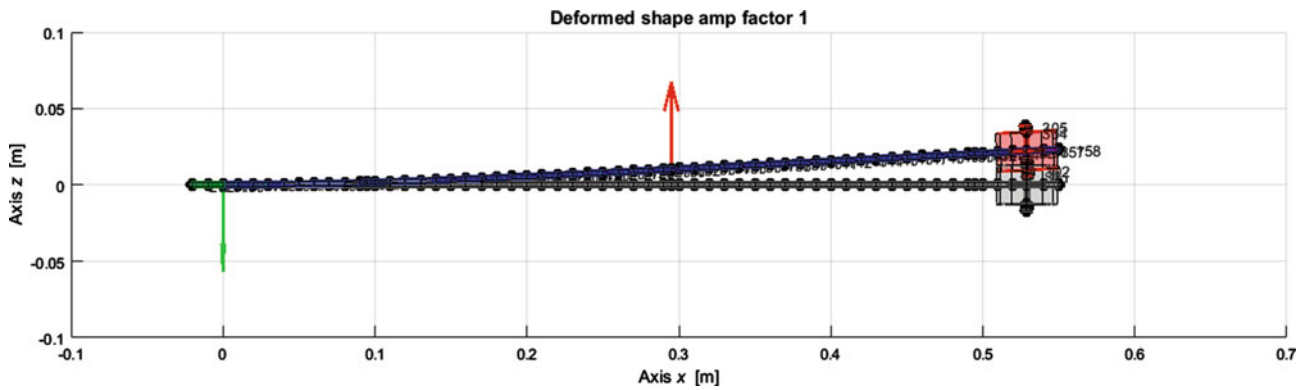


Fig. 38.7 Imposed non-null initial condition in the numerical model (undeformed state is overlapped in transparency)

The comparison of the free vibrations in terms of displacement for the three measured points is shown in Figs. 38.8, 38.9, and 38.10.

The time span in which the system is in the “free–free” level have white background, while the grey background indicates a contact condition between the beam and the support constraint.

The behaviour of node 1 in Fig. 38.8 is well predicted by the simulations. Both low frequency oscillations and high frequency excitations compare very well. The high frequency oscillations of the measured data have larger amplitude. This difference can be related to the non-ideal behaviour, with some degree of flexibility, of the constraint, with respect to the perfectly fixed boundary condition of the model. The initial condition of this point is significantly less than the experimental one, this is another prove of the non-perfectly rigid constraint that influence more the closest analysed point.

The comparison of the contact point displacement in Fig. 38.9 is much more interesting. The displacement is bounded in the lower part to the gap value in both the experimental and numerical simulation. The duration of the contact is very well predicted from the numerical method, even if it is visible a small flexibility of the experimental constraint that is not taken into account in the model. The time domain behaviour is very well predicted from the simulation, except the change of frequency of the experimental result already discussed for Fig. 38.5. It is very interesting to observe that both lower and

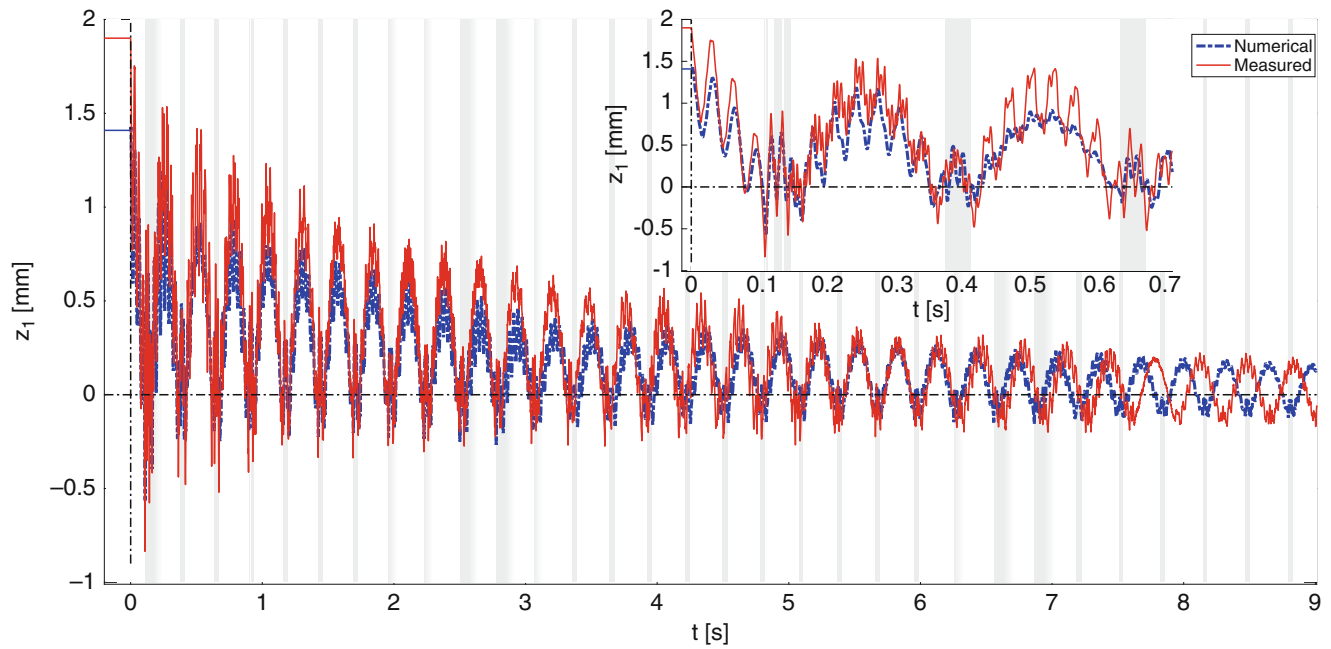


Fig. 38.8 Displacement of node 1: comparison between experimental data and numerical prediction

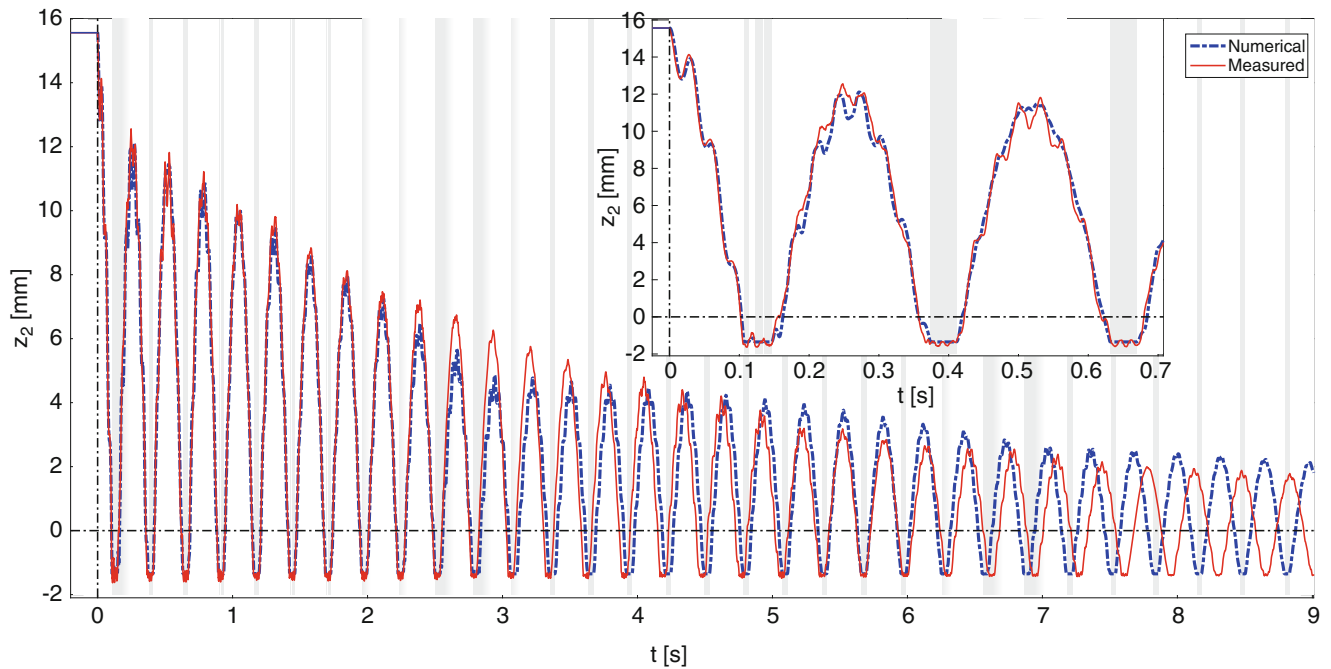


Fig. 38.9 Displacement of node 2: comparison between experimental data and numerical prediction

higher frequency and amplitude of oscillations are almost coincident between experimental and numerical result. Moreover, the behaviour of the system during the first contact is really surprising: some oscillations can be seen in the experimental curves, with bouncing of the beam on the support; the same behaviour is also numerically found, with the beam that loss the contact with the support two times inside the first contact in correspondence of the experimental bouncing.

In Fig. 38.10 the experimental measured data of the beam tip are compared with the numerical ones. This point is useful to understand the excited natural frequency of this system. The numerical initial condition in this case is really close to the experimental one. Also in this case the simulation results are almost coincident with the experimental one, except the phase

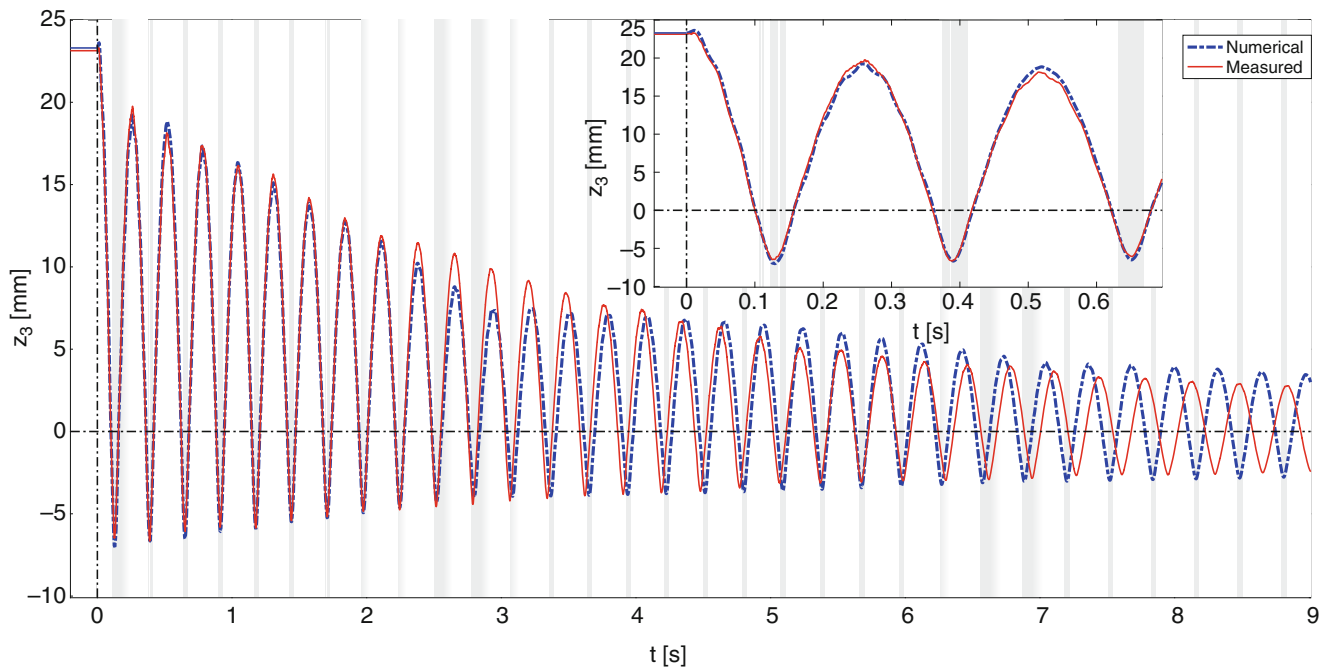


Fig. 38.10 Displacement of node 3: comparison between experimental data and numerical prediction

shift starting from 6 s. The detailed view on the first oscillations gives an idea of the level of accuracy of the simulation, which is very high.

38.5 Conclusion

The Multi-Phi method has been successfully applied to a non-smooth nonlinear system to predict the response in time domain. The basic theory of the method is evident: it lets to reduce the computational cost of a non-linear system integration by using only linearised discrete levels of the considered nonlinear system. The method has been valued against experimental results of the free vibrations of a laboratory test-rig. The predicted time domain displacements agree very well with the measured ones, even if the model could be substantially improved. Some aspects requires further investigations, in particular the flexibility of the clamp. Moreover support constraints are not actually considered and the hardening effect of the experimental system when the amplitude of oscillation is larger should be deeper investigated and eventually included in the numerical model.

References

1. Besselink, B., Tabak, U., Lutowska, A., van de Wouw, N., Nijmeijer, H., Rixen, D.J., Hochstenbach, M.E., Schilders, W.H.A.: A comparison of model reduction techniques from structural dynamics, numerical mathematics and systems and control. *J. Sound Vib.* **332**, 4403–4422 (2013)
2. Aizad, T., Maganga, O., Sumislawska, M., Burnham, K.J.: A comparative study of model-based and data-based model order reduction techniques for nonlinear systems. *Progr. Syst. Eng.* **330**, 83–88 (2014)
3. Géradin, M., Rixen, D.: *Mechanical Vibrations: Theory and Application to Structural Dynamics*, 2nd edn. John Wiley & Sons, West Sussex, UK (1997)
4. Rixen, D.J.: High order static correction modes for component mode synthesis. In: *Proceedings of the 5th World Congress on Computational Mechanics*, Vienna, Austria (2002)
5. Hurty, W.C.: Dynamic analysis of structural systems using component modes. *AIAA J.* **3**(4), 678–685 (1965)
6. Craig Jr., R.R., Bampton, M.C.C.: Coupling of substructures for dynamic analyses. *AIAA J.* **6**(7), 1313–1319 (1968)
7. Moore, B.C.: Principal component analysis in linear systems—controllability, observability and model reduction. *IEEE Trans. Automat. Contr.* **26**(1), 17–32 (1981)

8. Glover, K.: All optimal Hankel-norm approximations of linear multivariable systems and their L_∞ -error bounds. *Int. J. Contr.* **39**(6), 1115–1193 (1984)
9. Pillage, L.T., Rohrer, R.A.: Asymptotic waveform evaluation for timing analysis. *IEEE Trans. Comput. Aid. Design Integrated Circuits and Systems.* **9**(4), 352–366 (1990)
10. Feldmann, P., Freund, R.W.: Efficient linear circuit analysis by Padé approximation via the Lanczos process. *IEEE Transactions on Computer-Aided Design of Integrated Circuits and Systems.* **14**(5), 639–649 (1995)
11. E. Grimme: Krylov projection methods for model reduction. PhD Thesis, University of Illinois at Urbana-Champaign, USA (1997)
12. Kerschen, G., Golinval, J.C., Vakakis, A.F., Bergman, L.A.: The method of proper orthogonal decomposition for dynamical characterization and order reduction of mechanical systems: an overview. *Nonlinear Dyn.* **41**(1), 147–169 (2005)
13. Liang, Y.C., Lee, H.P., Lim, S.P., Lin, W.Z., Lee, K.H., Wu, C.G.: Proper orthogonal decomposition and its applications - Part I: theory. *J. Sound Vib.* **252**(3), 527–544 (2002)
14. Kerschen, G., Peeters, M., Golinval, J.C., Vakakis, A.F.: Nonlinear normal modes, part I: a useful framework for the structural dynamicist. *Mech. Syst. Signal Process.* **23**, 170–194 (2009)
15. Amabili, M.: Reduced-order models for nonlinear vibrations, based on natural modes: the case of the circular cylindrical shell. *Philos. Trans. Roy. Soc. A.* **371**, 1993 (2013)
16. Bond, B.N., Daniel, L.: A piecewise-linear moment-matching approach to parameterized model-order reduction for highly nonlinear systems. *IEEE Transactions on Computer-Aided Design of Integrated Circuits and Systems.* **26**(12), 2116–2129 (2007)
17. Rewieński, M., White, J.: A trajectory piecewise-linear approach to model order reduction and fast simulation of nonlinear circuits and micro-machined devices. *IEEE Transactions on Computer-Aided Design of Integrated Circuits and Systems.* **22**(2), 155–170 (2003)
18. Rewieński, M., White, J.: Model order reduction for nonlinear dynamical systems based on trajectory piecewise-linear approximations. *Linear Algebra Appl.* **415**, 426–454 (2006)
19. Brüls, O., Duysinx, P., Golinval, J.C.: The global parametrization for non-linear model-order reduction in flexible multibody dynamics. *Int. J. Numer. Meth. Eng.* **69**, 948–977 (2007)
20. Naets, F., Tamarozzi, T., Heirman, G.H.K., Desmet, W.: Real-time flexible multibody simulation with global modal parametrization. *Multibody Syst. Dyn.* **27**, 267–284 (2012)
21. Géraudin, M., Rixen, D.J.: A nodeless dual superelement formulation for structural and multibody dynamics application to reduction of contact problems. *Int. J. Numer. Meth. Eng.* **106**, 773–798 (2016)
22. Witteveen, W., Pichler, F.: Efficient model order reduction for the dynamics of nonlinear multilayer sheet structures with trial vector derivatives. *Shock Vib.* **2014**, 1–16 (2014)
23. Witteveen, W., Pichler, F.: Efficient Model Order Reduction for the Nonlinear Dynamics of Jointed Structures by the Use of Trial Vector Derivatives, pp. 1–8. IMAC, Orlando, FL (2014)
24. Starc, B., Čepon, G., Boltežar, M.: A mixed-contact formulation for a dynamics simulation of flexible systems: An integration with model-reduction techniques. *J. Sound Vib.* **393**, 145–156 (2017)
25. Bonisoli, E., Scapolan, M.: A Proposal of Multi-Dimensional Modal Reduction for Nonlinear Dynamic Simulations, pp. 1–8. IMAC 2017, Garden Grove, CA (2017)
26. Bonisoli, E., Scapolan, M.: Dynamic simulations of nonlinear systems using piecewise linear modeshapes. In: International Conference on Structural Engineering Dynamics, Ericeira, Portugal, pp. 1–11 (2017)
27. Mallat, S.: A Wavelet Tour of Signal Processing, pp. 205–432. Academic Press, Burlington, MA (2009)



Chapter 39

Dynamic Behavior and Output Charge Analysis of a Bistable Clamped-Ends Energy Harvester

Masoud Derakhshani and Thomas A. Berfield

Abstract Vibration energy harvesting systems are an excellent power source alternative to batteries or other green energy alternatives, given that many application environments feature vibration sources significant enough for power scavenging. The most important challenge faced by these types of energy harvesters is their general operating inefficiency when driven by the chaotic, low frequency vibration sources characteristic of most real-life scenarios. Prediction of power for these systems requires a detailed understanding of their performance under dynamic conditions. In this study, an analytical method is applied to dynamically analyze the output electrical charge of a piezoelectric-based bistable energy harvester under harmonic excitation. This system is made of a clamped-clamped buckled beam with attached piezo patches and a lump mass at the center. The bistability is created by a compressive load applied at the beam ends. In order to appropriately analyze the dynamic behavior of the structure, the beam is divided into two components in a way that the dynamic effect of the tip mass appears in the boundary conditions as a matching relation between two parts. First, natural frequencies and mode shapes of the system are found by theoretically solving the free undamped linear system. These obtained mode shapes are then used in a Galerkin approach to discretize the nonlinear equations of the buckled structure. By solving the nonlinear equations, Poincare' plot and output electrical charge for a buckled case under three different exciting frequencies are investigated to analyze the performance of the bistable energy harvester.

Keywords Vibration energy harvesting · Nonlinear dynamics · Piezoelectricity · Output charge · Bistability

39.1 Introduction and Model Description

Systems with the capability of harvesting ambient vibrational sources have been studied for several years [1, 2]. As shown previously in the literature, linear structures usually fail to fulfill the practical needs for energy harvesters due to their narrow frequency bandwidth and local vibrational motion for low input energy density, which in turn results in low efficiency [3, 4]. In order to address these issues, nonlinear structures with the ability to create snap-through motion have been considered as an alternative to linear systems [5–9]. A compressive buckled beam is a typical structure for such purpose which dynamic behavior has been heavily investigated by researchers in this area [10–12]. One of the common issues of buckled beam energy harvesters is their relatively high natural frequencies for small-scale systems. Adding concentrated mass to such a buckled structure significantly decreases the first natural frequency and consequently paves the way for having bistable motion at lower frequency range.

In most of the previous studies on the piezoelectric-based bistable beam energy harvesters, they have been simplified to a single degree of freedom vibrational system with the equivalent mass, stiffness, and damping coefficients. While such simplification could deliver a good estimation of the dynamic behavior of these systems, having a more accurate analysis of the dynamic behavior and possible output power of such devices would definitely lead to better understanding of their performance under various exciting situations. In this study, the dynamic analysis of a clamped-clamped buckled beam with a tip mass in the middle is theoretically being reviewed. A schematic view of this system is shown in Fig. 39.1. A unimorph setup with a piezoelectric layer attached to the top surface of the buckled beam is considered for this system. The buckling is created via a compressive load applied at the ends of the beam and the whole structure is subjected to a transversal harmonic base excitation. The parametric dimensions considered for this study are depicted in Fig. 39.1.

M. Derakhshani (✉) · T. A. Berfield
University of Louisville, Louisville, KY, USA
e-mail: masoud.derakhshani@louisville.edu

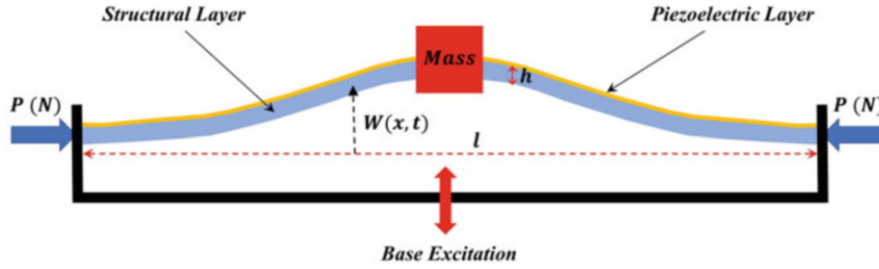


Fig. 39.1 Schematic view of the piezoelectric bisable energy harvester with an attached tip mass in the middle

To accurately model the described nonlinear system, the buckled beam is divided into two individual parts, so the effect of the concentrated mass can be considered as the boundary condition in the dynamic model. For each part, the nonlinear equation has been derived based on Euler-Bernoulli beam theory as:

$$\bar{m} \frac{\partial^2 W_1}{\partial t^2} + EI_y \frac{\partial^4 W_1}{\partial x^4} + P \frac{\partial^2 W_1}{\partial x^2} + C \frac{\partial W_1}{\partial t} - \frac{EA}{L} \frac{\partial^2 W_1}{\partial x^2} \left[\int_0^{L/2} \left(\frac{\partial W_1}{\partial x} \right)^2 dx \right] = -\bar{m} \ddot{W}_B \quad (39.1)$$

$$\bar{m} \frac{\partial^2 W_2}{\partial t^2} + EI_y \frac{\partial^4 W_2}{\partial x^4} + P \frac{\partial^2 W_2}{\partial x^2} + C \frac{\partial W_2}{\partial t} - \frac{EA}{L} \frac{\partial^2 W_2}{\partial x^2} \left[\int_{\frac{L}{2}}^L \left(\frac{\partial W_2}{\partial x} \right)^2 dx \right] = -\bar{m} \ddot{W}_B \quad (39.2)$$

where W_i ($i = 1, 2$) is the lateral deflection of the beam and W_B is the base excitation. Considering the fact that the thickness of the piezoelectric layer is very thin compared to the structural layer, its dynamic behavior is neglected in the model. To solve such a nonlinear system, Galerkin's method is chosen to discretize the nonlinear equations, for which a set of known spatial shape functions are required. These functions can be developed by solving the free vibration of the undamped linear system, in which all the damping, nonlinear, and external forcing terms are neglected. By shaping such functions, the following presumed solution can be written for each part of the beam:

$$W_i^j = \sum_{i=1}^N \psi_i^j(x) q_i^j(t) ; \quad (j = 1, 2) \quad (39.3)$$

where ψ_i and q_i are the linear shape function and the unknown generalized coordinate for mode i respectively. Applying Galerkin's discretization process, a set of nonlinear ordinary differential equations (ODE's) for each part of the beam is developed. Considering the matching conditions existing at the location of the concentrated mass, the coupling process of these obtained ODE's could be performed as described in [13], which yields the final form of the nonlinear equations as:

$$[M] \ddot{\underline{q}} + [C] \dot{\underline{q}} + [K] \underline{q} + \underline{f_{NT}} = \underline{F} \quad (39.4)$$

where $[M]$, $[C]$, and $[K]$ are the mass, damping, stiffness matrices respectively, $\underline{f_{NT}}$ is the vector of nonlinear terms, and \underline{F} is the external force vector for the coupled structure. Solving nonlinear Eq. (39.4) using Runge–Kutta numerical algorithm would deliver the vertical deflection of the beam under the harmonic excitation.

To estimate the electrical charge produced by the thin layer of piezoelectric attached to the top surface of the beam, the constitutional piezoelectric equation for the described arrangement in Fig. 39.1 can be written as:

$$D_z = d_{31} \sigma_{xx} + \epsilon_{33}^T E_z \quad (39.5)$$

where d_{31} is the coupling coefficient of the piezoelectric material, σ_{xx} is the longitudinal stress, ϵ_{33} is the electrical permittivity, and E_z is the electrical field across the device. By considering the short-circuit configuration (zero external resistance), the following relation is obtained for the output electrical charge of the studied bistable energy harvester:

$$Q(t) = bd_{31}E \left(\int_0^{\frac{L}{2}} \epsilon_{xx}^1 dx + \int_{\frac{L}{2}}^L \epsilon_{xx}^2 dx \right) \quad (39.6)$$

where ϵ_{xx} , and Q are the mechanical strain at the topside of the beam, and the output electrical charge of the piezoelectric layer due to mechanical deformation. Note that the mechanical strain shown in Eq. (39.6) could be found from the nonlinear Euler-Bernoulli beam relation between the strain and vertical deflection for each part individually.

39.2 Results and Discussion

The results of the Poincare plot and output electrical charge for the described system in Fig. 39.1 are developed under three different excitation frequencies. Table 39.1 shows the parameters of the model considered for developing such results. Acrylonitrile butadiene styrene (ABS) and lead zirconate titanate (PZT-5A) are considered as the structural and piezoelectric material respectively [14] and the compressive load is selected just above the critical buckling load ensuring a moderately buckled bistable system with a small base exciting amplitude ($B = 0.1$ mm).

As can be seen from Figs. 39.2, 39.3, and 39.4, the amplitude of the electrical charge captured for both 20 and 150 Hz excitations (Figs. 39.2 and 39.4) are pretty small due to the local vibration of the buckled beam around one of its stable states. However, the amplitude of the electrical charge obtained for the 50 Hz excitation (Fig. 39.3) is noticeably higher compared to the other two exciting situations. This difference occurs as a result of snap-through motion created in the beam

Table 39.1 The parameters of the studied bistable energy harvester used for the modeling results

Parameters	Beam length (mm)	Beam width (mm)	Beam thickness (mm)	Tip mass (g)	Young's Modulus (GPa)	PZT thickness (μm)
Values	100	10	2	50	2.3	10

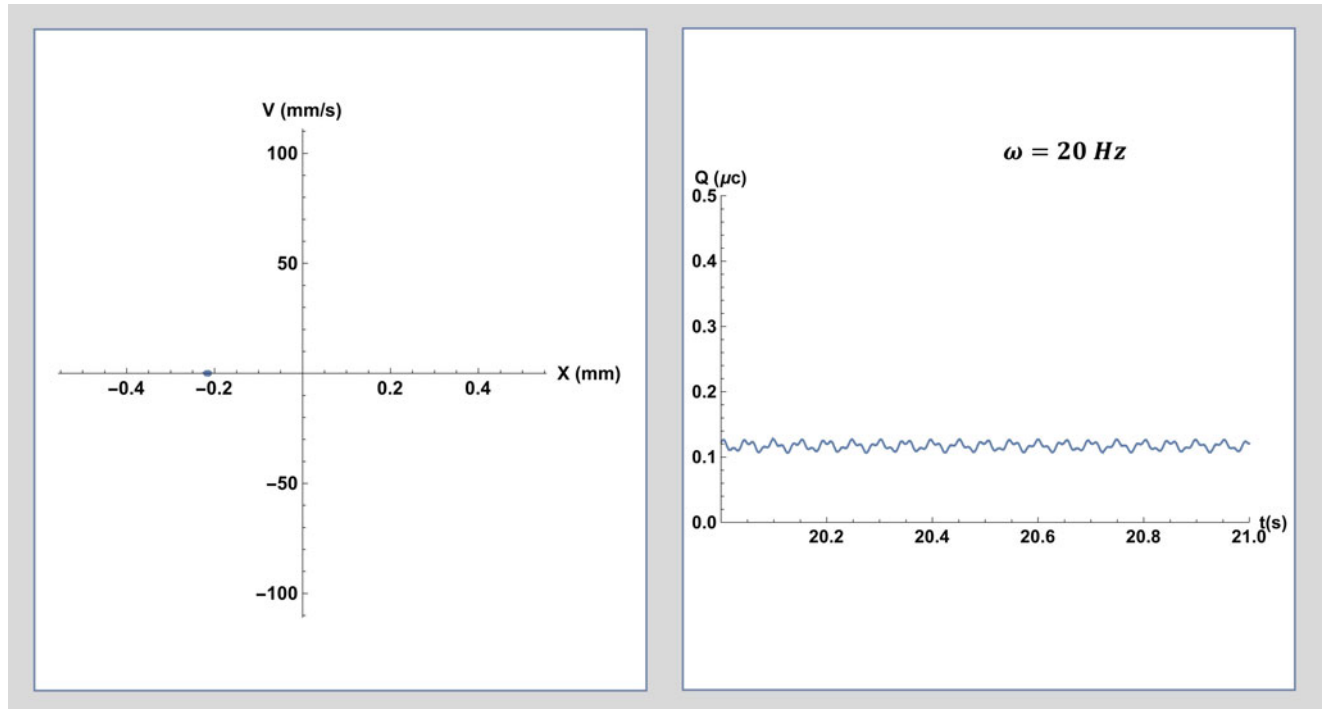


Fig. 39.2 Poincare plot and output electrical charge of the bistable system under 20 Hz excitation

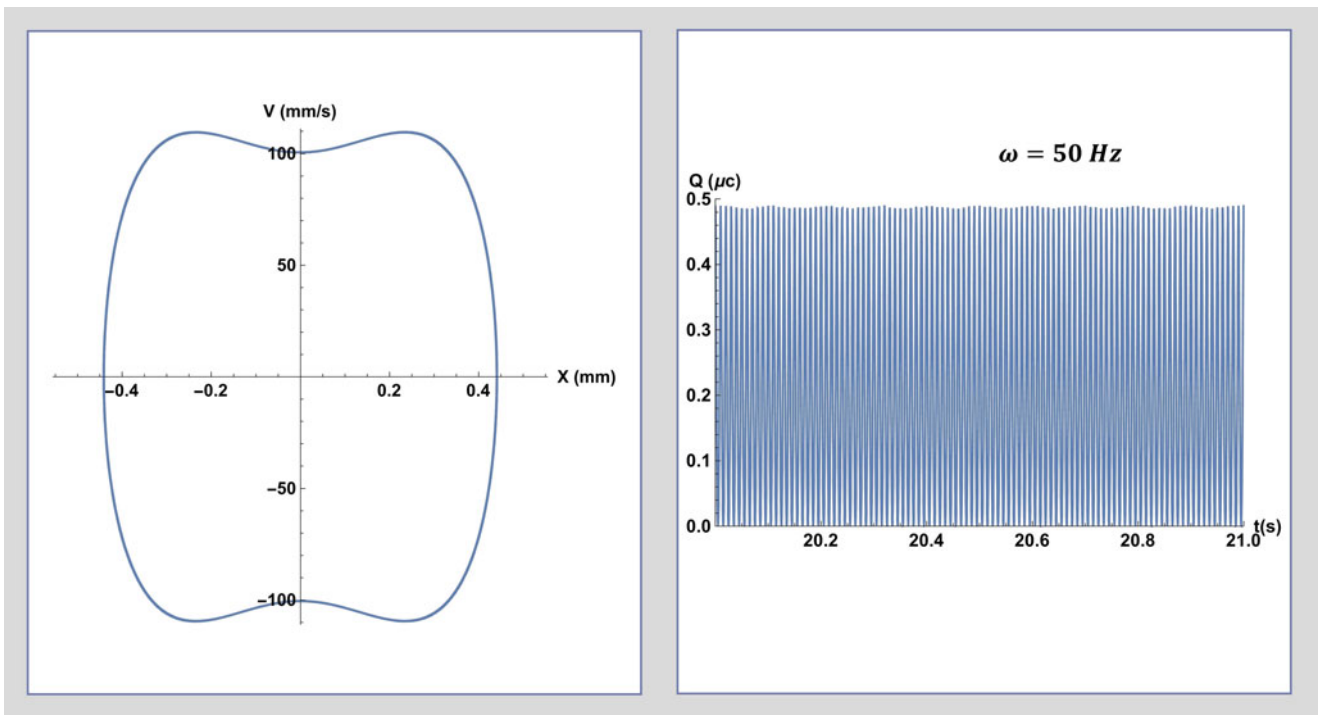


Fig. 39.3 Poincaré plot and output electrical charge of the bistable system under 50 Hz excitation

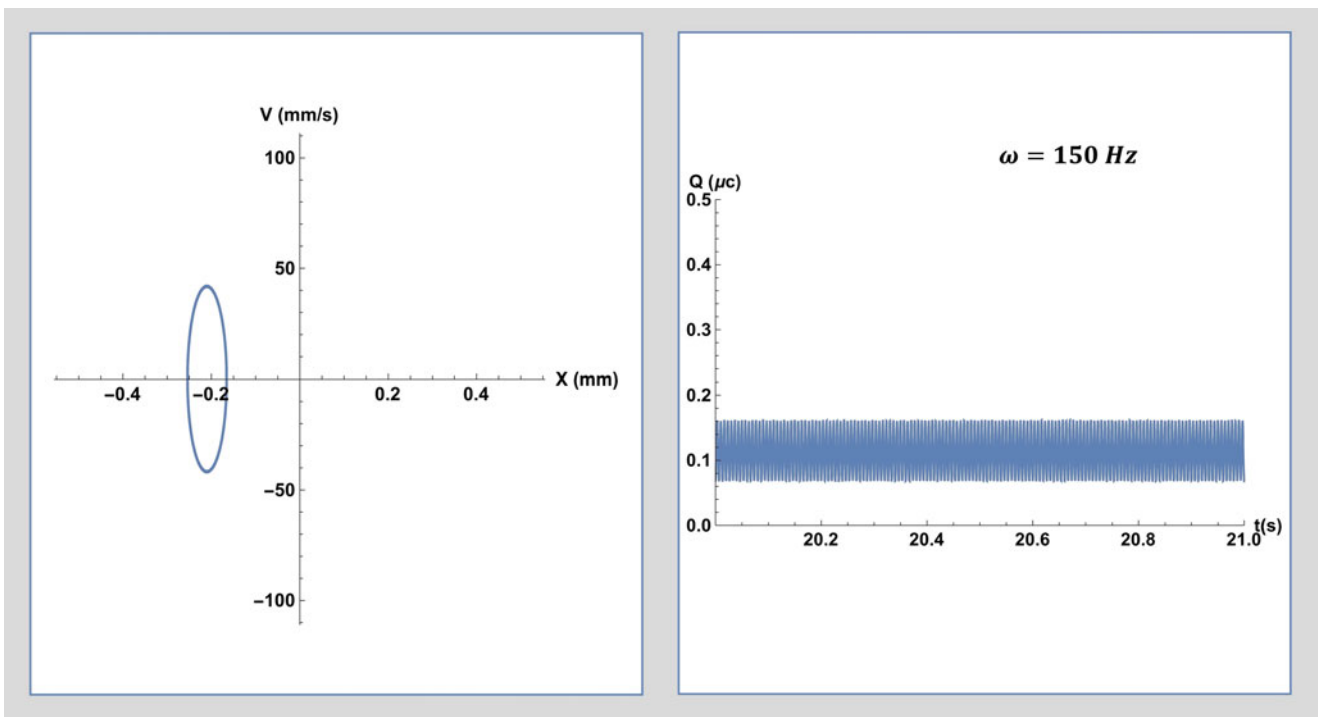


Fig. 39.4 Poincaré plot and output electrical charge of the bistable system under 150 Hz excitation

at around the first natural frequency obtained from solving the free vibration of the undamped linear system (first natural frequency of the described model is obtained as $\omega_n = 38.3242$ Hz). This indicates the significance of the concentrated mass added to the buckled beam to work as a low-frequency bistable energy harvester. Note that the compressive load applied to the system shifts the maximum amplitude toward the higher frequencies in the amplitude-frequency response due to the hardening behavior of the nonlinear structure.

39.3 Conclusion

The importance of snap-through motion in the efficiency of the vibration energy harvesters has been reviewed in this study by accurately modeling a nonlinear bistable structure suitable for low operating frequency range. It has been shown that dividing the bistable structure into its components with the possibility of considering the dynamic effect of the concentrated mass as a boundary condition could lead to a more accurate model of the studied nonlinear system. Furthermore, adding more inertia to a bistable structure could result in better performance as an energy harvester under low-frequency exciting conditions.

References

1. Kim, H.S., Kim, J.-H., Kim, J.: A review of piezoelectric energy harvesting based on vibration. *Int. J. Prec. Eng. Manuf.* **12**(6), 1129–1141 (2011)
2. Harn, R.L., Wang, K.W.: A review of the recent research on vibration energy harvesting via bistable systems. *Smart Mater. Struct.* **22**, 023001 (2013)
3. Cottone, F., Gammaitoni, L., Vocca, H., Ferrari, M., Ferrari, V.: Piezoelectric buckled beams for random vibration energy harvesting. *Smart Mater. Struct.* **21**, 035021 (2012)
4. Vocca, H., Cottone, F., Neri, I., Gammaitoni, L.: A comparison between nonlinear cantilever and buckled beam for energy harvesting. *Eur. Phys. J. Special Topics.* **222**, 1699–1705 (2013)
5. Cottone, F., et al.: Bistable electromagnetic generator based on buckled beams for vibration energy harvesting. *J. Intell. Mater. Syst. Struct.* **25**(12), 1484–1495 (2014)
6. Derakhshani, M., Allgeier, B.E., Berfield, T.A.: Study on the fabrication process of a MEMS bistable energy harvester based on coupled component structures. In: Grady, M., et al. (eds.) *Mechanics of Biological Systems & Micro-and Nanomechanics*, vol. 4, pp. 75–79. Springer, Cham (2019)
7. Pellegrini, S.P., et al.: Bistable vibration energy harvesters: a review. *J. Intell. Mater. Syst. Struct.* **24**(11), 1303–1312 (2013)
8. Navabi, M., Mirzaei, H.: θ -D based nonlinear tracking control of quadcopter. In 2016 4th International Conference on Robotics and Mechatronics (ICROM). IEEE (2016)
9. Samuel, C., Stanton, C.C.M., Mann, B.P.: Nonlinear dynamics for broadband energy harvesting: Investigation of a bistable piezoelectric inertial generator. *Physica D.* **239**, 640–653 (2010)
10. Emam, S.A., Nayfeh, A.H.: Nonlinear responses of buckled beams to subharmonic-resonance excitations. *Nonlinear Dyn.* **35**(2), 105–122 (2004)
11. Ghayesh, M.H., Amabili, M., Farokhi, H.: Global dynamics of an axially moving buckled beam. *J. Vib. Control.* **21**(1), 195–208 (2015)
12. Emam, S.A., Nayfeh, A.H.: On the nonlinear dynamics of a buckled beam subjected to a primary-resonance excitation. *Nonlinear Dyn.* **35**, 1–17 (2004)
13. Derakhshani, M., Berfield, T., Murphy, K.D.: Dynamic analysis of a bi-stable buckled structure for vibration energy harvester. In: *Dynamic Behavior of Materials*, vol. 1, pp. 199–208. Springer, Cham (2018)
14. Butt, Z., et al.: Generation of electrical energy using lead zirconate titanate (PZT-5A) piezoelectric material: analytical, numerical and experimental verifications. *J. Mech. Sci. Technol.* **30**(8), 3553–3558 (2016)